IMDC

Proceedings of the papers submitted to the
2020 TELEMAC-MASCARET
User Conference

October 2021

TUC 2020

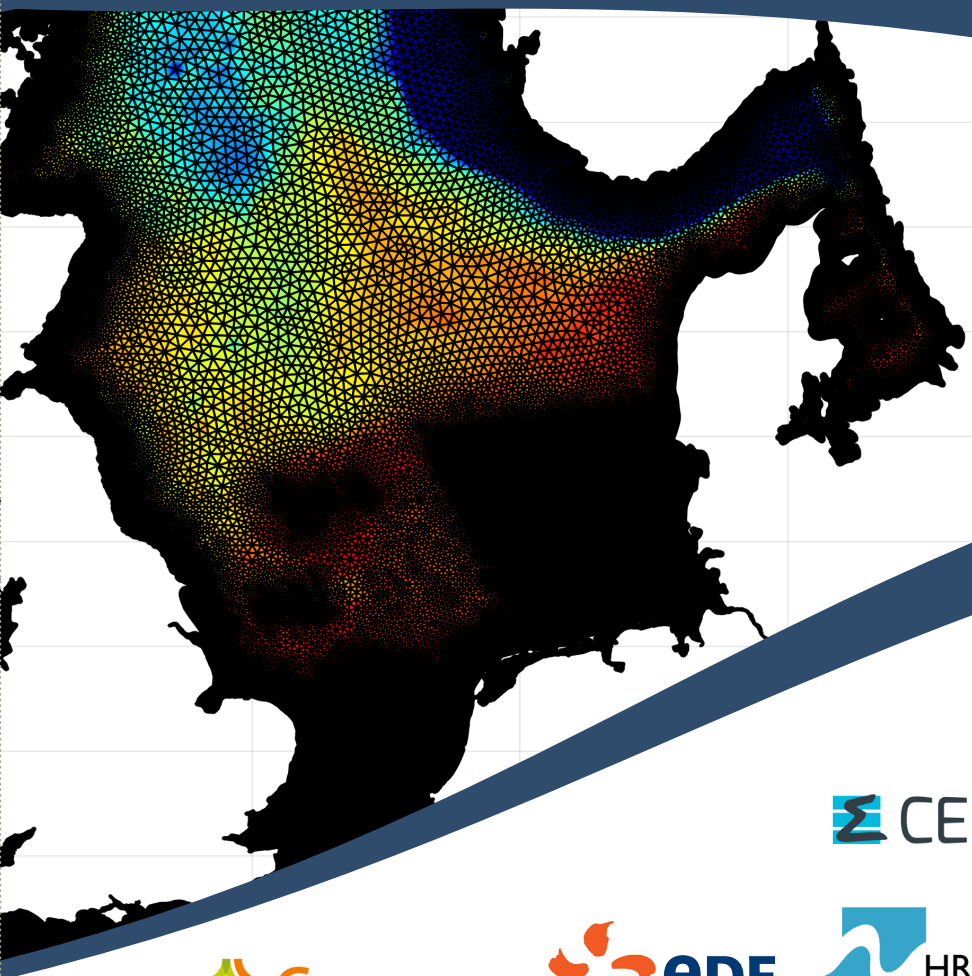

ARTELIA

CERFACS

Science & Technology Facilities Council

Cerema

eDF

HR Wallingford
Working with water

BAW
Bundesanstalt für Wasserbau

Proceedings of the papers submitted to the
2020 TELEMAC-MASCARET (2021)
User Conference

Organized by

International Marine & Dredging Consultants (IMDC)
Van Immerseelstraat 66
2100 Antwerp
Belgium
Tel: +32 3 270 92 95
tuc2020@imdc.be
https://tuc2020.org/

Edited by

W.A. Breugem
L Frederickx
T Koutrouveli
R Kulkarni
K Chu
B Decrop

Design

L Frederickx

Published by

ISBN 9789464447842

TELEMAC-MASCARET Core Group

Artelia

www.arteliagroup.com

Bundesanstalt für Wasserbau

Federal Waterways Engineering and Research Institute
www.baw.com

Centre d'études et d'expertise sur les risques, l'environment, la mobilité et l'amenagement

www.cerema.fr

Centre Européen de Recherche et de Formation Avancée en Calcul Scientifique

www.cerfacs.fr

Électricité de France

www.edf.com

HR Wallingford

www.hrwallingford.com

Science and Technology Facilities Council

www.stfc.ac.uk

Introduction by the organizing committee

October 2021

Dear TUC2020 delegates,

It is a great pleasure to welcome you at the TELEMAC/MASCARET User Conference 2020. The COVID-19 pandemic hit the world from 2019 on, sadly taking the lives of many people, and changing the lives of most other people on the planet, in a way we had not held possible before. Nevertheless, we had good hopes that a TELEMAC/MASCARET User Conference would be possible in 2020, but after the second wave of COVID-19 started in August 2020, it became clear that our hopes had been idle and that the TUC 2020 had to be postponed. Instead the TELEMAC webinar was organized, which was attended by more than 200 online participants from all over the world.

Meanwhile, successful vaccination campaigns against COVID-19 were started, leading to a gradual return to normal live. This made it possible that the TELEMAC/MASCARET User Conference 2020 can finally take place in October 2021. Nevertheless, travel limitations remain in place in many countries in the world. Therefore, for the first time in the history of the TUC, it is organized in hybrid form, with both participants on site in Antwerp as well as participating online in various countries around the world.

It was a privilege to organize this TUC, and in this way witness the latest developments in varying and interesting applications in which TELEMAC and MASCARET are used. These proceedings show that the TELEMAC community, despite the difficult times we have had, is very much alive.

This conference would not have been possible without the help from many people, which we would like to thank hereby. First of all we thank EDF, who have prepared two very interesting subjects for the workshop. We further thank everybody who submitted a paper to the conference. Without their contribution, the conference would not have been possible. We are also very grateful to all anonymous reviewers, who used their expertise in order to review all the submitted papers. Finally, we sincerely thank our colleagues at IMDC who helped us out in specific areas such as IT and finance.

The organizing committee of TUC 2020 (held in 2021),

Alexander Breugem
Theofano Koutrouveli
Lesley Frederickx
Kai Chu
Rohit Kulkarni
Boudewijn Decrop

Contents

Hydrodynamics and Hydrology

Sediment II and Numerical Methods

Water Quality

Vegetation

Influence of uncertainties of vegetation parameters in a 2D model

Frederik Folke, Rebekka Kopmann
Dept. of Hydraulic Engineering
Federal Waterways Engineering and Research Institute (BAW)
Karlsruhe, Germany
frederik.folke@baw.de

Amelie Hohnschop
Faculty of Architecture and Civil Engineering
Karlsruhe University of Applied Science
Karlsruhe, Germany

***Abstract*— The impact of terrestrial vegetation is becoming more important in federal German waterways for flood control and for a natural design of inland waterways. For estimating the hydraulic resistance of submerged and non-submerged vegetation, several vegetation approaches are available in Telemac-2D. The vegetation is characterized by selected parameters which serve as input parameters for the vegetation approaches. Hence, uncertainties in the modelling of roughness caused by vegetation results from both the natural variability of vegetation and the vegetation approaches themselves. In this paper, the interdependencies of relevant vegetation parameters and their mathematical description by allometric relations are analysed, deriving an interdependency between hydrodynamic density and stem diameter. The uncertainties of the vegetation parameters resulting from the natural range of variation are determined by allometric relations and by a literature review. By means of an uncertainty analysis using a 2D hydro-numerical model of a straight compound channel, it is apparent that the uncertainties of the vegetation parameters outweigh the uncertainties of the vegetation approaches.**

I. INTRODUCTION

Floodplain and riparian vegetation have a large impact on the flow field and morphological processes. In particular, the occurrence of terrestrial vegetation significantly increases the hydraulic resistance. A lot of research has been done on the interaction between flow and vegetation in the last decades. The result of these investigations are several promising approaches for non-submerged and submerged rigid or flexible vegetation. Several of these vegetation models for representing roughness effects have been implemented in TELEMAC-2D [1] and are available to the user in the official release. As input data different vegetation parameters such as vegetation density and height are needed. It should be noted that vegetation parameters can change over time (e.g. height and width growth), but are also subject to seasonal variations (e.g. foliage). In addition, these exhibit natural ranges of variation. However, uncertainties can also arise from the recording of the parameters. Therefore, the question arises what influence the total uncertainties of the vegetation parameters have on the resulting roughness effect of vegetation.

Some of the needed vegetation parameters are interdependent. For example, large trees have greater spacing than small trees and with the growth in height the plants also grow in width. In this paper relevant allometric relations are presented and a statistical description of the variability of individual vegetation parameters, e.g. by mean value and standard deviation or minima and maxima values with a corresponding distribution was derived.

The aim of the work was to evaluate different vegetation models considering the influence of the existing uncertainties of the input parameters. This was achieved by means of an uncertainty analysis with the uncertainty analysis tool Unantopy (Uncertainty Analysis Tool in Python) developed by BAW [2]. An uncertainty analysis can be used to investigate the influence of the variation ranges of the vegetation parameters on the roughness effect of the vegetation approaches. In this framework, the overall uncertainty of the vegetation parameters was analysed in comparison to the uncertainty of the vegetation approaches, but also the influence of the individual parameters.

The dependencies of relevant vegetation parameters on each other were analysed and described mathematically using allometric relationships. Furthermore, the uncertainties of the vegetation parameters were investigated by means of a literature research and allometric relations. This study focusses on natural variability of vegetation parameters. Other uncertainties, e.g. of measurement, were not considered.

II. VEGETATION MODELS AND VEGETATION PARAMETERS

The vegetation types tree and bush are considered in this study. Since the height of trees is usually greater than the flow depth on the floodplains, only non-submerged conditions have to be considered. For bushes both non-submerged and submerged conditions can occur. Furthermore, in this case flexibility of the plants can affect the vegetation-induced hydraulic resistance. Based on this, three categories were defined that are investigated within the framework of the study:

A. Rigid non-submerged tree

It is assumed that the crown is completely above the water level. In this case a simplified assumption of the vegetation elements to rigid cylinders is widely accepted (e.g. [3]). Petryk

and Bosmajian [4](referred to as P&B) introduced a vegetation model for rigid non-submerged vegetation based on the hydrodynamic density mD (unit m^{-1}) and the dimensionless drag coefficient c_D of a single element. The hydrodynamic density is defined as the sum of the projected areas of the vegetation elements divided by the ground surface multiplied by the water depth. For rigid regularly arranged cylinders, it simplifies to

$$mD = \frac{D}{\Delta^2} \quad (1)$$

with the stem diameter D and the spacing Δ between the individual trees. For the drag coefficient [4] indicates that this is approximately 1.0.

Lindner [5] and Pasche and Rouvé [6] (referred to as LIND) developed a method to quantifying the drag coefficient at the reach scale. The method assumes that the drag coefficient of a cylinder in the wake zone depends on the drag coefficient of a single non-submerged cylinder, the resistance due effects of the adjacent cylinders, and the resistance due to the gravity wave. The LIND vegetation model needs as input parameters the stem diameter and the spacing between the vegetation elements.

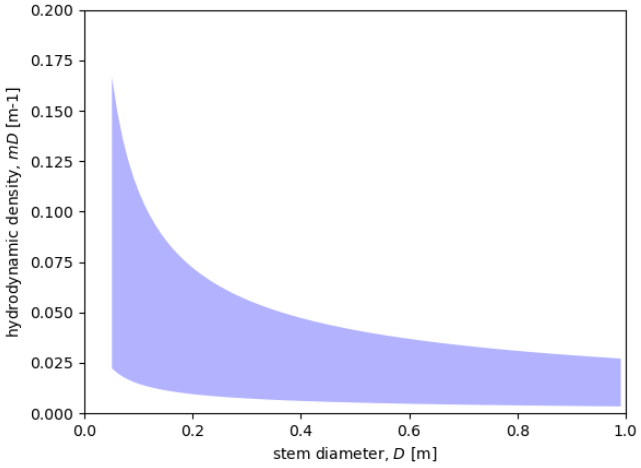

Figure 1: Allometric relation for trees of [7] between stem diameter and hydrodynamic denisty with allometric factor a in the intervall of 11 to 13 referred to [8]

The vegetation parameters stem diameter and spacing are interdependent. For this relation [7] formulated an allometric rule

$$N = e^a \left(\frac{0.25}{D}\right)^{-1.605} \quad (2)$$

with number of stems per hectare N, and breast height diameter D. For the species-specific and site-dependent allometric factor a, [8][8] determined a range of variation from 11 to 13 for stands in southern Germany. Using (1) and (2) a relation between the hydrodynamic density and the stem diameter can be derived for trees. In Fig. 1 the range of values is shown.

B. *Rigid non-submerged and submerged bush*

The roughness effect of bushes can only be adequately represented if a distinction is made between non-submerged and submerged conditions. Furthermore, a simplification of the vegetation elements to rigid cylinders is not valid.

The 2-layer approaches of Baptist et al. [3] (referred to as BAPT), Huthoff et al. [9] (referred to as HUTH) and van Velzen et al. [10] (referred to as VANV) are all based on the vegetation model of P&B and consider the vegetation as rigid. To account for the submerged case also the vegetation height h_p is needed as input parameter. The three models differ with respect to the assumptions for the vertical velocity profile within the free upper layer. Only HUTH needs additional information about spacing between the vegetation elements.

In literature higher values for the hydrodynamic density of bushes can be found compared to trees. E.g. [10] gives values for alluvial softwood forest (trees) from 0.027 m^{-1}, and for softwood bushes from 0.233 m^{-1} (young) to 0.097 m^{-1} (older) for the hydrodynamic density.

In forestry the focus is on trees. For this study no usable allometric relations for bushes could be found in literature.

C. *Flexible non-submerged and submerged bush*

Depending on the species and degree of foliage, the flexibility of the vegetation can have a significant impact on resistance behaviour. Järvelä [11] (referred to as JAER) introduced a 1-layer approach for flexible just-submerged and submerged vegetation based on the empirical concept of [12]. To account for vegetation density [11] is using the leaf-area index LAI and the vegetation height. Additionally, the species-specific parameters $C_{D\chi}$, χ and u_χ are needed.

Reference [13] extended the JAER approach for non-submerged conditions by assuming a logarithmic velocity distribution in the free layer above analogue BAPT (extended approach referred to as HYBR).

All vegetation models used and the corresponding vegetation parameters are summarized in Tab. 1.

TABLE 1: USED VEGETATION MODELS AND THE CORRESPONDING INPPUT PARAMETERS

Vegetation model	Approach	Parameters
P&B [4]	1-layer, rigid	C_D, mD
LIND [5], [6]	1-layer, rigid	Δ, D
BAPT [3]	2-layer, rigid	C_D, mD, h_p
HUTH [9]	2-layer, rigid	C_D, mD, Δ, h_p
VANV [10]	2-layer, rigid	C_D, mD, h_p
JAER [11]	1-layer, flexible	$C_{D\chi}$, χ, u_χ, LAI, h_p
HYBR [13]	2-layer, flexible	$C_{D\chi}$, χ, u_χ, LAI, h_p

III. NUMERICAL MODEL

In this study a TELEMAC-2D model of a straight compound channel was used. The cross-section had a total width of 300 m and was composed of a 60 m wide main channel, a 60 m wide bank with a slope of 1:10, and a 180 m wide vegetated floodplain as shown in Fig. 2. The total

channel length was 3600 m with a slope in streamwise direction of 0.5 ‰.

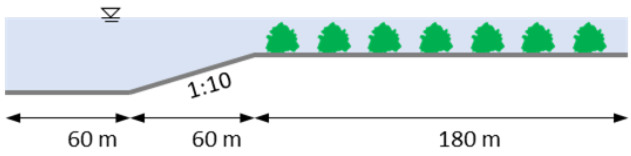

Figure 2: Cross-section of investigated compound channel

The bottom roughness was modelled using the Nikuradse roughness law. The equivalent sand roughness k_s of the main channel and the bank were set to 0.15 m, and of the floodplain to 0.10 m.

To consider the additional resistance caused by vegetation the principle of linear superposition is used. Thus, the total friction λ is the sum of the bed roughness coefficient λ' and the vegetation form resistance per unit surface λ''. In this study the vegetation on the floodplain is assumed to be uniform.

Three different flow events were investigated with flow depth on the floodplain (FP) of 1.0 m (h_FP_1m), 3.0 m (h_FP_3m) and 6.0 m (h_FP_6m). Flow depths were selected to both flow through and over brushy vegetation. Trees are always considered as non-submerged. To ensure normal flow conditions the discharges were calibrated using the vegetation P&B with a hydrodynamic density of 0.05 m^{-1} and a drag coefficient of 1.0. The boundary conditions are summarized in Tab. 2.

TABLE 2: BOUNDARY CONDITIONS

Event	Q_{inlet}	$h_{outlet,main}$	$h_{outlet,FP}$
h_FP_1m	1600 m³/s	7 m	1 m
h_FP_3m	2750 m³/s	9 m	3 m
h_FP_6m	4250 m³/s	12 m	6 m

All simulations were carried out with the open-source code TELEMAC-2D (v8p0r2) using the horizontal mixing length turbulence model. The total number of elements of the computational grid is 12798 and the average node distance is around 14 m.

IV. UNCERTAINTY ANALYSES

To investigate the effect of the uncertainties of the vegetation parameters on the hydraulic parameters water level and discharge distribution an uncertainty analysis was carried out. For this, the tool Unantopy (Uncertainty Analysis Tool in Python) developed at BAW [2] was used. The unique feature of this study is that the investigation was conducted with nature-based vegetation parameters.

As a first step all vegetation parameters used in the investigated vegetation laws (see Table 1) were assumed uncertain. Their natural variability was found in literature. The uncertain parameters need to be independent or the dependencies between them must be known. To ensure statistical independency the allometric relations described before were considered. In general, normal distribution was presumed for all parameters. The impact of uniform distribution was investigated exemplarily. For a statistical description of a normal distribution the mean value μ and the standard deviation σ are needed. For the present study minimal (Min) and maximal (Max) values of the uncertain vegetation parameters were taken from literature. It was assumed that the vegetation parameters are normally distributed. To determine the standard deviation, it was assumed that 99.73 % of all values lie within the min and max values. The mean values and standard deviation were approximated by the following formulas:

$$\mu = \frac{Max+Min}{2} \quad (3)$$

$$\sigma = \frac{Max-Min}{6} \quad (4)$$

In Unantopy three uncertainty quantification methods can be chosen: First-Order-Second-Moment (FOSM) method, Monte-Carlo method (MC) or metamodeling using a non-intrusive polynomial chaos method. For a steady state flow without sediment transport the FOSM method is recommended (e.g. [2], [14]). This method needs only a small number of simulation runs (two for each uncertain parameter plus one for the reference settings) but requires a linear system behaviour in the range of the parameter variability and normal distributed uncertain parameters.

The FOSM method was applied in this study. Exemplarily the assumption of the linear system behaviour was validated exemplarily using MC method.

For the uncertainty analysis the three categories described in Sec. II were used. For the category rigid non-submerged tree, several cases with different stem diameters were considered. The corresponding hydrodynamic densities were derived from the allometric relations. The category rigid non-submerged and submerged bush was subdivided into the two cases, small bush and large bush. To investigate the influence of flexibility only one case was analysed for the category flexible non-submerged and submerged bush.

Tab. 3 summarizes the mean values and the standard deviations of the uncertain vegetation parameters for the 7 cases. Reference velocity u_χ was not varied as it is defined as the lowest velocity used in the experiments to determine the species-specific vegetation parameters and was set constant to 0.1 m/s.

The final step in Unantopy is the statistical evaluation of the simulation runs. Unantopy provides automatically the sensitivity of all uncertain parameters, the probability interval or the failure probability. Further user defined evaluations can be done.

TABLE 3: USED PARAMETERS FOR THE VEGETATION LAWS

		mD	C_D	h_p	LAI	C_{D_χ}	χ
Tree D=0.10 m	μ	0.063 m^{-1}	1.0	-	-	-	-
	σ	0.016 m^{-1}	0.2				
Tree D=0.40 m	μ	0.027 m^{-1}	1.0	-	-	-	-
	σ	0.007 m^{-1}	0.2				
Tree D=0.70 m	μ	0.020 m^{-1}	1.0	-	-	-	-
	σ	0.005 m^{-1}	0.2				
Tree D=1.00 m	μ	0.016 m^{-1}	1.0	-	-	-	-
	σ	0.004 m^{-1}	0.2				
Bush small	μ	0.285 m^{-1}	1.35	1.50 m	-	-	-
	σ	0.062 m^{-1}	0.22	0.17 m			
Bush large	μ	0.224 m^{-1}	1.35	3.50 m	-	-	-
	σ	0.042 m^{-1}	0.22	0.50 m			
Bush flexible	μ	0.284 m^{-1}	1.35	3.00 m	2.45	0.45	-0.08
	σ	0.062 m^{-1}	0.22	0.67 m	0.68	0.12	0.03

V. RESULTS

Within this section the focus is on the resulting water depth on the floodplain. The water depth was evaluated at x=2200 m. Beside the mean value also the deviation within 95 % probability of occurrence was considered. The ratio of the discharge distribution between floodplain and main channel was also evaluated and can be found in [15].

A. *Uncertainty analysis using FOSM*

1) Rigid non-submerged tree: In Fig. 3 the resulting water depths on the floodplain are shown for the category rigid non-submerged tree. The results show a decreasing water depth with increasing stem diameter for all three flow events. This can be explained by the decreasing hydrodynamic density with increasing stem diameter (cf. Fig. 1) which induces decreasing roughness. In addition, it can be seen that the deviation increases with increasing diameter. Overall, the deviations are smaller for event h_FP_1m than for the other two.

The additional variation of the drag coefficient (light blue) to the hydrodynamic density (dark blue) within P&B's model results in an increase in the deviation of water level. The increase in the range of variation is about 12 to 27 %.

Both, mean values and deviations of the water levels of LIND (black) are in good agreement with the values of P&B, but generally show somewhat larger values. For all flow depths, the C_D value of LIND for stem diameter of 0.10 m was calculated from the LIND approach in a range from 0.90 to 1.20 which gives a percent range of variation of ±14 %. For steam diameter of 1.0 m, the calculated range of variation was 0.90 to 1.5 which gives the percentage range of variation of ±25 %. The calculated C_D values of LIND are in a plausible range. They have a larger mean value than those of P&B, which explains the larger mean values of LIND's water depths.

Overall, the results show good agreement between the vegetation approaches studied for the rigid non-submerged tree case. Moreover, the P&B shows a small variation due to the variation of the C_D value. The ranges of variation resulting from the uncertainties of the vegetation parameters outweigh the uncertainties of the individual vegetation approaches in the present case.

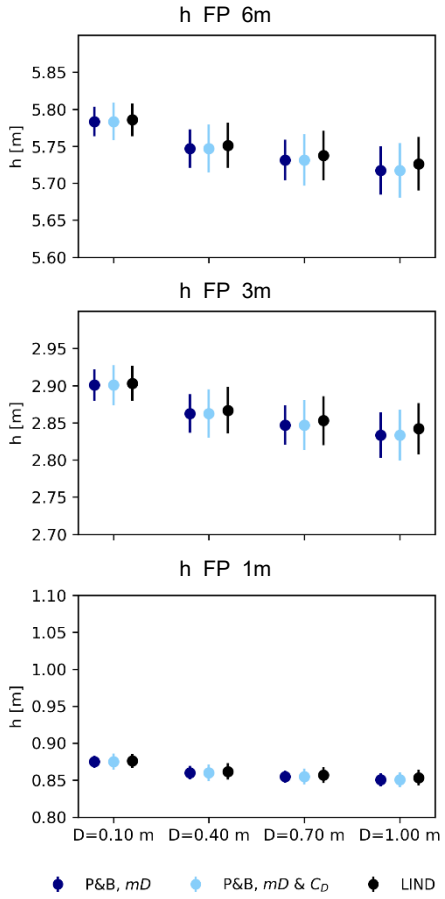

Figure 3: Water depth for the category rigid non-submerged tree for the events h_FP_1m (bottom), h_FP_3m (middle) and h_FP_6m (top) evaluated on floodplain at x=2200 m; mean value (circle) and deviation within 95 % probability of occurrence (errorbars)

2) Rigid non-submerged and submerged bush: Fig. 4 shows the resulting water depth and the corresponding deviations for the cases small (left) and large (right) non-submerged and submerged rigid bush. For the event h_FP_1m all models lead to the same results and the deviation are negligible. Here, both the small and the large bush are non-submerged. As described above, in this case the three models treat the vegetation analogue to P&B. Due to the lower hydrodynamic density the large bush leads to slightly lower water depth compared to the small bush.

For the event h_FP_3m and h_FP_6m the water depth in case of the large bush are higher compared to the small bush. The small bush is for both events submerged. In contrast to this, the large bush is for the event h_FP_3m non-submerged leading to only small deviations.

With exception of HUTH the uncertainty due to the vegetation height (light blue) is larger compared to the vegetation density (dark blue). The additional variation of the drag coefficient (black) results for all vegetation models in a

small increase in the deviation of water level. Overall, BAPT shows somewhat less deviation than the other two models.

In summary, the results for the small bush and the large bush show good agreement, although the considered vegetation approaches model the velocity profile in the free surface layer differently for the submerged case. The vegetation height has a large influence and the hydrodynamic density and the drag coefficient have a small influence on the output parameters water depth. However, the result of HUTH for the small bush is an exception, because in this case the hydrodynamic density has the largest influence and the vegetation height has a relatively small one. The ranges of variation resulting from the uncertainties of the vegetation parameters outweigh the uncertainties of the individual vegetation approaches in the present case.

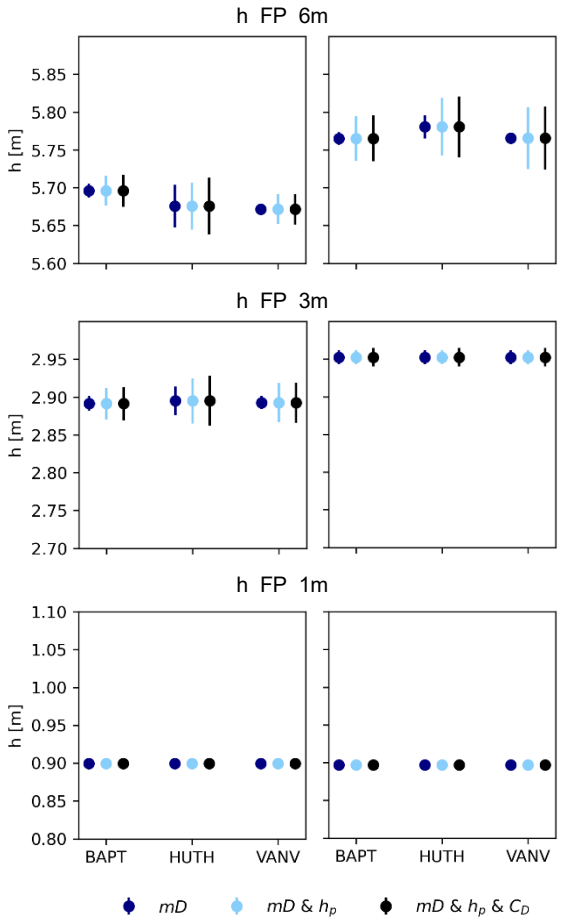

Figure 4: Water depth for the category rigid non-submerged and subermerged bush (left: small, right: large) for the events h_FP_1m (bottom), h_FP_3m (middle) and h_FP_6m (top) evaluated on floodplain at x=2200 m; mean value (circle) and deviation within 95 % probability of occurrence (errorbars)

3) Flexible submerged and non-submerged bush: In Fig. 5 the resulting water depths for the flexible submerged and non-submerged bush are shown. Beside the models for rigid vegetation, the JAER model was used in case of non-submerged vegetation and in case of submerged conditions the adapted HYBR model. For the rigid approaches BAPT, HUTH and VANV only the results for the case when all parameters are varied are shown.

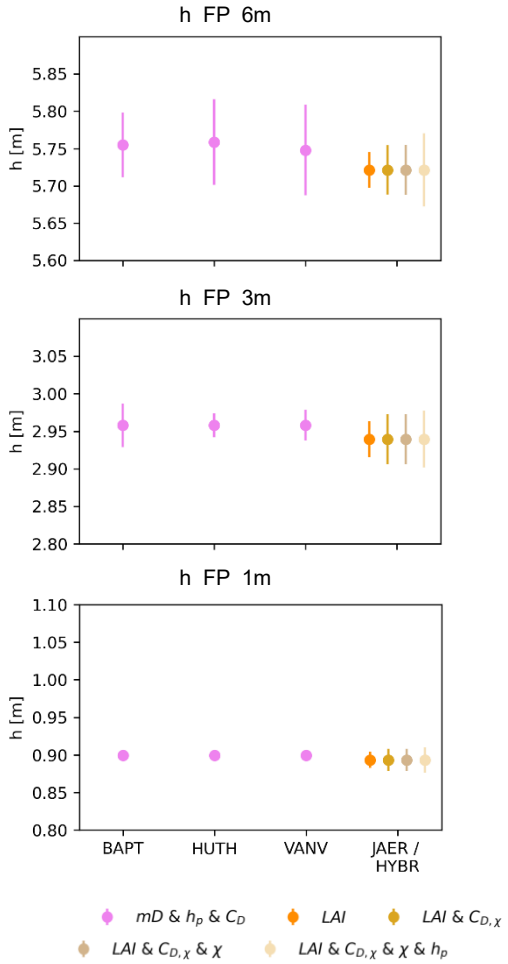

Figure 5: Water depth for the category flexible non-submerged and subermerged bush for the events h_FP_1m (bottom), h_FP_3m (middle) and h_FP_6m (top) evaluated on floodplain at x=2200 m; mean value (circle) and deviation within 95 % probability of occurrence (errorbars)

For all three events the mean water levels of the flexible approach are lower than the resulting of the rigid ones. In case of non-submerged (h_FP_1m) and just-submerged (h_FP_3m) conditions the flexible approaches show higher deviation of the water level and in the submerged case (h_FP_6m) lower ones compared to the rigid approaches.

The variation width of the flexible approach is composed of a large variation width of the leaf area index LAI, a large increase in the species-specific resistance coefficient $C_{D\chi}$, and a large increase in the vegetation height. The parameter χ causes a very small change in the variation widths of water depth and runoff partitioning. The increase in water depth is less than 1 %.

The results for the flexible submerged and non-submerged bush do not deviate strongly from each other and show a high overlap. The ranges of variation resulting from the uncertainties of the vegetation parameters outweigh the uncertainties of the individual vegetation approaches in the

present case. The approaches differ fundamentally from each other due to the modelling of a rigid vegetation on the one hand and a flexible vegetation on the other hand.

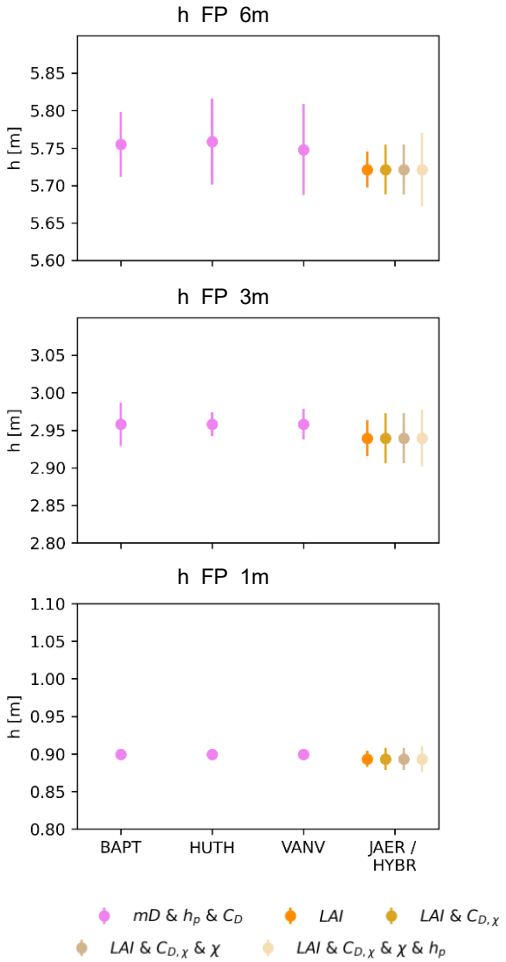

Figure 5: Water depth for the category flexible non-submerged and subermerged bush for the events h_FP_1m (bottom), h_FP_3m (middle) and h_FP_6m (top) evaluated on floodplain at x=2200 m; mean value (circle) and deviation within 95 % probability of occurrence (errorbars)

4) Comparision of vegetation types tree and bush (both considered as rigid): In the preceding analyses, the influence of the vegetation parameters for different vegetation approaches related to one vegetation category is considered in each case. In the following, the results of the vegetation categories tree and bush (rigid) are compared with each other. Only the results of BAPT are used for this purpose; and in the case of non-submerged tree, these correspond to the results of P&B.

Fig. 6 shows the ranges of variation in water depths on the floodplain. For the comparison, the two steam diameters 0.10 m and 1.00 m are focused on for the non-submerged tree.

The deviations of the water level are smallest for h_FP_1m. The tree is non-submerged at all flow depths. The tree with a steam diameter of 0.10 m has a higher mean water depth for all flow depths compared to the tree with a steam diameter of 1.00 m as shown above.

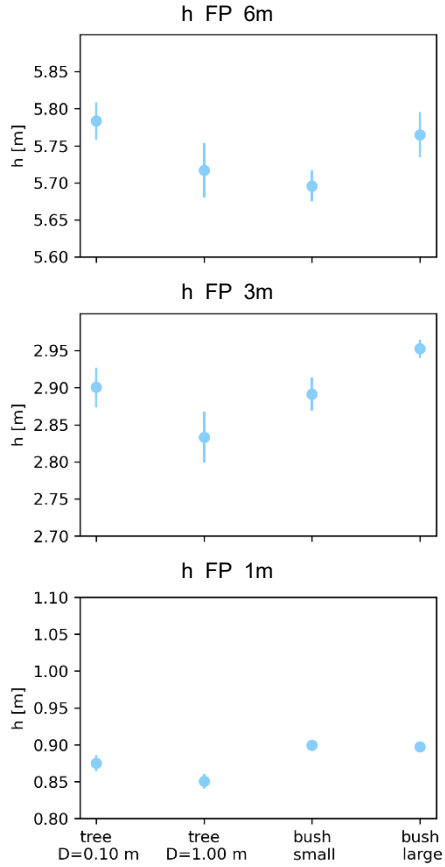

Figure 6: Water depth for the vegetation types tree and bush predicted by BAPT for the events h_FP_1m (bottom), h_FP_3m (middle) and h_FP_6m (top) evaluated on floodplain at x=2200 m; mean value (circle) and deviation within 95 % probability of occurrence (errorbars)

The bush is non-submerged for h_FP_1m. Compared to the tree, it has slightly larger water depth values for the VL-WT of 1 m. This results from larger assumed hydrodynamic densities for the small bush and for the large bush and a larger assumed C_D value compared to the tree. For h_FP_3m the mean value of water depths for the small bush is within the range of values for the tree with a steam diameter of 0.10 m. Here, the small bush is submerged but covers around half of the water depth with its vegetation height (varies from 1 m to 2 m). For h_FP_6m, the mean of the water depth of the small bush has the lowest water depth. The large bush in this case approaches the tree with the steam diameter of 0.10 m. Both types of bushes are submerged, but the large bush covers larger parts of the water depth with a variation in vegetation height from 2 m to 5 m.

Comparison of vegetation categories illustrates the different mechanisms of vegetation resistance under non-submerged and submerged conditions. At non-submerged conditions, the larger values of hydrodynamic density and drag coefficient are the primary factors that result in a higher water depth for bush compared to tree. For the submerged case, this is not apparent. In the submerged case, the mean values of the bush equal the mean values of the tree.

B. *Validation of methodology*

In order to verify the applicability of the FOSM method with the assumption of a linear system behaviour, the MC method was applied for the two cases small and large bush of the category rigid non-submerged and submerged shrub and the event h_FP_6m. In Unantopy the Latin Hypercube Sampling [16] is used to reduce the number of needed random experiments without compromising reliability. In the present case, 1000 samples were simulated. Previous tests at BAW have shown that such number of samples are satisfactory for simple hydrodynamic situations as in this study. Nevertheless, this corresponds to about 140 times more computation time compared to FOSM, which requires only 7 simulation runs for 3 uncertain input parameters.

Fig. 7 shows that the results of FOSM (light blue) and MC (dark blue) are nearly the same. The deviation ranges differ by a maximum of around 5 % while the mean values were computed slightly smaller (max 0.15 %) with MC method.

Furthermore, a uniform distribution (uni) instead of a normal distribution (normal) was used with the MC method. The results are presented in Fig. 7 (black). As expected a uniform distribution created more deviation of the water level as a normal distribution. Interestingly, the mean values were also slightly changed due to another probability distribution of the uncertain parameter. With the MC method the mean value was calculated slightly smaller than with FOSM method except for large bush and HUTH vegetation formula. The differences are larger for HUTH which shows again the higher sensitivity of this vegetation formula.

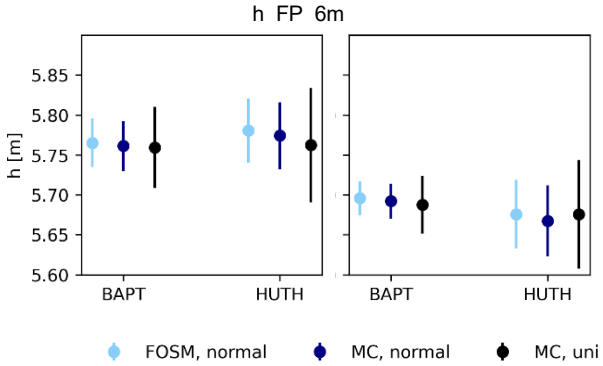

Figure 7: Water depth for the category rigid non-submerged and subermerged bush (left: small, right: large) for the event h_FP_6m evaluated on floodplain at x=2200 m; mean value (circle) and deviation within 95 % probability of occurrence (errorbars)

VI. Discussion

The wide range of vegetation appearance results in a large variability of vegetation parameters. In practice, the determination of the vegetation parameters can prove to be difficult. The results of the uncertainty analyses performed in this work show that the range of variation resulting from the uncertainties of the vegetation parameters outweighs the uncertainties of the vegetation approaches. The unique feature of this work is that the ranges of variation of the vegetation parameters were included.

To discuss the influence of the individual vegetation parameters, the deviations of water levels related to the relative standard deviations of the uncertain vegetation parameters hydrodynamic density, vegetation height and drag coefficient are shown in Fig. 8. The relative standard deviation (RSD) is a relative measure of dispersion of the parameters and defined as

$$RSD = \frac{\sigma}{\mu}. \quad (5)$$

Using the RSD values the uncertainty of the individual vegetation parameters can be compared with each other regardless of their absolute values.

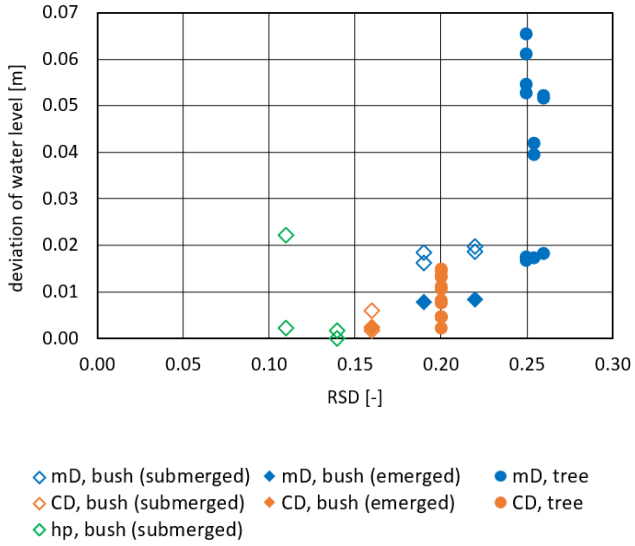

Figure 8: Deviation of the water level within 95 % probability of occurrence on floodplain at x=2200 m related to the RSD values of the vegetation parameters for the investigated rigid cases of BAPT

The vegetation categories tree and bush (both rigid) for all three flow events were considered. The results of BAPT are shown exemplarily for HUTH and VANV. The results of these approaches are comparable while HUTH shows little differences due to the influence of the individual parameters. For non-submerged (emerged) conditions, the results of BAPT, HUHT and VANV correspond to those of P&B.

The hydrodynamic density mD (blue) generates large ranges of deviation for the water depth. In contrast, the drag coefficient C_D (orange) has smaller RSD values and generates much smaller ranges of deviation for water depth. Thus, the influence of the mD value is larger than that of the C_D value for both submerged and non-submerged vegetation.

The vegetation height h_p (green, only relevant for submerged vegetation) has the smallest RSD values, but still relatively large ranges of variation in water depth are evident compared to mD and C_D. The influence of the vegetations height is strongly dependent of the level of submergence.

Since the coefficient of resistance has a small influence compared to mD and h_p, but still causes a change, it is further to be investigated whether the $C_D$value can be fixed or a calculation according to LIND should be done. The

calculation method of LIND was developed using rigid, uniformly arranged cylinders with flow. Therefore, it should be checked whether the calculation is also applicable for natural structures.

For practical application, it is advantageous that the vegetation parameters mD and h_p, which can be derived e.g. from remote sensing, have a larger influence than the drag coefficient C_D. Apart from the LIND calculation, the drag coefficient can only be determined by laboratory tests, which makes the effort not worthwhile for the relatively small influence compared to other vegetation parameters.

Reference [2] simulated different vegetation approaches using the FOSM method and the Monte Carlo method with a normal distribution, including for JAER, LIND, and P&B. They suspect that linearity of input and output parameters is present due to the direct relationship of vegetation parameters with vegetation resistance. Based on the study by [2], it is very likely that the results of the FOSM method in this work are robust despite the assumed linearity of the method. No conclusion could be made in the work as to whether the assumption of a normal distribution of vegetation parameters is justified. Furthermore, it has to be evaluated whether a uniform distribution, which generates similar results with larger ranges of variation, corresponds more to the statistical distribution of the vegetation parameters

VII. CONCLUSION

The results of the uncertainty analysis show that the natural uncertainties of the vegetation parameters outweigh the uncertainties of the vegetation approaches. Thus, the quality of the input parameters should be in focus. Furthermore, the range of application of the approaches should be considered when choosing the vegetation approach. Provided that the flow field is influenced by predominant vegetation we highly recommend to use an appropriate vegetation approach. The use of e.g. Nikuradse's roughness law is only valid if the roughness elements are in the order of ten times smaller than the flow depth.

When overflowing vegetation occurs, a two-layer approach is to be used. For flexible vegetation, the degree of flexibility is decisive. In this work, the results of the flexible approaches did not show significantly larger deviations compared to the approaches of rigid vegetation. Therefore, depending on the local conditions, it should be decided whether flexibility should be considered or not.

The hydrodynamic density and the vegetation height have a large influence on the output parameters. The vegetation height plays a crucial role for submerged conditions. The drag coefficient plays a minor role, and therefore a constant assumption is recommended in practice.

The admissible use of the more inaccurate but computation time saving FOSM method for uncertainty analysis could be confirmed by comparison with the Monte Carlo method for individual tests. This is consistent with the research of [2] on vegetation approaches.

REFERENCES

[1] F. Folke, R. Kopmann, G. Dalledonne, and M. Attieh, "Comparison of different vegetation models using TELEMAC-2D." XXVIth TELEMAC-MASCARET User Conference, Toulouse, 2019

[2] G. Dalledonne, R. Kopmann, and T. Brudy-Zippelius, "Uncertainty quantification of floodplain friction in hydrodynamic models." HESS, 23, 3373-3385, 2019

[3] M.J. Baptist, V. Babovic, J. Rodríguez Uthurburu, M. Keijzer, R.E. Uittenbogaard, A. Mynett, and A. Verwey, "On inducing equations for vegetation resistance", J. of Hydr. Res., 45:4, 435-450, 2007

[4] S. Petryk, and G. Bosmajian, "Analysis of Flow through Vegetation", In: Journal of the Hydraulics Division 101, pp. 871–884, 1975

[5] K. Lindner, "Der Strömungswiderstand von Pflanzenbeständen", Braunschweig, 1982

[6] E. Pasche, and G. Rouvé, "Overbank flow with vegetatively roughended flood plains", J. of Hydr. Eng.k, 111(9), 1985

[7] L.H. Reineke, "Perfection a stand-density index for even-aged forest", Journal of Agricultural Research, 46, 627-638, 1933.

[8] H. Pretzsch, "Grundlagen der Waldwachstumsforschung" (in German), Springer-Verlag, doi: 10.1007/978-3-662-58155-1, 2019

[9] F. Huthoff, D.C M. Augustijn, and S.J.M.H. Hulscher, "Analytical solution of the depth-averaged flow velocity in case of submerged rigid cylindrical vegetation", Water Resource Res., 43.6, 2007, doi: 10.1029/2006WR005625.

[10] E.H. Van Velzen, P. Jesse, P. Cornelissen, and H. Coops, "Stromingsweerstand Vegetatie in Uiterwaarden", 2003.029. RIZA, Arnhem, 2003

[11] J. Järvelä, "Determination of flow resistance caused by non-submerged woody vegetation", Int. J. of River Basin Manag., 2:1, 61-70, 2004

[12] S. Vogel, "Drag and Flexibility in Sessile Organisms", American Zoologist, 24.1, 37-44, 1994

[13] F. Folke, M. Attieh, and R. Kopmann, "In search of friction laws for vegetated flow within 2D large-scale applications", E-proceedings of the 38th IAHR World Congress, Panama City, Panama, 2019

[14] R. Kopmann, S. Hudjetz, and A. Schmidt, "Uncertainty quantification in hydrodynamic modeling using the example of a 2D large-scale model of the river Elbe", SimHydro 2021: Models for complex and global water issues – Practices and expectations, 16-18 June 2021, Sophia Antipolis, France.

[15] A. Hohnschop, "Analyse der Unsicherheiten von Vegetationsparametern als Grundlage für die HN-Modellierung" (in German), Masterthesis, University of Applied Science Karlsruhe, 2021

[16] J.R. Koehler and A.B. Owen, „Computer experiments, Handbook of Stat.", S. Ghosh and C.R. Rao ed., Elsevier Science B.V. 13, 261-308, 1996

Hydrodynamics

Implementing Effective Performance Turbine Model into TELEMAC-3D

Yi Man, Ioan Nistor, Colin D. Rennie
Department of Civil Engineering
University of Ottawa
Ottawa, Canada
aman070@uottawa.ca

Julien Cousineau
Ocean, Coastal and River Engineering
National Research Council Canada
Ottawa, Canada
Julien.Cousineau@nrc.ca

Abstract—River Energy Converters (REC) typically need to be installed in an array formation or farm layout to maximize their cost efficiency. Optimizing the arrangement of such formations plays a vital role in achieving the array's maximum effectiveness. In order to analyse the performance of the turbines, a high-definition numerical simulation using a fine computational grid is the most practical approach. The Laboratoire de Mécanique des Fluide Numérique (LMFN) of Laval University, Quebec City, Canada, developed, in collaboration with the National Resources Canada (NRCan), a model approach called the Effective Performance Turbine Model (EPTM) that accurately predicts the wake recovery of turbines in an array formation [1]. The EPTM was originally developed using a computational fluid dynamics (CFD) model and validated with laboratory experiments performed at the National Research Council [2]. However, simulations for fluvial, coastal and ocean domains, spanning several hundred kilometres, are often out of reach for CFD models due to high computational costs. The authors have undertaken the task to implement and validate the EPTM in TELEMAC-3D in the goal of properly simulating power extraction and wake recovery in array turbine formation. The paper presents the implementation of the EPTM in TELEMAC-3D with an example.

I. Introduction

A well-planned river energy converter layout will achieve the best price-quality ratio for economic return. High-fidelity CFD numerical modelling is the chosen approach due to its high precision and flexibility in modifying and adding parameters. The Laboratoire de Mécanique des Fluide Numérique (LMFN) of Laval University developed a fully resolved CFD reference simulation with about 60 million cells in a 20-meter simulated flume. This simulation displayed and described the wake characteristics and power extraction of a crossflow turbine in both 2D and 3D [2]. Their work selected Unsteady Reynolds-Averaged Navier-Stokes (URANS) method for flow resolution and used about 60 million cells to simulate the turbine and turbulence region. The results were highly accurate, with only about 2-5% difference from the results obtained by [3] in 2D and 3D for both crossflow turbine and axial-flow turbine simulations. Natural Resources Canada (NRCan) subsequently tasked LMFN with the development of an efficient simplified CFD tool to reduce the impractical computational expenses, which took a couple of months with hundreds of cores to resolve, for large river energy converter projects. Effective Performance Turbine Model (EPTM) was, as such, proposed. EPTM has been used to simulate axial flow turbine and cross flow turbine in 2D and 3D [1]. Instead of using URANS, EPTM employed steady-state RANS equation as the solver. Combined with a coarser mesh, the computation speed was significantly improved while maintaining similar results. The region of turbine with its simulated drag forces was simplified to an actuating region. In the case of a cross flow turbine (CFT), an actuating annulus or cylindrical region is preferred, as proven by [4] and [5]. The present study aims to implement the EPTM 3D cross flow turbine (EPTM-3DCFT) from Laval University into TELEMAC-3D. The TELEMAC-3D model can be further used for regional scale models spanning hundreds of kilometres across the domain of interest. Therefore, lowering the computational cost while maintaining reasonable accuracy is the focus and the aim of this project.

As will be shown, the downstream wake topology produced by the TELEMAC-3D simulation showed very good agreement to the EPTM result, but noticeably longer wake and near wake ($x/D > 5$) velocity discrepancies at about five turbine diameters downstream are found.

II. Methodology

A. *EPTM*

The EPTM is a simplified numerical model which replaced the turbine rotor by an actuating region to simulate the wake zone induced by the interactions between the flow and the turbine objects. The actuating region takes the time averaged drag coefficients from the fully resolved reference model, therefore eliminating the need to calculate the interactions between the fluid and the blades. The turbine flow zone is reproduced by mimicking the mean flowrate and the time-averaged forces passing through the turbine. Given similar parameters, the actuating region will determine the averaged power extracted by the system [6] using a drag force equation. Three turbine models are simplified using the EPTM model: the axial flow turbine, EPTM-AFT, and cross flow turbine in 2D and 3D, EPTM-2DCFT and EPTM-3DCFT. In the scope of this simulation using TELEMAC, only the data from EPTM-3DCFT is used.

B. Drag Force Equation

The drag force which the turbine experiences was calculated using the following formula:

$$F = \frac{1}{2}\rho C_d^* A V^2 \quad (1)$$

Where ρ is the density of the fluid (kg/m^3), C_d^* is the effective drag coefficient from EPTM simulation, A is the area of the turbine's center plane (m^2), and V is the total averaged velocity from every node inside of the turbine (m/s).

The effective drag coefficient, C_d^*, is the drag coefficient normalized with effective velocity, V^* (m/s). The effective velocity, V^*, or otherwise defined as the "axial disk-averaged velocity," is the time- and spatial-averaged velocity on the center mesh plane of the turbine object. The turbine centerplane is illustrated in Fig. 1.

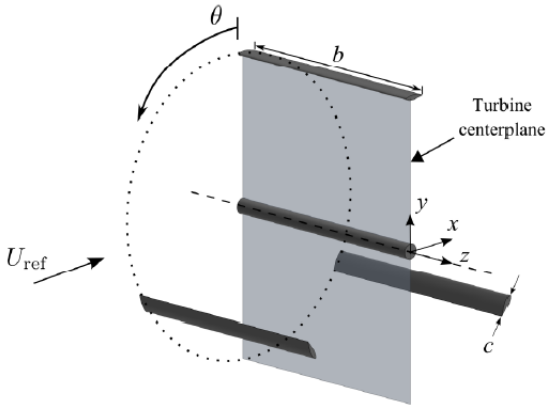

Figure 1 Turbine centerplane illustration [1]

In Fig. 1, U_{ref} is the inflow velocity, θ indicates the rotation of the turbine in radians, b is the turbine span, c is the blade chord length of the turbine, while x, y, z indicates the axes.

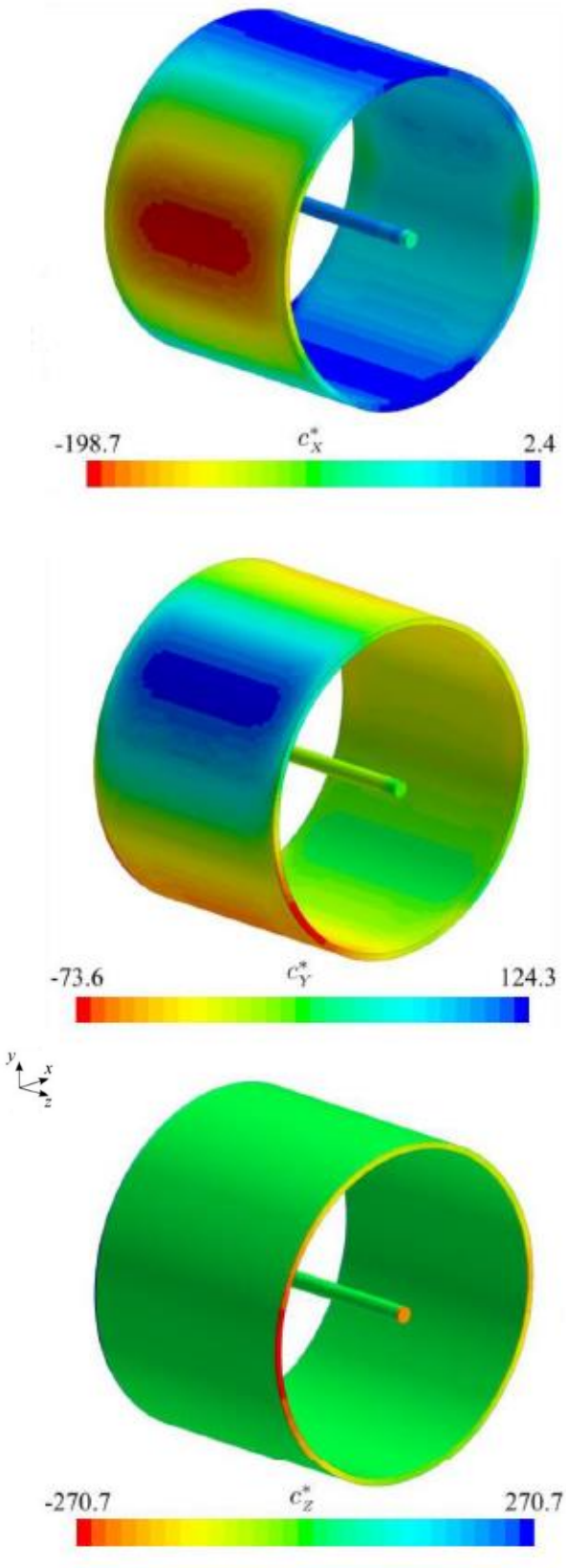

Figure 2 Effective force distribution for each component from EPTM-3DCFT [2]

Figure 2 represents the effective drag coefficient mapped on the turbine from the EPTM-3DCFT result. The notations c_X^*, c_Y^*, c_Z^* are the same effective drag coefficient discussed above (C_d^*). In the x-direction, the region that faces the incoming flow has large negative effective drag coefficients indicated in red, while the top and bottom regions have very low magnitude of effective drag coefficients. The turbine experienced large positive effective drag coefficients indicated in blue in the y-direction, and a significant negative value was observed on the span of the turbine blade on the lower half of the actuating region. Moreover, in the z-direction, the tip of the blade and shaft exhibited large C_d^* values, similar in magnitude but on the opposing side of the blade and shaft. It is noticeable that the forces vary with the changes of the positions of the blades. The model calculates the mean forces of a region in a narrow time interval. If the changes happen too rapidly, then there is a chance that the time interval will not capture the changes in the forces and disrupt the stability of the model [2].

III. Implementation in TELEMAC-3D

A. Drag Force as Source Term

`S1U%R()`, `S1V%R()`, and `S1W%R()` are defined as the implicit source terms on velocity in U, V, and W directions in [4] and [7]. These terms are used by TELEMAC-3D to update the velocity of each node at each time step. Since the source term is set to be drag force divided by volume, and the volume of the turbine object averaged in Laval University's study, the source term is $S1U = Drag\ force/Vol_{TEC}$. The complete formula is as follows:

$$S1U(I3) = (\tfrac{1}{2}\rho C_{dx}^* A U^2)/Vol_{TEC} \quad (2)$$

$S1U(I3)$ is the source term in the x direction (kg/s^2m^2), and $I3$ is referring to each individual node of the TELEMAC mesh. ρ is the density of the fluid (kg/m^3), C_{dx}^* is the effective drag coefficient of each node in x-direction obtained from the EPTM model. A is area of the turbine centerplane shown in Fig. 1. U is the fluid velocity in the x direction (m/s), and Vol_{TEC} is the sum of discretised mesh node volume within the defined turbine region (m^3).

B. Turbine Volume and Mean Velocity

EPTM-3DCFT takes the average of velocities from the center plane of the turbine as the averaged velocity the turbine experiences. Following the same logic, the velocity terms used for the drag force equation and the source term equation must also be the mean velocity of the turbine. Since the turbine is comprised of different mesh points in the TELEMAC simulation domain, by averaging the velocities from each mesh point inside the turbine object, turbine mean velocity can be calculated. Looping through all the mesh points and using `inpoly` function to check if the mesh point is inside the turbine, all turbine mesh points are collected. The volume of turbine, V_{TEC}, is the sum of the volumes of all the mesh nodes inside the turbine. The turbine mean velocity can be obtained by dividing the sum of all the velocities in three directions from each mesh point to the number of points.

C. Computational Domain

The TELEMAC simulation domain is set up with the same geometry as that of the EPTM-3DCFT test case. The channel is 30 meters long, 1.68 meters wide, and 2.24 meters in depth. With turbine diameter being 1 meter and a transverse span of 0.75 meters, the blockage ratio is calculated to be 20%, which is one of the EPTM simulation trials that this project is aiming to duplicate. The spacing between each TELEMAC-3D mesh node, Δx and Δy, is set to 0.021 meters throughout the domain, yielding 4.6 million nodes across the domain. The channel has a free surface. Both sides of the wall and channel bottom are defined as solid wall. The inflow follows prescribed constant water elevation, and outflow is considered to be open boundary with free velocity and elevation. The turbine origin is set at (0,0) of the simulation domain, meaning that the span of the flume is from -10 m to 20 m in x direction, -1.68 m to 1.68 m in y direction, and -1.12 m to 1.12 m in z direction.

BlueKenue is a data visualization software developed by National Research Council Canada. This tool supports direct data input from TELEMAC-3D simulation results. Various choices of perspectives enable users to have a graphical representation of the results, serving as a sophisticated tool for data analysis.

IV. Code Implementation

A. Supporting Modules

The main Fortran subroutine for TELEMAC-3D simulations cannot work without supporting Fortran modules. These modules contain functions that handle the mathematics, geometry, objects, etc., enabling the main subroutine to be written in a more concise and efficient manner. The steering file is the most important supporting file as it governs many properties of the simulation including, fluids, boundaries, time step, and which solver equation sets to be employed. Geometry, input, and boundary files are specified in the steering file as well. There are two formatted data files as input. TELEMAC-3D will read the data from these files and store them in memory in the form of arrays for the program to use. The formatted data file 1 (`FO1`) is a text file for the turbine energy convertor (TEC) properties. This file includes the TEC's name, diameter, thickness of the blade, position in the domain, and rotations in degrees along x, y, and z axis. The number of lines indicates the number of turbines to be put in simulation. Formatted data file 2 (`FO2`) is a csv file detailing the EPTM data of the effective drag coefficient around the turbine object. The values are presented in cylindrical coordinates (radius, theta, z-elevation). The radius and theta will give us the points in '*x* and *y* direction', unfortunately, due to the different coordinate convention, the *y* component from cylindrical coordinate system is the z in Cartesian coordinate system, as it signifies the depth. The *z* component becomes the y axis after the conversion, marking the width of the channel span. The *x* component stays the same, as both are describing the flow direction. The conversion to Cartesian coordinate system, along with rotation, transformation, and scaling of the turbine object are handled by `Mat4.f90` module. To identify

if a node is located within the turbine, one needs to be inside of TEC's XY and XZ (front and side view). `Qhull.f90`, adopted from Qhull, is used to draw convex hulls representing the two planes. Since the input arrays must be sorted in ascending order for the module to function, two quicksort modules were adapted and utilized, one for one-dimension array and another for two-dimension array. An intrinsic function `Inpoly.90` then identifies if the given point is within the boundary of both planes. If it is, then this point will be considered when calculating the TEC's volume and average velocities. A list of supporting files with descriptions is presented below:

- `A_qsort.f90`: provides quick sort function to a given array. "A_" was added for TELEMAC to load this file first, as the program takes in files alphabetically.
- `Check.f90`: checks if a is equal to b for different element types.
- `File_csv.f90`: writes computed 2D array results in an .csv file.
- `Geometry.f90`: handles the translation, scale, rotation, and transform of the turbine object represented a 3D array format.
- `Inpoly.f`: checks if a point is inside of a given 2D polygon
- `Mat4.f90`: handles a four by four array's reset, translation, scale, rotation, and transform function.
- `Math.f90`: uses qsort.f90, unique.f90, unique2.f90 to handle their functionalities.
- Polyarea.f: computes the area of a given enclosed polygon.
- `Qhull.f90`: computes the convex hull of a given array. See [8] for more information.
- `Quicksort_include.f03`: calculates scenarios before calling quick sort module for optimal speed.
- `Turbine.f90`: defines and creates the turbine object and its values and functions, including reading CFD values from input file.
- `Turbines.f90`: creates the formation of the turbine objects constructed.
- `Unique.f03`: Used by Math.f90 to check if the value is unique in a given series.
- `Unique2.f03`: Used by Math.f90 to check if a point is unique in a 2D array.
- `User_condi3d_uvw.f`: overwrites the default TELEMAC-3D input boundary condition of flow velocity in uvw direction. Works in conjunction with steering file.
- `User_mesh_transf.f`: overwrites the default TELEMAC-3D mesh transformation
- `User_source.f90`: the main source file which is explained in the following section

All supporting files can be found on the GitHub repository [9] : https://github.com/Julien-Cousineau/telemac3d-eptm.git.

`turbine.f90` is responsible for creating individual turbine objects, which can be considered as a 'class' in other programming languages. This type contains the numerical values read from `FO1` and `FO2`. It also contains procedures to allow users to modify its special properties, such as, rotation, translation, and scaling.

`turbines.f90` is set as an overall construction of the turbine formation. This module reads `FO1` to gain information on the number of TEC and the characteristics of each. A one-dimension array `TEC(:)` which holds objects of type `Turbine` is defined. in the module `turbine.f90` (to be differentiated from `turbines.f90`). There are two subroutines in the `turbines.f90`, `readTEC` and `readCD`. `readTEC` reads the number of turbines in `FO1` then it constructs `TEC(:)` with size equal to that number. Since each element within `TEC(:)` is of type *Turbine*, an initiation sequence called *initialize* is called with input arguments read from `FO1`. `readCD` follows the same logic, where it makes each turbine object to read the C_d^* values from `FO2`.

B. *Main Source File*

This module functions as the main program of this simulation as it overwrites the source file (user_source.f90) of TELEMAC. It uses a few intrinsic modules such as `BIEF`, `DECLARATIONS_SPECIAL`, and `DECLARATIONS_TELEMAC3D`.

a) *Turbine Initialization*

After declaring variables, upon the first iteration *(*`LT .EQ. 1`*)*, the program checks if the files (`FO1`, `FO2`) of turbine position and drag coefficient from the input files are in place, and will send error messages and calling the program to stop if they are not. `readTEC` *and* `readCD` are then called to read the data and store them into memory. Mesh points are saved into `meshIds` array if a given mesh point is inside of the TEC boundary in 2D view.

b) *Inverse Distance Weighting (IDW)*

To mimic the total drag force calculated in EPTM in TELEMAC, it is vital to use the same drag coefficient data. The spatially distributed drag coefficients data needs mapping into the coarser mesh grid of TELEMAC. To achieve this, IDW method was employed to approximate the spatially averaged drag coefficients around each node within the turbine location region in TELEMAC. Each turbine mesh node gathers scattered EPTM drag coefficient values within the defined search radius. The distance `dist` between each pair of EPTM and TELEMAC nodes is calculated using:

$$distance = \sqrt{(x-x_1)^2 + (y-y_1)^2 + (z-z_1)^2}$$

Since TELEMAC has an intrinsic coordinate value for each node, and EPTM node coordinates are stored in array `temptec`, the code is line 1 to 3 in the appendix. The unit is in meters.

A distance threshold `distThreshold` is defined; if the distance between two nodes is within the threshold, the value

of the EPTM node is used, instead of proceeding to obtain the value from the IDW method based on the surrounding nodes within the search radius. The defined threshold is a part of the variables that can be investigated in the sensitivity analysis. This procedure is to ensure the greatest accuracy and the most efficient use of computing power are taken into account. There is no need to use IDW to map EPTM value into TELEMAC grid if the two nodes are within a defined distance threshold. Furthermore, in order to maintain the highest accuracy of the approximated value, the closest EPTM node value is used. However, in most cases, there are no nearby EPTM nodes within the distance threshold, then the second order IDW method is employed to calculate the mesh node value from interpolating nodes within the search radius using:

$$C_{d_p} = \frac{\sum_{i=1}^{n}(\frac{C_d}{d_i{}^p})}{\sum_{i=1}^{n}(\frac{1}{d_i{}^p})} \quad (4)$$

In Fortran, this is achieved by calculating the sum of both numerator and denominator on the x, y, z direction for each node, then dividing them. The search radius is the most impactful variable in IDW method, and it is crucial for the users to determine the best radius for their project needs. A logical flag `pointsInRange` is set to check if there are any points within the search radius. Sample code is in the appendix from line 4 to 37.

Parameters are reset at the end of each loop going through the nodes. Lastly, the effective C_d values along with their node IDs are added to the `updateArray` for velocity update.

c) Source term update

The velocity of each node is updated by calculating the drag forces as implicit source terms using the drag coefficients obtained earlier using $F_D = \frac{1}{2}\rho v^2 C_d A$. The implicit source terms are defined by the drag force on each node divided by the volume of the turbine. Therefore, the drag force itself is the implicit source term multiplied by the volume of the turbine object in the simulation domain. Updating the implicit source terms along all axes and the collection of drag forces are coded as shown in the appendix line 38-40.

In the code, S1U, S1V, S1W are the implicit source terms in u, v, w flow direction, and `%R` represents its value. `I3` is the specification of the node ID being updated. `effX`, `effY`, and `effZ` are the effective drag coefficient imported and calculated from the EPTM csv file. `TcenterplaneA` is the turbine's centerplane area. `TECAvgU`, `TECAvgV`, and `TECAvgW` are the turbine objective's average velocity in u, v, and w direction from the last time step. `TECVolu` stands for the turbine objective volume in the mesh.

V. SIMULATION EXAMPLE

The CFD results are generated with the aim to validate the TELEMAC simulation results with coarser mesh against the EPTM-3DCFT results. The inflow flowrate is prescribed to be 3.763 m^3/s. With 1.68 m in width, and a prescribed fluid elevation of 1.12 m (2.24 m in flow depth), the inflow velocity is at 1 m/s, which is the reference velocity from the EPTM simulation. Several turbulence models were tested, and the most promising results were obtained when using the K-Epsilon model. This turbulence model can be activated by setting both horizontal and vertical turbulence model key words to 3 in the steering file. This model solves the balance equations for turbulent energy and turbulent dissipation [10] to determine the local eddy viscosity. The diffusion coefficient for fluid is set as 1E-6, the default, as instructed in the manual. The law of bottom friction in the steering file is set to model 3 which is the Strickler's law. And the friction coefficient is left at the default value of 60.

Figure 3(a) and (b) are the reference results generated by LFMN. Figure 3(a) is the high-fidelity CFD simulation result, and Fig. 3(b) is the EPTM version of the 3D crossflow turbine, which is scoped to be replicated using TELEMAC. Figure 4, 5, and 6 presented the simulation using TELEMAC. The color legends on the left-hand side are for all three TELEMAC figures. Fig. 4 used K-Epsilon model while the Fig. 5 and 6 employed the constant viscosity method with different diffusion coefficients. The simulation parameters are identical for all different scenarios. Time step Δt is 0.05 seconds for 1000 steps, yielding 50 seconds of simulation time. The center of the turbine is set at the origin (0,0). Spanning 1 meter long, eight meters downstream of the TEC origin, depending on the choice of turbulence model. The $k-\epsilon$ model yielded a more uniform and less turbulent wake similar to the reference results. The constant viscosity model produced a more chaotic and longer wake. The simulation results are similar to the result from Laval University; however, the key difference is that the TELEMAC generated wake is longer than the wake from EPTM [1], despite using the same effective drag coefficient; different turbulence models will produce different wakes. Therefore, the balance between computational resources and the accuracy of the results is left to the latitude of the researcher and to the requirements of specific project.

(a)

(b)

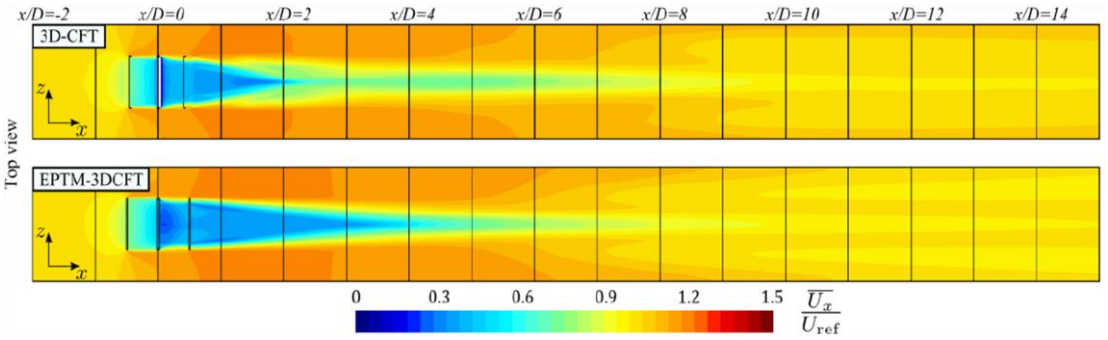

Figure 3 High-fidelity CFD and EPTM reference simulation result (Top View) [1]

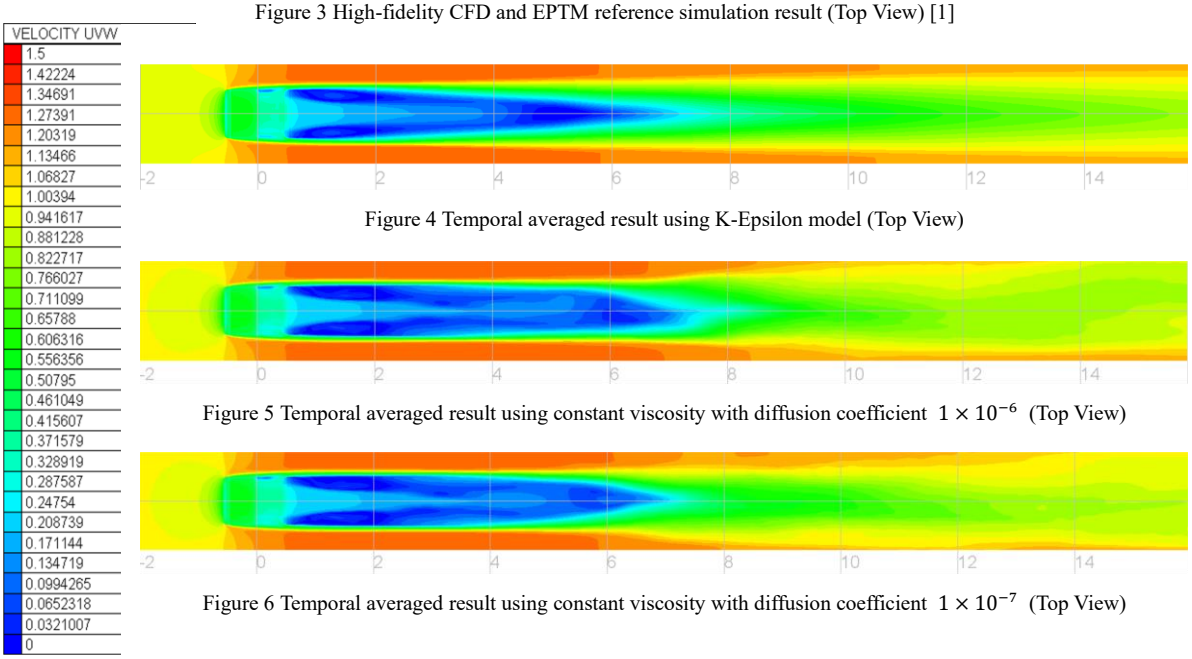

Figure 4 Temporal averaged result using K-Epsilon model (Top View)

Figure 5 Temporal averaged result using constant viscosity with diffusion coefficient 1×10^{-6} (Top View)

Figure 6 Temporal averaged result using constant viscosity with diffusion coefficient 1×10^{-7} (Top View)

the upstream and downstream of actuating cylinder representing the blades are located at x=-0.5 and x=0.5. The reduction of the velocity just upstream of the turbine is indicative of the blockage effect and the interaction between the turbine structure and the fluid. And the slight increase of fluid velocity near both walls in *y*-direction is the result of the fluid and boundary interaction. The reduction of velocity downstream of the turbine indicates energy loss in the fluid which is the energy extracted by TEC. The reference simulated wake from 3D-CFT takes a short distance to recover, and the simulated wake of EPTM-3DCFT requires more time to recover, resulting in a longer wake. The TELEMAC result of flow wake reaches to about seven to

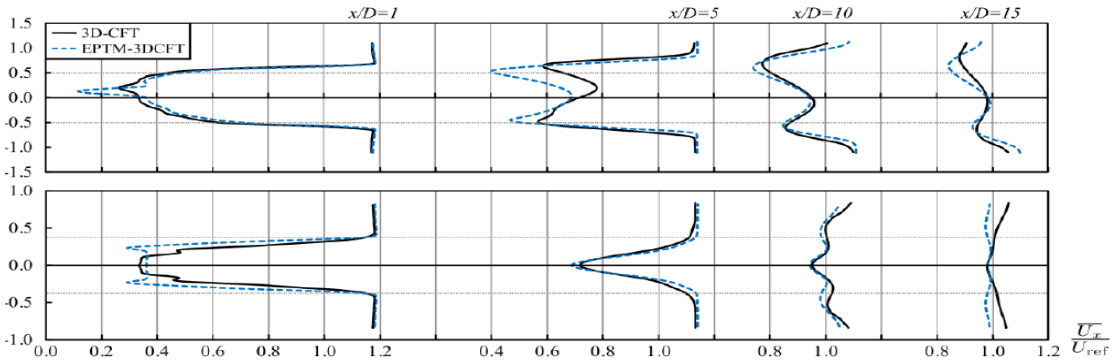

Figure 7 High fidelity and EPTM-3DCFT mean stream velocity profile at different locations, top: vertical direction, bottom: transverse direction [1]

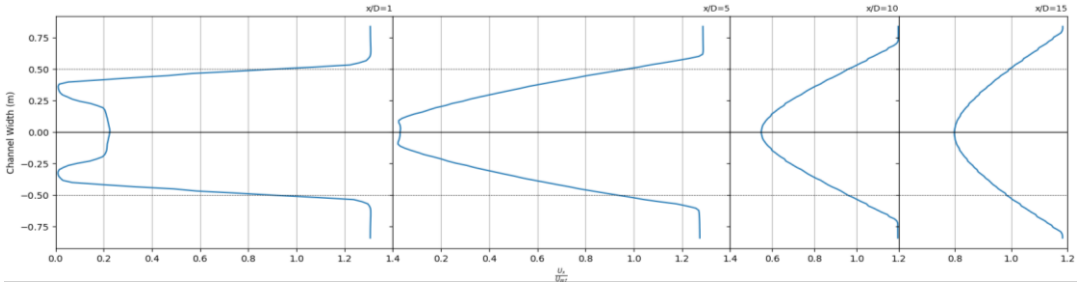

Figure 8 Velocity profile of the TELEMAC results using K-Epsilon method in vertical direction at different locations

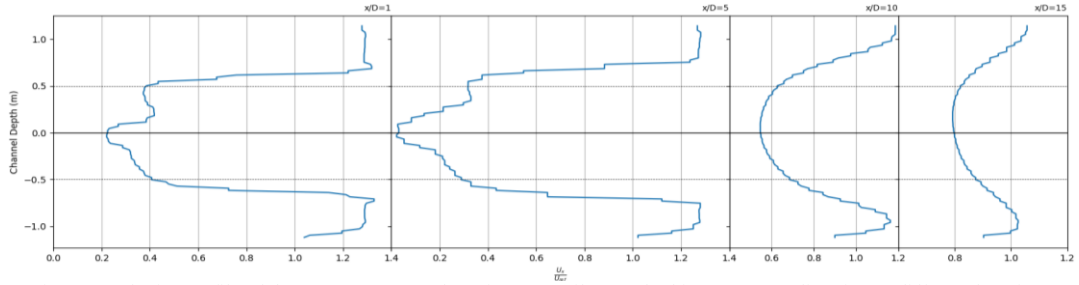

Figure 9 Velocity profile of the TELEMAC results using K-Epsilon method in transverse direction at different locations

Figure 7 showed the velocity profile of the high-fidelity reference simulation and EPTM-3DCFT velocity profile at 1, 5, 10, and 15 meters down stream of where the turbine is placed, given in this case the diameter of the turbine, D, is one meter. The black solid line represents the reference simulation while the blue dotted line shows the EPTM-3DCFT profile. Fig.8, and Fig. 9 are the velocity profile of the TELEMAC simulation using the K-epsilon method at different locations in vertical and transverse direction respectively. The jagged line in Fig. 8 is due to the fact that the data points had to be extrapolated from the 40 vertical layers defined. More vertical layers mean the result will be more refined at a cost of computational power. Both Fig. 8 and Fig. 9 resemble the velocity profile of the EPTM-3DCFT ones, except for when $x/D = 5$ in the transverse direction. As one can notice from the profiles, the simulated wake from TELEMAC takes notably longer to recover. the reduction in velocity is most prominent at both $x/D = 10$ and $x/D = 15$.

VI. CONCLUSIONS

This study utilized the Fortran programming language to add a module to TELEMAC-3D to mimic the results simulated using a high-fidelity CFD model and its simplified EPTM version. Actuating cylindrical region replaced the rotating blades, forming a time-averaged cylinder of drag coefficients around the turbine. Inverse distance weighting method was employed to distribute the input drag coefficients around the actuating region to ensure each mesh point has correct mappings of the drag coefficient, and therefore yields the correct drag force. A significant advantage of a coarser grid can reduce simulation time significantly, and the saved computing power can be allocated elsewhere or used to cover a large domain. The high-fidelity model 3D-CFT shown in Figure 3 took several months using 300 cores of a supercomputer centre. The EPTM-3DCFT model needed about 24 hours using 100 cores. The results obtained used the TELEMAC-3D model were achieved using a single core in a little more than half a day using the constant viscosity model.

The $k-\epsilon$ model adds about 25% to 40% of simulation time varying on the mesh resolution, including time step selection and the number of vertical layers. As suggested by the running time, the efficiency was significantly improved in magnitude by several hundred folds. The simulation was visualized using BlueKenue developed by the National Research Council, Canada. Results obtained were similar to the reference EPTM-3DCFT ones but exhibiting a longer wake region. Further sensitivity analysis, model improvement, and geometry adjustments are needed to achieve a better replication to the simulations obtained by [1].

Reference

[1] Bourget, Sébastien. "Development and assessment of a modeling method for hydrokinetic turbines operating in arrays." (2018).

[2] Gauvin-Tremblay, O., Kinsey, T., Descoteaux, P. and Dumas, G., 2019. *VALIDATION OF A SIMPLIFIED NUMERICAL MODEL USING LABORATORY TESTING RESULTS OF RIVER HYDROKINETIC TURBINE ARRAYS*. Quebec City: CFD Laboratory LMFN, pp.2-5, 18-22, 64

[3] Boudreau, M., Dumas, G. 2017. Comparison of the wake recovery of the axial-flow and crossflow turbine concepts. J. Wind Eng. Ind. Aerodyn. 165:137-152. doi: 10.1016/j.jweia.2017.03.010.

[4] Antoine Joly, Chi-Tuân Pham, Marc Andreewsky, Sylvain Saviot, Lauriane Fillot. Using the DRAGFO subroutine to model Tidal Energy Converters in TELEMAC-2D. TELEMAC User Club 2015, Oct 2015, Warrington, United Kingdom. hal-01702806

[5] Provan, Mitchel & Cornett, Andrew & Knox, Paul & Cousineau, Julien & Ferguson, Sean. (2019). EXPERIMENTAL STUDY OF THE WAKE PRODUCED BY SINGLE AND MULTIPLE CROSS-FLOW TURBINE. Journal of Ocean Technology. 14. 2-20. - Joly et al. (2015)

[6] Bourget S., Gauvin-Tremblay O., Dumas G. (2018): "Hydrokinetic turbine array modelling for performance analysis and deployment optimization", **Transactions of the CSME**, 42:370-381. http://dx.doi.org/10.1139/tcsme-2017-0088

[7] Wiki.opentelemac.org. 2020. User_Manual_TELEMAC-3D · Open TELEMAC-MASCARET. [online] Available at: <http://wiki.opentelemac.org/doku.php?id=user_manual_telemac-3d#modelling_turbulence> [Accessed 21 August 2020].

[8] Qhull.org. 2021. *Qhull code for Convex Hull, Delaunay Triangulation, Voronoi Diagram, and Halfspace Intersection about a Point*. [online] Available at: <http://www.qhull.org/> [Accessed 16 May 2020].

[9] *Man, Y., and Cousineau, J. (2021). "Julien-Cousineau/telemac3d-eptm". GitHub, <https://github.com/Julien-Cousineau/telemac3d-eptm.git> (Aug. 20, 2021).*

[10] Pham, C., & Joly, A. (2016). TELEMAC Modelling System [Ebook] (3rd ed., pp. 49-55). Opentelemac.org. Retrieved from http://www.opentelemac.org/downloads/MANUALS/TELEMAC-3D/telemac3d_user_manual_v7p1.pdf

Appendix

```
1.  dist = DSQRT((MESH3D%X%R(I3)-
2.  temptec%xyz(K,1))**2+(MESH3D%Y%R(I3)-
3.  temptec%xyz(K,2))**2+(MESH3D%Z%R(I3)-
    temptec%xyz(K,3))**2)

4.  IF (dist .LT. distThreshold) THEN
5.  IF (closest .EQ. -1.D0) THEN
6.  closest = dist
7.  effX = temptec%cd(K,1)
8.  effY = temptec%cd(K,2)
9.  effZ = temptec%cd(K,3)
10. ELSEIF (dist .LT. closest) THEN
11. closest = dist
12. effX = temptec%cd(K,1)
13. effY = temptec%cd(K,2)
14. effZ = temptec%cd(K,3)
15. ENDIF
16. ELSEIF (dist .LT. searchr) THEN
17. pointsInRange = .TRUE.
18. IDWSumX = IDWSumX+
        (temptec%cd(K,1))/(dist**2)
19. IDWSumY = IDWSumY+
        (temptec%cd(K,2))/(dist**2)
20. IDWSumZ = IDWSumZ +
        (temptec%cd(K,3))/(dist**2)
21. IDWSumDist = IDWSumDist + (1/dist**2)
22. ENDIF
23. IF (closest .EQ. -1.D0) THEN
24. IF (pointsInRange) THEN
25. L = L + 1
26. updateArray(L,1) = I3
27. updateArray(L,2) = IDWSumX/IDWSumDist
28. updateArray(L,3) = IDWSumY/IDWSumDist
29. updateArray(L,4) = IDWSumZ/IDWSumDist
30. ENDIF
31. ELSE
32. L = L + 1
33. updateArray(L,1) = I3
34. updateArray(L,2) = effX
35. updateArray(L,3) = effY
36. updateArray(L,4) = effZ
37. ENDIF

38. S1U%R(I3) = (0.5D0 * (-effX) *
    TcenterplaneA * TECAvgU**2.D0)/TECVolu
39. S1V%R(I3) = (0.5D0 * (-effY) *
    TcenterplaneA * TECAvgV**2.D0)/TECVolu
40. S1W%R(I3) = (0.5D0 * (-effZ) *
    TcenterplaneA * TECAvgW**2.D0)/TECVolu
```

Passing ship effects on water surface elevations

Juliette Parisi, Michael Turnbull, Nigel Tozer
Coasts and Ocean Group, HR Wallingford
Howbery Park, Wallingford, UK
j.parisi@hrwallingford.com
m.turnbull@hrwallingford.com
n.tozer@hrwallingford.com

***Abstract*— Following the work presented at the TELEMAC User Conference 2019 [1], about the ship-current interactions using TELEMAC and HR Wallingford's Navigation Simulator, the investigation of ship effects within TELEMAC has been expanded.**

TELEMAC-3D hydrodynamic model has been used to examine the effects of passing ships on water surface elevations at berth. A range of scenarios were modelled to investigate how water surface elevations varied as a result of the number of passing ships, variations in their speed, distance between passing ships, the effects of deceleration and altering slowing locations.

As well as estimating the free surface elevations, the TELEMAC model results were used to develop separate time series of surge and sway forces, and yaw moments that could be used as input to the SHIPMOOR dynamic mooring model. These time series were used to determine whether the effects of multiple passing vessels traveling in convoy, and decelerating upstream of a berth, are likely to result in increased vessel motions and mooring forces above certain thresholds.

I. INTRODUCTION

In an effort to understand the instances of mooring line failures at a berth located within a channel, HR Wallingford undertook a passing vessel study. A TELEMAC-3D hydrodynamic model was built and validated to determine the surface elevations at the berth for a range of variables, including ship speeds, distance between vessels and deceleration point.

II. MODEL SETUP

A. *Model extent and model bathymetry*

A TELEMAC-3D model (hydrostatic) was set up to cover approximately a 25 km length of channel, including the Port of interest. The area of the whole model is shown in Fig.1.

TELEMAC-3D is used for this study because it reduces the instabilities near the moving ship, compared to using TELEMAC-2D.

In terms of bathymetry, because of the limited available information outside the main navigation channel, the bathymetry in the shallow area to either side of the channel was estimated using two cross sections given: one cross section was at the north measurement site, the other one was at the south measurement site.

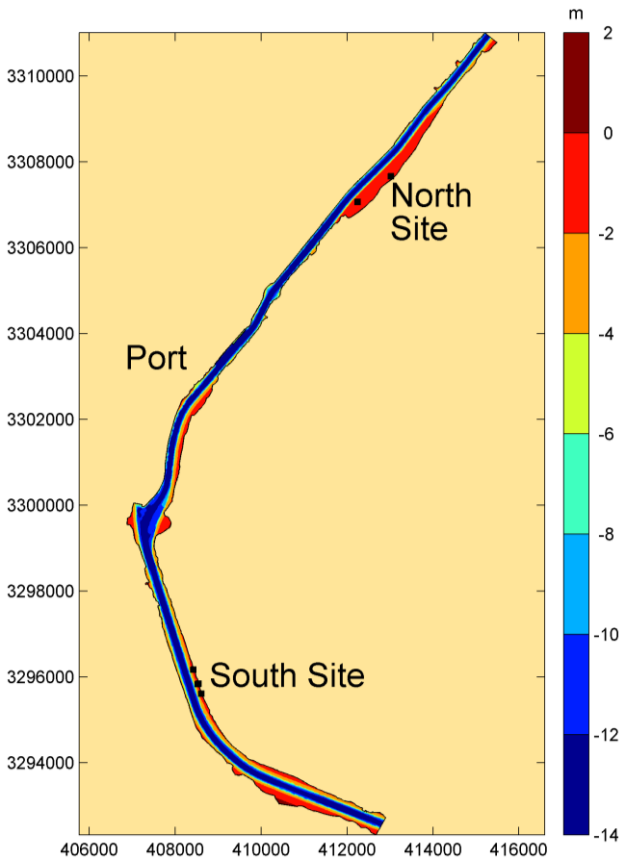

Figure 1: TELEMAC-3D model extent

B. *Model mesh*

The model horizontal mesh size is 5m along the centre line of the channel, where the ships travel. In the shallower areas, to the sides of the channel, the mesh size is 10m. In terms of vertical mesh size, the model was set up to use only three horizontal planes. Sensitivity tests were carried and the number of planes had little impact on model results at locations of interest. The model mesh for the area around the berth of interest is shown in Fig. 2.

C. *Ship representation*

The moving ships are modelled by imposing a pressure field on the surface corresponding to the hull shape. The applied pressure is proportional to the depth of the hull below the water free surface, according to the equation below:

$$P = \rho g d \qquad (1)$$

where P is the pressure (in kg/ms^2 or N/m^2), ρ is the sea water density (1,025 kg/m^3), g is the acceleration due to gravity (9.81 m/s^2) and d is the depth of the ship's hull below the water free surface (in m).

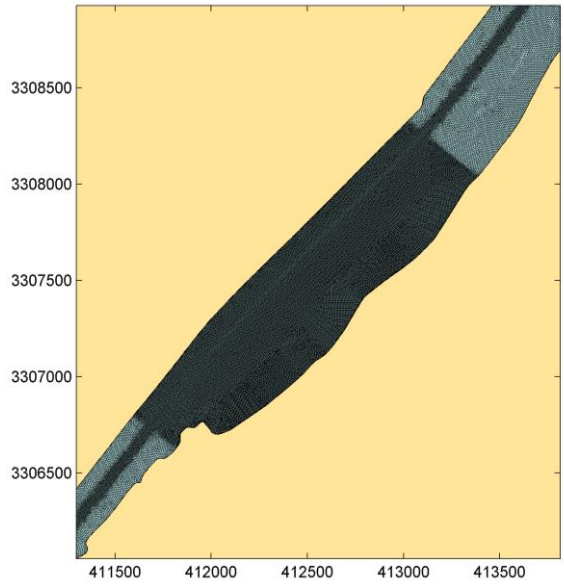

Figure 2: Model mesh at the berth of interest

III. Model Validation

To validate the TELEMAC-3D model, runs were carried out and compared against measured surface elevation and current speed data for passing ships. Model runs were carried out where the most complete information on vessel characteristics and measurements were presented.

The model was run for two scenarios (Ship 1 and Ship 2) where surface elevations and currents were measured at locations at the North site and South site, in relatively shallow water away from the main shipping channel. The model results are compared with time histories of observed level and current speed at a number of locations shown in Fig. 3 and Fig. 4.

A. *Ship 1*

Ship 1, a tanker 250 m long, 41 m wide with a 12 m draught, travelled inbound to the North at slack tide, so no mean flow has been imposed in the model. The ship was travelling at 8.6 knots past the South site and at 8.3 knots past the North site.

The modelled ship track was shifted 25 m west to the centre of the channel. The vessel track was not provided and was therefore part of the validation process.

Fig. 5 to Fig. 8 show comparison between predicted and measured water elevations. For the South Pressure Cell 1 and the South Capacitance Gauge, the modelled drop in level and subsequent rise in level is in good agreement with measurements. For the North pressure Cell (Fig. 7), the model matches the observations for the drop in the level and the start of the following rise in level, but does not rise to the observed level for the later time.

For the North Capacitance Gauge (Fig. 8), the drop in the model elevation agrees well with the observations, but the model rise in level occurs later than in the observations. An alternative point (40m away from the channel) was taken in the model to compare against the North Capacitance Gauge. The comparison for this point (Fig. 9) shows that the level rise in the model agrees better with the observed rise.

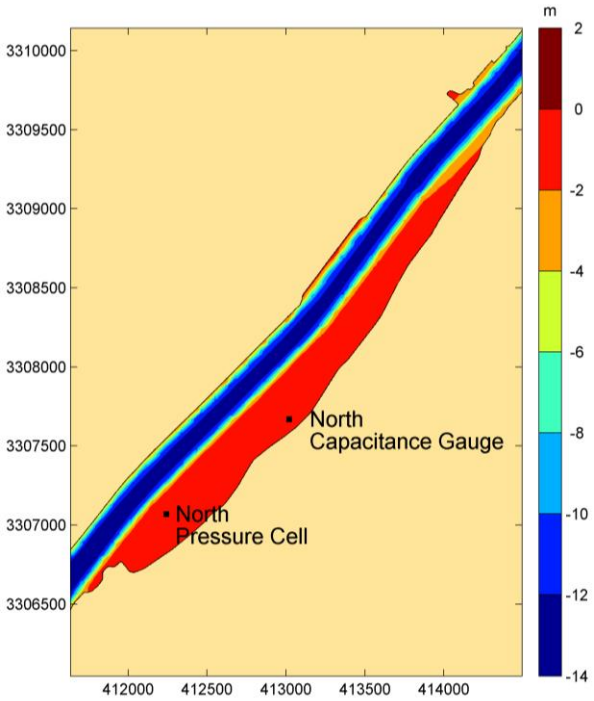

Figure 3: North Site

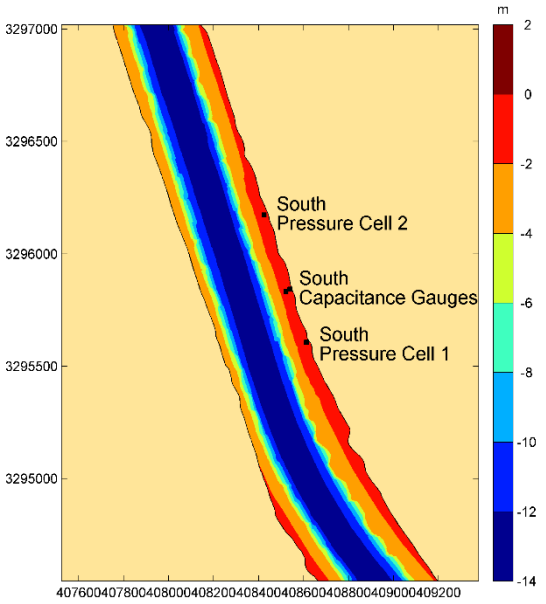

Figure 4: South Site

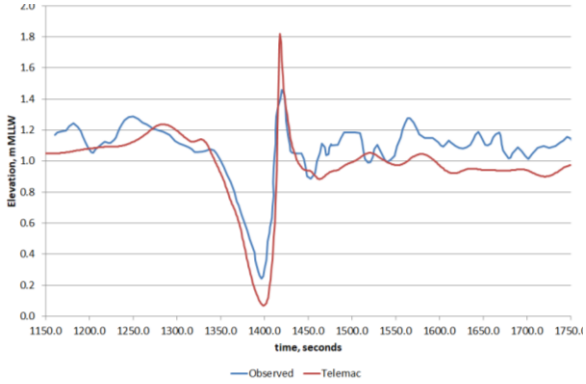

Figure 5: Ship 1. Elevation time series. South Pressure Cell 1.

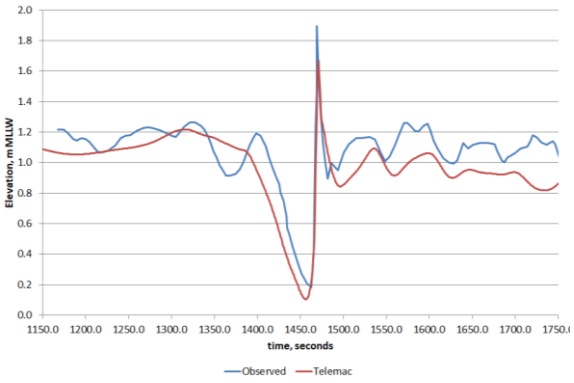

Figure 6: Ship 1. Elevation time series. South Capacitance Gauge (shoreline)

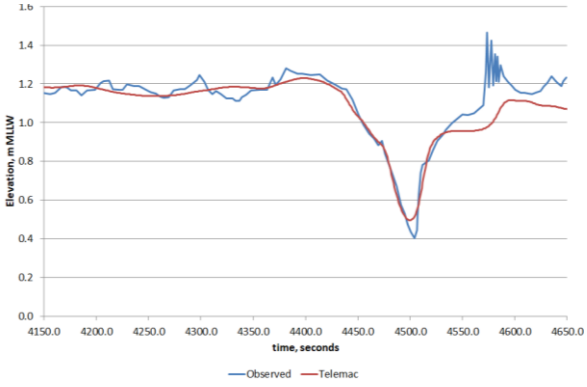

Figure 7: Ship 1. Elevation time series. North Pressure Cell

Figure 8: Ship 1. Elevation time series. North Capacitance Gauge

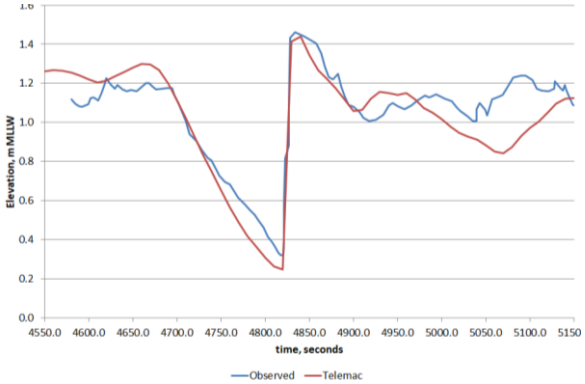

Figure 9: Ship 1. Elevation time series. North Capacitance Gauge. Alternative point

B. *Ship 2*

Ship 2, a tanker 250 m long, 42 m wide with a 11 m draught, travelled inbound at slack tide, so no mean flow has been imposed in the model. The ship was travelling at 8.2 knots past the South site.

Fig. 10 to Fig. 12 show comparison between predicted and measured water elevations.

Fig. 10 shows the model matches very well the observations for the drop in level and subsequent rise at South Pressure Cell 1. Fig. 11 shows that the model drop and rise are slightly bigger than observed and the rise occurs slightly earlier at South Pressure Cell 2. For South Capacitance Gauge (channel), Fig. 12 shows that the drop and rise are about the same magnitude as observed, but the rise occurs slightly later.

Predicted current speed were compared with observed speed at South Capacitance Gauge (channel), 0.6m above the bed. Fig. 13 shows that the value of the predicted peak speed is slightly smaller than the observed peak. However, the observed speed is noisy and seems to indicate a mean channel flow of about 0.3 m/s. If this mean speed is added on to the predicted peak, then the agreement between the predictions and the observations is better.

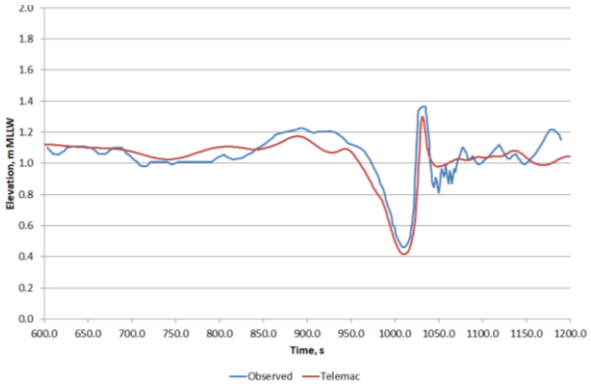

Figure 10: Ship 2. Elevation time series. South Pressure Cell 1.

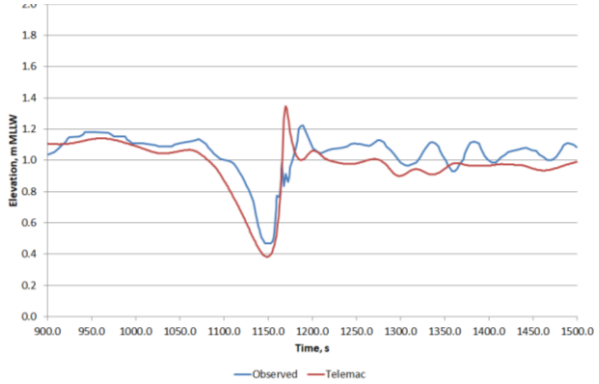

Figure 11: Ship 2. Elevation time series. South Pressure Cell 2.

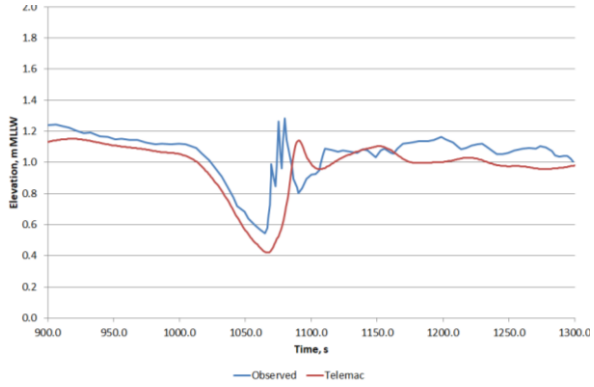

Figure 12: Ship 2. Elevation time series. South Capacitance Gauge.

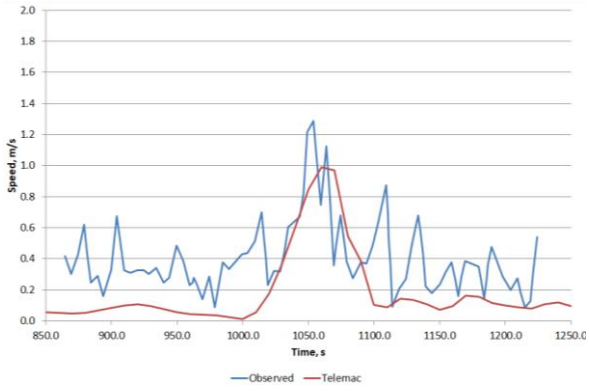

Figure 13: Ship 2. Speed time series. South Capacitance Gauge (channel).

C. *Model validation conclusions*

The overall conclusion from the validation of the TELEMAC-3D model is that the model reproduces the measured surface elevations and currents due to passing ships well. This is bearing in mind the limited information provided on which the model runs were performed, e.g. the bathymetry in the shallow regions where the measurements were taken and the vessel track.

IV. PASSING VESSEL STUDY

In order to gain a good insight into the important hydrodynamic processes, including the interaction of two ships and the deceleration approaching the berth, TELEMAC-3D model runs were carried out covering a range of scenarios. The scenarios, as summarised in Table 1, were selected to account for:

- 2 operating vessel speeds
- Up to 2 vessels in convoy
- Distance between vessels
- An example / typical deceleration profile based on data provided by the pilots.

Further tests were also performed to examine the sensitivity of the results to vessel transit direction and the effect of tidal currents. To generate the current in the model, a level difference at the two ends of the model was applied so that the target current speed was achieved. For example, for Case 15, with a current speed of 1.5knot ebb current the surface elevation level was raised by 0.15 m at the North and lowered by 0.15 m at the South. This method was used because imposing the desired current directly at a model boundary caused the model to become unstable.

All model runs were carried out with a ship moored starboard side alongside Berth 3 and a passing ship transiting along the centreline of the channel.

Track information for two ships, from data provided, was used to derive a representative deceleration profile for the modelling. Fig. 14 shows the ship speeds plotted against the distance north of the berth. For the test runs with deceleration, the ship moved at 8 knots until it was approximately 1.5Nm upstream of the berth. It then decelerated uniformly until it was at 3 knots, at the berth. The same deceleration profile was also applied to test cases where the point at which the ships start to decelerate was moved 1Nm further upstream (2.5Nm upstream). These two locations are shown in Fig. 15.

The results of the TELEMAC-3D modelling are presented as time series plots of the free surface elevation at a point along the centre of the navigation channel, adjacent to the Berth 3. Each time series graph shows the onset of the vessel generated pressure waves adjacent to the berth, the passing of the ship or ships, shown as the abrupt discontinuity in the time series record, and the residual disturbance after the vessel has passed, before returning back to a relatively undisturbed state.

The time series plots are grouped so that the relative differences can be compared between different simulations. For example, Cases 1, 5, and 9 are grouped together in Fig. 16, as these all show the results from one or two outbound vessels all travelling at constant speed of 4 knots, and if there are two vessels they have a separation of 1 or 2 nautical miles. This figure shows that although the time series are different, the general amplitude and maximum free surface elevation is higher for two vessels (Cases 5 and 9) compared with one vessel (Case 1).

Case	Number of ships	Constant overground speed (knots)	Passing ship course	Variable overground speed deceleration profile (knots)	Deceleration point (upstream of Berth 3)	Separation when Ship 1 is passing berth (Nm)	Current speed (knots)	Current direction
1	1	4	Outbound		n/a		0	
2	1	3	Outbound		n/a		0	
3	1		Outbound	8 to 3	1.5Nm		0	
4	1		Outbound	8 to 3	2.5Nm		0	
5	2	4	Outbound		n/a	1	0	
6	2	3	Outbound		n/a	1	0	
7	2		Outbound	8 to 3	1.5Nm	1	0	
8	2		Outbound	8 to 3	2.5Nm	1	0	
9	2	4	Outbound		n/a	2	0	
10	2	3	Outbound		n/a	2	0	
11	2		Outbound	8 to 3	1.5Nm	2	0	
12	2		Outbound	8 to 3	2.5Nm	2	0	
13	1	4	Inbound		n/a		0	
14	1	3	Inbound		n/a		0	
15	1	4	Outbound		n/a		1.5	Ebb
16	1	3	Outbound		n/a		1.5	Ebb
17	1	4	Outbound		n/a		1.5	Flood
18	1	3	Outbound		n/a		1.5	Flood
19	2		Outbound	8 to 3	1.5Nm	1	1.5	Flood
20	2		Outbound	8 to 3	2.5Nm	1	1.5	Flood

Table 1. Scenarios modelled

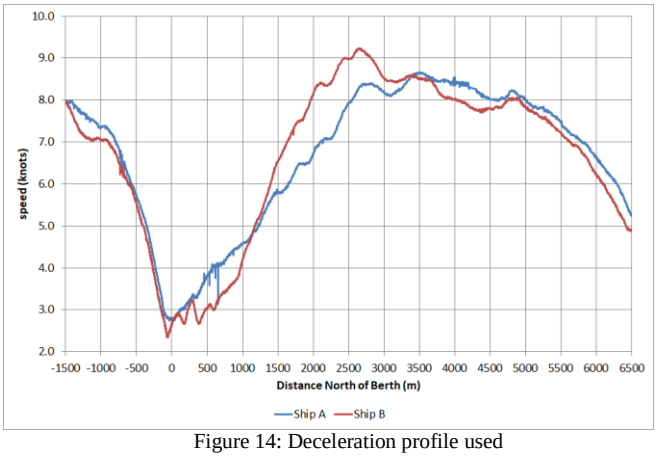

Figure 14: Deceleration profile used

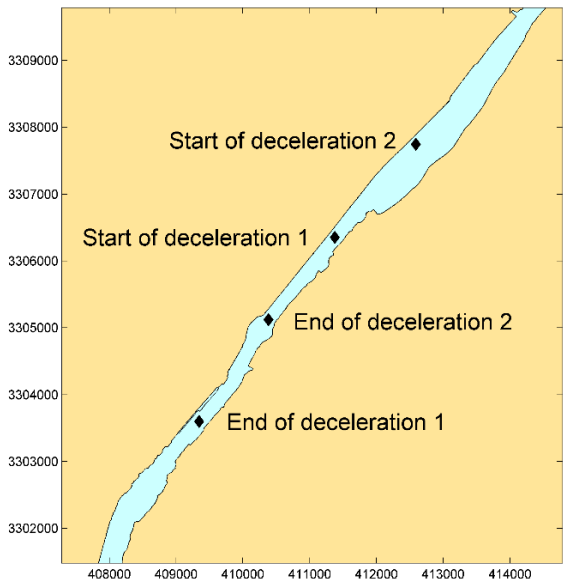

Figure 15: Location of deceleration points considered in the modelling

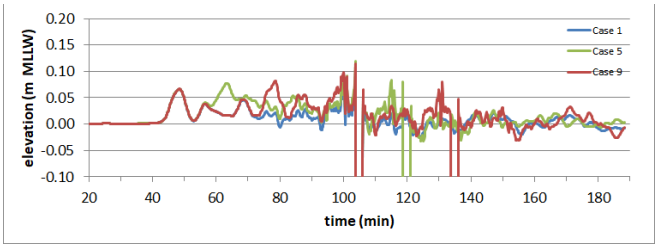

Figure 16: Model elevation time series at berth. Cases 1 (1 ship), 5 (2 ships 1Nm separation) and 9 (2 ships 2Nm seperation). Ship speed of 4 knots

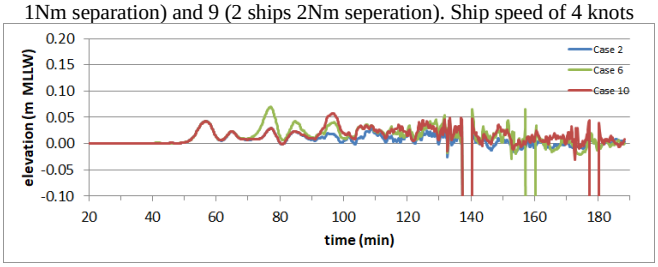

Figure 17: Model elevation time series at berth. Cases 2 (1 ship), 6 (2 ships 1 Nm separation) and 10 (2 ships 2 Nm seperation). Ship speed of 3 knots

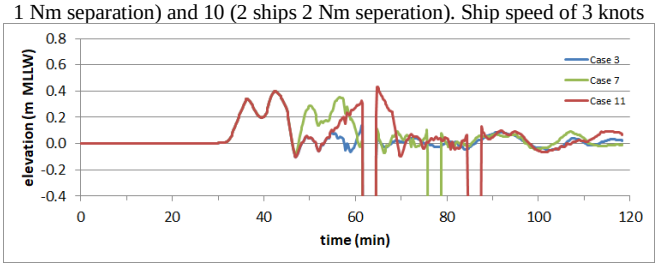

Figure 18: Model elevation time series at berth. Cases 3 (1 Ship), 7 (2 ships 1 Nm separation) and 11 (2 ships 2 Nm seperation). 8 to 3 knots, 1.5 Nm decleration

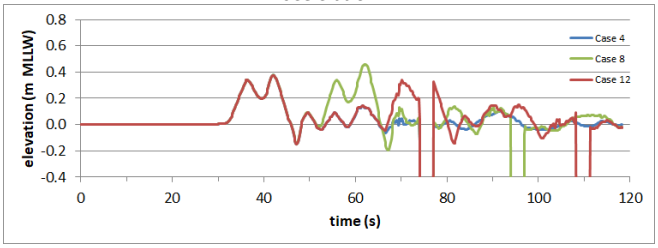

Figure 19: Model elevation time series at berth. Cases 4 (1 ship), 8 (2 ships 1 Nm separation) and 12 (2 ships 2 Nm seperation). 8 to 3 knots, 2.5 Nm deceleration

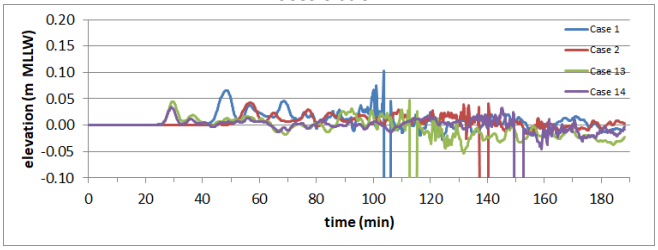

Figure 20: Model elevation time series at berth Cases 1 (inbound ship 4 knots), 2 (inbound ship 3 knots), 13 (outbound ship 4 knots) and 14 (outbound ship 3 knots)

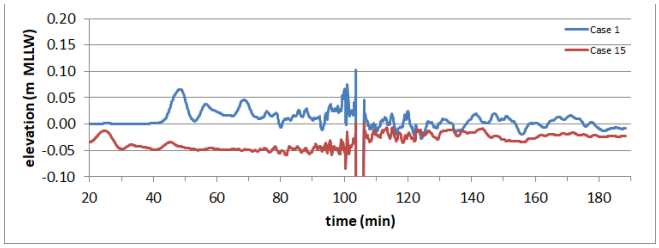

Figure 21: Model elevation time series at berth Cases 1 and 15 (effect of ebb current, 4 knots)

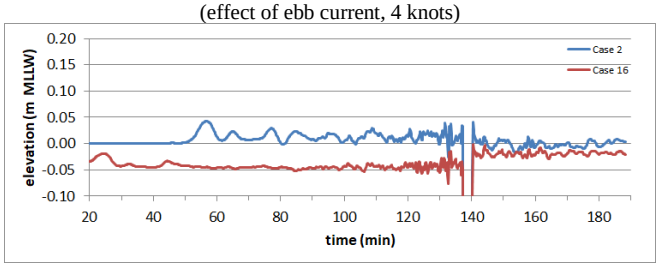

Figure 22: Model elevation time series at berth Cases 2 and 16 (effect of ebb current, 3 knots)

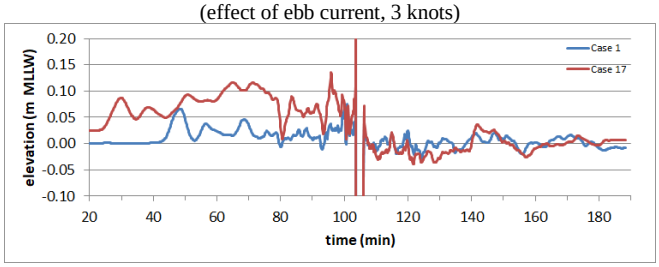

Figure 23: Model elevation time series at berth Cases 1 and 17 (effect of flood current, 4 knots)

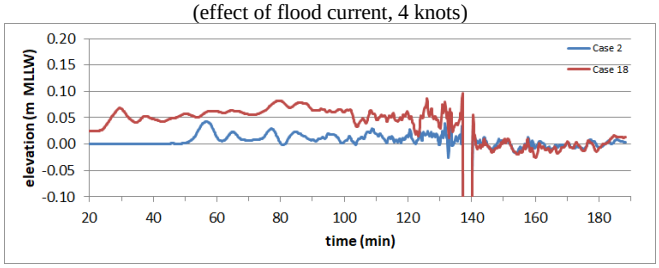

Figure 24: Model elevation time series at berth Cases 2 and 18 (effect of flood current, 3 knots)

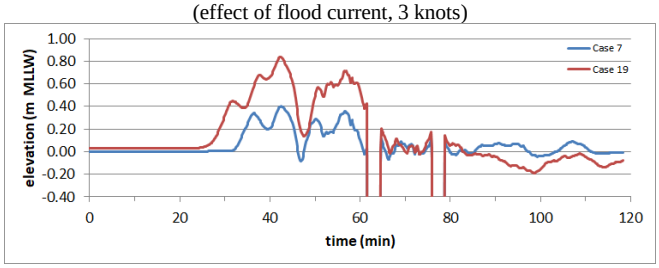

Figure 25: Model elevation time series at berth Cases 7 and 19 (effect of flood current, 8 to 3 knots, 1.5 Nm deceleration)

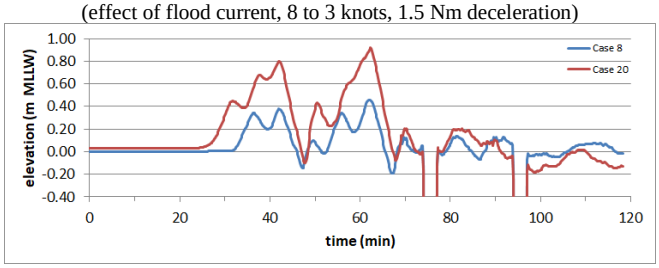

Figure 26 : Model elevation time series at berth Cases 8 and 20 (effect of flood current, 8 to 3 knots, 2.5 Nm deceleration)

Fig. 17 shows the corresponding results, but for vessels traveling at 3 knots. Compared with Fig. 16, this figure shows that travelling at 3 knots, leads to a noticeably lower free surface elevation, but again two vessels travelling in convoy leads to generally higher free surface elevations at the berth location.

The results of tests including vessel deceleration from 8 to 3 knots are shown in Fig. 18 and Fig. 19. Fig. 18 shows the results with the deceleration point (approximately 1.5Nm upstream of Berth 3), whereas Fig. 19 shows the results from beginning to decelerate approximately 2.5Nm upstream of Berth 3. Both sets of results show a significant increase in the water surface elevations when there are two ships (Cases 7 and 11 or Cases 8 and 12), compared with one ship (e.g. Case 3 or Case 4).

The effect of vessels travelling inbound (to north) as opposed to outbound (travelling south) is illustrated in Fig. 20. This figure show a similar range in the predicted free surface elevations, with the high speed (4 knots for Cases 1 and 13) leading to slightly higher surface elevations than when travelling at 3 knots.

Fig. 21 and Fig. 22 show the effect of an ebb current of 1.5 knots, i.e. in the same direction of the outbound ships being simulated. To generate the target current speed, a level difference at the two ends of the model was applied. For example, for Case 15 (Fig. 21) with an ebb current of 1.5 knots, the level was raised by 0.15 m at the North and lowered by 0.15 m at the South. This resulted in an initial condition at the berth where the level was below zero. This negative elevation continues throughout the run. For both ebb current cases, the predicted free surface elevation range is noticeably lower when including the tidal current effect.

In contrast, as shown in Fig. 23 to Fig. 26 the effect of the 1.5 knots opposing current, noticeably increases the predicted free surface elevations. To generate the flood current, a level difference at the two ends of the model was applied. This resulted in an initial condition at the berth where the level was above zero. This positive elevation continues throughout the run. The increase in predicted surface elevation shown is not surprising as the ship speed through the water is increased by the speed of the opposing current. For the Cases 19 and 20 the effect of the opposing current gives the highest predicted free surface elevations of all simulations.

A. *Vessel study conclusions*

If a single ship passing at a constant speed of 4 knots is taken as the reference case, representative of the limit of acceptable passing speeds from earlier analysis, the model predicts water surface elevations to increase slightly when ships are traveling at a constant speed in convoy. However, when the effects of deceleration are considered, model predictions of the water surface elevations are significantly greater than the reference case. Also important is when there is a current running against the direction of ship travel, as the associated water surface elevations also noticeably increase.

Whilst the model results presented provide a useful insight into the free surface elevations and currents associated with the different scenarios, it is not possible to conclude from these results alone that the increased water surface elevations will result in a corresponding increase in moored vessel motions and mooring line forces. TELEMAC-3D modelling results were then used to develop a force time series as input to the SHIPMOOR model in order determine whether the increased water surface elevations resulted in a corresponding increase in moored vessel motions and mooring line forces.

V. SUMMARY

A computational modelling study using a TELEMAC-3D model has been performed to examine the effects of passing ships on water surface elevations. After verifying that the model performed well against measurements, a range of scenarios were modelled to investigate how water surface elevations varied as a result of the number of passing ships, variations in their speed, distance between passing ships, the effects of deceleration and altering slowing locations.

As well as estimating the free surface elevations, the TELEMAC-3D model results were used to develop separate time series of surge, sway forces, and yaw moments that could be used as input to the SHIPMOOR dynamic mooring model. These time series were used to determine whether the effects of multiple passing vessels traveling in convoy, and decelerating, are likely to result in increased vessel motions and mooring forces above that estimated in the previous passing vessel study.

When compared against a case of a single passing vessel travelling at a constant speed, vessel surge motions and mooring forces are predicted to increase as a result of passing vessels travelling in convoy and decelerating upstream.

It has not been possible to fully understand the complex relationships between the forcing parameters as part of this study. Further research is required to further understand the relationship between the following parameters and the relative mooring forces and surge motions:

- the location of the deceleration point
- distance between vessels in convoy and passing speed
- width and draught of the ships
- direction and magnitude of the currents

REFERENCES

[1] J. Parisi, M. Turnbull, A. Cooper, and J. Clarke (2019) “Ship-current interactions with TELEMAC,” *XXVIth TELEMAC-MASCARET User Conference*, 2019.

Recent improvements for the Berre lagoon modelling with TELEMAC-3D

Elisabeth Justin-Brochet
EDF R&D – LNHE, ENPC, LHSV
6 quai Watier, 78400 CHATOU, FRANCE

Chi-Tuân Pham, Javier Vidal-Hurtado
EDF R&D – LNHE
6 quai Watier, 78400 CHATOU, FRANCE
chi-tuan.pham@edf.fr

***Abstract*— The Berre lagoon (South East of France near Marseille) is among the largest brackish lagoons in Europe, connected to the Mediterranean Sea through the Caronte channel, while receiving freshwater from two tributaries and a hydroelectric power plant. An average depth of 6 m makes the lagoon strongly sensitive to wind conditions, i.e. when the mistral is not blowing, thermohaline vertical stratification occurs in the lagoon. Anthropogenic activities (i.e. industry and urbanisation since mid-20th century) have seriously affected its ecosystem (strong variability of salinity, water column stratification, pollutants, and eutrophication). A continuous and real-time hydro-environmental monitoring program has been carried out since 2006. Previous TELEMAC-3D models of the Berre lagoon had been developed at Laboratoire National d'Hydraulique et Environnement (LNHE) for simulating hydrodynamics, salinity and temperature. The aim of this paper is to present recent improvements of the TELEMAC-3D model to accurately reproduce stratification and mixing in the Berre lagoon, with particular focus on the effects of the advection schemes and turbulence models. The use of the LIPS scheme for the advection of tracers salinity and temperature, combined with the Yap correction for the *k*-ε turbulence model are the options that have mostly improved the previous TELEMAC-3D model of the Berre lagoon without tidal flats.**

I. INTRODUCTION

EDF manages hydropower plants along the Durance-Verdon chain to produce electricity. This chain releases fresh water into the Berre brackish lagoon, which is connected to the Mediterranean Sea and has two tributaries. One of the main characteristics of the Berre lagoon is the strong haline stratification (i.e. freshwater and saltwater entering the lagoon do not mix easily due to the difference of density).

One of the goal of the TELEMAC-3D modelling of the Berre lagoon is to reproduce accurately stratification and mixing events, which is a key factor to represent the lagoon behaviour. It has been used and improved for years. The aim of this paper is to show recent improvements by using some recent features in TELEMAC-3D, dealing with less diffusive advection schemes and variants of turbulence models.

The second section of this paper presents the studied area and available measurements. The third section describes the preliminary TELEMAC-3D model of the Berre lagoon and the features that are tested (mainly advection schemes and turbulence models). Results of different tests and comparison with *in situ* measurements are given in section 4, followed by conclusions in section 5.

II. PRESENTATION OF THE STUDIED AREA

A. Location and environment

The Berre lagoon is located in the south of France (west of Marseille), at the end of the Durance canal (a chain of hydropower plants) that diverges the water from the Durance River (250 km long) to the lagoon. The lagoon has a surface of 155 km^2 with a volume of water around 980 Mm^3. Being connected to the Mediterranean Sea through the Caronte channel, the lagoon receives sea salty-water in tide-driven pulses. Two rivers (Arc and Touloubre) and the EDF Durance Canal releases fresh water (through the Saint-Chamas hydropower plant) into the lagoon, in addition inputs from rain, runoff and wastewater treatment plants. The mean annual flowrate through Saint-Chamas power plant is between 20 to 30 m^3/s (since 2006), whereas mean flowrate of rivers Arc and Touloubre is around 6 m^3/s. Dense seawater enters during rising tide and plunges to the bottom, whereas fresh water spreads over the surface where it mixes vertically in the first few meters. Therefore, the lagoon remains stratified when there is no strong wind (the salinity difference between the bottom and the surface can be up to 10 g/L). During summer and with weak wind, anoxia (oxygen depletion) often appears in the bottom layers. Anoxia enhances the release of unwanted components and lethal gases from the sediments as well as it produces mortality of organisms by asphyxia. Only long and strong wind events (mistral events) can mix completely the lagoon and re-oxygenate the bottom layer.

B. In situ measurements

Many *in situ* measurements are available in the lagoon: EDF owns four measuring stations where temperature and salinity (CTD Seabird SBE-19) have been recorded every hour since 2006. Three stations (SA1, SA2 and SA3) are located inside the lagoon, whereas the fourth (SA4) is located in the Caronte channel (Fig. 1). Measurements are recorded at five different depths. At SA4 station, velocity in the water column (Teledyne-RDI ADCP) is also measured every hour, so that flow rate exchanges between the lagoon and the Mediterranean Sea could be calculated. At the three other stations, a 3-month period in 2008 of velocity measurements is also available.

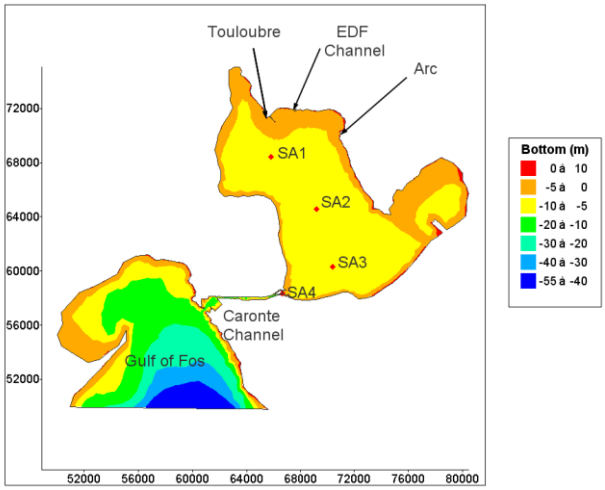

Fig 1: Berre lagoon extent and location of the measurement stations.

Metocean data are also used in this paper as input of the TELEMAC-3D model: meteorological data, flowrates of rivers or tidal levels. Meteo France data at Marignane are used, on the Berre lagoon bank: wind magnitude and direction, air temperature, relative humidity, air pressure, cloud coverage, rain and solar radiation. For the Gulf of Fos, tidal levels at Marseille and in the Gulf of Fos, as well as salinity and temperature in the Gulf of Fos are used. Flowrates and temperatures of the rivers are regularly measured by the Rhône-Méditerranée-Corse Water Agency. The flowrates and temperature of water released by the Saint-Chamas station are provided by EDF every hour.

III. Presentation of the TELEMAC-3D model

The previous release of the TELEMAC-3D Berre lagoon model was built in 2016. The main characteristics of the 3D model have been kept for this paper and are reminded here.

A. *Model domain and bathymetry*

The computational area includes the Gulf of Fos, the Caronte channel and the Berre lagoon (Fig. 1).

The mean depth of the lagoon is 6 m and maximum depth is around 10 m, reaching 45 m in the Gulf of Fos.

B. *Computational mesh*

The 2D mesh is made of 4,214 nodes and 7,707 triangular elements, refined where velocities are large: in the Caronte channel and the three freshwater intakes (Arc and Touloubre rivers, and Saint-Chamas power plant). The elements sizes vary from 1 km for the largest elements to 3 m for the smallest ones.

There are 41 horizontal planes over the vertical with fixed elevation (except the last one following the free surface). Combined with the 2D mesh, the 3D mesh is made of 172,774 nodes and 308,280 prisms. The horizontal planes are tightened where the salinity gradients are strong, around 8 m deep. As the bottom is not flat, and in order to prevent from artificial velocities, some planes are crushed, in particular near the solid boundaries.

The 3D mesh can be seen in Fig. 2 with the vertical direction distorted with a ratio of 250.

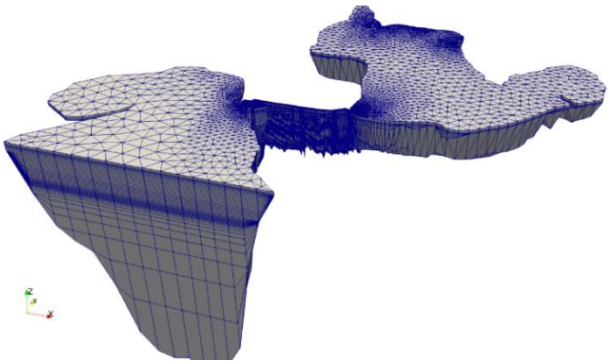

Fig 2: The Berre lagoon 3D mesh.

C. *Initial and boundary conditions*

The TELEMAC-3D model of the Berre lagoon has four open boundaries. Three of them where flowrates are prescribed corresponding to freshwater (Arc, Touloubre and Saint-Chamas power plant): daily data for the two rivers and hourly data for the power plant are interpolated at each time step. Salinity and temperature are also prescribed at these open boundaries with the same frequency.

The fourth and last liquid boundary corresponds to the interface between the Gulf of Fos and the Mediterranean Sea where the free surface elevation is prescribed, corresponding to the sea level estimated from both Marseille and Fos tidal gauges. At this location, the flowrate is not prescribed, so the flow can be entering or exiting. At every time step, if the flow comes in, temperature and salinity are prescribed; if the flow goes out, the two tracers are let free.

A few freshwater intakes have not been measured: they are mainly runoff on the banks (more than 70 km long). This flowrate has been estimated and is taken into account by increasing the Arc and Touloubre flowrates with a few cubic meters per second (~ 2 m^3/s).

Meteo data (wind, temperature, pressure, humidity, cloud coverage, rainfall, and solar radiation) are given as input of the TELEMAC-3D model since the THERMIC model of the WAQTEL module is coupled to TELEMAC-3D to take into account heat exchange of water with atmosphere. Meteo data are available hourly and linearly interpolated at every time step.

At the initial time step, zero velocities are taken. The water level is taken equal to the one prescribed at the Gulf of Fos boundary. Temperature and salinity are initialised in different areas, in particular with salted concentration = 38 g/L in the Gulf of Fos. In the Caronte channel and inside the Berre lagoon, the computation is initialised with the measurements at SA4 and SA3 respectively. As the stratification is usually around 8 m deep, initial values below 8 m are taken equal to

the deepest measurement, whereas above 8 m, initial values are taken equal to the average of the four other measurements.

D. Numerical settings

The initial setting for advection schemes is:

- Method of characteristics (MOC) for velocities and *k*-ε variables,
- PSI scheme for tracers (temperature and salinity).

Since TELEMAC release v7p2, recent advection schemes belonging to the MURD family are available in TELEMAC-3D after Sara Pavan's PhD [1]: Predictor-Corrector schemes (PC) [2] which does not work with tidal flats and LIPS (Locally Implicit Predictor-corrector Scheme) which works with tidal flats [3].

To prevent from issues with tidal flats, in the TELEMAC-3D model of Berre lagoon, which used the PSI scheme (this one also does not work with tidal flats as the PC scheme), the bottom elevation is lowered at a maximum value of -0.5 m to be always wet. To compare the results obtained from different advection schemes, the same modification of the bottom elevation is kept.

Accuracies to solve linear system are equal to 10^{-6} except for the diffusion of tracers where an accuracy of 10^{-9} is retained to ensure mass conservation of tracers (salinity and temperature).

E. Physical settings

Nikuradse law is chosen to model friction on the bottom with a roughness height equal to 0.1 mm in the Berre lagoon (fine sand) and 10 cm in the Caronte channel (concrete bottom covered by mussels).

To model thermohaline stratification of the lagoon, a density law of water depending on temperature and salinity is used (corresponding to keyword DENSITY LAW = 3):

$$\rho = \rho_0\left(1 - (7.10^{-6}(T - T_0)^2 - 750.10^{-6}.S)\right),$$

With ρ density, T temperature, S salinity, T_0 reference temperature (= 4° C) and ρ_0 reference density at T_0 (= 999.972 kg/m^3).

The non-hydrostatic version of TELEMAC-3D is used.

The Coriolis force is taken into account due to the wide surface of the Berre lagoon.

In 2016, the standard *k*-ε turbulence model was used both in horizontal and vertical directions. Other turbulence models (mixing length models with various mixing length formulae with or without damping functions, *k*-ω) have been tested and compared in this paper, but also variants of the *k*-ε model (limitation of the production term and the Yap correction).

F. Parallel setting

Every computation is run on a cluster with 112 cores (= 4 nodes of 28 cores, 128 Go RAM, Intel Xeon CPU E5-2680 v4 @ 2.4 Ghz).

IV. Results

In order to study the impact of advection schemes when modelling salinity, two 1-month periods have been chosen:

- September 2006 when hourly measurements of salinity started in the lagoon. During this month, two periods when mistral blew occurred, from 18th to 19th and from 26th to 27th. Large water releases from the power plant were observed during this period: from 13th to 16th and from 25th to 26th. This month is representative of how the lagoon behaves,
- January 2008, when four measurement stations were active. There was a lot of wind during the first half of this month and water releases from the power plant were often done, in particular during the second half of this month.

Salinity measurements are compared to computational results at stations SA3 and SA4 at the surface and at the bottom.

From this section, "reference" means the options used in 2016 (in particular PSI scheme for the advection of tracers, method of characteristics for the advection of velocities and *k*-ε, and a 10 s time step).

A. Advection of tracers salinity and temperature

Results with LIPS and PC schemes are compared to results from the PSI scheme (used as a "reference" computation) for the advection of tracers only. The advection of velocity components and *k*-ε is computed with the method of characteristics.

For the PC scheme, a 5 s time step has to be used (instead of 10 s for the "reference" model) so that advection steps converge. Although with other schemes, larger time steps can be used, comparisons are shown only with a 5 s time step. Whereas computations with PSI and LIPS schemes need similar CPU times (3 h 15 min, 4 h 15 min respectively), using the PC scheme requires nearly a time twice longer without sub-steps or corrections (8 h 20 min).

During September 2006, the succession of stratification and mixing is well reproduced by the computation. Nevertheless, the measured stratification (6-7 g/L between bottom and surface) is stronger than the modelled one (~ 4 g/L). (Fig. 3).

However, at SA3 station, using the LIPS scheme yields a stronger stratification than the "reference" PSI scheme (around 1 g/L), as the PC scheme but better modelled with the LIPS scheme (Fig. 3). We can assume that numerical diffusion is partly responsible for the stratification weakness and that the LIPS scheme (less diffusive) may correct this drawback. A longer simulation lasting one whole year confirms this idea for the LIPS scheme (Fig. 4). No result is given for one year with the PC scheme as CPU time is big.

As the LIPS scheme is suitable for CPU time and quality of results, it should be used when advecting tracers for this TELEMAC-3D model and is then used from subsection IV.C.

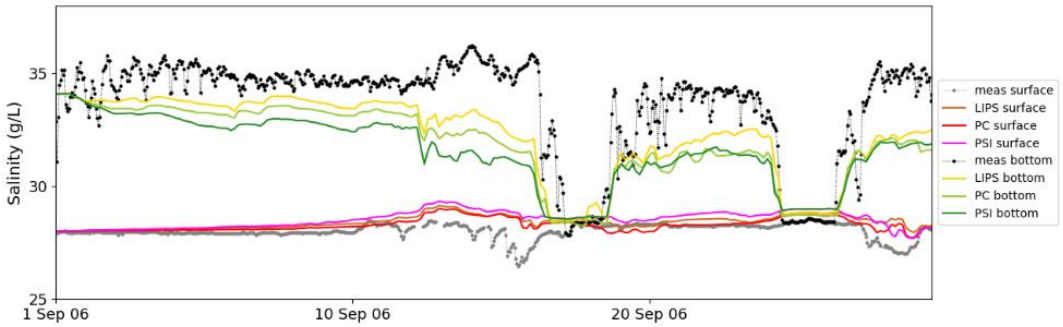

Fig 3: Salinity at SA3 in September 2006. Measurements (points), LIPS, PC and PSI schemes for tracers only (solid lines).

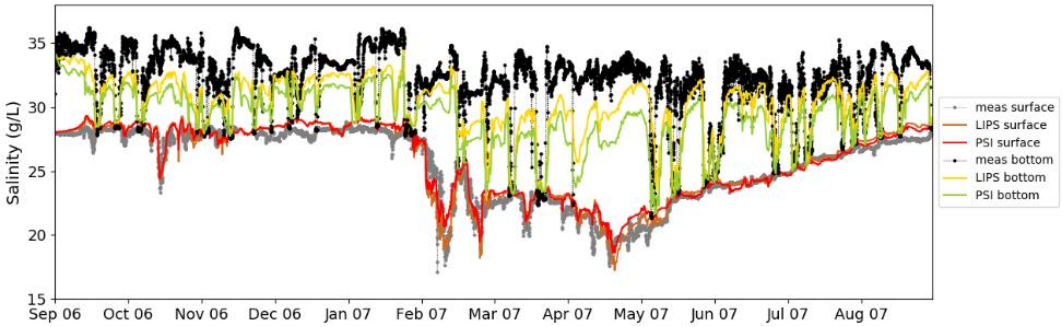

Fig 4: Salinity at SA3 from September 2006 to August 2007. Measurements (points), LIPS and PSI schemes for tracers only (solid lines).

B. *Advection of velocity components*

In this subsection only, the same advection scheme is used for the advection of both velocity components and tracers (replacing the method of characteristics for velocity components and PSI for tracers): PC and LIPS schemes are tested.

The PC scheme requires the use of a 2 s time step to converge, but the CPU time strongly increases (27 h). For that reason, this choice is dropped out.

Using the LIPS scheme does not require decreasing the time step. Comparisons are then done with the same time step as the "reference" model, i.e. 10 s. Using the LIPS scheme for velocity components is slower than the previous choice (method of characteristics): with the same time step, CPU time increases by 50 %.

Inside the lagoon at SA3 station, salinity values computed with LIPS and PC scheme are close to the ones from the "reference" model with PSI scheme. Contrary to the comparisons with advection schemes for tracers, no improvement is observed for stratification (Fig. 5).

On the other hand, using LIPS and PC schemes for velocities improves the salinity results in the Caronte channel. Fast variations of salinity due to tide (a few hours time scale) are better modelled (Fig. 6).

In the Caronte channel (direction East-West), velocity is directed alternatively toward the lagoon (rising tide) or toward the Gulf of Fos (falling tide) and maximum velocities are around 1 m/s. Velocity are well modelled, which is mandatory to reproduce correctly the exchanges between salted water and brackish water coming from the lagoon. When looking at velocity, small differences may appear depending on the advection scheme. If only the advection scheme is modified for tracers, the differences for velocity are minor. However, with LIPS for the advection of velocities, the maximum velocity is increased by around 25 % (Fig. 7), which may explain the fast variations of salinity above. Compared to measurements, this is also an improvement of the numerical model. Inside the Berre lagoon, velocities are very low (a few cm/s), which cannot be reproduced accurately.

Regardless of the advection scheme, during mistral events the surface current from North to South and the bottom current from South to North are well reproduced (Fig. 8).

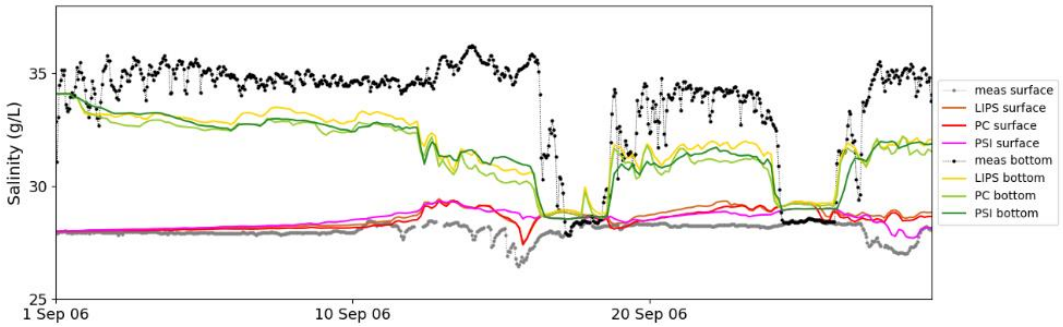

Fig 5: Salinity at SA3 in September 2006. Measurements (points), LIPS, PC and PSI+MOC schemes for tracers and velocities (solid lines).

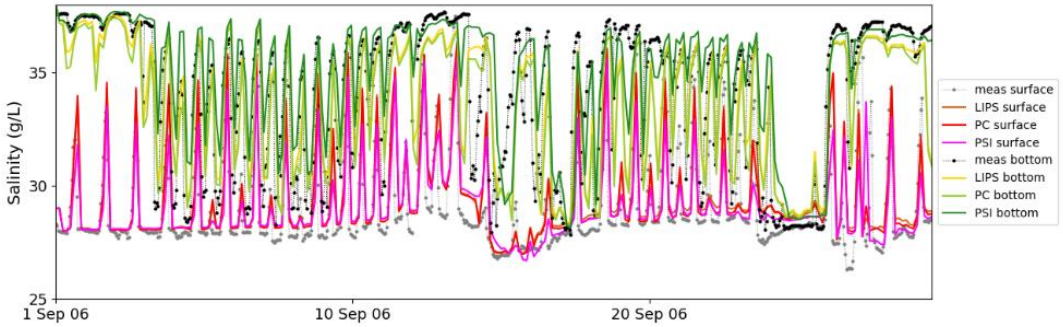

Fig 6: Salinity at SA4 in September 2006. Measurements (points), LIPS, PC and PSI+MOC schemes for tracers and velocities (solid lines).

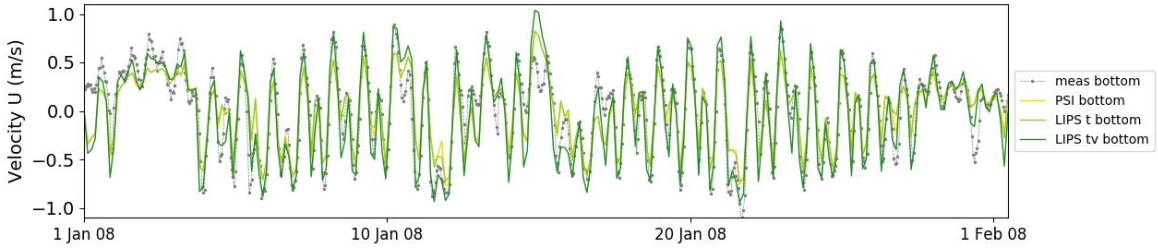

Fig 7: Velocity in the Caronte channel in January 2008 (LIPS t = LIPS for tracers only and MOC for velocities, LIPS tv = LIPS for tracers and velocities).

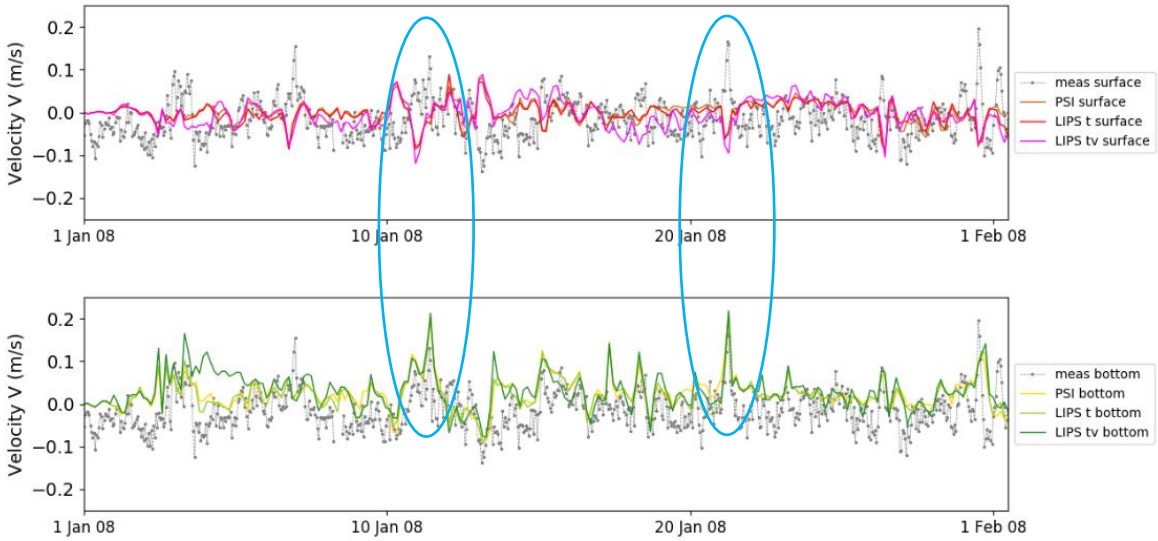

Fig 8: North-South velocity in the lagoon (SA3), January 2008 (LIPS t = LIPS for tracers only and MOC for velocities, LIPS tv = LIPS for tracers and velocities). In blue are shown events with strong mistral where a circular current appears in the lagoon.

Salinity of the lagoon is not well reproduced during a whole year (Fig. 9). On the one hand, the salinity difference between surface and bottom is divided by two compared to the measurements. On the other hand, a salinity shift of around 2 g/L can be seen after one year.

Although the exchanges through the Caronte channel fit the measurements, the results inside of the lagoon are not improved. This leads us not to retain this set of advection schemes (LIPS for tracers and velocity components).

C. *Sensitivity analysis for the advection schemes*

A 3 min time step accelerates the computation, but the results are worse. Using a time step below 30 s does not change the results: convergence with time step is reached. A balance between CPU time and accuracy has led us to choose a 60 s time step with LIPS for tracers (compared to 10 s with PSI for tracers) (Fig. 10). For the sensitivity to sub-iterations, nearly no influence on the results is observed but the CPU time increases: this feature is not chosen. For the sensitivity to the number of corrections, which is an option available with the LIPS scheme (at least and by default, one is done), tests with two and four corrections do not show modifications of results nor strong increase of CPU time: this feature is also not chosen.

The LIPS scheme for the advection of tracers enables a better modelling of stratification than the PSI previous "reference" scheme for tracers. The LIPS scheme for velocity components better replicates large velocities in addition to fast variations of salinity, but there is a salinity drift when modelling one whole year. The LIPS scheme is then chosen only for tracers and the method of characteristics is kept for velocity components and turbulent variables. No sub-iterations and additional correction are retained.

A whole year can be modelled with 7 h CPU time using a 60 s time step.

D. *Turbulence modelling*

After choosing the numerical parameters dealing with advection schemes, we would like to better model the physics of stratification. In particular, we would like to model succession of stratification and mixing correctly so that water quality can be studied afterwards. Modelling turbulence is then a key factor to take into account the exchanges in the Caronte channel, the mixing with incoming fresh water and weak exchanges between the two layers of different densities of water when the lagoon is stratified.

Some turbulence models available for TELEMAC-3D have been tested:

- Mixing length turbulence model with various mixing length formulae (Prandtl, Nezu & Nakagawa, Quetin, Tsanis) coupled with a damping function to better reproduce stratification (e.g. Toorman or Munk and Anderson functions),
- Transport equation turbulence model: k-ε as used in the "reference" model and some variations.

Mixing length turbulence model:

In case of a stratified lake like the Berre lagoon, a simple mixing length solution is not accurate without any damping function because the stronger the density gradient, the smaller the eddies: the turbulent kinetic energy k available is not sufficient to mix two layers of large density differences. Hence the use of a damping function equal to 1 in case of unstable stratification and decreasing with density gradient in case of stable stratification.

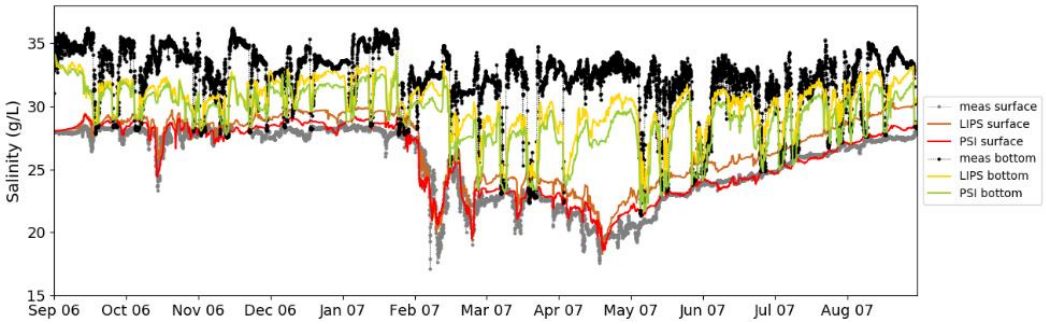

Fig 9: Salinity at SA3 from September 2006 to August 2007. Measurements (points), LIPS and PSI schemes for tracers and velocities (solid lines).

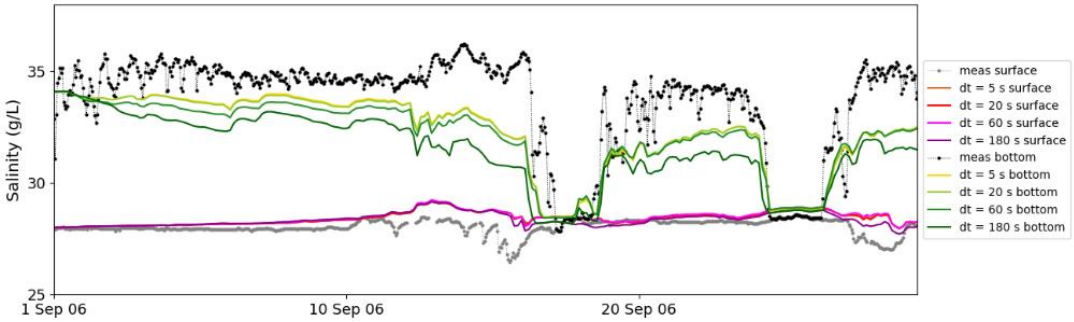

Fig 10: Salinity at SA3 in September 2006. Comparison between results with different time steps (5 s, 20 s, 60 s, 180 s).

The four mixing length formulae provide similar results. Fig. 11 shows results with Munk & Anderson damping function. Tsanis model seems to give better results as the modelled stratification is the strongest, but no model can reproduce a stratification as strong as the one measured.

Nevertheless, Toorman damping function combined with any mixing length model enables keeping a strong stratification, in particular when the lagoon is stratified. But the mixing periods and the mixing at stations SA1 and SA2 are not well reproduced (see Figs 12 and 13).

To summarize: although modelling stratification quite well, the mixing length model with damping function does not fit during strong mistral periods (in particular during the mixing of deep and surface layers).

k-ε turbulence variants:

Sensitivity to the Schmidt turbulent number (ratio between the turbulent viscosity and the turbulence diffusivity) has been tested. In the literature, this coefficient can vary from 0.8 to 1.3. As there are few variations of results, the default value of 1. is kept.

Among the options of the *k*-ε model, some can limit the turbulence production or the turbulence kinetic energy, what may *a priori* limit the mixing.

One first solution is to limit the production term:

$$P = C_\mu \frac{k^2}{\varepsilon} S^2,$$

With P production term, C_μ the Prandtl-Kolmogorov constant, S scalar mean rate of strain.

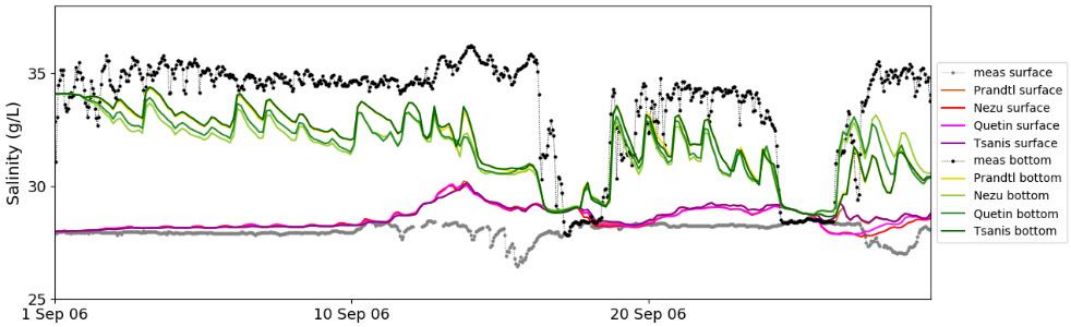

Fig 11: Salinity at SA3 in September 2006. Comparison between results with various mixing length models combined with Munk and Anderson damping function.

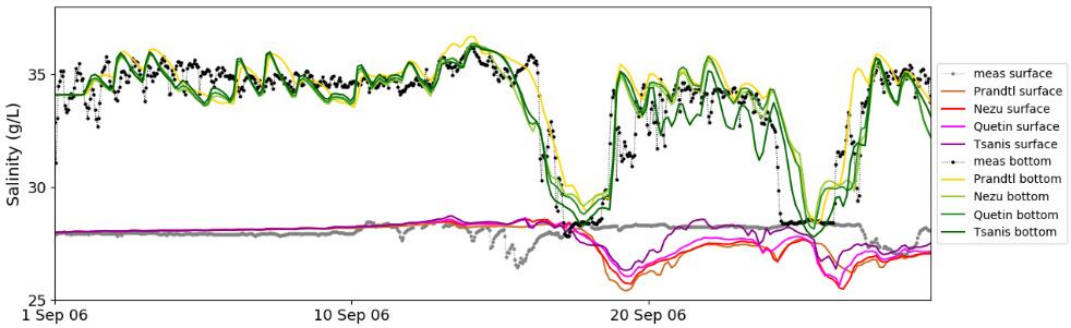

Fig 12: Salinity at SA3 in September 2006. Results with mixing length models combined with Toorman damping function.

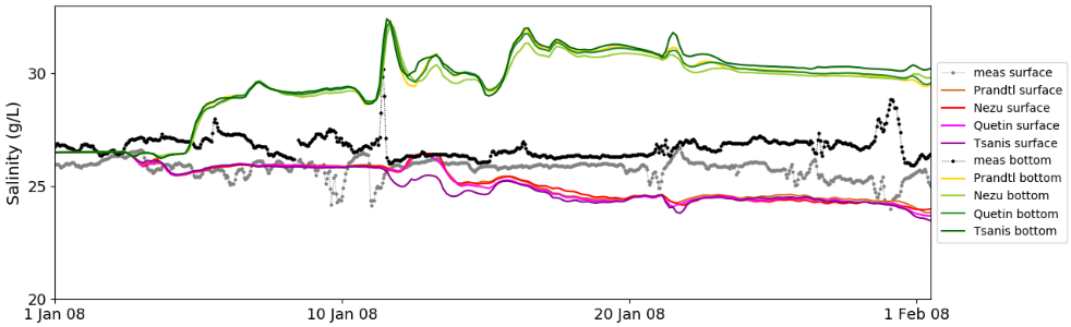

Fig 13: Salinity at SA2 in January 2008. Results with mixing length models combined with Toorman damping function.

If the dissipation is larger than the production, the production term is kept. If not, the production term is replaced by the square root of the product production times ε (*i.e.* $\sqrt{P\varepsilon}$). For the Berre lagoon, this variation has a slight positive effect for representing the stratification, around 0.5 g/L (Fig. 14). This can be done by setting the variable OPTPROD to 1 in the CSTKEP subroutine, and implementing this correction for the surface nodes in the SOUKEP subroutine.

A second limitation of turbulence comes from a physical criterion on the size of large vortices: the size cannot be larger than the distance between the considered point and the lagoon bottom. Yap (1987) suggested a correction to decrease the coefficient $C_{\varepsilon 2}$. This leads to the increase of dissipation ε:

$$C_{\varepsilon 2} \rightarrow C_{\varepsilon 2} - 0.83\left(\frac{LL}{\kappa\delta} - 1\right)\left(\frac{LL}{\kappa\delta}\right)^2,$$

With $LL = C_\mu^{3/4}\frac{k^{3/2}}{\varepsilon}$, κ Karman constant and δ is the distance to the bottom.

This correction strongly improves the modelling of stratification in the Berre lagoon: the salinity difference between the bottom and the surface increases around 1 g/L (see Fig. 14). A one-year simulation confirms this result. This Yap correction is then kept to model the Berre lagoon. It can be activated by setting YAP = .TRUE. in the CSTKEP subroutine.

Other modifications of the *k*-ε model have not been chosen, as they do not improve the results. Moreover, the GOTM module has not been investigated so much due to the lack of both relevant preliminary results and experience of this module.

Regarding the turbulence modelling of the Berre lagoon, the *k*-ε model seems to better fit the results. Contrary to the mixing length models, it enables to model alternating periods of stratification and vertical mixing, but also the mixing of incoming water (fresh or salted with brackish water of the lagoon).

Compared to the initial setup, two variations are chosen: the limitation of the turbulence production and the Yap correction. This leads to the modelling of stratification closer to the measurements with a slight trend to underestimate measured stratification.

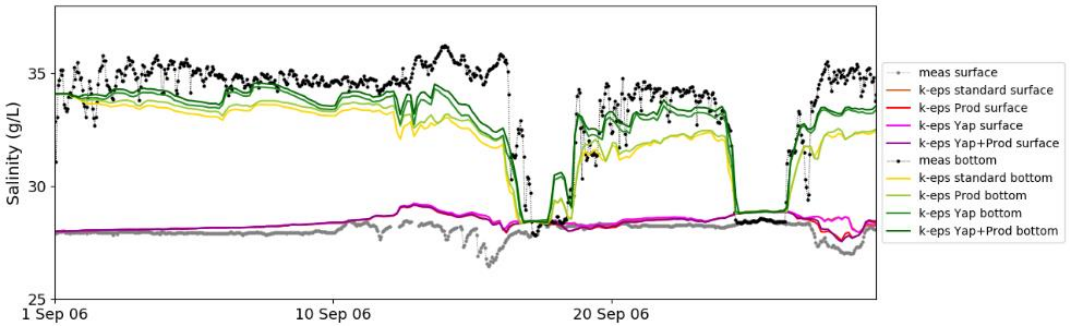

Fig 14: Salinity at SA3 in September 2006. Results with or without the modification of the production term and with or without the Yap correction.

V. CONCLUSION

Modelling the Berre lagoon is a tough task, which has been carried out for years. Reproducing stratification and mixing events is crucial to deal with water quality. In case of a TELEMAC-3D model without tidal flats, some improvements have been obtained using not so usual options:

- LIPS scheme for the advection of tracers salinity and temperature which is less diffusive,
- A variant to limit the turbulent production term and the Yap correction to tune the *k*-ε model.

ACKNOWLEDGEMENT

The authors thank Sara Pavan for her knowledge and explanations of the "recent" advection schemes (PC, LIPS), Martin Ferrand for his knowledge of turbulence models and Nathalie Durand for her large experience in hydraulics modelling and in particular the Berre lagoon.

REFERENCES

[1] S. Pavan, "Nouveaux schémas de convection pour les écoulements à surface libre" PhD thesis, Université Paris-Est, 2016.

[2] S. Pavan, J.-M. Hervouet, M. Ricchiuto, and A. Ata, "A second order residual based predictor-corrector approach for time dependent pollutant transport." JCP, vol. 318, pp. 122-141, 2016.

[3] J.-M. Hervouet, S. Pavan, and M. Ricchiuto, "Residual distribution advection schemes in Telemac," Research Report RR-9087, Inria Bordeaux Sud-Ouest, 2017.

[4] D. Violeau, and M. Ferrand, "Etude comparative de quelques modèles algébriques explicites pour les tensions de Reynolds et les flux turbulents de scalaires passifs et actifs, et application au cas d'un étang saumâtre. EDF R&D-LNHE Technical report, 2009.

Hydrodynamic modelling of the tide propagation in a tropical delta: overcoming the challenges of data scarcity

Ignace Pelckmans[1], Olivier Gourgue[1,2], Jean-Phillipe Belliard[1], Luis E. Dominguez-Granda[3], Cornelis Slobbe[4], Stijn Temmerman[1]

[1] Ecosystem Management (ECOBE), University of Antwerp, Antwerp, Belgium
[2] Department of Earth & Environment, Boston University, Boston, USA
[3] Centro del Agua y Desarrollo Sostenible, ESPOL, Guayaquil, Ecuador
[4] Geoscience & Remote Sensing, TU Delft, Delft, The Netherlands
ignace.pelckmans@uantwerpen.be

***Abstract*—Tropical river deltas are hotspots of human activity, but their vulnerability to flood risks is increasing due to sea level rise and worldwide conversion of mangroves, acting as natural buffers against marine flooding, into human land use. Moreover, extreme sea levels notably driven by climatic fluctuations such as the El Niño-Southern Oscillation, are projected to intensify with global warming. Hydrodynamic models offer a valuable tool in reaching a better understanding on the distribution of extreme sea levels in tropical deltas, but often their development is hampered by data scarcity. We combined state-of-the-art techniques to overcome that challenge by setting up a TELEMAC-2D model for the Guayas delta (Ecuador), a large (± 3,000 km²) delta with a complex geometry of branching river channels and mangrove forests. First, we used remote sensing to (1) obtain channel widths, which in turn determine the cell size in a flexible mesh, allowing us to capture both regional and local processes, (2) estimate intertidal flat topographies, and (3) delineate intertidal mangrove forests. Furthermore, we used an along-channel-coordinate interpolation to ensure channel connectivity in channels with scarce bathymetric observations. Finally, to capture the land-sea gradient in the water surface slope, we referenced all bathymetric and tide gauge data to a global geoid. Applying these techniques allows us to build a model which simulates tidal ranges (of 2 to 4 m) with an error ranging between 0.2 and 29 cm (i.e. 0.2 and 7.8 % of the observed tidal range), depending on tide gauge station. In a next stage, our model can be used to test how both El Niño and land use changes affect extreme sea levels in this tropical delta.**

I. INTRODUCTION

A. Coastal flooding in tropical deltas

Coastal deltas are highly vulnerable to flood risks which are very likely to increase in the near future [1]. Intensifying storms and climatic cycles such as the El Niño Southern Oscillation (ENSO) along with long-term sea level rise will trigger more frequent and more severe coastal floods [2,3,4] In addition, over 90 % of deltaic communities are located in developing countries with already dense populations expected to double before 2060 [5]. This increasing population pressure along with intensifying coastal hazards pose enormous risks to coastal communities, framing tropical deltas as communities which will be disproportionately hit by climate change [6].

B. Paper outline

Hydrodynamic models are valuable tools in understanding how extreme sea levels originate and propagate through deltas but especially in tropical areas, data scarcity often hampers the development of such models. This paper presents an integrated model setup where we combined several state-of-the art techniques to overcome the data scarcity challenge and setup a tidal model (no wind or short-period waves) model in the Guayas delta, Ecuador. The propagation of tides through a tropical delta is driven by ebb-and-flow currents in the open ocean but when these tidal waves enter the delta, geometric properties of tidal channels and vegetated wetlands, mangroves, govern deltaic hydrodynamics. In the first part, we describe how we used remote sensing and GIS-techniques to build an unstructured mesh in order to cover the multi-scale character of deltaic hydrodynamics. Secondly, we list two methods which were used to interpolate scarce bathymetric observations in order to ensure hydrodynamic connectivity over the entire domain. Thirdly, we stress the importance of using a vertical reference level which allows the model to include all major drivers, including a land-to-sea gradient. In the final section, we shed light on the calibration process of the channel's bottom friction and the mangroves forest floor elevation. The combination of these methods allowed us to build and calibrate a TELEMAC-2D model which in later stages will be used to further investigate the propagation of ENSO-driven extreme sea levels in a tropical delta.

C. Study area

The Guayas delta is the largest river delta along the Latin Pacific coast and flows into the Gulf of Guayaquil (Fig. 1). The gulf and delta are subject to semi-diurnal tides with a mean tidal range of ± 2 m at the SW seaward boundary of the gulf. When propagating landwards, the mean tidal range is amplified up to ± 5 m near the city of Guayaquil. Freshwater river discharge into the Guayas delta comes from the Babahoyo and Daule rivers in the North. Discharges vary strongly with values between 125 and 400 m³/s in the dry season (April – November) and values up to 1600 m³/s in the wet season (December – March) [7]. Similar to many other tropical deltas, the mangroves are heavily degraded after large parts of the delta were converted to aquaculture [8]. The tarnished ecosystem and its exposure to El Niño puts the delta under risk, a threat highlighted by a global study on risks of flood damage (relative to local GDP) in coastal cities, ranking Guayaquil on the 3rd highest place [9], highlighting the Guayas delta as a global hotspot of coastal hazards.

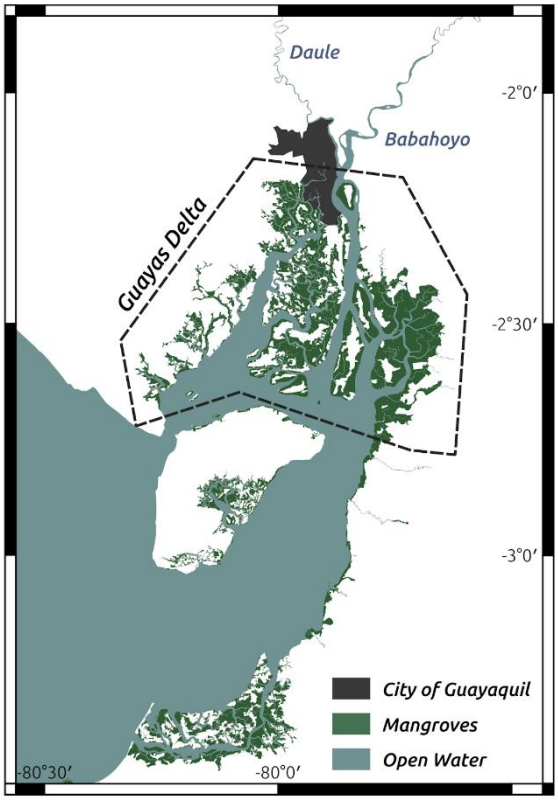

Fig.1: Map of the Gulf of Guayaquil, the western part of the domain containing the region of interest: the Guayas Delta. Both mangroves and open water are included in the model domain. The city of Guayaquil is not. The open ocean boundary is located east of the shown extent. Both freshwater boundaries are indicated (Daule and Babahoyo river).

II. Mesh Generation

A. *Model domain*

The domain of the model covers the entire Gulf of Guayaquil, stretching from the continental shelf at the open ocean (-81.25°) to 50 km upstream at the Babahoyo and Daule river from Guayaquil. The natural wetlands, mangroves, flood during high water levels and therefore, are included in the domain. After conversion to aquaculture, mangroves can no longer flood due to the construction of levees and therefore, aquaculture ponds are excluded from the domain.

B. *Delineation of mangroves and channels*

The use of satellite-borne remote sensing allowed us to delineate the mangroves and channels from aquaculture ponds, urban areas and surrounding agricultural land. ESA's Sentinel 2 is a collection of multi-spectral optical images which allows calculating the Normalized Difference Vegetation Index (NDVI) at a spatial resolution of 10 m. NDVI ranges from -1 to 1 with values above zero, indicating the presence of vegetation. In our study, mangroves were determined by pixels with a NDVI-value above a threshold value. To determine that value, we randomly selected 50 points in the mangroves and 50 points in other land cover types (e.g. aquaculture ponds, built-up areas, etc.). NDVI at all points in mangroves exceed the value of 0.6 while 49 of 50 in other land cover types did not. Consequently, mangroves were determined as all pixels with a NDVI-value > 0.6. To ensure channel connectivity, we applied a 1-pixel-wide dilation and erosion algorithm (Fig. 2). Afterwards, the entire domain was visually checked and compared with aerial pictures collected through Google Earth. If needed corrections were applied. Finally, manually delineated data of mangroves and channels for subareas within our study area were available through ESPOL, and after visual comparison, our NDVI-based results were considered satisfactory.

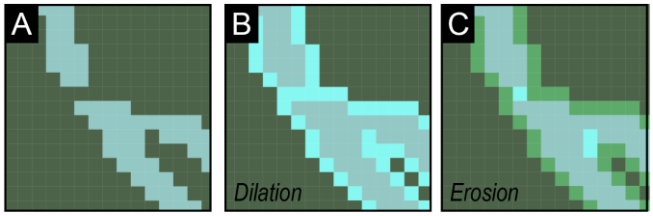

Fig 2.: (A) close up of original delineated channel (B) dilation process of 1 pixel wide (blue pixels) (C) erosion process after dilation, light green pixels indicate pixels which were removed again after erosion. Note how the channel kept its original width but is connected now.

C. *Cell size*

We constructed a mesh where cell sizes inside the delta are determined in function of the channel width. We developed a Python-based set of functions, '*tidealgeopro*' [10], to build a set of polylines representing the center line of the channel polygons (channel skeleton). In addition, as traditional stream order systems were insufficient because tidal channels do not have a clear flow direction, we developed a stream order system to rank all tidal channel segments (portion of channel in between the joining of tributaries) as illustrated in Fig. 3. To calculate channel width for each location in the channel, we first calculated the channel width for each vertex of the skeleton. Next, per segment, we applied a nearest neighbour interpolation to extrapolate the channel widths at the channel vertices to a raster (pixel size of 5m) in order to assign a channel width to each location in the channel. At tributary-joints, the interpolated channel-width rasters overlapped but priority was given to higher order streams. This resulted in a raster file representing channel width for all channels (Fig. 4A).

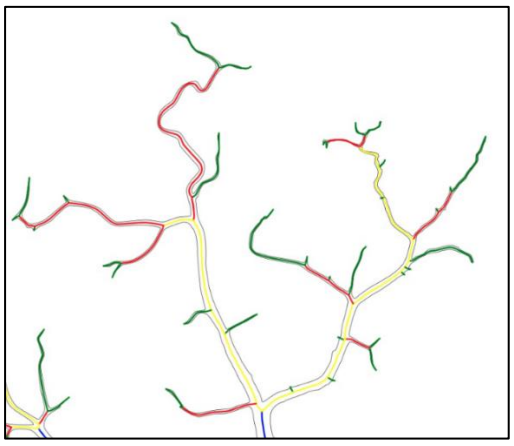

Fig. 3: Example of channel skeleton with colors representing stream orders per channel segment (green = 1, red = 2, yellow = 3, blue = 4).

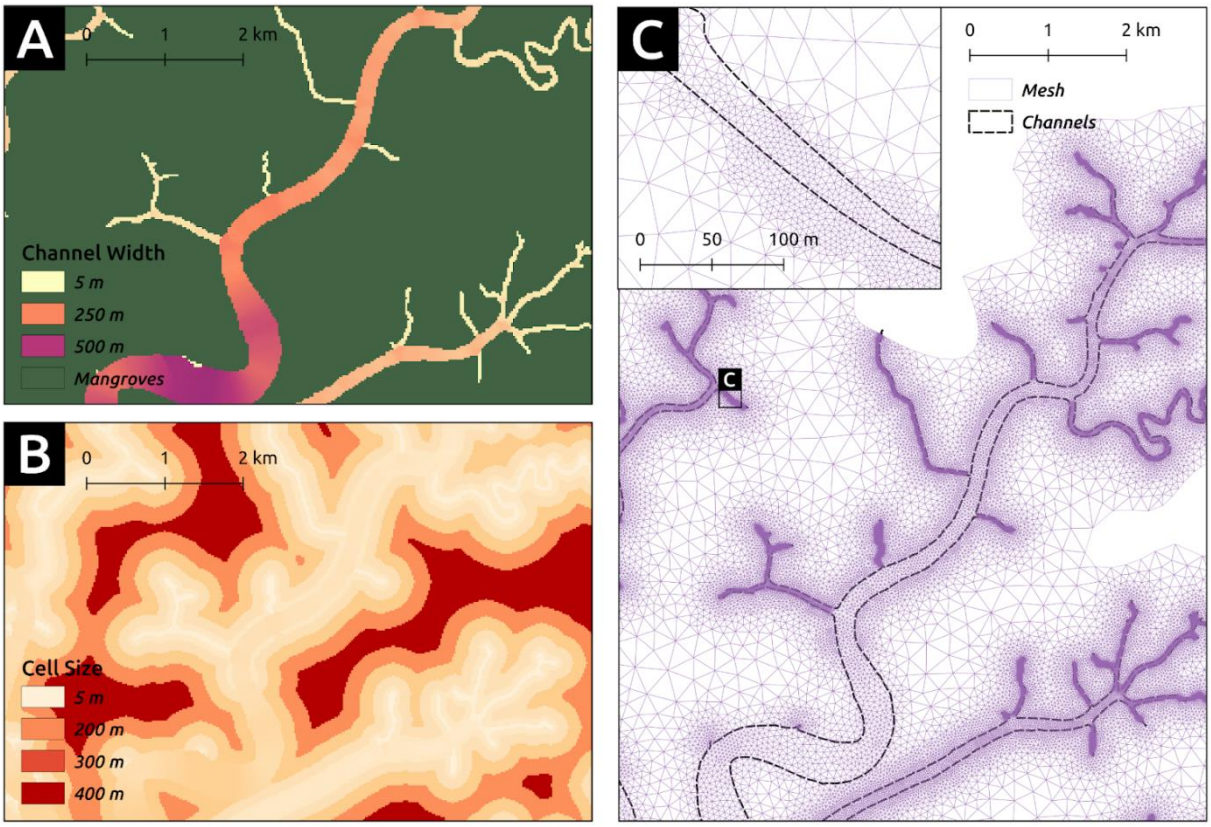

Fig. 4: (A) Example of channel width raster. (B) Example of raster file imposing the cell size of the eventual mesh (C) Example of mesh where the cell size has been calculated in function of the channel width.

Next, we expressed cell size in function of the channel width in order to ensure a minimum number (5) of mesh nodes broadwise. In addition, a minimum cell size of 5 m was enforced to limit the total number of elements. The cell size at the mangroves was set at 400 m. The latter might lead to strong gradients in cell size where narrow channels border mangrove forests, which could cause numerical instabilities. Therefore, we implemented stepwise buffers around the channels to impose smooth transitions in mesh cell size at the borders between channels and mangroves (Figure 4B & C). Cell sizes at the open ocean varied from 1000 m at the seaward boundary to 400 m at the entrance of the delta. The mesh was created using the finite element mesh generator GMSH [11].

III. Available Data

Water levels were obtained through 3 different sources: INOCAR shared water levels (1976 - 2019) from 8 tide gauge stations spread over the Gulf of Guayaquil, however many of the stations had significant gaps in the time series. Jan De Nul shared water levels from 11 tide gauge stations from which 10 are located along the main channels in the delta. Thirdly, water pressure sensors were installed at three different locations in the delta appr. 10 - 50 m inside the mangrove forests, permanently logging water depth since March 2019.

Bathymetry data at the open ocean were obtained from the General Bathymetric Chart of the Ocean (GEBCO, 2020). Limited bathymetric data inside the delta were shared by the Oceanographic Institute of the Navy (INOCAR) as well as nautical charts in JPG-format.

IV. Boundary Conditions

Boundary conditions at the seaward boundary were derived from the global tidal models TPXO9 [12]. Upstream river discharge data were obtained through INHAM. The available data did not cover the entire watershed of the Guayas river, but the available data was extrapolated by means of a linear precipitation-weighted interpolation with monthly precipitation data collected from OpenLandMap [13].

V. Bathymetry Interpolation

At the open ocean and major channels, bathymetry at the mesh nodes was derived by a linear TIN-interpolation of the available data. No bathymetric data covering intertidal flats were available. To interpolate the bathymetric data in the channels dissecting the mangrove forests, observations were too scarce to apply a simple linear TIN interpolation.

A. *Intertidal flat topographies*

Based on the nautical charts in JPEG-format and Sentinel 2 images, we delineated 20 zones covering significantly large (area > 40 km²) intertidal flats. Per zone, we collected a time series of all available cloud-free Sentinel 2 imagery through the Google Earth Engine. For each image, the Modified Normalized Difference Water Index (MNDWI) was calculated

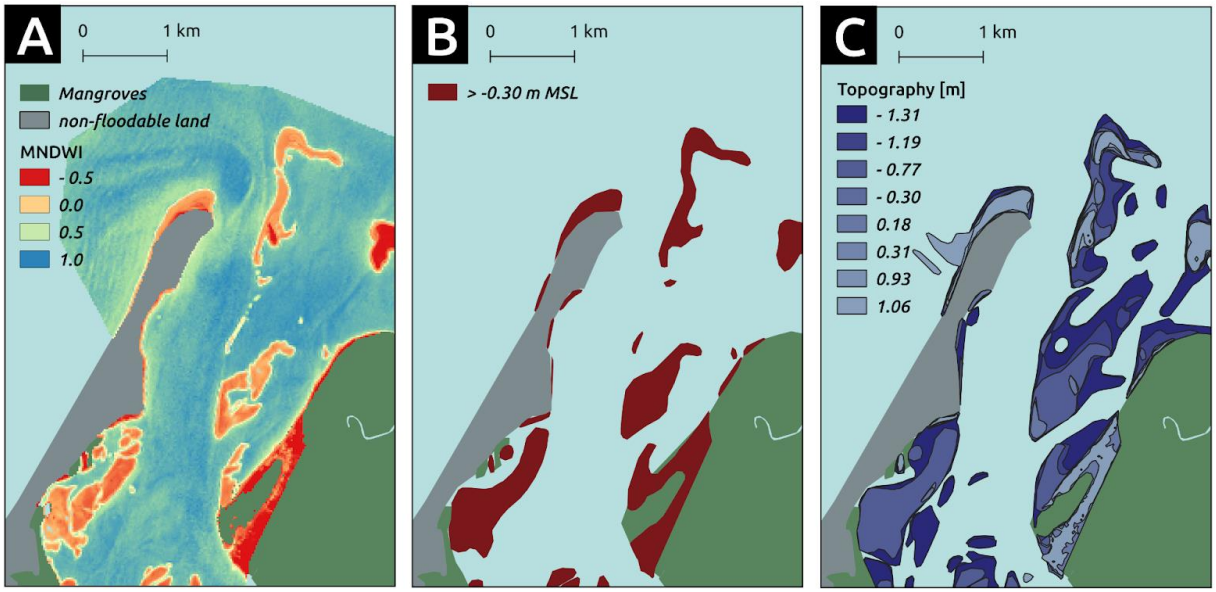

Fig. 5: (A) Modified Normalized Difference Water Index (MNDWI) of an intertidal mudflat. (B) Areas with MNDWI values lower than a given threshold, representing areas which were not submerged when a nearby tide gauge station measured a water height of 0.66 m below MSL. (C) Estimated topography of mudflat by combining MNDWI values at 4 different water heights.

(eq. 1), which ranges between -1 & 1 with positive values representing open water (Fig. 5A).

$$MDNWI = \frac{Green - SWIR}{Green + SWIR} \quad \text{(eq 1.)}$$

With *Green* and *SWIR* being the measured reflectance in the respectively, green part of the visible part of the electromagnetic spectrum and short-wave infrared part of the spectrum.

Submerged lands can be determined as cells with a MNDWI-index which exceeds a certain threshold value. Thus, the border between submerged and emerged cells is an estimation of the waterline at the timing of recording of that Sentinel 2 image [14, 15]. To define the value above which cells are considered submerged, we made use of an automatic thresholding technique called Otsu thresholding. In the latter, a threshold value is calculated to minimize intra-class variance (in our case of MNDWI) and maximize inter-class variance [16]. By obtaining the time of recording of each image, the obtained water lines could be linked to water levels of nearly located tide gauge stations. For instance, on Fig. 5B all areas which emerged when a nearby tide gauge station listed a water level of 0.66 m below mean sea level (MSL) are indicated by a red shade. The corresponding waterline can then be interpreted as contour lines of 0.66 m below MSL. By applying this algorithm for multiple Sentinel 2 images, acquired at different times and thus, different water levels, it is possible to build an estimated topography of an intertidal flat, as shown in Fig. 5C.

B. *Channel bathymetry interpolation*

Scarcely distributed point measurements of channel bathymetry were available to us, however, the resolution of the mesh strongly exceeded the resolution of the available observations, compelling an interpolation of the bathymetric observations. However, traditional cartesian interpolation techniques are insufficient. One could argue that the bed elevation within a channel is stronger related to its distance to the channel edge and position along the channel axis than its cartesian coordinates. Following this reasoning, we applied a linear TIN-interpolation after cartesian coordinates were projected to a channel fitted coordinate system [17]. Similar to section *II.C*, we first calculated the channel skeleton and divided the channel system into its different segments. On its turn, all bathymetry observations were assigned to a channel segment, which they were most closely located to.

Per segment and its related bathymetric observations, all cartesian coordinates of the bathymetry observations were projected to channel-fitted coordinates (see example in Fig. 6): (1) along-skeleton coordinate (*as*) which is the distance along the center line from the onset of the segment until the observation projected on the center line and (2) perpendicular-skeleton coordinate (*ps*) which is the distance from the observation to the center line. Such an approach conserves the geomorphic shape of a channel, even after interpolation. For instance, the interpolated channel bathymetry on the outside bends of channels will be more influenced by deep observations more down- and upstream than more closely located measurements at the inside bend.

VI. Vertical Reference Level

All collected data (bathymetry and tide gauge data) were referenced to the local mean sea level (MSL). However, when tidal waves enter and propagate through the delta, they are being pushed upwards, a process called tidal wave run-up. Along with significant freshwater river discharge, this creates a land-sea water surface slope in the MSL. Therefore, since MSL is derived from the hydrodynamics, it cannot act as an

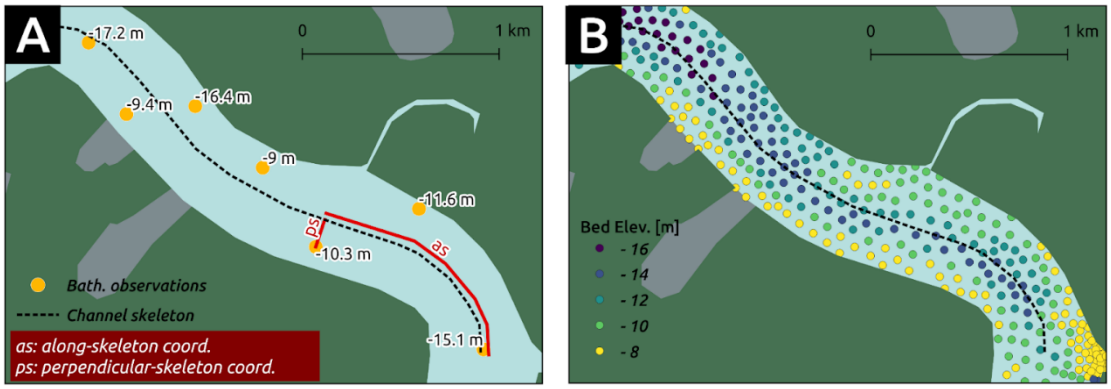

Fig. 6: (A) Example of channel segment with limited density of bathymetry observations (yellow markers). Channel coordinates are calculated as (as) the distance along the center line/skeleton measured from the start of that channel segment until each bathymetry observation projected on the center line and (ps) distance between the observation point and the center line. (B) Bathymetry of the channel segment after interpolation. Each marker represents a node on the final mesh. Nodes inside the mangrove forest are not shown.

independent reference level as it already includes an hydrostatic gradient from the ocean land inwards (Fig. 7). Therefore we referenced all data to a so-called geoid (XGM 2019). A geoid is a model describing an equi-potential gravitational field covering the entire globe. In other words, it is the shape which the ocean would take if the ocean's water level would only be governed by gravity and the rotation of the earth. Hence, if used as a vertical reference for hydrodynamic modelling, there would be no hydrostatic gradient between two locations with the same water surface level in reality as well [18].

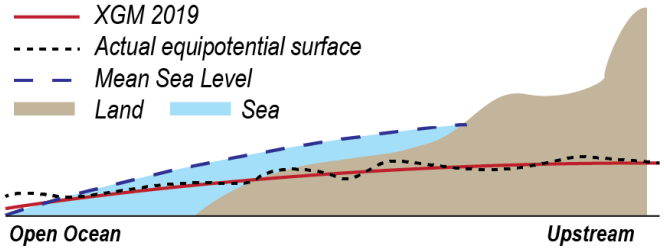

Fig. 7: Schematic representation of the geoid model (red line), the actual equipotential surface (black dashed line) and MSL (blue dashed line).

VII. Model Calibration

A. *Mangroves forest floor elevation*

No topographical data were available on the height of the mangrove forest floor. However, water depth measurements at the forest edge at three different locations, spread over the delta, were available. For instance, during the period 29th of September 2019 4:00:00 – 1st of October 2010 16:00:00, maximum water depths in the mangrove forest reached 60 cm, averaged over all three locations. Implicitly, we can estimate the mangrove forest floor elevation to be 60 cm lower than the high water mark surface in the mangroves. In other words, the mangrove forest floor elevation can be estimated based on the high water mark surface, however, the latter is affected by the mangrove forest floor elevation. Therefore, we set up an iterative process to estimate the mangrove forest floor elevation:

1. The first simulation excluded the mangroves from the floodable domain resulting in a high water mark surface which only included the channels. The high water mark surface was extrapolated to the mangroves by means of a 7th order polynomial surface and the mangrove forest floor elevation was set at this extrapolated high water mark minus 60 cm.
2. The updated mangrove forest floor was used as the input for a second simulation. This simulation resulted in a new high water mark, which did include the mangroves as the new mangrove topography allowed flooding in the mangroves since the forest floor elevation was set 60 cm below the high water mark in the channels.

   As all three surveyed locations are located near the border of the mangrove forest and channels, we can only assume that the forest floor is 60 cm below the high water mark at the edge of the forest. Hence, the newly updated elevation of the mangrove forest floor elevation was only set 60 cm lower than the high water mark at all nodes located on the border between mangroves and channels. Mangrove forest floor elevations inside the mangrove forest were again extrapolated by means of a 7th order polynomial surface.
3. On its turn, the resulting mangrove topography of the second simulation was used to simulate hydrodynamics, again resulting in a high water mark surface. The mangrove forest floor topography was updated by again, subtracting 60 cm for the last obtained high water mark and extrapolating the elevations to the inside of the mangrove forest. This iterative process was repeated until the RMSE of elevations at mangrove nodes between the two last iterations did differ less than 5 cm.

B. *Channel bottom friction*

Bottom friction in both the mangroves and open water areas is represented by the Manning's friction law. The dense network of aerial roots and branches in a mangrove forest adds

a significant amount of friction to the bottom friction and thus, an appropriate value of 0.14 was set as the Manning's friction coefficient *n*, based on previous studies (Zhang et al., 2012; Liu et al., 2014; Rhadarian & Niksokhan, 2017). One single value for the Manning's *n* was used to cover all open water areas, both the channels and the intertidal flats. To define this value, we ran model was with 7 different values for the Manning's n: 0.0050, 0.0075, 0.0100, 0.0125, 0.0150, 0.0175, 0.0200, 0.0225. Each simulation covered 60 hours and boundary conditions during a neap tide (the 5th of October 2019 22:00:00 - the 8th of October 2019 10:00:00, during which the mangroves do not flood) and a spring tide (the 29th of September 2019 4:00:00 - the 1st of October 2019 16:00:00). To evaluate each simulation, high and low water levels are compared at 11 separate stations spread over the delta. For both periods, simulated high and low water levels fitted best with observations, using a Manning's *n* of 0.0125. The time resolution of both the outputted model results and the observations were 5 minutes.

The model succeeded in simulating tidal propagation with errors in tidal range ranging from 2 mm to 24 cm (i.e. a relative error of 0.2 – 7.8 % of the observed tidal range). During the simulated spring tides, errors ranged from 15 cm to 39 (i. e. relative error of 4.4 – 8.73 % of the observed tidal range). Timing of high water levels and velocities did not contribute to the evaluation process.

VIII. Conclusion

Often, the development of hydrodynamic models is hampered by limited coverage of data on land use and topography & bathymetry. Here we have proven that the use of remote sensing and GIS-techniques such as waterline-extraction and channel-fitted coordinates could contribute in setting up a model, with relatively good agreement with observed water levels (errors on tidal range smaller then 9 % of the observed tidal range).

Acknowledgement

We would like to thank the Research Foundation Flanders, Belgium for funding this research (FWO, PhD fellowship for fundamental research I. Pelckmans, 11E0721N).

References

[1] J.W. Day, J. Agboola, Z. Chen, C. D'Elia, D. L. Forbes, L. Giosan et al. "Approaches to defining deltaic sustainability in the 21st century," Estuar. Coast. Shelf Sci., vol. 183, pp. 275–291, 2016.

[2] M. Oppenheimer, B. C. Glavovic, J. Hinkel, R. Van De Wal, A. K. Magnan, A. Abd-Elgawad et al. "Sea level rise and implications for low-lying islands, coasts and communities." In: IPCC Special Report on the Ocean and Cryosphere in a Changing Climate [H.-O. Pörtner, D.C. Roberts, V. Masson-Delmotte, P. Zhai, M. Tignor, E. Poloczanska, K. Mintenbeck, 2019.

[3] E. Kirezci, I. R. Young, R. Ranasinghe, S. Muis, R. J. Nicholls, D. Lincke and J. Hinkel "Projections of global-scale extreme sea levels and resulting episodic coastal flooding over the 21st Century." Sci. Reports 2020 vol 101 10, pp. 1–12, 2020.

[4] S. Vitousek, P. L. Barnard, C. H. Fletcher, N. Frazer, L. Erikson and C. D. Storlazzi "Doubling of coastal flooding frequency within decades due to sea-level rise." Sci. Reports 2017 vol 71 7, pp. 1–9, 2017.

[5] B. Neumann, A. T. Vafeidis, J. Zimmermann and R. J. Nicholls "Future coastal population growth and exposure to sea-level rise and coastal flooding - a global assessment." PLoS One vol 10, 2015.

[6] D. A. Edmonds, R. L. Caldwell, E. S. Brondizio and S. M. O. Siani "Coastal flooding will disproportionately impact people on river deltas." Nat. Commun., vol 111 11, pp. 1–8, 2020.

[7] INHAMI. Official INAMHI website. Accessed through http://www.serviciometeorologico.gob.ec/ on December 2019.

[8] S. E. Hamilton "Mangroves and aquaculture: a five decade remote sensing analysis of Ecuador's estuarine environments." Springer, 2019.

[9] S. Hallegatte, C. Green, R. J. Nicholls and J. Corfee-Morlot "Future flood losses in major coastal cities." Nat. Clim. Chang., vol 3, pp. 802–806, 2013.

[10] Gourgue, Olivier, Pelckmans, Ignace, Fagherazzi, Sergio, & Temmerman, Stijn. "ogourgue/tidalgeopro: Earth Surface Dynamics paper", 2021. accessible through: https://doi.org/10.5281/zenodo.5205285

[11] C. Geuzaine and J.F. Remacle "Gmsh: A 3-D finite element mesh generator with built-in pre- and post-processing facilities." International Journal for Numerical Methods in Engineering vol 79, pp. 1309–1331, 2007

[12] G. D. Egbert and S. Y. Erofeeva. "Efficient inverse modeling of barotropic ocean tides." Journal of Atmospheric and Oceanic Technology vol 19.2, pp. 183-204, 2002.

[13] T. Hengl "Monthly precipitation in mm at 1 km resolution based on SM2RAIN-ASCAT 2007-2018, IMERGE, CHELSA Climate and WorldClim (0.2)" accessible through https://doi.org/10.5281/zenodo.3256275, 2019.

[14] S. Sagar, D. Roberts, B. Bala, and L. Lymburner "Extracting the intertidal extent and topography of the Australian coastline from a 28 year time series of Landsat observations." Remote Sens. Environ., vol 195, pp. 153–169, 2017.

[15] J. U. Khan, M. D. N. Ansary, F. Durand, L. Testut, M. Ishaque, S. Calmant et al. "High-resolution intertidal topography from Sentinel-2 multi-spectral imagery: synergy between remote sensing and numerical modeling." Remote Sensing, vol 11 2888, 2019.

[16] R. Bishop-Taylor, S. Sagar, L. Lymburner, I. Alam and J. Sixsmith "Sub-pixel waterline extraction: characterising accuracy and sensitivity to indices and spectra." Remote Sensing, vol. 11 2984, 2019.

[17] V. Merwade, A. Cook and J. Coonrod "GIS techniques for creating river terrain models for hydrodynamic modeling and flood inundation mapping." Environ. Model. Softw., vol 23, pp. 1300–1311, 2008.

[18] P. Zingerle, R. Pail, T. Gruber and X. Oikonomidou "The combined global gravity field model XGM2019e." J. Geod., vol 94, 2020.

Sediment I

Innovative 3D hydrosedimentary modelling of migrating inlets

T. Oudart, R. Walther, A. Le-Dissez
1ARTELIA, 6 rue de Lorraine,
38130 Echirolles,
thibault.oudart@arteliagroup.com

***Abstract*—At its downstream part, the Bandama river flows into Tagba lagoon, located 150 km west of Abidjan on the Ivoirian coast. The large lagoon system is separated from the Atlantic Ocean by a 15 km-long and 200 m-wide ridge of sand interrupted by a 300 m wide inlet that allows hydraulic exchanges between fresh water and ocean due to tidal oscillations of sea level and hydraulic regime of Bandama river (flood and low water periods). Settled on this sandy ridge, the fishing village of Lahou Kpanda is the remains of the ancient wealthy colonial city of Grand-Lahou, and is highly vulnerable to coastal erosion, East-West migration of the mouth of the Bandama river with a speed of 160 m/year over the past 10 years, as well as coastal and river flooding.**

The TELEMAC-MASCARET modelling system, coupling TELEMAC-3D (3D hydrodynamic module) – TOMAWAC (wave propagation module) and GAIA (hydro-sedimentary module), calculates the 3D hydrodynamics and resulting sediment transport. This complex model succeeds in correctly simulating longshore coastal transport and seasonal inlet morphodynamics. The main significant result is the modelling of the mean annual migration rate of the inlet in the opposite direction of the littoral drift. This phenomenon is mainly due to the secondary currents generated at the extrados of the Bandama channel during lagoon drainage (Aubrey and Speer, 1984). However, the good results obtained for short-term morphodynamics get worse for mid and long terms: satisfying at the beginning of the simulation, the simulated erosion affecting the West side of the inlet and consecutive East-West inlet migration is stopped due to the non-inclusion of the cross-shore processes that are responsible for accretion of the sandy eastern ridge (for its emerged part). The correction of the cross-shore profile requires the development of a unique numerical tool able to re-profiling automatically the bathymetry between the coastline and the closing depth.

A preliminary review of the state of the art has shown that one-line models (based on equilibrium beach profile concept and bypassing cross-shore processes resolution) are perfectly suited for long-term shoreline evolution modelling. However, their validity domain is limited to simple shoreline shapes under quite simple hydrodynamic conditions. For complex configurations, 1D modelling has to be supported by a cross-shore calculation module in a so-called "hybrid modelling" (Kristensen et al, 2016). The main difficulty of this coupling is how to generate automatically a 1D mesh from any 2D mesh considering a time varying bathymetry. For that reason, since 2016, ARTELIA has been developing a hybrid model based on the unstructured triangular mesh used by TELEMAC-MASCARET. Automatic re-profiling of the seabeds located between the coastline and the closing depth is carried out considering principles of equilibrium profile and cross-shore mass transfer by ensuring mass conservation. This new hybrid model has been first validated on simple theoretical cases such as a growing sand spit and is applied for the first time to a complex concrete case: the Grand-Lahou site.

I. INTRODUCTION

The village of Lahou Kpanda (Ivory Coast), located immediately to the west of the Bandama river mouth, on the barrier island of Tagba lagoon (Fig 1 and 2), is subject to intense coastal erosion, threatened by the migration of the tidal inlet at an average speed of 160 m/year over the last decade with an acceleration of the migration observed during this period [1, 2 and 3].,

Since the 1960s it has migrated about 1.5 km. The entire colonial city is already destroyed and the remaining fishing village has been subjected to a significant shoreline retreat. As the sandy ridge is very low, the village is regularly flooded, as a proven consequence of climate change.

Despite the decision in 1973 to adopt a strategy of relocating the stakes to the site of N'Zida, located 18 kilometres to the north on a high plateau, some inhabitants of the fishing village reluctant to leave the lagoon, stayed in Lahou Kpanda objected to the risks of migration of the inlet, shoreline retreat, and coastal and river flooding. Their assets are threatened with programmed disappearance if no human intervention is undertaken. The call for help from the local population and the opportunity of economical development of the lagoon - make however question this passive strategy.

Thus, the WACA program has funded in 2017 a Multisectoral Investment Program (MIP) to study different scenarios for sustainable management of the inlet. This plan has notably concluded to the need for a more detailed study of the hydro-sedimentary dynamics of the system composed of Bandama outlet- lagoon - inlet - sandy ridge, a proper understanding of the system being an essential prerequisite for the choice and sizing of solutions of development and maintenance for a sustainable stabilization of the inlet.

Artelia was therefore commissioned to carry out a technical, environmental and social feasibility study for a sustainable management of Grand Lahou inlet. This study is based on a scientific investigation of the system, relying on a

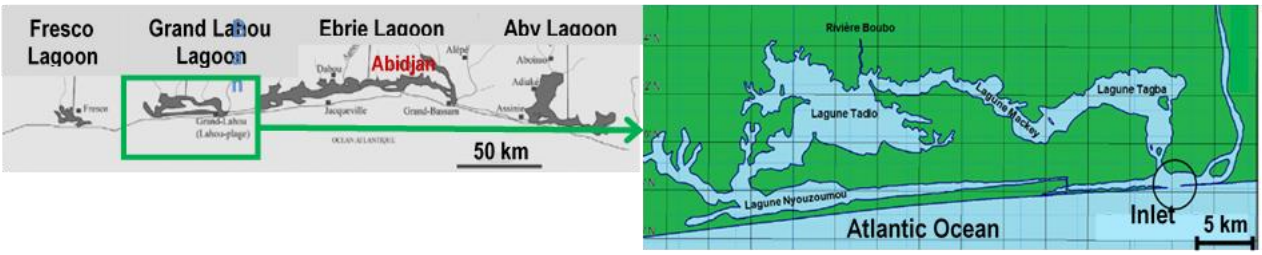

Figure 1. Location of the studied system, Grand Lahou, Ivory Coast

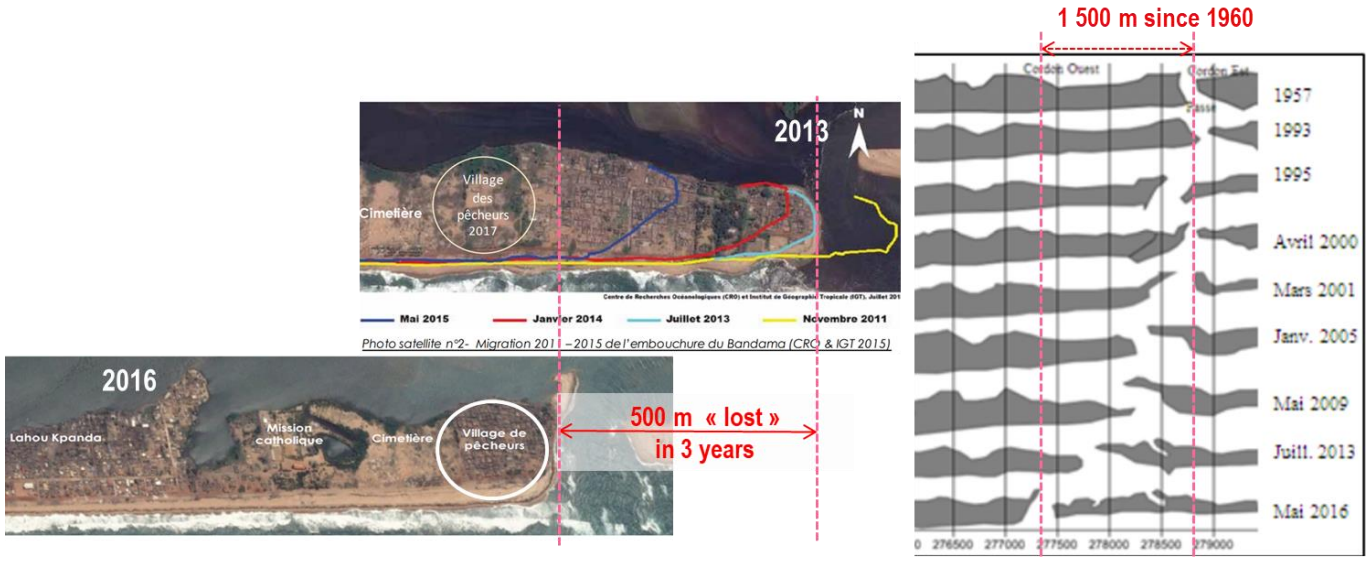

Figure 2. System evolution since 1960

numerical hydro-sedimentary modelling which aims at reproducing the observed morphodynamic evolutions of the system, in order to deduce future trends, with and without development, in order to compare the benefits of the different tested solutions for sustainable management of the mouth and to identify the better scenario.

The first goal of this feasibility study is to validate the model by reproducing past event, in particular the inlet migration opposite to the littoral drift **Error! Reference source not found.**. Adaptive solutions were then proposed and tested with the model.

II. Hydrodynamic Model

All the software used for this regional coastal numerical modelling comes from the TELEMAC-MASCARET software chain except the re-profiling tool. TELEMAC-3D (hydrodynamic), TOMAWAC (wave propagation) and GAIA (sediment transport) are all coupled together.

A. *TELEMAC-3D*

Telemac-3D allows simulating the dynamics of three-dimensional free surface flows. The software calculates, at all points of the mesh, the velocity fields in the 3 directions and the value of the scalar quantities possibly transported (temperature, salinity, suspended sediment...); on the surface mesh, we obtain the spatial and temporal evolution of the marine water layout.

The model is forced at its lateral boundaries by the astronomical tide (evolution of water levels and currents).

In addition, the model is forced in its momentum equations by the wave driving forces from the wave propagation model to reproduce the nearshore currents.

B. *TOMAWAC*

The TOMAWAC software, a 3rd generation/propagation model, allows studying the spectral propagation of sea states by using the main physical processes affecting the waves (refraction, shoaling, friction on the bottom, breaking waves, wind contributions, interaction with currents, diffraction ...). It calculates the evolution in space and time of the directional wave energy spectrum and can handle varied and complex sea conditions: ocean swells, splashes, sea states with several peaks in direction and/or frequency. From the directional wave energy spectrum, the software calculates, at all points of the mesh, the characteristics of the sea state: spectral significant wave height, mean wave direction, mean and peak frequencies, mean directional spread, radiation stresses, etc...

The TOMAWAC wave propagation code is coupled with the TELEMAC-3D calculation code and the GAIA sediment transport code.

It should be specified that a particular development was carried out in Telemac-3D to take into account the radiation constraints (2D) in 3D, as well as the energy induced by the surge, which makes it possible to better approximate the return currents [7].

The nesting of these models allows taking into account the consideration of wave currents due to surges in hydrodynamics as well as for sediment transport.

C. *GAIA*

The GAIA code coupled with TELEMAC-3D and TOMAWAC allows studying sediment transport under the combined action of currents and swell. The software calculates, at all points of the mesh, the evolution of the bottom and the solid flow at each time step. The local sediment sizes have been taken into account.

III. MODEL SETUP

A. *Bathymetry*

Different bathymetric sources (Fig. 3) have been used. SRTM data to compute the main slope of the Bandama river, PAA map in the lagoon, Shom map offshore, and more recent bathymetric survey near the inlet.

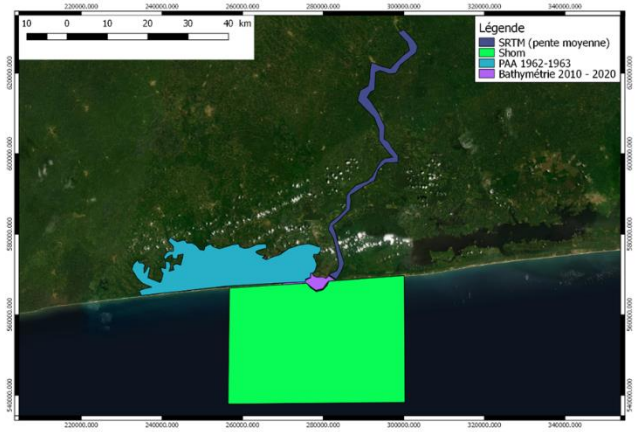

Figure 3. bathymetric data

B. *Mesh*

The horizontal mesh consists of triangular elements varying in size throughout the model from 1000 m offshore to about 30 m in the channel and at the dune cord, for a total of 48 342 knots and 90 044 elements (Fig. 4). The mesh size in the Bandama river is about 150 meters given the limited bathymetric data available in this area. For the same reason, the mesh size varies from 500 meters at the lagoon center, to about ten meters to ensure hydraulic connections in narrow areas. For the pass, as well as the dune cord, 30 metres mesh size were used in the dynamic zone (Fig. 5). This allows a free movement of the pass over a large area and does not constrain the morphodynamic calculation.

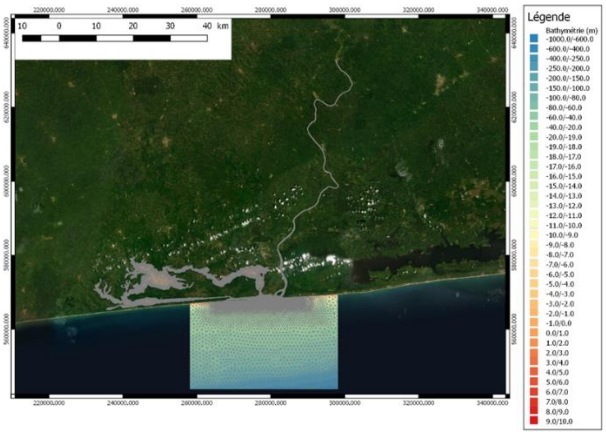

Figure 4. global mesh

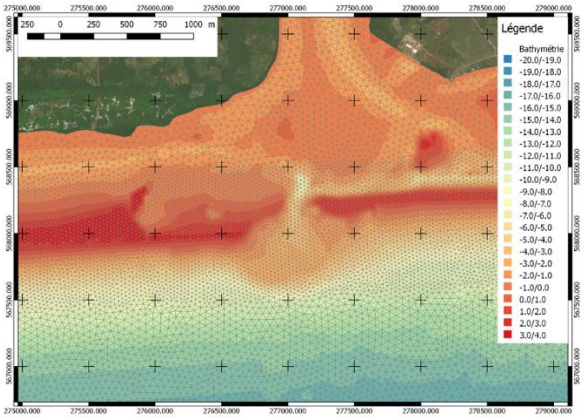

Figure 5. Mesh at the inlet localisation

IV. HYDRODYNAMIC VALIDATION

The hydrodynamic model is forced by taking into account the Bandama river flow rate, waves, tide, and general currents [6]. The model is then validated in three steps.

A. *Water level*

Water levels and currents are validated with two ADCP measurements (Fig. 6). One ADCP is located offshore of the inlet, the other one is located “inside” in the lagoon.

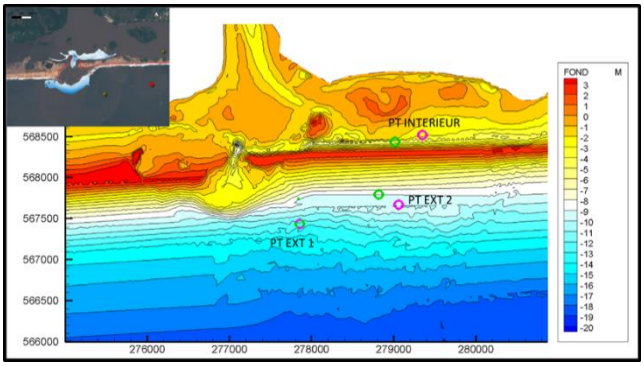

Figure 6. ADCP location inside and outside

The model is able to reproduce the water level at the two locations (Fig. 7), in particular the variation of the mean water level due to the variation of the Bandama river flow rate.

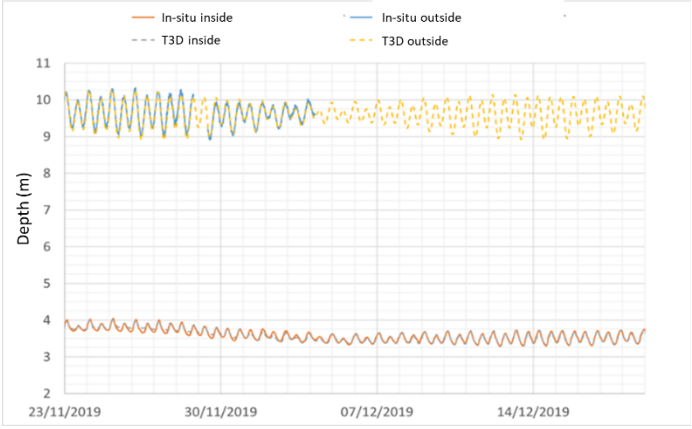

Figure 7. Water depth comparison at ADCP location

B. *Current validation*

River flow rate variations induce changes in velocity intensity and direction inside the lagoon which is well reproduced by the model (Fig. 8).

Figure 8. Velocity comparison at ADCP location

C. *Morphodynamic*

The morphodynamics is validated through three criteria: first through the global total sediment transport due to the littoral drift going east (while the inlet is migration westward, meaning updrift) with the CERC formula (Fig 9), secondly by mid term bathymetric evolution of the inlet observed between December 2019 and March 2020 (Fig 10 and 11); thirdly by the reproduction of seasonal inlet variations depending on the flowrate of the Bandama river.

The littoral drift is well reproduce, with 5 to 25% of difference with the CERC formula, but the system evolution has notable differences. The inlet start to move west, and sandy rerash east and west appear at expected localisation. The simulation was continued, but the model no longer evolves significantly following the expansion of the inlet.

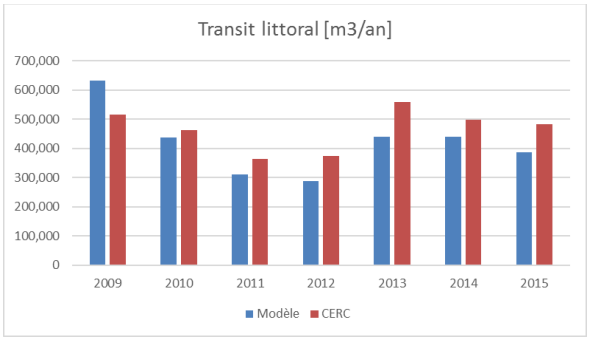

Figure 9. East littoral drift

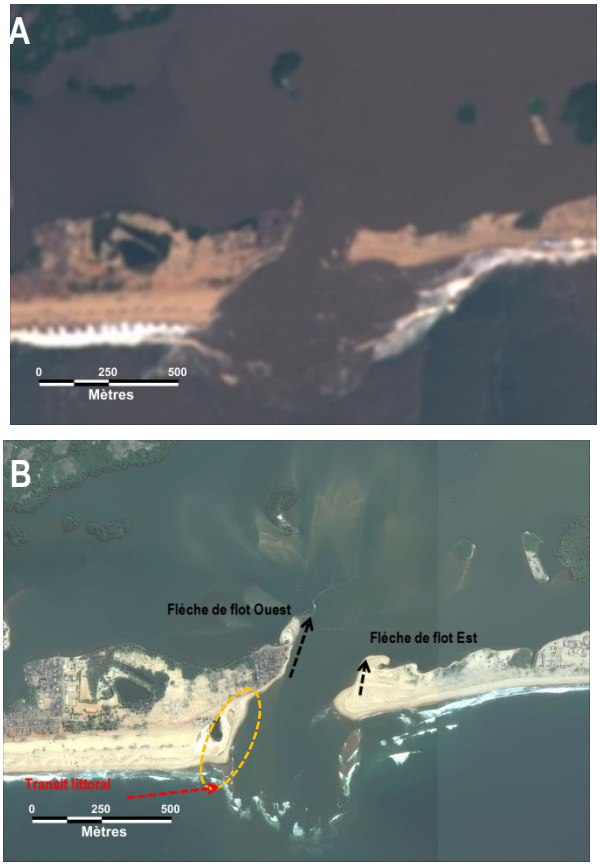

Figure 10. System evolution between December 2019 and March 2020

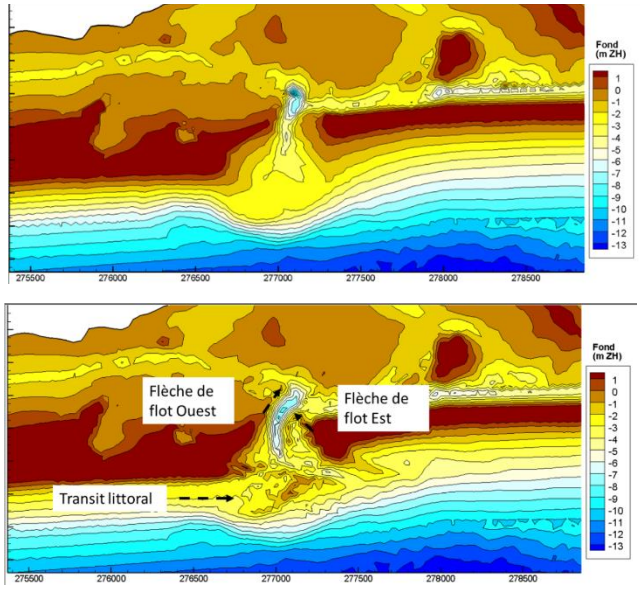

Figure 11. System evolutions modelled between December 2019 and March 2020

V. HYBRID ALGORITHM

The beach re-profiling tool (Fig 12, 13 and 14) is based on the equilibrium beach profile concept with a particular care for mass conservation. The tool is used every simulated month and any error in mass can lead to an overestimation or underestimation of beach nourishment and may lead to important errors in the global evolution of the system. To avoid mass errors, the tool is used directly on the mesh points, without intermediat grids.

The tools can be decomposed in four main steps:

- Determination of the profile for every point of the mesh
- Compute the theoretical profile
- Calculate the mass distribution over all the profile
- Apply the massProfile determination

In this step, the algorithm tries to define for every mesh point the profile from a top of the sand ridge to a bottom closure value. The profile path is determined from the slope of the bathymetry. For point where no profile can be found, especially peaks or troughs, their profiles are found by interpolating neighbour profiles. Many data are stored for every profile, like the main point associated, every neighbour to this profile, and the distance between the profile and the neighbours (Fig 12).

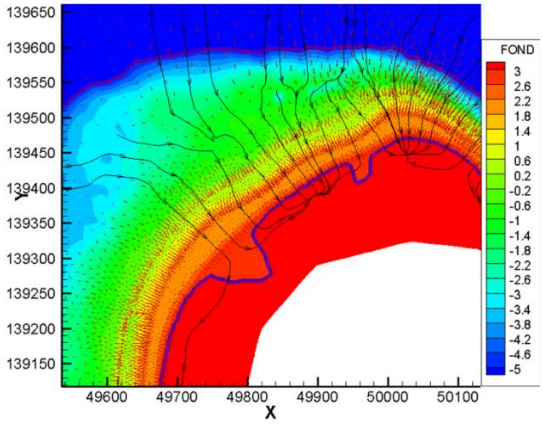

Figure 12. Profil determination

A. *Calculate the theoretical elevation*

For every mesh point where a profile has been found, the elevation from equilibrium profile is then calculated and an associated mass (to be added or removed) is computed (Fig 14, step 1 to 3). This theoretical elevation (1) takes only into account the curvilinear distance to the sand ridges, the closure altitude Z_0 and a coefficient A determined from the initial bathymetry slope.

$$Z(s)=Z_0-(A.s^{2/3}) \quad (1)$$

B. *Calculate the mass repartition*

For each profile, the mass added or removed is then distributed iteratively over all the points of the profile, ensuring mass conservation and weighting due to the distance to the profile (Fig 14, step 4). If a point exceeds the closing altitude (top and down), only the part of mass to reach the closure is applied, and the rest is redistribute iteratively along the profile.

C. *Apply the mass distribution*

For every mesh point, the sum of the mass from the previous step is calculated coming from all profiles. A coefficient common to all points is computed to avoid local exceeding of the closing altitude. Finally, it is only the mass sum weighting by this coefficient that is really applied to modify the bathymetry. Because no real modification is applied before this step, this is like applying the coefficient at the second step and correcting only partially the profile (Fig 14, step 5 and 6).

These last three steps are then repeated to slowly correct the bathymetry (Fig 14, step 7).

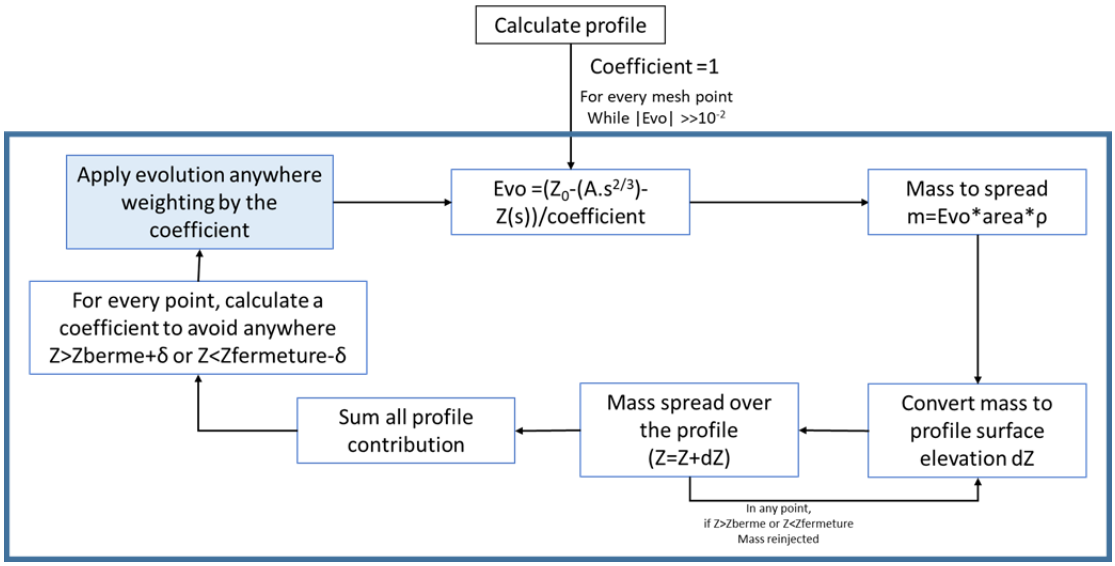

Figure 13. Re-profiling tool diagram

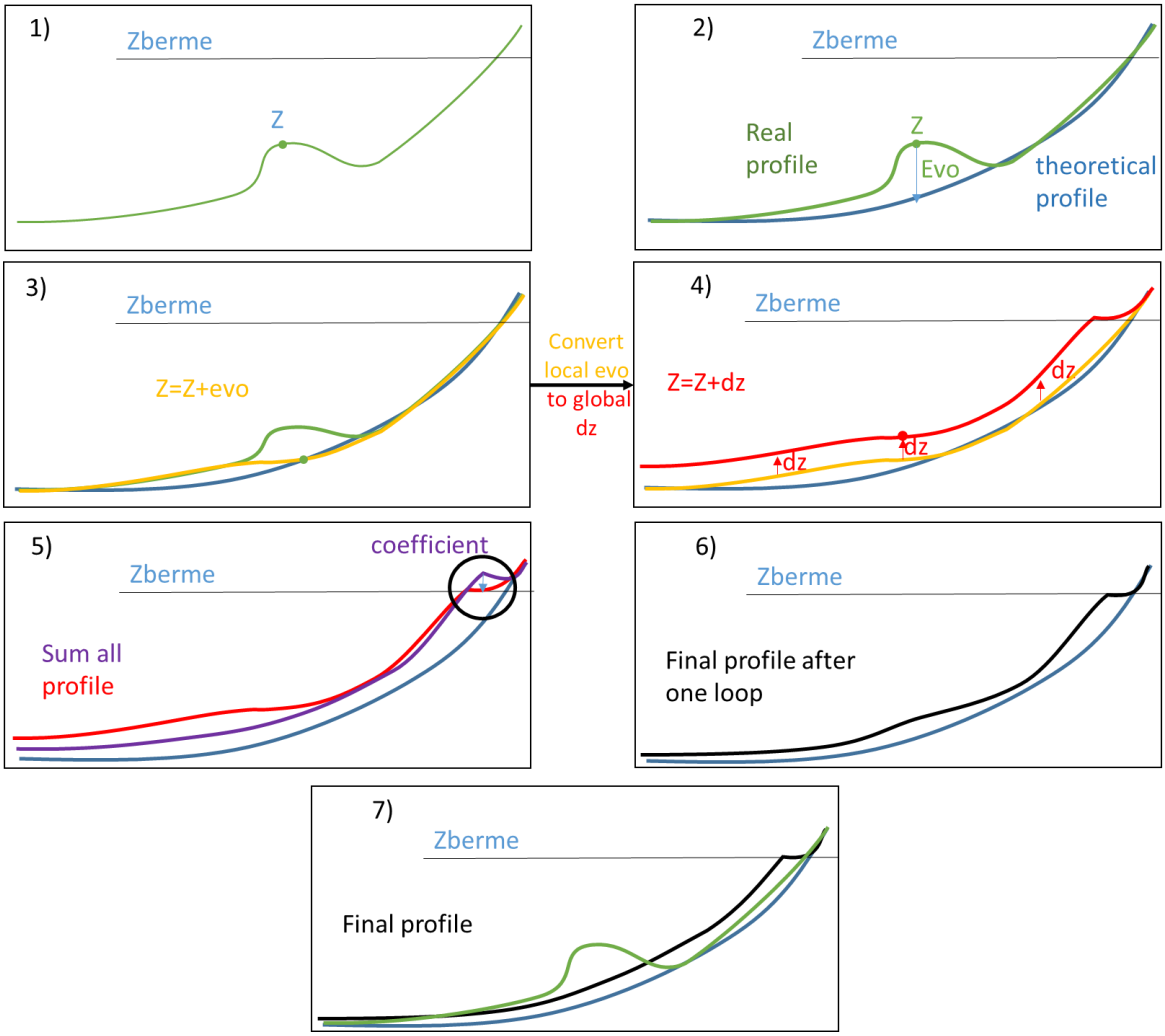

Figure 14. Re-profiling tool on one profile

VI. RESULTS

First, the hybrid model is tested over two inlet states, one representing the 2009 configuration (not presented here) to compare the velocity of translation of the inlet, the second representing the actual configuration (2020) but with 2009 Bandama flow rate (no data are available). The following figures (Fig 15) shows the improvements provided by the hybrid approach.

Without the tool, the inlet is widening and moving slowly westward (fig 11), while with the hybrid tool, the east sand bar is reconstructed and progresses westward allowing a faster westward migration of the inlet, as observed in nature. With the tool, the beach profile is maintained during the entire simulation at east and west of the inlet.

The model correctly reproduces the erosions due to the helical currents that allow the movement of the inlet eastward with an average rate of migration of 155 m/year. This average rate is correctly maintained for 2 consecutive years, what can be seen on the following figures: the dashed lines make it possible to materialize: the axis of the initial pass and the initial East and West dune. In the third year, the migration rate has slowed, due in particular to the increase in the width of the Western Cordon.

Other scenarios have been tested, like closing the actual inlet and opening the lagoon at different east location or also by adding structure to protect the west sand bar (Fig 16).

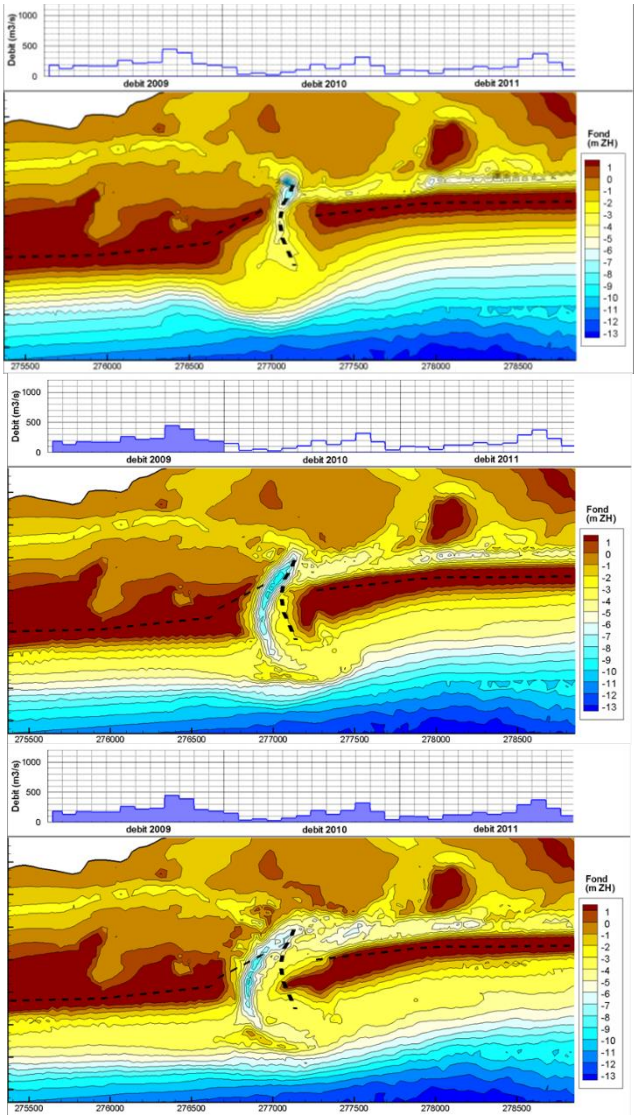

Figure 15. Initial bathymetry (top) and model result after one year and after 3 year (bottom) with reprofiling tool applied once a month

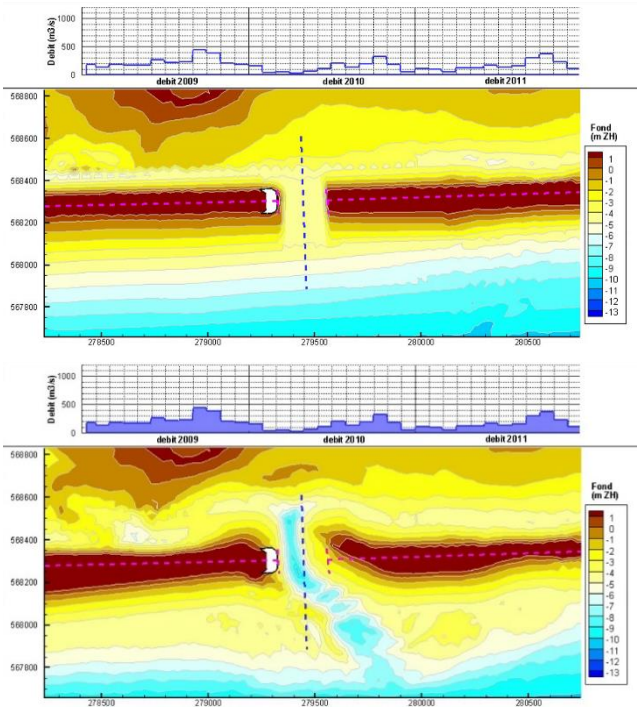

Figure 16. Scenario with one opening as in 1960 with structures to protect west sand bar, at initial state (top) and after three years (bottom).

VII. CONCLUSION

The hybrid model have been test and validated on the Grand Lahou system. It allows maintaining the beach profile and reconstructing sand bar. This tool can be used for long-term modelling.

ACKNOWLEDGEMENT

ARTELIA wants to thank the cooperation and efforts of WACA executive team led by Pr A.D. Ochou, Pr E.V. Djagoua and H. Ouattara, as well as the World Bank for its confidence.

REFERENCES

[1] BeDevelopment, 2017. Appui à la préparation du plan d'investissement pour la ville de Grand Lahou, République de Côte d'Ivoire. Rapport de synthèse – Atelier de validation.

[2] DHI, 2015. Projet d'aménagement et de réhabilitation de l'embouchure du Bandama à Grand-Lahou – Rapport final

[3] Kouassi Paul Anoh, 2010. Stratégies comparées de l'exploitation des plans d'eau lagunaire de Côte-d'Ivoire. Les Cahiers d'Outre-Mer. Revue de géographie de Bordeaux Vol 251 : Aspects de la Côte-d'Ivoire. Juillet-Septembre 2010

[4] Aubrey, D. G., & Speer, P. E. (1984). Updrift migration of tidal inlets. The Journal of Geology, 92(5), 531-545.

[5] Lemasson R., Rebert J-P., 1973. Les courants dans le golfe Ivoirien. Ed Orstom., sér. Octanogr., L~OI. XI, no 1: 67-95.

[6] Kristensen, S. E., Drønen, N., Deigaard, R., & Fredsoe, J. (2016). Impact of groyne fields on the littoral drift: A hybrid morphological modelling study. Coastal Engineering, 111, 13-22.

[7] P. Pechon and C. Teisson, 1994. "Numerical modeling of three dimensional currents in the surf-zone", 24 international conference Coastal engineering, ASCE, 2503-25012.

Sediment transport modelling (TELEMAC-3D + GAIA) case study: sand disposals in the Western Scheldt

T. Wolf, W.A. Breugem, K. Chu, B. Decrop,
G. Van Holland
International Marine and Dredging Consultants n.v.
Van Immerseelstraat 66, 2018 Antwerp, Belgium
thom.wolf@imdc.be

Y. Plancke, J. Stark
Flanders Hydraulics Research – Antwerp, Belgium
Berchemlei 115, 2140 Antwerpen

***Abstract*—In this study, the three-dimensional coupled (TELEMAC-3D + GAIA) morphodynamic Scheldt model is used to investigate the behaviour of sand disposals in the Western Scheldt by simulating the experimental disposal campaign of 2019 at the Put van Hansweert. A validation of the hydrodynamics shows that the Scheldt model is able to reproduce accurately water level predictions throughout the Scheldt estuary and good two/three-dimensional velocity patterns near the Put van Hansweert. By performing a Brier Skill Score analysis, it is shown that the simulated morpho-dynamics at the project site has the performance indication 'Good'. This reveals that the Scheldt model is suited for scenario analysis.**

By using the end state of a disposed sediment cloud from a multi-phase CFD simulation, realistic initial conditions of the sediment concentration are implemented by means of a horizontal & vertical interpolation on the TELEMAC-3D mesh. The results show that in the first five weeks during the disposals, 40% of disposed sediment is not encountered at the disposal local, which is in agreement with the measured loss rates. Most of the 0.9 [M m^3] disposed sediment tends to migrate in an upstream direction. By performing multiple sensitivity analyses, it is found that the stability of the disposed sediment is mostly affected by the choice of the equilibrium near-bed concentration formula and by the choice of the number and distribution of the vertical nodes in TELEMAC-3D.

I. INTRODUCTION

Maintenance of the navigation channel(s) in the Western Scheldt and Sea Scheldt is necessary in order to preserve the navigability for passing vessels. This maintenance encompasses the dredging of sand and other fine materials, as well as the disposal of these materials in strategically chosen areas in the Western Scheldt. These disposal areas are currently situated on shoals or in (side-) channels (Figure 1). A proposition to shift the disposal of sediment from these areas to deeper parts (pits) of the Western Scheldt exists, however the behaviour of the disposed sediment in these deeper parts is not fully understood.

Based on gathered bathymetric data during experimental disposal campaigns, volume evolutions have been analysed ([1]; [2]). Yet, the spreading and erosive behaviour of the disposed sediment in the deep pits on timescales of days to months remains unclear.

To answer these questions, several numerical models have been implemented [3]. These modelling studies showed that two-dimensional models show limitations to predict the transport of deposited sediment from the pits and showed the need for future studies using three-dimensional sediment transport models. The advantage of a three-dimensional model is that secondary circulations are resolved and hence, they do not need to be parametrized. This is particularly important, given the effect of the salinity on the secondary circulation in the study area, as these effects are not included in typical two-dimensional helicoidal flow parametrizations.

Therefore, in this study, a three-dimensional morphodynamical model is utilized to investigate the behaviour of the disposed sand in a hindcast of the experimental disposal campaign of 2019 at the Put van Hansweert ([2]; [4]).

The TELEMAC-3D module (version 8.1) is applied for the hydrodynamical calculations which solves the three-dimensional shallow water equations (with or without the hydrostatic pressure hypothesis) and the transport equations of intrinsic quantities (temperature, salinity, suspended sediment concentration). The sediment transport and morpho-dynamics are simulated using GAIA (version 8.1), which is the latest sediment transport code of the TELEMAC modelling suite.

II. HYDRODYNAMIC MODEL SETUP

The grid of the Scheldt model consists of unstructured triangular elements. Parts of the computational mesh and bathymetry of the Scheldt model are based on the SCALDIS model, which has been developed at Flanders Hydraulics Research [5]. The Scheldt model contains 214,416 calculation points in the two-dimensional grid and 397,889 elements. Twelve points are used for the vertical discretization. This leads to 2,572,992 calculation points for the entire three-dimensional model. These 12 vertical layers are located at 0%, 1%, 3%, 5%, 10%, 17%, 21%, 44%, 58%, 71%, 85% and 100% of the water depth. The high resolution near the bottom ensures that the model resolves the large sediment concentration gradient in the suspended sediment transport. The horizontal resolution (length of the sides of the

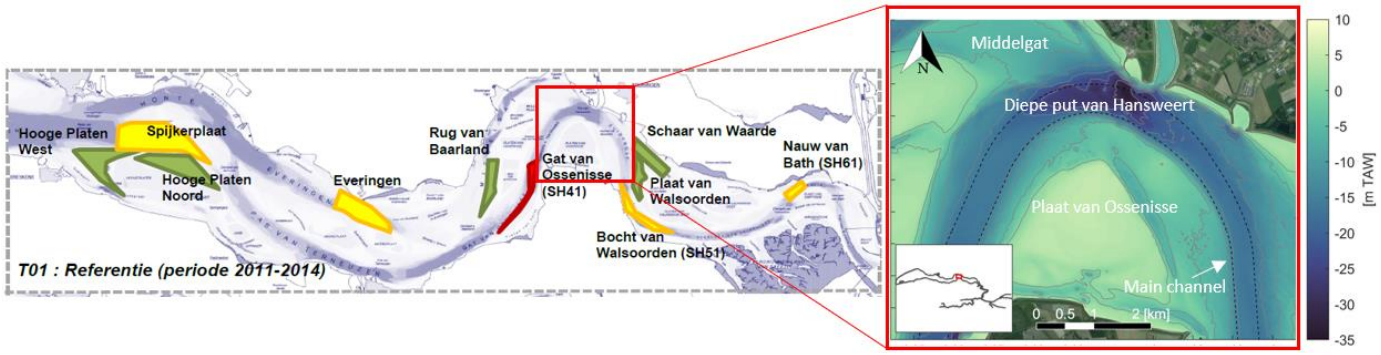

Figure 1 Left: Dumping strategy for the Western Scheldt (historical strategy for the period 2011-2014; colours indicate the intensity of the deposits; green to red = from low to high intensity).Source: [1]. Right: Zoomed-in red box with bathymetry of the Put van Hansweert disposal area.

triangular elements) varies between 3.6 [m] (mainly at Upper Sea Scheldt) and 400 m (Figure 2). In the coastal strip the resolution varies between 200 [m] and 400 [m] depending on the depth. The resolution in the Western Scheldt is approximately 120 [m], with refinements near the project area at the Put van Hansweert of up to 15 [m].

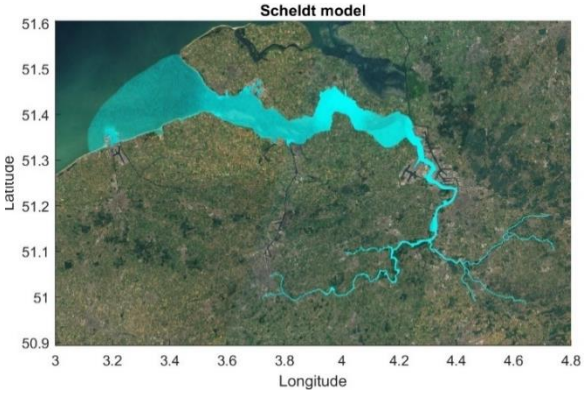

Figure 2 The computational mesh of the Scheldt model.

The model contains an open downstream boundary at the sea mouth of the Western Scheldt and eight upstream boundaries. Time series of water levels, velocities and salinity are imposed on the downstream open boundary. The time series of water levels and velocities come from the large-scale in-house developed iCSM model [6]. This model simulates tidal and wind-driven currents in the North Sea and other parts of the continental shelf. It is forced by hydrodynamic data from the OSU/TPXO model [7] for astronomical tidal components and by meteorological data (wind velocity and air pressure) obtained from the ERA-5 meteorological model. From the iCSM model, results of water levels and depth-average velocities are interpolated on the open downstream sea boundary of the Scheldt model via an in-house boundary nesting tool. The downstream precondition for salinity is based on either average representative values or measured values at the Vlakte van de Raan. There are eight upstream boundaries where flow rates and salinity are imposed.

Initial conditions of the model consist of spatially varying conditions for water levels and three-dimensional fields of velocity and salinity. These conditions are determined on the basis of a spin-up calculation of one day. An initial field has been created for the salinity from measured salinity data using horizontal interpolation.

The model is being used to simulate periods ranging from one day to two months. The following model settings have been used in the simulations of hydrodynamics and the salinity (Table 1).

TABLE 1 MODEL PARAMETERS SETTINGS OF THE SCHELDT MODEL

Parameter	Value
Time step	10 [s]
Initial conditions	Spin-up conditions for water levels, currents and interpolated salinity field
Number of vertical nodes	12 (three-dimensional model)
Version TELEMAC	TELEMAC-3D (goblinshark branch based on version 8.1)
Salt transport	On
Wind	Off
Roughness formula	Nikuradse
Bed roughness value	Spatially varying roughness field
Vertical turbulence model	6: GOTM (using K-epsilon model with second order closure for the buoyancy flux)
Horizontal turbulence model	4: Smagorinski
Scheme for advection of velocities	1: characteristic method
Scheme for advection of tracers	13: Leo Postma for tidal flats
Solver	7: GMRES

III. HYDRODYNAMIC VALIDATION

The RMSE value of water levels for the period of May-June 2017 is presented in Figure 3. It can be noted that, at the downstream part of the model (station Bol van Heist) the error is equal to 0.08 [m] and remains below 0.14 [m] along the estuary until Antwerp, which is the area of interest of the present paper. Near the Put van Hansweert at the measurement station of Hansweert, the error is 0.10 [m]. This is considered to be a good model performance.

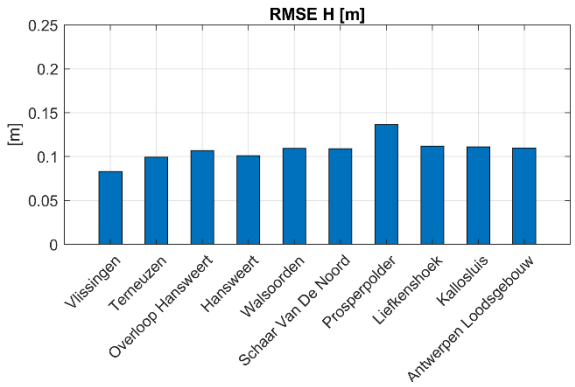

Figure3 RMSE [m] of the water level obtained for the various measuring points along the estuary, for the period 15/05/2017 - 02/06/2017

By using the model qualification based on the RMAE (relative mean absolute error) statistical parameter [8], which includes the accuracy of both the velocity magnitude and direction, comparisons between observed (with ADCP) and simulated depth-averaged velocities can be quantified. The RMAE statistics between simulated and measured velocities were calculated for the thirteen ADCP-campaigns near the project site. Values of the model qualification based on RMAE are provided in Figure 4. Thirteen available transects were used for the comparison and all, except for the 'Ossenisse_Dwarsraai -_20080407_Spring' transect, show a RMAE with the qualification 'Good' or 'Excellent'. Both the calculated RMSE and RMAE values of the five ADCP transect comparisons at the Diepe put van Hansweert are shown in Table 2.

Model qualification		RMAE [-]
Excellent		<0.2
Good		0.2-0.4
Reasonable/fair		0.4-0.7
Poor		0.7-1.0
Bad		>1.0
Not Applicable		-

Figure 4 Model qualification based on RMAE [8].

TABLE 2 COMPARISON OF RMSE AND RMAE OF VELOCITIES ALONG THE SELECTION OF ADCP TRANSECTS AT DIEPE PUT VAN HANSWEERT.

Campaign	RMSE [cm/s]	RMAE[-]
Diepe_Put_Hansweert_20170720	17.4	0.18
Diepe_Put_Hansweert_20181214_Dwarsraai	15.0	0.21
Diepe_Put_Hansweert_20181214_Langsraaien	18.0	0.26
Diepe_Put_Hansweert_20181220_Dwarsraai	13.0	0.15
Diepe_Put_Hansweert_20181220_Langsraaien	11.8	0.17

Figure 5 shows the comparison between simulated and measured vertical velocity profiles at the middle of the ADCP-transect during the rising of the tide. Both the shape of the velocity profile and its magnitude are well represented in the model.

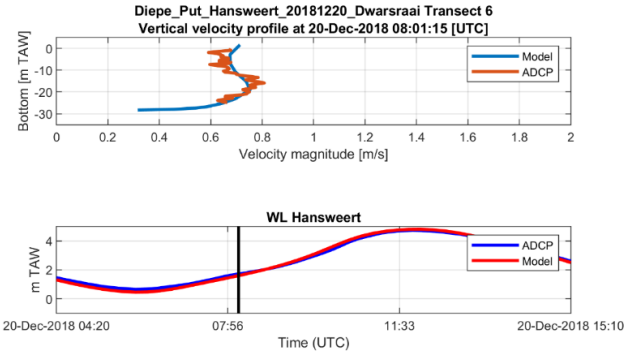

Figure 5 Top: Comparison of vertical velocity profiles between measurement velocities (ADCP campaign 20-Dec-2018 06:54:29, Diepe put van Hansweert) and simulated velocities. Bottom: Comparison of measured and simulated water level at Hansweert. The black line indicates the moment of comparison in the tide.

The three-dimensional behaviour of the simulated flow is further validated by comparing multiple times instances with measured ADCP-velocities taken during two ADCP-campaigns of December 2018 at the Put van Hansweert. An example is shown in (Figure 6). It shows that the overall patterns of the simulated transversal velocity components are in agreement with the measured ADCP transversal velocities. During the rise of the tide after slack water, both the simulated and measured transversal flows are at the bottom directed towards the outer bend and at the surface towards the inner bend.

A comparison of timeseries of the measured and modelled salinity near the water surface, just downstream and upstream of the Put van Hansweert, shows that the simulated salinity amplitude at the Overloop van Hansweert is underestimated by approximately 1 [psu]. Upstream of the Put van Hansweert at Baalhoek, both the amplitude and temporal variation of the salinity are well represented. A more quantitative analysis using statistical parameters (Table 3) shows that along a significant part of the Scheldt estuary, the salinity patterns are simulated well and that maximum RMSE reaches merely 0.93 [psu].

TABLE 3 STATISTICAL ANALYSIS BETWEEN SIMULATED AND MEASURED SALINITY VALUES (PERIOD 15/05/2017 - 02/06/2017) ALONG STATIONS IN THE SCHELDT ESTUARY.

Nr	Station	Correlation coefficient R [-]	RMSE [psu]	Bias [psu]
1	Overloop Hansweert	0.91	0.51	-0.11
2	Baalhoek	0.96	0.93	0.82
3	Prosperpolder	0.93	0.46	0.01
4	Liefkenshoek	0.93	0.67	0.50
5	Oosterweel	0.97	0.91	0.65
6	Hemiksem	0.98	0.54	0.44

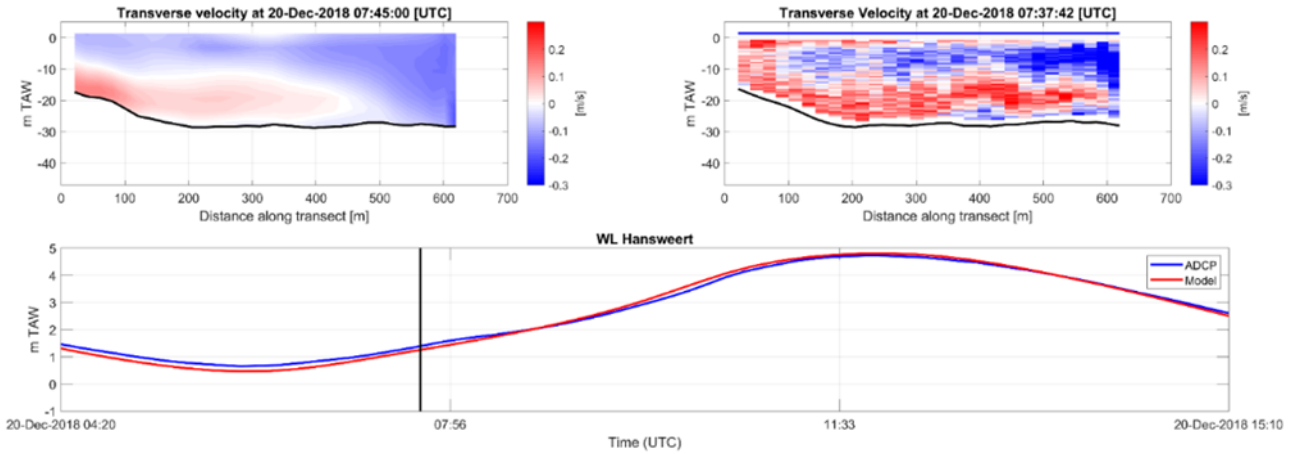

Figure 6 Comparison between simulated transverse flow velocity along transect in the 'Put van Hansweert' (top left) and measured transverse flow velocity (ADCP) along transect (top right). Red colour (positive velocity to the right (outer bend)), blue colour (negative velocity to the left (inner bend)). The bottom figure shows the measured (blue) and simulated (red) water level, the black vertical line indicates the moment of the ADCP-measurement

IV. HYDRODYNAMIC RESULTS

For the investigation of the spatial distribution of the secondary circulation patterns near the Put van Hansweert, multiple transects along the thalweg with mean transversal velocities for spring tidal conditions are displayed in Figure 7. It shows that the upslope bottom velocities are present along a large part of the inner bend of the channel of Hansweert. The most pronounced circulation patterns are observed at the sharp bend of the Put van Hansweert transect 9. Furthermore, it is observed that transects 11 till 13 do not show similar tide averaged flow patterns as the upstream transects. This is likely due to the influence of the tidal flow coming from and going towards the side-branch of the Middelgat (location indicated in Figure 7 and right subfigure of Figure 1).

The effect of lateral flow is substantially influenced by the density gradient due to the presence of salinity. This can be demonstrated by performing a run without salinity. When the effect of salinity is not included in the simulation, the simulated transversal velocity pattern changes significantly, and shows at patter that does not correspond to the ADCP transversal velocity (not shown). The tidally averaged transversal velocities along cross-sections in the channel near Hansweert show that multiple circulation cells are no longer present. Especially near the Put van Hansweert, the flow behaves as a typical helicoidal flow with a transversal surface

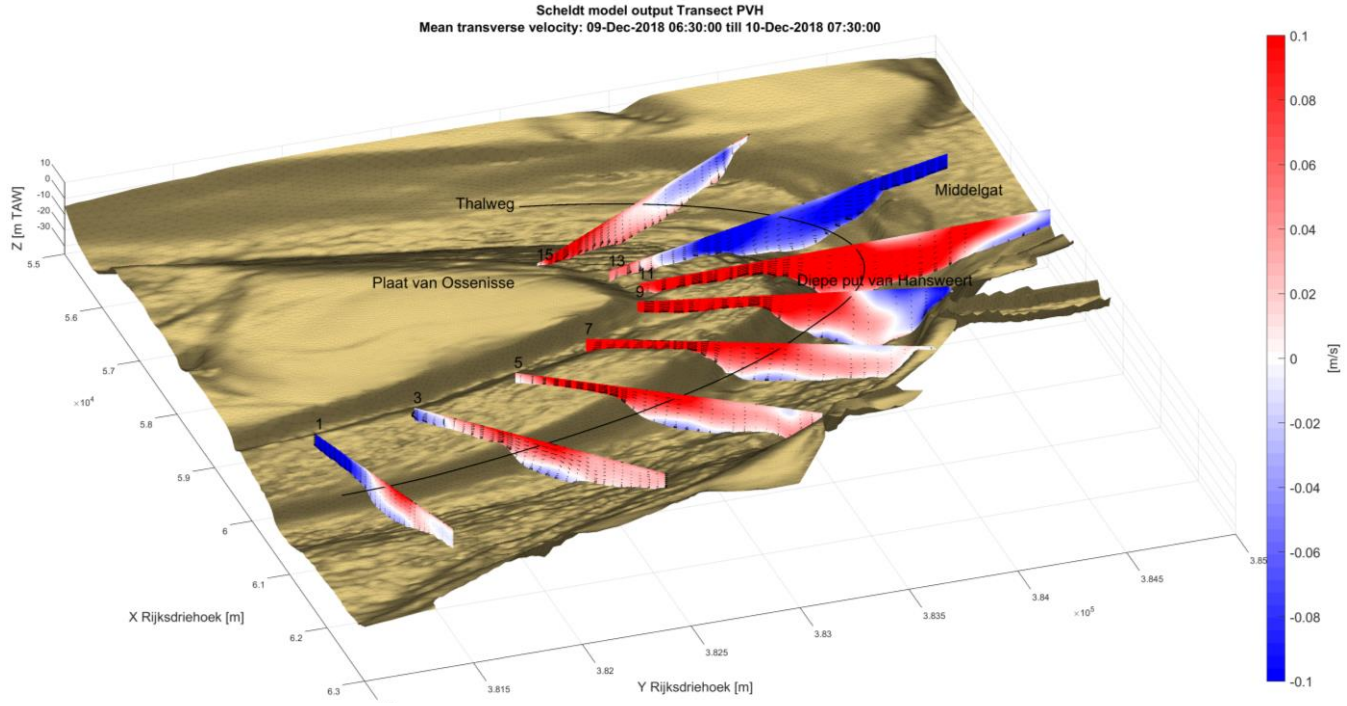

Figure 7 Simulated mean transverse flow velocities (for spring tidal conditions) at multiple transect perpendicular to the thalweg near the 'Put van Hansweert'. Red colour (positive velocity to the outer bend), blue colour (negative velocity to the inner bend).

flow directed towards the outer bend and a bottom flow directed towards the inner bend. This shows that the presence of salinity is vital to correctly simulate the complex local flow pattern and that it therefore should be included in the morpho-dynamic calculations.

V. MORPHODYNAMIC MODEL SETUP

A. GAIA settings

The used physical and numerical settings when coupling TELEMAC-3D to the sediment transport module GAIA are provided in Table 4. The sediment transport model is utilized to simulate two different sand fractions, hereafter called fraction1 and fraction2. Fraction1 is the disposed fraction with a d_{50} of 170 [µm] based on the analysis of barge samples performed by [4], which [9] applied as well in their study.

Fraction2 is the background sediment which is naturally present in the model through the definition of an initial layer thickness and has an attributed d_{50} of 220 [µm]. The choice of the natural sediment grain size is based on a grain size map shown from [10], where the d_{50} ranges between 200 - 250 [µm]. Furthermore, sediment samples [4] show that coarser sediments (d_{50} = 250 [µm]) are to be found downstream of the project site at the Overloop van Hansweert and finer sediments (d_{50} = 170 [µm]) upstream at the Drempel van Hansweert. A value in between this range is therefore representative to be used as d_{50} for the project site.

TABLE 4 MORPHOLOGICAL SETTINGS GAIA MODULE

Parameter (keywords GAIA)	Value
Finite volumes	YES
Minimal value of the water height	0.5 [m]
Number of sediment fractions	2
Classes sediment diameters	170; 220 [µm]
Classes initial fraction	0.0; 1.0
Bed-load transport formula for all sands	7 Van Rijn 1984)
Suspension transport formula for all sands	3 (Van Rijn 1984)
Hindered settling	YES
Hindered settling formula	1 (Whitehouse 2000; the equation is adapted for sand)
Skin friction correction	1
Formula for slope effect	1 (Koch and Flokstra, default β=1.3)
Formula for deviation	1 (Koch and Flokstra)
Sediment slide	NO
Layers non cohesive bed porosity	0.4 (default)
Active layer thickness	0.01 [m]
Number of layers for initial stratification	3
Layers initial thickness	1.E-6; x; x [m] (latter two spatially varying, in `user_bed_init.f`)

As initial layer thickness of the natural background sediment (fraction2 in GAIA) in the Western Scheldt, a spatially varying layer thickness has been applied in the Fortran function '*user_bed_init.f*'. The height of the sediment layer is based on a combination of an existing TNO dataset [11] and the knowledge of the known locations of hard structures in the Western Scheldt [12].

B. Sediment sources

Initial conditions of the disposed sediment (fraction1 in GAIA) originate from multi-phase CFD simulations [13]. In these simulations a realistic amount of sediment, corresponding to a hopper volume of 4000 [m^3], was disposed at the Put van Hansweert under flood flow conditions. The CFD model simulates 380 seconds, after which sediment concentration of the generated sediment plume (Figure 8) is extracted and horizontally & vertically interpolated on top of the TELEMAC-3D mesh.

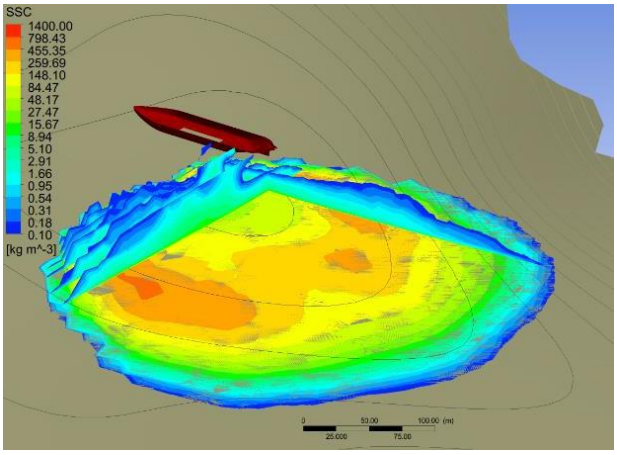

Figure 8 Contour plot of the suspended sediment concentration [kg/m^3] from the CFD simulation scenario [13] at time instant t=380 s (end of the simulation). Black contour lines show the local bathymetry.

The disposal campaign of autumn 2019 has been reconstructed with the morpho-dynamic Scheldt model to investigate the disposed sediment loss over 2.5 months' time. The start of the simulation period is in accordance with the hydrodynamic starting period of May 2017. The disposed sediment volumes and disposal times are used from the recorded dredging data from the Flemish Ministry of Public works. The TELEMAC code was modified, such that the disposed volume was added to the suspended sediment in the model at the moment of each disposal where the amount of sediment from the CFD run is adjusted to match the volumes of the recorded disposal data. To take the flow direction into account on the disposal processes, the sediment plume is mirrored along the flow direction in case of ebb tide.

During the disposal campaign of 2019, two different sites were used in the Put van Hansweert for disposal. These are the outer bend (solid green bins 155 & 156 in Figure 9, hereafter called Northern disposal location) and the inner bend (solid yellow bins 292, 293 & 326 in Figure 9, hereafter called Southern disposal location). At the Northern disposal site, a total of 300,000 [m^3] of sediment is disposed within the first three weeks of the simulation period and at the

Southern disposal site, a total of 700000 [m^3] is disposed within the first eight weeks of the simulation period.

Measured bathymetric datasets from multibeam-echosounder campaigns reveal that the location of the disposal inside the bend of the Put van Hansweert is of key importance (Figure 9). The donut shape of the disposed sediment at the northern outer bend (bins 155 and 156) seems to be relatively stable, whereas at the same time, it is clearly visible that bedforms are actively migrating along the inner bend. From the small bed evolution in bins 223 till 225 it seems that there is a distinct border between these two regions. Approximately two months after the start of the disposal campaign, the disposed sediment is still visible in its confined spot in the deep part of the Put van Hansweert and maintains its donut shape.

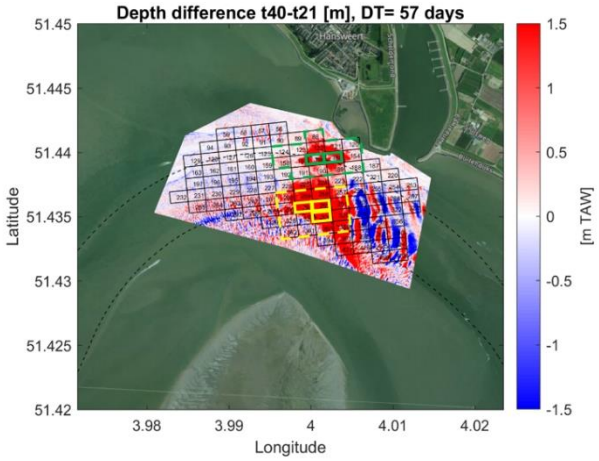

Figure 9 Observed bed level difference [m] in 57 days' time from multibeam-echosounder datasets T40 and T21. Overlaid with black polygons of disposal bins and the navigation channel. Green polygons display the location of the Northen disposal bins (155,156) and the corresponding volume calculation area (dashed line). Yellow polygons display the location of the Southern disposal bins (292, 293 & 326) and the corresponding volume calculation area (dashed line).

C. *GAIA adaptations*

Multiple adaptations have been implemented in separate FORTRAN files of the GAIA code to perform the simulations, which are treated below.

ZREF: The Van Rijn (1984) equilibrium near-bed concentration formula is given as:

$$C_{eq} = 0.015 d_{50} \frac{\left(\frac{\theta'}{\theta_{cr}} - 1\right)^{1.5}}{z_{ref} {D_*}^{0.3}} \quad (1)$$

where d_{50} is the median grainsize of the sediment, θ_{cr} is the critical Shields parameter, $\theta' = \mu\theta$ the shear stress due to skin friction, $D*$ is the dimensionless grain diameter of the sediment and z_{ref} is the reference height defined in GAIA as $z_{ref} = 0.5 k_s$ with k_s the total bed roughness. However, following the original paper [14], it is stated that for stability reasons the value of k_s should have a minimal value of $0.01h$, were h denotes the water depth. This formulation was implemented in the '`zref_gaia.f`' subroutine and has been applied accordingly in this study. Note that there is no physical reason for the bed load thickness (and hence z_{ref},) to depend on the water depth. This dependence was added by Van Rijn merely on numerical reasons (namely to avoid the exponential peak in the Rouse profile close to the bed). Therefore, an additional calibration simulation with a constant z_{ref} = 0.15 [m] was performed. The results of this simulation are provided in the chapter VI.

POROSITY EFFECTS: A correction factor has been applied to account for the porosity effect on the dilatancy of the sand which influences the erosion. Reference [15] found that in the high velocity range (> 1.5 [m/s]), shearing of sand occurs. Due to this, the porosity increases slightly after which dilatancy yields an inward hydraulic gradient causing a reduction in erosion. Using results from a recent study [16], the following modification to the Van Rijn equilibrium near-bed concentration formula has been made in '`suspension_vanrijn_gaia.f`':

$$C_{eq} = 0.015 d_{50} \frac{\left(\frac{\theta'}{\theta_{cr}} - 1\right)^{1.5}}{z_{ref} {D_*}^{0.3}} f_d \quad (2)$$

Here, f_d stands for the correction factor which is defined as

$$f_d = \begin{cases} 1, & \theta' \leq 1 \\ \frac{1}{\theta'}, & \theta' > 1 \end{cases} \quad (3)$$

The inclusion of the correction factor has a limited impact on the local morphodynamics near the project site of the Put van Hansweert, but tends to effectively stabilize excessive morphological instabilities.

HYBRID-SCHEME AND DISTRIBUTION VERTICAL NODES: In the simulations, the vertical advection and diffusion was calculated using the '`set_dif.f`', subroutine, which solves the suspended sediment vertical profile using an implicit scheme and a tridiagonal matrix solver. This subroutine is fast and stable. However, the settling of sediment is calculated using a upwind numerical scheme, which leads to substantial numerical diffusion. Therefore, a hybrid numerical scheme was used [17]. In such a hybrid scheme, an upwind scheme is used for high Peclet numbers (Pe>2, with Pe = uΔz/ν, and u is the velocity, Δz the vertical mesh spacing and the ν diffusivity, when advection is dominant over diffusion), whereas a central scheme is used for low Pe numbers, (i.e. where the physical diffusivity is already high). The results are shown in Figure 10 for a test case in straight uniform open channel flow. The hybrid scheme shows less numerical diffusion than the original scheme. Note that this simulation was performed with a refined mesh near the bottom (twelve vertical nodes).

Initial tests with coarser layer distributions (five & ten sigma layers) revealed very large numerical diffusion, leading to sediment concentrations that are too high, and hence too strong bed erosion. It should be noted that even though the current selected twelve vertical nodes (section II) are the best option so far, since the choice of it is a trade-off between accuracy and computational time & data usage, the selection could be further optimized in future studies.

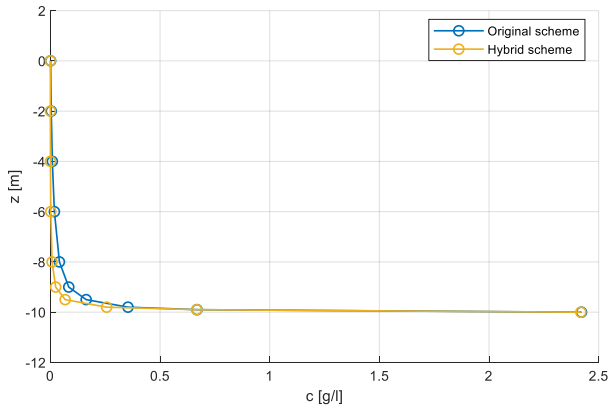

Figure 10 Comparison of original and hybrid advection scheme in straight channel flow simulation.

C-VSM VS HIRANO: Initial tests were performed using the continuous vertical sorting model (C-VSM) [18]. The continuous vertical sorting model is an alternative model for calculating the sorting in the bed, which leads to the formation of stratified sediment layers. This model has the advantage that the stratigraphy of the bed is taken better into account, thus leading to less artificial mixing of sediment in the bed , at the expense of a larger calculation time. In order to use this, the code was changed, such that bed changes due to suspended sediment transport as well as due to bedload were taken into account. However, the results of these tests showed that the C-VSM, in its current form, does not conserve the amount of material, which is essential for the current study, where the amount of fraction1 is used to determine the spreading of the disposed sediment. Some investigations were performed to find the cause of this, and it was found the almost all of the changes in the volume of a certain fraction occurred in the Douglas-Peuker algorithm that is used to simplify the stratigraphy profiles.

VI. MORPHODYNAMIC CALIBRATION

A qualitative and quantitative validation of the natural morpho-dynamics has been performed by comparing the bed level difference after 46 days from measured multibeam-echosounder datasets, with the simulated bed level difference. In order to determine which of the available equilibrium near-bed concentration equations in GAIA is best suited for the morpho-dynamic modelling tasks of the current study, several simulations with different equations were performed. Results show that there are large differences between the individual equations. Using the Zyserman-Fredsoe formulation, the simulated bed evolutions are extremely high, causing the model to crash within a few simulated days' time. The same holds true when using the Smith and McLean equation (implemented in a user defined Fortran file). Only the Van Rijn (1984) formulation provides realistic bed evolutions, Therefore this equation is selected for further comparison with the observed bed level differences in this section, together with the total load equation of Engelund-Hansen, which is used without advection-diffusion of suspended sediment. This latter applied formula acts as a benchmark equation for river/estuarine morpho-dynamics.

By comparing the measured bed evolution from Figure 11 with the simulated evolutions in Figure 12 (using Van Rijn (1984) equation), it is visible that there is a dynamic area along the inner bend where large-scale bars are migrating upstream. A less dynamic area is visible in the outer bend, which partially corresponds to the region where a stiff non-erodible clay layer is situated. Both measurements and simulation show that there is on average sedimentation on the shoal near the inner bend.

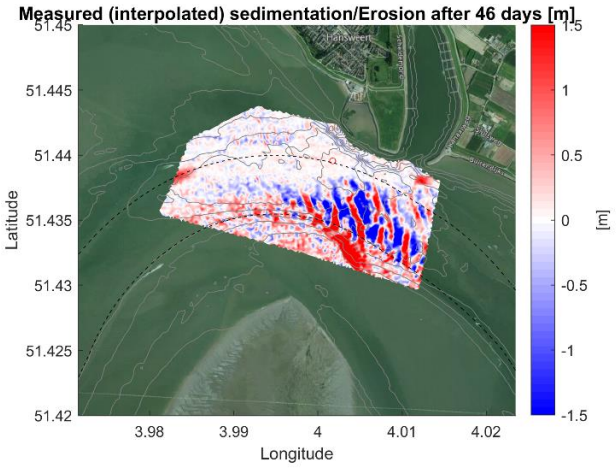

Figure 11 Bed level difference [m] between multibeam-echosounder datasets T20 and T21 (46 days apart), interpolated on top of model mesh.

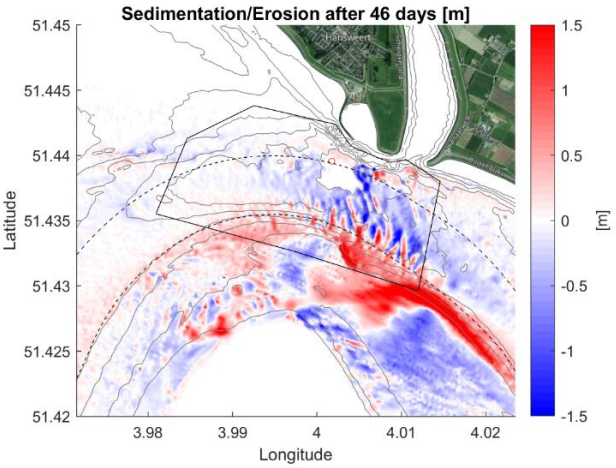

Figure 12 Simulated bed evolution [m] after 46 days with Van Rijn (1984) formula.

The model, using the Van Rijn (1984) equation, has a moderate correlation R = 0.67 [-] with the observed bed evolution and a calculated bias of -0.05 [m]. This shows that simulated bed evolution tends to be slightly more erosive than the measured evolution. Table 5 gives an overview of the statistical parameters for different tested equations. A performed Brier Skill Score (BSS, [19]) analysis of the models with different transport equations, shows that all morpho-dynamic validation simulations perform well. The model using the Van Rijn (1984) equation has a BSS of 0.44 [-]. This implies that the morphodynamical performance of the model has the classification 'Good' (Table 5-3). The BSS of the model with the modified Van Rijn (1984, with constant

z_{ref} = 0.15 [m]) equation has a smaller value (0.34 [-]), but still the classification 'Good'.

The simulation with the Engelund-Hansen total load equation performs even better than the Van Rijn simulations, having the classification 'Excellent'. Though, this total load formula cannot be further used for the analysis of the sediment disposals since three-dimensional sediment concentration fields are applied in the model to simulate the initial spreading of the sediment plume. For this, suspended load transport needs to be calculated by the advection-diffusion equation in TELEMAC-3D.

TABLE 5 OVERVIEW OF STATISTICAL PARAMETERS, CALCULATED FROM THE MEASURED AND MODELLED BED EVOLUTIONS FOR THE DIFFERENT TESTED EQUATIONS.

Equation	Bias [m]	RMSE [m]	Correlation [-]	BSS [-]
Engelund-Hansen	-0.11	0.50	0.75	0.54 (Excellent)
Van Rijn (1984)	-0.05	0.56	0.67	0.44 (Good)
Van Rijn (1984) modified	-0.15	0.60	0.61	0.34 (Good)
Van Rijn (1984) hybrid scheme	-0.12	0.57	0.67	0.41 (Good)

Overall, based on both a qualitative and quantitative validation, the model performs well at the Put van Hansweert and is ready to be used for studying the disposal of sediment.

VII. MORPHODYNAMIC RESULTS

The disposed sediment loss in the first 2.5 months of the realistic reconstructed disposal campaign of autumn 2019 are shown in this section. In this simulation, disposals of both the northern and southern sites are included. From the simulated results, using the Van Rijn (1984) formulation, it can be computed that the loss (i.e., volume outside the northern and southern calculation areas) in the first five weeks of disposal is higher in the model than in the multibeam-echosounder measurements (Figure 13, comparing difference between orange and light-blue lines with difference between red and dark blue lines). To be exact, 40% is lost in the model compared to 36% in the measurements. After this period, the simulated decrease is smaller than the measured decrease. Compared to the estimated measured (linear) loss rate of 2130 [m^3/day] in the two months after the last disposal, the modelled loss rate of 1411 [m^3/day] is 34% less. It is found that the disposed volume in the model is slightly less than the actual disposed volume, especially in the southern site. This can be explained by volume correction factor that is applied to the CFD sediment plume for every single disposal. Due to a bottom evolution which is more prominent in the southern area, the correction factor is underestimated more than for the northern area. For future iterations, the implementation of the correction factor needs to be improved by taking the effect of the bed evolutions throughout the simulation better into account.

Figure 14 shows that most of the disposed sediment is still confined to its original disposal location after 2.5 months of simulation. Most of the sediment that moves out of the disposal area, tends to migrate in an upstream direction of the main channel. In case of the Northern disposal site, most of the sediment moves along the outer bend, with some sediment moving downstream in the direction of the side channel entry (Middelgat). For the Southern disposal site, most sediment moves along the inner bend. A clear distinction between the sediment disposed in the Northern and Southern bins is visible. This could be explained from a hydrodynamics point of view by the, two individual secondary circulation cells in the bend of the Put van Hansweert (Figure 6). As a result of this, there is a tide averaged flow division in the middle of the channel by which the disposed sediment in the outer bend stays in the outer bend and does not migrate as usual with a helicoidal flow towards the inner bend.

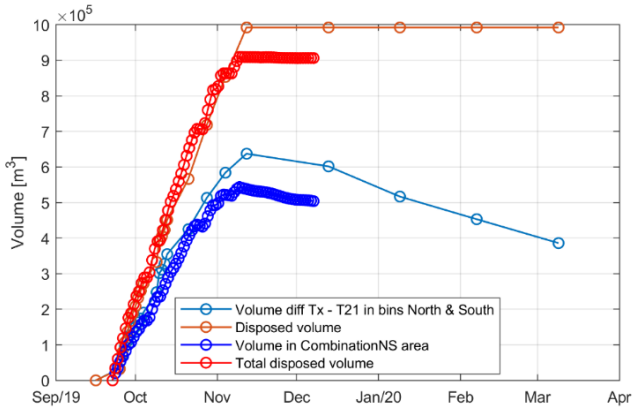

Figure 13 Volume evolution (measured and modelled) of disposed sediment [m^3]. Light-blue: observed remaining volume in the Northern & Southern calculation polygons. Orange: total volume of disposed sand. Dark blue: simulated remaining volume of sand in the Northern & Southern calculation polygons. Red: volume of disposed sand in model.

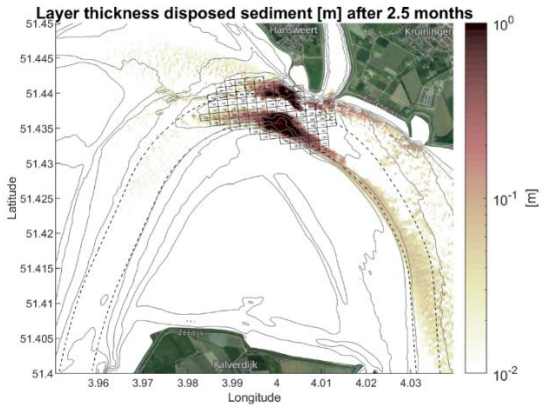

Figure 14 Layer thickness of disposed sediment (northern & southern area) after 2.5 months. Layer thickness scale is saturated.

In order to provide an estimation of the migration directions of the disposed sediment, the region surrounding the Put van Hansweert is divided into ten separate calculation polygons in which the volumes of disposed sediment are calculated. Figure 15 shows that the largest amount of sediment, aside from the disposal polygons, is found upstream in polygon 8 (8.1%) and on the outer bend of the

Put van Hansweert in polygon 10 (6.9%). Of the sediment found in the relatively large polygon 10, the layer thickness map (Figure 14) indicates that the largest amount is found at the outer bend of the Put van Hansweert and at the edge of the main navigation channel. Of the total disposed 0.9 [M m^3] sediment, only 2.3% is found back downstream in the Middelgat side channel (polygon 1).

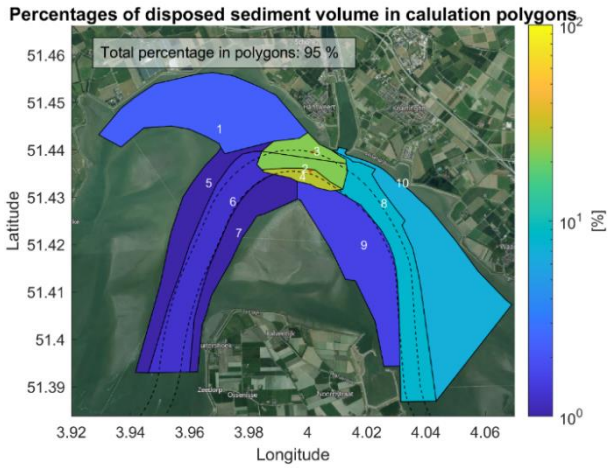

Figure 15 Percentage of disposed volume found in polygons after 2.5 months.

VIII. CONCLUSIONS

In this study, numerical simulations were performed with the morpho-dynamic TELEMAC-3D Scheldt model to investigate the behaviour of disposed non-cohesive sediment in the Put van Hansweert. More specifically, the model has been deployed to reproduce the experimental disposal campaign of autumn 2019 at the Put van Hansweert.

From the hydrodynamical validation process, it has become evident that the salinity plays a crucial role in the generation of the local (secondary) cross-currents at the Put van Hansweert. Without the effect of salinity, the usual helicoidal flow is observed. However, when salinity is included in the model, the generation of two circulation cells is observed which can act as a barrier for sediment to move from the outer bend towards the inner bend.

A scenario simulation has been constructed which reproduces the experimental disposal campaign of autumn 2019 at the Put van Hansweert in a long-term 2.5-month simulation. Results show that the modelled sediment losses are close to the measured values of losses. The majority of the in total 0.9 [M m^3] disposed sediment in the model is still confined to its original disposal location after 2.5 months of simulation. Most of the sediment that moves out of the disposal area tends to migrate in an upstream direction. In case of sediment disposals in the Northern disposal area, the main migration route is along the outer bend of the channel with limited potential transport to the side channels. In case of the Southern disposed area, the main migration is along the inner bend of the main channel.

By performing multiple sensitivity analyses, it is found that the stability of the disposed sediment is mostly affected by the choice of the equilibrium near-bed concentration formula and by the choice of the number and distribution of vertical nodes in TELEMAC-3D. Numerical schemes for the vertical sediment transport in TELEMAC show a substantial amount of numerical diffusion. Therefore, a new hybrid upwind/central advection schemes was used, which shows less numerical diffusion. Nevertheless, the morphological results are not very sensitive to the choice of the scheme, provided that proper calibration of the model is performed.

REFERENCES

[1] Huisman B.J.A., Huismans Y. & Vroom J. (2021). Effecten van storten in diepe putten van de Westerschelde. Synthese van proefstortingen en modelanalyses. Deltares rapport 1210301-015-ZKS-0012.

[2] IMDC (2021). Analyserapport proefstortcampagne Inloop van Ossenisse en Put van Hansweert. I/RA/11498/20.063/API/

[3] IMDC & Deltares (2018). Detailanalyse Morfologische respons op de proefstortingen in de put van Hansweert. I/RA/12161/18.013/THL/.

[4] Plancke Y., Bastiaensen E. & Mostaert, F. F. (2020a). Proefstortingen Westerschelde Deelrapport 2 – Analyse beun- en boxcorerstalen bij de uitvoering van de stortproef 2019 in de diepe put van Hansweert. Versie 4.0. WL Rapporten, 19_079_2.

[5] Vanlede J., Smolders S., Maximova T. & Teles M.J. (2015). The unstructured Scaldis model: A new 3D high resolution model for hydrodynamics and sediment transport in the tidal Scheldt. Proc Scheldt Estuary Phys. Integr. Manag. Sess. 36th IAHR World Congr.

[6] Chu K., Breugem A., Wolf T. & Decrop B. (2020). Improvement of a Continental Shelf Model of the North Sea. TELEMAC User Conference, Antwerp, Belgium.

[7] Egbert G.D. & Ray R.D. (2001). Estimates of M2 tidal energy dissipation from TOPEX/Poseidon altimeter data. J. Geophys. Res. Oceans, 106(C10), 22475–22502.

[8] Sutherland J. & Soulsby R. (2003). Use of model performance statistics in modelling coastal morphodynamics. Proc. Int. Conf. Coast. Sediments.

[9] Huismans Y., van der Vegt H., Huisman B. & Colina Alonso A. (2021). Westerschelde: storten in diepe putten. Technische rapportage: mesoschaal morfologische ontwikkelingen rond de Put van Hansweert. Deltares rapport 1210301-015-ZKS-0011.

[10] McLaren (1994). sediment transport in the westerschelde between baarland and rupelmonde.

[11] S.H.L.L. Gruijters, Schokker J. & Veldkamp J.G. (2004). Kartering Moeilijk Erodeerbare Lagen in Het Schelde Estuarium, Rapport nr 03-213-B1208.

[12] Van der Vegt H., Mastbergen D. & Van der Werf J. (2019). Moeilijk-erodeerbare lagen in de Westerschelde. Onzekerheden en gevolgen voor morfodynamiek.

[13] IMDC (2020b). VNSC Project Diepe Delen - Report on CFD calculations of disposal plumes. I/RA/12161/20.005/BDC/FKY

[14] Van Rijn L.C. (1984). Sediment transport, Part II: Suspended load transport. J. Hydraul. Eng., 110(11), 1613–1641.

[15] van Rhee C. (2010). Sediment entrainment at high flow velocity. J. Hydraul. Eng., 136(9).

[16] Rijn L.C.V., van Rhee C. & Bisschop R. (2019). Modified Sediment Pick-Up Function. J. Hydraul. Eng., 145(1).

[17] Patankar, S. V. (1980). Numerical heat transfer and fluid flow(Book). Washington, DC, Hemisphere Publishing Corp., 1980. 210 p.

[18] Merkel, U. (2017). C-VSM-II: Large scale and long time simulations with Sisyphe's continuous vertical grain sorting model. In Proceedings of the XXIVth TELEMAC-MASCARET User Conference, 17 to 20 October 2017, Graz University of Technology, Austria (pp. 131-138).

[19] Sutherland J., Peet A. & Soulsby R. (2004a). Evaluating the performance of morphological models. *Coast. Eng.*, 51, 917–939.

Simulation of embayment lab experiments with TELEMAC-2D/GAIA

Rebekka Kopmann
Hydraulic Engineering in Inland Areas
Federal Waterways Engineering and Research Institute (BAW)
Karlsruhe, Germany
Rebekka.kopmann@baw.de

Javier Perez Obreque
Institute for Water and River Basin
Karlsruhe Institute of Technology
Karlsruhe, Germany

***Abstract*— For the inland river projects at BAW, sediment transport was usually considered as bedload only. This simplification was acceptable as long as the interest of investigations focusses to the main channel. However, lateral exchange between main channel, groyne fields, and floodplains is of increasing interest.**

Within a new BAW internal R&D project the capability of TELEMAC-2D / GAIA to simulate the lateral sediment exchange was examined by re-modelling the laboratory experiment conducted by [1]. In this experiment the distribution of suspended sediment and its deposits in different configurations of lateral embayment for three constant discharges were investigated. The embayment deposits and the concentrations at two significant locations were measured and were used to validate the numerical model. The numerical model could be calibrated reasonably to one embayment configuration and the lowest discharge. However, the calibration could not be transferred to the higher discharges or other embayment configurations. Furthermore, three differences between the numerical and the laboratory model made the comparisons difficult: the procedure of sediment recirculation, the loss of material in the pores of the laboratory model and the embayment pumping effect.

Further investigations are required to improve the hydrodynamics in an embayment using a 2D depth averaged numerical model. To account for the mainly 3D nature of the sediment transport in the embayment requires advances in 2D turbulence models and a numerical scheme that allows pumping effects. In any case it would be helpful to find or conduct an experiment with suspension and lateral sediment exchange that avoids the pumping effect and material losses in pores and provides measurements needed for validation of numerical models.

I. INTRODUCTION

For the inland river projects at BAW, sediment transport is usually considered as bedload only. The limitation due to this simplification is small as long as the interest of investigations focusses to the main channel. There, the main part of the suspended sediment is not involved in the river bed building process and is called “wash load”. However, the requirements of the European Water Framework Directive cause investigations at the floodplains and of the interaction between floodplain and main channel. Therefore, the focus of investigation is changing and suspended sediment transport becomes more and more important. At the floodplains, the deposition is dominated by suspended load. In the numerical model the simulation of the bed load is based on empirical formulations, but a lot of data are available in the main channel for calibration. Contrary to that, the suspended load is based on the advection-diffusion equation but data at the floodplains are rare. The simulation of the sediment processes at the floodplains and the interaction between main channel and groyne fields and floodplains are an interesting and challenging topic.

The aim of a new BAW internal R&D project is to demonstrate the numerical modelling capability of the lateral sediment exchange of non-cohesive material between floodplain or groyne field and main channel on German federal inland waterways and to improve long-term morphodynamic numerical modelling by considering suspension. For long-term morphodynamic modelling TELEMAC-2D/SISYPHE resp. TELEMAC-2D/GAIA is applied in BAW. The computer capacity and model efficiency are still not good enough to use three-dimensional models with the wanted space and time resolution.

From literature a laboratory experiment with lateral suspended sediment exchange was chosen for comparison with the depth-averaged numerical modelling. Reasons for the choice were the simple geometry, the presence of concentration and deposition measurements and the excellent description of the laboratory experiment. But even an intensive calibration process did not lead to a satisfying numerical simulation of the laboratory experiment. In this study it could not fully proven if a two-dimensional numerical model is generally able to reproduce the lateral sediment exchange found in the experiment.

Furthermore, the question needs to be answered whether the important processes of the laboratory experiment are also dominant in inland waterways. Nevertheless, the current state of investigation is presented as it is not only valuable to know the possibilities of numerical simulation, but also its limitations.

In section II the embayment flume experiment of [1] is presented. The numerical modelling with TELEMAC-2D / GAIA of this lab experiment is shown in section III. In section

IV the numerical results are compared with the measurements and in the section V the results are discussed and concluded.

II. EMBAYMENT FLUME EXPERIMENT

[1] investigated in a 7.5 m long and 1 m wide flume with a longitudinal slope of 0.1 % four different embayment configuration (see Fig. 1). Artificial sediments of polyurethane were recirculated and mixed in upstream and downstream tanks. With a mean grain size of d_{50} = 0.2 mm and a density of 1160 g/m^3 the artificial material corresponds to non-cohesive fine sediments with grain sizes 0.062 – 0.5 mm. [1] determined the settling velocity (0.00276 m/s). Each configuration was modelled with three different discharges. The initial concentration was determined experimentally to the maximum suspended capacity of the flow. The amount of recirculating sediment was calculated from the known water volume in the flume and the tanks, and the required sediment concentration. The values are summarized in Table 1. The recirculating sediment procedure did not produce a constant feed but a decreasing probably slightly oscillating feed. At the boundaries neither the concentrations nor the incoming sediment masses were measured. At two positions in the main channel orientated at the embayment configuration, (see Fig. 1) turbidimeters were installed which monitored the concentrations. The vertical position of the turbidimeters was experimentally chosen to the vertical averaged value of the concentration profile. The experiments were finished after 3, 4 and 5 hours reaching a quasi-equilibrium concentration state for low, medium and high discharges, respectively (see Table 1). Equilibrium was assumed when the bottom evolution in the lateral embayment were not measurable anymore.

The total sediment mass trapped in the embayment was collected, dried and weighed. The results were presented in Fig. 2 as trapping efficiency which is the mass divided by the total embayment area.

In the reference configuration without embayment (3.0) some sediments were trapped in small gaps between bricks and walls which led to a significantly decrease of sediment concentration (see Fig. 3). In this configuration no bed evolution appeared, so the loss resulted from the bricks and walls. For the low discharge nearly 80 % of the concentration was lost due to this phenomenon. For higher discharges it was only nearly 65 % (medium) resp. 40 % (high).

The measurements of the water levels show an oscillation phenomenon for all embayment configurations. This phenomenon is induced by a seiche, which occurs in dead zones of a flow like the embayment configurations 3.1 – 3.4 (e.g. [2], [3]). The seiche phenomenon is related to the geometry of the cavities and was observed stronger for configuration 3.1 and 3.2. The configurations differed in the roughness aspect ratio. This is defined as the lateral depth of the cavities (0.25 m) divided by the distance between two cavities. The configuration 3.1 has smaller roughness aspect ratio of 0.5 than configuration 3.2 which has one of 0.6.

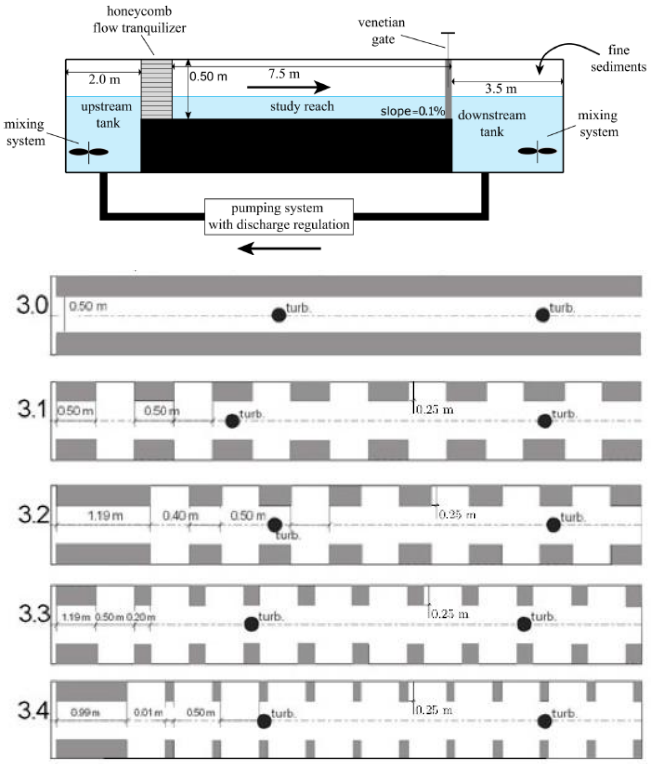

Figure 1: Side view of the set-up of the flume experiment (top) and topview on embayment configurations group 3 (bottom) (from [1]).

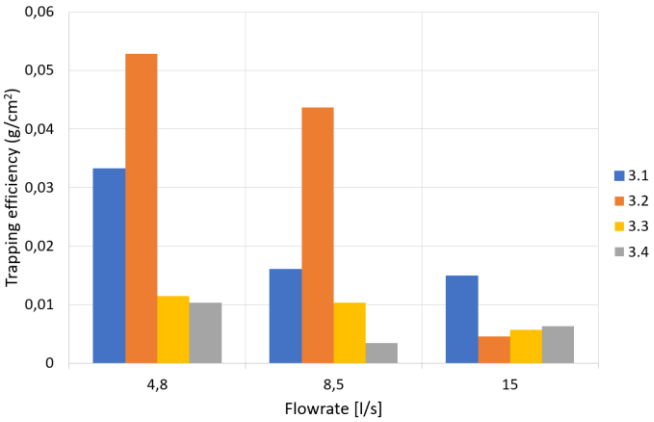

Figure 2: Measured trapping efficiency for all embayment configurations and all discharges (values are taken from [1]).

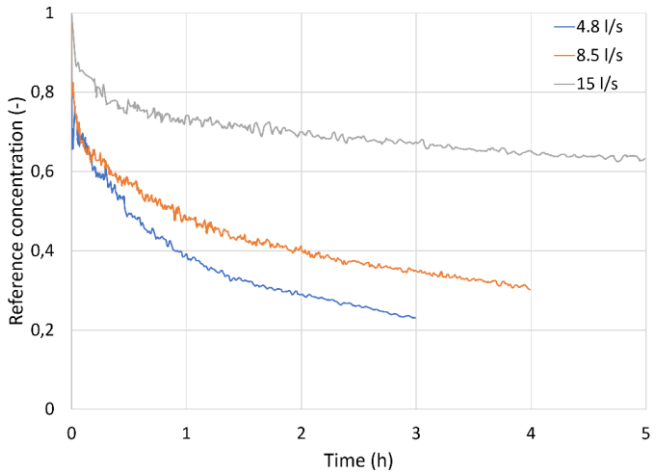

Figure 3: Measured concentration for the configuration without embayment (3.0) (values are taken from [1]).

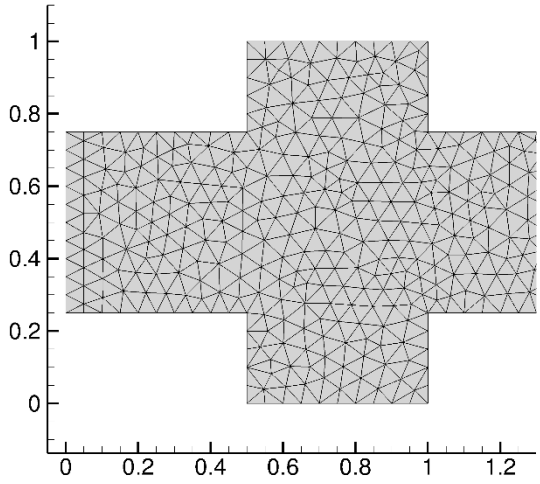

Figure 3: Part of the simulation grid for embayment configuration 3.1.

III. NUMERICAL SIMULATION WITH TELEMAC-2D / GAIA

For long-term hydro-morphodynamic modelling of German federal inland waterways usually TELEMAC-2D/SISYPHE and in future TELEMAC-2D/GAIA is applied in BAW. Therefore, 2D models with a typical BAW resolution of about 10 grid points in the main channel was used for the simulations of the embayment lab models. The number of nodes for the five models are between 1454 and 2559 with maximum edge lengths of 5 cm. Fig. 3 shows the first 1.2 meters of the simulation grid for model 3.1. No increased resolution was chosen for the embayment areas as the embayment gyre could be simulated.

At the inlet boundary the discharge and the velocity distribution were imposed. The distribution was taken from the outlet boundary of a previous made steady state simulation. This procedure minimises the boundary impact. At the outlet boundary the water level was set.

Unfortunately, the boundary sediment concentration at the inlet was not measured and was not a direct recirculating due to the two tanks. After some investigations with sediment recirculating procedures, the best compromise was to use the measured sediment concentration as inlet boundary condition.

Applying the given initial concentration uniformly along the whole flume did not seem plausible. In order to fit best to the laboratory experiment, the initial condition was found as a steady state with a concentration distribution at the inlet according to the outlet. The sediment input flux was adapted to meet the initial concentration as an average value at the two measurement points. Fig. 4 shows exemplarily the initial sediment concentration for the embayment configuration 3.1. The initial and boundary conditions are summarised in Tab. 1.

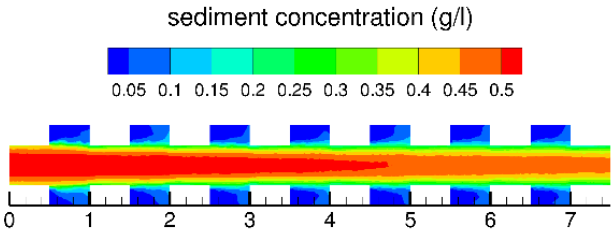

Figure 4: Initial concentration from a previous steady state simulation for embayment configuration 3.1 and the discharge 4.8 l/s.

TABLE 1: INITIAL AND BOUNDARY CONDITIONS.

Boundary conditions:			
Discharge (l/s)	4.8	8.5	15
Water depth (m)	0.035	0.05	0.07
Sediment concentration (g/l)	Measured concentration (see Fig. 3)		
Experiment duration (h)	3	4	5
Initial conditions:			
Velocities	Steady state from previous simulation		
Water depth			
Sediment concentration			
Initial concentration at the measurement points (g/l)	0.5	1.0	1.5
Recirculating sediment mass (kg)	2.75	5.5	8.25

Beside the unknown sediment boundary conditions another source of uncertainty in the measurements came from the loss of sediments in the small gaps between the bricks and walls. Both aspects lead to a high degree of uncertainty which prevents a good comparability between the experimental and numerical results. This fact was not so clear in the choosing process of the experiment. The structured simple geometry, the presence of concentration and deposition measurements and the excellent description of the laboratory experiment were good arguments for the choice.

A. *Hydrodynamic calibration*

The roughness coefficients were initially taken as Manning values from literature for wooden bottom (0.011 s $m^{-1/3}$) and for lateral bricks (0.014 s $m^{-1/3}$). For calibration the values were converted to Nikuradse roughness coefficients of 0.5 mm for the wooden bottom and of 2.1 mm for the lateral bricks. With both turbulence models, k-epsilon and horizontal mixing length, the embayment vortices could be reproduced. For further simulations k-epsilon model was chosen as it promised to apply better for complex flow situations. In Fig. 5 streamlines visualises the measured and simulated flow situation in the embayment for configuration 3.1. Measurements and also simulations show quite similar flow patterns for all discharges. In the measurements a vortex occurs with a centre moved in flow direction (x/l ≈ 0.7). In case of high discharge, the size of the vortex seems smaller and a second small vortex could be interpreted at the upstream boundary. The numerical simulation calculated just one vortex which covers the whole embayment area. The vortex centre is only slightly upstream at x/l ≈ 0.55.

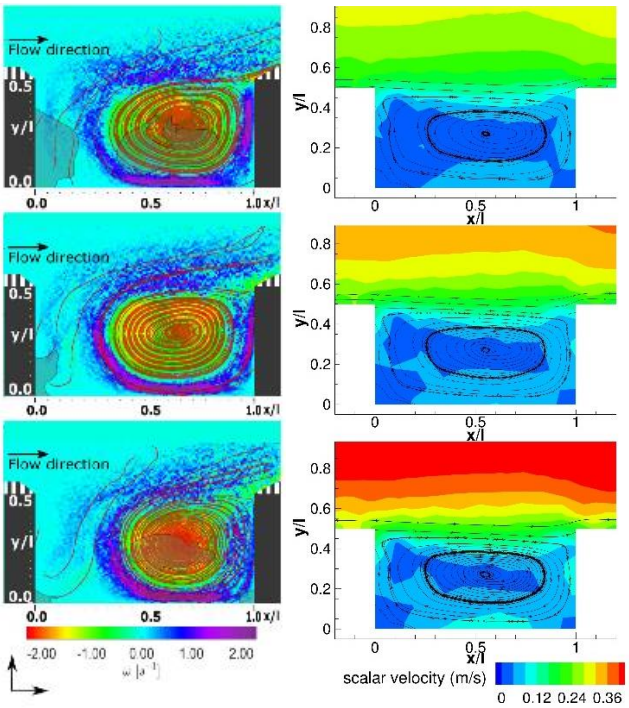

Figure 5: Comparison of measured vorticity and streamlines of the groyne gyre (left, from supplementary online data of [1]) and simulated scalar velocity and streamlines of the groyne gyre (right) for low (top), medium (middle) and high (bottom) discharges for configuration 3.1.

The uniformity of the flow was checked between the two concentration measurement points (see Figure 1). The water level slopes were found only slightly larger than the bottom slopes except for the largest discharge. The water level difference between the two measurement points and the uniform water depth was less than 1 % for the low and mean discharges but nearly 5 % for the high discharge. Tests were done using lower roughness for the high discharge, which led to the same hydrodynamic calibration quality as reached for the lower discharges. But this did not improve the sediment results significantly. Therefore, all results presented here used the same roughness coefficients.

IV. Comparison of Numerical Results of Lateral Sediment Exchange to Measurements

The numerical model was calibrated using the offered sediment measurements of the embayment experiment. The settling velocity, the grain size and grain density were taken from the measurements. The following numerical and physical parameters were used for calibration:

- Reference height
- Bed shear stress
- Equilibrium concentration formulation
- Settling lag
- Diffusion of tracers
- Time step
- Numerical scheme for sediment (finite Element / finite volume / PSI-scheme / N-scheme)

The best calibration was found for the minimal reference height (1 % of the water depth), a bed shear stress which includes turbulence according to [4] with the parameter 2r=0.0119, van Rijn equilibrium concentration, settling lag, no diffusion of tracers, a time step of 0.05 s and PSI-scheme. For sensitivity studies the impact of the mesh resolution and the settling velocity were investigated as well.

The time evolution of the concentration averaged from the two measurement points and normalised by dividing with the initial concentration shows an exponential decrease until asymptotically reaching a constant value. Fig. 6 shows the comparison between the measurements and the calibrated numerical results exemplarily for embayment configuration 3.1 and all three discharges. The differences between the measurements which were also set as boundary conditions and the simulated concentration at the measurement points are very small. Therefore, no further adaption of the initial sediment concentration was done.

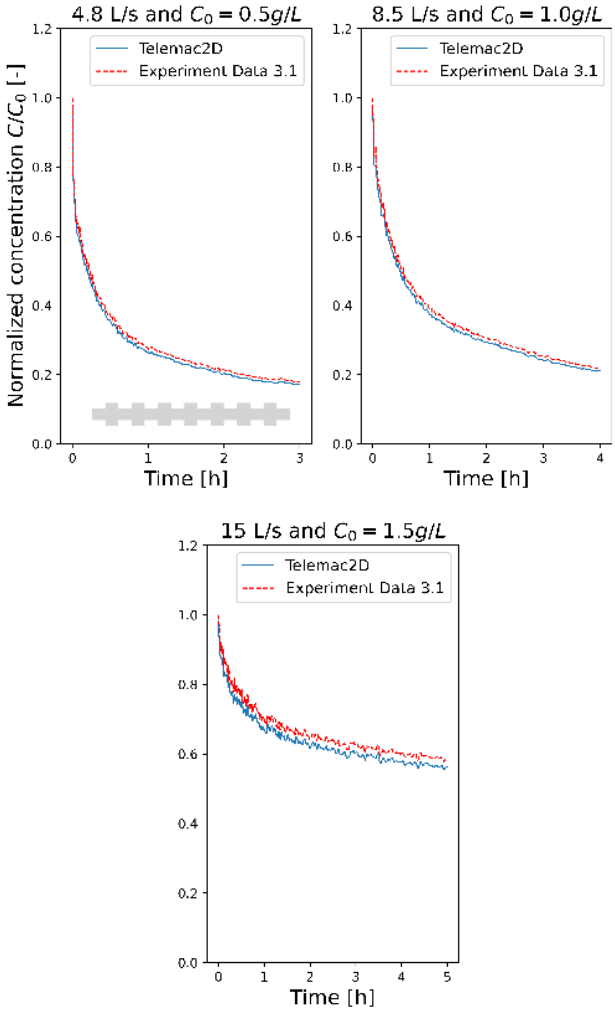

Figure 6: Simulated (blue) and measured (red) time evolution of the normalised concentration for embayment configuration 3.1.

In Table 2, the deposited masses are compared between the calibrated simulation and the measurements. Due to the recirculating procedure the temporal evolution of the sediment concentration corresponds to the deposited masses in the embayment areas of the experiment. A smaller final concentration implies a higher mass deposition. With increasing discharges, the deposition masses decreased in the experiment. Because of the set boundary condition instead of a recirculation in the numerical simulation, higher final concentrations did not lead to smaller masses. Contrary to the small differences between measurements and numerical results for the concentration the deposition masses fit only reasonable for low discharge. For mean discharge the masses were computed 5 times and for high discharge even 20 times too high. For the other configurations the behaviour for higher discharger is equivalent or even worse. The effect of smaller lateral sediment exchange for increasing discharges could not be captured by the numerical model at all.

A sensitivity study was conducted to investigate the range of deposition masses. Figure 7 presents the variation of deposition masses for several numerical and physical parameter settings for the low discharge and configuration 3.1.

From the physical parameters the settling velocity was the only one which decreased the mass compared to the calibration set up (red mark). But the chosen values are far from the measured ones and should not be taken for calibration. A finer grid resolution and a smaller time step decrease the numerical diffusion. This leads to less sediment input to the embayment areas. The fine grid with node distances of 1 cm instead of 5 cm cut the deposition masses roughly into half (258 g / 1018 g / 2203 g). Unfortunately, the trend that increasing discharges resulted in decreasing deposition masses could also not captured with a finer mesh.

Fig. 8 shows the comparison of the hydrodynamics and the final sediment concentration in the embayment area between coarse and fine grid for the mean discharge. The velocities are slightly higher in the main channel due to less numerical diffusion in the fine grid and the centre of the embayment gyre is moved more downstream like in the experiment with the finer grid. Moreover, the concentration is more mixed with the coarser mesh than in the fine mesh. Neither with the coarse mesh nor with the fine mesh the water level oscillated like in the experiment. In the experiment [1] reported water level oscillations between 1 and 3 mm.

TABLE 2: SIMULATED AND MEASURED MASSES DEPOSITED IN THE EMBAYMENT AREAS FOR CONFIGURATION 3.1.

	Measured deposition mass (g)	simulated deposition mass (g)
Low discharge	583	428
Mean discharge	282	1464
High discharge	262	5174

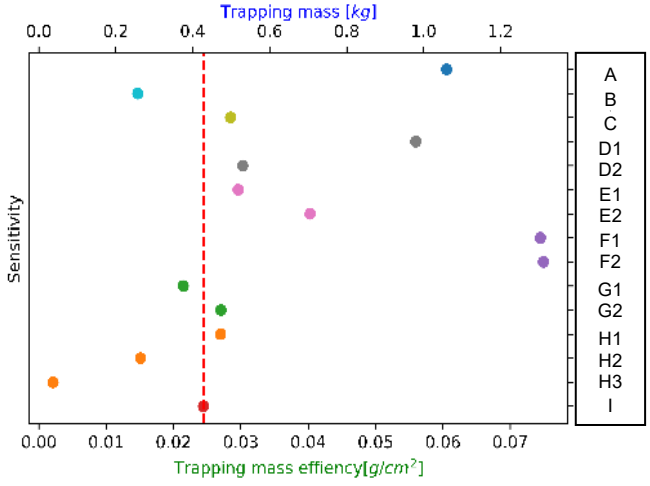

Figure 7: Simulated deposition masses for different parameter settings for low discharge and configuration 3.1 (A: settling lag, B: finer mesh, C: with diffusion of tracer, D1: equilibrium concentration Soulsy D2: equilibrium concentration Zyserman, E1: bed shear stress + TKE with 2r=0.119 E2: bed shear stress + TKE with 2r=0, F1: Finite Volume parallel F2: Finite Volume seriell, G1: timestep 0.01s G2: time step 0.1s, H1: settling velocity 0.005 m/s H2: settling velocity 0.001 m/s H3: settling velocity 0.0001 m/s, I: reference)

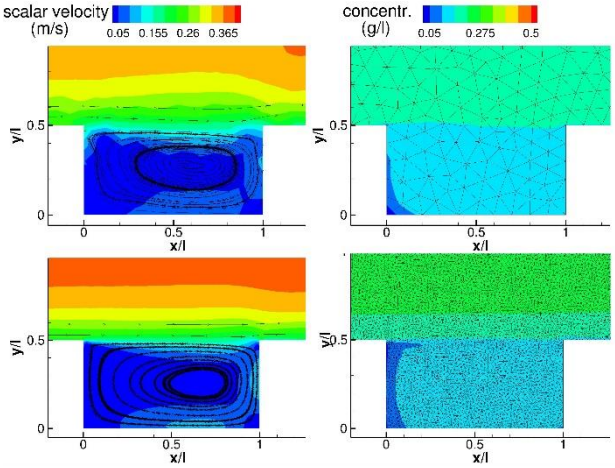

Figure 8: Comparison of the hydrodynamics and the final concentrations in the embayment area between the coarse (left) and the fine (right) mesh for mean discharge and configuration 3.1.

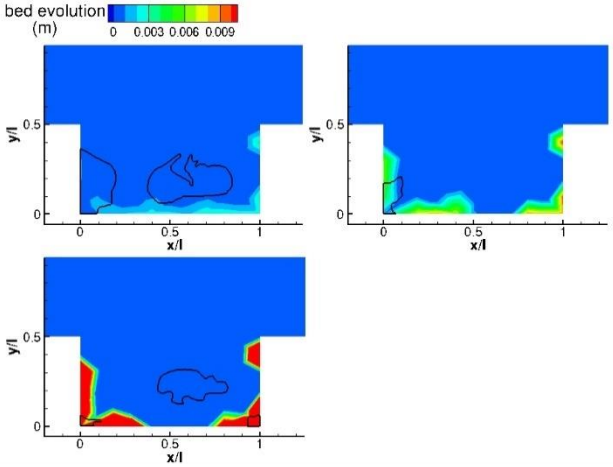

Figure 9: Comparison of simulated deposition to the measured deposition areas (black polygons) in the embayment for configuration 3.1 for low discharge (top left), mean discharge (top right) and high discharge (bottom left).

Furthermore, the transfer of the calibration to the other embayment configurations was investigated. In the experiments the deposits nearly doubled for configuration 3.2 and halved for configurations 3.3 and 3.4. Again, this was not predicted by the numerical model (see Table 3). At least the numerical model computed significant different values for configuration 3.3 and 3.4 but in the wrong direction. It must be stated that the calibration can neither be transferred to other discharges nor to other embayment configurations.

A qualitative comparison was made with the deposition areas. It is well known that sediment will be deposited in the middle of a vortex according to the spiral flow. The deposition pattern in the embayment areas show deposition in the middle of the embayment and additionally at some corners (see black polygons in Fig. 9). In the 2D simulation the deposition only occurred at the boundaries of the embayment where the velocities minimised (see Fig. 9). Again, the finer mesh did not improve the results. The missing deposition at the centre of the embayment gyre was expected because the secondary currents effect is a three-dimensional effect. An approximation exists in TELEMAC-2D but requires a slope in the free surface. The velocities of the embayment gyre are so small that no significant free surface flow appears.

TABLE 3: SIMULATED AND MEASURED MASSES DEPOSITED IN THE EMBAYMENT AREAS FOR THE LOW DISCHARGE AND ALL EMBAYMENT CONFIGURATIONS.

Embayment configuration	Measured deposition mass (g)	simulated deposition mass (g)
3.1	583	428
3.2	925	437
3.3	287	605
3.4	284	729

V. CONCLUSION AND OUTLOOK

At BAW the lateral sediment exchange between main channel and groyne fields is a topic of interest. The embayment experiment of [1] was chosen to investigate the capability of TELEMAC-2D / GAIA to simulate lateral sediment exchange. The numerical model was compared to the experimental results for four different embayment configurations and three different discharges. With some calibration it was possible for a single configuration and the lowest discharge to fit reasonable to the measurements. But with this calibration set up neither other embayment configurations nor higher discharges could be predicted. It is presumed that the numerical model missed significant physical processes. Of course, a three-dimensional simulation would enhance the numerical results. Deposits in the center of the embayment vortex are expected for a three-dimensional simulation (see e.g. [5]). But it is doubtable that the effect of decreasing lateral sediment exchange with increasing discharges can be captured by a 3D model with the same resolution.

Some aspects hinder the analysis of the present flume experiment. The procedure of sediment recirculation did not reproduce the boundary condition for the sediment concentration in the numerical model. Together with the loss of material in the pores of the laboratory model the masses can only be examined qualitatively. Additionally, in the experiment an oscillating water level was observed. Compared to the water depth the oscillating amplitude was high. Amplitudes of 1-3 mm were reported by [1] which correspond to 2 – 6 % of the water depth. Nevertheless, the simple geometry, the presence of concentration and deposition measurements and the excellent description of the laboratory experiment were good arguments using this experiment as a validation case for lateral sediment exchange. But it would be helpful to find or conduct an experiment with suspension and lateral sediment exchange that avoids the pumping effect and mass loss.

In the numerical model no oscillating of the free surface was simulated as it was observed in the experiment. This seiche effect producing low-frequency fluctuations in the water level is a typical phenomenon for embayment and groyne field hydrodynamics (e.g. [2], [6], [7]). Further investigations are needed to evaluate whether this effect influences the lateral sediment exchange significantly. In addition, it needs to be investigated whether this effect also plays an important role in groyne field morphodynamics. Investigations with oscillating boundary conditions could be proof whether these oscillations create a substantial amount of sediment exchange.

The "CAVITY" validation test case of TELEMAC-2D simulates a straight flume with one embayment and constant flow using a very fine grid [8] and Smagorinsky turbulence model. The flow was found unsteady and large and periodically small eddies were observed moving into the embayment. Although the configuration of the model is different to the investigated flume it seems promising that the pumping effect could be simulated even with a 2D very fine grid. Further investigations should be done with a very fine grid and different turbulence models.

Another idea to enhance the 2D simulation was an adaption of the secondary current approach. In TELEMAC-2D the secondary currents effect is classically using the free surface flow but could also take a given radius of the flow. For this experiment the radius could be set according to the radius of the streamlines of the embayment gyre. This should improve the position of deposition in the embayment areas. For the application to river stretches with groynes this idea needs some more investigations. Typically, the radius of a river stretch is constant. In case of overtopped groynes the gyre will disappear and the radius must be adapted.

Even if a wide range of calibration already have been done some further ideas could be followed like a modification of the settling velocity due to turbulence, other formulation for the reference level or other integration of turbulence in the shear stress computation.

Applying TELEMAC-3D/GAIA to this flume experiment will be the next step. Even if a three-dimensional model cannot be used for long river stretches and long time periods it would be helpful to see how far a three-dimensional simulation can improve the model results. Furthermore, the grade of resolution needed for a reasonable improvement would be of high interest. If applicable, a coarse resolution three-dimensional model could be used at least for medium-scale river stretches.

From a user perspective, GAIA needs to include some variables in the results file for a verification process of the suspended sediment calculation (e.g. equilibrium concentration) and new keywords to enhance calibration of the model (Schmidt number, reference elevation, user increase of bed shear stress, flux redistribution, etc).

ACKNOWLEDGEMENT

The authors thank Carmelo Juez for his helpful answers to the questions about the laboratory experiment.

REFERENCES

[1] C. Juez, I. Bühlmann, G. Maechler, A. J. Schleiss, & M. J. Franca, Transport of suspended sediments under the influence of bank macro-roughness. Earth Surface Processes and Landforms, 43 (1), 271–284, 2018, https://doi.org/10.1002/esp.4243.

[2] I. Kimura, T. Hosoda, Fundamental properties of flows in open channels with dead zone, Journal of Hydraulic Engineering 123: 98–107, 1997.

[3] Y. Akutina, Experimental investigation of flow structures in a shallow embayment using 3D-PTV. PhD thesis, McGill University, Montreal, 2015.

[4] A. Goll, 3D Numerical Modelling of Dune Formation and Dynamics in Inland Waterways. PhD thesis, Université Paris-Est, École du Pont ParisTech 2017, https://hdl.handle.net/20.500.11970/104213.

[5] P. Ouro, C. Juez, M. Franca, Drivers for mass and momentum exchange between the main channel and river bank lateral cavities, Advances in Water Resources, 137, 103511. 2020, 10.1016/j.advwatres.2020.103511.

[6] C. Wirtz, Hydromorphologische und morphodynamische Analyse von Buhnenfeldern der unteren Mittelelbe im Hinblick auf eine ökologische Gewässerunterhaltung. PHD thesis, Freie Universität Berlin. 2004.

[7] C. Anlanger, Field-scale experiments and analysis of turbulent flow structures in a river reach with groynes. Master thesis at University of Natural Resources and Applied Life Sciences, Vienna, 2008.

[8] TELEMAC-2D Validation Manual, Version v8p2, Dec, 2020, http://wiki.opentelemac.org/doku.php?id=documentation_latest.

Modelling the impacts of Hurricane Ike on the Texas coast using a fully coupled TELEMAC-TOMAWAC-SISYPHE model

Connor McCarron, Michiel Knaapen, Belen Blanco, Mike Dearnaley, Richard Lewis, Maria di Leo
HR Wallingford
Wallingford, United Kingdom
c.mccarron@hrwallingford.com

Hurricane Ike, a category 4 hurricane, made landfall near Galveston, Texas on the 13th of September 2008. A fully coupled TELEMAC-TOMAWAC-SISYPHE model was developed to predict sediment transport and associated morphodynamics resulting from the passage of Hurricane Ike. The predicted hydrodynamics were validated against observed tidal elevations, currents, waves and inundation. The predicted sediment transport pathways and resulting bed elevation change were compared with assessments of coastal impacts associated with Hurricane Ike. The model results show good agreement with observations and demonstrate the ability to predict hydrodynamics, sediment transport and morphodynamics associated with hurricanes using a fully coupled TELEMAC-TOMAWAC-SISYPHE model.

I. INTRODUCTION

Hurricane Ike, a category 4 hurricane, made landfall near Galveston, Texas, at 0700hrs UTC on the 13th of September, 2008. On landfall, the hurricane was downgraded to a strong category 2 but sustained winds of 175 km/h with maximum sustained wind swaths estimated at 180 km [1]. The track of the hurricane, its landfall at Galveston, and the sustained wind swaths are illustrated in Figure 1. Peak wind speeds were observed east of Galveston and extended east into Louisiana (Figure 1).

The development of a fully coupled TELEMAC, TOMAWAC and SISYPHE model used to predict sediment transport pathways and magnitudes as a result of Hurricane Ike along the coastline of Galveston, Texas is presented herein. The predicted hydrodynamics are compared with observations of tidal elevations and currents, waves and inundation recorded during the passage of Hurricane Ike. The predicted morphodynamics are compared with observations of coastal impacts as a result of Hurricane Ike.

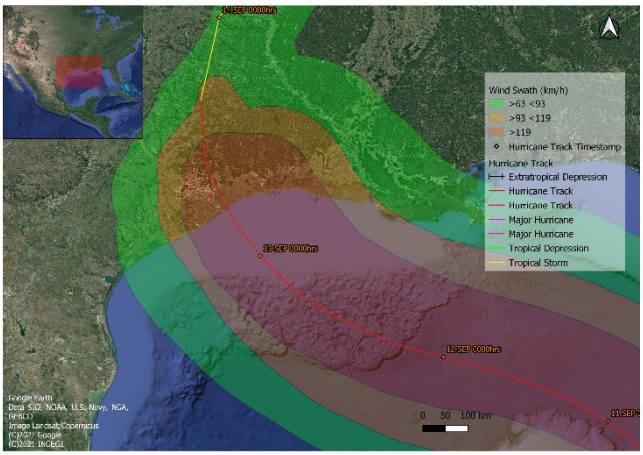

Figure 1 Storm track of Hurricane Ike from the National Hurricane Centre's HURDAT2 dataset illustrating the sustained wind swaths

II. THE MODEL

TELEMAC-2D (*v8p1r1*) was used to model the hydrodynamics associated with Hurricane Ike along the Galveston coastline. The model domain extended from Bay City, west of Galveston, Texas to Holly Beach on the Louisiana border, and extended up to 100 km offshore to a depth of 90 m MSL (Figure 2). The model grid comprised approximately 470,000 nodes and 930,000 elements which ranged in length from approximately 4 m in the nearshore to 7 km along the offshore boundary.

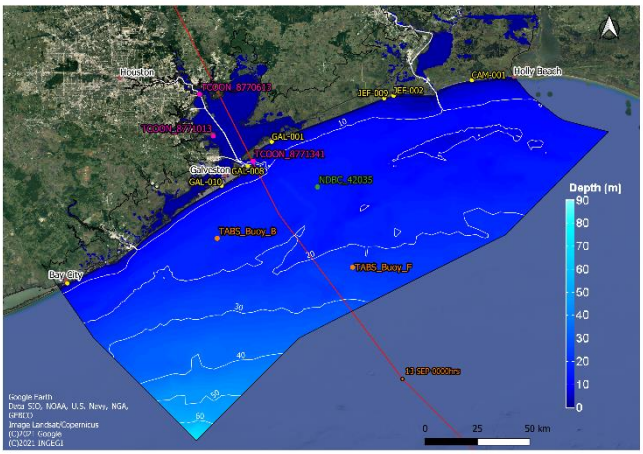

Figure 2 Model bathymetry including the locations of tidal level (pink), tidal current (orange), waves (green) and inundation (yellow) observations

A. *Bathymetry*

A subset of bathymetric data was extracted from the United States Army Corps of Engineers (USACE) ADCIRC model grid used in the Coastal Texas Protection and Restoration Feasibility Study [2] which covers the gulf facing beaches and inlets along the Texas coast, extending approximately 16.9 km offshore to a depth of approximately 10 m MSL. The USACE grid was extended beyond the 10 m depth contour using GEBCO bathymetry data [3]. The bathymetry employed in the model is shown in Figure 2.

B. *Tidal boundary conditions*

The model was forced with tidal elevations and currents using data extracted from the Hybrid Coordinate Ocean Model of the Gulf of Mexico (HYCOM + NCODA Gulf of Mexico 1/25° Reanalysis, GOMl0.04/expt_50.1). Hourly predictions of sea surface elevation (ssh), eastwards- and northward- velocities (u,v) were interpolated using a 2-dimensional linear interpolation and applied to the offshore nodes of the boundary of the model domain.

C. *Wave boundary conditions*

Wave boundary conditions were extracted from the European Centre for Medium Range Weather Forecast's (ECMWF) ERA5 wave reanalysis dataset which provides hourly wave spectra across a 0.5° (30 km) grid. Time-varying wave spectra from ERA5 output locations bordering the offshore boundary of the model domain were used to force the TOMAWAC model by interpolating the wave spectra along the offshore nodes of the model boundary.

D. *Atmospheric conditions*

Hourly atmospheric pressure (mean sea level) and 10 m wind speeds were also extracted from the ECMWF's ERA5 reanalysis dataset with a spatial resolution of 0.25°. The ERA5 wind speed and pressure fields were interpolated spatially on to the model mesh and used to account for wind stress in TELEMAC and wave generation in TOMAWAC.

E. *River discharge*

Within the model domain, the major rivers flowing into the Gulf of Mexico include the Neches, Sabine, Trinity, San Jacinto, and Brazos rivers, as well as the Buffalo and Chocolate Bayous (Figure 3). Extreme run-off events related to hurricanes have been shown to significantly affect flows in the bays [4]. River discharge data were obtained from the United States Geological Survey's National Water Information System (NWIS). NWIS stations closest to the model boundary which recorded discharge data were used to force the model. No discharge data were available for the Trinity or Brazos rivers during the passage of Hurricane Ike. These rivers were therefore not included in the model. Discharge from the remaining rivers were included and are shown in (Figure 3). The Buffalo Bayou and Neches River recorded the highest peak flood discharges during the passage of Hurricane Ike reaching 280 m^3/s and 580 m^3/s, respectively (Figure 3).

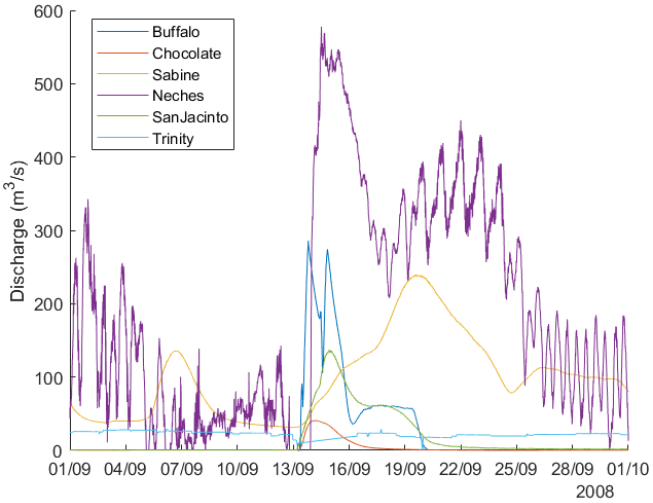

Figure 3 Discharge for the 6 largest rivers within the model domain entering the Gulf of Mexico during September 2008

F. *Bed composition*

A spatially varying grain size distribution and bed friction was employed in the model. The bed comprised 5 separate grain classes ranging from medium silt to medium sand: 30 µm (medium silt); 70 µm (coarse silt); 125 µm (very fine sand); 0.25 mm (fine sand); and 0.5 mm (medium sand). The mean grain size calculated from the employed sediment fractions is illustrated in Figure 4. These sediment classes were derived from an assessment of available sediment data collected between 1899 and 2015 by various sources including: the Texas General Land Office's coastal sediment database (TxSeD); the USGS's usSEABED database; the Bureau of Ocean Energy Management's Marine Mineral Information System; core logs collated by the University of Texas Institute for Geophysics; and shear strength maps of shallow water sediments in the Gulf of Mexico compiled by Texas A&M University's Offshore Technology Research Centre. The bed composition in the model was corrected to account for areas likely to be non-erodible:

- structures such as groynes, jetties and sea walls;
- areas where the clay content exceeded 40%;
- areas where maximum velocities exceeded 1.5 m/s.

III. Observational Data

During the passage of Hurricane Ike, water levels, tidal currents and winds were recorded by a number of buoys maintained by the Texas Automated System (TABS), as well as tide gauges on the Texas Coastal Ocean Observation Network (TCOON) hosted by the National Oceanic and Atmospheric Administration (NOAA). Within the model domain, waves were recorded by one National Data Buoy Centre wave buoy (NDBC 42035). This buoy became adrift on the 12th of September passing through the eye of the hurricane and recorded a maximum significant wave height of 6 m at 0450 UTC on the 13th of September. The location of these buoys and tide gauges are shown in Figure 2 and the data recorded by each is indicated in Table 1.

Table 1 Observations available from buoys which successfully recorded data during the passage of hurricane Ike

Station ID	Tidal Elevations	Tidal Currents	Waves	Winds
NDBC 42035			X	X
TABS Buoy B		X		X
TABS Buoy F		X		
TCOON 8770613	X			X
TCOON 8771013	X			X
TCOON 8771341	X			X

The coastal inundation which occurred as a result of the storm surge driven by Hurricane Ike was recorded by a number of temporary USGS rapid deployment gauges [5] which are also shown in Figure 2.

The tidal, wave, wind and inundation observations recorded at these locations were used to validate the hydrodynamics predicted by the model during the passage of Hurricane Ike.

IV. Model Calibration

The hurricane model is based on a model that was calibrated for normal conditions. For January 2018, the model results were compared to measured values in 8 locations; one for waves; three for water level elevation and four for flow velocities.

The model uses a spatially and temporally varying wind for waves and currents and spatially varying bed friction using the Nikuradse coefficient. There were remarkably few changes from the default setting required. For the waves, Yan's formula was used for the wind generation, but otherwise default settings produced the best results. For the currents, the method of characteristics and the wave equation were used to minimise the computational requirements. No upwind discretisation for the water depth and free surface gradient compatibility of 0.7 were needed to stabilise the water levels. For the sediments the active layer thickness was reduced to 1m, to allow for some bed composition changes. Soulsby van Rijn was used for bedload transport (5) and for the reference concentration formula (4).

The skill of the model to predict the hydrodynamics observed during Hurricane Ike is quantified by the mean error (ME), mean absolute error (MAE), root mean square error (RMSE) and the Willmott (1981) skill score (1):

$$\mathrm{WS} = 1 - \frac{\sum_{i=1}^{n}(M_i - O_i)^2}{\sum_{i=1}^{n}(|M_i - \langle O\rangle| + |O_i - \langle O\rangle|)^2} \qquad (1)$$

in which M and O are the measured and observed values, respectively, and angled brackets denote an average. A perfect fit has a value of 1 and predicting a constant equal to the mean of the measured data has a value of 0. The model is deemed adequate with values between 0.55 and 0.65, sufficient between 0.65 and 0.75, good between 0.75 and 0.85, and very good for values >0.85.

The calibration results (Table 2) show that the model is very good for the waves and water levels, good to very good for currents near the inlets where tidal currents dominate (g6010 and Sn0101) and sufficient for the offshore locations where the wind driven ocean currents dominate.

Table 2 Error statistics analysis between model prediction and observations for January 2018

Forcing	Station ID	ME	MAE	RMSE	Skill Score
Elevation (m)	TCOON 8772471	-0.03	0.09	0.11	0.92
Elevation (m)	TCOON 8771013	-0.31	0.34	0.43	0.89
Elevation (m)	TCOON 8771341	-0.09	0.10	0.13	0.89
Currents (m/s)	g6010	0.01	0.10	0.13	0.92
Currents (m/s)	Sn0101	-0.06	0.10	0.11	0.72
Currents (m/s)	NDBC 42050	-0.01	0.08	0.10	0.41
Currents (m/s)	NDBC 42051	0.01	0.05	0.06	0.56
Waves (m)	NDBC 42035	-0.02	0.11	0.15	0.95

Units of the ME, MAE and RMSE are in m for elevations and waves, and m/s for tidal currents

V. Model Validation

Validation of the model was completed by first comparing the predicted tidal elevations, currents and waves with observations from the buoys and tide gauges which successfully recorded data during the passage of Hurricane Ike. The predicted inundation as a result of Hurricane Ike was then compared with observations of inundation from the USGS rapid deployment gauges.

A. *Tidal elevations, currents and waves*

The error statistics for the model are presented in Table 2. The model performs well when compared with observations with skill scores ranging from 0.67 to 0.98 (Table 2). The results are even better than for the calibration period.

Table 3 Error statistics analysis between model prediction and observations during Hurricane Ike

Forcing	Station ID	ME	MAE	RMSE	Skill Score
Elevation (m)	TCOON 8770613	0.05	0.12	0.15	0.96
Elevation (m)	TCOON 8771013	0.02	0.11	0.17	0.98
Elevation (m)	TCOON 8771341	0.02	0.09	0.13	0.98

Forcing	Station ID	ME	MAE	RMSE	Skill Score
Currents (m/s)	TABS Buoy B	-0.12	0.16	0.20	0.67
Currents (m/s)	TABS Buoy F	-0.09	0.12	0.18	0.72
Waves (m)	NDBC 42035	-0.15	0.24	0.34	0.96

Units of the ME, MAE and RMSE are in m for elevations and waves, and m/s for tidal currents

Predicted and observed tidal elevations at TCOON station 8771013 are shown in Figure 4. The skill score of the predicted tidal elevations were deemed to be very good (> 0.85). The model slightly overpredicted water elevations as indicated by a ME of between 0.02 m and 0.05m (Table 3). The model accurately resolved the phase and magnitude of the tidal elevations pre-, post-, and at the peak of Hurricane Ike (Figure 4).

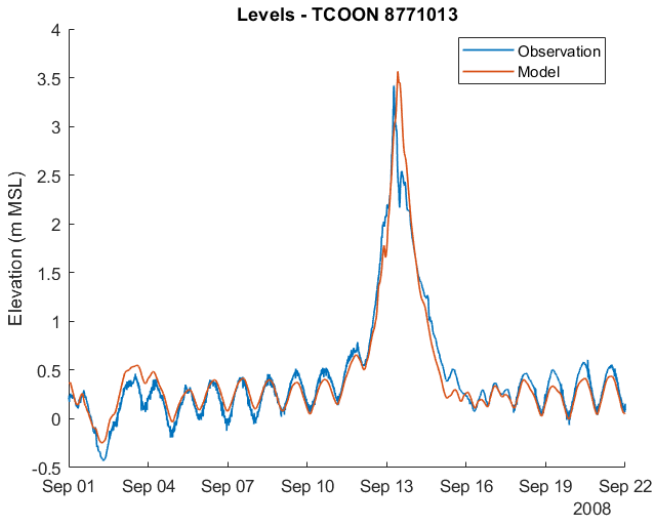

Figure 4 Modelled and observed elevations at TCOON station 8771013

Predicted and observed tidal current magnitudes and directions at TABS buoy B are shown in Figure 5. The model predicted the phase of the tidal currents well both pre-Ike and during the peak of the Hurricane, however, the predicted tidal currents were lower than observed and there was a noticeable phase shift between the predicted and observed tidal currents post-Ike (Figure 5). This was reflected by the skill score which was deemed to be sufficient (0.65 – 0.75) (Table 2). The model predicts larger tidal currents during the landfall of Hurricane Ike then observed (Figure 5), however, previous studies have noted that the TABS buoys do not resolve current speeds greater than 1 m/s well [6]. Therefore, it is likely that the skill score for current speeds at TABS Buoys B and F are underestimated. The lower predicted current speeds compared with observations is possibly related to the hourly temporal resolution of the boundary forcing which may act to alias peak current flows.

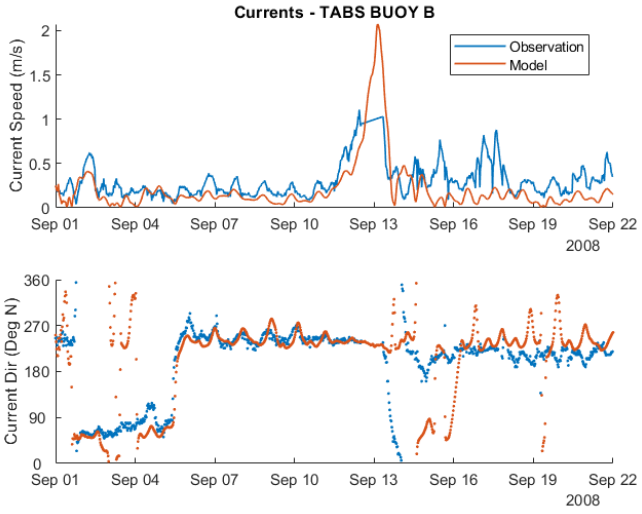

Figure 5 Modelled and observed currents at TABS buoy B

Predicted and observed significant wave heights and directions at for NDBC buoy 42035 are shown in Figure 6. The model accurately predicted the wave heights and directions during the passage of Hurricane Ike (Figure 6) which is reflected by a skill score of 0.96, deemed as very good (Table 2).

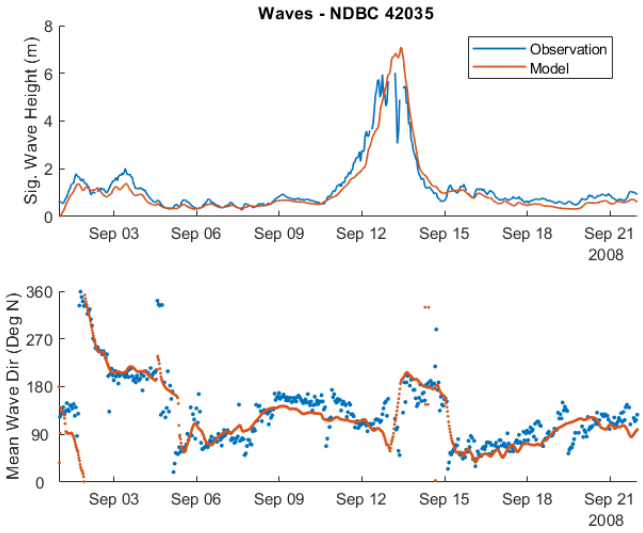

Figure 6 Modelled and observed waves at NDBC buoy 42035

B. *Inundation*

The inundation predicted by the model was compared with observations at 7 USGS rapid deployment gauges along the coastline within the model domain (Figure 2). The error statistics for the model are presented in Table 3 and the predicted inundation at GAL-010 is compared with the observed inundation in Figure 7. The model predicted the inundation observed at each of the USGS stations well with skill scores between 0.80 and 0.97, except for station MAT-008 where the skill score was 0.49 (Table 3). The poorer skill score at this station is attributed to its proximity to the model boundary, and the short duration of inundation observed at the station. The

model skill is very good considering there is likely large variability in the permeability of the surfaces (i.e. roads, paths, etc.) close to the locations of the rapid deployment gauges which the model does differentiate.

TABLE 4 ERROR STATISTICS ANALYSIS BETWEEN INUNDATION PREDICTED BY THE MODEL AND OBSERVATIONS

Station ID	ME (m)	MAE (m)	RMSE (m)	Skill Score
CAM-001	0.11	0.18	0.40	0.88
GAL-001	0.06	0.07	0.27	0.91
GAL-008	-0.04	0.09	0.25	0.92
GAL-010	0.01	0.07	0.16	0.97
JEF-002	0.27	0.30	0.53	0.80
JEF-009	0.03	0.20	0.44	0.85
MAT-008	0.00	0.01	0.01	0.49

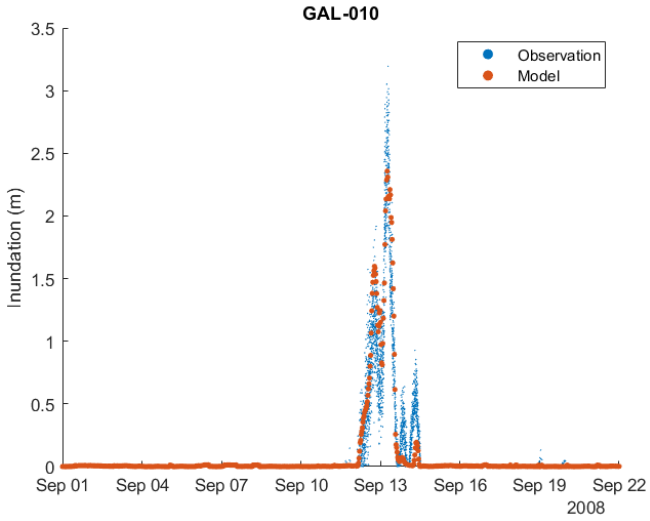

Figure 7 Modelled and observed tidal inundation at GAL-010

VI. RESULTS

A. *Sediment Transport*

The sediment transported predicted during the landfall of Hurricane Ike is shown in Figure 8. Sediment was predicted to be transported dominantly onshore east of the Galveston bay entrance channel across Bolivar Peninsula into Galveston bay, along the coastline of the McFaddin National Wildlife Refuge, and into Sabine Lake and the surrounding areas (Figure 8). West of the Galveston entrance channel the direction of sediment transport veers alongshore with little onshore sediment transported predicted (Figure 8).

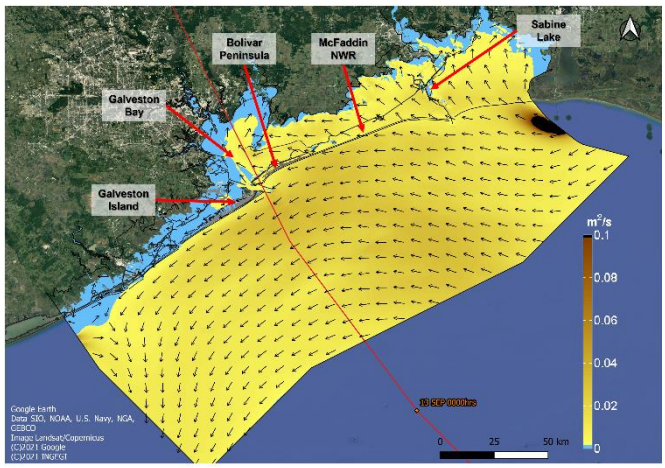

Figure 8 Predicted sediment transport rates during the landfall of Hurricane Ike on the 13th of September 2008 at 0700hrs

B. *Erosion/Deposition*

The patterns of erosion and deposition predicted as a result of Hurricane Ike are shown in Figure 9. The impacts of Hurricane Ike were predicted to occur dominantly along the coastline to the east of the Galveston entrance channel with lesser impacts predicted along the coastline to the west (Figure 9). Doran et al. [7] relate the difference in the impacts observed east and west of the entrance channel to the location of the hurricane track. The eye of the Hurricane travelled over the Galveston entrance channel (Figure 1), which resulted in onshore winds to the east, and offshore winds to the west of the entrance. These offshore winds reduced the height of the storm surge and dampened the waves to the west of Galveston. Conversely, the onshore Hurricane wind eastward of the Galveston entrance increased the storm surge and waves on that side [7].

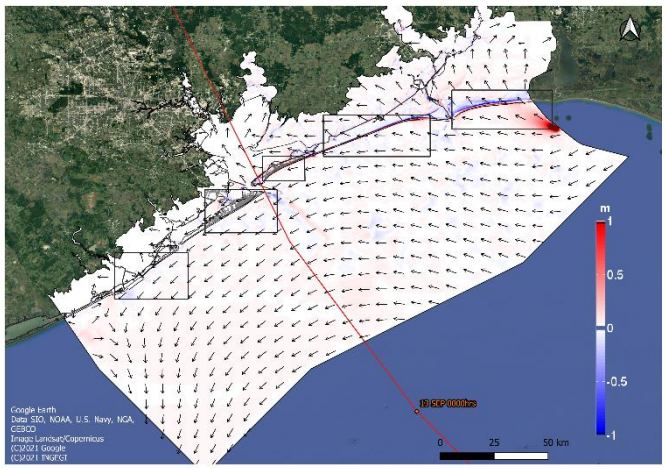

Figure 9 Bed elevation change predicted during the passage of Hurricane Ike. The black boxes indicate the areas assessed for coastal impacts by Doran et al. [7]

Along Galveston Island, the impacts of Hurricane Ike were confined to the beaches west of the Galveston Island seawall where the shoreline was eroded landward [7]. The Galveston Island seawall acted to protect the city of Galveston, however, beach erosion was observed in front of the seawall and to a

section on the eastward section of the Island not protected by the seawall [7]. The model correctly predicted shoreline erosion to the west of the sea wall indicated by band of red west of the seawall and blue to the north of it; the erosion of the unprotected section of the coastline at the eastern end of Galveston Island; and the protection of Galveston City by the seawall and some beach lowering in front of the seawall (Figure 10).

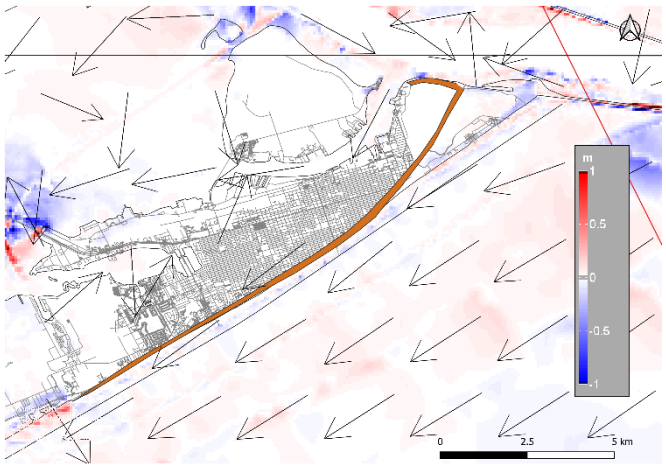

Figure 10 Predicted bed elevation change across the Galveston Island assessment area. The orange polygon shows the location of the seawall protecting Galveston City

Bolivar Peninsula experienced significant impacts due to the landfall of Hurricane Ike close to the Galveston entrance channels and the combined force of the storm surge, onshore winds and associated waves [7]. The combination of 5 m storm surge and waves, with low-lying dunes (approx. 2 m elevation) providing little protection, resulted in sand being eroded from the beach and dunes and transported onshore which was subsequently deposited across Bolivar Peninsula [7]. The erosion of the beach and dunes and subsequent deposition of the sediment onshore is reflected well by the model (Figure 11).

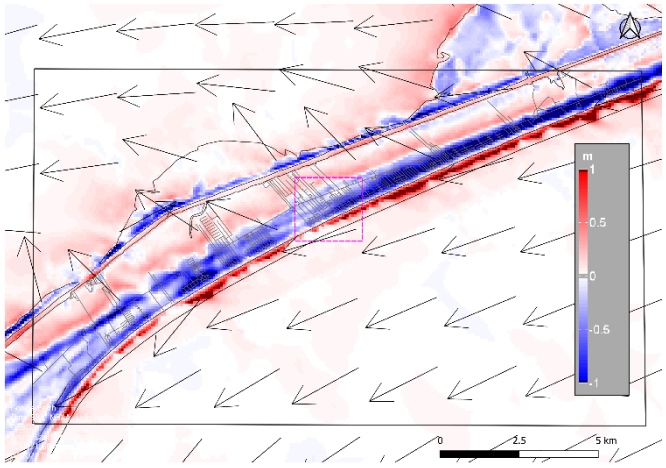

Figure 11 Predicted bed elevation change across the Bolivar Peninsula assessment area. The pink dashed box indicates the area of topographic change assessed from pre- and post-Ike LIDAR by Doran et al. [7] at Chrystal beach

Doran et al. [7] completed an assessment of topographic change at Crystal Beach, Bolivar Peninsula using lidar data collected in September 2005 and September 2008. The observed topographic change is compared with the model prediction in Figure 9. Bed lowering of up to 1 m was observed along the coast at Crystal Beach which was predicted by the model, however, the model did over predict the landward extent of erosion (Figure 9). This is attributed to the reduced resolution of the model mesh in this area compared to the resolution of the lidar data and the presence of small scale hard layers such as building foundations and roads - which may act like revetments - not represented in the model.

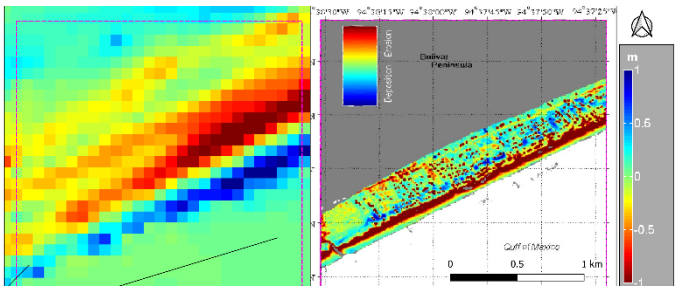

Figure 12 Comparison of the bed elevation change predicted by the model (left) and the bed elevation changed at Crystal Beach, Bolivar Peninsula assessed by Doran et al. [7] (right)

VII. Discussion and Conclusions

The model presented herein was developed to predict sediment transport pathways and magnitudes, and resulting coastal impacts along the coastline of Galveston, Texas arising from the passage of Hurricane Ike. The predicted hydrodynamics were calibrated and validated against observations of tidal elevations, currents, waves and inundation which show good agreement.

The validation of the hydrodynamics predicted by the model illustrates that predicted tidal elevations, waves and inundation were in good agreement with observations. Discrepancies between the predicted and observed tidal current speeds and directions are attributed to the applied boundary forcing and issues with TABS instrumentation [6].

The predicted sediment transport pathways and morphodynamics were compared with observations of coastal impacts associated with Hurricane Ike. Although no observational data (i.e. channel surveys or infill) were available with which to assess the validity of the predicted sediment transport rates, model predictions of bed elevation change are in line with observed bed elevation change from pre- and post-Ike LIDAR data. The predicted sediment transport pathways also reflect that assessed by Doran et al. [7].

The lack of a detailed map of small scale hard structures, such as roads and buildings is the main source of the model errors.

The results of this work demonstrate the ability to predict hydrodynamics, sediment transport and morphodynamics associated with hurricanes using a fully coupled TELEMAC-TOMAWAC-SISYPHE model.

ACKNOWLEDGEMENT

The authors thank the USGS, NDBC, NOAA, TCOON, NHC, ECMWF, HYCOM, the Texas General Land Office, the Bureau of Ocean Energy Management's Marine Mineral Information System, the University of Texas Institute for Geophysics, Texas A&M University's Offshore Technology Research Centre, and the USACE for making the data used herein publicly available.

REFERENCES

[1] Berg, R. (2009). Tropical cyclone report Hurricane Ike: National Oceanic and Atmospheric Administration National Hurricane Centre Report AL092008.

[2] USACE (2020). Appendix D: Engineering Design, Cost Estimates and Cost Risk Analysis for the Coastal Texas Protection and Restoration Feasibility Study.

[3] GEBCO Compilation Group (2019) GEBCO 2019 Grid (doi:10.5285/836f016a-33be-6ddc-e053-6c86abc0788e).

[4] Du, J., & Park, K. (2019). Estuarine salinity recovery from an extrem precipitation event: Hurricane Harvey in Galveston Bay. Science of the Total Environment, 1049-1059.

[5] East, J.W., Turco, M.J., and Mason, R.R., Jr., (2008). Monitoring inland storm surge and flooding from Hurricane Ike in Texas and Louisiana, September 2008: U.S. Geological Survey Open-File Report 2008–1365 [https://pubs.usgs.gov/of/2008/1365/].

[6] Hope, M.E., et al. (2013). Hindcast and validation of Hurricane Ike (2008) waves, forerunner, and storm surge. J. Geophys. Res. Oceans, 118, 4424–4460.

[7] Doran, K.S., Plant, N.G., Stockdown, H.F., Sallenger, A.H., Serafin, K.A. (2009). Hurricane Ike: Observations and analysis of coastal Change. USGS Open-File Report 2009-1061.

Coastal and Ocean modelling

Implementation of Overtopping Discharges in a 2D Coastal Flood Model of the Mont Saint-Michel Bay

J.-B. Saulnier, T. Paquereau--Gaboreau, J.-V. Delemasure
EGIS Water & Maritime
Guyancourt, France
jean-baptiste.saulnier@egis.fr

***Abstract*—In the framework of a regulatory hazard assessment study applied to the coastal protection system of the Mont Saint-Michel Bay, a coupled TELEMAC-2D/TOMAWAC dynamic flood model was set-up and run in storm conditions. Besides considering hazard scenarios such as dyke breaching or culverts (due to e.g. electric failure of tidal gates), overtopping is also considered. To that end, a specific module dedicated to the computation of wave overtopping discharges over the coastal dykes and transfer to the rear of the structures was developed in TELEMAC-2D. The EurOtop 2018 formulations for overtopping discharges were implemented as a decision tree algorithm. The coastal protection system was segmented in a number of sections along which structural, geometric and incident hydrodynamic characterictics were deemed homogeneous. Such an implementation has the advantage of introducing overtopping discharges in an automated way along the simulation, being robust and computationally efficient.**

I. INTRODUCTION

Coastal and flood modelling is more and more required in a context of sea level rise and increasing frequency of erosion/submersion issues worldwide. A good integration of all physical processes occurring on the sea-land interface in models is crucial for a realistic simulation of water intrusion (overflow, overtopping, erosive processes, breaching etc.) through or over protection systems such as dykes, embankments, tidal gates, dams etc.

In France, regulatory hazard assessment studies – also known as "Etudes de dangers" – are required from communities in order to define the so-called 'protection level', which corresponds to the storm water level (tide + surge) the coastal protection system is able to withstand. In this frame, a set of regulatory scenarios at the protection water level or above (with/without dike, working failure of the hydraulic system, natural breaches etc.) is to be run in order to identify – and account for – the residual water intrusions, if occurring. The modelling steps usually are three-fold : 1/ "upstream" simulation for the determination of wave/level conditions at the toe of structures at each time step, 2/ calculation of overtopping discharge series – using e.g. the EurOtop formulations [1] – along the protection system, 3/ "downstream" simulation wherein discharges are introduced as hydraulic source terms at the rear of structures.

In the framework of a hazard assessment study for the *Syndicat Mixte du Littoral de la Baie du Mont Saint-Michel*, a maritime-terrestrial model was built with the open TELEMAC-MASCARET suite by coupling the TELEMAC-2D and TOMAWAC codes. The coupled model simulates various processes such as tidal oscillation, propagation of offshore sea states up to the coastline, related wave-current interactions and overtopping over structures, which is responsible for the flooding over the protected terrestrial area – if not for dyke breaching. Overtopping is represented as the addition of two specific phenomena: 1) overflow by local exceedance of the structure's crest by the static water level (including wave setup), and 2) overtopping discharge due to waves running up the face of the structure (green water) and/or wave breaking (splash). The first phenomenon is natively handled in TELEMAC-2D by the resolution of the Saint-Venant equations over high-resolution topo-bathymetric relief (Digital Elevation Model, DEM). Due to its dynamic nature, the second phenomenon is dealt with by implementing the EurOtop probabilistic formulae for overtopping discharges, reported as source terms at the rear of the coastal protection system, following previous works (see e.g. [2]). A specific methodology was adopted, which involved the input of structural parameters into the model as well as the implementation of a decision tree for the overtopping discharge formulae to be used in TELEMAC-2D as source term at each time step. Such an approach allows to merge the three steps evoked earlier into one simulation only, which saves a considerable amount of time while rationalising the calculation methodology.

This paper presents the TELEMAC-2D/TOMAWAC model (v7p3) specifically constructed for the hazard study of the Bay of Mont Saint-Michel (Sections II and III) and the implementation of the EurOtop formulations into TELEMAC-2D (Section IV). The promising results obtained for wave overtopping occurrences (among others) in one representative regulatory scenario are then illustrated and commented (Section V). Conclusions are finally drawn with further work avenues (Section VI).

II. STUDY AREA

The bay of Mont Saint-Michel is located in North-Western France, in the English Channel. It extends over about 30km (~500km^2) from Avranches in Normandy to the Grouin Head Point in Brittany. A large part of the bay is a tidal sand-mud flat covered by the sea at high tide and the tidal oscillation can reach 15m in spring tide – the largest one in continental Europe. A continuous protection against flooding made of successive dykes (with or/without road) is present all along the coastline, namely (from West to East, see Fig. 1) : the Duchess Ann dyke (starting South from Cancale), the Western/Eastern polders dykes (at either side of the Mont Saint-Michel) and the Guintre dyke (ending in

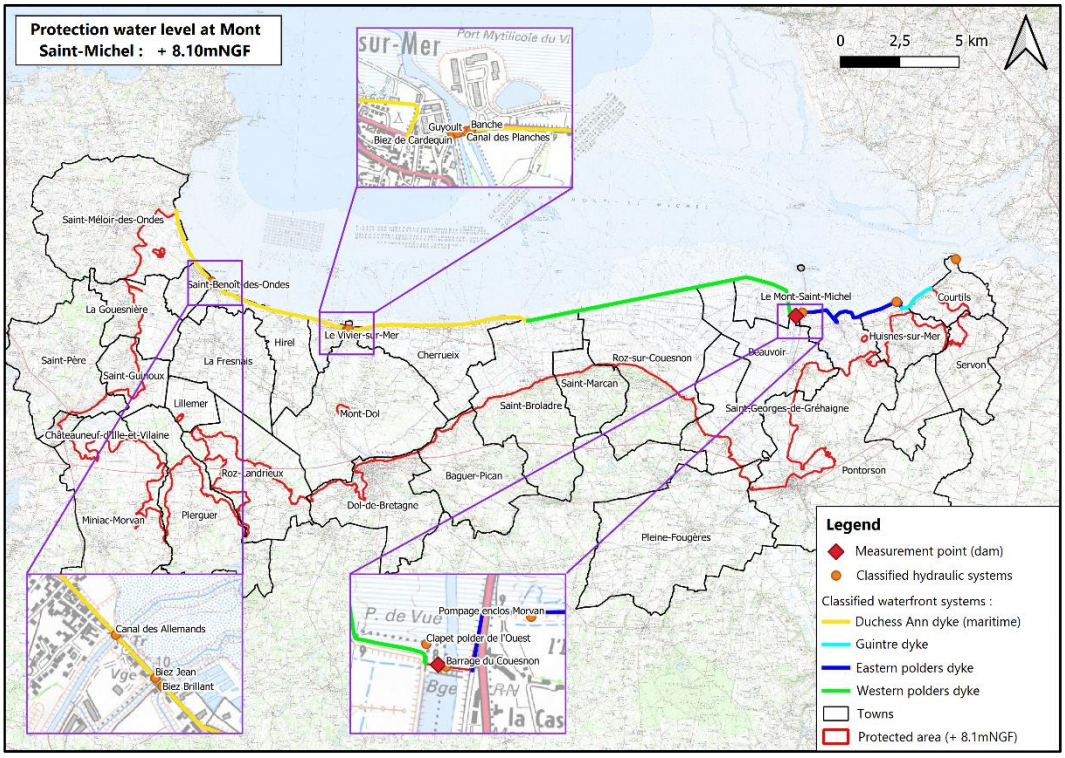

Figure 1 – Area protected from flooding in the Bay of the Mont Saint-Michel and description of the coastal protection system (dykes).

Courtils). In some places, the dykes are bordered by emerged, grassy zones (*schorres* or "herbus"), which can extend up to 2km seawards in the polders zones. Various rivers are flowing out in the bay, among which the Sée and the Sélune in the easternmost part of the bay, and the Couesnon, close to the Mont Saint-Michel rock, whose flow mixes with sea water and is controlled by a dam for sediment flushing purposes. Other hydraulic systems (mechanic/electric gates) are also present along the dykes in order to control the inland drainage. The maximum tidal currents reach 2 to 3m/s in the North of the Mont Saint-Michel so that the flow usually covers the bay at a speed far lower than that "of a galloping horse", as a famous saying erroneously goes. Swells and storm waves (peak period $T_p > 8$s) mostly come from W-NW ([270°N;300°N]) while wind-sea systems ($T_p < 6$s) from NW to NE generally are observed when offshore wave systems are weak. The largest incoming sea states have a significant wave height H_{m0} of 4-4.5m with typical peak period of 10-11s. In storm conditions, water levels up to +8.50mNGF (+8.34mNGF during Xynthia in 2010) have been recorded at the toe of the Mont Saint-Michel.

III. SETUP OF THE HYDRODYNAMIC MODEL

A. *Domain extent and meshing*

The hydrodynamic model was built by combining two spatial domains – a maritime one and a terrestrial one – , which intersect along the 37 km-long coastal protection system (dykes) containing water works like dams, tide gates, sluices etc. The whole domain covers an area of 893km² (almost one fourth of which is land), including the whole Mont-Saint-Michel Bay from the Grouin Head Point to Granville, offshore, and to the southern coastal lowland, onshore (up to level +9.50mNGF).

The maritime mesh was built with refined resolution around the Grouin Head Point (and the scattered islands located close-by), the Mont-Saint-Michel and Tombelaine rocks. The resolution ranges from 5m in *schorres* and around coastal protection structures to 1 000m offshore.

The terrestrial domain contains a number of drainage channels, hydraulic connections between local water systems and coastal protection dykes as well as inland embankments. Only the main drainage channels (78 over a few thousands, with fine 3m wide / 10m long resolution) and the inland embankments (set back dykes, with 5m wide resolution and 5 parallel constraint lines) were included in the mesh. The lowland default mesh resolution was loosened to 100m for optimisation purposes. The final maritime+terrestrial mesh is composed of 369 112 nodes (Fig. 2).

B. *Digital Elevation Model*

The Digital Elevation Model (DEM, see Fig. 3) was created by merging two topo- and bathymetric datasets :

- the coastal topo-bathymetric DEM (20m-resolution) partly covering the Normand-Breton Gulf and produced by the SHOM in 2020 [3] ;
- the LIDAR-based DEM of the Bay of Mont Saint-Michel (1m-resolution) produced in the frame of a regulatory action plan against flooding in 2012.

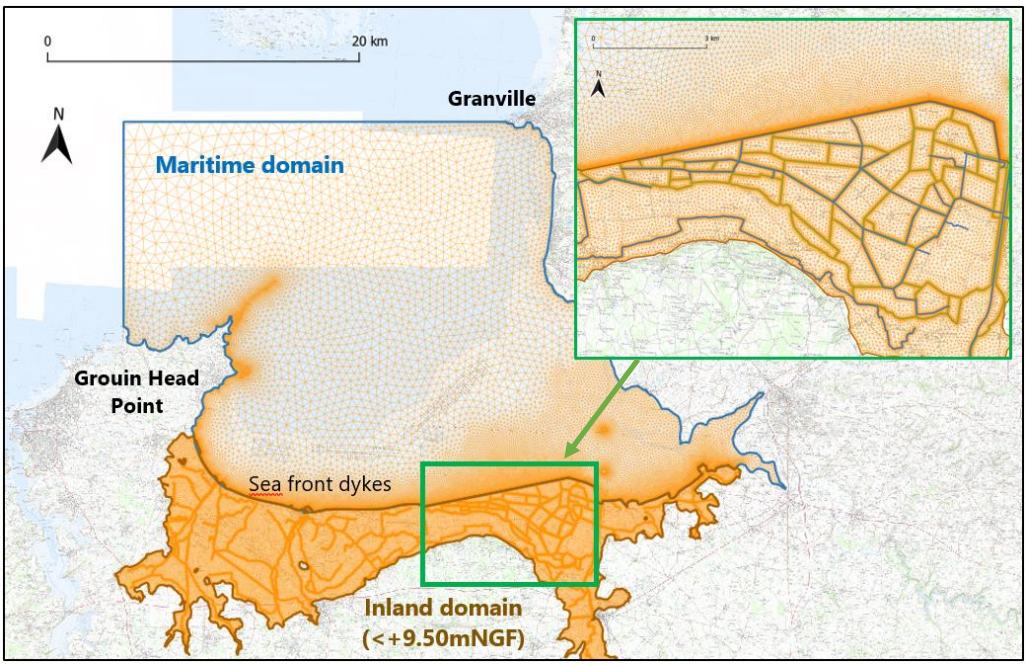

Figure 2 – Mesh of the flood model (maritime + terrestrial) in the Bay of Mont Saint-Michel (369 112 nodes).

The altimetry of the maritime area is entirely based on the 20m-resolution DEM (2020). The altimetry of the terrestrial and intermediate areas is based on the finest (1m) data (2012), although those be less recent.

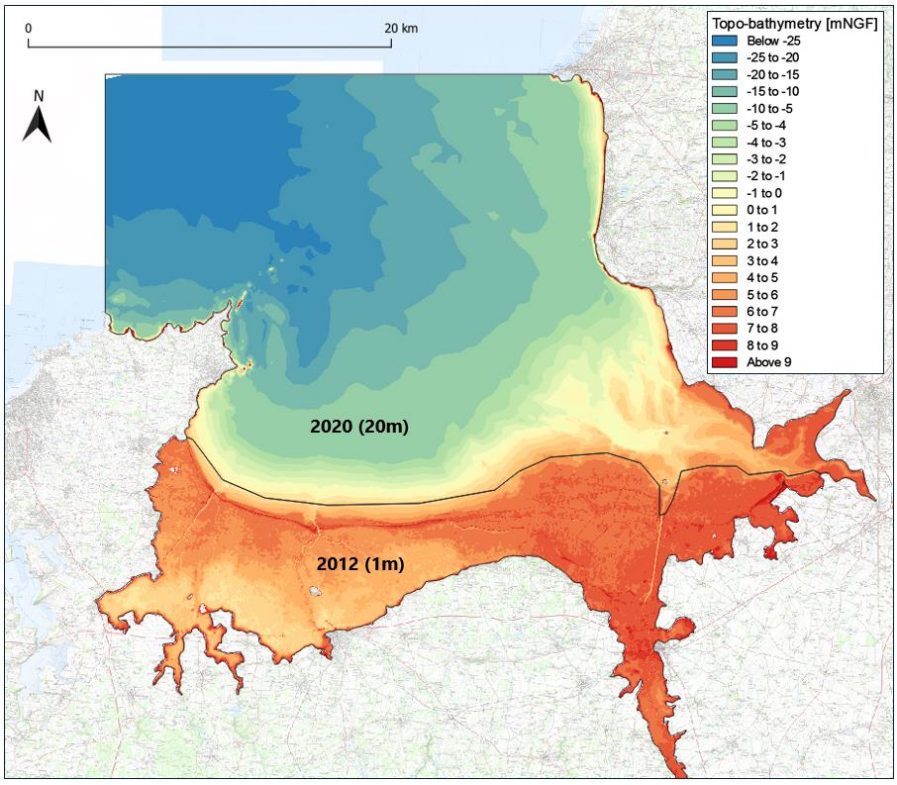

Figure 3 – DEM of the flood model in the Bay of Mont Saint-Michel : fusion of 1m topo-bathymetric data (2012) and 20m bathymetric data (2020).

C. *Boundary conditions*

The environmental conditions are defined as: 1/ a given water level (protection value Z_w = +8.10mNGF or above) and 2/ sea state parameters (H_{m0}, T_p, θ_p). An analysis based on existing extrapolated data on water level in the bay and HOMERE offshore sea state data [4] was conducted in order to produce water level/significant wave height couples with same return period following the "desk study" method described in [5]. This joint-probability analysis was used to determine adequate scenarios for the hazard study (see §V.A).

As tidal oscillation is required for model validation and running regulatory scenarios, the PREVIMER atlas covering the Western English channel area ("MANW", 250m-resolution) was used to prescribe heights and velocities along the open boundary. To this end, the amplitude and phase of 37 tidal constituents were interpolated on each boundary node.

Sea state conditions were imposed along a part of the liquid boundary only (the north-westernmost one), for sea states are predominantly coming from W-NW. The input offshore sea states were modelled as JONSWAP/$\cos^{2s}$ directional spectra with γ = 1 (Bretschneider-like shape) and s = 14 – these mean values were determined by inspection of the spectral shapes and mean spreading values provided in the HOMERE dataset. As stormy conditions are simulated only, the assumption of unimodal spectra is valid here.

The effect of wind on currents was not taken into account in the modelling because the potential wind setup possibly generated onshore does not affect the most critical part of the protection system, from which the overall protection level is determined. River outflows (Sée, Sélune) were not taken into account in the model boundaries either, as it was verified, beforehand, that their impact on water level was very limited.

Space-varying bottom friction conditions were defined according to the Corine Land Cover 2018 occupation database [6]. The Strickler coefficients set up over the domain were based on the recommendations of Paris *et al.* [7], as : K = 30m$^{1/3}$/s in salt marsh/grassy areas along the coast, K = 20m$^{1/3}$/s in marshes, fields and polders, K = 10m$^{1/3}$/s in urban areas and K = 40m$^{1/3}$/s on the sea bed (sand-mud, value obtained after calibration, see §III.D.2)).

D. *Model calibration and validation*

A calibration of two parameters in TELEMAC-2D and TOMAWAC, namely bottom friction coefficient K and breaking parameters γ_2[-], was conducted from available *in situ* datasets in the bay in order to adjust the simulated current velocities and significant wave height to measurements. As it is weakly sensitive to bottom friction, water level was directly validated against reference data.

1) Water level (tide): The simulated water level was compared to two water level datasets: one near Cancale and another one at the St Aubert's chapel, at the toe of the Mont-Saint-Michel. Figure 4 compares the modelled level to *in situ*-validated EPSHOM forecast levels near Cancale on 1-4 January 1991. A very good agreement (R^2 = 0.99) was found,

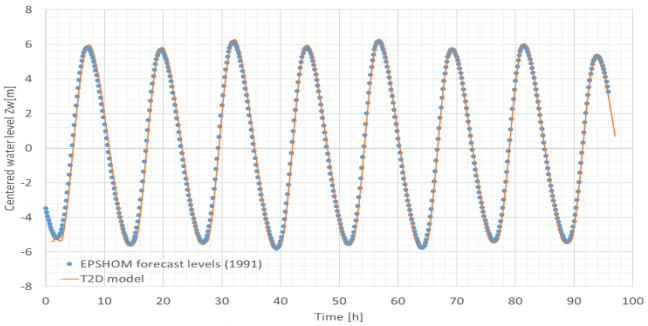

Figure 4 – Comparison of tidal oscillations predicted by EPSHOM and by the flood model near Cancale (1-4 January 1991).

which validated the water level modelling in the western part of the bay.

Figure 5 compares the model results with piezometer measurements at the St Aubert's chapel recorded on 5-12 April 2012 (near highest astronomical tide). The observed level offset at low tide and phase lag are most probably due to topo-bathymetric changes since 2012 (maritime DEM of 2020) and local water catchment. Indeed, sediment dynamics lead to permanent changing in the eastern bay around the Mont Saint-Michel, in particular since the construction of the new access bridge in 2014. The TELEMAC-2D model showed, however, very realistic high tide levels (R^2 = 0.81), which validated the modelling in the eastern part of the bay.

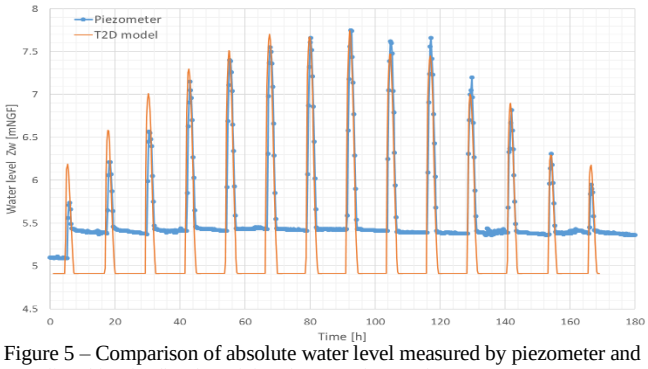

Figure 5 – Comparison of absolute water level measured by piezometer and predicted by the flood model at the St Aubert's chapel (5-12 April 2012).

1) Current velocity: The model was compared to available *in situ* current velocity data, provided by the University of Caen and collected using an electro-magnetic current/wave meter deployed 300m north from the Mont-Saint-Michel between December 2007 and February 2008 [8]. A sensitivity analysis to bottom friction Strickler parameter K was conducted (see Fig. 6). The simulated velocities were found of the same order of magnitude as the measured (depth-averaged) ones and the value K = 40m$^{1/3}$/s was adopted for bottom friction – although this parameter have a limited influence on velocity results in that location.

2) Waves: The same device recorded significant wave height, period and direction data. Because of significant topo-bathymetry changes between 2008 and 2020, and in order to perform relevant comparisons, a depth-based correction was applied to the measured data assuming a conservation of the ratio between significant wave height (H_{m0}) and depth (h).

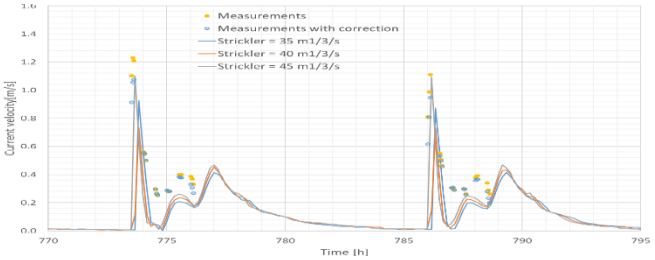

Figure 6 – Comparison of depth-averaged current velocity modulus measured by current meter and predicted by the flood model near the Mont Saint-Michel (~24h in January 2008, [8]).

Also, a sensitivity analysis to breaking parameter γ_2 in TOMAWAC was conducted. Figure 7 depicts the comparison between simulated and measured H_{m0} values around high tide: the obtained range of heights was found in agreement with measurements and the value $\gamma_2 = 0.7$ was eventually adopted. This calibration choice ensured conservative wave penetration and wave breaking modelling over the intertidal zone in view of assessing the performance of coastal protection as regards overtopping and flooding issues.

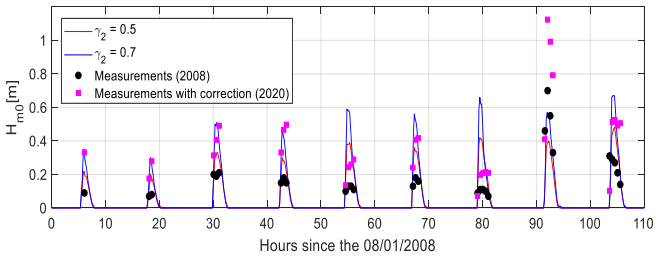

Figure 7 – Comparison of (depth-corrected) significant wave height estimated by wave meter and predicted by the flood model near the Mont Saint-Michel (8-13 January 2008, [8]).

II. IMPLEMENTATION OF OVERTOPPING DISCHARGES IN TELEMAC-2D

C. *EurOtop definitions, formulae and hypotheses*

The EurOtop manual [1] gives a set of empirical probabilistic formulations for the analytical calculation of overtopping-related quantities in given sea state and water level, among which discharge q (in m^3/s per linear meter of structure). This quantity includes the phenomena of green water (wave running up on the structure's seaward face and passing over the crest, see Fig. 8) and the splash effect due to wave breaking on the structure (droplets passing over due to momentum or wind). This wave-related overtopping quantity is different from overflow, schematically illustrated in Fig. 9. The input parameters in the EurOtop formulae therefore are related to hydrodynamics (Table 1) and geometry (Table 2) parameters and some influence factors related to slope roughness, wave attack, presence of a wall or promenade etc. (Table 3).

The basic formulation for the overtopping discharge q is :

$$\frac{q}{\sqrt{g \cdot H_{m0}^3}} = A \cdot exp\left[-\left(B \cdot \frac{R_c}{H_{m0} \cdot \Pi_j \gamma_j}\right)^C\right] \quad (1)$$

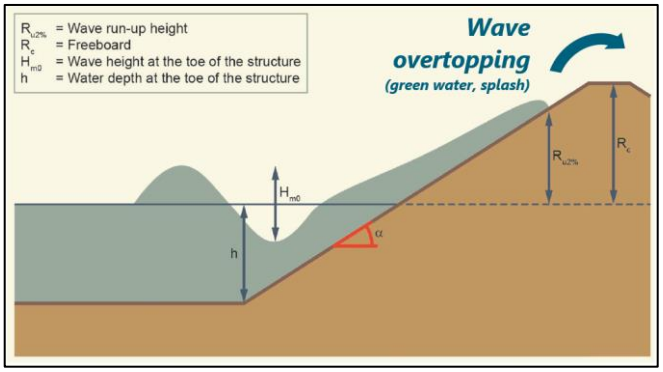

Figure 8 – Sketch of wave overtopping phenomenon [adapted from EurOtop 2018].

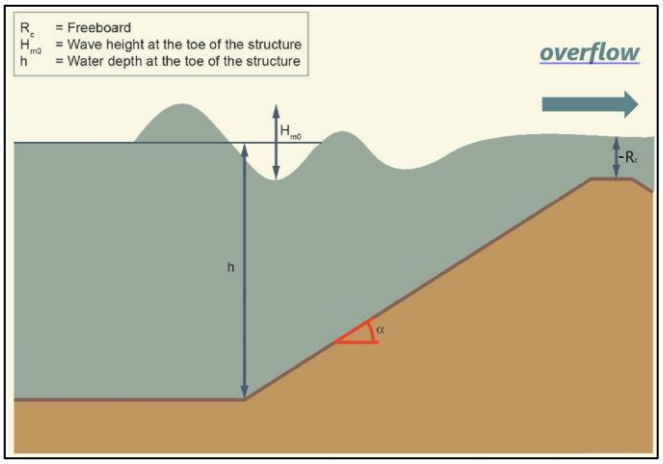

Figure 9 – Sketch of overflow phenomenon [adapted from EurOtop 2018]; Rc < 0 here.

where A, B, C are (empirical) constant values or functions of other input parameters, according to the case. Parameters γ_j stand for appropriate influence factors, where required. The parameterisation depends on the type of structure (coastal dykes and embankment seawalls, armoured rubble slopes and mounds, vertical and steep walls, respectively in chapters 5, 6 and 7 of the EurOtop manual), and roughness (γ_f), geometry (cot α, berm…) and hydrodynamic parameters (e.g., ξ_{-10}).

TABLE 1 – EURTOP HYDRODYNAMIC INPUT PARAMETERS (AT THE TOE OF STRUCTURE)

Symbol	Unit	Name/ Formula
H_{m0}	m	Spectral significant wave height ($\neq H_s$)
T_p	s	Spectral peak period
T_{-10}	s	Energy mean period: $T_{-10} = 1.1 * T_p$, mean experimental value
T_m	s	Mean period : $T_m = T_p/1.2$, mean experimental value
Z_w	mNGF	Water level (in given vertical reference level)
ξ_{-10}	-	(Energy) Breaker parameter : $\xi_{-10} = \tan\alpha/(H_{m0}/L_{-10})^{0.5}$
L_{-10}	m	(Energy) Mean wavelength : $L_{-10} = g*T_{-10}^2/(2\pi) \sim 1.56*T_{-10}^2$
s_{m-10}	-	(Energy) Mean steepness : $s_{m-10} = H_{m0}/L_{-10} = 2\pi*H_{m0}/(g*T_{-10}^2)$

TABLE 2 – EURTOP GEOMETRY INPUT PARAMETERS

Symbol	Unit	Name/ Formula
cot α = 1/tan α	-	Structure slope (cot α = 0 corresponds to a vertical wall)
Z_c	mNGF	Crest level (in given vertical reference level)
R_c	m	Crest freeboard of structure : $R_c = Z_c - Z_w$
H_{wall}	m	Height of storm wall on top of slope or at promenade
G_c	m	Promenade width
B	m	Berm width (horizontal)

TABLE 3 – EURTOP INFLUENCE FACTORS

Symbol	Unit	Name/ Formula
γ_b	-	Influence factor for a berm
γ_f	-	Influence factor for the permeability and roughness of or on the slope
γ_β	-	Influence factor for oblique wave attack
γ_v, γ^*	-	Influence factors for a vertical storm wall on the slope and/or a promenade

When the static water level exceeds the structure's crest, i.e., when $R_c < 0$ (negative freeboard), the EurOtop discharges may still be valid by considering $R_c = 0$. Hence, the formulae do not depend on freeboard any longer. This assumption has a limit however, as suggested by Hughes and Nadal [9], given as:

$$R_c/H_{m0} < -0.3 \quad (2)$$

meaning that as soon as the dimensionless freeboard (R_c/H_{m0}) is lower than -0.3, the residual wave overtopping may be seen as negligible.

In this work, the *mean value approach* formulations of the EurOtop manual have been implemented as the goal is to perform realistic simulations of hydraulic processes on the sea-land interface. However, in a conservative approach, the definition of influence factors was made simpler by considering no berm, storm wall or promenade ($\gamma_b = \gamma_v = 1$) and frontal wave attack ($\gamma_\beta = 1$). Only roughness/permeability factor γ_f was varying according to the structure (e.g., $\gamma_f = 1$ for concrete/grass slopes, $\gamma_f = 0.40$-0.60 for rocky layers etc.).

D. *Methodology and implementation*

The first task consists in subdividing the coastal protection system into a set of individual sections (length of e.g. some tens to some hundreds of meters) where local hydrodynamic, structural (roughness, berm…) and geometrical (crest width, slope…) characteristics are deemed homogeneous. An example along the Duchess Ann dyke is given in Fig. 10.

Then, the implementation of overtopping discharges in TELEMAC-2D simply boils down to introducing a set of culverts along the coastal protection system. The main difference with the default culvert module is the fact the discharges do vary in time and depend on TELEMAC-2D and TOMAWAC hydrodynamic variables calculated by the model at each time step (namely Z_w, H_{m0}, T_p…). For each section, these variables are extracted at a given "upstream" node (standing for "toe" conditions as required in the EurOtop manual) and used for calculating the corresponding wave overtopping discharge (in a specific routine), which is then conveniently prescribed as a source point in a given "downstream" node at the rear of the structure (see Fig. 11). The location of both the up- and downstream nodes is freely defined by the user. Here, it is taken approximately between 10 and 25m at both sides of the dykes' crestline depending on the topo-bathymetry and dyke slope.

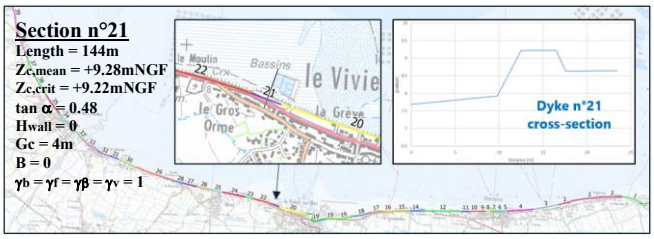

Figure 10 – Map of coastal sections of the Duchess Ann dyke and focus on section n°21 (cross-section and characteristics).

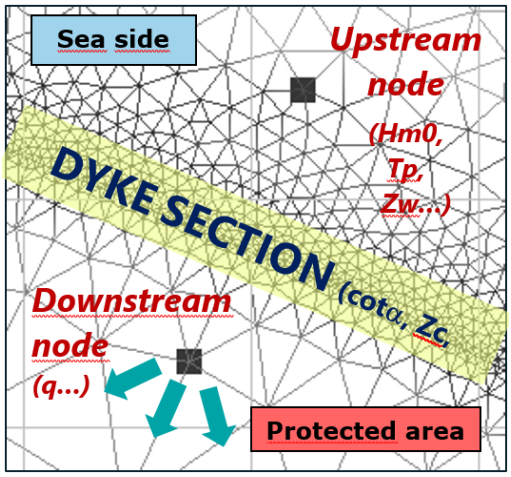

Figure 11 – Sketch of sinks/sources implemented in TELEMAC-2D for overtopping discharge calculation.

The main routine to be modified in TELEMAC-2D is PROSOU, wherein wave parameters have been made available (HM0_TEL, TPR5_TEL…). As the model is expected to be run in parallel mode, it must be ensured that the couple of upstream/downstream nodes defined for each section complies with the partitioning scheme, that is, both nodes belong to the same submesh. Otherwise, the simulation is forced to crush.

A specific output variable is created in order to allow for extracting time series of wave overtopping discharge over each section, which can also be useful for checking the order of magnitude of the computed values.

Such an implementation therefore is straightforward. The limitations may be, however, the fact the realism of the model rests on a sufficiently accurate dyke sampling (one source point per section only), which means a larger effort has to be made prior to running the simulation, so that a satisfying trade-off is found. Also, the location of both up- and downstream nodes might be sensitive. In any case, the upstream work devoted to the discretization of the coastal protection system is fundamental for a good accuracy of the model and should require due attention.

III. SIMULATIONS

A. Simulated scenario

Among the regulatory scenarios simulated in the frame of the risk study, scenario n°3 (SC3) is considered here for illustrative purposes. The scenario corresponds to a 50-year return period event (Z_w = +8.40mNGF in Mont-Saint-Michel, H_{m0} = 2.1m, T_p = 15s et θ_p = 290°N) and includes structural failures (breaches) throughout the coastal defence system. A 24-hour high spring tidal event was simulated and a constant surge component was added to the tidal level so that the extreme water level is reached in the Mont Saint-Michel approximately 5 hours after the simulation start. The surge then decreased linearly up to the second tidal peak where it is zero from there on. Such a definition allows a better understanding of the flood expansion over the lowland topography right after the storm peak (i.e., the first high tide in the simulation). The prescribed water level was adjusted so that the highest level simulated at the Mont Saint-Michel matched the target value (Z_w). Due to local transformation effects in the bay (flow, wave setup…), indeed, the water level is always higher on the coast and varies alongshore: high tide is e.g. delayed by approximately 30 min between the Mont Saint-Michel and the Nielles, in the western part of the bay.

SC3 is expected to exhibit three types of phenomena: 1/ direct wave overtopping discharges inducing (limited) flooding at the rear of the coastal defence, 2/ direct overflow and 3/ breaching occurrences due to large overtopping discharges. The breaching scenario is based on a preliminary analysis – a regulatory part of the risk study, – which aims to characterise the incident hydraulic conditions at each coastal section in the various storm events previously defined. This means each storm event – among which, that of SC3 – was simulated for this purpose (here, on the maritime domain only and over a shorter time span, up to the first high tide) and the overtopping module was used in order to produce the discharge curves related to the critical crest level of each coastal section. According to these results and to the EurOtop recommendations for maximum tolerable discharge regarding structural design (e.g. typical value of 5l/m/s over seawalls with grass covered crest and landward slope), the risk of potential breaching could be assessed. In SC3, 21 natural breaches have been set up in TELEMAC-2D among which 16 are assumed to be due to an excess of overtopping discharge. The other breaches defined in the scenario were due to other types of risks (e.g. excessive overflow, toe scouring, slipping or external/internal erosion, etc.). For all breaches, the embedded breaching module was used with trigger criterion based on water level in front of the structure (to the so-called "safety level"). Figure 12 shows the location of the breaches with highlight on those specifically initiated by overtopping (red line) and those due to other type of risk (orange line). Some of them are located in the westernmost part of the bay (Nielles, Le Vivier-sur-Mer) while others are located in the polders region. Along the rest of the coastal defence system (green line), no structural failure is expected but flooding due to overtopping discharge may occur, namely on those sections indicated by an arrow.

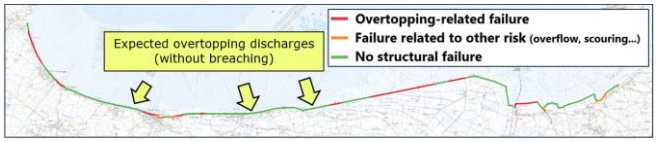

Figure 12 – Location of breaches along the coastal defence system in the bay of Mont St-Michel in SC3; location of expected wave overtopping discharges not causing breaches.

B. Results

1) Direct wave overtopping discharges: Figure 13a illustrates the maximum water height reached during the 24-hour simulation along a part of the Duchess Ann dyke, where inland expansion due to wave overtopping is observed, namely on sections 16, 17, 19, 20 and 21. The orange points denote the downstream node of each coastal section. As the tidal range is large, the overtopping duration is rather short – approximately 1.4h according to the discharge and cumulated volumes curves plotted in the figure. In every such section, only one discharge peak is obtained during the simulation, which occurs at the first high tide – around the 5th hour – when water level is highest. The largest discharge value – exceeding 0.30m^3/s along the section – is obtained in section 20, with a final transmitted volume of water of about 530m^3. The implemented overtopping module therefore looked to behave satisfactorily.

2) Breaches: Lower crested dykes and breaches let large volumes of water flow into the terrestrial domain as compared with overtopping discharges, as shown in Fig. 13b. The order of magnitude is 10^{5}m^3, which is 1 000 times as big as those due to overtopping discharges: as expected due to breaching assumptions, overflow is the dominant phenomenon causing flooding in the protected area of the bay of Mont St-Michel in this scenario. The curves exhibit an overflow discharge peak as soon as the breach is triggered. The discharge generally becomes negative after the first peak because a part of the water volume returns to the sea with ebb-tide. Section 56 is an exception as the water expansion is too wide (with the aid of the drainage channel) to let a significant volume of water flow back into the sea. A second, smaller overflow discharge peak is also observed at the second high tide due to the locally lowered altimetry.

IV. CONCLUSIONS

A coastal flood model including automatic overtopping discharge calculation following the EurOtop formulations has been constructed and successfully run in the frame of the hazard assessment study of the Bay of Mont Saint-Michel. To this end, the coastal protection system was discretised as a sequence of homogeneous sections whose characteristics were introduced in the model. The flooding occurrences due to overflow, wave overtopping discharges and overtopping-related breaches could be satisfactorily simulated and analysed in storm conditions. Based on these first encouraging results, the methodology and related implementations can be extended and improved by considering more coastal contexts and types of structure, involving more EurOtop parameters and quantities.

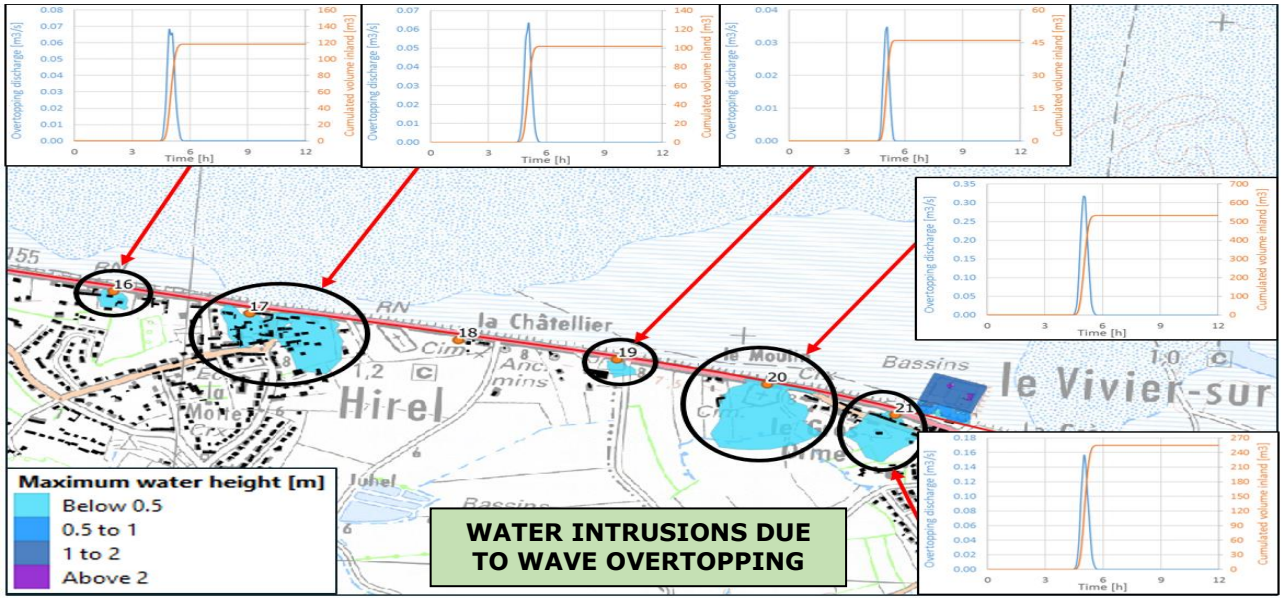

(a)

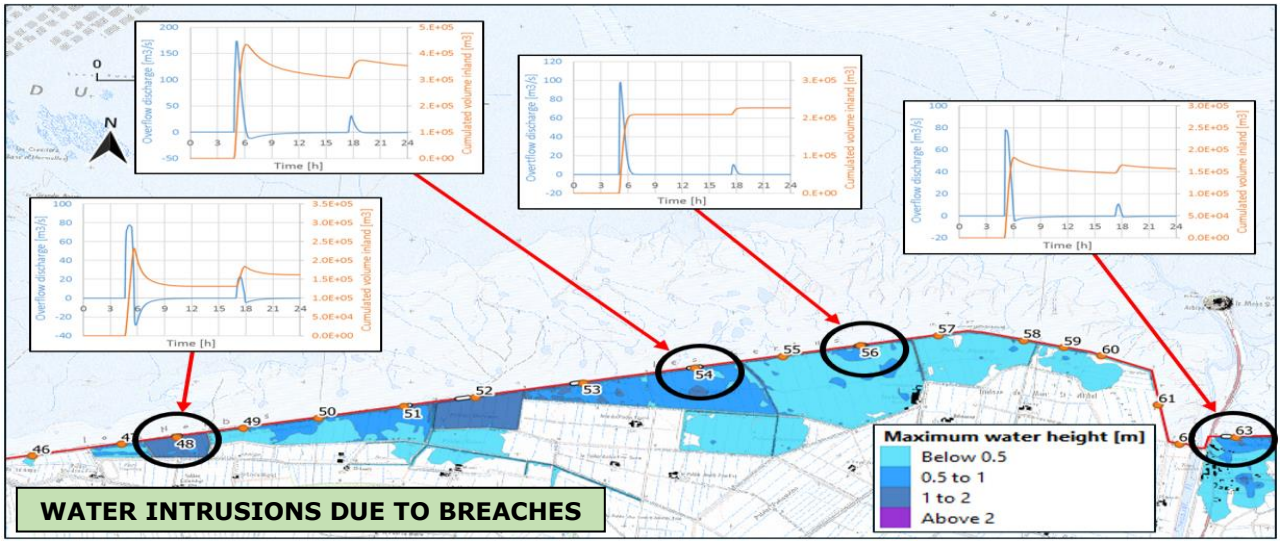

(b)

Figure 13 – Examples of water intrusions at the storm peak (maximum water height) due to wave overtopping (a) and wave-overtopping-related breaches (b) simulated by the flood model in SC3; instantaneous discharge (left axis) and cumulated volume inland (right axis) curves.

ACKNOWLEDGEMENT

The authors wish to thank the *Syndicat Mixte du Littoral de la Baie du Mont Saint-Michel* for authorising to publish this work.

REFERENCES

[1] J.W. Van der Meer, N.W.H. Allsop, T. Bruce, J. De Rouck, A. Kortenhaus, T. Pullen, H. Schüttrumpf, P. Troch, and B. Zanuttigh, EurOtop – Manual on wave overtopping of sea defences and related structures. An overtopping manual largely based on European research, but for worldwide application. 2nd ed., 2018. www.overtopping-manual.com

[2] J. Dugor, D. Rihouey, and P. Lang, "Flood modelling on Île de Ré during Xynthia," 21st Telemac User Conference, Grenoble, October 2014, 8pp.

[3] SHOM, Coastal topo-bathymetric digital elevation model of the Normand-Breton Gulf, 2020.

[4] E. Boudière, C. Maisondieu, F. Ardhuin, M. Accensi, L. Pineau-Guillou and J. Lepesqueur, "A suitable metocean hindcast database for the design of Marine energy converters," *Int. Jour. of Marine Energy*, pp. 40-52, 2012.

[5] DEFRA/Environment Agency (P. J. Hawkes), "Use of Joint Probability Methods in Flood Management, A Guide to Best Practice,' R&D Technical Report FD2308/TR2, March 2005, 77pp.

[6] Corine Land Cover database, 2018: https://land.copernicus.eu/pan-european/corine-land-cover

[7] F. Paris, R. Pedreros, A. Stépanian, T. Bulteau and S. Lecacheux, "Modélisation de la submersion marine en Camargue," Final report BRGM/RP-66804-FR, 176pp.

[8] R. Desguée, "Etude des processus hydro-sédimentaires et évolutions morphodynamiques autour du Mont-Saint-Michel, " Ph.D Thesis Report, Univ. Caen / Basse-Normandie, France, 2008, 366pp.

[9] S. A. Hughes and N. Nadal-Caraballo, "Laboratory study of combined wave overtopping and storm surge overflow of a levee," *Coastal Engineering*, vol. 56, March 2009, pp. 244-259.

Wave overtopping and overflow hazards: application on the Camargue sea-dike

Thomas Paul, Clément Lutringer, Adrien Poupardin, Abdelkrim Bennabi, Jena Jeong
Institut de Recherche en Constructibilité, Ecole Spéciale des Travaux Publics
Université Gustave Eiffel
6-8 avenue Blaise-Pascal Cité Descartes – Champs-sur-Marne – 77455 Marne La Vallée, France.
apoupardin@estp-paris.eu

Philippe Sergent
CEREMA EMF
134 rue de Beauvais, CS 60039, 60280 Margny les Compiègne Cedex, France
Philippe.Sergent@cerema.fr

***Abstract*— Dike breaches occurs regularly during storm events. This phenomenon contributes to amplify considerably the impact of floods on coastal areas. It represents an important cost for repairing existing infrastructures in the vicinity of the sea-dike. Then, they must be upgraded to prevent breaches.**

In the present study, ANEMOC and REFMAR dataset were analysed, off Camargue coasts, to quantify the storm hazards in terms of wave height and sea level wind set-up. Repartition laws were adjusted on dataset to build a 2D-copula which is used to estimate events return periods.

As we were interested in the physical parameters around the sea-dike, waves were propagated from the deep water by using TOMAWAC module which takes into account the actual bathymetry. As a first approximation, only a 1D propagation was considered.

From estimated local parameters, overtopping formula were used to estimate the overtopping discharge, the crest velocity, and the water level over the sea-dike. These latter were used to assess a potential erosion on the dike rear-side.

A set of several wave heights – sea-level wind set-up couple were tested and each of them were relied to a probability of occurrence given by the 2D-copule.

I. INTRODUCTION

Hazards studies are of a great importance to size infrastructures which protect a city or a socio-economic area. In particular, in the case of coastal storms, we consider wave spectra and their propagation to coasts, mean water level and dike dimensions which impact flood probability of occurrence.

Previous works in storm hazards ([1] and [2]) allow to estimate the wave height and water level return periods, in particular, concerning extreme events.

Depending of these deep water parameters, waves can be propagated using empirical formula [3] or tools based on wave spectrum propagation by considering the dispersion relation, in particular in intermediate water depths (TOMAWAC module for example [11]). The wave breaking impacts greatly the propagation by decreasing linearly wave heights and increasing the wave set-up to the coast with a maximum at toe of sea-dike.

From local parameters, coupled software can be used to compute water discharges over the dike (by using the TELEMAC suit for example). Water discharge estimation can also be deduced from empirical laws ([4], [5] and [6] for example).

In the scope of this study, several approaches were combined and compared to estimate the water discharge over the sea-dike and his corresponding water crest velocity which may be responsible for dike rear-side erosion.

In Part II, input parameters and numerical model are presented. Part III is focused on numerical results and their interpretations. Part IV deals with water discharges and particularly run-off velocities. Finally, we conclude this study in Part V.

II. INPUT PARAMETERS AND NUMERICAL MODEL

A. *Probabilistic data*

For this study, two sets of data were considered: REFMAR data extracted from the tide gauge located in Marseille harbour and ANEMOC data from a synthetic wave gauge located at a depth of 30 m and 3.6 km off the coast. Event were selected by identifying a local maximum and by considering a minimum time interval of 24 h between two events.

Both datasets were analysed to extract storm events by considering a two-thresholds method. Then, we use a Generalized Extreme Value Distribution (GEV) to fit REFMAR and ANEMOC treated data independently [7].

Finally, a Gumbel Copula, called F in the following of the text, was used to merge both distributions by sector and we determined the interdependency parameter α by using a likelihood maximum method.

The computed Gumbel Copula is given in Figure. 1.

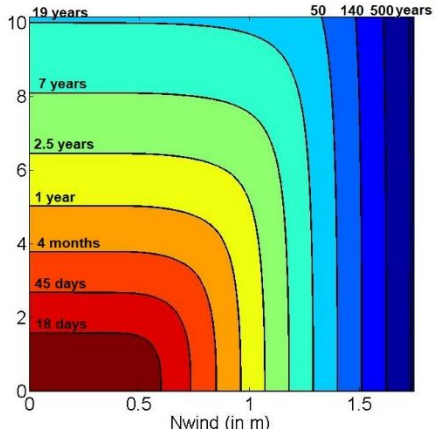

Figure. 1. Gumbel copula built from ANEMOC and REFMAR dataset and by fitting events with a Generalized Extreme Value Distribution (GEV)

B. *Physical input Parameters*

TOMAWAC module [8], from TELEMAC software suite, was used to propagate the wave from deep waters to the coast.

Bathymetry was built from Litto3D products (see www.shom.fr for more details) for shallow water ($d < 10$ m) and GEBCO (see www.gebco.net for more details) data for deeper water. A representation of the two-dimensional bathymetric map is given in Figure. 2.

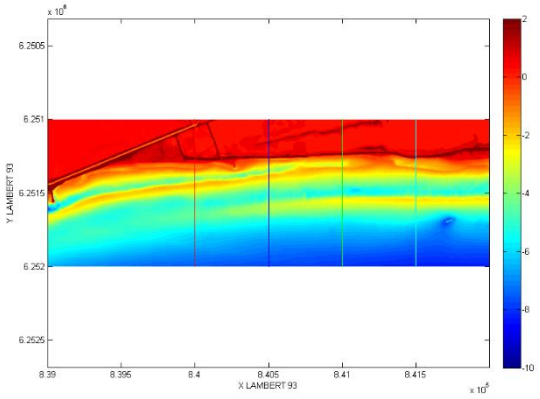

Figure. 2. Bathymetric map in Lambert 93 coordinates system from Litto3D products

As a preliminary work, we consider a one-dimensional wave propagation from the south (deep water) to the north on the profile $X = 841000$ (in green in Figure 2) in Lambert 93 coordinates system (see Figure 3) although three event classes were detected (REFMAR data) and separated according to their propagation direction: north-west (315° for most energetic and frequent extreme events), north (0°) and east (80°). Then, we neglected refraction effects in the scope of this paper.

Concerning other physical parameters, simulations were realized by varying: significant wave height H_{m0} from 2 to 10 m each 2 m and; mean water level $\overline{\eta_{wind}}$ from 0 to 2 m each 0.5 m.

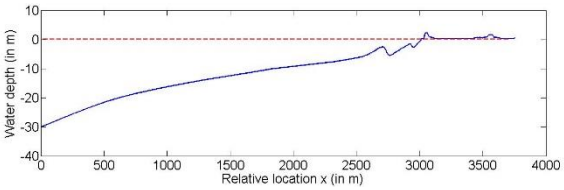

Figure. 3. Bathymetric profile $X = 841000$ in Lambert 93 coordinates system. Water depth was replaced in a relative coordinate system with x designing the propagation direction and the new reference $x = 0$ corresponding to $Y = 6254300$ in Lambert 93 coordinates system. Waves propagates from the south to the north.

C. *Numerical input Parameters*

We chose to propagate a JONSWAP spectrum in the TOMAWAC options by adjusting the significant wave height and pic frequency to simulate the case described section II-B. To simplify the problem, ANEMOC data were used to fit relation (1) which rely the significant wave height to the wave peak period.

$$\frac{1}{f_p} = 3.72\, {H_{m0}}^{0.37} \qquad (1)$$

We verified that (1) is not so far from the constant curvature hypothesis in deep water. Furthermore, the exponent in (1) is slightly inferior to the one given in the literature, as in [9].

The frequency sampling was adjusted from $f = 0.05$ Hz (20 s) to $f = 0.5$ Hz (2 s) with a frequency ratio of 1.1.

The spatial grid was sampled by using a spatial step of 3 m (in x and y-directions). We considered a flume width of 60 m.

The total time was fixed to ensure that a permanent state is reached in TOMAWAC at the simulation end. The time step of simulation was fixed to 0.5 s.

Battjes and Janssen's model (1978) was used to take into account the wave breaking in the simulation, and we chose the Miche's criterion to rely the local wave height to the water depth by using typical values for α, γ_1 and γ_2.

D. *Laws for wave overtopping*

Finally, TOMAWAC results (local wave height H_m and mean water level $\overline{\eta_t} = \overline{\eta_{wind}} + \overline{\eta_{wave}}$) were extracted at toe of dike at a water depth of $d = 0.5$ m (see Figure 4).

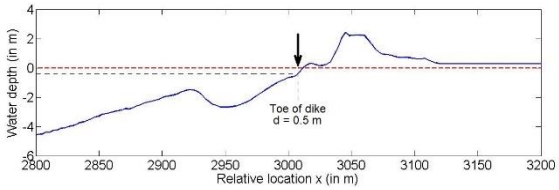

Figure 4. Bathymetric profile: zoom on the dike

The wave set-up $\overline{\eta_{wave}}$ was computed at each point from the deep water by using the radiative stress Sxx gradient.

As shown in Figure 4, the upstream bank of the dike is located near an emerged reef flat which must be taken into account when applying overtopping formula. In this paper, the form developed by [10] was considered:

$$\frac{q_w}{\sqrt{g\,Hm^3}} = 0.06\frac{\xi_{op}}{\sqrt{\tan(\alpha)}}\exp\left(-5.2\frac{R_c}{Hm}\frac{1}{\xi_{op}}\frac{1}{\gamma_r\gamma_b\gamma_h\gamma_\beta}\right) \text{ for } \xi_{op} < 2 \quad (2)$$

$$\frac{q_w}{\sqrt{g\,Hm^3}} = 0.2\exp\left(-2.6\frac{R_c}{Hm}\frac{1}{\gamma_r\gamma_b\gamma_h\gamma_\beta}\right) \text{ for } \xi_{op} > 2 \quad (3)$$

with q_w the overtopping discharge, α the slope of the dike front-side, R_c (vertical distance between the still water elevation and crest elevation) the freeboard, ξ_{op} the Iribarren number and γ-factors reduction factors (see [5]). For applying these formulas, we measured $\alpha = 26°$, ξ_{op} depended on the simulated case, $\gamma_r = 0.6$ (for one natural blocks layer) and γ_b depending on the local water level and on the reef flat elevation and length (see [4]).

These estimated values were compared with discharge computed with results given by using Dean formula (4) and Henderson law (5) [11]:

$$\overline{\eta_t} = \overline{\eta_{dean}} = \overline{\eta_{wind}} + 0.191H_{m0} \quad (4)$$

$$q_w = 0.5443\sqrt{g\,{h_0}^3} \quad (5)$$

with h_0 corresponding to the vertical distance between the still water elevation $\overline{\eta_{dean}}$ and crest elevation.

The two methods will be referred as Met. a) (TOMAWAC for wave propagation and (2) or (3) for discharge estimation) and as Met. b) ((4) for water level and (5) for discharge estimations). A diagram describing both methods is given Figure 5.

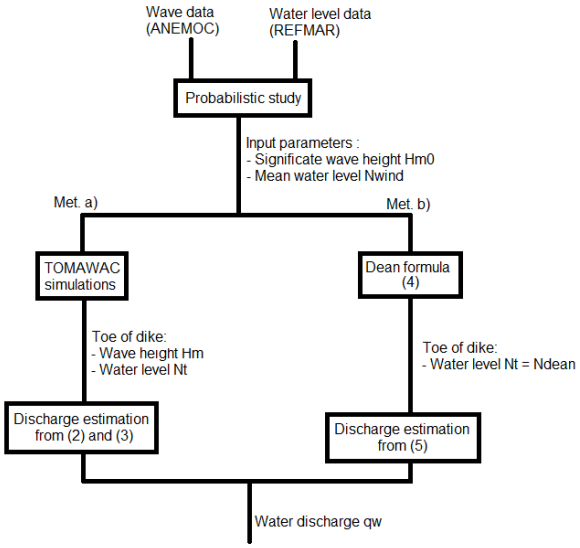

Figure 5. Methodology for water discharge estimation

Finally, TELEMAC-2D (Shallow-Water equations) was used to submerge the dike in two cases: moderate and severe flooding and to compare results with Met. a) and b). For these simulations, we considered results of TOMAWAC simulations as input parameters. To simplify the problem, we considered a monochromatic wave signal with wave height equal to the corresponding significate wave height computed with TOMAWAC and water level impacted by the wave set-up. The bathymetric grid input boundary is located at toe of dike (see Figure 4). We measured wave discharges, water heights and velocities by using synthetic gauges located on the dike crest and the dike rear-side.

III. RESULTS

A. *TOMAWAC results*

Each case was simulated by using TOMAWAC module. Significant wave heights H_m and mean water level $\overline{\eta_t}$, at toe of dike ($d = 0.5$ m), are shown in Figure 6.

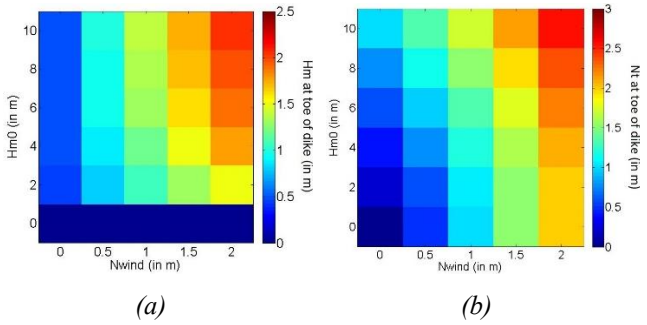

(a) *(b)*

Figure 6. Hydraulics parameters at a water depth $d = 0.5\ m$ at toe of dike: (a) significate wave height $Hm(d = 0.5$ m); (b) mean water level $\overline{\eta_t}(d = 0.5$ m)

By considering a crest elevation of 2.31 m, overtopped discharges were computed by using Met. a) and Met. b). Data were oversampled on a slightly more resolved grid (see Figure 7a) and b)). We remind that the horizontal distance between toe of dike and crest elevation is around 33 m.

Generally, Met. a) (Figure 7a) induces higher discharge for higher wind set-up and lower significant wave height whereas Met. b) (Figure 7b) induced higher discharge for lower wind set-up and higher significant wave heights.

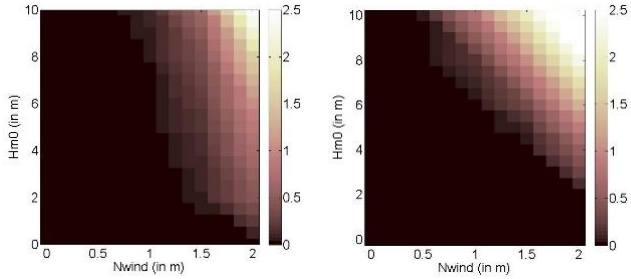

(a) *(b)*

Figure 7. Overtopping discharge in $[m^3/s/m]$ computed from: (a) Met. a); (b) Met. b)

As expected, Met. b) (Figure 7b) give linear iso-discharge lines whereas Met. b) (Figure 7a) shows curbed iso-discharge lines.

B. *Discharge occurrences on the dike*

By combining the Gumbel copula shown in Figure 1 and discharge grids obtained in Figuire 7, each event can be associated to an overtopping discharge and a return period. For example, a 5 m significant wave height and 1 m wind set-up event corresponds to a 2.5 years return period event but it doesn't generate high discharge over the dike (0.011 and 0

$m^3/s/m$ with Met. a) and Met. b) respectively). Whereas a 6 m significant wave height and 1.5 m wind set-up event corresponds to a 130 years return period and it generates high flooding: 0.2 and 0.33 $m^3/s/m$ with Met. a) and Met. b) respectively.

Then, we wanted to know what is the cumulative probability to reach: a moderate discharge (0.01 $m^3/s/m$), a severe discharge (0.2 $m^3/s/m$). Cumulative probabilities of Gumbel copula were integrated on the two latter iso-discharge lines for Met. a) and b).

Knowing what couple $(\overline{\eta_{wind}}, H_{m0})$ of variables would give us a specified discharge, we then had to integrate the copula represented in Figure1 on all the points that would give us this amount of discharge (or worse). We decide to integrate the derivative of the copula $\frac{\partial F(\overline{\eta_{wind}}, H_{m0})}{\partial H}$ on the iso-discharge line, which should be the same according to theory.

$$P(\eta > \overline{\eta_t}) = \iint_C \left(\frac{\partial^2 F(\overline{\eta_{wind}}, H_{m0})}{\partial H \partial \eta}\right) d\eta dH \quad (6)$$

$$P(\eta > \overline{\eta_t}) = \int_0^{+\infty} \left[\frac{\partial F(\overline{\eta_{wind}}, H_{m0})}{\partial H}\right]_{g(H)}^{+\infty} dH \quad (7)$$

$$P(\eta > \overline{\eta_t}) = -\int_0^{+\infty} \left(\frac{\partial F(\overline{\eta_{wind}}, H_{m0})}{\partial H}(H, g(H))\right) dH \quad (8)$$

with $P(\eta > \overline{\eta_t})$ the exceedance probability over a water level $\overline{\eta_t}$ and $g(H)$ the law relying η and H which can be easily deduced from data of Figure 7a and 7b (we assume that iso-discharge lines can be converted into iso-water level lines).

Components of the copula derivative $\frac{\partial F(\overline{\eta_{wind}}, H_{m0})}{\partial H}$ were summed onto the line $\overline{\eta_t} = g(H)$ for Met. a) and Met. b) by varying the discharge (0.01 and 0.2 $m^3/s/m$). Results are shown in Figure 8.

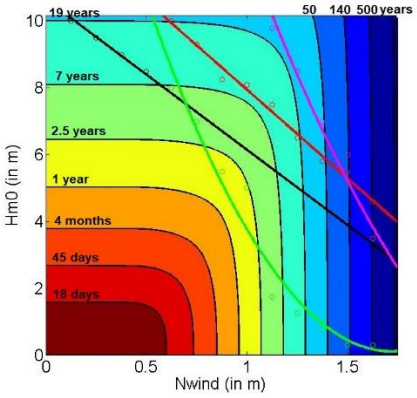

Figure 8. Gumbel copula in logarithmic scale and iso-discharge lines for: a discharge exceedance of 0.01 $m^3/s/m$ by using Met. a) (in green) and Met. b) (in black); a discharge exceedance of 0.2 $m^3/s/m$ by using Met. a) (in magenta) and Met. b) (in red)

The return period (computed from (8)) for discharge exceedances of 0.01 and 0.2 $m^3/s/m$ are respectively of 1 year (Met. a)), 2 years (Met. b)) and 75 years (Met. a)), 7 years (Met. b)). As Met. b) is supposed to be used as a first estimation, the return period of a 0.2 $m^3/s/m$ water discharge must be closer to probability of occurrence given by Met. a).

C. *Comparison with TELEMAC-2D simulations*

For TELEMAC-2D, cases described as moderate (0.011 $m^3/s/m$) and severe (0.2 $m^3/s/m$) in section III-B were simulated.

In the scope of this paper, we focused our analysis on the first wave which overtopped the dike.

Figure 9 shows differences between both cases. In particular, the severe event gives a maximum water discharge of 2.5 $m^3/s/m$ followed by a positive discharge during the whole wave period (7.2 s for a wave height of 6 m). Whereas the moderate event gives a smaller peak discharge of 0.03 $m^3/s/m$ with a water discharge more regular in time.

By integrating these water discharges on a period, we retrieved a mean water discharge of 0.012 $m^3/s/m$ (closed from results of Met. a)) for the moderate event and of 0.322 $m^3/s/m$ (closed from results of Met. b)) for the severe event.

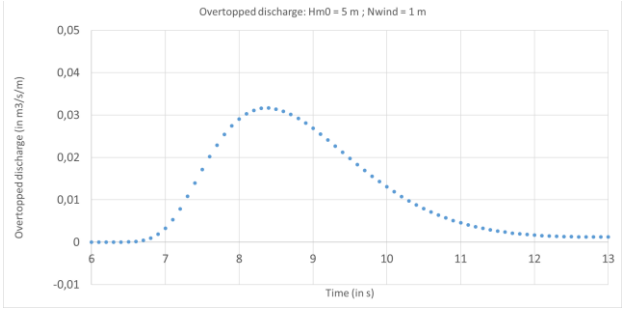

(a)

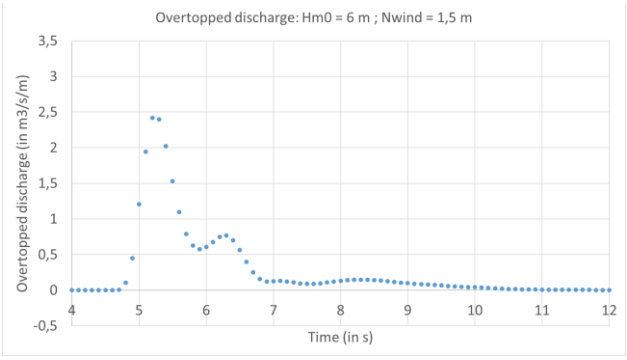

(b)

Figure 9. Overtopping discharge in $[m^3/s/m]$ computed with TELEMAC-2D by considering the following simulated cases: (a) a 5 m significant wave height and 1 m wind set-up event; (b) a 6 m significant wave height and 1.5 m wind set-up event

IV. Discussion

A. *In terms of peak velocity*

As, we are interested in the dike rear-side erosion, we used the relation (9) given by [6] to convert the water volume V into a peak velocity u_p:

$$u_p = 4.5V^{0.3} \quad (9)$$

The volume depends on the considered point onto the iso-discharge lines $\overline{\eta_t} = g(H)$. Indeed, the discharge is linked to the wave period which is linked to the significate wave height. Then, by considering parameters described in section III-B and eq. (9), mean water discharges of 0.01 and 0.2 $\mathrm{m^3/s/m}$ correspond to peak velocities of 2.1 and 5 $\mathrm{m/s}$.

By using results from TELEMAC-2D, peak velocities of 0.7 m/s and 2.6 m/s respectively were obtained on the dike rear-side.

Orders of magnitude seem to be respected but results from TELEMAC-2D present the advantage to take into account for the actual topography.

Depending on the soil characteristics, these peak velocities, corresponding to return periods of 100 and 1000 years, should generate erosion as we observed periodically breaches onto the Camargue sea-dike.

V. Conclusion and Perspectives

Wave parameters (local water level $\overline{\eta_t}$ and wave height H_m) were estimated at toe of dike for several initial parameters couples ($\overline{\eta_{wind}}, H_{m0}$) and their corresponding return periods.

Two methods were proposed to estimate the water discharge over the sea-dike and we found distributions of water discharges depending on initial parameters couples. We used it to compute cumulative probabilities associated to moderate (0.01 $\mathrm{m^3/s/m}$) and severe (2 $\mathrm{m^3/s/m}$) events. Return periods around 1.5 and 75 years respectively were found.

As, we were interested in the dike stability, water peak velocities on the dike rear-side were also estimated. For these kind of events, we retrieved that erosion may occur depending on the critical velocity of the dike soil composition.

In perspectives of this work, the use of TOMAWAC in two dimensions is expected to take into account effects of refraction and we will compare our results with the approach developed by [3].

Finally, for future works on Camargue sea-dike rear-side erosion, we will, particularly, pay attention to the peak water discharge which may be responsible for the erosion process beginning.

It remained important to improve our results precision to adapt the dike against extreme events.

Acknowledgement

We thank IGN and SHOM for Litto3D products localized in the study area. We thank also the SHOM for tide gauge data and EDF R&D LNHE for ANEMOC data.

References

[1] Salvatori, G., 2004. Bivariate return periods via 2-Copulas, Statistical Methodology, vol. 1, pp. 129-144.

[2] Brunner, M. I., Favre, A.-C., Seibert, J., 2016. Bivariate return periods and their importance for flood peak and volume estimation, WIREs Water, 3(6), pp. 819-833.

[3] Goda, Y., 1970. Numerical experiments on wave statistics with spectral simulation, Rep. Portand Harbour Res. Inst.

[4] EurOtop, 2018. Manual on wave overtopping of sea defences and related structures, Van der Meer, J.W., Allsop, N.W.H., Bruce, T., De Rouck, J., Kortenhaus, A., Pullen, T., Schüttrumpf, H., Troch, P. and Zanuttigh, B., www.overtopping-manual.com.

[5] Hughes, S.A., Nadal, N.C., 2009. Laboratory study of combined wave overtopping and storm surge overflow of a levee, Coastal Engineering 56, pp. 244–259.

[6] Van der Meer, J., van Hoven, A., Paulissen, A., Steendam, G., Verheij, H., Hoffmans, G., Kruse, G., 2012. Handreiking toetsen grasbekledingen op dijken t.b.v het opstellen van het beheerdersoordeel (bo) in de verlengde derde toetsronde. Tech. rep., Rifkswatershaat, Ministerie van Infrastructuur en Milieu.

[7] Muraleedharan, G., Guedes Soares, C., Lucas C., 2010. Characteristic and Moment Generating Functions of Generalised Extreme Value Distribution (GEV), Sea Level Rise, Coastal Eng., Shorelines and Tides, Chapter 13, Publisher: Nova Science Publishers, New York.

[8] Fouquet, T., 2016. Telemac Modeling System, Tomawac Software, Release 7.1, operating manual,

[9] Goda, Y. 2000. Random seas and design of maritime structures (2nd edition). World Scientific, Singapore, ISBN 981-02-3256-X.

[10] van der Meer, J.W., Janssen, W., 1995. Wave run-up and wave overtopping at dikes; In: Kabayashi, Demirbilek (Eds.), Wave Forces on Inclined and Vertical Wall Structures; American Society of Civil Engineers, pp. 1–27.

[11] Henderson, F.M., 1966. Open channel flow. MacMillian Publishing Co., New York

Modeling the world oceans with TELEMAC

T. Saillour, G. Cozzuto, F. Ligorio, G. Lupoi
Studio SPERI,
Rome, Italy

S.E. Bourban
EDF R&D LNHE / LHSV
Paris, France

***Abstract*—This paper presents the development and application of a highly detailed metocean model of the world oceans. Thanks to its adaptive resolution, the model is able to resolve the main ocean processes (tides, surges, tsunamis), using the TELEMAC suite [1][2], with an unrivalled level of spatial and temporal resolution at global, regional and local scale.**

I. THE SMARTWAVE PROJECT

The model of the oceans has been developed in the context of the SmartWave project, funded by Regione Sicilia. The SmartWave platform aims to support a broad range of activities linked to the Blue Economy. The platform refers to the most up-to-date metocean databases and assimilates them with state-of-the-art evolution models. Advanced analysis techniques are used to provide a new class of services to the actors of the sea. The metocean data on the SmartWave platform will be made available using different thematic layers. The quality of data is ensured by the quality of both the databases and the modelling tools. Input data are combined and completed by SmartWave models, allowing a timely and constant update of forecasts over the blue planet.

II. GLOBAL MODELLING

A. *Short literary review*

Constant advance in computational power and efficiency has enabled modelling of metocean processes at global scale with increasing accuracy and spatial/temporal resolution. While a full review of the state of the art global models is outside of the scope of this paper, a brief overview of some among the most established models is useful to set the context within which the development is happening and is therefore given in what follows.

- ERA5 [4] dataset by the European Centre for Medium-Range Weather Forecasts (ECMWF) is the fifth generation ECMWF reanalysis for the global climate and weather; it combines model data with observations from across the world into a globally complete and consistent dataset using the laws of physics; it provides metocean data over the entire globe at a spatial and temporal resolution of ~ 0.25° (~ 25km) and 1hrs, respectively for the atmosphere and ~ 0.5° (~ 50km) and 1hrs, respectively for the ocean waves;
- WaveWatch III [7] reanalysis is a thirty-year global wave hindcast generated from the NCEP Climate Forecast System Reanalysis and Reforecast (CFSRR) homogeneous dataset of hourly high-resolution winds. The time period covers from 1979 through 2009. The spatial resolution is 0.5° (~ 50km).
- CMEMS [8] reanalysis datasets. The Copernicus Marine Service provides various datasets; forecasts and hindcasts and information on waves or circulation parameters at a global and regional scale (Mediterranean and other seas around Europe). The global models deliver metocean data on a 0.083° (~ 9km) resolution grid with an hourly time step.

A case study of the world oceans has already been done [3] on a regular unstructured mesh using different components of the multipurpose finite element hydrodynamic suite TELEMAC [2]. This paper presents the preliminary results of a further improved global model of the Earth, using a further advanced mesh capable of resolving various physical processes.

III. A MODEL OF THE BLUE PLANET

A. *The world oceans as we know it*

Constant improvement of the bathymetric and atmospheric databases and increasing availability of field observations are improving the reliability of metocean evolution models at both regional and global scale.

Global bathymetric data sets include:

- GEBCO [10], General Bathymetric Chart of the Oceans, operates under the joint auspices of the International Hydrographic Organization (IHO) and the Intergovernmental Oceanographic Commission (IOC) (of UNESCO); it provides gridded bathymetry data which covers lands and oceans around the whole globe with a resolution of ~ 0.004° (~ 460m);
- EMODnet [11], European Marine Observation and Data Network; it provides bathymetry data which covers lands and oceans mainly around Europe and Northern Africa with a resolution of ~ 0.001° (~ 110m).
- SRTM [12], the Shuttle Radar Topography Mission is an international research effort. It provides terrestrial digital elevations models at a resolution of 1 arc-second (~30m) resolution.

As part of the SmartWave project, an assessment has been conducted of datasets around the world (including but not limited to the above) to create a bathymetric datasets that is "fit for purpose".

Similarly, datasets exist of forcing system, to include surface winds that are provided, among others, by:

- ERA5 [4] dataset, detailed in I.A above.

- CFSR [5] dataset, by National Centre for Atmospheric Research (NCAR) is a third generation reanalysis product; it is a global, high resolution, coupled atmosphere-ocean-land surface-sea ice system designed to provide the best estimate of the state of these coupled domains over this period.; it provides wind over the entire globe at a spatial and temporal resolution of ~ 0.25° (~ 25km) and 1hrs, respectively;
- GFS [6], the Global Forecast System is a National Centre for Environmental Prediction (NCEP) weather forecast model that generates data for dozens of atmospheric and land-soil variables; among which, the dataset provides wind, pressure and temperature over the entire globe at a spatial resolution of ~ 0.25° (~ 25km) and an hourly timestep from now to 16 days in the future, respectively;

These were assessed to identify the best database subset to be used to force the system for specific areas and period of time.

B. *Global unstructured meshes*

The need to resolve multiscale, multiphysics metocean processes points to the use of unstructured over structured meshes, which adapt to enable efficient modelling of the relevant processes: offshore deep ocean dynamics as well as coastal processes.

C. *Framework for modelling*

The triangle mesh has an adaptive resolution, an optimised procedure has been developed to size the mesh elements to effectively resolve the features of the bathymetry and the coastlines, this has allowed us to optimise the computation and reproduce the processes we are interested in, in the most efficient way.

As a certain range of different physical processes - tides, storm surges, waves, tsunamis or a combination of these – are modelled for the purpose of the SmartWave project, an unstructured mesh that would be able to resolve all of these processes is meant to be generated. Whilst higher resolution meshes have been created and are used in the SmartWave project, this paper presents the results of a 10 km mesh and give insights on the quality and the limits of this model resolution. This has been found to provide reliable boundary condition for use in higher definition regional meshes (discussed in the twin paper Cozzuto et al. 2021). The boundary conditions are critical for a good generation of a regional model, especially for those processes that evolve on a global scale, i.e. the tides.

The main focus in this paper will then be on the tides, since boundary condition for waves can be inferred from the world most renowned open databases [7].

Meshes with various resolutions have been generated for the purpose of the SmartWave project. The coarsest one (50km) was used for testing purposes, as its resolution was not sufficient to resolve coastal hydrodynamics.

TABLE 1 MESH SPECIFITIES DEPENDING ON THE TARGET RESOLUTION

Mesh target resolution	Number of triangles	Number of nodes
50 km	145,639	76,029
10 km	2,011,308	1,021,527
5 km	5,166,806	2,586,806
2 km	19,539,778	9,773,292

The more detailed meshes are better suited for the scope of project i.e. resolving deep ocean dynamics as well as coastal processes up to a resolution of a few kilometres close to the coastline. For the equivalent resolution, the unstructured meshes generated allow us to have 30 to 40 times less nodes compared to the regular triangles meshes presented in “The Earth by TELEMAC”.

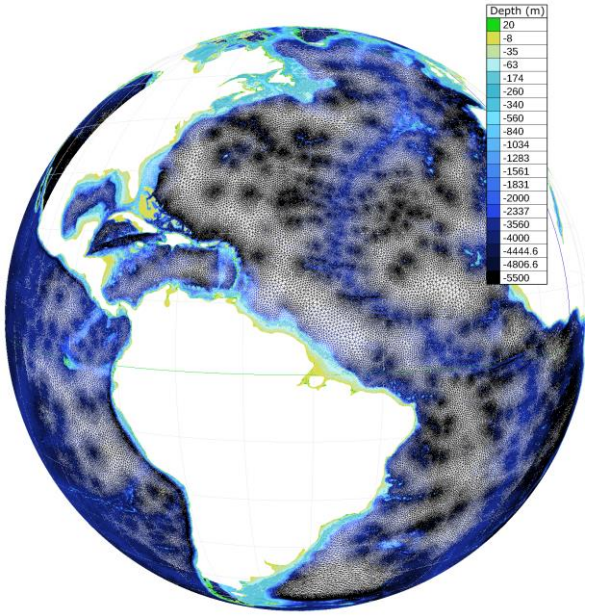

Figure 1. Mesh of the whole world. This version has a 10 km resolution at the coasts. Visualisation on BlueKenue

III. GLOBAL SCALE PROCESSES

A. *Tsunamis*

For the purpose of this paper, historical tsunamis have been modelled using the TELEMAC 2D model. This has been found to be adequate given the spatial and temporal scale of the events considered in this analysis (large seismic events generating transoceanic tsunamis), that are expected to be well represented by a model solving the non-linear shallow water equations. Given the seismic nature of the tsunami-genic events considered in this paper, the tsunami events have been initiated using the Okada model (Okada, 1985) which allows determining the initial free surface deformation resulting from a given seismic event.

B. *Tides*

Tides have been modelled cold-starting the model from a "still water condition" and applying gravitational forces only. Working with a global mesh defined in spherical coordinates has facilitated accounting for the Coriolis force.

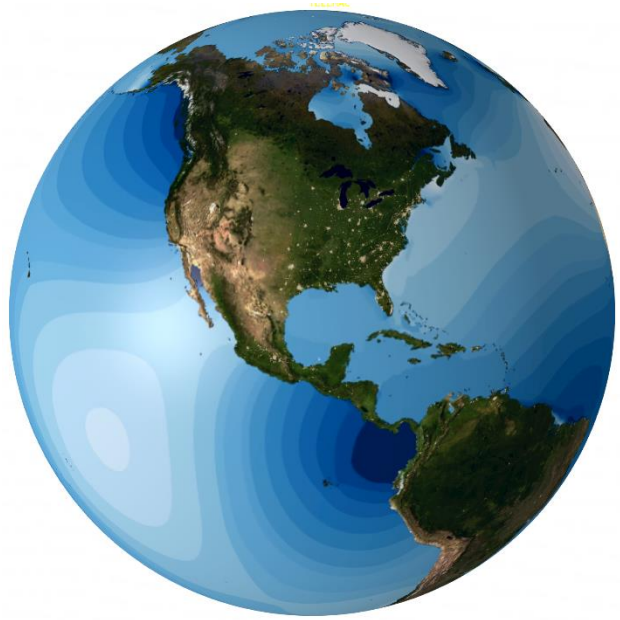

Figure 2. Representation of the global tides around the globe

IV. GLOBAL TSUNAMIS

Once the model had been created, a set of simulation were run of global tsunamis to validate the ability of the model to reproduce the propagation and transformation of very long waves over the world oceans.

- *Historical Tsunamis*

Some of the most known and research tsunamis of the history have been remodelled in order to assess the ability of the TELEMAC model to simulate the propagation of tsunamis (i.e. waves with important wavelengths).

TABLE 2 HISTORICAL TSUNAMIS USED TO VALIDATE THE MODEL

Tsunami location	a	Seismic magnitude
Lisbon, Portugal	1755	8.5-8.7
Kamtchatka, Russia	1952	9.0
Valvidia, Chile	1960	9.5
Prince William sound, Alaska, USA	1964	9.2

D. *Forcing the model*

Given the seismic nature of the tsunami-genic events considered here, these have been forced by imposing an initial free surface elevation derived using the model proposed by Okada [13]. This latter computes the deformation of the ground using the theory of elasticity in an idealized homogenous medium. The deformation of the free surface is obtained with an instantaneous translation of the ground distortion.

C. *Model validation*

To test the performances of the model, a qualitative comparison with the TTT (per Tsunami Travel Time) contour plots published by NOAA has been conducted for the tsunami events in Table 2.

Lisbon, Portugal, 1755

Model predictions of the evolution of the 1755 Lisbon tsunami at different times from its activation are compared in Figure 3 with the tsunami travel time maps published by [14] NOAA.

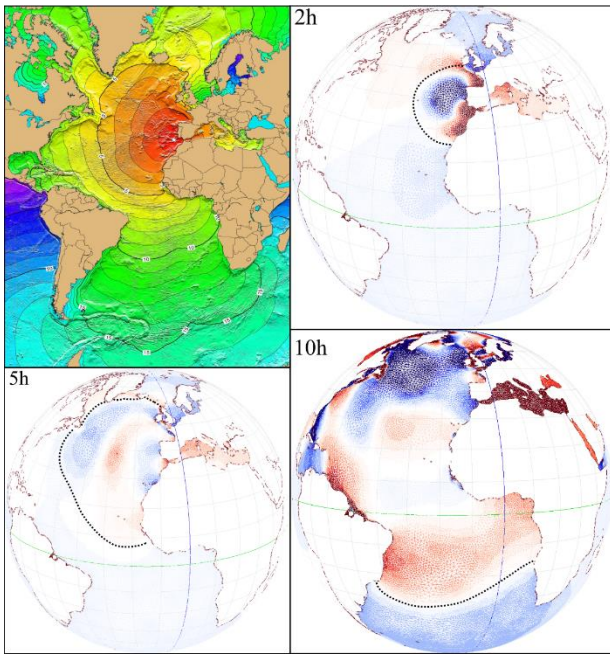

Figure 3. TTT maps from NOAA (top-left) and TELEMAC-2D results 2 hours (top-right), 5 hours (bottom-left) and 10 hours (bottom-right) after the seism for the tsunami of Lisbon, Portugal in 1755.

Kamtchatka, Russia, 1952

Model predictions of the evolution of the 1952 Kamtchatka tsunami at different times from its activation are compared in Figure 4 the tsunami travel time maps [14] generated by NOAA.

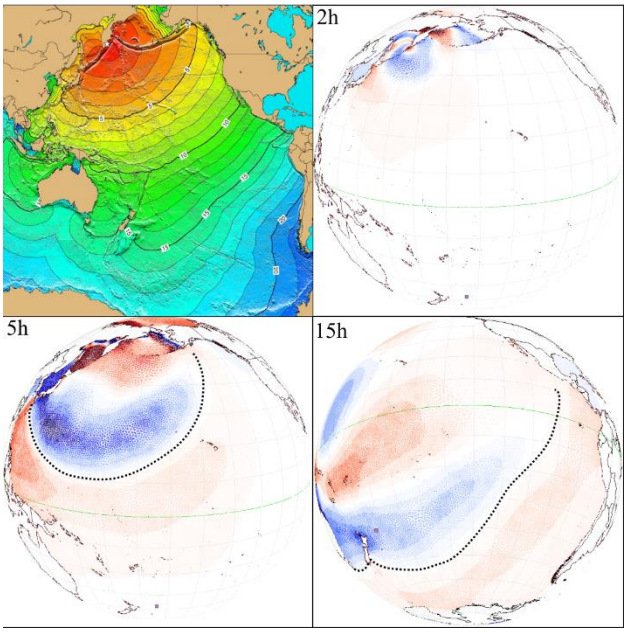

Figure 4. TTT maps from NOAA (top-left) and TELEMAC-2D results 2 hours (top-right), 5 hours (bottom-left) and 15 hours (bottom-right) after the seism for the tsunami of Kamtchatka, Russia in 1952.

Valvidia, Chile, 1960

Model predictions of the evolution of the 1960 Chilean tsunami at different times from its activation are compared in Figure 5 with the tsunami travel time maps published by the [14] generated by NOAA.

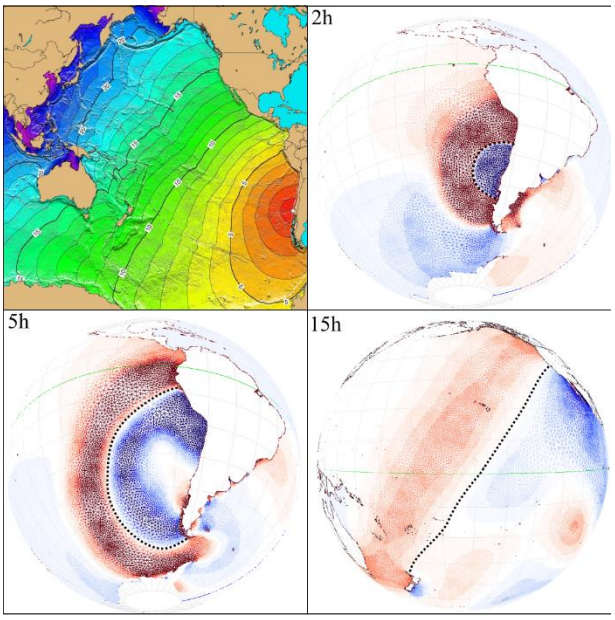

Figure 5. TTT maps from NOAA (top-left) and TELEMAC-2D results 2 hours (top-right), 5 hours (bottom-left) and 15 hours (bottom-right) after the seism for the tsunami of Valvidia, Chile in 1960.

Prince William sound, Alaska, USA, 1964

Model predictions of the evolution of the 1964 Alaska tsunami at different times from its activation are compared in Figure 6 with the tsunami travel time maps published by the [14] generated by NOAA.

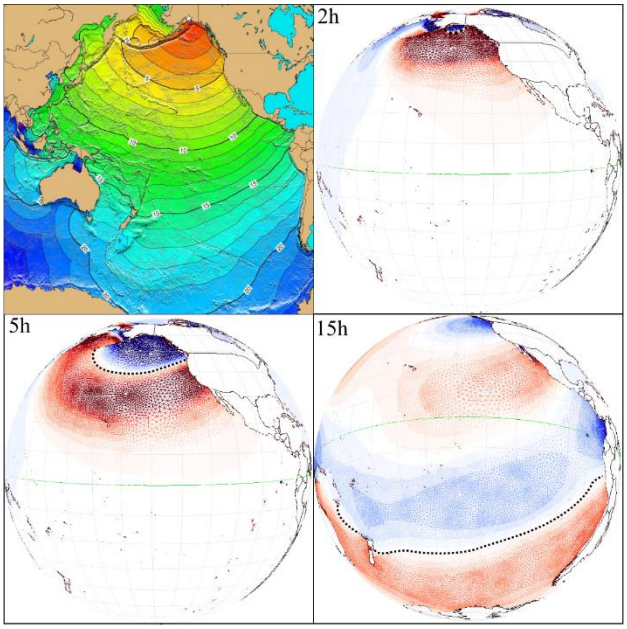

Figure 6. TTT maps from NOAA (top-left) and TELEMAC-2D results 2 hours (top-right), 5 hours (bottom-left) and 15 hours (bottom-right) after the seism for the tsunami of Prince William sound, Alaska, USA in 1964.

V. GLOBAL TIDES

A. *Tide forcing*

Since we are working with a global mesh, which is defined in spherical coordinates, the Coriolis force is automatically switched on. Global tides, were forced directly by imposing a gravitational field varying in time and space in a similar fashion to what done for “The Earth by TELEMAC”. Indeed, the TELEMAC code offers the particular feature to activate the known gravitational forces (from the relative rotations of the Sun, the Moon, the Earth and various corrections).

E. *Model validation using satellite data*

The results of the model were then compared to the TPXO model [9]. To validate the results from the global tidal model, more than 60 random points were taken into the ocean and the result of the TELEMAC-2D model (solid line) were compared to satellite observations (TPXO model, dashed line) respectively. Two comparisons are shown in the Figure 7 and Figure 8 and are represented by a yellow star in the Figure 9.

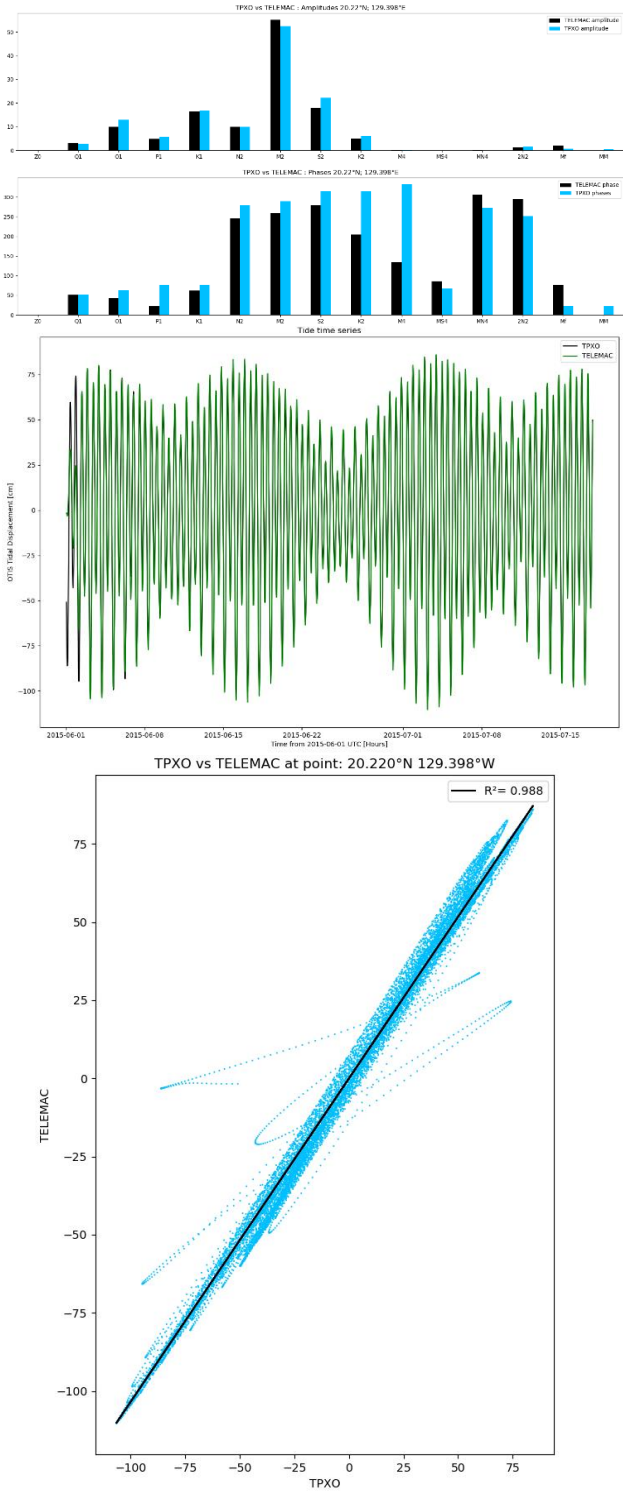

Figure 7. Harmonic (top) and temporal (middle) comparison between the TELEMAC results and the TPXO model at the latitudes and longitudes 20.22N, 129.398E respectively. The correlation between both signals is shown on the bottom graph.

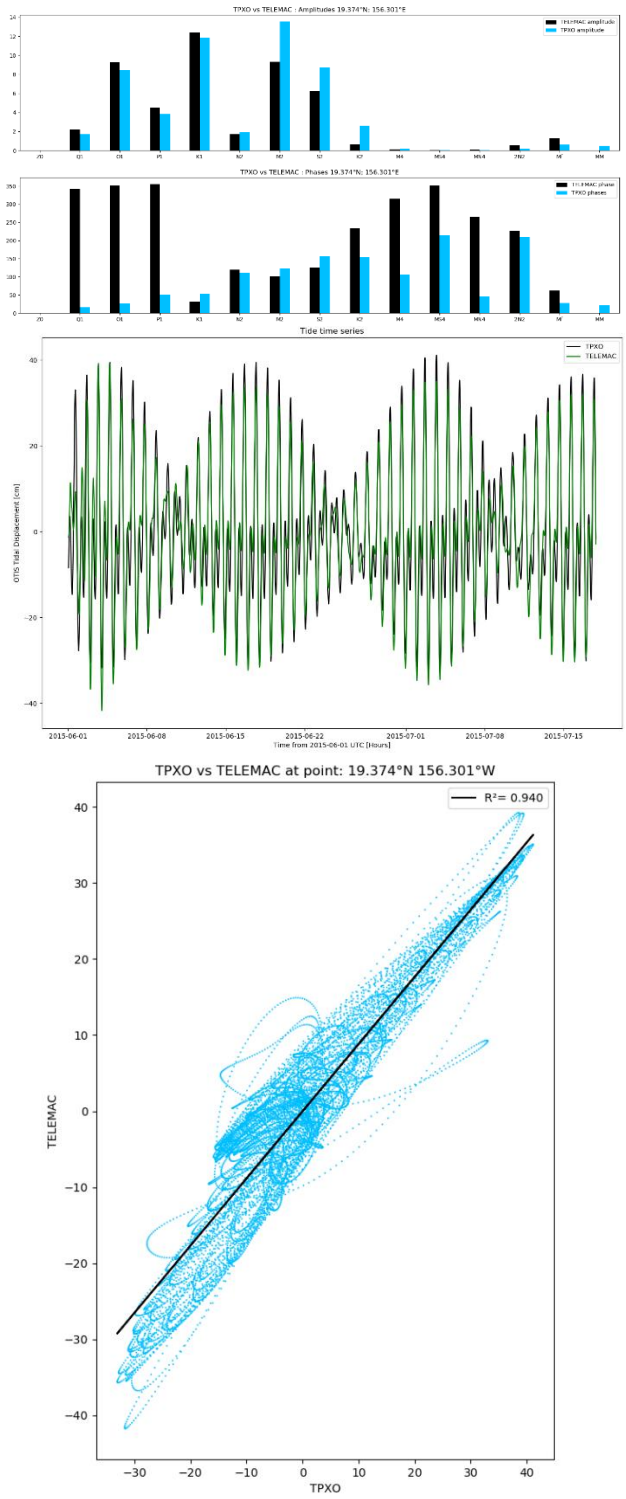

Figure 8. Harmonic (top) and temporal (middle) comparison between the TELEMAC results and the TPXO model at the latitudes and longitudes 19.374N, 156.301E respectively. The correlation between both signals is shown on the bottom graph.

The correlation between the TELEMAC results and the TPXO model has been calculated at all random locations mentioned above and represented in the map of Figure 9. Correlations at all locations has been identified with a colour from worst (red) to best (green) fitting.

The distribution of the correlation coefficients is represented in the histogram of Figure 9.

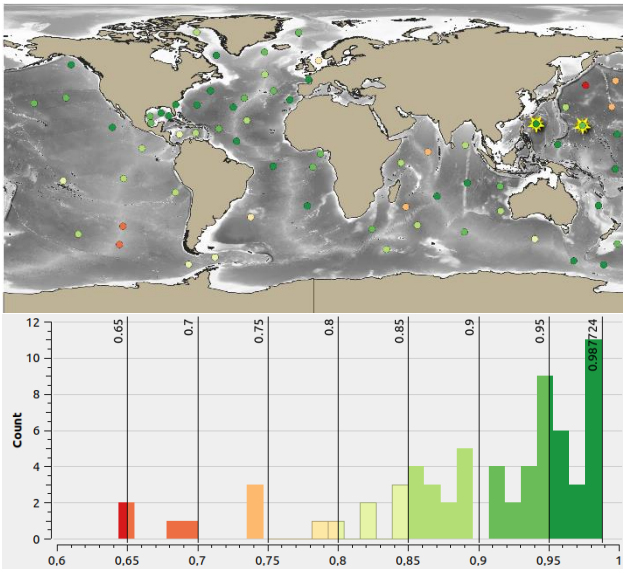

Figure 9. Localisation of the random points (top) taken for the comparison between the TELEMAC-2D model and the TPXO model and the distribution of all correlation values r^2 (bottom).

VI. INITIAL CONCLUSION AND ON-GOING WORK

Within the framework of the SmartWave project funded by Regione Sicilia, a global hydrodynamic model has been developed using TELEMAC which is capable of modelling the evolution of tsunamis and tides over the world oceans.

The model has been validated using both field observations and satellite data.

Whilst the system is capable of higher resolutions, all results presented in this paper have been obtained for demonstration purposes using a desktop machine and computational times shorter than 30 minutes.

At time of writing we are tackling the following challenges:

1) Higher resolution

Higher resolution inevitably implies more complex mesh that comport a higher number of elements and nodes. As the resolution increases, the time step decreases to respect of the CFL conditions. The processing power required for the computation thus increases.

Deep ocean dynamics

Internal tides is a specific type of internal waves that is critical to a number of offshore applications [3]. These waves are the result of a combination of a strong stratification and tides, and are not currently represented in any of the global models or datasets.

ACKNOWLEDGE

This research is being carried out as part of the SmartWave Project, funded by Regione Sicilia within the POR2014/20 EU framework.

REFERENCES

[1] Galland J.C., Goutal N., Hervouet J.M. (1991) – "TELEMAC: A new numerical model for solving shallow water equations", Advances in Water Resources, Volume 14, I. 3.

[2] JM Hervouet, R. Ata (2017). User manual of open software TELEMAC-2D, Report, EDF-R&D, http://www.opentelemac.org/, ISBN:9780470035580.

[3] Bourban, SE; Turnbull, MS; Cooper, AJ (2017): The Earth by TELEMAC. Proceedings of the XXIVth TELEMAC-MASCARET User Conference (Dorfmann, Clemens; Zenz, Gerald (Hg.)), 17 to 20 October 2017, Graz University of Technology, Austria. Graz University of Technology. S. 1-8.

[4] Hersbach, H. et al. (2020) The ERA5 global reanalysis. Q. J. R. Meteorol. Soc. 146, 1999–2049.

[5] E. Kalnay et al. (1996) The NCEP/NCAR 40-Year Reanalysis Project. Bulletin of the American Meteorological Society.

[6] National Centers for Environmental Prediction/National Weather Service/NOAA/U.S. Department of Commerce. 2015, updated daily. *NCEP GFS 0.25 Degree Global Forecast Grids Historical Archive*. Research Data Archive at the National Center for Atmospheric Research, Computational and Information Systems Laboratory. https://doi.org/10.5065/D65D8PWK. Accessed 20 mar 2021.

[7] Chawla, A., and H. L. Tolman, 2007: Automated grid generation for WAVEWATCH III. NOAA / NWS / NCEP / OMB Technical Note 254, 71 pp.

[8] F. Ardhuin et al. (2010) Semi empirical dissipation source functions for wind-wave models : Part I, definition and calibration and validation at global scales. Journal of Physical Oceanography.

[9] Egbert, Gary D., and Svetlana Y. Erofeeva. "Efficient inverse modeling of barotropic ocean tides." Journal of Atmospheric and Oceanic Technology 19.2 (2002): 183-204.

[10] GEBCO, "The General Bathymetric Chart of the Oceans, the most authoritative, publicly-available bathymetry data sets for the world's oceans", 2017, http://www.gebco.net/

[11] Martin Miguez, Belen & Novellino, A. & Vinci, Matteo & Claus, Simon & Calewaert et al. (2019). The European Marine Observation and Data Network (EMODnet): Visions and Roles of the Gateway to Marine Data in Europe. Frontiers in Marine Science. 6. 10.3389/fmars.2019.00313

[12] Farr, T. G. et al. (2007), The Shuttle Radar Topography Mission, Rev. Geophys., 45, RG2004, doi:10.1029/2005RG000183.

[13] Okada Y (1985) Surface deformation due to shear and tensile faults in a half-space. Bull Seismol Soc Am 75:1135–1154

[14] Shokin, et al. (1987). Calculations of tsunami travel time charts in the Pacific Ocean, Science of Tsunami Hazards, vol. 5, p. 85-113

[15] R. Ata, M. Le Gal and D. Violeau (2017). An overview on the capabilities of the TELEMAC-MASCARET system to deal with tsunamis: feedbacks from TANDEM project. Proceedings of the XXIVth TELEMAC-MASCARET User Conference (Dorfmann, Clemens; Zenz, Gerald (Hg.)), 17 to 20 October 2017, Graz University of Technology, Austria. Graz University of Technology. S. 1-8.

Metocean regional models using TELEMAC

G. Cozzuto, T. Saillour, F. Ligorio, G. Lupoi
Studio SPERI,
Rome, Italy

S.E. Bourban
EDF R&D LNHE / LHSV
Paris, France

***Abstract*—Metocean regional models of the Mediterranean Sea, the Gulf of Mexico and the Persian Gulf have been developed as part of the SmartWave project, funded by Regione Sicilia. The models, which use state of the art, multipurpose finite element hydrodynamic model TELEMAC [1][2] allow generation of metocean information with an unrivalled level of spatial and temporal resolution, enabling accurate determination of metocean climate at both regional and local scale.**

I. THE SMARTWAVE PROJECT

Sustainable development is the strength of the Blue Economy: it drives opportunities and pushes funds to invest in social and financial growth as well as productive activities on a global scale. All this translates into the need to use state-of-the-art tools and up-to-date, reliable and high-resolution data. In this context, the SmartWave project, funded by Regione Sicilia, has developed an advanced modelling framework to provide decision-makers with reliable and accessible management tools.

The tools available in SmartWave are developed as part of the technological chain that supports the planning and management of Blue Economy's most important sectors' needs, such as: management, protection and development of the marine environment; products and services for maritime, coastal and offshore engineering; risk assessment, management and mitigation; renewable marine energies and site prospections; logistics and transportation; fisheries and recreational activities.

This paper presents metocean regional models of the Mediterranean Sea, the Gulf of Mexico and the Persian Gulf developed as part of the SmartWave project. The models are described in Section II and the mesh set-up illustrated in Section III. Model predictions have been calibrated and validated using extensive datasets of direct (field) and indirect (satellite) measurements and compared with predictions by a selection of some among most established global and regional models.

II. REGIONAL AND GLOBAL MODELLING

A. General overview

Constant advance in computational power and efficiency has enabled modelling of metocean processes at global scale with increasing accuracy and spatial/temporal resolution. While a full review of the state-of-the-art global models is outside of the scope of this paper, a brief overview of some among the most established models is useful to set the context within which the development is happening and is therefore given in what follows.

B. Climate models

For what concerns metocean data, a wide set of databases, catalogues and models are developed by international institutions and organizations that provide metocean climate information at both a global and regional scale. The following list shows a selection of these datasets (not exhaustive); it includes:

- ERA5 [4] dataset by the European Centre for Medium-Range Weather Forecasts (ECMWF) is the fifth generation ECMWF reanalysis for the global climate and weather; it combines model data with observations from across the world into a globally complete and consistent dataset using the laws of physics; it provides wind over the entire globe at a spatial and temporal resolution of ~ 0.25° (~ 25km) and 1hrs, respectively;
- CFSR [5] by National Center for Atmospheric Research (NCAR) is a third generation reanalysis product; it is a global, high resolution, coupled atmosphere-ocean-land surface-sea ice system designed to provide the best estimate of the state of these coupled domains over this period.; it provides wind over the entire globe at a spatial and temporal resolution of ~ 0.25° (~ 25km) and 1hrs, respectively;
- COSMO [6] by the German Meteorological Service (DWD) is a high-resolution reanalysis system based on the NWP model COSMO; it provides wind over European regions at spatial and temporal resolution of ~ 0.055° (~ 6km) and 15min for 2d field data, respectively;
- TPXO [7] by Oregon State University (CEOAS) is a global, regional and local model of barotropic tide, obtained with the software package OTIS (OSU Tidal Inversion Software); it provides complex amplitudes of MSL-relative sea-surface elevations and transports/currents for eight primary (M2, S2, N2, K2, K1, O1, P1, Q1), two long period (Mf, Mm) and 3 non-linear (M4, MS4, MN4) harmonic constituents (plus 2N2 and S1 for TPXO9 only).

C. Bathymetric data

Global and regional topo-bathymetric databases mapping the bottom of the oceans and the orography of lands are made available by national and international institutions and organizations. The following list shows a selection of these databases (not exhaustive); it includes:

- GEBCO [8], General Bathymetric Chart of the Oceans, operates under the joint auspices of the International Hydrographic Organization (IHO) and the

Intergovernmental Oceanographic Commission (IOC) (of UNESCO); it provides gridded bathymetry data which covers lands and oceans around the whole globe with a resolution of ~ 0.004° (~ 460m);

- EMODnet [9], European Marine Observation and Data Network; it provides bathymetry data which covers lands and oceans mainly around Europe and Northern Africa with a resolution of ~ 0.001° (~ 110m).

III. METOCEAN PREDICTION MODELS

Three different metocean regional models (Figure 1, Figure 2 and Figure 3) have been developed to simulate wave climate of the Mediterranean Sea, the Gulf of Mexico and the Persian Gulf. The models use state of the art, multipurpose hydrodynamic modelling suite TELEMAC [1][2] (including TOMAWAC and TELEMAC2D), which is capable of resolving various metocean processes at different scales [3].

Figure 1. Meshing of the regional model of the Mediterranean Sea.

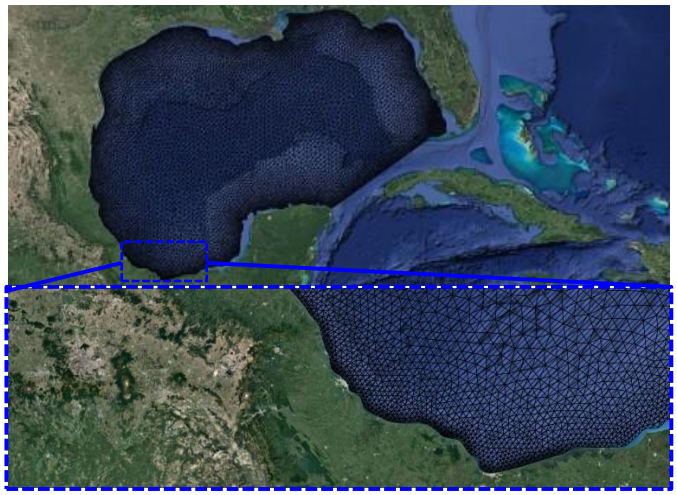

Figure 2. Meshing of the regional model of the Gulf of Mexico.

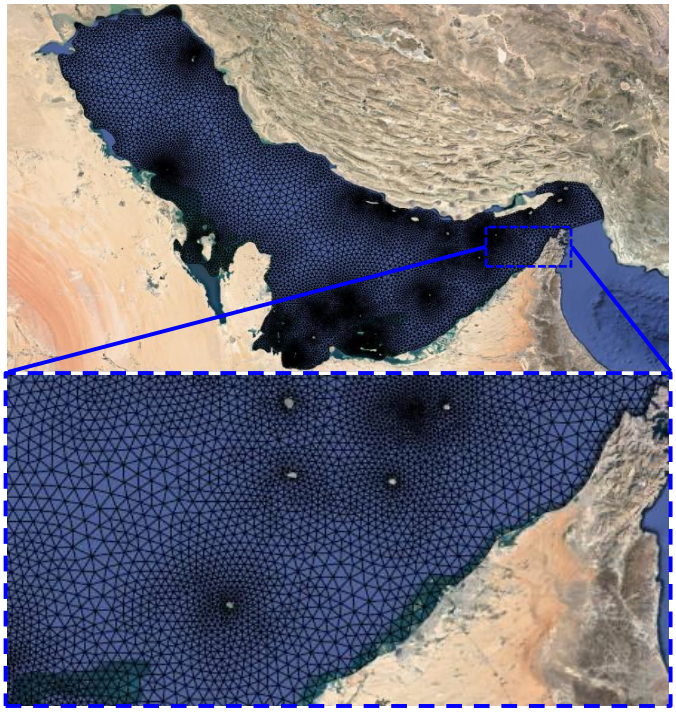

Figure 3. Meshing of the regional model of the Persian Gulf.

IV. MODEL SET-UP

A. *Atmospheric forcing*

Sensitivities have been performed with respect to model setup and input parameters to determine an optimum model set-up for use in both hindcasting and forecasting mode. The use of different atmospheric data to force the model has been assessed to determine the best performing setup.

B. *Bathymetric features*

A good compromise has to be made between the accuracy of the model and its efficiency. The size of the elements has been determined by means of a set of functions inferred, among other parameters, from the local value of the bathymetry and the distance from the shore. The bathymetric input data adopted for the numerical models have been derived from the most up-to-date and informative databases available.

C. *Meshing*

As a certain range of different physical processes like waves are modelled for the purpose of the project, an unstructured mesh that would be able to resolve all of these processes was generated. The triangle mesh has an adaptive resolution, and the size of the triangles depends on the features of the bathymetry and the coastlines.

The modelling of wave transformation processes and of water level fluctuations has been carried out on the meshes of the Mediterranean Sea, Gulf of Mexico and Persian Gulf, presented in Figure 2 and Figure 3, respectively.

V. CASE STUDIES

Numerical simulations have been performed to prove the capability of the SmartWave framework to derive metocean parameters to serve the Blue Economy sectors in different regions of the world.

A. *Mediterranean Sea*

In order to calibrate and validate the capability of the framework to predict wave and tide of the Mediterranean Sea, waves and tides measurements from the directional wave buoy networks of Italy RON and levels stations RMN, managed by ISPRA, and wave data from CANDHIS network, managed by the French Centre d'Archivage National de Données de Houle In-Situ, have been used (Figure 4).

An example comparison with measurements is shown for the period from January 2013 to May 2013. The model has been forced with different wind input (i.e. ERA5 and COSMO) and the results presented in this paper are those obtained using the best performing. Wave results are plotted against in-situ field data (from Figure 5 to Figure 8). To provide a quantitative assessment of the performance of the model, the correlation coefficient (R) is also presented in each figure. Results have been produced at a higher time resolution (30min) and show that the model compares well when predicting the wave field.

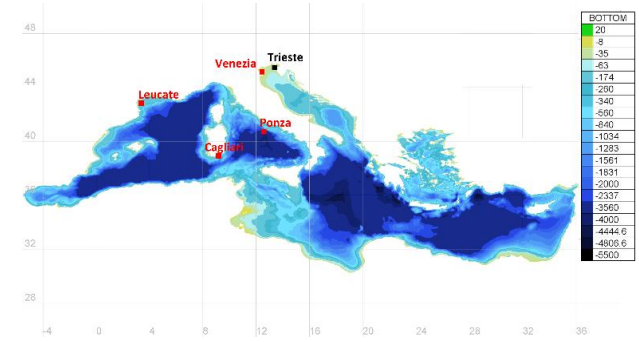

Figure 4. ISPRA RON and RMN stations adopted to calibrate and validate the numerical model (wave buoys and water level stations in red points and black points, respectively). Colour contours show bathymetric data of the Mediterranean Sea.

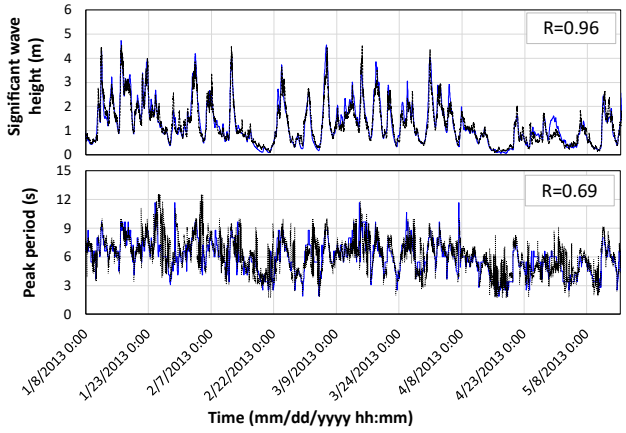

Figure 5. Ponza RON buoy measurements (black dots) plotted against model results. Top panel: wave height plot. Bottom panel: wave period plot.

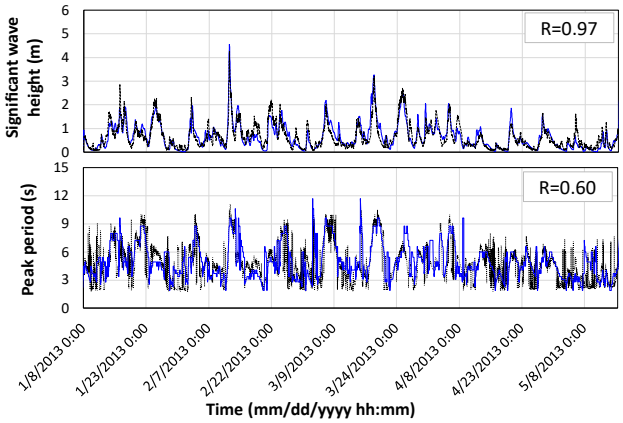

Figure 6. Venezia RON buoy measurements (black dots) plotted against model results. Top panel: wave height plot. Bottom panel: wave period plot.

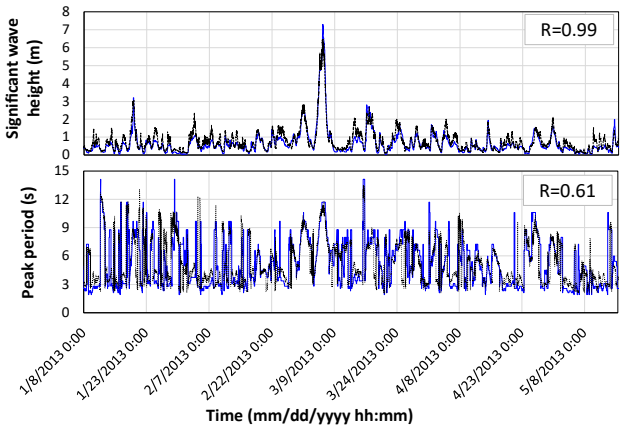

Figure 7. Leucate CANDHIS buoy measurements (black dots) plotted against model results. Top panel: wave height plot. Bottom panel: wave period plot.

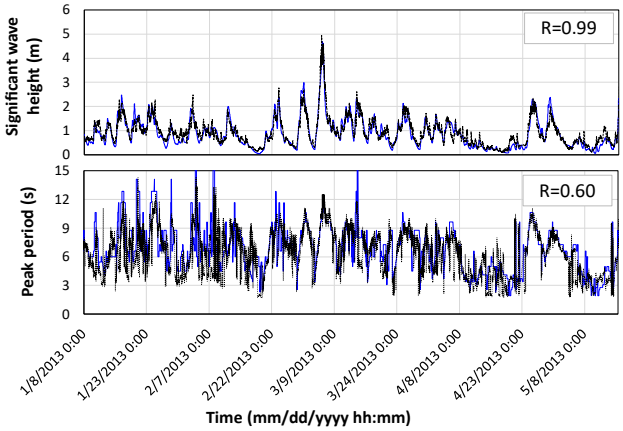

Figure 8. Cagliari RON buoy measurements (black dots) plotted against model results. Top panel: wave height plot. Bottom panel: wave period plot.

Results of the water levels modelling at selected points along the coast (Figure 4) are shown in Figure 9 and Figure 10. Plots illustrate tide-and-wind-induced results in terms of water level fluctuations obtained using a mesh resolution of 5km at the coastline. For the Mediterranean Sea, predictions are less satisfactory, probably due to the fact that the tide regime within the gulf is driven by the interaction with the

Atlantic Ocean, which requires a larger scale model (see twin paper by Saillour et al. 2021).

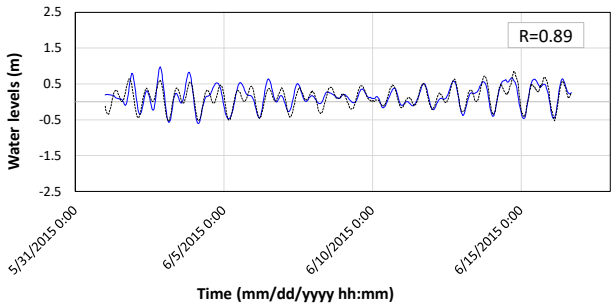

Figure 9. RMN station measurements in Venezia (black dotted line) plotted against model results (blue line).

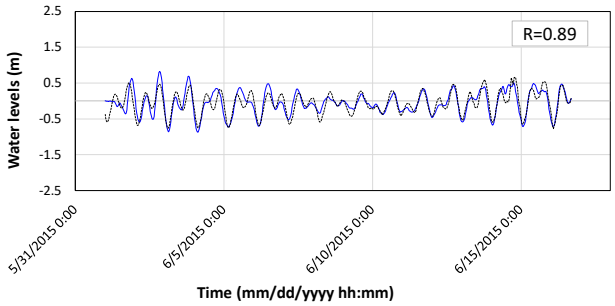

Figure 10. RMN station measurements in Trieste (black dotted line) plotted against model results (blue line).

B. *Gulf of Mexico*

In order to calibrate and validate both the wave and tide model of the Gulf of Mexico, waves measurements from the American network "National Data Buoy Center (NDBC)" and "Tides and Currents" managed by the National Oceanic and Atmospheric Administration (NOAA) have been used, respectively (Figure 11).

An example comparison with measurements is shown for the period from November 2015 to May 2016. The model has been forced with different wind input (i.e. ERA5 and CFSR) and the results presented here correspond to the best performing setup. Wave results are plotted against in-situ data (from Figure 12 to Figure 15) and the correlation coefficient R given.

Results of the water levels modelling at selected points along the coast (Figure 11) are shown in Figure 16 and Figure 17. Plots illustrate tide-and-wind-induced results in terms of water level fluctuations obtained using a mesh resolution of 5km at the coastline. For the Gulf of Mexico, predictions are less satisfactory, probably due to the fact that the tide regime within the gulf is driven by the interaction with the Atlantic Ocean.

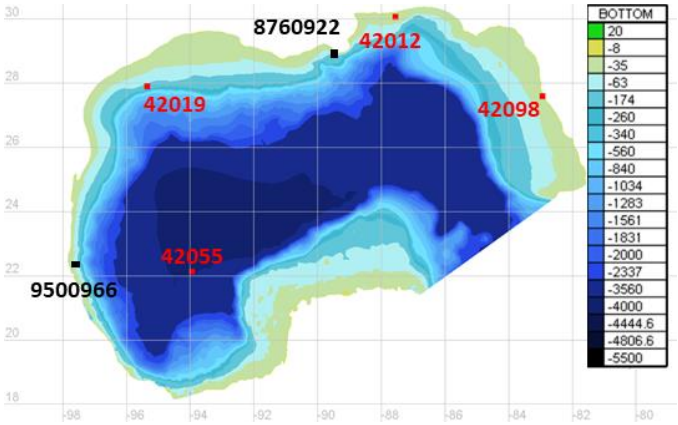

Figure 11. NOAA NDBC buoys adopted to calibrate and validate the numerical model (wave buoys and water level stations in red points and black points, respectively). Colour contours show bathymetric data of the Gulf of Mexico.

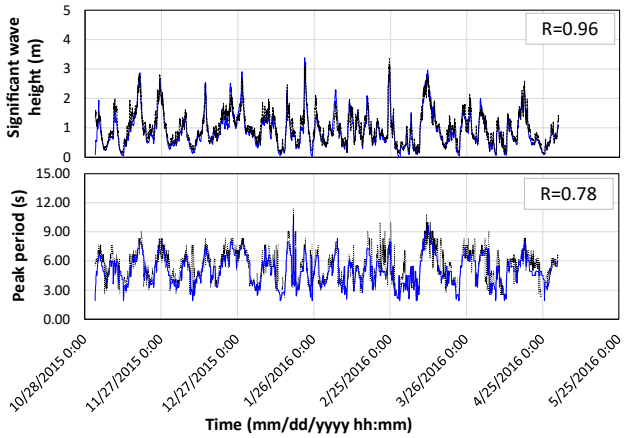

Figure 12. NDBC buoy 42012 measurements (black dots) plotted against model results. Top panel: wave height plot. Bottom panel: wave period plot.

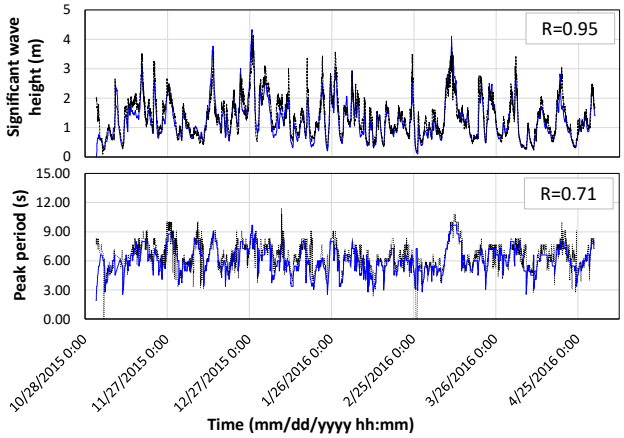

Figure 13. NDBC buoy 42019 measurements (black dots) plotted against model results. Top panel: wave height plot. Bottom panel: wave period plot.

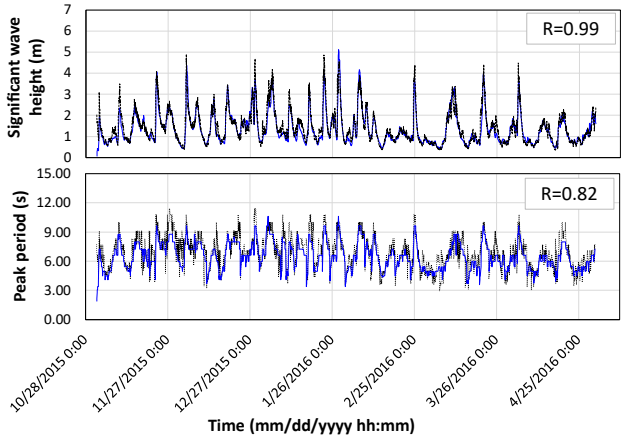

Figure 14. NDBC buoy 42055 measurements (black dots) plotted against model results. Top panel: wave height plot. Bottom panel: wave period plot.

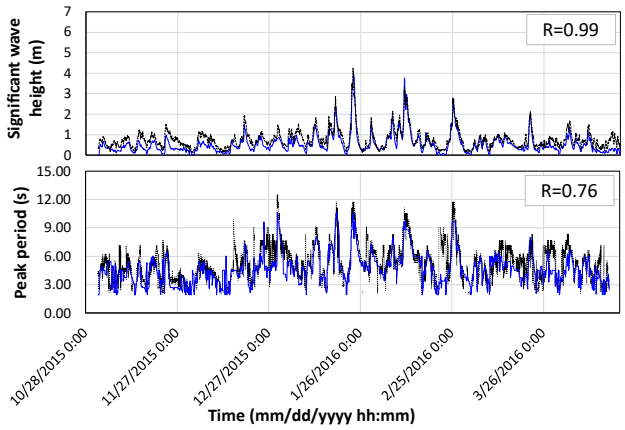

Figure 15. NDBC buoy 42098 measurements (black dots) plotted against model results. Top panel: wave height plot. Bottom panel: wave period plot.

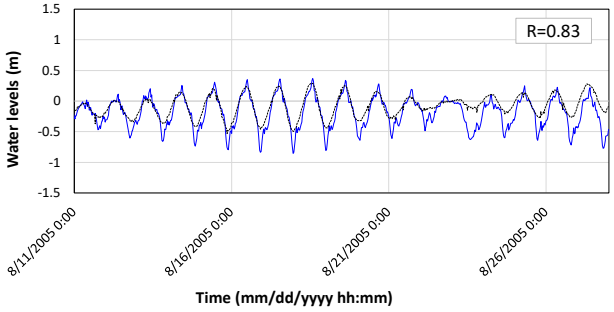

Figure 16. NDBC station 8760922 measurements (black dotted line) plotted against model results (blue line).

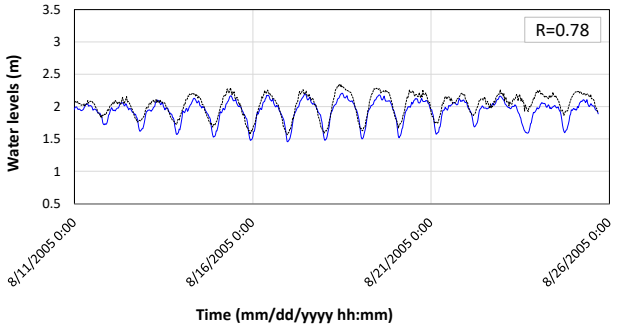

Figure 17. NDBC station 9500966 measurements (black dotted line) plotted against model results (blue line).

C. Persian Gulf

In order to calibrate and validate the wave model of the Persian Gulf, waves from the European reanalysis of historical data ERA5 have been used (Figure 18).

An example comparison with measurements is shown for the period from November 2015 to May 2016. The model has been forced with different wind input (i.e. ERA5 and CFSR) and the results presented here correspond to the best performing setup. Wave results are plotted against historical data (from Figure 19 to Figure 22) and the correlation coefficient R is given.

Results of the water levels modelling at selected points along the coast (Figure 18) are shown in Figure 23 and in Figure 24. Plots illustrate tide-and-wind-induced results in terms of water level fluctuations obtained using a mesh resolution of 5km at the coastline. For the Persian Gulf, model compares well with TPXO data for which the boundary is relatively neatly defined.

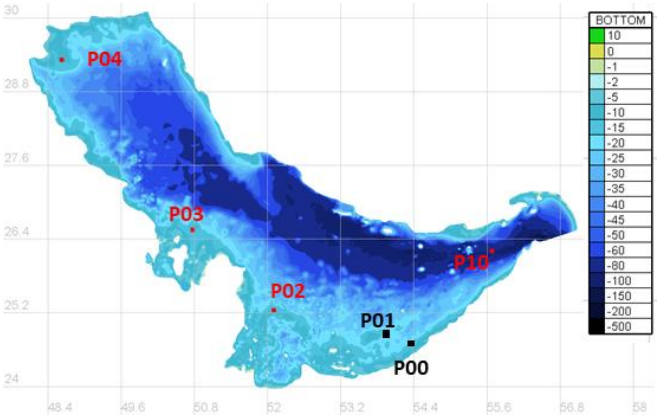

Figure 18. Numerical buoys adopted to calibrate and validate the numerical model (wave buoys and water level stations in red points and black points, respectively). Colour contours show bathymetric data of the Persian Gulf.

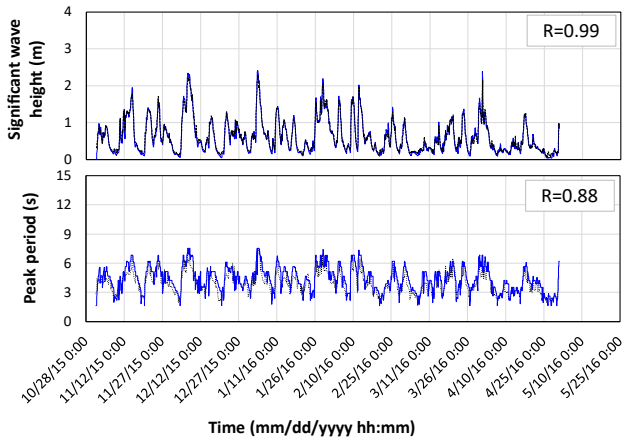

Figure 19. Virtual buoy P02 data (black dots) plotted against model results. Top panel: wave height plot. Bottom panel: wave period plot.

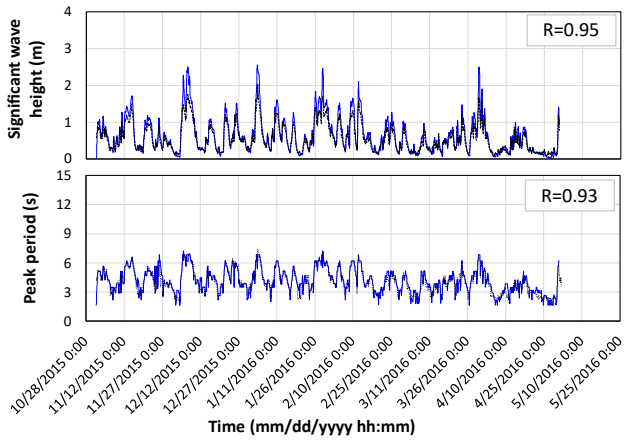

Figure 20. Virtual buoy P03 data (black dots) plotted against model results. Top panel: wave height plot. Bottom panel: wave period plot.

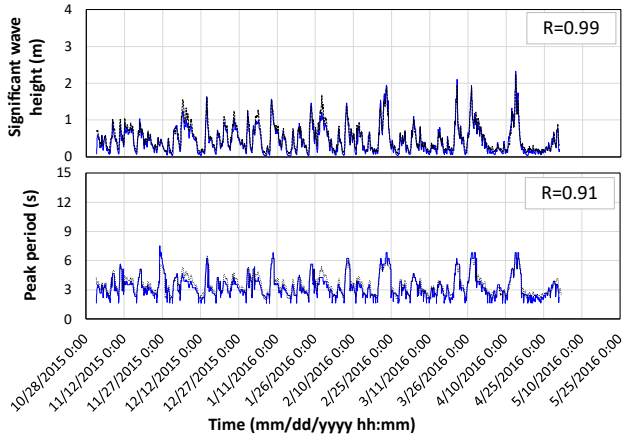

Figure 21. Virtual buoy P04 data (black dots) plotted against model results. Top panel: wave height plot. Bottom panel: wave period plot.

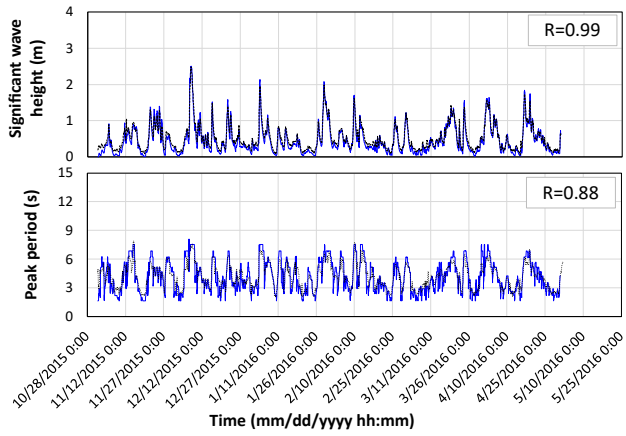

Figure 22. Virtual buoy P10 data (black dots) plotted against model results. Top panel: wave height plot. Bottom panel: wave period plot.

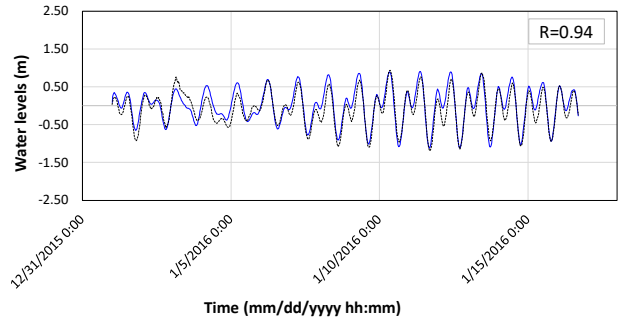

Figure 23. P00 station data (black dotted line) plotted against model results (blue line).

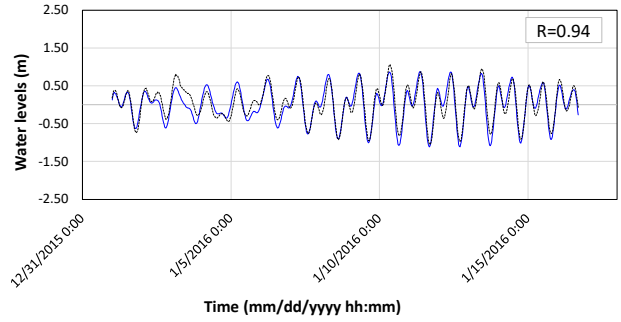

Figure 24. P01 station data (black dotted line) plotted against model results (blue line).

VI. CONCLUSIONS AND ON-GOING WORK

The model has been proved to provide robust predictions of wind waves regimes in three different regions of the world. The model has also highlighted the limitation of using regional models for predicting tide fluctuations which requires the use of a global evolution model, as the processes involved evolve on a global scale (see twin paper by Saillour et al. 2021).

ACKNOWLEDGEMENTS

This research is being carried out as part of the SmartWave Project, funded by Regione Sicilia within the POR2014/20 EU framework.

REFERENCES

[1] Galland J.C., Goutal N., Hervouet J.M. (1991) – "TELEMAC: A new numerical model for solving shallow water equations", Advances in Water Resources, Volume 14, I. 3.

[2] JM Hervouet, R. Ata (2017). User manual of open software TELEMAC-2D, Report, EDF-R&D, http://www.opentelemac.org/, ISBN:9780470035580.

[3] Bourban, SE; Turnbull, MS; Cooper, AJ (2017): The Earth by TELEMAC. Proceedings of the XXIVth TELEMAC-MASCARET User Conference (Dorfmann, Clemens; Zenz, Gerald (Hg.)), 17 to 20 October 2017, Graz University of Technology, Austria. Graz University of Technology. S. 1-8.

[4] Hersbach, H. et al. (2020) The ERA5 global reanalysis. Q. J. R. Meteorol. Soc. 146, 1999–2049.

[5] E. Kalnay, M. Kanamitsu, R. Kistler, W. Collins, D. Deaven, L. Gandin, M. Iredell, S. Saha, G. White, J. Woollen, Y. Zhu, A. Leetmaa, R. Reynolds. The NCEP/NCAR 40-Year Reanalysis Project. Bulletin of the American Meteorological Society. March 1996.

[6] Bollmeyer, C., J. D. Keller, C. Ohlwein, S. Bentzien, S. Crewell, P. Friederichs, A. Hense, J. Keune, S. Kneifel, I. Pscheidt, S. Redl, S. Steinke (2015): Towards a high-resolution regional reanalysis for the European CORDEX domain, Q. J. Royal Met. Soc., 141 (686), 1-15.

[7] Egbert, Gary D., and Svetlana Y. Erofeeva. "Efficient inverse modeling of barotropic ocean tides." Journal of Atmospheric and Oceanic Technology 19.2 (2002): 183-204.

[8] GEBCO, "The General Bathymetric Chart of the Oceans, the most authoritative, publicly-available bathymetry data sets for the world's oceans", 2017, http://www.gebco.net/

[9] Martin Miguez, Belen & Novellino, A. & Vinci, Matteo & Claus, Simon & Calewaert et al. (2019). The European Marine Observation and Data Network (EMODnet): Visions and Roles of the Gateway to Marine Data in Europe. Frontiers in Marine Science. 6. 10.3389/fmars.2019.00313.

Hydrodynamics and Hydrology

Validation and Improvement of Data Assimilation for Flood Hydrodynamic Modelling Using SAR Imagery Data

Thanh Huy Nguyen[1], Anthéa Delmotte[1], Christophe Fatras[2], Peter Kettig[3], Andrea Piacentini[1], and Sophie Ricci[1]

[1] CECI, CERFACS/CNRS UMR 5318, Toulouse, France
[2] Collecte Localisation Satellites (CLS), Toulouse, France
[3] Centre National d'Etudes Spatiales (CNES), Toulouse, France

Corresponding author: thnguyen@cerfacs.fr

***Abstract*—Relevant comprehension of flood hazards has emerged as a crucial necessity, especially as the severity and the occurrence of flood events may intensify with climate changes. Flood simulation and forecast capability have been greatly improved thanks to advances in data assimilation. This approach combines in-situ gauge measurements with hydrodynamic models, which aims at correcting the hydraulic states and reducing the uncertainties in the model parameters, e.g., friction coefficients, inflow discharge. These methods depend strongly on the availability and quality of observations, thus requiring other data sources to improve the flood simulation and forecast quality. Sentinel-1 images collected during a flood event were used to classify an observed scene into dry and wet areas. The study area concerns the Garonne Marmandaise catchment, and focuses on the recent flood event in January-February 2021. In this paper, seven experiments are carried out, two in free run modes (FR1 and FR2) and five in data assimilation modes (DA1 to DA5). A model-observation bias was diagnosed and corrected over the beginning of the flood event. Quantitative assessments are carried out involving 1D metrics at Vigicrue observing stations and 2D metrics with respect to the Sentinel-1 derived flood extent maps. They demonstrate improvements on flood extent representation thanks to the data assimilation and bias correction.**

I. Introduction

Simulations based on hydrodynamic numerical models in analysis and forecast modes are crucial to mitigate flood impacts. The analysis mode could be carried out to obtain better estimates of the dynamic footprints of past flood events, as well as to assess flood damages and design future flood defense systems, whereas the forecast mode is used by civil security services and industry. However, these numerical models remain imperfect because the uncertainties inherently existing within the models and the inputs, e.g., friction and boundary conditions, seemingly translate into uncertainties in the model outputs. A well-established method for reducing uncertainties and generating more reliable predictions is to periodically adjust these models, for instance, by assimilating various observations as they become available [1].

Indeed, flood simulation and forecast capability have been greatly improved thanks to the advances in data assimilation (DA). Such methods, notably Ensemble Kalman Filter (EnKF), aim at combining in-situ gauge measurements with numerical models to correct the hydraulic states and reduce the uncertainties in the model parameters (e.g., friction coefficients, upstream inflow). These filters rely on the stochastic computation of the forecast error covariance matrix, within a limited number of simulations. The sources of uncertainty, represented by the control vector, is updated over each assimilation window. Nevertheless, this approach depends strongly on the availability and quality of observations, as its performance relies on the spatial and temporal density of the observing network [2]. As a matter of fact, limnimetric in-situ observations providing water levels are only available at a few sparse locations along a river catchment, due to installation and maintenance costs [3]. This is a limiting factor for numerical model precision in simulation and forecast, especially in the floodplains. Such a situation requires efforts to leverage other sources of data such as remote sensing-derived flood maps to validate and improve the flood simulation and forecasting performance. In this work, we carry out the flood extent mapping by applying a Random Forest (RF) segmentation on Synthetic Aperture Radar (SAR) images such as Sentinel-1 (S1) [4]. The inferred flood extent maps are then compared with the flood extents simulated by TELEMAC-2D with EnKF assimilation.

This work highlights the merits of using SAR-derived flood extent maps to validate and improve the simulation results based on hydrodynamic numerical models with EnKF DA. It illustrates how SAR imagery data could be used to overcome the limits of the calibration and validation process which was done using river-gauge data only. For instance, a bias between the models and in-situ observations has been identified and corrected, yielding better flood extent representation. Quantitative performance assessments are carried out by comparing the simulated and observed water level time-series at several in-situ gauge locations, as well as involving Critical Success Index measured between the simulated flood extent maps and the SAR-derived maps. They underline the benefits of using spatially distributed remote sensing data that inform on the floodplain dynamics.

II. Study Area, Data, Model

Hydrodynamic numerical models, such as TELEMAC-2D (www.opentelemac.org), are used to simulate and predict water surface elevation and velocity from which the flood risk can be assessed for lead times ranging from a couple of hours to several days. TELEMAC-2D solves the Shallow Water Equations (SWE) with an explicit first-order time integration scheme, a finite element scheme and an iterative conjugate gradient method [5]. At each point within the mesh representing the model topography and bathymetry (for mesh nodes in the river channel), the results of the simulation are water depth and velocity averaged over the azimuth axis.

A. Shallow Water Equations (SWEs) in TELEMAC-2D

The non-conservative form of SWEs is written in terms of water depth (h [m], also called water level) and horizontal components of velocity (u and v [m.s^{-1}]). They express mass and momentum conservation averaged in the vertical dimension while assuming that:

- The horizontal length scale is significantly greater than the vertical scale;
- Vertical pressure gradients are hydrostatic;
- Horizontal pressure gradients are due to the displacement of the free surface.

As such, using similar mathematic notations to [6], the SWEs read:

$$\frac{\partial h}{\partial t}+\frac{\partial}{\partial x}(hu)+\frac{\partial}{\partial y}(hv)=0 \quad (1)$$

$$\frac{\partial u}{\partial t}+u\frac{\partial u}{\partial x}+v\frac{\partial u}{\partial y}=-g\frac{\partial z}{\partial x}+F_x+\frac{1}{h}div\left(hv_e\,\overrightarrow{grad}(u)\right) \quad (2)$$

$$\frac{\partial v}{\partial t}+u\frac{\partial v}{\partial x}+v\frac{\partial v}{\partial y}=-g\frac{\partial z}{\partial y}+F_y+\frac{1}{h}div\left(hv_e\,\overrightarrow{grad}(v)\right) \quad (3)$$

where z [m NGF69] is the water surface elevation ($h = z - z_b$ with z_b [m NGF69] being the bottom elevation) and v_e [m^2.s^{-1}] is the water diffusion coefficient. g [m.s^{-2}] is the gravitational acceleration constant. div and $\overrightarrow{grad}$ are respectively the divergence and gradient operators. F_x and F_y [m.s^{-2}] are the horizontal components of external forces (friction, wind and atmospheric forces), defined as follows:

$$\begin{cases} F_x = -\dfrac{g}{K_s^2}\dfrac{u\sqrt{u^2+v^2}}{h^{4/3}}-\dfrac{1}{\rho_w}\dfrac{\partial P_{atm}}{\partial x} \\ \qquad +\dfrac{1}{h}\dfrac{\rho_{air}}{\rho_w}C_D U_{w,x}\sqrt{U_{w,x}^2+U_{w,y}^2} \\ F_y = -\dfrac{g}{K_s^2}\dfrac{v\sqrt{u^2+v^2}}{h^{4/3}}-\dfrac{1}{\rho_w}\dfrac{\partial P_{atm}}{\partial y} \\ \qquad +\dfrac{1}{h}\dfrac{\rho_{air}}{\rho_w}C_D U_{w,y}\sqrt{U_{w,x}^2+U_{w,y}^2} \end{cases}$$

where ρ_w/ρ_{air} [kg.m^{-3}] is the water/air density, P_{atm} [Pa] is the atmospheric pressure, $U_{w,x}$ and $U_{w,y}$ [m.s^{-1}] are the horizontal wind velocity components, C_D [-] is the wind drag coefficient that relates the free surface wind to the shear stress, and lastly, K_s [m$^{1/3}$.s^{-1}] is the river bed and floodplain friction coefficient using the Strickler formulation [7]. In order to solve Eq. (1)-(3), initial conditions $\{H(x,y,t=0)=H_0(x,y);\ u(x,y,t=0)=u_0(x,y);v(x,y,t=0)=v_0(x,y)\}$ are provided, and boundary conditions (BC) are described with a time-dependent hydrograph upstream and a rating curve downstream. The Strickler coefficient is prescribed as uniform over subdomains, and calibrated according to the observing network.

B. Study area

The study area concerns the Garonne Marmandaise catchment (Southwest France) which extends over a 50-km reach of the Garonne River, between Tonneins, downstream of the confluence with the river Lot, and La Réole. This part of the valley is identified as an area at high flood risk. Since the 19th century, it has been equipped with infrastructures to protect the Garonne floodplain from flooding events such as the historic flood of 1875. A system of longitudinal dykes and weirs was progressively constructed to protect floodplains and manage submersion and flood retention areas.

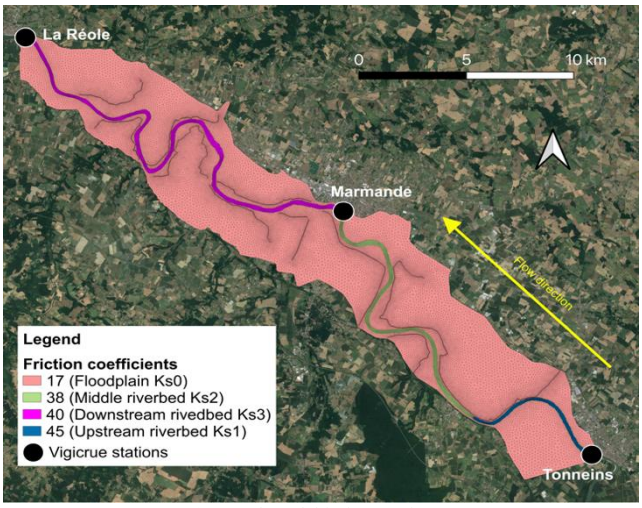

(a) Mesh and friction zoning

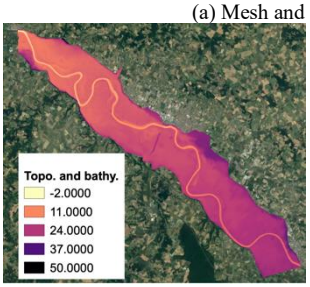

(b) Topography and bathymetry

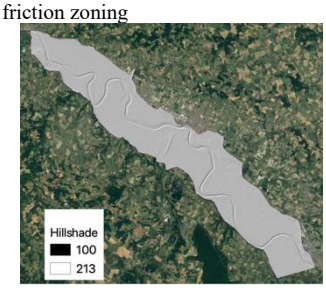

(c) Hillshade representation

Figure 1: Garonne Marmandaise TELEMAC-2D model.

A TELEMAC-2D model (Figure 1) was developed and calibrated over this catchment, which was built on a mesh of 41,000 nodes using bathymetric cross-sectional profiles and topographic data [8]. It involves a triangular unstructured mesh, with an increased mesh resolution around the dykes and in the river bed. The local rating curve at Tonneins (established from a number of water level-discharge measurements) translate the observed water levels into a discharge that is then

applied over the entire upstream interface, both river bed and floodplain boundary cells. This modeling strategy was implemented by Electricité de France R&D to allow a cold start of the model with any inflow value. However, it prompts an over-flooding of the upstream first meander (near Tonneins), until the water returns to the river bed. The downstream BC at La Réole is described with a local rating curve. Over the simulation domain, the friction coefficient K_s is defined over four areas. Their values resulted from a calibration procedure over a set of non-overflowing events and are set respectively equal to: $K_{s_1} = 45$, $K_{s_2} = 38$ and $K_{s_3} = 40$ [$m^{1/3}s^{-1}$] for the upstream, middle and downstream part of the river bed and $K_{s_0} = 17$ [$m^{1/3}s^{-1}$] for the floodplain. They are characterized by a discrete zoning of uniform K_s values into subdomains within the catchment, restricted by the limited number of in-situ measurements. Such a friction coefficient setting is indeed prone to uncertainty related to the zoning assumption, the calibration procedure and the set of calibration events. This uncertainty is more significant in the floodplain area where no observing station is available.

The probability density function (PDF) for the Strickler coefficients is assumed to follow a gaussian distribution with mean and standard deviation set accordingly to the calibration process and expert knowledge. The limited number of in-situ observations also yields errors in upstream inflow as the expression of the inflow relies on the use of the local rating curve, usually involves extrapolation for high flows. In order to account for uncertainties in the upstream BC (i.e., time-dependent discharge $Q_{up}(t)$) while limiting the dimension of the uncertain input space, the perturbation added to BC is applied via a parametric formulation that allows for a multiplicative, an additive and a time-shift error, as proposed by [9]:

$$\tilde{Q}_{up}(t) = a \times Q_{up}(t - c) + b \qquad (4)$$

where $(a, b, c) \in \mathbb{R}^3$, and their PDF follows gaussian distribution, centered at their default values. The characteristics of the friction- and inflow-related uncertainty PDFs are summarized in Table 1. Other works dealing with this uncertainty have been put forth using EnKF [10] or Extended Kalman filter [11].

TABLE 1: GAUSSIAN PDF OF UNCERTAIN INPUT VARIABLES RELATED TO FRICTION AND INFLOW DISCHARGE COEFFICIENTS.

Variables	*Unit*	*Calibrated/default value* $\mathbf{x_0}$	*Standard deviation* σ_x	*95% confidence interval*
K_{s_0}	$m^{1/3}s^{-1}$	17	0.85	17 ± 1.67
K_{s_1}	$m^{1/3}s^{-1}$	45	2.25	45 ± 4.41
K_{s_2}	$m^{1/3}s^{-1}$	38	1.9	38 ± 3.72
K_{s_3}	$m^{1/3}s^{-1}$	40	2.0	40 ± 3.92
a	-	1	0.06	1 ± 0.118
b	m^3s^{-1}	0	100	0 ± 196
c	s	0	900	0 ± 1760

C. 2021 flood event and observations

A substantial flood event occurred in late January and February 2021 as it exceeded the yellow risk level alert set out by the French national flood forecasting center (SCHAPI) in collaboration with the departmental prefect, and reached its peak on February 4. In this work, we examine an extended length of this event, i.e., between January 16 and February 15.

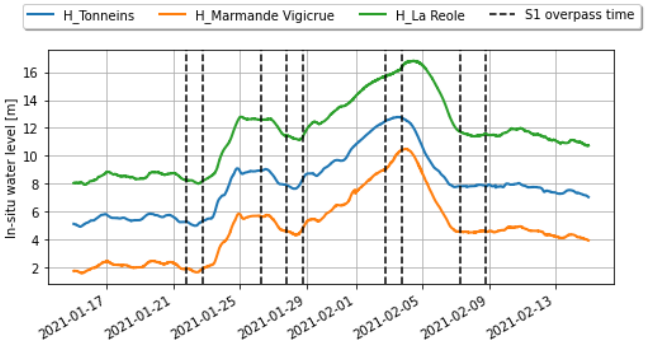

Figure 2: Water level time series at Vigicrue observing stations, and Sentinel-1 overpass times.

Figure 2 depicts the in-situ water level (15-minute time step) observed during the flood event at Vigicrue observing stations: Tonneins (blue curve), Marmande (orange curve) and La Réole (green curve). The event is observed by nine S1 images, indicated by the vertical black dashed lines in Figure 2. S1 works as a constellation of two satellites in a phased orbit, S1A and S1B, each with a 6-day revisit frequency. They are part of the Copernicus program launched by ESA with contributions from CNES. The flood peak was covered by the ascending orbit 30 on February 2 18:55 and by the ascending orbit 132 the next day on February 3 18:48.

III. METHODS

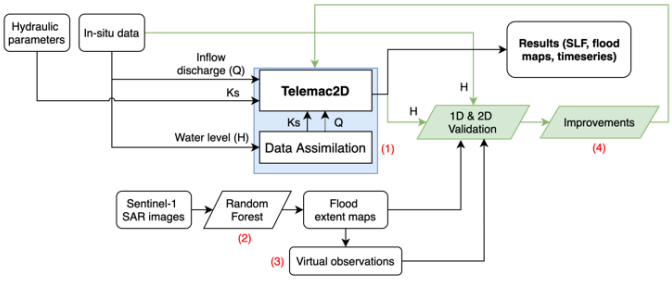

Figure 3: Proposed methodology.

The merits of the complementary use of in-situ data for assimilation and remote sensing (RS) data for validation are assessed with different deterministic and ensemblist numerical experiments. Four main steps to sum up the dynamic and novelty of the proposed methodology (Figure 3):

(1) DA combines in-situ data with this TELEMAC2D model to reduce the uncertainties within the model and inputs. The control variables are the friction coefficients and inflow parametric coefficients;
(2) S1 imagery data is used to generate flood extent maps, represented by binary flood maps (black pixels: dry, white pixels: wet);
(3) Several virtual observation regions are defined with expertise at important areas within the simulation domain. They measure the number of wet pixels within

defined boxes and allow to validate local performance of the flood simulations;

(4) Based on the performed 1D and 2D validations, improvements are made upon the model and simulation setting, allowing to better configure the control space, correct the existing bias between the model and observation, and so on.

A. Ensemble-based data assimilation algorithm (EnKF)

Continuous time-series of measured water levels and/or discharges recorded at discrete locations are traditionally used for model calibration and validation of DA algorithms for real-time constraints of hydraulic flood prediction models [1] [12]. In this work, the measured water levels at the 3 Vigicrue stations (Tonneins, Marmande and La Réole) are assimilated with the EnKF algorithm in the TELEMAC-2D Garonne model presented previously to sequentially correct the friction and inflow discharge.

1) Description of the control vector:

The DA algorithm consists in a cycled stochastic EnKF, where the control vector $\mathbf{x}$ is composed of the friction coefficients (four scalars $K_{s_i}, i \in 0,..,3$) and parameters that modify the time-dependent upstream BC (three scalars a, b, c). n denotes the size of the control vector. These seven parameters are assumed to be constant over a DA cycle, yet their evolution in time is made possible by DA between cycles. The DA cycle k covers a time window, noted $W_k = [t_{start}, t_{end}]$ of 12-hour length over which N_{obs} in-situ observations are assimilated. The cycling of the DA algorithms consists in sliding the window by a period $T_{shift} = 6$ hours so that the cycles W_k and W_{k+1} overlap. The EnKF algorithm relies on the propagation of N_e members with perturbed values of $\mathbf{x}$ (denoted by $\mathbf{x}^i$) into the forecast values denoted by $\mathbf{x}_k^{f,i}$ with $i \in [1, N_e]$ represents the ensemble member index.

2) EnKF forecast step:

The EnKF forecast step stands in the propagation in time of the control and model state vectors over the assimilation window W_k that gathers N_{obs} observations. The EnKF is here applied to model parameters that, by definition, do not evolve in time over the W_k. In order to avoid ensemble collapse, artificial dispersion is introduced within the sampling with the addition of perturbations $\boldsymbol{\theta}$ to the difference between the mean of the analysis from the previous cycle $(k-1)$ and the previous cycle analysis. The two terms are weighted by the hyperparameter λ. The forecast step thus reads:

$$\mathbf{x}_k^{f,i} = \begin{cases} \mathbf{x}_0 + \boldsymbol{\theta}_k^i & if\ k = 1 \\ \overline{\mathbf{x}_{k-1}^a} + \lambda_1\left(\mathbf{x}_{k-1}^{a,i} - \overline{\mathbf{x}_{k-1}^a}\right) + (1-\lambda_1)\boldsymbol{\theta}_k^i & if\ k > 1 \end{cases} \quad (5)$$

with $\overline{\mathbf{x}_{k-1}^a} = \left(\sum_{i=1}^{N_e} \mathbf{x}_{k-1}^{a,i}\right)/N_e \in \mathbb{R}^n$ and $\boldsymbol{\theta}_k^i \sim \mathcal{N}(\mathbf{0}, \sigma_{\mathbf{x}}^2)$.

For the first cycle, the perturbed friction and upstream forcing coefficient values are drawn within the PDFs described in Table 1. For the next cycles, the set of coefficients issued from the analysis at the previous cycle is further dispersed by combining the analysis anomalies with perturbations $\boldsymbol{\theta}$ drawn from the gaussian distribution centered at 0 and with the standard deviation described in Table. This technique is an alternative to anomalies inflation for avoiding the ensemble collapse, while preserving part of the information from the background statistical characteristics. In the following implementation, λ is respectively set equal to 0.3. The background hydraulic state, denoted by $\mathbf{s}_k^{f,i}$, associated with each member of the ensemble results from the integration of the hydrodynamic model $\mathcal{M}_k: \mathbb{R}^n \to \mathbb{R}^m$ from the control space to the model state (of dimension m) over W_k:

$$\mathbf{s}_k^{f,i} = \mathcal{M}_k\left(\mathbf{s}_{k-1}^{a,i}, \mathbf{x}_k^{f,i}\right) \quad (6)$$

The initial condition for $\mathcal{M}_k$ at t_{start} is provided by a user-defined restart file for the first cycle. For the following cycles, it stems from the analyzed model state $\mathbf{s}_{k-1}^{a,i}$, saved from the previous cycle. The control vector equivalent in the observation space for each member, noted $\mathbf{y}_k^{f,i}$, stems from:

$$\mathbf{y}_k^{f,i} = \mathcal{H}_k\left(\mathbf{s}_k^{f,i}\right) \quad (7)$$

where $\mathcal{H}_k: \mathbb{R}^m \to \mathbb{R}^{N_{obs}}$ is the observation operator from the model state space to the observation space (of dimension N_{obs}) that selects, extracts and eventually interpolates model outputs at times and locations of the observation vector $\mathbf{y}_k^o$ over W_k. It should be noted that, in the following, the observation operator may also include a bias correction to take into account a systematic model error. Eq. (7) thus reads

$$\mathbf{y}_k^{f,i} = \mathcal{H}_k\left(\mathbf{s}_k^{f,i}\right) - \mathbf{y}_{bias} \quad (8)$$

where $\mathbf{y}_{bias}$ is an a priori knowledge of the model-observation bias.

3) EnKF analysis step:

The EnKF analysis step stands in the update of the control and model state vectors. When applying a stochastic EnKF [13], the observation vector $\mathbf{y}^{o,i}$ is perturbed, thus an ensemble of observations $\mathbf{y}_k^{o,i}$ $(i \in [1, N_e])$ is generated:

$$\mathbf{y}_k^{o,i} = \mathbf{y}_k^o + \boldsymbol{\epsilon}_k \text{ with } \boldsymbol{\epsilon}_k \sim \mathcal{N}(0, \mathbf{R}_k) \quad (9)$$

where $\mathbf{R}_k = {\sigma_{obs}}^2 \mathbf{I}_{N_{obs}}$ is the observation error covariance matrix, here assumed to be diagonal, of standard deviation σ_{obs} (and $\mathbf{I}_{N_{obs}}$ is the $N_{obs} \times N_{obs}$ identity matrix), as the observation errors are assumed to be uncorrelated, Gaussian and with a standard deviation proportional to the observations $\sigma_{obs,k} = \tau \mathrm{y}_k^o$. The innovation vector over W_k is the difference between the perturbed observation vector $\mathbf{y}_k^{o,i}$ and the model equivalent $\mathbf{y}_k^{f,i}$ from Eq. (7) (or Eq. (8)) and Eq. (9). It is weighted by the Kalman gain matrix $\mathbf{K}_k$ and then added as a correction to the background control vector $\mathbf{x}_k^{f,i}$, so that the analysis control vector $\mathbf{x}_k^{a,i}$ is computed in Eq. (10),

$$\mathbf{x}_k^{a,i} = \mathbf{x}_k^{f,i} + \mathbf{K}_k\left(\mathbf{y}_k^{o,i} - \mathbf{y}_k^{f,i}\right) \quad (10)$$

The Kalman gain reads:

$$\mathbf{K}_k = \mathbf{P}_k^{x,y}\left[\mathbf{P}_k^{y,y} + \mathbf{R}_k\right]^{-1} \quad (11)$$

with $\mathbf{P}_k^{y,y}$ being the covariance matrix of the error in the background state equivalent in the observation space $\mathbf{y}_k^f$ and $\mathbf{P}_k^{x,y}$ the covariance matrix between the error in the control vector and the error in $\mathbf{y}_k^f$, stochastically estimated within the ensemble:

$$\mathbf{P}_k^{x,y} = \frac{1}{N_e}\mathbf{X}_k^T\,\mathbf{Y}_k \in \mathbb{R}^{n\times N_{obs}}$$

$$\mathbf{P}_k^{y,y} = \frac{1}{N_e}\mathbf{Y}_k^T\,\mathbf{Y}_k \in \mathbb{R}^{N_{obs}\times N_{obs}}$$

with

$$\mathbf{X}_k = \left[\mathbf{x}_k^{f,1} - \overline{\mathbf{x}_k^f}, \cdots, \mathbf{x}_k^{f,N_e} - \overline{\mathbf{x}_k^f}\right] \in \mathbb{R}^{n\times N_e}$$

$$\mathbf{Y}_k = \left[\mathbf{y}_k^{f,1} - \overline{\mathbf{y}_k^f}, \cdots, \mathbf{y}_k^{f,N_e} - \overline{\mathbf{y}_k^f}\right] \in \mathbb{R}^{N_{obs}\times N_e}$$

where

$\overline{\mathbf{x}_k^f} = \frac{1}{N_e}\sum_{i=1}^{N_e}\mathbf{x}_k^{f,i} \in \mathbb{R}^n$ and $\overline{\mathbf{y}_k^f} = \frac{1}{N_e}\sum_{i=1}^{N_e}\mathbf{y}_k^{f,i} \in \mathbb{R}^{N_{obs}}$

The analyzed hydrodynamic state, associated with each analyzed control vector $\mathbf{x}_k^{a,i}$ is denoted by $\mathbf{s}_k^{a,i}$. It results from the integration of the hydrodynamic model $\mathcal{M}_k$ with updated friction and upstream forcing over W_k, starting from the same initial condition (for the first cycle), then from each background simulation within the ensemble:

$$\mathbf{s}_k^{a,i} = \mathcal{M}_k\left(\mathbf{s}_{k-1}^{a,i}, \mathbf{x}_k^{a,i}\right) \quad (12)$$

B. Flood extent mapping using S1 images

In recent years, SAR image data has been widely used in flood management due to its ability to collect day and night images in all weather and to map flood extents in large areas in near real-time. Water bodies and flooded areas usually appear on SAR images with low backscatter intensity because most of the incident radar signals are reflected away from the SAR antenna. Therefore, with a few exceptions such as the built environment and vegetation areas, the detection of such areas is straightforward on SAR images.

In this work, a Random Forest (RF) segmentation [14] was trained over a training dataset with 223 S1 images from 12 non-coastal Copernicus EMS Rapid mapping flood cases from multiple regions of the world. The training dataset consists of permanent water pixel samples selected according to the Global Surface Water Occurrence products [15].

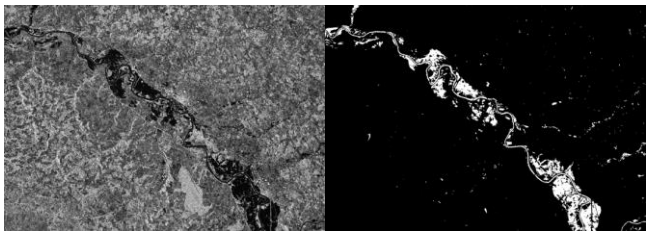

Figure 5: SAR S1 image (left) acquired on 2021-02-02 and the flood extent map inferred by RF (right).

Both VV and VH polarizations of S1 were used, in conjunction with the use of the local slope derived from the MERIT DEM [16]. The S1 images are calibrated and orthorectified, then inferred by the RF algorithm to produce the binary flood map, indicating flood (white pixels) and non-flood areas (black pixels), as shown in Figure 5. Using cuML, an open-source GPU-accelerated machine learning library, the RF algorithm is able to generate a flood extent map in a couple of minutes. To remove noises and artifacts in the resulting detected binary flood maps, a majority filter (with size of 3) was applied on the resulting flood binary map. The ground sampling distance of the S1 images and the derived flood binary map is 10 x 10 meters. The generated flood extent maps are used to improve flood visualization and reduce modeling uncertainty.

C. Experimental setup

Two free run simulations and five DA simulations were implemented, summarized by Table 2. Their variations concerns whether the experiment consists in a Free Run or involves a DA approach, as well as whether or not the model-observation bias $\mathbf{y}_{bias}$ is taken into account, and the value of τ (for σ_{obs}). The diagnosed bias was estimated during the 24 hours of January 15 which are composed of quasi-stationary non-overflowing discharge, result in $\mathbf{y}_{bias,Tonneins} = 0.72$, $\mathbf{y}_{bias,Marmande} = 0.4$, and $\mathbf{y}_{bias,LR} = -0.24$ meters.

TABLE 2: SUMMARY OF THE REALIZED EXPERIMENTS.

Exp. name	*Bias correction*	*DA*	N_e	τ *(%)*	*Control variables*
FR1	No	No	1	-	-
FR2	Yes	No	1	-	-
DA1	No	Yes	24	15	$K_{s[0:3]}, a, b, c$
DA2	Yes	Yes	24	15	$K_{s[0:3]}, a, b, c$
DA3	Yes	Yes	24	1	$K_{s[0:3]}, a, b, c$
DA4	Yes	Yes	24	99	$K_{s[0:3]}, a, b, c$
DA5	Yes	Yes	24	15	$K_{s[0:3]}$

IV. RESULTS AND DISCUSSIONS

In terms of validation, two assessments are carried out. First, a 1D validation between the simulated and observed time-series water levels at Vigicrue observing stations was achieved. Second, 2D assessments between the flood extent maps simulated by TELEMAC-2D and those derived from Sentinel-1 images by RF algorithm was carried out in order to validate the overall performance of simulated flood extents, and to analyze the local behavior at individual virtual observation locations.

A. *Simulated water levels*

Figure depicts the water levels simulated by the performed experiments (from FR1 to DA5) represented by solid curve with respect to the observed water levels (black dashed curve) at the 3 Vigicrue observing stations. These plots focus on the period near the flood peak, i.e., between January 31 and February 9. The bottom panel on each sub-figure shows the differences between the simulated and observed water levels.

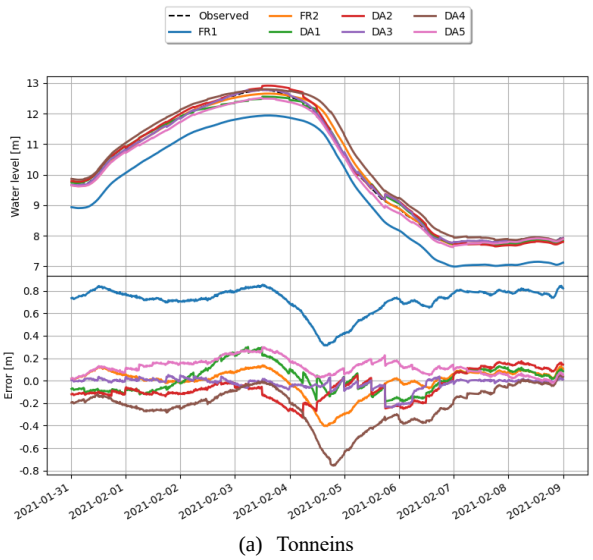

(a) Tonneins

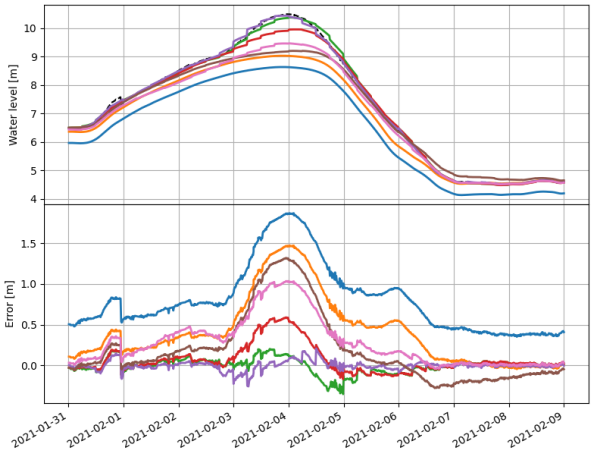

(b) Marmande

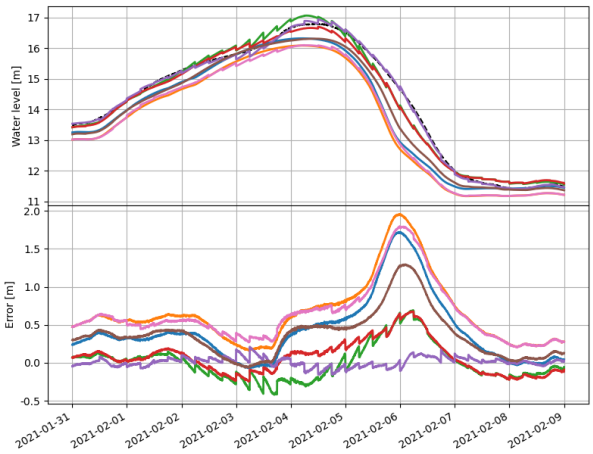

(c) La Réole

Figure 6: Simulated and observed time-series water levels around the flood peak, between January 31 and February 9.

B. *1D Assessment Metrics*

Table 3 summarizes the 1D assessment metrics (RMSE and maximum absolute error) computed over the whole simulation duration, from January 16 to February 15, between the water levels simulated by TELEMAC-2D and the observed water levels. For each metrics (each column) the best score (i.e., lowest RMSE and lowest maximum absolute error) is highlighted in boldface, whereas the second best is underlined.

Considering the free run experiments (FR1 and FR2), Table 3 shows that the bias correction leads to a better agreement between the model and observations at Tonneins and Marmande. This is however not the case for La Réole. Next, with the involvement of DA, the resulting water level errors have been reduced significantly. For example, from FR1 to DA1, the RMSE are reduced by 88.1%, 90.6% and 63.8% at Tonneins, Marmande and La Réole, respectively. Overall, DA3 yields the water levels the closest to the observations at every Vigicrue stations (as highlighted by the boldfaced values), both the RMSE and maximum absolute error, as a result of the σ_{obs} set equal to 0.01 in which the observation vector was considered with very little perturbation (Eq. (9)). On the other hand, high uncertainty of observation vector is

assumed for the DA4 experiment ($\sigma_{obs} = 0.99$), which leads to the resulting errors greater than DA2 and DA3.

In practice, an inflow discharge used as input for a hydraulic model like TELEMAC-2D may originate from a hydrologic model in which statistical corrections were also carried out [17]. This leads to the assumption that no uncertainty exists in the inflow discharge, based on which the DA5 was realized. However, the comparison between DA2 (with 7 parameters in the control vector) and DA5 (with only 4 friction coefficients in the control vector) demonstrates the improvements from DA5 to DA2 emphasized by the water level errors, which are reduced both in terms of RMSE and maximum absolute errors. This advocates for the consideration of uncertainty within $Q_{up}(t)$.

TABLE 3: 1D ASSESSMENT METRICS W.R.T. IN-SITU DATA MEASURED AT VIGICRUE OBSERVING STATIONS, COMPUTED OVER THE WHOLE SIMULATION DURATION.

	Root-Mean-Square Error (m)			***Max Absolute Error (m)***		
Exp. name	***Tonneins***	***Marmande***	***La Réole***	***Tonneins***	***Marmande***	***La Réole***
FR1	0.756	0.625	0.409	1.062	1.870	1.721
FR2	0.102	0.338	0.505	0.404	1.472	1.956
DA1	0.090	0.059	0.148	0.456	0.352	0.690
DA2	0.084	0.104	0.138	0.330	0.590	0.676
DA3	**0.034**	**0.034**	**0.043**	**0.238**	**0.258**	**0.212**
DA4	0.171	0.260	0.298	0.756	1.319	1.295
DA5	0.093	0.226	0.480	0.299	1.036	1.796

C. *Control vector analysis*

The analyzed values from DA experiments for friction and inflow parameters are shown in the first seven panels on Figure 7. The inflow discharge $Q_{up}(t)$ is also depicted on the eighth panel, and the two bottom panels reveal the water level errors from FR1 and FR2 at the Vigicrue stations. Since the model-observation bias is not taken into account in DA1, a larger increment is required in the control vector to make up for the difference between the model and observation. In order to make the model as close to the observation as possible, DA3 (with $\sigma_{obs} = 0.01$) commits very large correction upon the control vector, as shown by the large margin from the violet curves in all 7 control variable panels. Due to this constraint, the friction coefficient for the floodplain K_{s_0} is even diminished below 10 $m^{1/3}s^{-1}$ near the flood peak which is not a realistic value for the floodplain in this catchment. On the other hand, DA4 with a σ_{obs} set equal to 0.99, i.e., full uncertainty on the observation vector, presents very small corrections upon the control vector. As such, the brown curves remain quite stable from the calibrated and default values. Even though DA2 and DA5 experiments were configured with the same σ_{obs}, the respective increments on friction coefficients of DA5 (magenta curves) are much higher than those of DA2 (crimson curves). This is due to the fact that the control vector in DA5 is only composed of the friction coefficients, whereas DA2 involves all 7 variables, hence the contribution to compensate the water level error was shared among them.

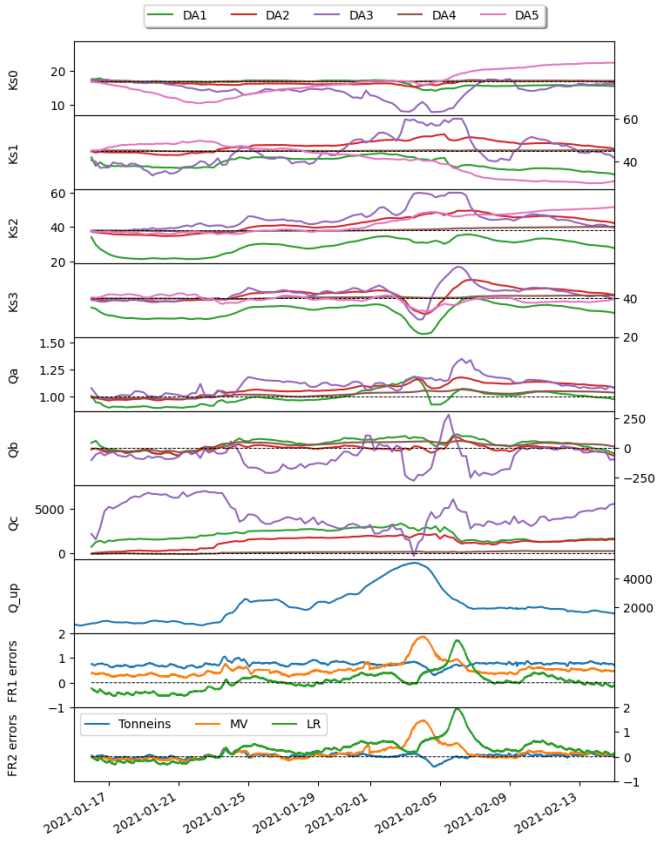

Figure 7: Evolution of controlled variables.

D. *Assessment of simulated flood extents*

The flood extent maps simulated by TELEMAC-2D from the experiments are generated by applying a threshold of 5cm above which the node is considered wet (and dry otherwise). A rasterization of TELEMAC-2D water level output field onto a regular grid is also carried out. They are then compared with the flood extent maps generated from the RF algorithm on S1 images. Critical Success Index (CSI) is widely used to assess the performance of flood extent mapping, it is defined as follows:

$$\mathrm{CSI} = \frac{TP}{TP + FP + FN} \tag{13}$$

where True Positives (TP) is the number of pixels correctly predicted as flooded, False Positives (FP) or *over-prediction* is the number of non-flooded pixels incorrectly predicted as flooded, True Negatives (TN) is the number of pixels correctly identified as non-flooded, and False Negatives (FN) or *under-prediction* is the number of missed flooded pixels. The RF-inferred flood extent maps are considered the reference flood map based on which the TELEMAC-2D flood extent map will be evaluated.

Table 4 summarizes the CSI measured from the experiments with respect to the RF-inferred flood extent maps. On each day, the best score (i.e., highest CSI) is highlighted in boldface, whereas the second best is underlined. At the beginning of the event, the water prevails mainly in the river bed and only occupies a small portion of the simulation domain. However, the CSI scores during these non-flooding times were degraded because of several over-predicted regions

such as the numerical artificial flooding of the upstream first meander (previously mentioned in subsection II.B). Let us focus on the 2021-02-03 which is the S1 overpass time the nearest to the flood peak. DA4 with the most uncertainty hypothesized on the observation vector allows the highest CSI score. However, reducing the σ_{obs} from 0.99 (DA4) to 0.15 (DA2) only decreases the resulting CSI 0.13 points (i.e., from 63.97% to 63.84%). DA3, by forcing the simulated water levels to be as close to the observation as possible, yields significantly lower CSI, even smaller than the free runs. After the flood peak, the interpretability of the CSI may also be limited due to a number of water puddles that remain in the floodplain as the model struggles to simulate the water recession.

TABLE 4: CSI METRIC WITH RESPECT TO S1-DERIVED FLOOD EXTENT MAPS.

	CSI (%)					
Exp. name	***Jan 26 07:00***	***Jan 27 19:00***	***Jan 28 19:00***	***Feb 2 19:00***	***Feb 3 19:00***	***Feb 7 7:00***
FR1	**28.13**	**27.81**	**25.09**	44.39	55.86	22.10
FR2						
DA1	25.82	25.92	23.58	41.91	61.97	20.00
DA2	27.66	27.49	24.95	43.98	63.84	20.87
DA3	27.65	27.49	24.93	44.22	50.82	23.75
DA4	27.52	27.44	24.84	**47.08**	**63.97**	20.92
DA5	27.74	27.59	24.92	44.60	49.31	**25.41**

E. Analyzing local behavior at virtual observation regions

Several locations within the simulation domain were selected to analyze local behavior of the flood simulation, especially in the floodplains, as shown by the rectangular boxes in Figure 8. From these boxes, the number of wet pixels is counted from the flood extent maps (there are 9 in total, cf. Figure 2). These counts from the experiments (represented by the dashed curves) and the RF-inferred flood extent maps (black solid curve) are depicted in Figure 9.

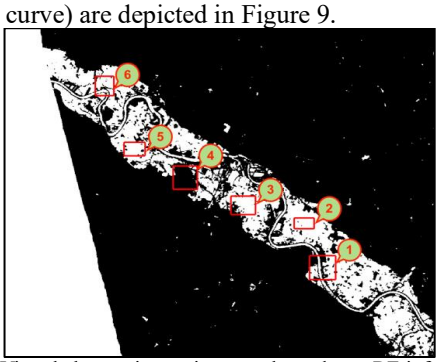

Figure 8: Virtual observation regions overlapped on a RF-inferred flood extent map, generated from S1 image on February 3.

All of virtual observation regions are filled very quickly with respect to the S1 observations. One particular region is box number 4 in which the number of flooded pixels is very low according to the observation, but it is over-flooded in the experiments, with varying degree (FR2 and DA4 by a small margin, and the others by a lot). Such different behaviors between boxes number 3, 4, and 5, despite they are all on the floodplain and near to each other, advocate for an adjustment, e.g., DA, which corrects the friction of the area around box number 4. DA1, without taking into account the bias correction, tends to overflood the whole catchment (i.e., for all boxes). Lastly, the flood recession period associated with the last two S1 overpass times is poorly modelled, particularly for box number 2. This stems from the fact that evaporation and ground infiltration physical processes are not accounted for in the Garonne model.

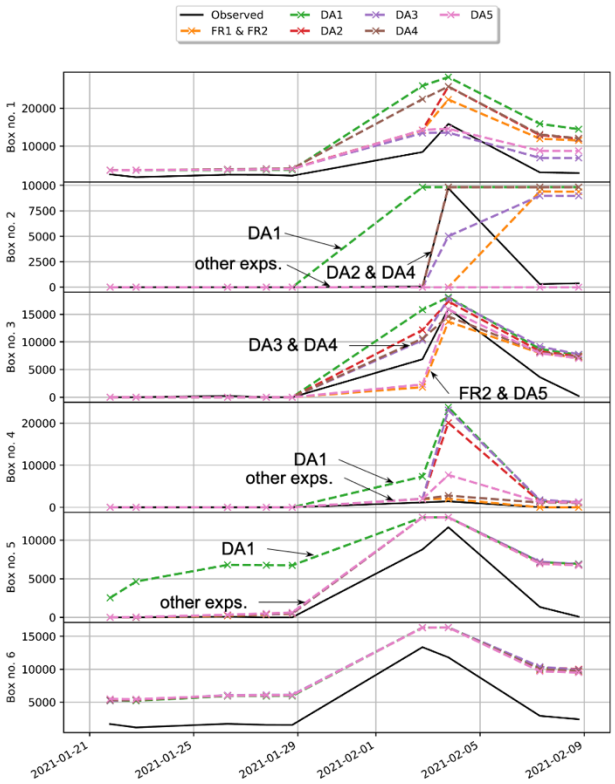

Figure 9: Wet pixel counts at virtual observation regions.

V. CONCLUSIONS

In this paper, flood extents observed from Sentinel-1 images were extracted using Random Forest and compared with the flood extent maps simulated by TELEMAC-2D. The study was carried out over the Garonne Marmandaise catchment, focusing on the flood event occurred in January and February 2021. Seven experiments were realized, namely two in free run mode and five in DA mode. The DA was performed using only in-situ observations, and it was implemented by an EnKF with a 12-hour assimilation window sliding with 6-hour overlapping between windows.

Several key remarks can be drawn from this work. First, ensemble-based data assimilation allows time-varying correction of friction and inflow leading to improved simulation and forecast in the river bed and the flood plain. Second, it was shown that the bias correction leads to properly corrected water levels in the river bed and floodplains. The uncertainty assumed on the observation vector through parametrization of σ_{obs} was also demonstrated, for which the compromise between a good fit on simulated water level (i.e., DA3) and a high CSI/good agreement between flood extents (i.e., DA4). Lastly, several limitations concerning local behaviors of the flood simulation have been revealed with the virtual observation regions.

Moving forward, a particular perspective for this study concerns resolving the limitation of the control vector size and refining the spatial friction zoning definition, assimilating information from RS data such as number of wet pixels in the flood plain (which were used for validation in this work) and/or flood extent information to improve the description of the refined friction subdomains in the floodplains and to calibrate them. This study paves the way toward a cost-effective and reliable solution for flood forecasting and flood risk assessment over poorly gauged or ungauged catchments, thanks to the use of remote sensing data. Such developments, once generalized, could potentially lead to hydrology-related disaster risk mitigation in other regions. Future progresses built upon this work will involve a more refined approach for friction zoning and calibration, especially for the floodplains, as well as improving the current models by assimilating flood extent maps.

ACKNOWLEDGEMENT

This work was supported by CNES, CERFACS and SCO-France. The authors gratefully thank the Electricité de France R&D for providing the TELEMAC-2D model for the Garonne River, SCHAPI, SPC Garonne-Tarn-Lot and SPC Gironde-Adour-Dordogne for providing the in-situ data. Lastly, the authors would like to thank the anonymous reviewer whose comments and suggestions helped improve this manuscript.

REFERENCES

[1] J. Neal, P. Atkinson, and C. Hutton, "Flood inundation model updating using an ensemble Kalman filter and spatially distributed measurements," *J. Hydrol.*, *336*(3-4), 2007, pp. 401-415.

[2] I. Mirouze, S. Ricci, and N. Goutal, "The impact of observation spatial and temporal densification in an ensemble Kalman Filter," in *26th TELEMAC-MASCARET User Conference,* 2019, Toulouse.

[3] D. Mason, G. Schumann, J. Neal, J. Garcia-Pintado, and P. Bates, "Automatic near real-time selection of flood water levels from high resolution Synthetic Aperture Radar images for assimilation into hydraulic models: A case study," *Remote Sens. Environ.*, *124*, 2012, pp. 705-716.

[4] P. Kettig et al., "The SCO-FloodDAM Project: New Observing Strategies for Flood Detection, Alert and Rapid Mapping," in *2021 IEEE International Geoscience and Remote Sensing Symposium*, 2021, in press.

[5] J. M. Hervouet, "Hydrodynamics of free surface flows: modelling with the finite element method," John Wiley & Sons, 2007.

[6] Laborie, V., Ricci, S., De Lozzo, M., Goutal, N., Audouin, Y. and Sergent, P., 2020. Quantifying forcing uncertainties in the hydrodynamics of the Gironde estuary. Computational Geosciences, 24(1), pp.181-202.

[7] P. Gauckler, "Etudes Théoriques et Pratiques sur l'Ecoulement et le Mouvement des Eaux," Gauthier-Villars, 1867.

[8] A. Besnard and N. Goutal, "Comparison between 1D and 2D models for hydraulic modeling of a floodplain: case of Garonne River," *Houille Blanche-Revue Internationale De L'Eau*, vol. 3, 2011, pp. 42-47.

[9] Ricci, S., Piacentini, A., Thual, O., Pape, E. L., & Jonville, G. (2011). Correction of upstream flow and hydraulic state with data assimilation in the context of flood forecasting. *Hydrology and Earth System Sciences*, *15*(11), 3555-3575.

[10] Laborie, V., 2020. Quantification d'incertitudes et assimilation de données pour la modélisation hydrodynamique bidimensionnelle: application au modèle de prévision des hautes eaux de l'estuaire de la Gironde (Doctoral dissertation, Université Paris-Est).

[11] Habert, J., Ricci, S., Le Pape, E., Thual, O., Piacentini, A., Goutal, N., Jonville, G. and Rochoux, M., 2016. Reduction of the uncertainties in the water level-discharge relation of a 1D hydraulic model in the context of operational flood forecasting. *Journal of Hydrology*, *532*, pp.52-64.

[12] Zaoui, F., Goeury, C., & Audouin, Y. (2018). Ensemble Integrations of Telemac-Mascaret for the optimal model calibration. *In Proceedings of the XXVth TELEMAC-MASCARET User Conference,* 9th to 11th October 2018, Norwich (pp. 169-175).

[13] M. Asch, M. Bocquet, and M. Nodet, "Data assimilation: methods, algorithms, and applications," Society for Industrial and Applied Mathematics, 2016.

[14] M. Pal, "Random Forest classifier for remote sensing classification," *Int. J. Remote Sens.*, *26*(1), 2005, pp. 217-222.

[15] J. Pekel, A. Cottam, N. Gorelick, and A. Belward, "High-resolution mapping of global surface water and its long-term changes," *Nature*, 540(7633), 2016, pp. 418-422.

[16] D. Yamazaki et al., "MERIT Hydro: a high-resolution global hydrography map based on latest topography dataset," *Water Resources Research*, 55, 2019, pp. 5053– 5073.

[17] R. Hostache et al., "Near-real-time assimilation of SAR-derived flood maps for improving flood forecasts," *Water Resour. Res.*, 54(8), 2018, pp. 5516-5535.

Simplified physically-based modelling of overtopping induced levee breaching with TELEMAC-2D

L. Kheloui, K. El Kadi Abderrezzak, S.E. Bourban
EDF R&D, LNHE
Université Paris-Est, LHSV
6 quai Watier, 78400 CHATOU, FRANCE

***Abstract*— Flood events related to dike breach and failure are a major concern throughout the world due to the severe human and economic damages they cause. An important research effort is made to improve flood risk assessment through the detailed prediction of breach temporal and spatial evolutions, which remains essential to accurate prediction of the breach outflow discharge. In this study, a simplified modelling approach is demonstrated to reproduce a field scale experiment of fluvial levee breach induced by overtopping. The hydrodynamics module TELEMAC-2D is used with several empirical laws, now implemented within its breach module, to prescribe the gradual expansion (widening and deepening) of the breach. The numerical results are compared to measurements in terms of breach discharge and breach opening evolution and assess the performances of the implemented parametric models.**

I. INTRODUCTION

Levee breach and failure can lead to destructive floods with severe economic, social and environmental damages. Levees are commonly used as flood-defence structures but were mostly built with erodible material and designed for specific ranges of river discharges and water levels. Their breaching can occur due to several mechanisms, such as internal erosion with seepage flows and external erosion due to overflow. The latter being the most common failure mechanism [1, 2].

Populations living in flood-prone areas are continuously increasing, which makes the risk of important fatalities and property destruction in case of flooding even greater. Therefore, an important research effort is made in terms of physical and numerical modelling of levee breaching to improve available flood resilience and risk assessment techniques [3]. In the framework of numerical modelling of levee breach due to overflows, three different approaches for levee failure simulation emerge [1, 4]: (i) parametric models, which consist of simple regression equations for breach peak discharge and breach width and duration, resulting from the statistical analysis of reported historical failure events and mostly related to dams, (ii) simplified physically-based models, where flow variables are computed using one or two dimensional hydrodynamic models and breach expansion defined with parametric equations, and (iii) detailed physically-based models, which simulate both hydrodynamic and sediment transport processes.

The aim of this study is to simulate a field scale experiment of overtopping induced levee failure with a simplified physically based approach, which includes newly implemented empirical equations for gradual breach expansion in TELEMAC-2D. The capabilities and limitations of this model are discussed and the performance of each empirical equation to provide accurate estimation of breach discharge and expansion are evaluated.

II. FIELD SCALE EXPERIMENT MODELLING

A. *Description of the field scale experiment*

Kakinuma and Shimizu [5] presented full-scale experiments of side-overflow levee breaching performed in Chiyoda test channel, the largest river experimental facility in Japan built on Tokachi River, Hokkaido. Levee failure tests triggered by overtopping were conducted for various channel inflow discharges, dike soil composition and geometry as well as location. Further information on these experiments can be found in Shimada et al. [6].

In this paper, “Case 4” is considered (Fig. 1). This test was carried out in an 8 m wide and 176 m long main channel with a longitudinal bed slope of 1/500. The levee was built along the right side of the main channel toward an 80 m wide floodplain. The erodible part of the levee was 100 m long, 3 m high and its crown width was equal to 6 m with 1:2 (V:H) side slopes. Its soil composition consisted of non-cohesive sand (median diameter d_{50} = 0.74 mm) and 19% of silty soil and clay. In order to trigger overtopping an initial trapezoidal-shaped notch was carved 20 m far from the upstream end of the dike. The notch was 0.5 m deep, 3 m wide at the crest and 1 m wide at the bottom. The main channel inflow discharge was gradually increased to approximately 80 m^3/s to reach the required water level for overtopping at the notch location. Measurement data included breach outflow hydrographs, water levels, levee-breaching process estimated from acceleration sensors observations.

B. *Numerical model*

The two-dimensional shallow water equations code TELEMAC-2D is used to compute flow characteristics and combined with its BREACH module (Fig. 2). We implemented selected empirical laws within this module to simulate the gradual expansion of the breach in time (widening and deepening). Since sediment transport is not simulated, the use of such simplified models requires some

user-defined parameters. First, the breach location is specified with a polygon created from a polyline along the dike crest and a bandwidth corresponding to dike bottom width. For the breaching A initiation, a criterion has to be selected among three different options implemented in the breach module : the user can directly specify (i) a start time, (ii) a threshold value for the average overflow water level above the entire breach location previously defined, or (iii) a threshold water level at a specific node. The user can then select a breach development mode among two options: (i) breach expansion is performed by lowering the breach bottom level for the complete breach zone (i.e. breach final width is reached instantaneously), or (ii) both breach widening and deepening are performed gradually. For this latter option, the user can choose a parametric model among newly implemented empirical laws in TELEMAC-2D (see Section C). Depending on that, information needed *a priori* can also include final breach dimensions, erosion rate, erosion duration and eventual empirical parameters values.

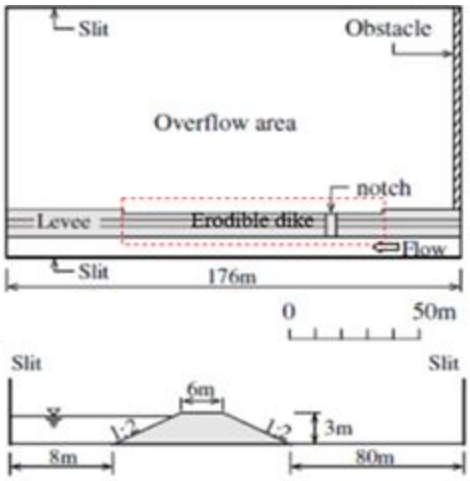

Figure 1. "Case 4" experiment - Plan view and cross-sectional profile (adapted from Kakinuma and Shimizu [5]).

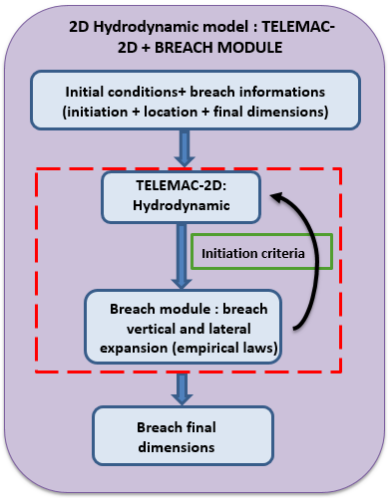

Figure 2. Simplified physically based approach for levee breach modelling in TELEMAC-2D.

C. *Computation of breach widening and deepening*

The breach lateral expansion is performed in a symmetrical way upstream and downstream of the initial notch location. The longitudinal breach cross-sectional profile is assumed rectangular, except for the Froehlich model [7] for which the profile is nearly trapezoidal (see Eqs.10-13).

Breach lateral expansion

The simplest description of breach widening is a time dependent linear equation: the breach width grows at a user-defined uniform rate. To mimic the real breach widening, another option is to split the process into two main phases (Eqs. 1 and 2), where the breach grows quickly in the first phase, and then slows down toward the end of the development time:

$$B(t) = E_{w1}t + B_0 \qquad \text{for } t \le T_1 \qquad (1)$$

$$B(t) = E_{w1}T_1 + E_{w2}(t - T_1) + B_0 \quad \text{for } T_1 \le t \le T_f \quad (2)$$

where t is time in hours (after the breach initiation), B the breach width in meters, B_0 the initial breach width in meters, T_1 is the duration of phase 1 in hours, T_f total duration of the breach expansion (phase 1 and phase 2) in hours, E_{w1} and E_{w2} are breach growth rates (m/hr) for phase 1 and 2, respectively.

Growth rates could be obtained from literature or physically-based models ([2, 8, 9]). Using available datasets, Resio et al. [10] reported that the rate of breach widening is ranging between 9 m/hr for erosion-resistant soils (cohesive dikes) and 60 m/hr for erodible alluvial material (sand and gravel soils). The widening rate can rarely reach 300 m/hr for very erodible dikes.

USBR [11] recommended a single breach widening rate of 91 m/hr for embankment dams:

$$B(t) = 91t + B_0 \qquad \text{for } t \le T_f \qquad (3)$$

Von Thun and Gillette [12] developed two equations for breach widening in dikes of low and high erodibility. For erodible dikes (*i.e.* non-cohesive dikes), the law reads as:

$$B(t) = (4h_w + 61)t + B_0 \qquad \text{for } t \le T_f \qquad (4)$$

with h_w the water depth above the breach invert in meters at failure time and notch location. For resistant dikes (*i.e.* cohesive dikes), the law is:

$$B(t) = 4h_w t + B_0 \qquad \text{for } t \le T_f \qquad (5)$$

Verheij [13] provided a simple relationship between the breach width B and time for sand and clay levees, based on field and laboratory data sets. For sand levees (*i.e.* non-cohesive dikes), the equation is:

$$B(t) = 37.2t^{0.51} + B_0 \qquad \text{for } t \le T_f \qquad (6)$$

For clay levees (*i.e.* cohesive dikes), the law reads as:

$$B(t) = 13.4\sqrt{t} + B_0 \qquad \text{for } t \le T_f \qquad (7)$$

Verheij and Van der Knaap [14] improved the previous formulations by including the effect of the difference in water levels at both sides of the dike at the breach location, and the critical flow velocity for the initiation erosion of the dike material. The empirical equation reads as:

$$B(t) = f_1 \frac{g^{0.5}\Delta H^{1.5}}{u_c} log\left(1 + f_2 \frac{g}{u_c} t\right) + B_0 \quad \text{for } t \leq T_f \tag{8}$$

with u_c the critical flow velocity for the initiation of erosion of dike material (m/s), f_1 and f_2 are empirical factors for breach width, g is the gravitational acceleration (m/s^2), and ΔH (m) denotes the difference in water level between the upstream and downstream sides of the breach.

In the implemented version within TELEMAC-2D, we consider the difference of water head instead of water level, *i.e.* ΔH (m) = $h_{up} - h_{down}$ with h_{up} the hydraulic head upstream of the breach (channel side) and h_{down} the hydraulic head downstream of the breach (floodplain side); this term allows a natural balance, meaning that breach width stabilises when the hydraulic head's difference is close to zero. Therefore, the user is not expected to give final breach width to run the model. Default values and ranges have been proposed for f_1 and f_2 (Table 1) [14]. Table 2 shows characteristic values of the critical velocity u_c for the surface erosion according to the dike material.

TABLE 1. DEFAULT AND RANGE OF VALUES FOR COEFFICIENTS F_1 AND F_2.

Type of Soil	Default	Range
f_1	1.3	0.5 – 5
f_2	0.04	0.01 – 1

TABLE 2. STRENGTH CHARACTERISTICS OF VARIOUS SOIL TYPES [13].

Type of Soil	u_c (m/s)	τ_c (Pa)	c_E (m^{-2}/s^2)
Grass, good	7	185	0.01×10^{-4}
Grass, moderate	5	92.5	0.02×10^{-4}
Grass, bad	4	62	0.03×10^{-4}
Clay, good (compact ; $\tau_{undrained}$ = 80-100 kPa)	1.0	4	0.50×10^{-4}
Clay with 60% sand (firm ; $\tau_{undrained}$ = 40-80 kPa)	0.80	2.5	0.60×10^{-4}
Good clay with less structure	0.70	2	0.75×10^{-4}
Good clay, heavily structured	0.60	1.5	1.5×10^{-4}
Bad clay (loose ; $\tau_{undrained}$ = 20-40 kPa)	0.40	0.65	3.5×10^{-4}
Sand with 17% silt	0.23	0.20	10×10^{-4}
Sand with 10% silt	0.20	0.15	12.5×10^{-4}
Sand with 0% silt	0.16	0.10	15×10^{-4}

τ_c : critical shear stress; c_E: strength coefficient. These characteristics are given as indicative values, as they are not used in Verheij and Van der Knaap's formula [14]).

Breach deepening

For the empirical models described above the time-evolution of the breach invert elevation is simulated according to the following linear-time progression law:

$$Z_B(\mathrm{t}) = Z_{B0} - \frac{Z_{B0} - Z_{Bmin}}{T_d} t \qquad \text{for } t \leq T_d \tag{9}$$

with Z_B the elevation of breach invert, Z_{B0} = initial elevation of breach invert, T_d is the required duration to reach Z_{Bmin} in hours. The breach minimum bottom level Z_{Bmin} (elevation of the dike foundation, main channel bottom or of a rigid layer) is reached in a shorter period than lateral expansion till ultimate breach width. By default, the duration T_d is taken 10 times smaller than the total duration of breach lateral expansion T_f.

Froehlich model (2008) (adapted)

Froehlich [7] proposed an empirical model, composed of three breach evolution variants [15] to approximate breach expansion (widening and deepening). Each of the three models assumes that a breach begins to form at the top and grows with time into a trapezoidal shape. Froehlich [7] used the concept of Brunner [16] who proposed a sine-curve time breach progression (instead of the common linear time evolution), reflecting slower growth at the start; then acceleration followed by another slow phase close to the end of breach development. The longitudinal cross-sectional profile of the breach is trapezoidal.

In TELEMAC-2D, an adapted version is implemented for two-dimensional simulations. The instantaneous top width of the breach is computed as:

$$B(t) = \beta(t)(B_f - B_0) + B_0 \quad \text{for } t \leq T_f \tag{10}$$

$$\text{with } \beta(t) = \frac{1}{2}\left\{1 + \sin\left[\pi\left(\frac{t}{T_f} - \frac{1}{2}\right)\right]\right\} \tag{11}$$

and B_f as the final top width of the breach in meters. The breach bottom elevation evolves as:

$$Z_B(t) = Z_{B0} - \beta_1(t)(Z_{B0} - Z_{Bmin}) \quad \text{for } t \leq T_d \tag{12}$$

$$\text{with } \beta_1(t) = \frac{1}{2}\left\{1 + \sin\left[\pi\left(\frac{t}{T_d} - \frac{1}{2}\right)\right]\right\} \tag{13}$$

D. Computational domain and parameters

The 2D computational domain was discretized into structured triangular elements with an edge of 0.5 m. Boundary conditions (Fig. 3) consisted in imposing the measured inflow discharge at the main channel inlet (Fig. 4) and a rating curve at the downstream end to achieve the required water level in the main channel and trigger levee overtopping at the notch location. A supercritical outflow with free water depth and velocity was set in the floodplain and a solid boundary was imposed elsewhere. The Strickler coefficient was set to 43 m$^{1/3}$ s^{-1}, and a constant eddy viscosity of 10^{-3} m$^{1/3}$ s^{-1} was applied for turbulence closure. The time step was set to 0.1 s. The solver was the conjugate gradient with an accuracy of 10^6, while the mass-conservative PSI scheme and NERD scheme were used for water depth and velocity, respectively.

The breach initiation time was 105 min and breach final width was predefined at 74.8 m as a criterion to stop breach

widening (except for Verheij and Van der Knaap [14] formulation); These values were extracted from experimental data.

The simulation using the time dependent linear breach width growth law was performed with a lateral erosion rate E_w equal to 65 m/hr. The same value was adopted to describe breach evolution following two phases: during the first phase (E_{w1} = 65 m/hr) of the dual breach dynamics model during a period T_1 = 45 min, while the second phase was characterised by a slower growth rate E_{w2} = 30 m/hr.

For the Verheij and Van der Knaap [14] formulation, the critical erosion velocity u_c was taken equal to 0.23 m/s, as proposed by authors in Table 2 for sandy dikes with silt soil fractions. Default values were taken for f_1 (=1.3) and f_2 (= 0.06). Because the breach deepened faster than it widened, and because this model doesn't require user input breach final width or widening period, the duration of the breach deepening T_d was limited to 5 min, following the experimental observations. Finally, the total breach widening duration T_f was set to 50 min for Frohlich [7] model to achieve the best estimation of breach discharge.

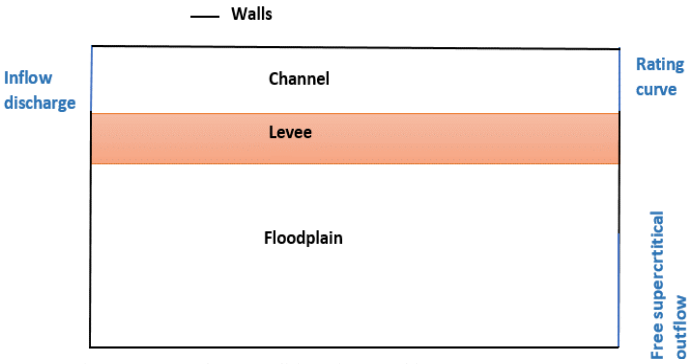

Figure 3. Boundary conditions imposed in TELEMAC-*2D*.

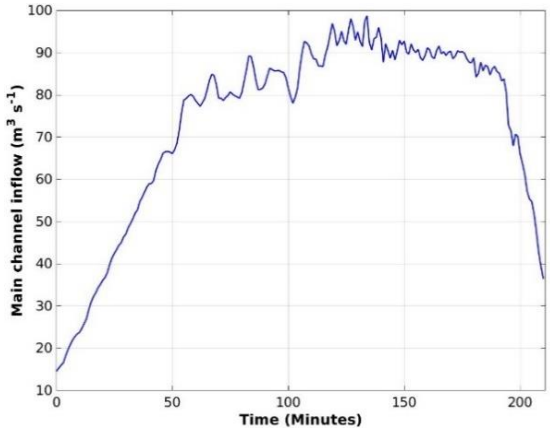

Figure 4. Measured main channel inflow discharge.

III. RESULTS AND DISCUSSION

In this section, simulated breach discharge and width time series are evaluated against experimental measurements and the performance of each parametric model is discussed. On Figures 5, one can see that the trend of fast increase in breach discharge followed by a quasi-stabilization step around a maximum value close to 70 m^3/s before dropping at test end (due to the limitation of channel inflow discharge at test end as shown in Figure 4) is well reproduced by the simplified modelling approaches. The results display a higher simulated amplitude of breach discharge with USBR formula as it estimates a higher breach width (Fig. 6), which induces a greater breach section to convey the flow.

Except for Froehlich's model, the breach discharge was slightly overestimated during the early stage of breach opening as the models predicted a faster breach lateral expansion. During quasi-stabilisation stage, computed breach dynamic with Verheij's (2002) model was too slow and the maximum breach discharge was missed, while USBR (1988) model overestimated breach widening rate and resulted in a higher breach outflow. The other laws successfully captured the breach discharge, although the breach width was underestimated by some laws such as Verheij and Van der Knaap's model (Run 5 in Table 4). This could be related to the preferential orientation of the flow through the breach section leaning toward the downstream end of the dike due to the lateral incident flow in the main channel, a dead water area usually forms near the upstream levee end [4, 5].

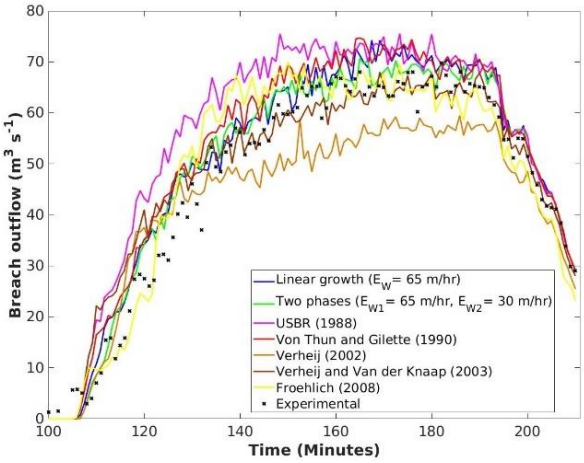

Figure 5. Computed and measured breach discharges.

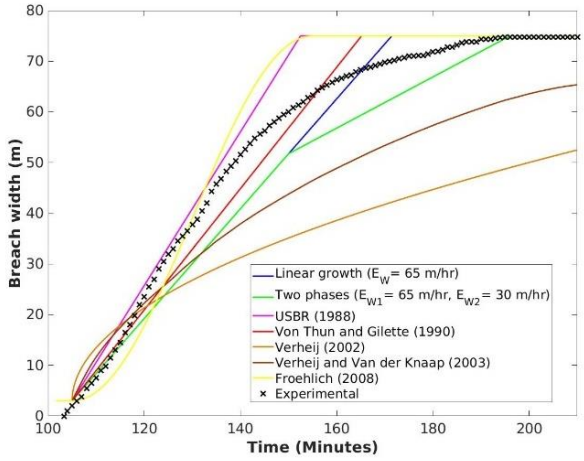

Figure 6. Computed and measured time-evolution of breach width.

For the user defined linear expansion models (both simple and two stages), a short sensitivity analysis was performed to assess the effect of the breach growth rate. Resulting breach outflow and widening are presented in Figures 7 and 8 and Normalized Root-Mean-Square Error (NRMSE) values are compared in Table 3. For the simple linear model three different widening rates were tested. In terms of NRMSE values test with E_w = 55 m/hr achieved the best agreement, but test with E_w = 65 m/hr displayed a more conservative estimate of breach outflow and was therefore retained. For the two phases linear representation of breach growth, two tests were performed and a good compromise between breach lateral growth and discharge prediction was obtained for E_{w1} =65 m/hr and E_{w2} =30 m/hr, although breach width is best estimated for E_{w1} =76 m/hr and E_{w2} =19 m/hr.

TABLE 3. LINEAR GROWTH MODEL INPUTS AND NRMSE.

Model	E_{w1} =76 m/hr	E_{w1} =65 m/hr	E_{w1} =55 m/hr	E_{w1} =76 m/hr, E_{w2} =19 m/hr	E_{w1} =65 m/hr, E_{w2} =30 m/hr
NRMSE	11.5%	7.5%	5%	10.2%	6.8%

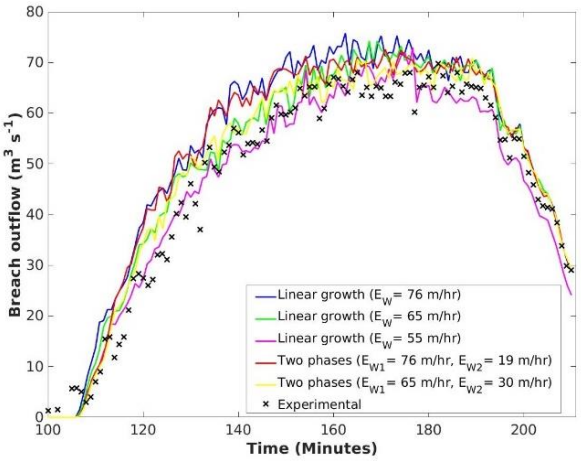

Figure 7. Computed breach discharges with the simple linear and two stages model compared to measurements.

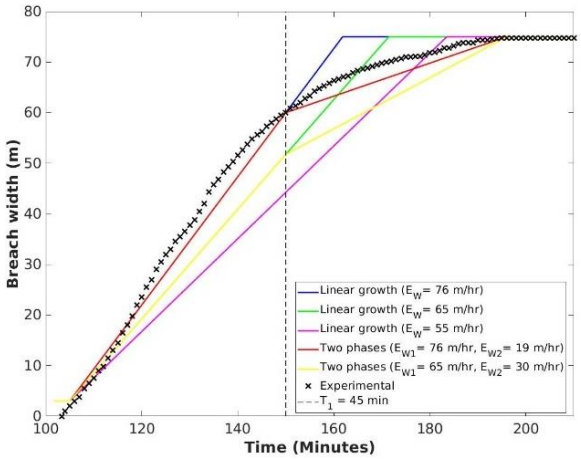

Figure 8. Computed breach widths with the simple linear and two stages model compared to measurements.

For the Froehlich model, a first run was performed with a lateral expansion period equal to that observed experimentally, as the ultimate breach width was reached 90 min after the initiation time, but this value did not allow a satisfactory concordance with measurements. As shown in Figures 9 and 10, the breach discharge fast increase was not captured using a duration of 90 min. The duration T_f was then adjusted and set to 50 min, which led to a better agreement with reported measurements. Figure 11 shows the computed longitudinal breach profile at the crest level (y = 89 m) for T_f = 50 min, evolving in a trapezoidal-like shape.

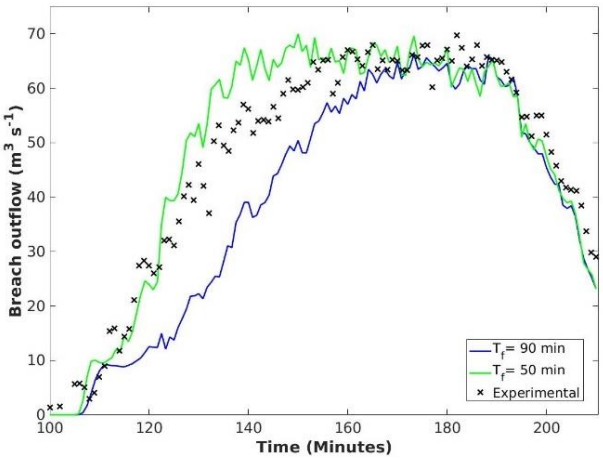

Figure 9. Computed breach discharge with Froehlich's model compared to measurements.

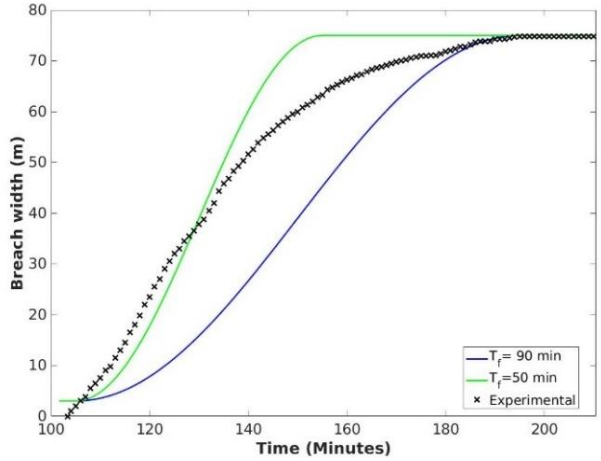

Figure 10. Computed breach width with Froehlich's model compared to measurements.

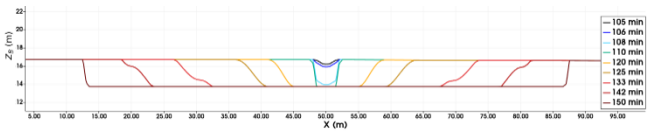

Figure 11. Longitudinal breach profile at the crest level (y=89 m) computed with Froehlich's model for T_f = 50 min.

For the Verheij and Van der Knaap formulation [14], a short analysis was carried out. The model was first tested in its original formulation considering water level difference upstream (channel side) and downstream (floodplain side)

the dike. A comparison is made in Run 1 and 2 (Table 4) between two different methods to compute this difference. First, by taking the average value of the computed water level differences along the dike defined location from the channel and floodplain side (Run 1). In the second run, the maximum value is used (Run 2). The two additional runs (Run 3 and 4) used the hydraulic head instead of water level to account for the effect of flow velocity. In the same way as Runs 1 and 2, the average and maximum hydraulic head difference values were used in Run 3 and Run 4, respectively. The additional Run 5 is similar to Run 4, but the coefficient f_2 was set to 0.06 instead of 0.04 (Run 4). Figures 12 and 13 highlight an influence of both considered hydraulic variable (water level and hydraulic head) and computation method of the difference term (maximum or average value). One can see improved results in Run 2 and Run 4 when compared to Run 1 and Run 3, respectively. In the same way, breach dynamics and discharge are better captured in Run 4 and Run 3 than Run 2 and Run 1, respectively.

The formulation with maximum value of hydraulic head difference was the version conserved in the Breach module of TELEMAC-2D, as it is demonstrated here to achieve the best performance in terms of breach evolution and discharge prediction. Run 5 highlights the effect of breach width empirical parameters, which default values, can be adapted and bring further improvements into Verheij and Van der Knaap formula capabilities.

TABLE 4. PERFORMED RUNS WITH VERHEIJ AND VAN DER KNAAP [14] FORMULA.

Run 1	Average $(h_{up} - h_{down})$ h denotes water level	
Run 2	Max $(h_{up} - h_{down})$	$f_1 = 1.3, f_2 = 0.04,$ $u_c = 0.23$ m/s
Run 3	Average $(H_{up} - H_{down})$ H denotes head	
Run 4	Max $(H_{up} - H_{down})$	
Run 5	Max $(H_{up} - H_{down})$	$f_1 = 1.3, f_2 = 0.06,$ $u_c = 0.23$ m/s

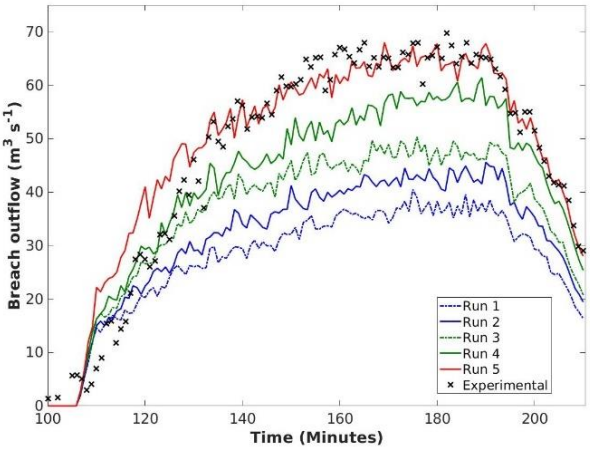

Figure 12. Verheij and Van der Knaap formulation - Computed and measured breach discharges.

Table 5 summarises the different parametric models required for each law as well as values of NRMSE calculated for the breach discharge. When the performances of these models are compared with each other, the best result is obtained from the two stages linear breach development model as it gives the lowest NRMSE values, while the highest values were calculated for the USBR (1988) and Verheij (2002) laws. When selecting a breach model, one should not only consider model performances on a particular case but also include the reliability and availability of data and information about the case of interest and their compatibility with available models. The Verheij and Van der Knaap (2003) formula led to satisfactory results and seems to be a good choice when poor information is available about breach dimensions and lateral expansion duration process as there is no need to pre-define the latter parameters.

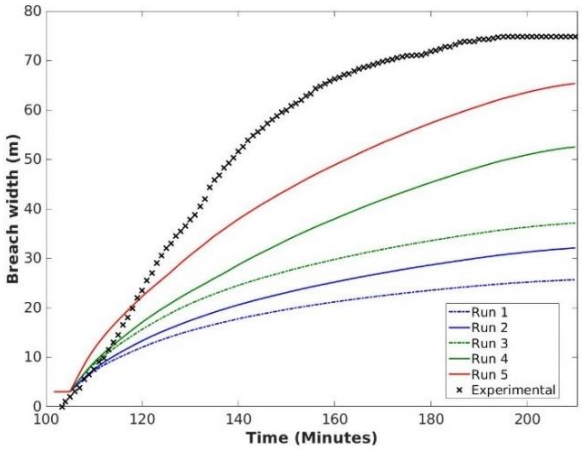

Figure 13. Verheij and Van der Knaap formulation - Computed and measured breach widths.

TABLE 5. EMPIRICAL LAW INPUTS AND BREACH DISCHARGE NRMSE

Empirical model	B_f or T_f	T_d	Other parameters	NRMSE Breach discharge
Linear		⊠		7.5%
Two stages	⊠	⊠	T_1, E_{w1}, E_{w2}	6.7%
USBR [11]	⊠	⊠		15.6%
Von Thun and Gillette [12]	⊠	⊠		8.2%
Verheij [13]	⊠	⊠		12.4%
Verheij and Van der Knaap [14]		⊠	f_1, f_2, u_c	8.3%
Froehlich [7]	⊠	⊠		8.6%

IV. CONCLUSION

In the present paper a set of parametric laws for breach expansion were presented and implemented in the breach module of TELEMAC-2D. Their performances were investigated through a field case experiment of a non-cohesive dike breaching highlighting the ability of the 2D hydrodynamic model and parametric breach models to predict breach discharge, which is a critical parameter for flood risk assessment and management. Although the simplified laws assume symmetrical breach widening and idealized breach longitudinal sectional profile (rectangular or trapezoidal shape), they have been shown to provide accurate results provided they are calibrated.

The use of simple geometric breach simulation methods is time efficient. On the other hand, they require user input choices and information about breach initiation, shape, and dimensions to be defined *a priori*. It is thus important to choose a model according to data availability and reliability about input parameters (reported erosion rates for similar cases, soil composition, breach duration and durations). It was also demonstrated that the modified Verheij and Von der Knaap formula, in which we used the head differences instead of the water level difference, performed better than the original formulation on the simulated case and represents an interesting possibility for levee breach modelling, as it only requires a few input parameters without the need to specify final breach width or widening duration. Further work will integrate additional field scale experiments and historical levee failure cases modelling to investigate the validity of the present conclusions.

REFERENCES

[1] ASCE/EWRI Task Committee on Dam/Levee Breaching, "Earthen embankment breaching," Journal of Hydraulic Engineering, 2011.

[2] M. West, M. Morris and M. Hassan, "A guide to breach prediction," HRPP770, Craig Goff, HR Wallingford, 2018.

[3] EUCOLD Working Group on Levees and Flood Defences, "European and US levees and flood defences: characteristics, Risks and Governance," 2018.

[4] I. Rifai, "Physical and numerical modelling of overtopping induced fluvial dike failure," Ph.D. thesis, University of Paris-Est and University of Liège, 2018.

[5] T. Kakinuma and Y. Shimizu, "Large-scale experiment and numerical modeling of a riverine levee breach," Journal of Hydraulic Engineering, 2014.

[6] T. Shimada, Y. Watanabe, H. Yokoyama and T. Tsuji, "Levee Breach Experiment by Lateral Overflow at the Chiyoda Experimental Flume," Journal of Japan Society of Civil Engineers, Ser. B1 (Hydraulic Engineering), 2009.

[7] D. C. Froehlich, "Embankment dam breach parameters and their uncertainties," Journal of Hydraulic Engineering, 2008.

[8] FERC, USA Federal Regulatory Commission, "Notice of Revised Emergency Action Plan Guidelines," 1988.

[9] T. Wahl, "Prediction of embankment dam breach parameters: a literature review and needs assessment," U.S. Department of the Interior, Bureau of Reclamation, 1988.

[10] D. Resio, S. Boc, S. Maynord, D. Wal, D. Abraham, D. Dudeck and B. Welsh, "Development and Deployment of Rapid Repair of Levee Breaching Technology" Report to Southeastern Regional Research Initiative, Department of Homeland Security, 2009.

[11] USBR (United States Bureau of Reclamation), "Downstream hazard classification guidelines," ACER Technical Memorandum No. 11, United States Department of the Interior, 1988.

[12] J. L. Von Thun and D. R. Gillette, "Guidance on breach parameters," Internal Technical Memorandum, United States Bureau of Reclamation, Denver, Colorado, 1990.

[13] H. Verheij, "Time dependent breach development in cohesive material," Internal Research Summary Report, Delft Hydraulics Laboratory, 2002.

[14] H. Verheij and F. Van der Knaap, "Modification breach growth model in HIS-OM," Technical report, WL | Delft Hydraulics, Delft, The Netherlands, 2003.

[15] D. L. Fread and T. E. Harbaugh, "Transient hydraulic simulation of breached earth dams," Journal of. Hydraulic Division, 1973. G. L. Brunner, "HEC RAS - River analysis system user's manual, version 3.1." Rep. No. CPD-68, U.S. Army Corps of Engineers, Hydrologic Engineering Center, Davis, CA, 2002.

Determination of initial soil moisture for a small highly erodible mountain basin with TELEMAC

Cécile Delcourt
Polytech Sorbonne
Paris, France

Florent Taccone
Laboratoire d'Hydraulique et Environnement
EDF R&D
Chatou, France
florent.taccone@edf.fr

Olivier Delestre
Laboratoire J.A Dieudonné
UMR CNRS 7351
Université Côte d'Azur
Nice, France
olivier.delestre@univ-cotedazur.fr

***Abstract*— Modelling the hydro-sedimentary dynamics of highly erodible watersheds is a difficult task. Indeed, some conceptual models are flawed in highly erodible watersheds. Physically based model can be more efficient to model the hydro-sedimentary dynamics in these cases.**

A physically based model governed by the Saint-Venant equations, and the advection equation was therefore created under the TELEMAC-MASCARET system. This model is composed of two modules: a hydraulic module and a sedimentary module. In this study, the hydraulic model and especially the infiltration model based on a two layers Green-Ampt model is implemented. The infiltration depends on the initial soil moisture. However, this infiltration model has some limitations and cannot be considered as fully predictive. Indeed, the initial soil moisture has a significant impact on the simulated outlet discharge. Therefore, the main goal of this study is to improve the predictability of this initial soil moisture and find if a correlation between previous rainfalls, seasonality and initial soil moisture exists.

To carry out this study, the Roubine, a small watershed basin tributary of the river the Bléone located on the Draix site in the Southern French Alps is chosen. This watershed is a gully-sized watershed (0.13 ha) with steep slopes of about 35-45° and low vegetation cover (21%). The Roubine is a part of the sub-catchments monitored for about 30 years by the INRAE Observatory of Draix/Bléone. These watersheds, sensitive to erosion, have been equipped to monitor discharge and sediment concentration at the outlet. The multitude of data measured during various seasons over different years are particularly interesting for hydrological modelling.

23 rainfall events corresponding to intense rainfall and generating high outlet discharge (2 l/s to about 20 l/s) were selected. The selected events cover spring, summer, and early fall. For each event, calibration of simulated outlet discharge on measured outlet discharge by adjusting the initial soil moisture is carried out. From this, the initial soil moisture is deduced for each considered event.

Among the results of this study, the main finding of this study is the clear correlation between initial soil moisture and previous rainfalls for a specific period.

I. INTRODUCTION

The poorly vegetated watershed of the Bléone, the Roubine is located at an altitude of 800-900 m on the Draix site in the Southern French Alps as Fig. 1 shows. The Roubine is characterized by the presence of black marl. The climate is Mediterranean mountain with an average rainfall of 900 mm per year. Winter is characterized by a period of freeze-defreeze and low rainfall, spring by a period of more sustained rainfall, summer by a period of heavy thunderstorms and fall by a period of low but continuous rainfall [3]. The two rainiest periods are April/May and September/October, October being is the wettest month of the year. Usually, only two or three isolated thunderstorms make up the rainfall in August [12]. Hortonian runoff is particularly associated with Mediterranean and Cevennes-type storms with short and very intense rainfall. When the intensity of rainfall exceeds the infiltration capacity of the soil, it creates a runoff on the slopes [8].

The climate, the geology and the topography are fully involved in natural phenomena encountered in the region. All these characteristics make the watershed susceptible to erosion and are the cause of variations in initial soil moisture.

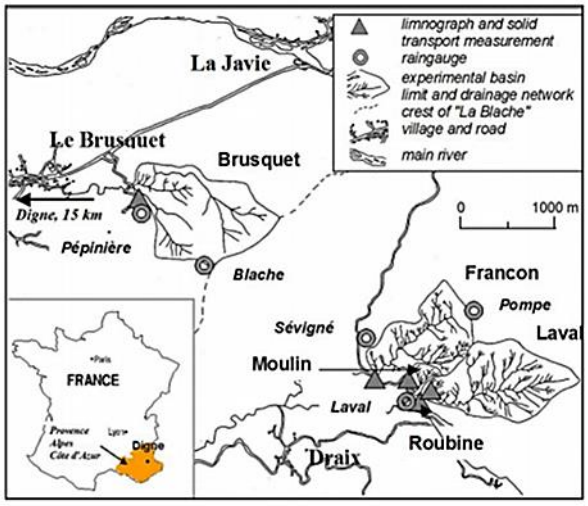

Figure 1. The experimental basins of Draix (Mathys et al., 2005)

Modelling the hydro-sedimentary dynamics of highly productive watersheds is part of a natural hazard forecasting approach. There are numerous EDF structures located downstream of this watershed. In order to prevent damages and to protect the EDF structures, it seems interesting to estimate the quantity of sediments causing the eventual filling of the reservoirs and to predict the arrival of sediments at those structures. Establishing a link between precipitation and the dynamics of sediment uptake and storage towards the hydrographic network is searched. This is the subject of modelling.

Conceptual models intent to answer this question. MORDOR TS is a software developed by EDF to quantify the filling of reservoirs. However, this type of model does not allow to easily represent the inflows from highly productive sub-basins such as the watersheds located near Draix. Physically based models seem to be more appropriate: many have been developed in recent years at the watershed scale for example CASC2D [10], MIKE SHE [6], WaSiM [18], openLISEM [9]. Most of them use kinematic or diffusive wave equations to model hydraulic transfers [14]. However, this may be insufficient for some cases, especially in the presence of debris flows or mudflows [15]. Therefore, a physically based model governed by the Saint-Venant equations has been created under TELEMAC-MASCARET and validated on the Laval [19]. This model is used for this study and the Roubine is considered.

The main limitation of the model is the predictability. Indeed, this model cannot be considered predictive regarding some parameters such as the initial soil moisture, cohesion-shear stress and sediment availability. The precise knowledge of this hydric state and its consideration in rainfall-flow modelling remains one of the current problems in hydrology. This study focuses on the initial soil moisture being one of the major controlling factors of the runoff process. The moisture content of the watershed at the start of a hydrological model forecast has a strong influence on the simulated discharge [17] [20] [23]. Properly estimating the corresponding state variables is crucial for obtaining a suitable simulation. This initial soil moisture has already been studied. Usually, field measurements are made to determine the initial soil moisture [11] [15] [22]. However, in-situ measurements are too punctual and difficult to generalize. In this paper, modelling is used to determine initial soil moisture. For each event, the initial soil moisture is adjusted to calibrate the simulated outlet discharge on measured outlet discharge. Thus, this calibration allows to deduce the initial soil moisture for each event. Then this initial soil moisture will be related to the rainfall that occurs before each rain event.

In this paper, the methodology and a presentation of the TELEMAC 2D model above-mentioned are presented. Then examples of discharge simulations and initial soil moisture results will be presented.

II. Materials and Methods

A. *Method used*

To find a link between initial soil moisture and rainfalls/seasonality, it was decided to choose rain events and for each one we intent to calibrate the simulated discharge on measured flow. These data are taken from Draix-Bléone Observatory [4].

These events were selected because they correspond to intense rainfalls and generated high outlet discharge for the Roubine. Indeed, the model has difficulty to reproduce low rainfall events [19]. What was shown on the Laval turned out to be also the case for the Roubine. In addition, low flows (<2 l/s) are not very interesting for the study, they do not cause significant sediment transport. A few extreme events per year give most sediment exports at the catchment outlet [1]. Therefore, these events cover the period of spring, summer and early fall, the most intense rainfalls and highest flows occurring in this period.

Then the model is calibrated to reproduce the peak discharge. This consists in finding the initial soil moisture that minimizes the difference between the simulated and measured peak discharges for each selected event.

If the peak discharge is well reproduced, the rain event is considered to deduce link between initial soil moisture, seasonality and previous rainfall. Tab. 1 shows the 23 rain events selected.

Table 1 Events considered

F. Months	*G.* Date
H. May	*I.* 11 May 2001, 14 May 2011, 26 and 29 May 2012
J. June	*K.* 5 June 2003, 4 and 5 June 2007, 10 June 2008, 22 June 2005, 28 June 2001
L. July	*M.* 4 July 2005, 7 July 2013, 8 July 2004, 13 July 2011, 16 July 2014, 25 July 2001, 29 July 2013
N. August	*O.* 3 and 5 August 1998, 18 August 2004, 20 August 2010
P. September	*Q.* 11 September 2005
R. October	*S.* 13 October 2014

B. Modelling with TELEMAC 2D

A physically based model governed by Saint-Venant equations, and the advection equation was therefore created under TELEMAC-MASCARET. For this case study the V8P2 version of TELEMAC-MASCARET is used and an infiltration module has been added. We are considering the hydraulic model and especially the infiltration model which represents only a vertical infiltration profile in each cell of the domain [16]. Therefore, the equations presented will be one-dimensional equations.

Eq. 1 represents the Saint-Venant system:

$$\begin{cases} \dfrac{\partial h}{\partial t} + \dfrac{\partial hu}{\partial x} = R - I \\ \dfrac{\partial hu}{\partial t} + \dfrac{\partial \left(hu^2 + \dfrac{gh^2}{2} \right)}{\partial x} = gh(-\dfrac{\partial z}{\partial x} - S_{fx}) \end{cases}; \quad (1)$$

where one has:

- g the gravity constant (m/s^2) ;
- h the water depth (m);
- S_{fx} the friction term according to x axis;
- t the time (s);
- u the flow velocity (m/s);
- z the bottom depth (m);
- R the precipitation rate (m/s);
- I the infiltration rate (m/s).

h, u and z are the unknows.

The friction term S_{fx} is calculated using the Chézy friction formula as Eq. (2) shows:

$$S_{fx} = \frac{q|q|}{C^2 h^3}; \quad (2)$$

where one has:

- q is the linear flow rate (m^2/s);
- C is the Chézy coefficient (m$^{1/2}$/s);
- h is the water depth (m);

The first equation is the continuity equation and represents the water runoff in the watershed. This equation uses the infiltration model. It is this infiltration rate that relies on the initial soil moisture.

The Infiltration model (3) is based on Green-Ampt model [7].

$$I = \left(1 + \frac{h_f + h}{z_f} \right) . K; \quad (3)$$

where one has:

- h_f a constant representing the capillarity head of the wetting front (m);
- h representing the water depth (m);
- z_f is the wetting front position (m) which depends on the initial soil moisture θ_i, the total cumulative infiltration I_t and the water content of the saturated soil θ_s as shown in Eq. 4:

$$z_f = \frac{I_t}{\theta_s - \theta_i}; \quad (4)$$

- K the hydraulic conductivity (m/s).

To estimate the hydraulic conductivity, two layers are considered [7]. The thickness of the first layer is noted Z_c, its hydraulic conductivity K_c and its porosity θ_1. The second layer is considered infinite. Its hydraulic conductivity is noted K_s and its porosity θ_2. The layers are considered as homogenous in the horizontal directions.

The equivalent hydraulic conductivity K depends on the position of the wetting front. If the wetting front is in the first layer, K is equal to a constant corresponding to the hydraulic conductivity of the first layer. When the wetting front exceeds the first layer, K becomes variable as Eq. 5 shows:

$$K = \frac{z_f}{\dfrac{z_f - Z_c}{K_s} + \dfrac{Z_c}{K_c}}; \quad (5)$$

The values retained are the following:

- $Z_C = 0{,}08$ m;
- $\theta_1 = 0{,}35$;
- $\theta_2 = 0{,}25$;
- $K_c = 30$ mm/h;
- $K_s = 1$ mm/h.

The low conductivity of the second layer allows to compensate the exfiltration neglected in this model.

The Z_c value comes from basin measurements [13]. The other ones have been chosen to obtain a porous first layer and a more structured base layer [1].

C. Discretization of the study domain

To solve the equations (1), the finite volume method is chosen. The numerical scheme is the Kinetic scheme [2] using Chen and Noelle hydrostatic reconstruction [5].

SALOME-HYDRO V2.2 is chosen to create the geometry and the mesh. To discretize the domain, one 2D triangular mesh is applied on the study domain as shown in Fig. 2.

The interest of this triangular mesh is it allows to faithfully represent the geometry of the study area. In addition, a 1D sub-mesh of the same size was applied to the polylines extracted by computing the flux accumulation method of QGIS in order to obtain a better representation of riverbank. This stress line represents the hydrographic network

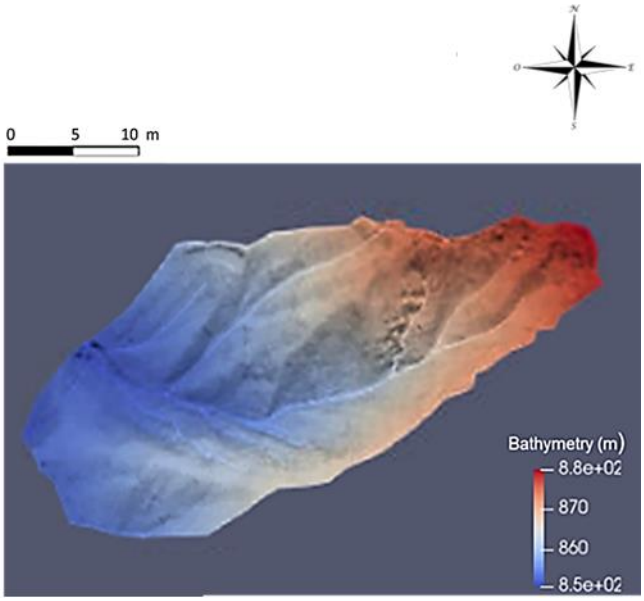

Figure 2. Bathymetry of the studied area, Paraview

The mesh size chosen is 20 cm. Fig.3 displays a part of this mesh. This mesh size allows to reconcile accuracy of the simulated solution and computational time. Mesh sizes of 10 cm and 50 cm were tested. The advantage of the 50 cm mesh size is its computation time, 15 times lower than 20 cm. However, the program has difficulties to converge (ill-posed problem). On the other hand, a 10 cm mesh size sees its computation time increase compared to 20 cm (three times higher than that of 20 cm).

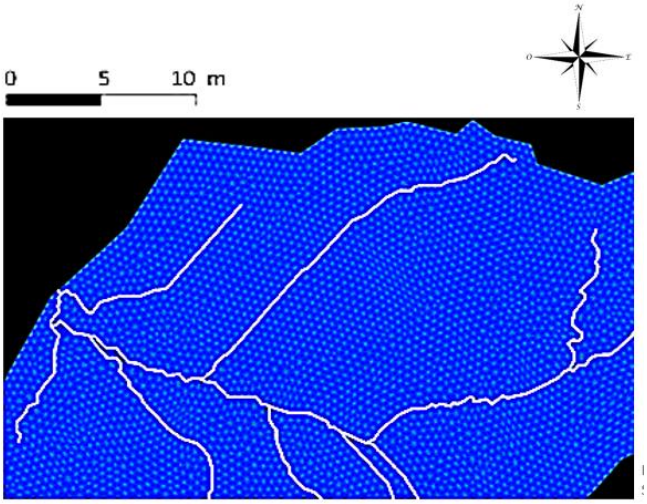

Figure 3. Mesh with the hydrographic network, Salomé Hydro

III. RESULTS

Not all rain events are well simulated. As previously stated, low intensity rain events are difficult to reproduce in their entirety. Three examples have been chosen to illustrate this point.

A. *Examples of simulations results*

Intense and brief rainfall events are well reproduced as shown in Fig.4. An event can be considered as intense when the instantaneous rainfall intensity is greater than about 40 mm/h.

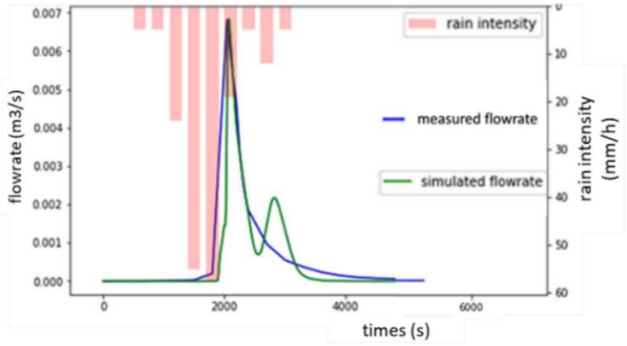

Figure 4. Simulated and measured discharges on May 29, 2012

For this event, the increase in discharge is in phase with the increase in measured flow.

Nevertheless, the model has difficulty reproducing the discharges generated by low (less than 40 mm/h) but continuous rainfall. Fig. 5 presents the simulated and measured outlet discharges for a low spring rainfall event.

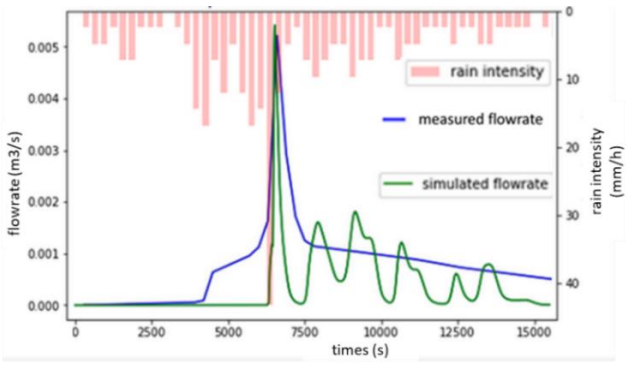

Figure 5. Simulated flow and measured discharge on May 11, 2001

Furthermore, two consecutive flow peaks are poorly reproduced. One is underestimated or overestimated. If we try to represent the maximum flow peak first when there are two consecutive flow peaks, the increase of the initial soil moisture leads to an overestimation of the second lower peak The Fig. 6 presents the result of the simulation of two consecutive peaks flows for an intense rainy event.

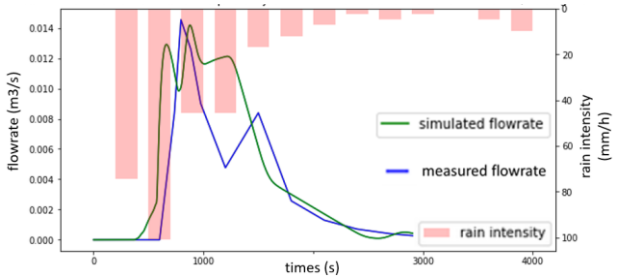

Figure 6. Simulated flow and measured flow on July 29, 2013

This difficulty to represent two peaks seems to be even truer, the more intense the rains are. For instance, the model seems to have difficulties in representing events with one peak due to very intense rainfall (instantaneous rainfall greater than 80 mm/h) and a second peak due to a less intense rainfall.

B. General Results

The initial soil moistures of each event are then grouped by month and previous rainfall is displayed for each event. These results show a strong correlation between initial soil moisture and previous precipitation and a specific trend by season as Fig. 7 demonstrates.

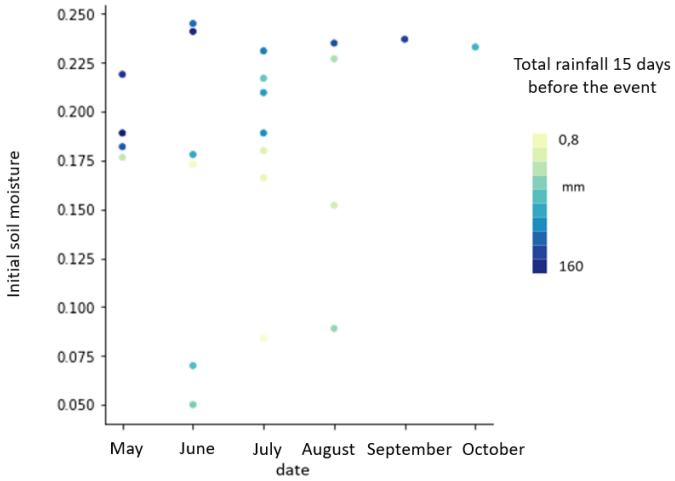

Figure 7. Initial soil moisture as a function of the month of the year and cumulative rainfall 15 days before

C. Cumulative rainfall and initial soil moisture

To identify the link existing between cumulative rainfall and initial soil moisture, cumulative rainfall over the 30 days, 15 days, 10 days and 5 days preceding the events are chosen.

The Fig. 8 and Fig. 9 allow to deduce that the initial soil moisture does not be explained by the cumulative rainfall over the 5 and 10 days prior to the events considered.

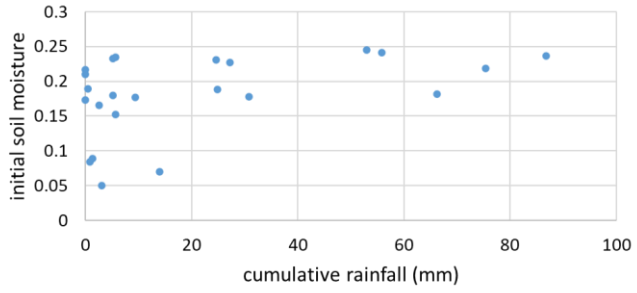

Figure 8. Initial soil moisture as a function of cumulative rainfall over the 5 days preceding the events considered

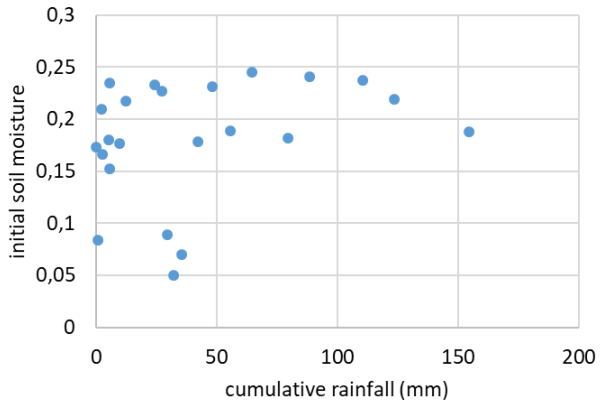

Figure 9. Initial soil moisture as a function of cumulative rainfall over the 10 days preceding the events considered

At the opposite, if cumulative rainfall over 15 and 30 days before the selected events are considered, a logarithmic trend curb can be drawn as illustrated in Fig. 10 and 11. Some initial soil moistures can be explained by cumulative rainfall.

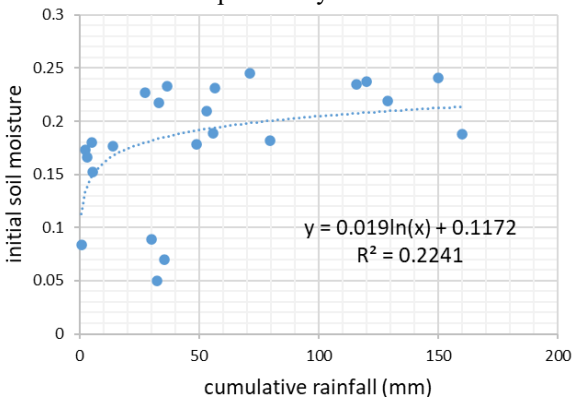

Figure 10. Initial soil moisture as a function of cumulative rainfall over the 15 days preceding the events considered

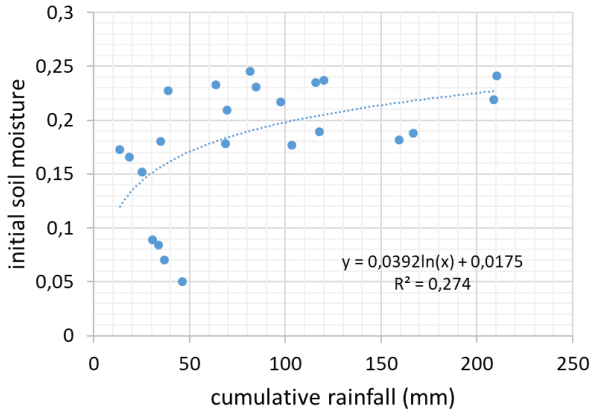

Figure 11. Initial soil moisture as a function of cumulative rainfall over the 30 days preceding the events considered

Then, we intent to group the events by periods of the year in order to obtain a best logarithmic trend curb.

First only spring events are selected. Regarding cumulative over 30 days before, it is possible to draw a trend curb with a high correlation coefficient (60 %) as shown in Fig. 12.

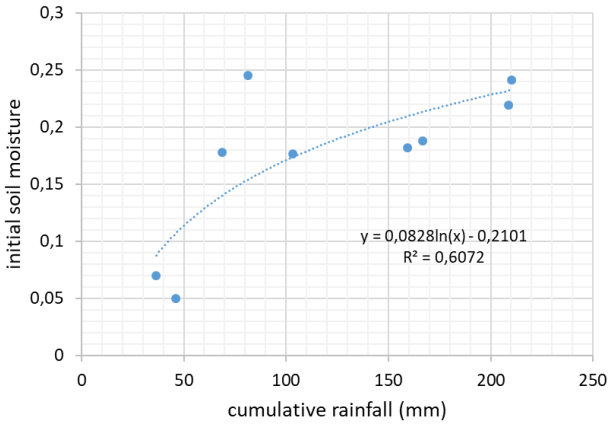

Figure 12. Initial soil moisture as a function of cumulative rainfall over the 30 days preceding the events considered (spring)

Secondly, the months of end of June, July, August, September and early October are grouped and cumulative rainfall over 15 days preceding the events are considered. This allows to explain in the best way the initial soil moisture. Fig. 13 shows the curb trend and the correlation coefficient which is about 47 %. However, the regression is not as good as in spring regression.

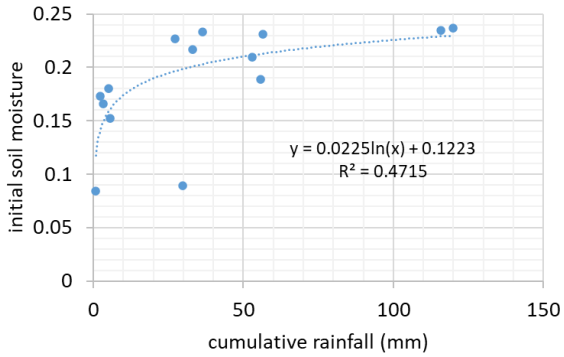

Figure 13. Initial soil moisture as a function of cumulative rainfall over the 15 days preceding the events considered (summer and early fall)

IV. DISCUSSION

This work has provided strong trends and restricted the initial soil moisture to a much smaller range than before. It can be said that the model has gained in predictability. It is therefore possible to consider certain ranges of initial soil moisture if the model is to be used without having discharge measurements, for example on another catchment with little vegetation.
Moreover, this demonstration allowed us to better understand the effects of seasonality on this type of watershed with the effects of previous rainfall.

Nevertheless, these results have some limitations.

The limited number of simulated events can raise the question of reliability of inferences. Adding more events would give us more confidence in our results.
In addition, the measured data quality can impact the results. Firstly, this is linked to the flow and rainfall measurement system. The measurement uncertainties are due to the accuracy of the sensors. Float gauges have an accuracy of 1 cm that leads to an uncertainty on the validated dimension which cannot be less than 0.5 cm. Discharges are similarly impacted being deduced from water height. For a height of less than 30 cm the relative error on the flow is 20 % for 0.5 cm of error on the level [13].
The second reason is related to the recording of the rain gauge. As soon as 2 mm of rain have accumulated on it, the trough is titled. For low rainfall, the intensity of the rain tends to be underestimated.

Furthermore, the DEM chosen for this model is from 2010. The events chosen dating from 1998 to 2013, Roubine topography may have evolved between the date of these events and 2010. So, it may affect the value of the simulated discharge.

The limitations of the model used can also influence the results.

This model is only 1D vertical, without exfiltration, therefore even with a good peak flow setting, the volumes can be wrong. The model also considers uniform conductivities and friction, which is a significant approximation, even if this allows the arrival times of the peaks to be well reproduced.

The method used also has drawbacks. A rain that occurred 30 days before is taken as equivalent to a rain that occurred 2 days before, although this will not have the same impact on the initial soil conditions.

V. CONCLUSION

The purpose of this study was to improve the predictability of the model by trying to establish the relationship between season, precipitation and initial soil moisture. The Roubine watershed, which is very erosive and poorly vegetated, was selected to carry out this study.

The method adopted was as follows. Several intense rainfall events with relatively high flows were selected. For each rainfall event, the model was calibrated to reproduce the peak discharge. This consisted in finding the initial soil moisture minimizing the difference between the simulated and measured peak discharges.

Simulations showed a strong correlation between previous rainfall and initial soil moisture.
The events that took place in summer and early fall could be grouped together to find the relationship between initial soil moisture and previous cumulative rainfall. For summer and early fall, it is sufficient to consider 15 days of previous rainfall.

The same thing could be done for the months of spring. To estimate the initial soil moisture, the cumulative rainfall that occurred 30 days earlier should be considered. The initial soil moisture does not seem to vary a lot.
For some months, it is also possible to consider the cumulative rainfall over 5 rainy days. However, as this requires an even more precise time breakdown, it is less interesting for forecasting.

As a close prospect, to improve the quality of deductions, it can be contemplated to increase the number of simulations and doing the same work with other DEM.
Besides, another way to improve the predictability of the model is to couple TELEMAC-2D with a reservoir model such as MORDOR TS that produces continuous soil moisture indicators using past rainfall and evapotranspiration. This would overcome the difficulty of the TELEMAC-2D model to reproduce the hydraulic part.

REFERENCES

[1] G. Antoine, O. Delestre, N. Goutal, F. Taccone, "A new gravity-driven runoff and erosion model for TELEMAC", TELEMAC-MASCARET User Conference, 2017.

[2] E. Audusse, F. Bouchut, M.-O Bristeau, R. Klein, and B. Perthame, "A fast stable well-balanced scheme with hydrostatic reconstruction for shallow water flows", SIAM Journal on Numerical Analysis, vol.25, pp. 2050-2065, 2004.

[3] J. Bechet, J. Duc, A. Loye, M. Jaboyedoff, C. Le Bouteiller, J.P Malet, N. Mathys, Jacques, B. Rudaz, J. Travelletti,, "Detection of seasonal cycles of erosion processes in a black marl gully from a time series of high-resolution digital elevation models (DEMs)", 2016. Copernicus Publications. doi:10.5194/esurf-4-781-2016

[4] J-P. Cambon, M. Esteves, S. Klotz, C. Le Bouteiller, C. Legout, F. Liebault, N. Mathys, M. Meunier, J.-E. Olivier, and D. Richard. Observatoire hydrosedimentaire de montagne Draix-Bleone. Irstea, 2015. https://doi.org/10.17180/obs.draix.

[5] G. Chen and S. Noelle, "A new hydrostatic reconstruction scheme based on subcell reconstructions", SIAM Journal on Numerical Analysis, vol. 55, pp. 758-784, 2017.

[6] D.N. Graham and M.B. Butts, "Watershed models" in chapter Flexible integrated watershed modelling with MIKE SHE, pp. 245–272, 2005.

[7] W. H. Green and G. A. Ampt, "Studies on soil physics", The Journal of Agricultural Science, vol. 4, pp. 1-17, 1911.

[8] R.E Horton, "The role of infiltration in the hydrologic cycle", American Geophysical Union, pp. 446–460, 1933.

[9] V. Jetten, "OpenLISEM - a spatial model for runoff, floods and erosion", 2013, http://blogs.itc.nl/lisem/.

[10] P.Y. Julien, B. Saghafian, "CASC2D user's manual: a two-dimensional watershed rainfall-runoff model", 2016

[11] F. Mallet, "Spatialisation et modélisation de l'état hydrique des sols pour l'étude des processus de formation des écoulements en contexte torrentiel : application au bassin versant marneux du Laval (ORE Draix-Bléone, Alpes-De-Haute-Provence, France)", Université d'Avignon, 2018. HAL Id: tel-01914950 https://tel.archives-ouvertes.fr/tel-01914950

[12] N. Mathys, D. Richard, "Historique, contexte technique et scientifique des BVRE de Draix. Caractéristiques, données disponibles et principaux résultats acquis au cours de 10 ans de suivi" in Les bassins expérimentaux de Draix, Laboratoire d'étude de l'érosion en montagne, Cemagref, october 1997 (Colloque Draix, le Brusquet, Digne, p.11 -27)

[13] N. Mathys, "Analyse et modélisation à différentes échelles des mécanismes d'érosion et de transport de matériaux solides Cas des petits bassins versants de montagne sur marne (Draix, Alpes-de-Haute-Provence) ", Grenoble INP, 2006. HAL Id: tel-02588905 https://hal.inrae.fr/tel-02588905

[14] E. Meyles, A. William, L. Ternan, J. Dowd, "Runoff generation in relation to soil moisture patterns in a small Darmoor catchment, Southwest England", Hydrological Processes 17, pp. 251–264, 2003.

[15] T. Pellarin, J.-C Calvet, W. Wagner, "Evaluation of ERS scatterometer soil moisture products over a half-degree region in sout western France", Geophysical Research Letters n°33, American Geophysical Union, 2006.

[16] J.B, Philip, "The infiltration equation and its solution" in The Theory of Infiltration, pp. 345-357, 1957.

[17] G, Ravazzani, M. Mancini, I. Giudici, P. Amadio, "Effects of soil moisture parameterization on a real-time flood forecasting system based on rainfall thresholds", Proceedings of Symposium HS2004 at IUGG2007, Perugia, July 2007, vol. 313. IAHS Publ., pp. 407–416.

[18] J. Schulla, "Model Description WaSiM". Swiss Federal Institute of Technology, 2012.

[19] F. Taccone, "Modélisation numérique du transfert sédimentaire en bassin versant montagneux fortement érodable", Université Paris-Est, 2018. https://pastel.archives-ouvertes.fr/tel-02138069

[20] M. Uber, J.P. Vandervaere, I. Zin, Isabelle Braud, M. Heisterman, C. Legout, G. Molinié and G. Nord. "How does initial soil moisture influence the hydrological response? A case study from southern France", Hydrology and Earth System Sciences, European Geosciences Union, vol. 22, pp. 6127-6146, 2018.

[21] V.P. Singh, "Is hydrology kinematic?", Hydrological processes, vol. 16, pp. 667-716.

[22] J.P. Walker, G.R Willgoose, G.R., J.D Kalma, "In situ measurement of soil moisture: a comparison of techniques". Journal of Hydrology n°293, pp. 85–99, 2004.

[23] E. Zehe, R. Becker, A. Bárdossy, E. Plate, "Uncertainty of simulated catchment runoff response in the presence of threshold processes: role of initial soil moisture and precipitation", Journal of Hydrology n°315, pp. 183–202, 2005.

Two and three-dimensional numerical modelling of flow patterns in shallow rectangular reservoirs

El Mehdi CHAGDALI[1,2], Cédric GOEURY[2], Jacques FONTAINE[2], Matthieu SECHER[3], Sébastien ERPICUM[4], Benjamin DEWALS[4], Kamal EL KADI ABDERREZZAK[1,2]

[1] EDF R&D, National Laboratory for Hydraulics and Environment, France
[2] Saint Venant Laboratory for Hydraulics, University Paris-Est, France
[3] EDF Hydro – CIH, France
[4] University of Liege (ULg), Research Group of Hydraulics in Environmental and Civil Engineering, Belgium

Email: el-mehdi.chagdali@edf.fr

***Abstract*—Two- and three-dimensional numerical models TELEMAC-2D and TELEMAC-3D are used for simulating laboratory experiments of steady flow in shallow rectangular reservoirs. Using TELEMAC-2D, various user-defined parameters and options are tested. In particular, six turbulence models are evaluated, along with a grid size sensitivity. Using the finite element and finite volume approaches, several numerical schemes for solving the advection step for velocity and turbulence are compared. For all laboratory configurations, the measured and computed horizontal velocity fields are compared. Satisfactory results are obtained with TELEMAC-2D using the Spalart-Allmaras turbulence model. The effect of numerical scheme is very weak. A comparison between TELEMAC-2D and TELEMAC-3D is performed using the k–ε turbulence model with LIPS scheme for the particular C-C reservoir configuration. The 3D simulations slightly improve the results.**

I. INTRODUCTION

The loss of effective storage capacity in shallow reservoirs due to sediment accumulation decreases reservoir's functionality for flood control, hydropower generation, irrigation and water supply. Sedimentation within these reservoirs depends on the flow, which can exhibit different patterns depending on the reservoir shape, boundary conditions and sediment input characteristics [4, 10]. The flow field can feature symmetric and asymmetric patterns with reattachment points [7] or a meandering jet [8]. Optimal design and management of shallow reservoirs need accurate prediction of the sedimentation areas and thickness, which can be supported by detailed analyses of flow patterns.

Previous numerical studies of flow in shallow basins have dealt mainly with laboratory configurations [2, 10, 12], and to a lesser extent with real basins [3], using generally 2D depth averaged models. These studies did not examine the effect of different model parameters and options, such as numerical schemes, turbulence models and mesh grid size. The present work focuses on the numerical modelling of flow in shallow rectangular reservoirs with varying boundary conditions [4]. A detailed study of the effects of various user-defined parameters is performed with TELEMAC-2D. Additionally, a comparison between TELEMAC-2D and TELEMAC-3D is conducted for a particular reservoir configuration.

II. DESCRIPTION OF LABORATORY EXPERIMENTAL CASES

Laboratory experiments conducted at Ecole Polytechnique Fédérale de Lausanne (EPFL), Switzerland, are simulated [1]. The experimental setup consisted of a rectangular PVC basin, L = 4.5 m long and B = 4 m wide, and two rectangular free surface channels, l = 1 m long and b = 0.25 m wide each (Figure. 1). The reservoir and channels were at the same bottom elevation. In the present work, one symmetric and three asymmetric cases are simulated, referred to as C-C, L-L, L-R and C-R, respectively. The inlet channel was fed with a clear, constant water discharge of Q = 7 L/s, while a flap gate located at the outlet channel end regulated the flow depth in the reservoir at h = 0.2 m. The horizontal velocity field was measured using UVP transducers placed at 8 cm (= 0.4h) from the bottom. The Froude and Reynolds numbers in the inlet channel are $\mathrm{Fin} = Q/(bgh^{3/2}) = 0.1$ and $\mathrm{Rin} = V_{in}\,4h/\nu = 4Q/(b\nu) = 112,000$, with g as the gravitational acceleration and V_{in} the flow velocity in the inlet channel.

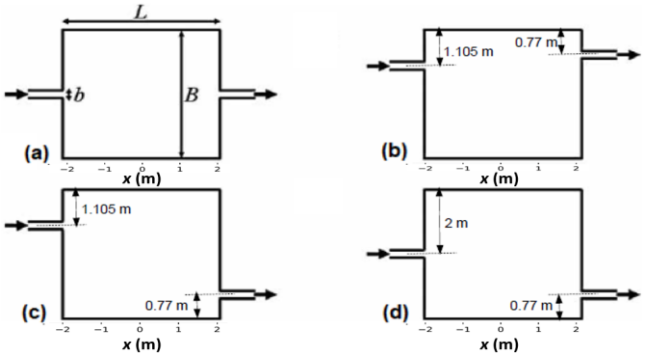

Figure 1. Plane view of laboratory configurations: (a) C-C, (b) L-L, (c) L-R, and (d) C-R. Note the origin of x-axis is taken at middle of the basin.

III. BRIEF DESCRIPTION OF NUMERICAL MODELS

The simulations are performed with the 2D hydrodynamic model TELEMAC-2D [5], which solves the Saint-Venant equations, and the 3D model TELEMAC-3D [5], which solves the Navier-Stokes equations. Several numerical schemes for

solving the advection step of velocity and turbulence as well as several turbulence closure models are available [5]. The Strickler formula is used for the friction term; a value of 80 $m^{1/3}s^{-1}$ (corresponding to PVC) is retained for the bed. The effect of sidewall friction was tested and no influence on the numerical results was noted. For the sake of brevity, results are shown for selected configurations.

IV. 2D-NUMERICAL STUDY

A. *Effect of numerical schemes*

Using the finite element approach, the method of characteristics, the N scheme, the Positive Streamwise Invariant (PSI) distributive scheme, the PSI scheme with Locally semi-Implicit Predictor-corrector Scheme (LIPS), and the Element by element Residual distributive Iterative Advection scheme (ERIA) for solving the advection step for velocity and turbulence are compared [9, 11]. In all the configurations, a CFL number lower than 0.8 is used; the mesh size is 0.025 m. Figure 2 illustrates measured and computed cross-sectional profiles of the longitudinal velocity for k–ε and Spalart-Allmaras turbulence models for the C-C configuration. The effect of numerical schemes is very weak. This finding remains valid for other reservoir configurations and turbulence models.

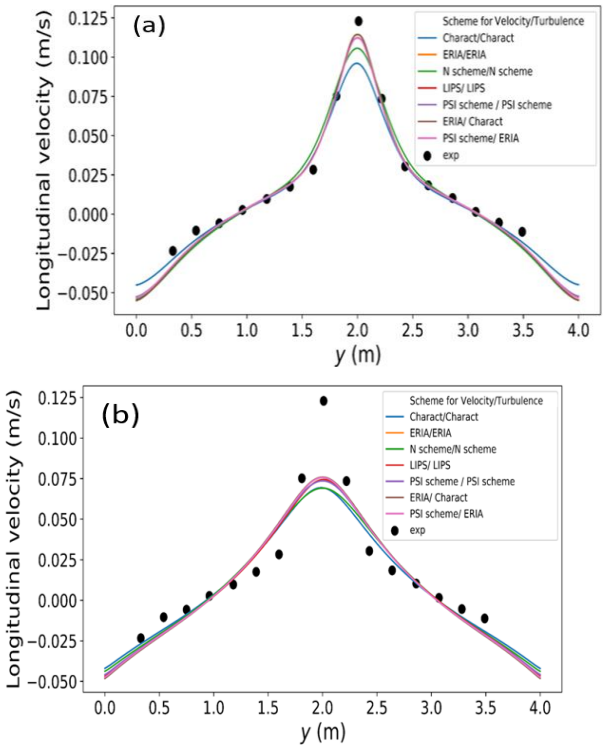

Figure 2. C-C configuration: Results for (a) k–ε turbulence model, and (b) Spalart-Allmaras (SA) turbulence model. Measured and computed cross-sectional profiles of longitudinal velocity at $x = 0.71$ m using finite element approach, with different numerical schemes for advection. Mesh size of 0.025 m.

Using the finite volume approach, the second order scheme in time and space WAF (Weighted Average Flux) for advection of velocity and turbulence is tested. The CFL number is set at 0.8. The finite volume approach with WAF scheme yields an oscillatory flow pattern that was not observed experimentally (Figure 3). Changing the mesh size (0.0125 m and 0.05 m, instead of 0.025 m) does not improve the numerical results. With this version of TELEMAC-MASCARET (V8P1), the finite element approach provides better results than the finite volume approach.

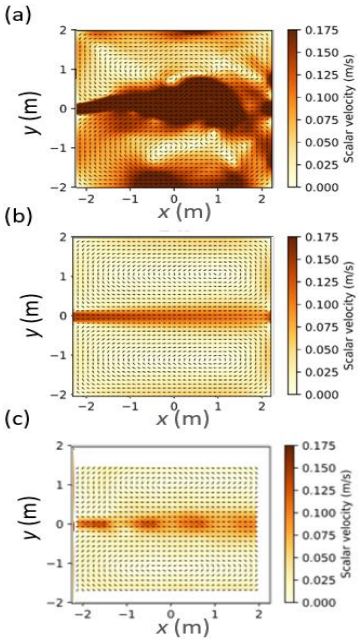

Figure 3. C-C configuration: (a) Oscillatory flow state found using finite volume approach, (b) finite element results, and (c) measurements. Numerical results for k–ε turbulence model, WAF for finite volume and LIPS for finite element for advection of velocity and turbulence. Mesh size of 0.025 m.

B. *Effect of turbulence models*

Using the finite element method, six turbulence models are evaluated: the Spalart-Allmaras (SA) model [6], the standard k–ε model, the constant viscosity model, the Elder model, the Smagorinsky scale model, and the depth-averaged Mixing Length turbulence model. The Locally semi-Implicit Predictor-corrector Scheme (LIPS) is used with a CFL number lower than 0.8 and a mesh size equal to 0.025 m. Model-data comparisons are shown in Figure 4.

The Spalart-Allmaras (SA) model reproduces correctly the measurements for the four configurations (Figure 4b). Spalart-Allmaras, which is one-equation model, has also the advantage to be less computational time consuming, but reproduces less well the velocity magnitude (Figure 2b).

The standard k–ε model reproduces fairly well the velocity magnitude and vector, except for the L-R case, where a flow field with one reattachment point was observed experimentally, but not numerically (Figure 4c). Using a k–ε turbulence model, Camnasio et al. [10] showed that employing a steady flow pattern with lateral reattachment as initial conditions allowed for more satisfactory model-data agreement. Similar results are obtained with TELEMAC-2D (Figure 5).

(a) Experimental

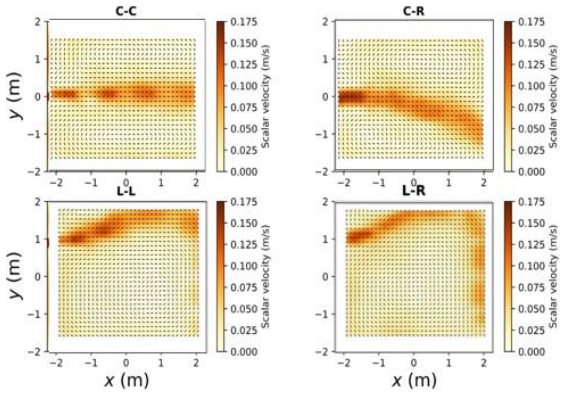

(b) Spalart-Allmaras (SA) turbulence model

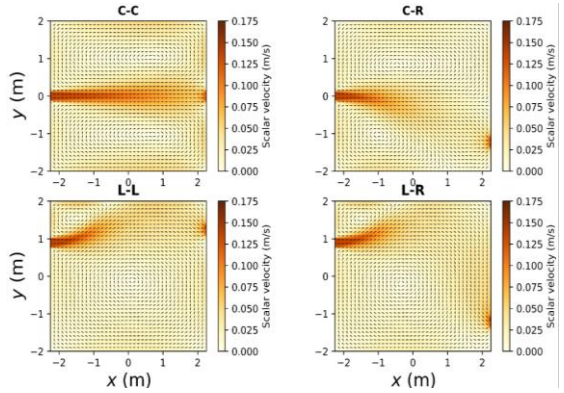

c) k–ε turbulence model

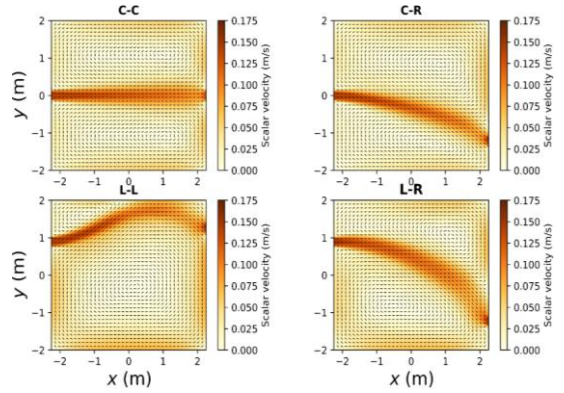

(d) Constant viscosity (10^{-3} m² s^{-1}) turbulence model

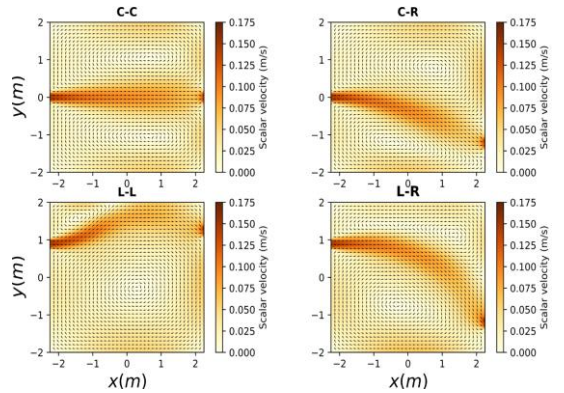

(e) Elder turbulence model

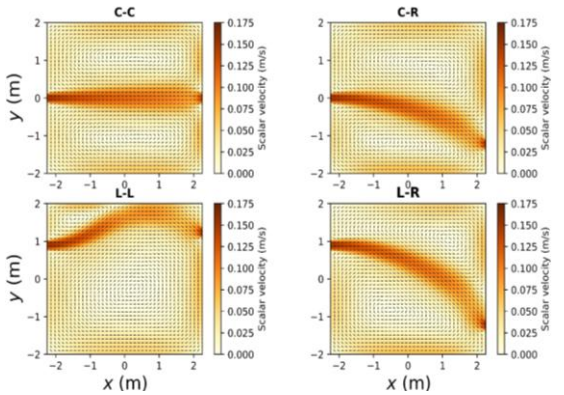

(f) Smagorinsky turbulence model

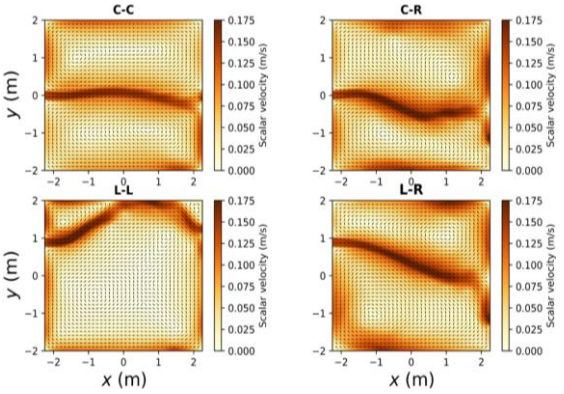

(g) Mixing Length turbulence model

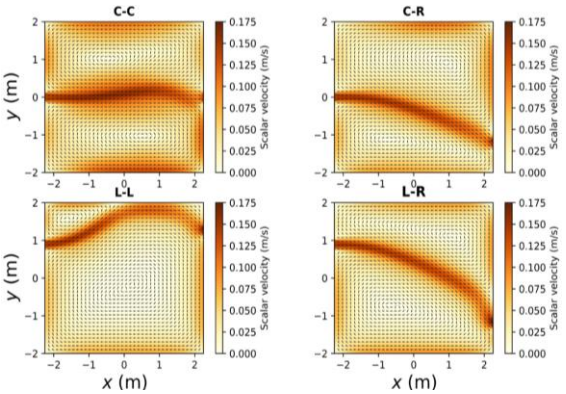

Figure 4. Experimental and computed velocity fields for C-C, C-R, L-L and L-R configurations using different turbulence models (LIPS and mesh size of 0.0025 m).

Various viscosity coefficient values are tested for the constant viscosity (molecular and turbulence viscosity) turbulence model, i.e. 10^{-6}, 10^{-5}, 10^{-4}, 10^{-3}, 10^{-2}, and 10^{-1} m² s^{-1}. Results show that a value of 10^{-3} m² s^{-1} reproduces correctly the velocity magnitude and vectors for C-C, C-R and L-L configurations (Figure 4d), but not for L-R configuration.

The Elder model considers the role of dispersion and includes two coefficients for calculating the longitudinal ($K_l = a_l u_* h$) and transversal ($K_t = a_t u_* h$) diffusion terms (u_* as the shear velocity stress, and a_l and a_t are dimensionless coefficients of dispersion, set in TELEMAC-2D by default to 6 and 0.6,

respectively). Similarly to the standard k–ε and constant viscosity models, Elder's model fails in replicating the flow patterns for the L-R configuration (Figure 4e). The effect of K_l and K_t has been evaluated by changing values of (a_l, a_t): (1, 0.1), (2, 0.2), (3. 0.3), (4, 0.4), (5, 0.5), (7, 0.7), (10, 1). Model-data comparison does not show any noticeable improvement of the results, as illustrated for L-R configuration in Figure 6.

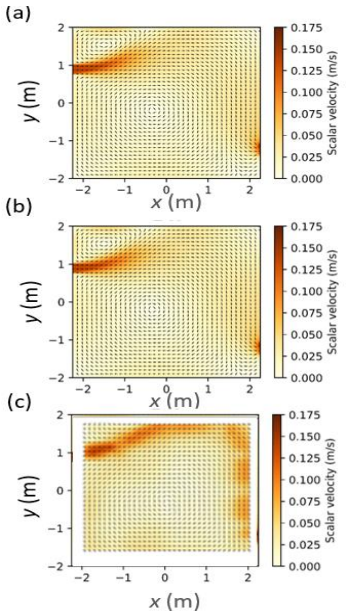

Figure 5. L-R configuration - (a) Initial condition with reattached jet used in TELEMAC-2D simulations, (b) model results obtained at steady state using k–ε turbulence and initial conditions shown in Figure 5a, and (c) measurements. LIPS and mesh size of 0.025 m.

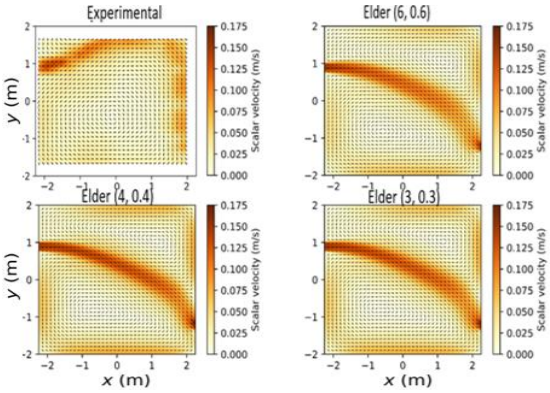

Figure 6. L-R configuration - Computed velocity fields using Elder's turbulence model with different dimensionless coefficients a_l and a_t (LIPS and mesh size of 0.0025 m).

The Smagorinsky scale model calculates the viscosity as $\nu_t = C_s\Delta^2(S_{ij}S_{ij})^{1/2}$, with C_s a dimensionless coefficient to be calibrated, Δ the mesh size derived from the surface, and S_{ij} the stress tensor. This model ignores the effect of dispersion due to heterogeneity of velocities on the vertical direction. The numerical results are not satisfactory (Figure 4f). Using C_s= 0.12, 0.15, 0.18, 0.25, 0.3, or 0.4 instead of the defaults value of 0.2 yields also inaccurate results. The steady state is not reached; an oscillatory state is found which can be due to numerical diffusion (Figure 7).

The Mixing Length turbulence model reproduces correctly the velocity vector maps for C-R and L-L configurations. However, the model does not replicate the steady state for the C-C configuration and the reattachment point observed for the L-R configuration. (Figure 4g).

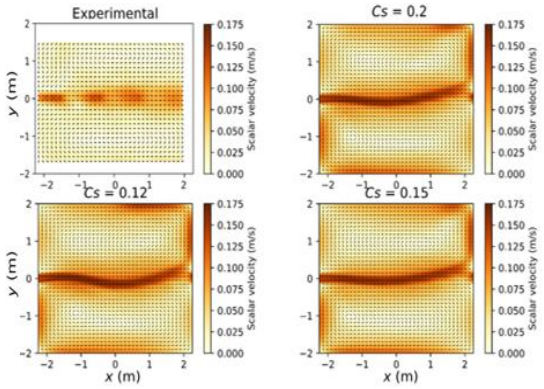

Figure 7. C-C configuration - Oscillatory state found using Smagorinsky turbulence model with C_s=0.12 (LIPS and mesh size of 0.0025 m).

C. *Mesh grid size sensitivity*

A mesh sensitivity is performed with each turbulence model for the C-C configuration. Mesh sizes of 0.0125 m, 0.025 m, 0.05 m, 0.1 m are tested. Results show that mesh size does not improve results for the depth-averaged Mixing Length turbulence model and Smagorinsky model.

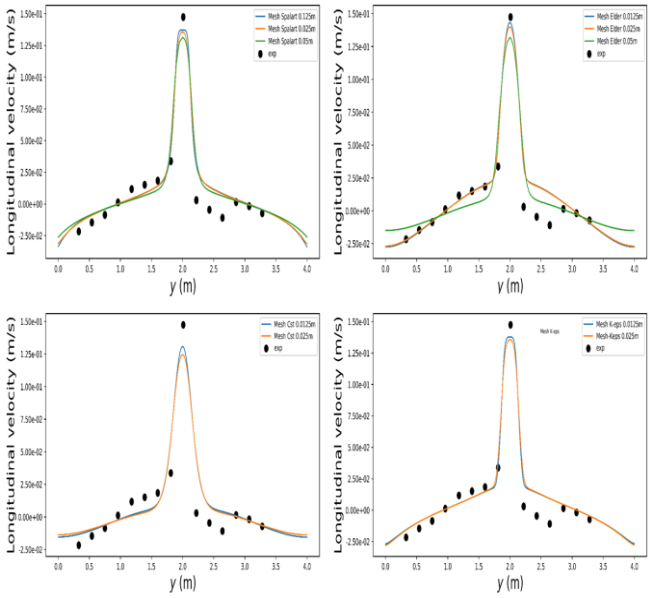

Figure 8. C-C configuration - Measured and computed cross-sectional profiles of the longitudinal velocity at x = 1.73 m using different turbulence models for different mesh sizes. LIPS is used for advection.

Figure 8 shows profiles of the longitudinal velocity at x = 1.73 m for (i) Elder and Spalart-Allmaras turbulence models with mesh sizes of 0.0125 m, 0.025 m and 0.05 m, and for (ii) constant viscosity (10^{-3} m² s^{-1}) and k–ε models with mesh sizes of 0.0125 m and 0.025 m; results with mesh size of 0.05 m are not satisfactory for the flow recirculation features, and thus are not shown for these two models. All the numerical

results are obtained using LIPS and a fixed CFL number of 0.8. Overall, the optimal mesh grid size is 0.025 m.

V. TELEMAC - 3D SIMULATIONS

TELEMAC-3D is applied with non-hydrostatic pressure distribution for C-C, L-L, L-R and C-R configurations using k–ε model in both horizontal and vertical directions, and LIPS scheme for advection of velocity and turbulence. The 3D model is composed of five layers uniformly distributed on the vertical, based on 2D unstructured mesh (0.025 m space step). For TELEMAC-3D, the standard k–ε model reproduces correctly the measured velocity vector field for C-C and C-R cases but does not reproduce the reattachment point for L-L and L-R configurations.

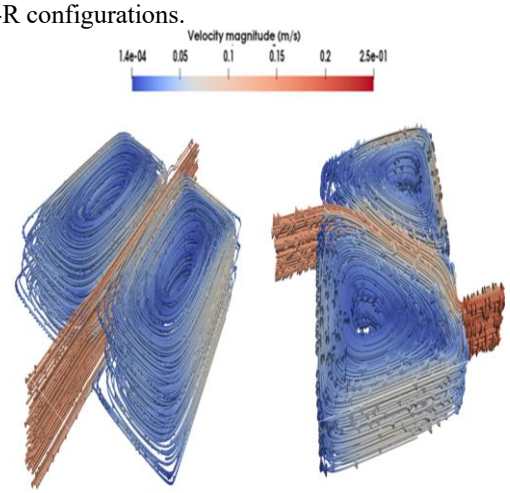

Figure 9. TELEMAC-3D simulations - Streamlines and velocity vectors for configurations C-C (left) and L-R (right) with standard k–ε turbulence model.

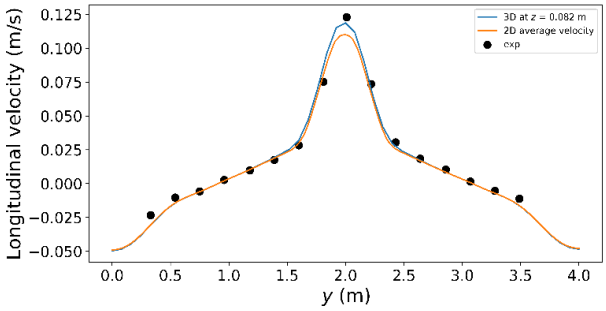

Figure 10. C-C configuration - Measured and computed cross-sectional profiles of longitudinal velocity at $x = 0.71$ m calculated with TELEMAC-3D and TELEMAC-2D. Results with the standard k–ε turbulence model.

Figure 9 shows the 3D streamlines and velocity vectors for C-C and L-R configurations. Figure 10 compares the experimental velocity recorded at a height of 8 cm from the reservoir bottom with the numerical results of TELEMAC-2D (averaged values) and TELEMAC-3D extracted at a height 8.2 cm. A slightly better results of the peak velocity are obtained by the 3D model.

VI. CONCLUSIONS

A numerical modelling of flow in shallow rectangular reservoirs with varying boundary conditions is performed using TELEMAC-2D and TELEMAC-3D. For TELEMAC-2D simulations, the Spallart-Allmaras turbulence model provides satisfactory results for the four configurations, although it shows a less good representation of the velocity magnitudes in comparison with k–ε, Elder and constant viscosity (10^{-3} m² s^{-1}) models. These three models yield satisfactory results for C-C, L-L and C-R configurations, but do not allow replicating the point of attachment for configuration L-R. The Mixing Length turbulence model reproduces the velocity vectors and magnitude for C-R and L-L configurations only. The effect of numerical schemes for advection of velocity and turbulence is very weak. The mesh sensitivity allows improving the results, but the improvement becomes very weak for mesh sizes less than 0.025 m. TELEMAC-2D and TELEMAC-3D are compared for the particular C-C configuration using the k–ε turbulence model. The 3D simulations slightly improve the results. Future work will complete the current study by quantifying the numerical diffusion, investigating further the effect of initial flow conditions, turbulence in both horizontal and vertical directions and numerical schemes using TELEMAC-3D.

REFERENCES

[1] E. Camnasio, E. Orsi and A.J. Schleiss, “Experimental study of velocity fields in rectangular shallow reservoirs,” Journal of Hydraulic Research, 49(3), 2011, pp. 352-358.

[2] B. Dewals, SA. Kantoush, S. Erpicum, M. Pirotton and A.J. Schleiss, “Experimental and numerical analysis of flow instabilities in rectangular shallow basins,” Environmental Fluid Mechanics, 8, 2008, pp. 31-54.

[3] N. Claude, M. Secher, J. Deng, E. Valette and M. Duclercq, “2D and 3D numerical modelling of the flow and sediment transport in shallow reservoirs: application to a real case,” XXVIth Telemac & Mascaret User Club, 2019.

[4] M. Dufresne, B. Dewals, S. Erpicum, P. Archambeau and M. Pirotton, “Experimental investigation of flow pattern and sediment deposition in rectangular shallow reservoirs,” International Journal of Sediment Research, 25, 2010, pp. 258-270.

[5] J.-M. Hervouet, “Hydrodynamics of free-surface flows- Modelling with finite element method: John Wiley & Sons,” 2007, 341p.

[6] A. Bourgoin, K. El kadi Abderrezzak, S. Benhamadouche and R. Ata, “An adoption of the Spalart-Allmaras turbulence model for two- and three-dimensional free surface environmental flows,” Journal of Hydraulic Research, 59(2), 2021, pp. 314-328.

[7] S.A. Kantoush, “Experimental study on the influence of the geometry of shallow reservoirs on flow patterns and sedimentation by suspended sediments,” PhD thesis, EPFL, Lausanne, Switzerland, 2008.

[8] Y. Peltier, S. Erpicum, P. Archambeau, M. Pirotton and B. Dewals, “Experimental investigation of meandering jets in shallow reservoirs,” Environmental Fluid Mechanics, 14(3), 2014, pp. 699-710.

[9] J.-M. Hervouet, “Residual distribution advection schemes in Telemac,” INRIA. Research Report n°9087, 2013.

[10] E. Camnasio, E. Orsi, S. Erpicum, A.J. Schleiss, M. Pirotton and B. Dewals, “Coupling between flow and sediment deposition in rectangular shallow reservoirs,” Journal of Hydraulic Research, 51(5), 2013, pp. 535-547.

[11] J.-M. Hervouet, “Latest news on distributive advection schemes and dry zones: the ERIA schemes,” Proceedings of the XXIIIrd TELEMAC-MASCARET User Conference, 2016, pp. 201-208.

[12] M. Dufresne, B. Dewals, S. Erpicum, P. Archambeau and M. Pirotton, “Numerical investigation of flow patterns in rectangular shallow reservoirs,” Engineering Applications of Computational Fluid Mechanics. 5(2), 2011, pp. 247-258.

Sediment II and Numerical Methods

3D Modelling for the Dispersion of Sediments Dredged in the Port of La Rochelle with Open TELEMAC-MASCARET

J.-B. Saulnier, E. Escobar-Valencia, M. Grognet
EGIS Water & Maritime
Guyancourt, France
jean-baptiste.saulnier@egis.fr

B. Waeles
BW-CGC
Brest, France

***Abstract*— In view of the future deepening operations in the port of La Rochelle (France), a 3D coastal model – including Ré and Oléron islands – was built with TELEMAC-3D and SEDI-3D to simulate the dispersion of the fine dredged sediments to be released at sea. The release scenario combined different sites and methods: two dumping zones with hopper dredger in the Lavardin shallows and in the Antioche Strait, and one submarine outfall in the La Pallice Strait. The model was adapted, firstly, to take wave contribution into account in the calculation of total (wave+current) bed shear stress, and secondly, to introduce the part of sediments maintained in suspension in the water column and the part deposited on the sea bottom during each release. The model proved to reproduce very satisfactorily the hydrodynamics in the straits as well as the known capacity of each disposal site to accumulate or disperse dumped sediments.**

I. INTRODUCTION

The mid- and long-term effect of fine sediment dumping at sea during port dredging operations often need to be simulated so that excessive turbidity and deposits – and associated mitigation measures – may be assessed. Finite-element-based softwares such as the open TELEMAC-MASCARET suite are commonly used to model the hydro- and sediments dynamics in complex environmental areas (tide, waves, wind, shallows…), see e.g. [1]. However, this kind of modelling is not always available off-the-shelf and programming adaptations are required to reproduce at best the release scenarios.

In view of predicting the effects of future deepening operations in the port of La Rochelle – PALR – (France), a 3D coastal model was built with TELEMAC-3D and SEDI-3D to simulate the fate of the fine sediments released after dredging and rock-breaking operations. The release scenarios involve two immersion types : dumping by trailing suction hopper dredger over two authorised sites (Antioche offshore in 24m mean water depth; the Lavardin shallows, close to La Rochelle, in 6m mean water depth) and submarine outfall discharge in the La Pallice Strait, after a decantation process of cuttings (tailings) inside a dedicated basin (La Repentie). The induced turbidity and deposits must be compared to the "natural" order of magnitude for the same period of the year (i.e. background turbidity and deposition) mainly due to the Gironde River discharges, strong hydrodynamic forces and low altimetry in the straits (mud flats). Concentrations up to several hundreds of mg/L may be observed, for instance, in the Bay of Aiguillon during spring tide and severe sea conditions. Also, the "Pertuis Charentais" are well known for the many aquaculture farms deployed all over the area (e.g., Marennes-Oléron oysters), which are sensitive to natural turbidity conditions and deposits but possibly also to suspended matter dispersion from dumping sites.

Simulating such a scenario implies: 1/ the consideration of a directionally oriented outfall for the suspended load coming from the decantation basin – which is easy to set-up using default TELEMAC-3D options –, and 2/ a specific consideration of two sediment compartments released from the barge : the fine sediments maintained in the water column during the descent phase and the sediments deposited on the sea bed after collapsing. As TELEMAC-3D and SEDI-3D are used in a far-field approach, both types of releases need to be introduced as schematic source terms in the domain. Also, even if the transport of suspended sediment is mainly driven by the tidal current, both tidal currents and waves contribute to erode and/or to maintain in suspension fine sediments (see e.g. [2]). Therefore, wave conditions must be included in the calculation of the total bed shear stress at each time step. A previous "background" 2D wave simulation (including the effect of tidal currents and free surface elevation variations) is used here as an input of the 3D dispersion model.

This paper presents the TELEMAC-3D/SEDI-3D model that has been set-up in order to simulate a particular release scenario, whose results are plotted and mapped for illustrative purpose.

Section II introduces the study area (The "Pertuis Charentais"). Section III presents the construction of the model, including the validation of the 3D hydrodynamics, the sediment dynamic parameterisation, the source terms and the related implementations. Section IV highlights the relevance of the modelling strategy according to the simulation results, in particular the time evolution of the sediment mass deposited in each dumping zone and subject to local erosion. Section V finally concludes this work with some further perspectives.

II. STUDY AREA

The study area covers the whole "Pertuis Charentais" located on the French Atlantic coast, including the region of La Rochelle (La Pallice Strait), the Aiguillon Bay, the Ré and Oléron islands, the Breton and Antioche Straits, as depicted in Fig. 1. The macrotidal regime (3 to 6m range) – in a maritime area with islands, straits, shallows and bays alternatively filled and emptied – induces significant flows that can reach 1 to 1.5m/s in Antioche and La Pallice straits in spring tide conditions. Oceanic swells

propagate through the Breton and Antioche straits where their energy is dissipated mainly due to refraction and bottom friction, in particular in the Breton Strait. Strong winds can also generate short-wave, wind-sea systems locally, which propagate through the straits and may therefore dominate over swells in these areas. In common situations, crossed seas are likely to be observed in the La Pallice Strait as the result of the meeting of waves from the Breton and Antioche straits.

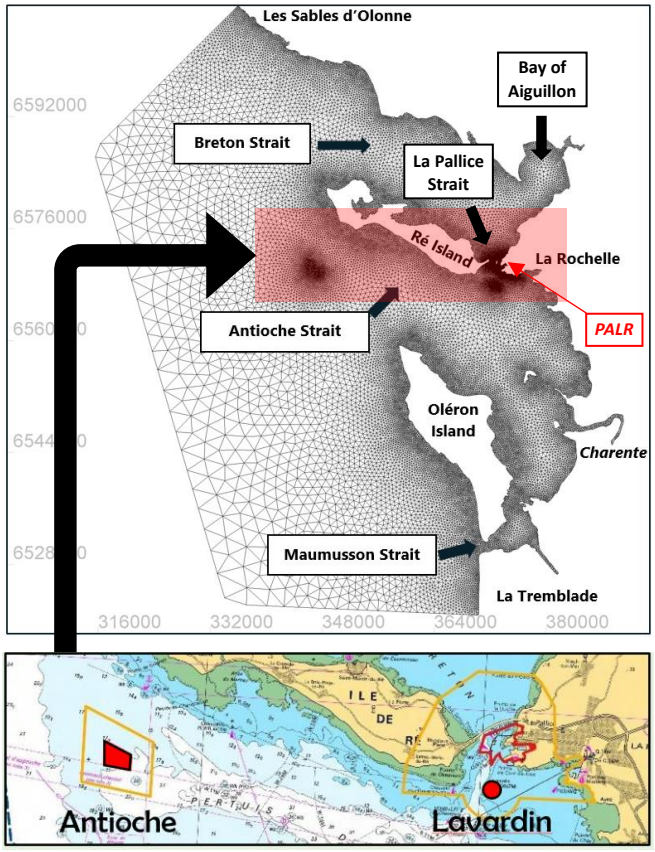

Figure 1 – Mesh of the "Pertuis Charentais" model with focus (below) on the two authorised dumping sites

Two main river outlets are present within and outside the domain, namely the Sèvre Niortaise, the Charente and the Gironde (further South). However, their contribution in terms of fine sediment input is not taken into account in this study.

The two authorised dumping sites – Antioche and Lavardin – are respectively located in the Antioche and La Pallice Straits (Fig. 1). The Lavardin site is defined within a 500m radius circle in the South of the La Pallice Strait (see Fig. 1). The bathymetry ranges between -4mCD and 0mCD and the seabed is a mix of sand and mud (mostly dredging material). The Antioche site is located South-West from Ré Island and is defined as an offshore trapezoidal (~2km^2 wide) area with sandy seabed around -20mCD.

The whole area is subject to environmental (Natura 2000 protected areas…) and socio-economic (fishing, shellfish farming, tourism…) concerns related to sediment transport and turbidity variations.

III. Setup of the Dispersion Model

A. *Modelling scheme*

The scheme for the 3D dispersion modelling rests on an offline coupling (chaining) strategy. As the total contribution wave+current to the bed shear stress needs to be calculated at each time step by the 3D dispersion model for the calculation of erosion/deposition fluxes, a wave history is produced beforehand using a TELEMAC-2D/TOMAWAC coupled model. This option was preferred to a direct TELEMAC-3D/TOMAWAC coupling to reduce CPU times. The wave spectral peak period (TPR5) and spectrum-averaged bottom velocity (UWB) calculated by TOMAWAC – and influenced by tidal oscillations thanks to the coupling with TELEMAC-2D – are stored. Then, TELEMAC-3D and the embedded SEDI-3D module simulate the sediments release scenario : they respectively solve the 3D hydrodynamics (Navier-Stokes in hydrostatic mode) and suspended sediment concentration (SSC) transport-diffusion equations taking sediment source terms into account, as direct inflow in the water column, on the one hand, and bed deposits, on the other hand. The deposition and erosion fluxes are a function of an excess or lack of bed shear stress (relatively to critical bed shear stress for erosion or deposition), which is computed in SEDI-3D based on the hydrodynamic variables UWB and TPR5 at each time step. This, in turn, allows an update of the bed elevation, which may have an effect on 3D currents, especially over the Lavardin area. A general sketch of the modelling scheme is given in Fig. 2. The final output variables are the 3D SSC denoted by C [kg/m^3 or g/L] and mud deposit thickness denoted by Δz_b [m].

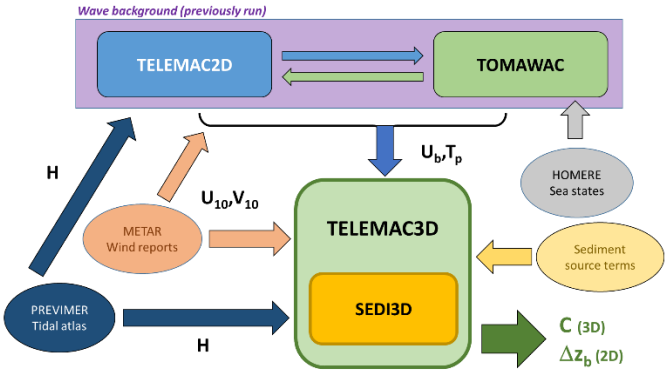

Figure 2 – Modelling scheme of the 3D dispersion model

IV. Hydrodynamics

A. *Currents (TELEMAC-3D)*

The hydrodynamic model is meshed using about 35 000 nodes with coarsest (2.5km) and finest (15m) resolution respectively along the open boundary and in the harbour zone. The resolution is also refined over the two deposit areas, as 50m in the Lavardin and 100m in Antioche. The water column is discretized as 5 σ-distributed planes, which is deemed sufficient in a macrotidal context with limited depth. Height and velocities are prescribed on the liquid offshore boundary

using the PREVIMER tidal atlas (37 constituents with 250m resolution) and a time-varying homogeneous wind field drags the surface layers using the default Flather formulation [3]. The wind history is produced using METAR data (La Rochelle airport/LFBH). A homogeneous Strickler coefficient of $40 m^{1/3}/s$ is set up over the whole domain and the Smagorinsky model is adopted for horizontal and vertical turbulence closure. The Digital Elevation Model (DEM, Fig. 3) interpolated on the mesh was produced by merging different sets of data, including both the HOMONIM topo-bathymetric DEM for the Pertuis Charentais (0.0002°) [4] and bathymetric DEM for the Atlantic coast (0.001°) [5], a local bathymetric multibeam survey conducted in the harbour before 2018 and some recent bathymetric complements.

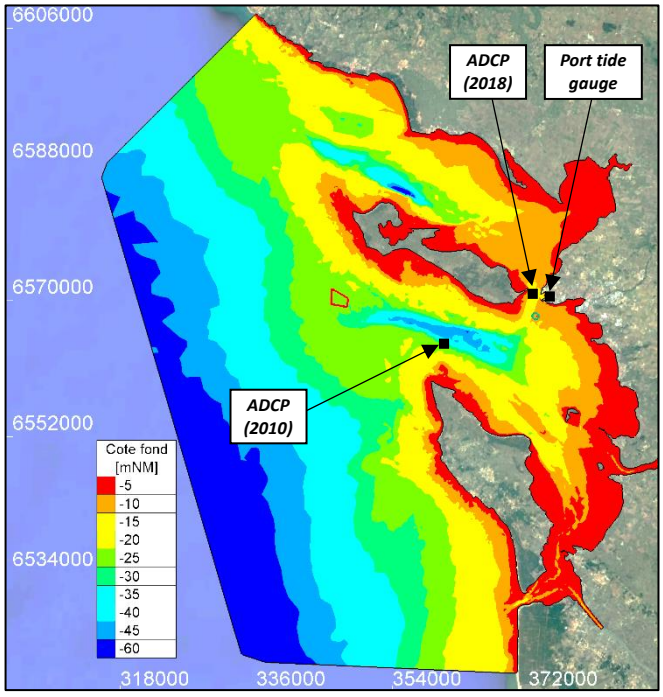

Figure 3 - DEM in reference to mean water level (=+3.90mCD in La Rochelle) in Lambert 93 projection; location of available *in situ* level/current/wave measurement devices

The water level variations and 3D currents were validated against *in situ* measurements (see Fig. 3):

- tide gauge records in octobre-novembre 2016 in the harbour of La Rochelle-La Pallice (46.158501°N, 1.22065°W),
- data from ADCP deployed in February-March 2010 by the SHOM in the Antioche Strait (46.0919°N, 1.3940°W) (currents mostly going W<>E)
- data from ADCP deployed in october-november 2016 in the La Pallice Strait (46.1596°N, 1.2423°W) (currents going mostly N<>S).

The comparison between measurements and results is shown in Fig. 4. For 3D currents, surface and bottom signals along the dominant axis only are shown (i.e., U-component in Antioche and V-component in the La Pallice Strait) for the sake of conciseness.

Water level in the harbour was satisfactorily reproduced, with a RMSE of 16cm. Simulated 3D currents (surface, mid-height and bottom) were also found in good agreement with measurements, with 13 to 27cm/s RMSE for U-component in Antioche and 15 to 21cm/s for V-component in La Pallice. In particular, ebb/flow asymmetries appeared to be well predicted.

B. *Waves (TELEMAC-2D/TOMAWAC)*

The wave history was generated by coupling TELEMAC-2D and TOMAWAC with the following boundary conditions: PREVIMER atlas for water level and currents; HOMERE reanalysis data [6] for sea states, through wave parameters H_{m0}, T_p and θ_p (virtual buoy "W184N4598"). These parameters were shown to vary little along the offshore boundary so that a homogeneneous JONSWAP/$\cos^{2s}$ directional spectrum could be assumed at each time step (mean shape parameters γ and s were estimated based on the HOMERE data). As in the TELEMAC-3D model, METAR wind data have been considered for surface current driving and wave generation.

The sea states simulated by the model in the La Pallice Strait were compared to the ADCP wave measurements covering the October-November 2016 period. The simulated significant wave heights H_{m0} showed to be in good agreement with ADCP data (RMSE of 15cm), as depicted in Fig. 4. Due the limited information on sea state multimodality (superposition of swell(s) and wind-sea) in the offshore data used as boundary conditions, the peak period (T_p) could not be accurately reproduced in calm situations, when the wind-sea dominates in the straits. Wave directionality was not deemed useful either for comparison, also because of many disturbance effects in the deployment site (wave diffraction and reflection, boat wakes…). However, as wave directionality is not taken into account in the deposition/erosion flux calculations (see §V), suspended sediment dynamics are not affected by the quality of directional results. Moreover, as bottom orbital velocities tend to be overestimated in calm wave situations due to the own T_p overestimation, this results in conservative calculated bed shear stress values – which, in turn, induces conservative turbidity levels – an acceptable approach for our study.

V. SEDIMENT RELEASES

A. *Characterisation of released sediments and work scenario*

The deepening works in the port consist in dredging the superficial muddy layer and cutting/dredging the underlying marl/limestone layers up to a certain operational level.

A total of 375 $000 m^3$ of sediment (the figure is only illustrative, here) is dredged in the port from which the fine – cohesive (∅<63µm) – part is then released into the sea. A sandy fraction is also expected in the mix but not studied here as it does not contribute to turbidity. The representative dry concentration of mud fraction is estimated around $650 kg/m^3$ based on PALR's assumptions. According to the capacity of the hopper dredger, a mass of about 600t of sediments is to be

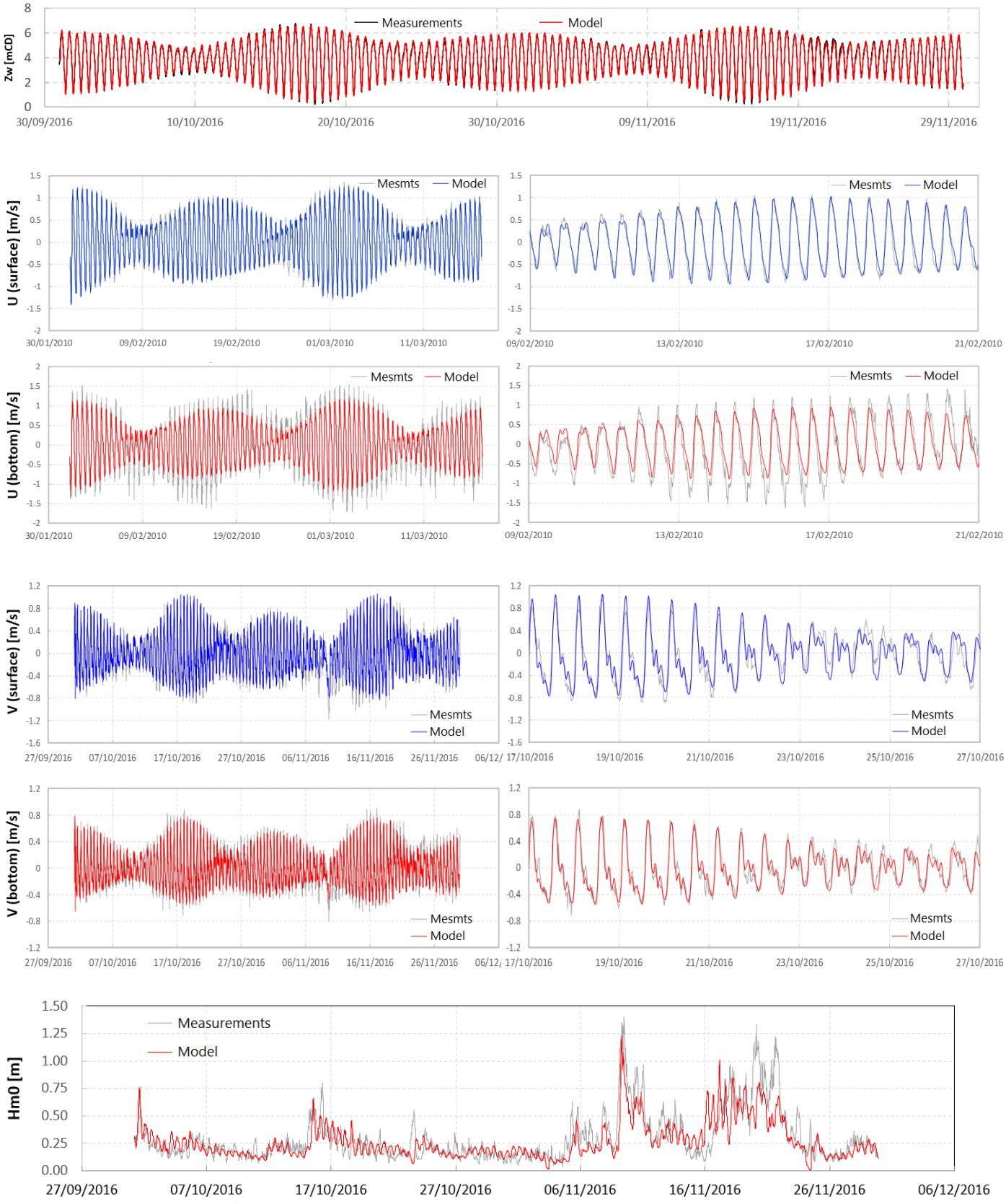

Figure 4 – Comparison of simulated 3D currents and significant wave height against in situ ADCP measurements (Antioche, La Pallice)

released at each rotation (in the Lavardin or Antioche). A 30% Lavardin / 70% Antioche repartition is assumed so that 122 and 284 rotations are planned for disposal at each site respectively. Releases at high tide are required at the Lavardin because of the shallow bathymetry.

The volumes of marl excavated by the cutter suction dredger (rock-breaking) are deposited into the close-by decantation basin of La Repentie. Due to aspiration and continuous disintegration, a significant load of suspended matter is obtained in the basin, which can be partly adjusted using flocculating agents. It is assumed here that the SSC never exceeds 1g/L. As the basin is progressively filled with sediments, the corresponding volume of water is sent back to the sea with an outfall pipe located under the bridge leading to the oil terminal in the middle of the La Pallice Strait (Fig. 5). The release – SW-oriented on the sea bottom – is supposed to be continuous during the rock-breaking operations, with maximum authorized flow rate of 10 000m^3/h (i.e., 2.78m^3/s) and constant SSC of 1g/L.

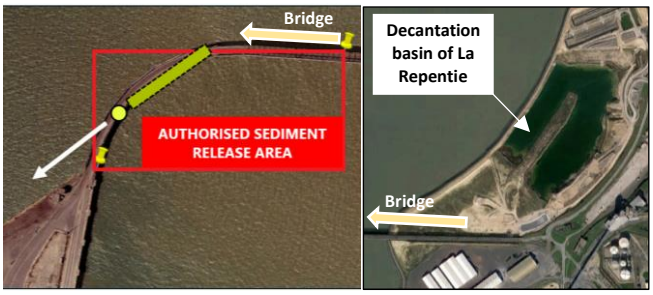

Figure 5 – (Left) Location of submarine outfall in the La Pallice Strait for the release of turbid waters from the decantation basin; (Right) decantation basin of La Repentie

A timeline of the release scenario simulated in this study is depicted in Fig. 6. The dumping operations in Antioche and Lavardin are planned over 63 days: they start as soon as the port deepening dredging starts, with one release around each high tide in the Lavardin and 2 or 3 releases in Antioche in between. After 28 days, the outfall release in the La Pallice Strait is launched for about 10 weeks (duration of rock-dredging operations in the port). "T0" here refers to the work start in mid-December of year N, after a 24h transient phase for hydrodynamics setting up. The rock-breaking and releases stop around mid-March of year N+1.

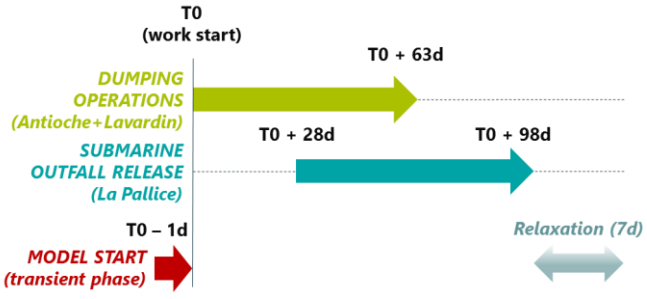

Figure 6 – Timeline (not scaled) of release operations during the port deepening works in La Rochelle

B. *Sediment dynamics and source terms*

The modelling of sediment dynamics in SEDI-3D rests on the usual formulations for cohesive sediments, namely the Krone law for deposition flux :

$$D = w_s C \left[1 - \frac{\tau_b}{\tau_{cd}}\right] \quad (1)$$

where w_s [m/s] denotes settling velocity and τ_{cd} [N/m^2] the critical bed shear stress for deposition, and the Partheniades law for erosion flux:

$$E = Max\left(0; M\left[\frac{\tau_b}{\tau_{ce}} - 1\right]\right) \quad (2)$$

with M the erosion constant [kg/m^2/s] and τ_{ce} [N/m^2] the critical bed shear stress for erosion.

The total bed shear stress (τ_b) needs to be calculated at each node and each time step. In SEDI-3D, the wave-induced stress is not included by default. As this contribution must be taken into account, it was included in the CLSEDI routine as follows.

The total stress is calculated in a conservative approach as:

$$\tau_b = \tau_c + \tau_w \quad (3)$$

where:

- $\tau_c = \rho u_*^2$, the shear stress due to currents, with ρ = 1 025kg/m^3 the sea water mass density and u_* the friction velocity, calculated here using the Nikuradse formula with rugosity coefficient k_s = 1mm ;
- $\tau_w = \frac{1}{2}\rho f_w U_w^2$, the shear stress due to waves expressed as a function of the maximum orbital velocity U_w [m/s] (UWB from TOMAWAC here) and f_w [-] the wave friction factor following the default Swart [7] formula (involving UWB and TPR5).

Directional difference between currents and waves is not taken into consideration for simplicity.

As parameters like deposition/erosion critical bed shear stresses (τ_{cd}, τ_{ce}) and bed concentration (denoted as c here) may be different for partly aggregated muds immediately deposited on the bottom and released particles deposited after having been advected (fresh deposits), two classes of sediments were setup in SEDI-3D (Fig. 7). The same critical stress values were used for both classes here (τ_{cd} = 0.1N/m^2 and τ_{ce} = 0.2N/m^2) but the deposits were modelled as slightly denser (c_1 = 300kg/m^3 vs. c_2 = 200kg/m^3, typical value for fresh deposits), which has an impact on bed thickness only. The settling velocity (w_s) was set to 2.2 10^{-4}m/s and the erosion constant M was given the value 5.10^{-5}kg/m^2/s. Most of these values were obtained in previous studies commissioned by PALR.

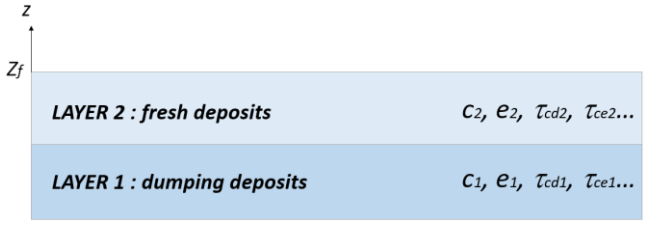

Figure 7 – Sediment layer definition in SEDI-3D

For simplicity, the dredger is assumed to release sediments from the same location in both Lavardin and Antioche sites. The released mass of sediments is divided in two parts: 13% are maintained in suspension during the descent phase (78t) while 87% of the mass (522t) remains on the sea bed after dynamic collapsing. This repartition is estimated based on dredger experience but might as well be approached using specific nearfield modelling softwares like e.g. ST-FATE [8].

At the centre of each disposal site, source points are defined at all planes but the first one (seabed), with identical mass flux (~65kg/s on each plane), as depicted in Fig. 8. The total duration of each release is 5min.

In order to introduce the right amount of sediment deposited on the sea bottom at each time step during the release, a sediment layer increment is applied as soon as suspended matter is released from the dredger (in ERODC subroutine). The layer increment is restricted to a certain area representing the footprint of the release and deemed homogeneous on that area. The dumping area can be estimated using, nearfield modelling, among others. Here, as a unit release simulated with ST-FATE was shown to induce a rather limited deposit area at both sites (10 000 to 100 000m^2), an averaged dumping area – standing for all rotations – was assumed, extending over 150 000m^2 in the Lavardin and 1 000 000m^2 in Antioche (within the zones depicted in Fig. 1). It is checked *a posteriori* that the mass of sediments introduced on the bottom at each rotation (522t) is correct.

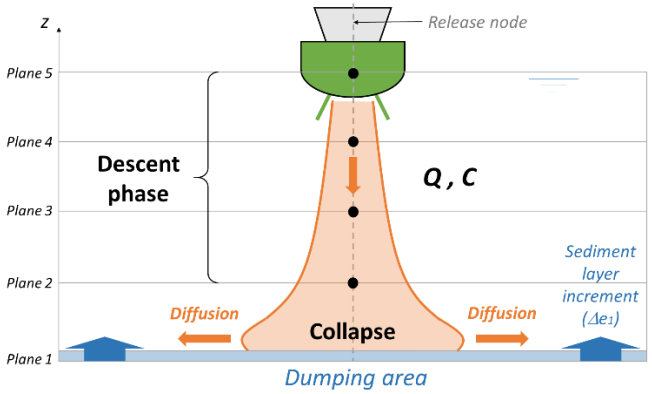

Figure 8 – Source term definition in SEDI-3D for dumping: four source points (planes 2 to 5 at release node) with prescribed suspended matter discharge and sediment layer increment on the disposal area

The submarine outfall is simulated as a typical source point located on the sea bed with given discharge, SSC, duration and direction (SW-oriented jet), as described earlier.

VI. MODELLING RESULTS

A. *Hydrodynamic conditions*

The wave-, current-induced and total bed shear stresses calculated by the model along the simulation at one representative point in both deposit sites are depicted in Fig. 9 and 10 (top). The simulated wave-induced stress (τ_w) generally is an order of magnitude higher than the current-induced stress (τ_c). The total stress (τ_b) never exceeds 3N/m^2 over the Antioche area, with peaks in the range [0.5;2.5N/m^2]. In the Lavardin site, waves are weaker than in Antioche so that their contribution to the total stress is also smaller : peak stress values are calculated in the range [0.1;1.5N/m^2]. All stress signals are influenced by tide, either due to the oscillatory flow or the effect of depth variation on waves.

B. *Turbidity*

The bottom/surface SSC (in mg/L) at both sites is also depicted in Fig. 9 and 10 (centre). As most of the dumped volumes are deposited on the seabed (87%) and also due to the own SSC gradient induced by settling velocity, bottom concentrations are systematically found higher than surface ones, especially in Antioche. In the Lavardin shallows, bottom and surface SSC are closer to each other due to stronger mixing and limited depth, which reduce the vertical SSC gradient. The calculated bottom concentration peaks reach 100mg/L (up to 280mg/L) in Antioche and 200mg/L (up to 340mg/L) in the Lavardin. A correlation to the total bed shear stress is found for bottom (and surface, to a lesser extent) SSC in Antioche. Although this be less clear on the curves, the same kind of dependence is observed in the Lavardin, where outfall releases also are contributing – although not significantly – to the resulting turbidity.

Figure 11 illustrates a sequence of bottom SSC in Antioche and the Lavardin at different stages of the tide on day 47 of the simulation – when dumping operations and outfall discharges are both ongoing and erosion rates are high. Dumping releases are taking place in flow- and ebb-tide in Antioche and just before high tide in the Lavardin. The simulated plumes are due to the releases at both dumping sites as well as resuspension of previously deposited sediments.

C. *Evolution of sediment deposits*

The instantaneous mass of sediment integrated over each dumping area is plotted in Fig. 9 and 10 (bottom). It is verified (see figure insets) that a mass of approximately 522t is introduced on the bottom (layer 1) at both sites during each dumping phase. In Antioche, the high bed shear stress levels cause a rapid erosion of the deposits. During calm periods, sediments may accumulate (up to 12 000-13 000t here around days 20 and 60) but do not remain longer than about ten days. On day 60, the accumulation stops because in the release scenario, dumping ceases in Antioche and is continued for about 4 days in the Lavardin only. The site of Antioche as simulated with the 3D model is therefore highly dispersive, which is consistent with PALR's experience. In the Lavardin, the deposited sediments tend to accumulate in spite of a slight, regular erosion – too small, however, to erode the whole of the dumped volume. The sediment mass therefore is continuously increasing during the barge rotations up to about 38 000t (over nearly 64 000t if no erosion occurred). On day 64, the dumping ceases and the deposits erode progressively. At the end of the simulation, nearly half of the volume has been eroded, so that a duration of about 3 months would be probably required to disperse it entirely. This is also consistent with PALR's experience (frequent bathymetric surveys), evoking no long-term accumulation trend in the Lavardin.

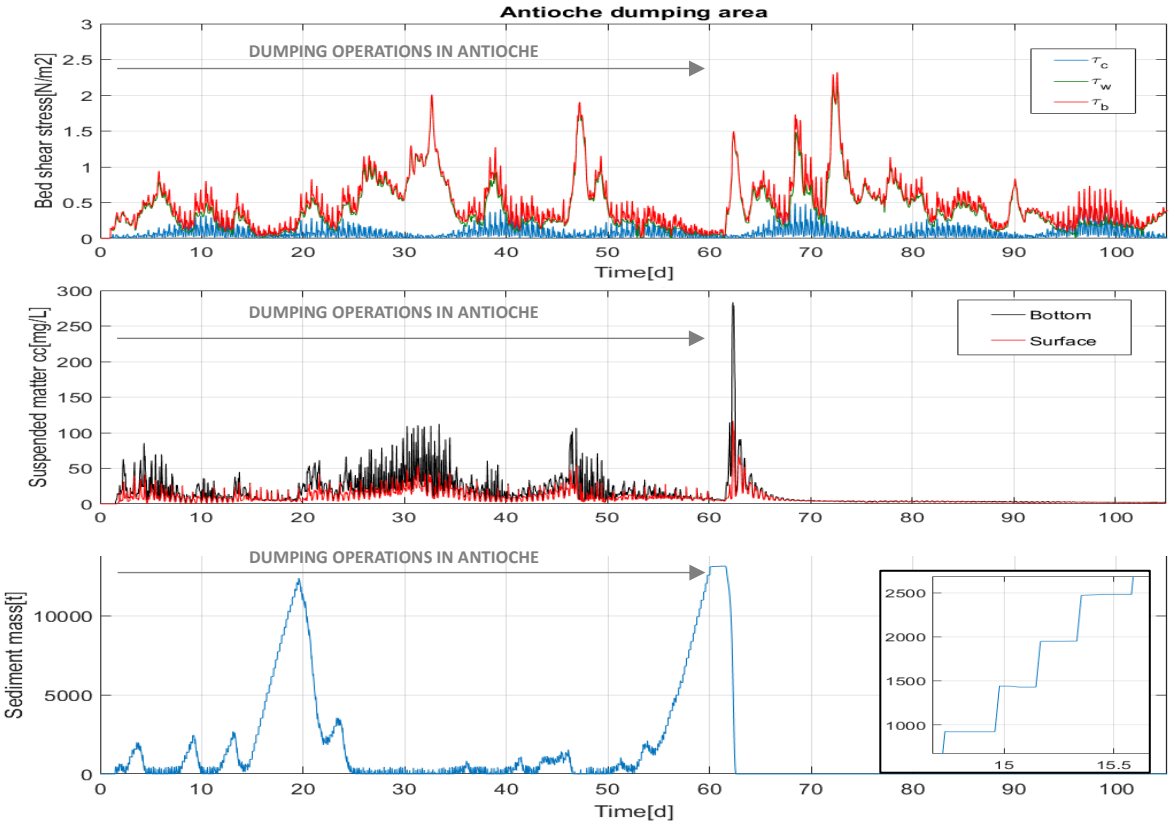

Figure 9 – Current-, wave-induced and total bed shear stress (top), SSC (centre) and total sediment mass deposited (bottom) in the Antioche dumping site as simulated by the 3D model; dumping in Antioche stops on day 60.

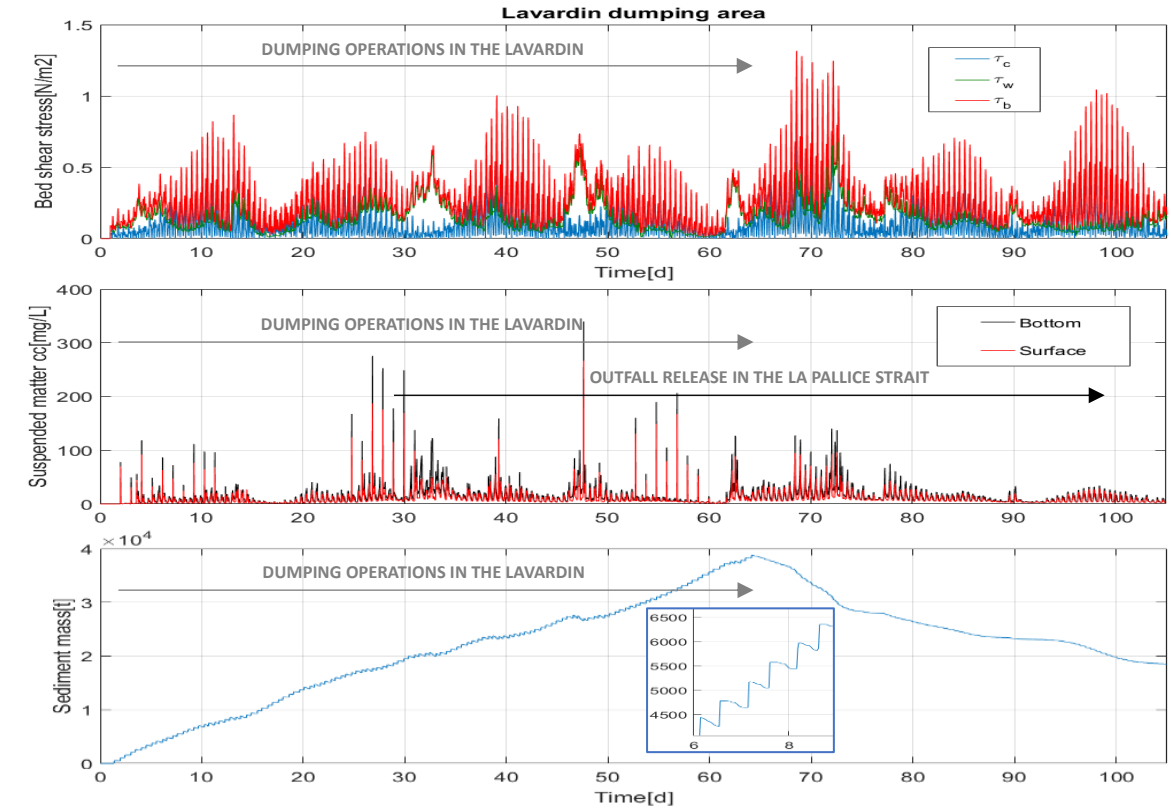

Figure 10 – *Idem* fig. 9 in the Lavardin dumping site; dumping stops in the Lavardin on day 64; outfall release starts in the La Pallice Strait on day 29 and stops on day 99.

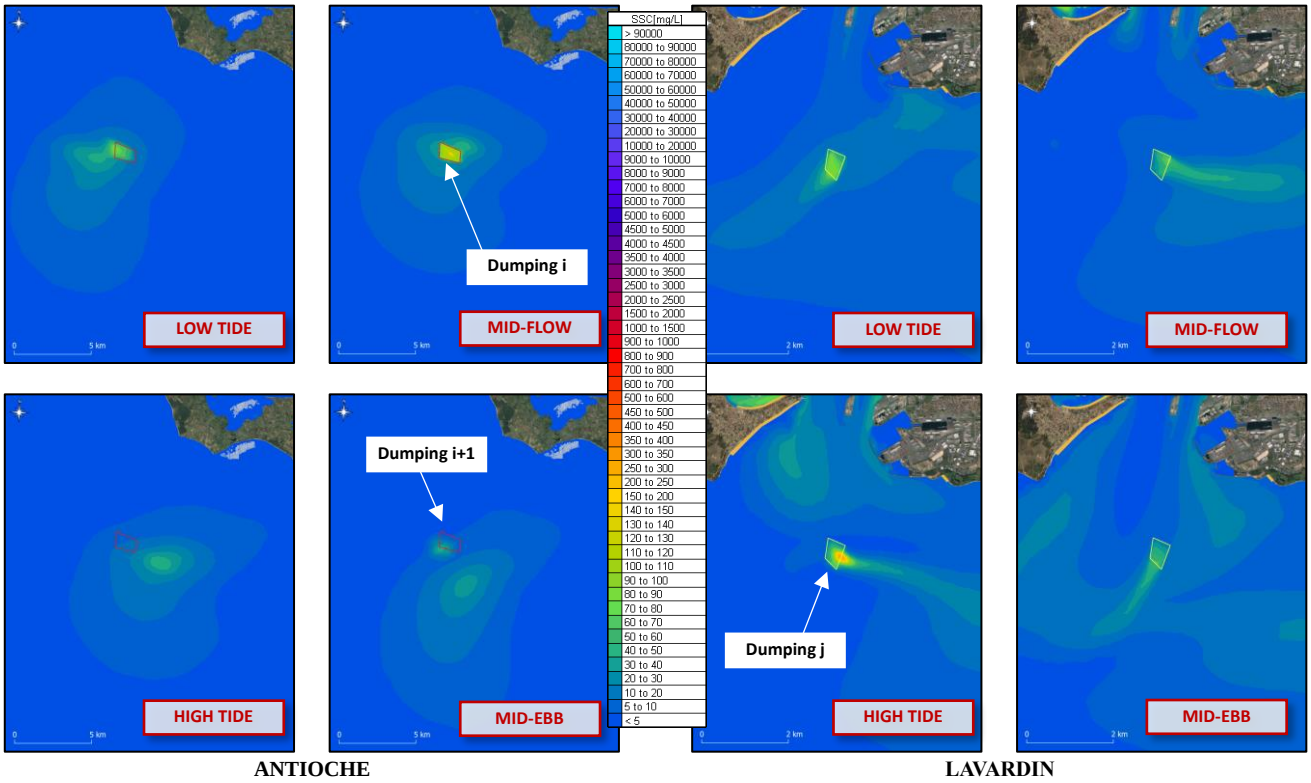

Figure 11 – Sequence of (bottom) SSC[mg/L] around high tide on day 47 of the simulation in Antioche (left) and Lavardin (right) dumping sites (dumping occurring during flow- and ebb-tide in Antioche and near high tide in the Lavardin).

VII. CONCLUSIONS AND FURTHER WORK

The TELEMAC-3D/SEDI-3D dispersion model constructed in view of assessing the effects of the future deepening works in the port of La Rochelle (PALR) has shown to behave very satisfactorily as regards hydrodynamics and the main trends of sediment dispersion. In particular, the simulated capacity of the Antioche and Lavardin dumping sites to store or disperse the deposited sediments confirmed PALR's empirical knowledge, that is : no persistence of sediments in Antioche and persistence over a period of time not exceeding a couple of weeks/months in the Lavardin, according to the volume of dredged sediments considered (375 000m^3 *in situ* here distributed on both sites). Such a modelling strategy can be applied to any release scenario in coastal areas with limited depths. Further refinements could be conducted, namely on the calculation of the total bed shear stress (current-wave interaction) in association with a better representation of the sea state contents in the domain in case field data are available.

ACKNOWLEDGEMENTS

The authors wish to thank Port Atlantique La Rochelle (PALR) and SDI/DEME for authorising to publish this work.

REFERENCES

[1] R. Walther, C. Cayrol, L. Hamm, A. Delouis and D. Lehay, "Evaluation of an offshore disposal site in the Loire estuary through field monitoring and 3D numerical modelling," *Proc. of Int. Conf. on Coastal Engineering*, vol. 1, n°34, pp. 1-15, 2014.

[2] P. Le Hir, S. Kervella, P. Walker and I. Brenon, "Erosions, dépôts et transits sédimentaires associés dans le bassin de Marennes-Oléron," *La Houille Blanche (SHF)*, n°5, pp. 65-71, 2010.

[3] O. Mattic, "Telemac3d – User Manual, Version v7p3," 90pp., 2018.

[4] SHOM, "MNT Topo-Bathymétrique Côtier des Pertuis Charentais (Projet Homonim)," 2015 [https://diffusion.shom.fr].

[5] SHOM, "MNT Bathymétrique de Façade Atlantique (Projet Homonim)," 2015 [https://diffusion.shom.fr].

[6] E. Boudière, C. Maisondieu, F. Ardhuin, M. Accensi, L. Pineau-Guillou and J. Lepesqueur, "A suitable metocean hindcast database for the design of Marine energy converters," *Int. Jour. of Marine Energy*, pp. 40-52, 2012.

[7] D. H. Swart, "Offshore sediment transport and equilibrium beach profiles," Technical report, Delft University, Delft Hydraulics Publication 131, 1976.

[8] B. H. Johnson, "User's guide for models of dredged material disposal in open water," U.S. Army Engineer Waterways Experiment Station. Dredging Operations Technical Support Program, Technical Report D-90-5, 1990.

Implementation of cross-shore processes in GAIA

E Fonias[1,2], WA Breugem[1], L Wang[1,2], A Bolle[1]
[1] International Marine and Dredging Consultants
Antwerp, Belgium
efstratios.fonias@imdc.be

G Kolokythas[2], B De Maerschalck[2]
[2] Flanders Hydraulics Research
Antwerp, Belgium

***Abstract*—In the present paper, a first attempt is presented to add cross-shore sediment transport processes within the module GAIA of TELEMAC-MASCARET. Consideration of Stokes drift, return flow and wave non-linearity mechanisms was implemented. A comparison was performed with a laboratory experiment, showing promising results.**

I. INTRODUCTION

Cross-shore transport processes are quite complex phenomena because they depend on the balance between wave effects and mean currents that can cause either onshore or offshore transport. Thus, cross-shore sediment transport gradients can be significant and cause morphological changes that can be intense spatially and temporally, particularly in storm events [9]. For example, convergence in cross-shore sediment transport rates result in the formation of bars, observed in the vicinity of the breaking zone. As shown by [5], nearshore bars move offshore within storm periods, whereas in cases of mild waves they propagate onshore. In particular when the ratio of the significant wave height to water depth above crest is higher than 0.6 the bars move offshore and when it is smaller than 0.3 they move onshore.

Accurate computation of cross-shore sediment transport in the nearshore is a rather challenging procedure. Several mechanisms with different effect and intensity are in motion balancing onshore and offshore transport processes. Onshore transport mechanisms include Stokes drift, streaming and wave non-linearity (skewness and asymmetry). Offshore processes include return flow, gravity, and long waves.

Stokes drift is causing net mass transport towards the coast. Due to continuity, a return flow or *undertow*, is formed. Streaming is a steady current induced by surface waves close to the boundary layer and contributes to onshore sediment transport [17] (see Figure 1).

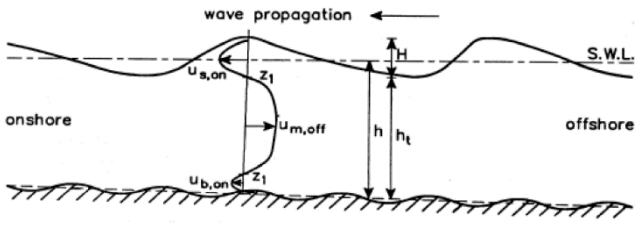

Figure 1 – Time averaged velocity profile [17] showing from top to bottom: Stokes drift (u_s), return flow (u_m) and streaming (u_b). From [17]

Wave non-linearity (skewness and asymmetry) contributes to the onshore transport by higher waves but with shorter crests than troughs (skewness) and a steeper wave front than the tail of the crest (asymmetry). Skewness is often considered as the dominant mechanism for onshore transport. However, this argument is still under debate and depends on sediment characteristics [8], [4]. Wave roller quantifies the energy dissipation due to wave breaking that occurs within an amount of time. Due to this temporal delay, the location of wave breaking and sediment concentration moves closer to the coast and this results in offshore transport due to the return flow from these rollers. Finally, 3D effects are important to explain cross-shore transport phenomena, as longshore transport is combined with cross-shore transport. For instance, 3D effects such as shear waves, edge waves and rip currents are important to reproduce coastal bars formation [1], [21].

Long waves result in offshore transport. Their contribution is smaller than wave non-linearity in sediment transport [6]. Long waves or surf beat result in dune erosion. In those cases, long waves and return flow have a stronger effect than wave non-linearity [15].

Gravity stabilizes sediment and smooths out morphological features especially in bars. It tends, on average, to transport sediment offshore due to foreshore slope.

In addition, vertical pressure gradients result in infiltration and exfiltration in the seabed and contribute to both onshore and offshore transport [7]. During exfiltration, those pressure gradients result in destabilized sediment and increasing near-bed concentrations. At the same time, the boundary layer thickness increases as turbulent eddies are released, which results in lower near bed velocities. Those mechanisms are reversed in case of infiltration.

Turbulence, fall velocity, bed forms, wind stress, wave roller and 3D effects are mechanisms that could result in either onshore or offshore transport.

Turbulence is the basic reason for the different transport behavior in shoaling zone and in surf zone. In the shoaling zone, there are high sediment concentrations in the near bed region, which are transported onshore. In the surf zone, turbulence occurs due to wave breaking, which results in sediment concentrations in the full water column and thus return flow becomes dominant resulting in offshore transport [6]. Based on the magnitude of the fall velocity, the suspended sediment particles can be caught in the crest or the trough of the wave, which determines whether they will be moving onshore or offshore [23].

Bed forms can affect the flow through secondary mechanisms such as changes in bed roughness [1], and depend on the intensity of local flow conditions. That is the reason why spatial variability of bed forms is evident on cross-shore profiles. Wind stress can impose a more intense flow by means of a shear stress on water surface, especially during storm events. This is compensated by a

bottom flow towards the opposite direction in the nearshore. When wind stress is combined with a Coriolis force, this generates upwelling and onshore transport or downwelling and offshore transport [14]. Those mechanisms will not be investigated in the present paper.

TABLE 1– RELATIVE IMPORTANCE OF PROCESSES FOR ONSHORE TRANSPORT, OFFSHORE TRANSPORT AND BAR BEHAVIOR [18]. THE "+" SIGN INDICATES HIGH IMPORTANCE OF THE MECHANISM, THE "-" LOW , AND THE "=" BALANCED EFFECT. MORE INTENSE CONTRIBUTIONS ARE INDICATED BY DOUBLE PLUS OR MINUS SIGNS.

Process	Onshore transport	Offshore transport	Bar behavior
Stokes drift	-		-
Return flow		++	++
Streaming	-		-
Wave asymetry	+		+
Wave skewness	++		++
In- and Exfiltration	--	--	--
Gravity		=	+
Turbulence	=	=	+
Wind stress	-	-	-
Fall velocity	--	-	--
Bed forms	-	-	=
Long waves	-	++	++
Wave roller			+
3D effects			- → ++

The relative importance of each process determines whether the sediment is transported onshore or offshore and depends on hydrodynamic conditions which are milder in summer and more intense in winter. The relative importance is shown in Table 1 for onshore transport, offshore transport and bar behavior [18]. The "+" sign indicates high importance of the mechanism, the "-" low , and the "=" balanced effect. More intense contributions are indicated by double plus or minus signs.

Several of the processes that are important for offshore and onshore transport have not yet been included in the TELEMAC-MASCARET suite. The present work is focused on the implementation of the Stokes drift, return flow, and wave non-linearity (both due to wave asymmetry and wave skewness), inspired by the available physical parametrizations in XBeach. The implementation of surface rollers was discussed in a separate paper [24], whereas the effect of long waves is also significant but it has not been implemented in the present work. The developments presented here were implemented in the framework of developing a morphological model of the Belgian Coast: the Scaldis-Coast model [11]. It shows the first step in implementing cross-shore processes in TELEMAC-MASCARET. The new implementations are tested for a laboratory test case coupling TELEMAC-2D, TOMAWAC and GAIA presented here, and the patterns in the bed morphology are discussed.

II. MATHEMATICAL MODEL AND CODE IMPLEMENTATION

A. *General features*

The GAIA modification for considering the cross-shore sediment transport processes include modification of the depth averaged flow velocities that will be used for computation of suspended sediment transport using the advection-diffusion equation:

$$\frac{\partial hC}{\partial t}+\frac{\partial hU^E C}{\partial x}+\frac{\partial hV^E C}{\partial y}=\frac{\partial}{\partial x}\left(h\varepsilon_s\frac{\partial C}{\partial x}\right)+\frac{\partial}{\partial y}\left(h\varepsilon_s\frac{\partial C}{\partial y}\right)+E-D \quad (1)$$

where C is the depth-averaged concentration, t is time, x and y are the two horizontal dimensions of the numerical domain, U^E,V^E are the Eulerian velocities , h is the water depth, ε_s is the eddy viscosity, and E and D are the non-cohesive erosion and deposition, respectively.

The additional velocity components accounting for cross-shore transport are based on formulations implemented in XBeach [12] and they are explained in detail in the following sections. This is achieved within the newly added subroutine `GAIA_CROSS_SHORE`.

In our approach, the generalized Lagrangian mean velocities U^L,V^L are given as:

$$U^L = U^E + U^S \ , \ V^L = V^E + V^S \quad (2)$$

where U^S,V^S are the velocities due to Stokes drift. The sediment transport needs to be calculated using the Eulerian velocity in the advection-diffusion equation. However, the velocities calculated by TELEMAC-2D are the Lagrangian velocities U^L,V^L. Therefore, one can take the effect of Stokes drift and the return current generated by the Stokes drift into account using:

$$U^E = U^L - U^S \ , \ V^E = V^L - V^S \quad (3)$$

In case we have waves moving towards the coast in a stationary situation, we have U^L=0 (no net flow of water towards the coast, and therefore U^E=-U^S, showing that the return current (U^E) is opposite to the Stokes drift [10].

The depth averaged flow velocities used for accounting for cross-shore sediment transport have the form of:

$$U^{tot} = U^L + \sin\theta\,(U_{NL} - U_{ST}) \quad (4)$$
$$V^{tot} = V^L + \cos\theta\,(U_{NL} - U_{ST})$$

The terms in these equations due to Stokes drift (U_{ST}, and wave non-linearity U_{NL}) are explained in the next sections and θ is the wave direction (TOMAWAC convention, i.e. 0 degrees for waves going to the North).

B. *Stokes drift and Return flow*

The Stokes drift occurs in the nearshore in the upper part of the water column (see Figure 1), because the motion of water particles do exhibits a perfectly circular track. As the horizontal orbital velocity increases with the distance from seabed [16], it leads to lower seaward velocities under the wave trough than the shoreward velocities under the wave crest.

This velocity difference has a magnitude of the order of 0.1 m/s in shallow water. The Stokes drift is taken into account by adding an extra velocity with magnitude U_{ST} and components U^S,V^S, based on the expression [12]:

$$U_{ST} = {}^{E_w}/_{\rho hc} \quad (5)$$
$$U^s = U_{ST}\sin\theta \quad , \quad V^s = U_{ST}\cos\theta$$

where U^s and V^s are the velocity components due to the Stokes drift [19], E^w is the wave-group varying short wave energy computed by:

$$E^w = {}^{\rho g H_s^2}/_{16} \quad (6)$$

In the above expression ρ is the water density, c is the phase velocity, g is the gravitational acceleration and H_s is the significant wave height.

C. Wave non-linearity

The wave non-linearity consists of wave skewness and wave asymmetry.

The wave skewness (*Sk*) indicates that wave crests are higher and shorter in duration than the troughs. The shoreward velocity under the crest is higher than the seaward velocity under the wave trough (skewness). Even though the mean orbital velocity is zero, the resulting mean bed shear stress is directed onshore.

Wave asymmetry (*As*) refers to the higher acceleration of the wave front compared to the wave tail. Phase lag effects (asymmetry) between maximum velocity and flow reversal has effect on sediment stirring [8]. Finally, horizontal pressure gradients can result in plug flow, or loosening up of sediment blocks from the bed. This phenomenon is more intense for asymmetric waves [10] resulting in onshore transport.

The contribution of wave non-linearity is calculated by means of an extra velocity with magnitude U_{NL} and components U^a,V^a:

$$U_{NL} = (f_{Sk}Sk - f_{As}As)u_{rms} \quad (7)$$
$$U^a = U_{NL}\sin\theta \quad , \quad V^a = U_{NL}\cos\theta$$

where f_{Sk} and f_{As} are calibration factors with values from 0 to 1.0 and a recommended value of 0.1, u_{rms} is the root-mean square velocity computed as:

$$u_{rms} = U_w\sqrt{2} \quad (8)$$

and U_w is the orbital velocity, calculated in TOMAWAC. Then, the skewness and asymmetry can be computed using the Boltzmann sigmoid through the expressions [12]:

$$Sk = B\cos\psi \quad , \quad As = B\sin\psi$$
$$\psi = -90 + 90\tanh\left({}^{p_5}/_{Ur^{p_6}}\right) \quad (9)$$
$$B = p_1 + {}^{(p_2 - p_1)}\Big/\left(1 + exp\,\tfrac{p_3 - logUr}{p_4}\right)$$

where Ur is the Ursell number computed by:

$$Ur = {}^3/_4 \cdot \left[{}^{0.5H_s k}/_{(kh)^3}\right] \quad (10)$$

and k is the wave number. $p_{1:6}$ are parametrization factors based on field observations [3]. In the present work we considered the mean values as:

$$p_1 = 0.000\ ,\ p_2 = 0.875\ ,\ p_3 = 0.471 \quad (11)$$
$$p_4 = 0.297\ ,\ p_5 = 0.815\ ,\ p_6 = 0.672$$

Variables including local orbital velocity, significant wave height, water depth and wave direction are communicated directly from TOMAWAC, whereas the wave celerity is calculated form the wave period and the wave number, which is computed using the subroutine `WNSCOU` using the local water depth and the wave period from TOMAWAC.

D. Bed slope effect

The bed slope can influence sediment transport, favouring sediment transport down the slope. This can result in different transport rate in terms of magnitude and/or direction. Inspired by the implementation in XBeach [12], the effect of the bed slope is parametrized by changing the sediment transport velocity shown in equation (4), using the following expression (with β as calibration coefficient) :

$$U^{tot} = U^{tot}\left(1 - \beta\frac{\partial\eta}{\partial x}\right) \quad (12)$$
$$V^{tot} = V^{tot}\left(1 - \beta\frac{\partial\eta}{\partial y}\right)$$

E. An updated advection scheme

The application of the above modifications leads to a sediment transport velocity field, that is not divergence free. The residual distribution schemes in TELEMAC were designed for the computation of advection for flow fields calculated in TELEMAC, that exactly conserve the water mass. Adding extra velocity components to schematize the cross-shore components, the velocity field used to advect the sediment is not mass conservative anymore. The added effects are merely parametrization that did not consider any mass balance in their derivation.

In order to have mass conservation for cross-shore transport, an updated advection scheme was implemented, based on the NERD scheme (`SCHEME FOR ADVECTION OF TRACERS = 13 or 14`) and for the ERIA scheme (`SCHEME FOR ADVECTION OF TRACERS = 15`). This scheme was specifically developed in order to perform well for flow fields that are not mass-conservative.

In deriving this scheme, we start from the continuity equation in the conservative form:

$$\frac{\partial hC}{\partial t} + \frac{\partial hCU}{\partial x} + \frac{\partial hCV}{\partial y} = 0$$

It can clearly be seen, that the product hC is the quantity that needs to be conserved. Therefore, we perform advection on the sediment volume ξ=hC. Using this substitution, and applying the product rule on the spatial derivatives we get the non-conservative form of the advection equation, (because all TELEMAC residual distribution schemes are based on the non-conservative form):

$$\frac{\partial\xi}{\partial t} + U\frac{\partial\,\xi}{\partial x} + V\frac{\partial\,\xi}{\partial y} = -\xi\left(\frac{\partial U}{\partial X} + \frac{\partial V}{\partial Y}\right)$$

This shows the following consequences for the updated advection scheme:

- The sediment volume in the time derivative is discretised by:

$$\frac{c^{n+1}H^{n+1} - c^{n}H^{n}}{\Delta t}$$

Hence, in order to get the sediment volume the concentration is multiplied by the water depth at time step *n*. To return to the depth-averaged concentration, the depth-integrated concentration needs to be divided by the water depth at time step *n+1* after the calculation of the advection.

- The sediment volume needs to be advected by the depth-averaged velocity field (in TELEMAC given by 'VGRADP', rather than by the depth integrated fluxes that are originally used in the NERD and ERIA schemes (variable; ' HUGRADP'))
- An extra source term is needed to take into account the fact that the velocity field is not divergence-free (this is the term on the right hand-side of the equation). This source term is added to the advection scheme. It is discretised implicitly in case the right hand side of the equation is negative (i.e. when it is a sink term) and explicitly when it is positive (i.e. when it is a source).

II. VALIDATION OF THE ADVECTION SCHEMES

A. *Constant velocity in increasing water depth*

The first validation case concerns a channel flow case of 2500 m length, with constant flow of 0.5 m/s in a channel with a uniformly increasing water depth. The spatial grid size is equal to 50 m and the time step equal to 10 s. The ERIA scheme has been used for this simulation. In this case the water depth is linearly increasing as it can be seen in Figure 2. The resulting solution of sediment concentration (solid line) is compared to the analytical solution (dashed line) derived using the method of characteristics. The results compare reasonably well, but the used advection scheme shows a substantial amount of numerical diffusion. A check of the mass balance showed that the mass of the advected tracer was conserved in this test case (not shown).

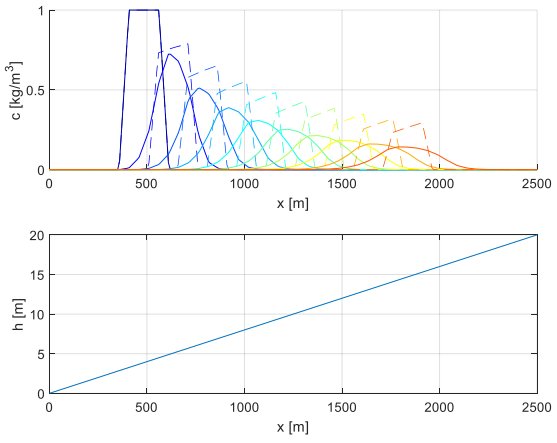

Figure 2 – Upper figure: temporal variation of suspended sediment concentration calculated using the updated ERIA scheme (solid lines) and comparison with the analytical solution (dashed lines). Lower figure: increase of the water depth along the channel.

B. *Accelerating flow*

The second validation case concerns a flow on the same channel where this time the water depth is remaining constant and the velocity increases from 0 m/s to 0.4 m/s. The ERIA scheme is used in this case as well. In Figure 3 the temporal variation of suspended sediment concentration along the length of the trench has been shown for the original ERIA scheme and for the modified ERIA scheme. In this case, the derivation of an analytical solution was not possible. In Figure 4, the mass is plotted for the original and modified schemes proving that the mass is conserved for the modified ERIA advection scheme, whereas in the original ERIA scheme, there is an issue with the mass balance.

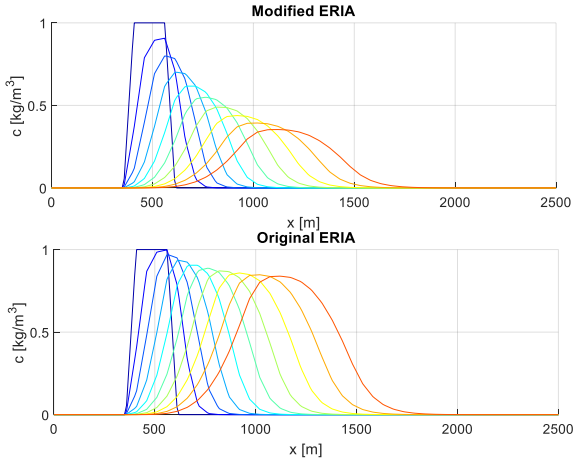

Figure 3 – Temporal variation of suspended sediment concentration along the channel for the modified ERIA scheme (upper figure) and the original ERIA scheme (lower figure).

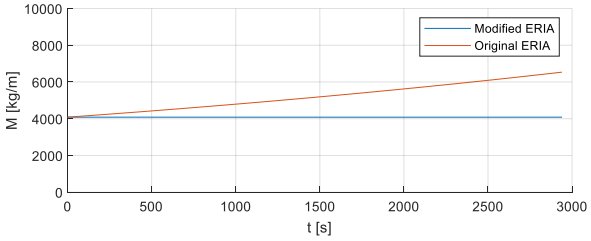

Figure 4 – Temporal variation of the sediment mass for the original ERIA advection scheme (red solid line) and the modified ERIA scheme (blue solid line).

III. APPLICATION: BAR EVOLUTION OVER A SLOPED BEACH IN A LABORATORY EXPERIMENT

A. *Model bathymetry and mesh*

The above improvements have been applied in one of the CROSSTEX experiments [20]. The experiments took place on a wave flume 104 m long, 3.7 m wide and 4.6 m deep. A bar formation has been placed on a 1:20 sloped beach as shown in Figure 5.

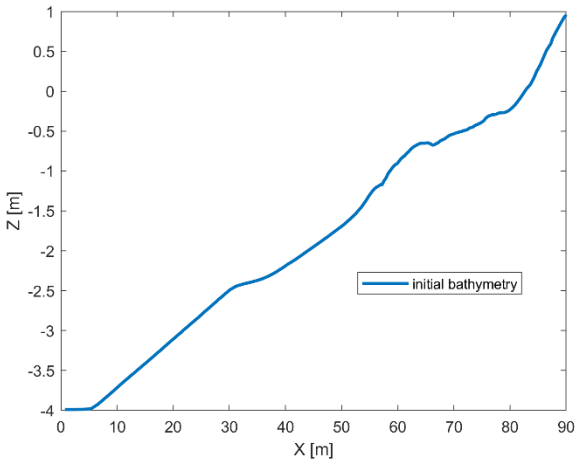

Figure 5 – Initial bathymetry for the CROSSTEX experiments under investigation [20].

An erosive event was studied. This event is generated under wave conditions of TMA spectrum with $H_s = 0.60$ m, $T_p = 4$ s and $\gamma = 2$. In this event the bar migrates from $x = 64$ m to 61 m. The experiment consisted of 14 sets of 15 minutes runs (hence a total time of 3.5 hours).

The numerical domain of length equal to 90 m has been considered according to Figure 5. The mesh resolution was set to 0.2 m, using a channel mesh with a width of three grid nodes, in order to have a quasi one-dimensional setting similar to the laboratory case. The sediment diameter is equal to $d_{50} = 0.2$ mm.

For the TELEMAC-2D simulation a timestep of 1 s was used. The advection scheme considered for tracers was the modified NERD scheme. The Nikuradse bottom friction with constant equal to 0.02 m was used. In TOMAWAC, only advection, shoaling and depth-induced wave breaking, were applied using the new numerical schemes developed in [25]. Monodirectional waves are applied at the boundary. The coupling period with TOMAWAC was set to 300. For GAIA, the Soulsby & van Rijn suspension transport formula has been considered for all sands. The sediment slide has been activated with a friction angle for sediment equal to 30°. The beta parameter for the slope effects, and the cross-shore skewness and asymmetry factors have been calibrated in order to verify the values that give the best results. It has been concluded that beta equal to 0, cross-shore skewness factor equal to 0.3 and cross-shore asymmetry factor equal to 0.1 give the best results that are shown in Figure 6.

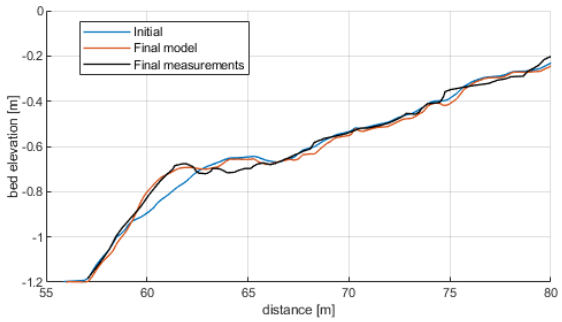

Figure 6 – Initial (blue solid line) and final (red solid line) simulated beach profile and comparison with CROSSTEX experiment under investigation [20] (black solid line).

The resulting beach profile shown in Figure 6. The current development manages to reproduce the migration of the bar to the offshore remarkably similar as observed in the experiment. Nevertheless, there is an area around $x = 63$ m to 66 m from which the results of the model do not show the erosion that occurred in the experiment. This can indicate that the occurring erosion resulting in the bar formation occurs in a much wider area instead of the immediate vicinity of the bar in the initial bathymetry.

In addition, the sediment mass throughout the simulation is shown in Figure 7. The sediment mass difference between the start and the end of the simulation is in total equal to 0.3 kg. This indicates that using the previously described numerical schemes a good conservation of mass is achieved, as the observed error of 0.3 kg is considered sufficiently small, not to have any influence in practical computations. Nevertheless, more research seems desirable to identify the cause of this small mass balance error.

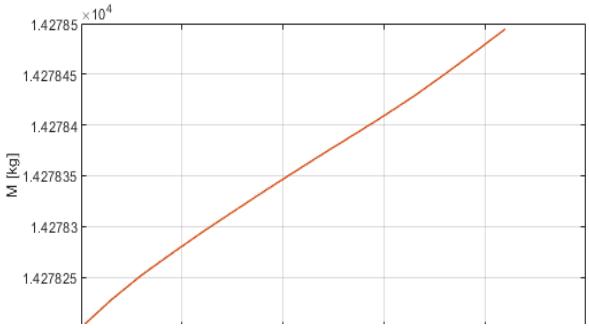

Figure 7 – Temporal variation of the total sediment mass (in suspension and in the bed) for the numerical simulation.

IV. CONCLUSIONS

This paper presents implementations within GAIA module to account for cross-shore sediment transport processes in the nearshore. The mechanisms taken into account include Return flow, Stokes drift, bed slope effects, and non-linear wave effects. The implementations were based on the processes currently implemented in XBeach for cross-shore sediment transport processes. A modified advection scheme was implemented, which advects the sediment volume in the water

column, rather than the depth-averaged sediment concentration, and which uses a correction term to compensate for flow fields that are not divergence-free. A first comparison with cross shore sediment transport in a laboratory experiment was performed, showing promising results. However, more testing is needed to further validate the implemented developments.

REFERENCES

[1] B. Castelle, B. G. Ruessink, P. Bonneton, V. Marieu, N. Bruneau and T. D. Price "Coupling mechanisms in double sandbar systems. Part 1: Patterns and physical explanation," Earth Surface Processes and Landforms, 35(4), pp. 476-486, 2010.

[2] B. Grasmeijer, Process-based cross-shore modelling of barred beaches. PhD thesis, pp.251, University of Utrecht, The Netherlands, 2002.

[3] B.G. Ruessink, G. Ramaekers and L.C. van Rijn, "On the parametrization of the free-stream non-linear wave orbital motionin nearshore morphodynamic models," Coastal Engineering, vol. 65, pp. 56-63, July 2012.

[4] B.G. Ruessink, H. Michallet, T. Abreu, F. Sancho, D.A. Van der A, J.J. Van der Werf and P.A. Silva, "Observations of velocities, sand concentrations, and fluxes under velocity-asymetric oscillatory flows," J. Geophys. Res., 116 (C03004), 2011.

[5] B.G. Ruessink and J.H.J. Terwindt, "The behaviour of nearshore bars on the time scale of years: A conceptual model," Mar. Geol., vol. 163, pp. 289–302, 2000.

[6] B.G. Ruessink, Y. Kuriyama, A.J.H.M. Reniers, J.A. Roelvink and D.J.R. Walstra, "Modelling cross-shore sandbar behaviour on the timescale of weeks," J. Geophys. Res., 112 (F03010), 2007.

[7] C. Berni, Processus de mibilisation et de transport de sédiments dans la zone de déferlement. PhD thesis at Laboratoire des Ecoulements Géophysiques et Industriels (LEGI), Grenoble University, 2011. In French.

[8] D.A. Van der A, T. O'Donoghue and J.S. Ribberink, "Sheet flow sand transport processes in oscillatory flow with acceleration skewness," Proceedings Coastal Dynamics '09, World Scientific, Singapore, 2009.

[9] D.C. Conley and R.A. Beach "Cross-shore sediment transport partitioning in the nearshore during a storm event," Journal of Geophysical Research: Oceans, 108(C3), 2003.

[10] D.L. Foster, A.J. Bowen, R.A. Holman and P. Natoo, "Field evidence of pressure gradient induced incipient motion," Journal of Geophysical Research, 111 (C05004), 2006.

[11] G. Kolokythas, B. De Maerchalck, L. Wang, E. Fonias and W.A. Breugem, "Scaldis-Coast: An Integrated Numerical Model for the Simulation of the Belgian Coast Morphodynamics," In: Geophysical Research Abstracts (Vol. 21), January 2019.

[12] J.A. Roelvink, A. Reniers, A. van Dongeren, J. van Thiel de Vries, R. McCall and J. Lescinski, "Modelling storm impacts on beaches, dunes and barrier islands," Coastal Engineering, 56(11-12), pp. 1133-1152, 2009.

[13] J. Groeneweg. Wave-current interactions in a generalized Lagrangian mean formulation. PhD Thesis, Delft University of Technology, 1999.

[14] J. Jung and Y.-K. Cho, "Persistence of coastal upwelling after a plunge in upwellingfavourable wind," Scientific reports, 10(1), pp. 1-9, Nature Scientific Group, 2020.

[15] J.S.M Van Thiel de Vries, M.R.A. van Gent, D.J.R. Walstra and A.J.H.M. Reniers, "Analysis of dune erosion processes in large-scale flume experiments," Coastal Engineering 55, pp. 1028-1040, 2008.

[16] L. van Rijn and D. Walstra, "Modelling of sand transport in Delft3D," WL | Delft Hydraulics, project Z3624, 2003.

[17] M.S. Longuet-Higgins, "Mass transport in water waves," Phil. Trans. R. Soc., Ser. A 245(03), pp. 535-581, London, 1953.

[18] N. Zimmermann, K. Trouw, B. De Maerschalck, F. Toro, R. Delgado, T. Werwaest and F. Mostaert, "Scientific report regarding hydrodynamics and sand transport in the coastal zone: Evaluation of XBeach for long-term cross-shore modelling," Version 3.0. WL Rapporten, 00_072. Flanders Hydraulics Research & IMDC. Antwerp. Belgium, 2015.

[19] O.M. Phillips, The dynamics of the upper ocean. Cambridge University Press, 1977, pp.366.

[20] P. T. Cobo, J. T. Kirby, M. C. Haller, H. T. Ozkan-Haller, J. Magallen and G. Guannel,. "Model simulations of bar evolution in a large scale laboratory beach, " In Coastal Engineering 2006: (In 5 Volumes), pp.2566-2578, 2007.

[21] R. Soulsby, Overview of Coast3D project. Coast3D project, Paper A1, HR Wallingford Ltd, 2003.

[22] R. Soulsby, Dynamics of marine sands. H.R. Wallingford, 1997.

[23] USACE Coastal Engineering Manual, Chap. III-3-2-a, 2008.

[24] W.A. Breugem, "Ongoing developments in TELEMAC and TOMAWAC in IMDC," XXVIth TELEMAC-MASCARET User Conference, Antwerp, 14-16 October 2020 (submitted).

[25] W.A. Breugem, E. Fonias, L. Wang, A. Bolle, G. Kolokythas and B. De Maerschalck, "TEL2TOM: coupling TELEMAC2D and TOMAWAC on arbitrary meshes," XXVth TELEMAC-MASCARET User Conference, Toulouse, 15-17 October 2019.

[26] WA Breugem, S. Doorme, A. Bakhtiari, J. Figard, and E. Di Lauro, Speeding up TOMAWAC by means of improved numerical methods, submitted to TELEMAC USER CONFERENCE , 2021.

Speeding up TOMAWAC by means of improved numerical methods

WA Breugem, S. Doorme, A. Bakhtiari, J. Figard, and E. Di Lauro
IMDC NV
Antwerp, Belgium
abr@imdc.be

***Abstract*— TOMAWAC is a third generation spectral wave model. It is used as a stand-alone wave prediction tool, as well as coupled to TELEMAC and GAIA/SISYPHE in order to perform morphological simulations. Due to the fact that energy is calculated for a full wave spectrum, the wave calculation tends to be relatively slow. Therefore, improvements to the numerical calculations in TOMAWAC were implemented, with the objective to increase the speed of the code, but at the same time also to increase the robustness and stability. The results are illustrated in various test cases.**

I. INTRODUCTION

The calculation of wave energy resources using numerical models become a necessity in order to completely understand the wave climate and reduce the uncertainties. Despite considerable advances in computational power, speeding up wave modelling calculations and improving numerical performance continue to be a challenge. As a part of Blue Energy Resource Assessment (BluERA) research, improvements to the TOMAWAC model were implemented. The results of these improvements are presented in this paper.

II. OVERVIEW OF NUMERICAL TECHNIQUES IN THIRD GENERATION WAVE MODELS

At the moment, various third generation wave models are being used in the coastal and oceanographic community. WAVEWATCH [1] and SWAN [2], two of the most used wave models were reviewed in order to understand their numerical behaviour and to find inspiration for possible improvements in TOMAWAC. Each of these models solve the wave action balance, which is given by:

$$\frac{\partial N(\theta,\sigma)}{\partial t}+\frac{\partial c_j N(\theta,\sigma)}{\partial x_j}=S \qquad 1$$

Here, N is the wave action defined as N=E/σ, with E the two dimensional wave energy spectrum, and σ the wave frequency ,c_j is the propagation velocity of the wave energy along the different dimensions (x, y, θ and σ) and S are the source and sink terms that parametrize physical processes such wind input, non-linear wave interactions and whitecapping.

WAVEWATCH has a numerical architecture that is rather similar to TOMAWAC. It uses a fractional step method, where different physical processes are solved one after the other, starting with intra-spectral propagation (such as refraction, and frequency shifting due to currents) for half a time step, followed by spatial advection, and the second half time step of intra-spectral propagation (i.e. using Strang splitting). After the spatial advection, the source terms are integrated. For each of these processes, sub-time steps are used to improve the accuracy and stability. For unstructured meshes, the spatial advection schemes are based on the work by Roland (2008) [3], including an explicit and implicit N-scheme as well as an explicit PSI-scheme (second order accurate in space). For intra-spectral propagation, different explicit advection schemes are used, namely a first order upwind scheme, the second order UNO scheme and the third-order Ultimate QUICKEST scheme. Each of these advection schemes is fully conservative and non-oscillatory.

SWAN was specially designed for shallow water wave modelling. Thereto, it uses a fully implicit method, leading to a large matrix. The individual blocks of this matrix are solved using different methods. The intra-spectral propagation typically leads to tridiagonal or pentadiagonal block matrices, which can be solved efficiently using direct matrix solvers. The spatial propagation is solved using a Gauss-Seidel iteration method. However, the Gauss-Seidel method convergences in one iteration in case the solution in the Gauss-Seidel step is advanced in downwind direction. In order to make sure that the solution is in downwave direction, SWAN uses multiple sweeps (four in the version for a structured mesh), in which a quadrant of the spectrum is solved. Iteration is used to account for non-linearities (such as depth-induced breaking). This method has the advantage that arbitrary large time steps can be used (at the cost of a larger cost per time step), and it is very suited for a structured mesh. However, its application is more difficult on an unstructured mesh and is difficult to parallelize (such that the unstructured SWAN version uses OpenMP, rather than MPI, leading to a limited maximum number of parallel processes that can be used). Note that in the unstructured version, SWAN uses the N-scheme, which is only first order in space. However, for spectral propagation a mixture between an upwind and central scheme is used, as it was found that the use of an upwind scheme leads to smoothing of the refraction. Note that the methods used in SWAN can, in some situations, lead to negative wave energies. Hence, in SWAN, a correction routine is implemented that corrects the spectrum after the calculation in order to remove the negative wave energy.

TOMAWAC [4] uses a fractional step method, where advection is solved first using the method of characteristics (for both the intra-spectral and spatial propagation terms. The roots needed for the characteristic methods are not calculated

every time step. Instead, they are calculated at the beginning of the calculation and when the hydrodynamics (flow velocities and water depths) are updated. This procedure leads to a fast and unconditionally stable advection scheme. However, this advection scheme is not fully energy conservative and is only first-order accurate such that there is a reasonable amount of numerical diffusion. Furthermore, the parallel scaling of this method worsens in case the Courant number increases (as for an increasing time step, it can lead to streamlines extending to a larger neighbouring subdomain, leading to more parallel communication). After the advection terms, the source terms are solved. A sub-time step can be used for rapidly varying processes (e.g. depth-induced breaking, and triad interactions), which are solved after the slower varying physical processes (wind input, whitecapping, bottom friction and quadruplet interaction). A disadvantage of the fractional step approach is that it leads to a time step restriction (e.g. [3]) for accuracy reasons. A clear example of this occurs in case of breaking on a bar. In case the time step used is too large, the waves will not break at the bar, but instead, they will be advected over the bar, leading to wave heights that are too high behind the bar.

III. New TOMAWAC numerical architecture

Based on the findings of the review of these different wave models, a new architecture of TOMAWAC was implemented (Figure 1).

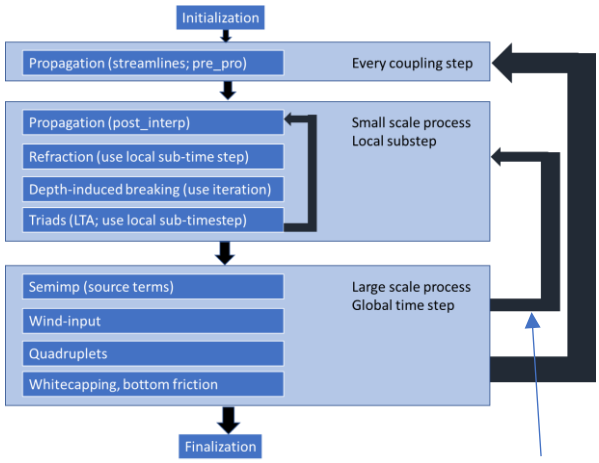

Figure 1 New numerical architecture in TOMAWAC

In this new architecture, a separation is made between fast and slow physical processes. The fast processes, which occur locally in space, need to be resolved using a small time step. These process include spatial advection, intra-spectral propagation (such as refraction), depth-induced breaking and triad interactions. Within these individual processes, sub steps are still used for some of these processes (notably advection and triad interactions, which will be discussed below). The slow physical processes (wind-input, quadruplet interactions, whitecapping and bottom friction) are now solved with a large global time. In this way, calculation time can be reduced substantially, as the calculation of these source terms can be quite slow (especially the calculation of quadruplet interactions). This method resembles what is used in WAVEWATCH, and has also been used in WAM by Monbaliu et al [5]. The loops for small scale and large scale processes are included an even slower loop, which is to update the hydrodynamic data, and update the calculation of the roots of the characteristics. This latter loop is already present in the current version of TOMAWAC.

Furthermore, the review indicates the need for alternative advection methods, in order to have the possibility to use:

- a second order spatial advection scheme that leads to less numerical diffusion
- higher order advection schemes for intra-spectral propagation
- advections schemes that are fully energy conservative

IV. Improvements of the individual source terms/ processes

A. *Advection*

Different changes were made to the advection routines. For the currently available characteristic method, a sub time step was implemented. The objective of this sub time step is to speed-up the code, by calculating shorter streamlines, which in parallel extend less to other subdomains, in order to improve the parallel scaling of the advection, at the expensive of some increase in the numerical diffusion. Furthermore, a fractional step method was implemented similar to WAVEWATCH, where spatial advection and intra-spectral propagation are calculated separately. This has various advantages compared to the original method:

- Fully-conservative intra-spectral schemes are now possible (discussed in the next paragraph).
- As the spatial propagation is now two-dimensional, various existing advection schemes from TELEMAC can now be used in TOMAWAC. In this way, three additional advection schemes become available to TOMAWAC:
  - Two-dimensional characteristic method. This method was newly implemented in the module *streamline.f*. It was found that for efficiency in parallel, it is necessary to have the parallel communication for all streamlines (for all spectral bins) together. This leads to the need of a slightly different version of this method.
  - The first-order accurate NERD residual distribution scheme [11]. This advection scheme was modified in order to be able to deal with velocity-fields that are not divergence free (as discussed in [12]), such that the advection scheme conserves energy exactly.
  - The second-order accurate ERIA residual distribution scheme [11]. This advection scheme was also modified in order to deal with velocity fields that are not divergence free [12], such that the advection scheme conserves energy exactly.

- As the spatial and intra-spectral calculation are decoupled, it is not necessary to calculate the advection for all spectral bins. Instead, in case spectral bins do not contain wave energy, it is not necessary to calculate the advection. The wave energy content of a spectral bin can be checked with a threshold criterium. This threshold method is currently only implemented for ERIA and NERD schemes.

  The disadvantage of this approach is that it can be slower than the original four-dimensional characteristic method (as now a separate method is needed for intra-spectral propagation) and that there is a time step criterion due to the use of a fraction step method.

B. Intra-spectral propagation

The intra spectral propagation methods that were newly implemented uses the same numerical methods as WAVEWATCH. Three different schemes were implemented, each of which is explicit, non-oscillatory and fully energy conservative:

- Upwind scheme (first order accurate).
- UNO scheme (second order accurate).
- Ultimate QUICKEST scheme (third order accurate; this scheme is currently only implemented for refraction, not for frequency shifting).

As these method are explicit, they have a strong time step restriction. In order to make the calculation as performant as possible, the local advection time step is divided into sub steps, to ensure that CFL number is lower than one. The number of sub steps is chosen individually for each point in space, leading to an optimal time step in each spatial point.

C. Shoaling

Shoaling is the change in wave height that occurs by the change in the propagation velocity of the wave energy due to changes in the water depth. In his book, Holthuijsen [10] explains shoaling by the conservation of Ec_g, with E the wave energy and c_g the wave group velocity. In order to simulate this effect a fully conservative discretization of the advection is needed. However, the characteristic method does not use the conservative form, and hence does not fully simulated the effect of shoaling (a test to show this is presented in section VI). Therefore, shoaling is implemented as an extra source term that determined by applying the product rule to the spatial advection term in equation 1:

$$\underbrace{\frac{\partial c_{g,j} N}{\partial x_j}}_{conservative\ form} = \underbrace{c_{g,j}\frac{\partial N}{\partial x_j}}_{non-conservative} + \underbrace{N\frac{\partial c_{g,j}}{\partial x_j}}_{shoaling\ term} \quad 2$$

This term is discretised implicitly in case the divergence of the wave velocity field is negative (i.e. when it acts as a sink term) and explicitly when it is positive and works as a source of wave energy. This source term is currently only included for the two-dimensional characteristic method, not for the original three and four-dimensional characteristic methods (a similar term in included in the ERIA and NERD schemes see [12]).

D. Refraction velocity limiter

As the new refraction schemes are explicit, the CFL number needs to be lower than one, which can lead to small time steps and hence large calculation times. On the other hand, the mesh spacing or time step used in the spatial advection may lead to rather strong changes in the direction of the wave energy. Dietrich et al [6] therefore present a limiter on the propagation velocity in spectral space, in order to prevent excessive turning of wave energy as well as frequency shifting, which is given by:

$$|c_\theta| < \alpha_\theta \Delta\theta \left(\frac{|c_x|}{\Delta x} + \frac{|c_y|}{\Delta y}\right) \quad 3$$

$$|c_\sigma| < \alpha_\sigma \Delta\sigma \left(\frac{|c_x|}{\Delta x} + \frac{|c_y|}{\Delta y}\right) \quad 4$$

Here, the Δx and Δy, are the spatial mesh spacing, c_x and c_y, the spatial wave energy propagation velocity components, c_θ and c_σ, the intra-spectral propagation velocities, $\Delta\theta$ and $\Delta\sigma$ the mesh spacing in spectral space, and finally α_θ and α_σ are both tuning parameters, which are set to 0.90. This limiter has a similar effect as the smoothing of the bathymetry used in WAVEWATCH, which leads to more gentle bathymetric gradients and hence smaller refraction velocities $|c_\theta|$. These limiters are implemented in TOMAWAC in a new subroutine, called *limit_celerity.f*. This subroutine is called after c_θ and c_σ are calculated in the subroutines *conwac.f* or *conw4d.f*. In this subroutine the calculated values of $|c_\theta|$ and $|c_\sigma|$ are decreased to the values in equation 3 and 4, in case the originally calculated values were higher.

E. Depth induced breaking

Depth induced breaking is taken into account in the inner local loop. Hence it is called often, leading to the need for a fast subroutine for the calculation of depth induced breaking. Nevertheless, profiling of the TOMAWAC code showed that the calculation of the depth-induced breaking term used a substantial amount of calculation time. The exact amount depends strongly on the keyword NUMBER OF BREAKING TIME STEPS, which is rather hard to estimate a priori. Therefore, a new implementation was made for depth induced breaking (currently only for the breaking parametrization of Battjes-Janssen [9], which is the default in TOMAWAC). This new implementation of the source term speeds up the calculation of the depth-induced breaking significantly by the following modifications:

- The use of an implicit numerical scheme with Newton-Raphson iteration similar to SWAN. This has the additional advantage that it makes the computation more robust and that the user does not need to specify the number of time steps for the breaking iterations; the number of iterations is determined automatically using a convergence criterion.
- The use of a threshold insures the depth-induced breaking is only calculated on the mesh points, where depth induced breaking is important (i.e. shallow points).

- The calculation of the energy dissipation for the mean action density only, because the source term of Battjes-Janssen leads to an energy dissipation that is constant for each component in the spectrum. Hence, multiple iterations are performed, adapting the wave energy variance. After all iterations are performed, the calculated change in the wave energy variance is distributed over the wave spectrum.

The new breaking term can be activated by setting the keyword DEPTH-INDUCED BREAKING DISSIPATION = 10.

F. Triad interactions

It was found that the triad interactions (using the LTA parametrization [13]) can lead to numerical problems. In this source term, energy is transformed from the spectral peak to higher frequencies (Figure 2). The strength of this transfer depends on the energy difference between a frequency and twice this frequency. In case this energy difference is large, the transfer is fast. In combination with a large time step, this leads to transfer that is so large, that negative wave energies are generated around the peak frequency. These negative energies are later set to zero, leading to changes in the wave energy. In order to prevent this issue, a new source term was implement for triad interactions, with the following properties:

- The discretisation is implicit for the points in the spectrum where the wave energy decreases and explicit where it is increasing (thereby strongly decreasing the probability that the wave energy becomes negative).
- Sub steps in time are used that increase according to:

$$\Delta T_{i+1} = \mathrm{n}\Delta \mathrm{T_i}$$

  with *n* a used defined parameter. This is the same method that is currently used in the breaking loop in TOMAWAC).
- The number of sub time steps that is used, is determined using a heuristic equation, based on the energy at the peak of the spectrum.

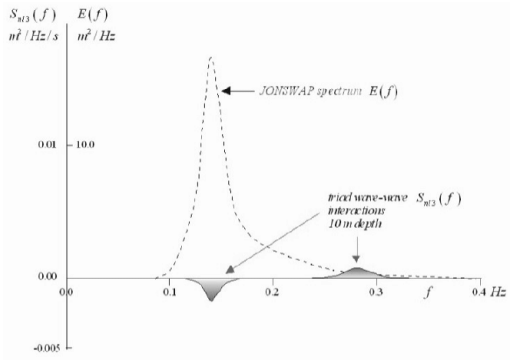

Figure 2 Schematic of the triad interaction source term (from [10])

The new triad source term can be activated by setting TRIAD INTERACTIONS= 10

G. MDIA

Some test showed that the use of the Multiple Direct Interaction Approximation (MDIA) [7] took considerable calculation time. A code restructuration was done, changing the ordering of the loops, in order to limit the number of cache losses. This lead to a speedup of this term by 50%, without changing the results (at the expense of a slightly larger use of RAM memory). Nevertheless, this source term remains relatively slow, compared to the DIA. This source term is nevertheless interesting, because it is a more complete approximation of the quadruplets interactions than the DIA, leading amongst others to a better prediction of the directional spreading (which typically is too broad when using DIA). However, the other source terms (wind-input and whitecapping) have typically been calibrated in combination with DIA, rather than MDIA, such that those source terms would have to be retuned for its use in combination with the MDIA.

H. Linear wind input

The linear wind input term [8] appeared to take a substantial amount of calculation time (about a factor four more than other source terms such as the whitecapping or non-linear wind input). The reason for this was that there was a substantial number of evaluations of geometric and exponential functions in the inner loop (i.e. evaluated for each spectral points). The code has been restructured, to bring these terms as much as possible to the outer loops, which results in a speed-up of a factor four for this specific source term, bringing the calculation speed in line with the other source terms.

V. NEW KEYWORDS IN TOMAWAC

In order to use the new functionalities, the following keywords were added:

ADVECTION SCHEME: this determines the advection scheme. The options are:

- 1= classical streamlines
- 11=2d streamlines + separate refraction
- 14=NERD + separate refraction
- 15=ERIA 1st order in time + separate refraction
- 16=ERIA 2nd order in time + separate refraction

NUMBER OF ITERATIONS FOR SMALL SCALE PROCESSES: this determines the number sub steps taken in the inner loop (for advection, refraction, depth-induced breaking and triads), thus determining the local time step.

NUMBER OF ITERATIONS FOR ADVECTION: this determines the number of sub steps for spatial advection within the local sub step (as set by the previous keyword). This keyword is only used for ADVECTION SCHEME 1 or 11.

SHOALING: if yes, the effect of shoaling is taken into account (only for ADVECTION SCHEME 11).

ADVECTION SCHEME FOR THETA: determines the advection scheme for propagation along the directions (i.e. refraction). The possible options for the this keywords are:

- 0=off; this option is useful for theoretical test cases but should not be used in practical simulations.
- 1=first order upwind
- 2=second order UNO
- 3=third order ULTIMATE QUICKEST

ADVECTION SCHEME FOR F: determines the advection scheme for propagation along the frequencies (i.e. frequency shifting due current velocity gradients). The possible options for the two keywords are:

- 0=off; this option
- 1=first order upwind
- 2=second order UNO

LIMITER FOR REFRACTION VELOCITY: switches the limiters of the intra-spectral propagation velocities on or off. The options are:

- 0=off
- 1=only for directions
- 2=only for frequencies;
- 3=for frequencies and directions

VI. RESULTS

In this section, a number of test cases is presented that were performed using the new schemes. This is part of ongoing work, for which still some extra test cases need to be added in a later stage.

A. *Simple shoaling test*

In the first test case, a shoal with a steep bathymetry gradient is studied (Figure 3). Only advection, refraction and shoaling are considered for different advections schemes. Source terms are switched off. The mesh is made of cells with a size of 100m in the wave direction; the time step is 30 s. A rather fine spectral mesh is used, with 72 directional bins. A JONSWAP spectrum is applied at the boundary (monodirectional waves by using a very low directional spreading value, by setting BOUNDARY DIRECTIONAL SPREAD 1 = 500) with H_s = 3.0 m and T_p = 5.0 s.

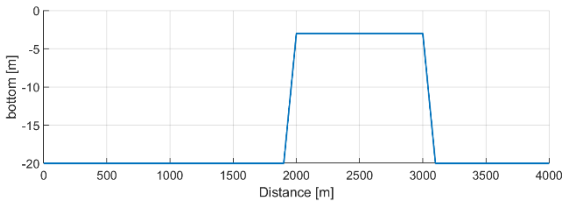

Figure 3 Bathymetry for the simple shoaling case

TABLE 1 OVERVIEW OF THE SETTINGS FOR THE DIFFERENT CALCULATIONS

RUN	SCHEME FOR ADVECTION	SCHEME FOR ADVECTION OF THETA	SHOALING
1	1	n/a	n/a
2	11	0	NO
3	11	1	NO
4	11	0	YES
5	14	0	n/a

The calculated wave heights are shown in Figure 4 for the different simulations that are shown in Table 1. The results are compared with the analytic solution for shoaling of monochromatic waves [10]:

$$\frac{H_s}{H_{s0}} = \sqrt{\frac{c_{g0}}{c_g}} \qquad 5$$

From the result it appears that the case with shoaling on (run 4) as well as with the NERD scheme (run 05) correctly calculate the change in the wave height due to the changes in the bathymetry. For the new two-dimensional characteristic method without refraction or shoaling (run02), the wave height remains constant in the whole model domain. In case refraction is switched on (run03), the wave height increases on the shoal, rather than decreases. This is not very dramatic for the run with two-dimensional -streamlines in combination with the new energy conservative intra-spectral calculation scheme (run03). Note that an additional simulation using the limiter of Dietrich et al [6] eliminated this effect completely and for that simulation, the resulting wave height was the same as the one obtained in run02. Furthermore note that the simulation with the limiter on was substantially faster than the simulation without the limiter.

Simulations with the original scheme in TOMAWAC (run01) show large unphysical increases in the wave height. The reason for this is that some of the streamlines calculated at the downwind side of the bar turn in such a way, that the bring wave energy from the mean wave propagation direction to other directions. This shows the importance of having an energy conservative scheme for the intra-spectral propagation. Hence this test case, clearly shows the improved robustness of the new two-dimensional advection scheme with separate refraction schemes. It furthermore demonstrates the need to take a separate shoaling term into account, in order to correctly reproduce this effect.

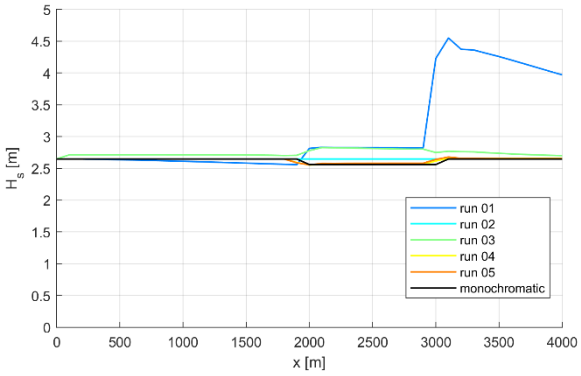

Figure 4 Resulting significant wave height in the simple shoaling case for different advection schemes.

B. *Beach case (breaking test)*

In order to test the new breaking implementation, a test is performed on a beach, with a constant slope of 1/100 and a mesh resolution of 10 m in the wave direction (Figure 5). Monodirectional waves were applied at the boundary condition using a JONSWAP spectrum with H_s = 1.0 m and T_p = 10.0 s. The simulations are performed using advection scheme 11 (two-dimensional streamlines) without shoaling. The only source term that is considered is depth-induced breaking using the method of Battjes-Janssen. Both the original explicit method and the new implicit method are considered.

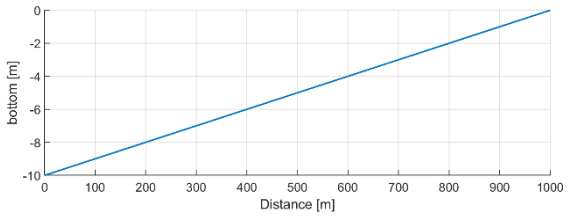

Figure 5 Bathymetry of the beach case.

The results of the different simulations are shown in Figure 6. The results are compared to a simple analytic approximation, which is determined by setting the significant wave height to 0.78 the water depth. The results of both methods are rather similar. The wave height using the original method appears smoother. The result of the new scheme is closer to the analytical approximation. As the results are inconclusive, it is the intention to perform more test for depth induced breaking, in which the results for the different schemes are compared to measurements form literature.

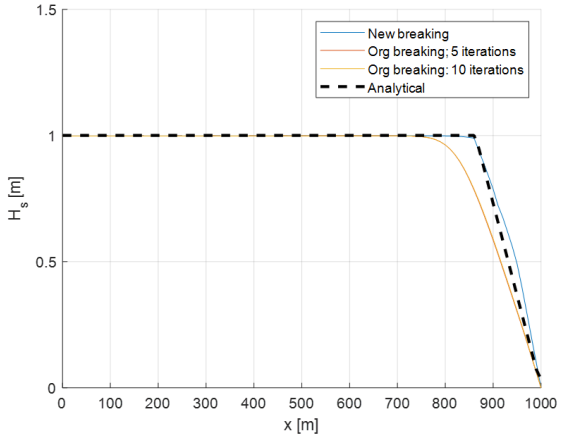

Figure 6 Significant wave height for the beach case for different advection schemes.

C. *Energy conservations (North Sea model test)*

The energy conservation of the different advection schemes was checked in a large scale TOMAWAC model of the North Sea, developed by IMDC. In order to test the energy conservation, an initial wave field with a significant wave height of 2.0 m was applied in the middle of the North Sea (Figure 3). The model was run with different advection schemes, but without any source terms. The water depth was kept constant in time (implying that the streamlines were only calculated once in the beginning of the calculations). The wave height at the open boundaries was set to 0.0 m. The runs were executed on 32 processors. The time step was set to 2 minutes.

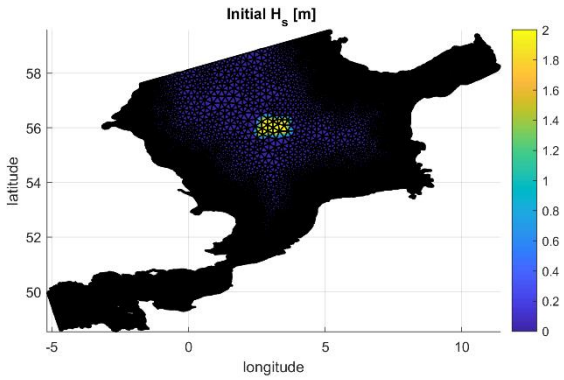

Figure 7 Initial significant wave height in the North Sea model.

In this test, the total initial wave height should stay constant, until the waves arrive at the coast or at the open boundary. Then the wave energy should start to decrease. The settings of the different calculations are shown in Table 2. The results of the total wave energy in the domain are shown are shown in Figure 4. From this figure, it is clear that energy is not conserved for the characteristic method (run 1). The new two-dimensional streamline scheme in combination with a separate method for refraction and the shoaling parametrization (run 3) ,shows a similar energy loss as the original scheme in TOMAWAC (run 1), whereas the same scheme without shoaling (run 2) actually gains energy (but the

difference with the exact conservation is lower than for run 1 and 2). The original method is faster than the two new methods (with a very limited change in calculated speed due to the inclusion of shoaling). This is due to the extra calculation time needed in the refraction calculation. Note that the limiter from Dietrich et al. [6] was not used in these calculations. A simulation similar to run 2 with the limiter switched on, finished in 154 s (substantially faster). Then the simulation with the new scheme is only 15% slower than the calculations with the original scheme (run01), this difference is not substantial for real calculations, as then the calculation time is for a large part determined by the source terms, or updating of the streamlines in the case of varying currents or water depths. The residual distribution schemes (run 4 to 6) conserve energy, but are substantially slower than the schemes based on the characteristic method. Especially the ERIA scheme is slow. Note hereby that limited effort was put into optimizing the calculation speed of these schemes for TOMAWAC, such that some improvements still might be possible for these advection schemes.

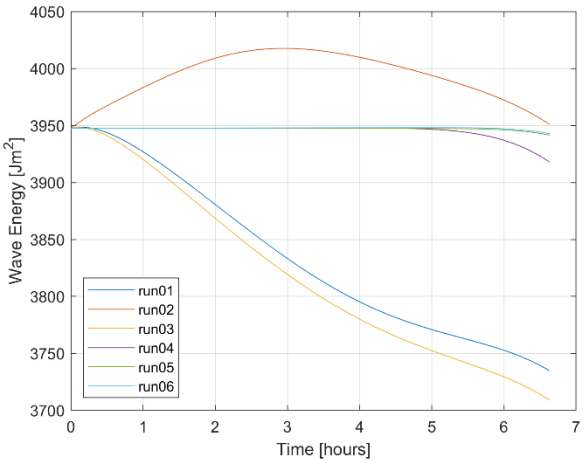

Figure 8 Total wave energy in the domain as function of time for the different simulations.

TABLE 2 SETTINGS AND CALCULATION TIME FOR THE DIFFERENT RUNS.

RUN	Advection scheme	Advection scheme for theta	Shoaling	Calculation time [s][
1	1	n/a -	n/a	134
2	11	1	NO	181
3	11	1	YES	185
4	14	1	n/a	360
5	15	1	n/a	790
6	16	1		880

D. Beji-Battjes bar (triads)

In order to test the new implementations for the triad interactions, the experiment Beji- and Battjes [15] is simulated in TOMAWAC. In this experiment, waves are approaching a shallow bar (Figure 3), where triad interactions occur. A model of a channel was made, with a mesh resolution of 0.1 m. The only source-term that is considered are the triad interactions. Advection is simulated using the original characteristic method (ADVECTION SCHEME =1). Monodirectional waves with a JONSWAP spectrum were used as boundary condition with H_s = 2.9 cm and T_p = 2.5 s. the different simulations that were performed are shown in Table 3.

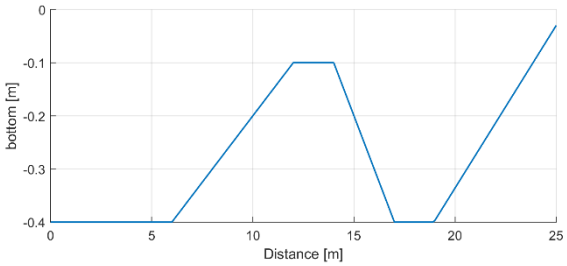

Figure 9 Bathymetry of the Beji-Battjes test case. The water level is at 0.0m.

TABLE 3 OVERVIEW OF THE DIFFERENT SIMULATIONS FOR THE BEJI-BATTJES TEST CASE

RUNS	Time step	nr of sub steps for triad interactions	triads scheme	calculation time
run01	0.5	1	1	45
run02	0.5	5	1	97
run03	0.5	10	1	168
run04	0.05	1	1	421
run05	0.5	1	10	58

The wave spectra at x = 17 m (behind the bar) are shown in Figure 4. It appears that all schemes give the transfer of energy to the higher frequencies. There is a substantial difference with the measured spectra, where the peaks are much less pronounced. This difference is likely due to deficiencies in the LTA method used for the parametrization of triad interactions. The results of the simulations with the new scheme (run05) resemble the results from the original scheme, for simulations which uses multiple sub steps for triads (run02 and run03) or a smaller global time step (run04). The increase in calculation time of the new scheme is limited, compared to the simulation using the original scheme with one sub step for triads (run01). However, the results in run01 are somewhat different for the high frequencies, suggesting that more iterations are needed. The increase in calculation time is modest (30%) compared to run01. However, the new method is faster than the other runs (02 to 04).

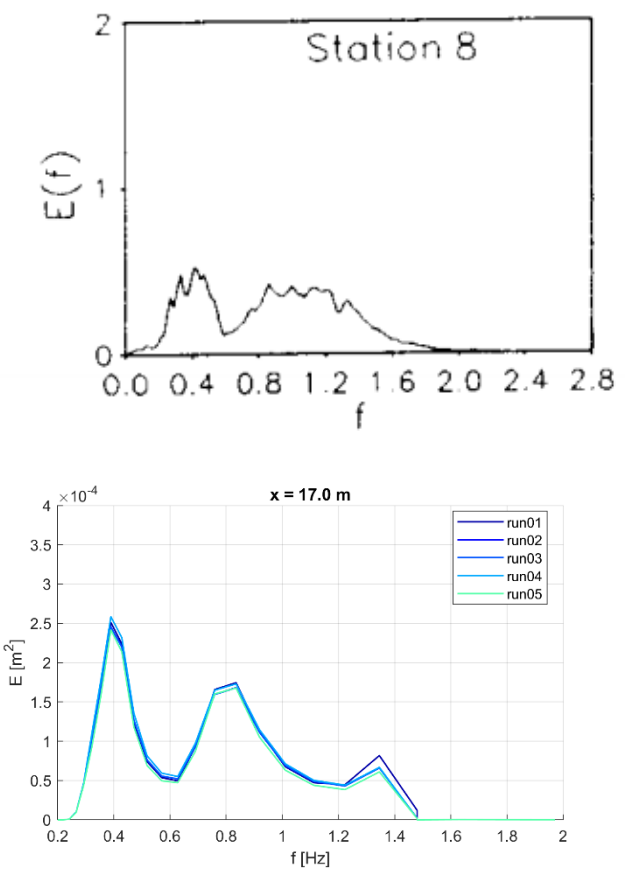

Figure 10 Wave spectra at 17 m (behind the bar) for the different simulations Top: measurement [15]. Bottom TOMAWAC result

In recapitulations, for this specific test cases, the issues with energy loss due time steps that are too high (see section IV) do not occur and both the original and the new give adequate results. The new method automatically choses the number of sub time steps, and hence leads to converged results with a relatively modest increase in calculation time

E. Haringvliet case (SWAN)

Finally, the new methods were applied in a real test case. The case that was used for this is the model of the Haringvliet, which is used to validate the SWAN unstructured mesh version [14]. The bathymetry is shown in Figure 3. The model contains 5961 nodes. The model is run with one single processor for some time until the wave conditions are in equilibrium, using advection scheme 1 (full characteristics). The source terms that were considered are wind-input (linear and exponential), whitecapping, quadruplets (DIA), bottom friction and depth induced-breaking.

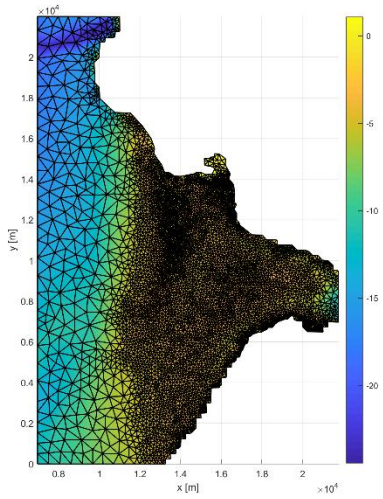

Figure 11 Bathymetry and mesh of the Haringvliet model

The different runs that were performed are:

- Run 1: Original TOMAWAC code
- Run 2:using improved version for linear wind-input.
- Run 3: Run 2 + new implicit depth induced breaking scheme
- Run 4: Run3: + five sub time step for local processes.

The results were compared between all four simulations, and it appeared that the results were very similar between the different runs, except for the change of the depth-induced breaking scheme (i.e. comparing run 2 and 3). This is not unreasonable, as a different numerical method is used. Calculation times of the different simulations are shown in Figure 4. It can be seen that the total speed up is about a factor four in this case, with the largest speed-up obtained from the change in numerical scheme for depth-induced breaking.

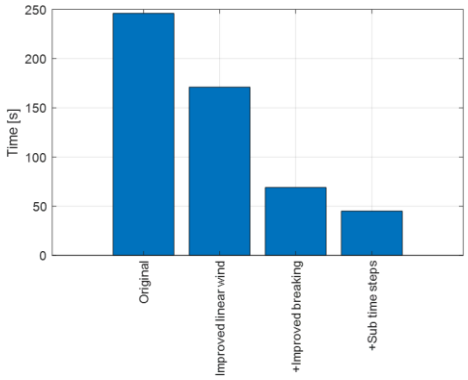

Figure 12 Calculations times

V. Conclusions

In this paper, a new computational architecture for TOMAWAC was presented, in which separate time steps are used for local, small scale processes (depth-induced breaking, advection, intra-spectral propagation and triad interactions) and for large scale slow processes (quadruplets, wind input, whitecapping and bottom friction). New numerical algorithms were introduced for triad interactions and depth-induced breaking. Additional advection schemes, as well as intra-spectral propagation schemes were introduced and the effect of shoaling was added to these schemes, which was previously not taken into account. The robustness of the new methods is shown in various academic test case. In a small real-life example case, it is shown that a speedup of a factor of four can be achieved using the newly developed functionalities.

Acknowledgement

This projects is executed in the framework of the bluecluster research into blue energy the financial support from bluecluster is highly appreciated.

References

[1] Tolman, H. L. (2009). User manual and system documentation of WAVEWATCH III TM version 3.14. Technical note, MMAB Contribution, 276, 220.

[2] Booij, N., Holthuijsen, L. H., & Ris, R. C. (1997). The" SWAN" wave model for shallow water. In Coastal Engineering 1996 (pp. 668-676).

[3] Roland, A. (2008). Development of WWM II: Spectral wave modelling on unstructured meshes (Doctoral dissertation, Ph. D. thesis, Technische Universität Darmstadt, Institute of Hydraulic and Water Resources Engineering).

[4] Benoit, M., Marcos, F., & Becq, F. (1997). TOMAWAC. A prediction model for offshore and nearshore storm waves.

[5] Monbaliu, J., Padilla-Hernandez, R., Hargreaves, J. C., Albiach, J. C. C., Luo, W., Sclavo, M., & Guenther, H. (2000). The spectral wave model, WAM, adapted for applications with high spatial resolution. Coastal engineering, 41(1-3), 41-62.

[6] Dietrich, J. C., Zijlema, M., Allier, P. E., Holthuijsen, L. H., Booij, N., Meixner, J. D., ... & Westerink, J. J. (2013). Limiters for spectral propagation velocities in SWAN. Ocean Modelling, 70, 85-102.

[7] Tolman, H. L. (2004). Inverse modeling of discrete interaction approximations for nonlinear interactions in wind waves. Ocean Modelling, 6(3-4), 405-422.

[8] Phillips, O. M. (1957). On the generation of waves by turbulent wind. Journal of fluid mechanics, 2(5), 417-445.

[9] Battjes, J. A., & Janssen, J. P. F. M. (1978). Energy loss and set-up due to breaking of random waves. In Coastal engineering 1978 (pp. 569-587).

[10] Holthuijsen, L. H. (2010). Waves in oceanic and coastal waters. Cambridge university press.

[11] Hervouet, J. M., Pavan, S., & Ricchiuto, M. (2017). Residual distribution advection schemes in Telemac (Doctoral dissertation, Inria Bordeaux Sud-Ouest).

[12] E Fonias, WA Breugem, L Wang, A Bolle, G Kolokythas, B De Maerschalck (2021), Cross-shore processes implementation in GAIA, submitted to TUC 2021

[13] Eldeberky, Y. (1997). Nonlinear transformation of wave spectra in the nearshore zone. Oceanograpy

[14] Zijlema, M. (2010). Computation of wind-wave spectra in coastal waters with SWAN on unstructured grids. Coastal Engineering, 57(3), 267-277.hic Literature Review, 4(44), 297.

[15] Beji, S., & Battjes, J. A. (1993). Experimental investigation of wave propagation over a bar. Coastal Engineering, 19(1-2), 151-162.

A Lossy Compression Experiment of Telemac Data

Fabrice Zaoui
EDF R&D – National Laboratory for Hydraulics and Environment (LNHE)
6 quai Wattier, 78401 Chatou, France
E-mail: fabrice.zaoui@edf.fr

***Abstract*— The Telemac-Mascaret system can require or produce large amount of data to address complex problems in geoscience or industry. This statement is verified with the availability of new databases and the increase of problem sizes solved by numerical simulation nowadays. But how to efficiently deal with such data when file sizes can range from several gigabytes to terabytes, or more? Dealing with a vast volume of data is not always possible. Copy, transfer or storage of large files can quickly become an issue to carry out a study in a short period of time. The high memory usage is mainly due to the double precision floating point representation of billions of real numbers, which can hardly be avoided except with doing a compromise between necessity and feasibility. For example, the latter can be the frequency of saving results in file which may differ from the calculation time step. In this paper, another compromise is presented. It is the possibility of reducing the insignificant part of the information by compressing the data with a lossy algorithm. The acceptance of a loss of accuracy may have meaning in view of the uncertainty present in data especially if it is linked to the definition of error values that cannot be exceeded. To this end, the lossy compressor SZ is tested on hydrodynamic data coming from very large Selafin files. This tool can highly decrease the size of the data with compression ratio values directly depending on the user's choice for the error bounds. Some limitations and perspectives of this experiment are also discussed.**

I. INTRODUCTION

Many sources of uncertainty lie in real-world problems. The underlying data needed to describe and analyse a case study always has a high level of numerical accuracy when stored on disk leading to large file sizes. However, this level of accuracy does not necessarily reflect the reliability of the information whether it comes from observations or calculation results. Telemac simulations can require or produce large amount of disk data, in the range of several gigabytes to terabytes, which can cause copy, transfer or storage issues.

Such a vast volume of data is not still possible or tractable. Even if the floating-point representation of real numbers in 64 bit double-precision format helps keep rounding errors within an acceptable range for the convergence of many numerical algorithms, it is not always necessary or relevant when storing a database with millions of samples for example. The well-known lossless compressors like gzip or 7z are possible solutions to decrease file sizes but with a low compression ratio for binary data. With the help of HPC, this paper proposes to investigate better compression rates by accepting certain but controlled losses on hydraulic data.

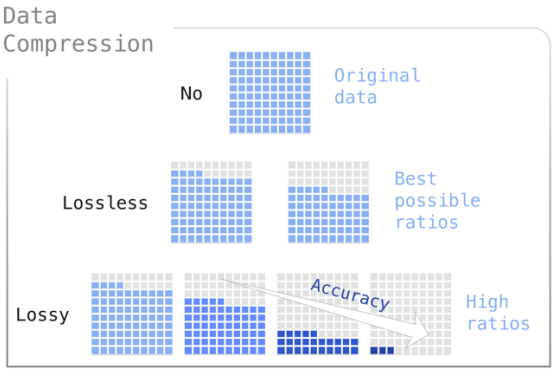

Figure 1. Lossless and lossy data compression

Accuracy is one of the criteria to evaluate or measure data quality, see Fig. 2. It tells how far the data is from reality, considering this last one is known with certainty. Other criteria exist like: *Completeness* (is the data diversity sufficient to fulfill the requirements of phenomena studies?); *Consistency* (is there any kind of contradictory information in the database?); *Timeliness* (how old is the data and does it still reflect a possible new reality?); *Validity* (is the available data in the correct structure and format?); *Uniqueness* (does a recording with specific characteristics only appear once?); *Integrity* (can the relevant information always be found in the database whatever the request?); and *Auditability* (are data changes traceable?).

Figure 2. Data quality criteria

Accuracy should not be confused with precision. Accuracy is important to depict reality well but is not directly related to precision where the concepts of repeatability and reproducibility dominate. Accuracy refers to how close data is to a known value while precision refers to data dispersion. Consequently, accuracy and precision are not correlated, see Fig. 3.

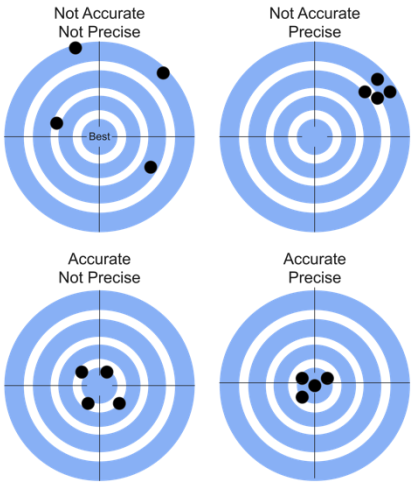

Figure 3. Accuracy vs Precision

A higher numerical accuracy in data does not necessarily reflect, paradoxically, a better reality. This is due to the uncertainty that occurs at all stages of data acquisition and processing. Indeed, data acquisition is prone to errors because it can be intrusive and then change reality, or it uses measurement or communication devices with limited specifications or reduced performance over time (perhaps in addition of one or more human operations) or it can be simply partial. The simulation of physics is also error prone. Nowadays it mainly relies on numerical modeling with incomplete or approximative consideration of complex phenomena. Moreover, all the real numbers can not exactly be represented by computers and rounding operations are performed. This is due to the binary representation in memory with a limited number of bit. With this drawback in mind, the best possible accuracy in the floating-point representation of real numbers still remains primordial for the numerical computations as it mainly governs the convergence of solving algorithms and confidence in output results.

Thus, the level of accuracy for data storage must be fixed according to the knowledge of the errors involved in the processing chain (uncertainty, see Fig. 4).

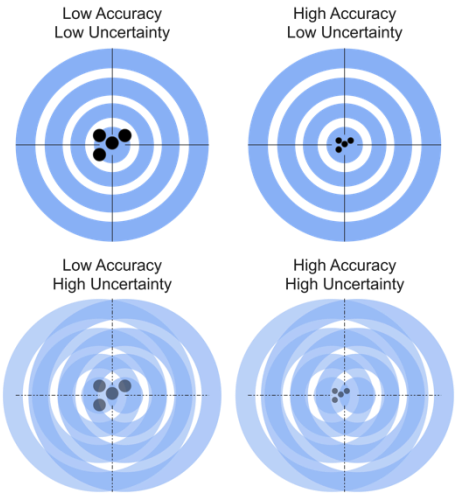

Figure 4. Accuracy vs Uncertainty

II. Data Compression

When considering the study of a geoscience problem with the help of numerical modeling, one will sooner or later face the huge size of data in the input sets or output results. Even with a supercomputing infrastructure, the data file sizes without any compression can be a restriction on what it is really possible to study, save and share because of the limited amount of memory and network bandwidth.

Data compression for reducing the logical file size is usually done without any loss of information but with a limited power (ratio between the uncompressed and compressed sizes). Lossy compressors (SZ, ZFP, ISABELA, NUMARCK…) have better ratio performances but with a loss of accuracy when compressing information.

SZ is an open framework designed for scientific data and has the advantage of providing several criteria to control loss of accuracy error [1]. It can be used for many purposes involving data processing and has implementations on CPU, GPU and FPGA. It supports different languages like C, Fortran, Java and Python. It is also included in I/O libraries like HDF5.

The version of June 2020 (v2.1.8.3) has been installed on EDF GAIA HPC cluster with the default options (no OpenMP, Intel Xeon Gold 6140 2.3 GHz, 384 GB per node). It is used on some Mascaret and Telemac hydraulic results but not directly on Selafin files as it is designed for the (de)compression of floating-point arrays in byte stream format. Thus, before using SZ, the Selafin files are first converted into raw binary two-dimensional files: a number of mesh nodes and a number of time steps. If this file is named 'telemac.dat' with results on a mesh of 10,000 nodes for 2,000 time steps, its compression based on SZ is simple:

> sz -z -d -c sz.config -i telemac.dat -2 10000 2000

where:

-z is for compression;

-d for double precision;

-c for the configuration file (user criteria on the errors produced);

-i for the input data file;

-1, **-2**, **-3**, **-4** for the array sizes.

The result of this command will be the creation of a new file 'telemac.dat.sz' whose size will depend on the configuration file 'sz.config'. For the decompression, the command is similar:

> sz -x -d -s telemac.dat.sz -2 10000 2000

where:

-x is for decompression;

-s for the input file.

The result of this last command will be the creation of the file 'telemac.dat.sz.out' whose size is the same as 'telemac.dat' but with a loss of accuracy.

More options and combinations are possible, see the in-line help information (> ***sz -h***) if needed.

Eight options are available in the configuration file to control different types of error bounds. Only three of them are presented and tested int this work:

- The absolute error bound (ABS) is to limit the errors to be within an absolute error. For instance, if this value is 10^{-3} then all the (de)compressed values will be in $[V - 0.001, V + 0.001]$ where V are original values;
- The relative bound ratio (REL) is to limit the errors by considering the global data value range size. For instance, if this value is 10^{-3} and the dataset is $\{0, 1, 2, 3, \dots, 100\}$ then the error bound will be $0.1 = (100 - 0) \times 10^{-3}$;
- And the point-wise relative bound ratio (PW_REL) is to limit the errors by considering each value. For instance, if this value is 10^{-3} and the dataset is $\{0,1,2,3, \dots ,100\}$ then (de)compression errors will be limited to $\{0, 0.001, 0.002, 0.003, \dots, 0.1\}$.

III. CASE STUDY

A. *Mascaret*

The case is a water quality study on the Rhine river where the discharge is saved on file at every time step. This allows to compute the hydraulics only once for the tracer part (convection and diffusion of constituents) and thus speeding-up the overall simulation as the tracer part is generally less computational time-consuming compared to the hydraulic part of Mascaret.

The resulting file is named 'Q.masc' whose description is given in Table 1.

TABLE 1: MASCARET ORIGINAL FILE DESCRIPTION

Number of nodes	1,170
Number of time steps	1,848,961
Number of values (8 Bytes)	2,163,284,370
Original file size (GB)	16
Original file size (Bytes)	17,306,274,960
Min. value ($m^3.s^{-1}$)	15.3
Max. ($m^3.s^{-1}$)	866.51
Mean ($m^3.s^{-1}$)	114.18
Median ($m^3.s^{-1}$)	77.11

The compression of the file 'Q.masc' with SZ is:

> sz -z -d -c sz.config -i Q.masc -2 1170 1848961

This file of 17 GB has been zipped with two lossless compressors (gzip and 7z with default options) to get some comparison items shown in Table 2.

TABLE 2: PERFORMANCES OF LOSSLESS COMPRESSORS

Tool	Output file size	Ratio	Compression time	Decompression time
gzip	14 GB	1.19	20'28"	3'58"
7z	11 GB	1.54	12'05"	17'23"

B. *Telemac*

For testing the compression of Telemac results, the 2D example case of Malpasset is considered, see Fig. 5 (fine grid mesh version with 104,000 triangular elements). The water depth is saved on the file 'H.tel' at each time step.

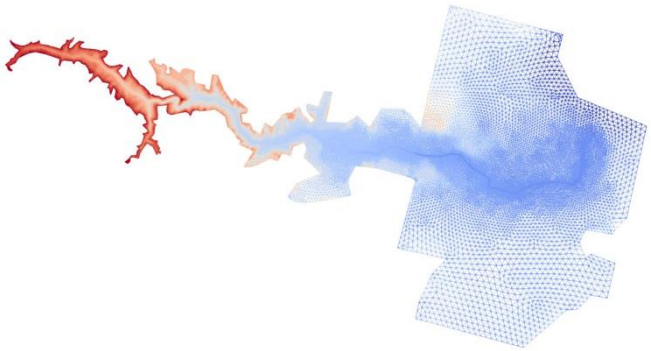

Figure 5. Malpasset triangular mesh

The compression of the file 'H.tel' with SZ is:

> sz -z -d -c sz.config -i H.tel -2 53081 400000

TABLE 3: TELEMAC ORIGINAL FILE DESCRIPTION

Number of nodes	53,081
Number of time steps	400,000
Number of values (8 Bytes)	21,232,400,000
Original file size (GB)	158
Original file size (Bytes)	169,859,200,000
Min. value (m)	0.
Max. (m)	193.92
Mean (m)	4.46

The data file 'H.tel' of 158 GB is too large to conduct all the tests of compression for the different criteria (ABS, REL and PW_REL) due to a lack of RAM on the computational node. It is also the reason why the median value of the water depths is not in Table 3.

IV. RESULTS

A. *Mascaret*

The first exercise is to test the compression of the file 'Q.masc' with the ABS criterion. Eight error threshold values have been set in the configuration file and all corresponding compression results are presented in Table 4.

TABLE 4: MASCARET ABS TESTS

ABS	Size	Compression time	Decompression time	Ratio	Check
1	5.7 MB	1'14	31"	2932	YES
0.1	33 MB	1'15	31"	509	YES
0.01	125 MB	1'23	34"	133	YES
0.001	215 MB	1'26	37"	77	YES
10^{-6}	533 MB	1'29	42"	31	YES
10^{-9}	2.8 GB	1'53	2'14"	6	YES
10^{-12}	8.3 GB	2'42	2'23"	1.94	NO
10^{-15}	12 GB	2'46	1'24"	1.45	NO

A systematic check of the ABS error on the decompressed data was performed. For the seventh and eighth test, the error threshold check did not work. Indeed, the value of 1.023×10^{-12} for the maximal error was obtained instead of 10^{-12} as requested, and 1.78×10^{-15} instead of 10^{-15}. This difference remains nevertheless very acceptable in view of the accuracy value to be satisfied (near the machine precision for floating point numbers stored in eight bytes).

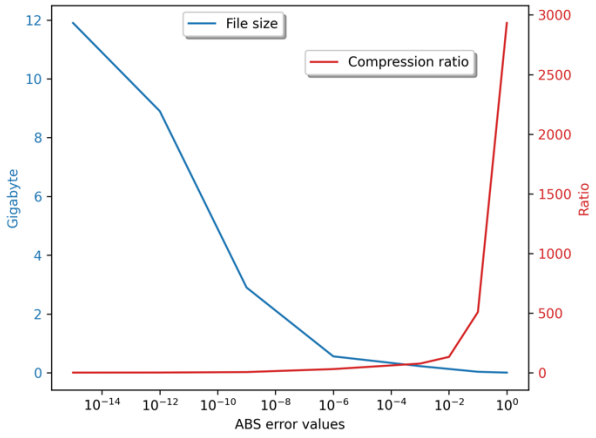

Figure 6. PCA representations of the eight tests

A Principal Component Analysis (PCA) of this dataset is shown in Fig. 7 and 8. PCA is a dimensionality reduction technique that is used here to bring out trends and strong patterns in the dataset. The dataset can be divided into three subsets according to the first two dimensions (with an explained variance of 92%), see Fig. 7. The first point is clearly an extreme value with a very high compression ratio but also with the highest error on the hydraulic discharge of $1\ m^3.s^{-1}$.

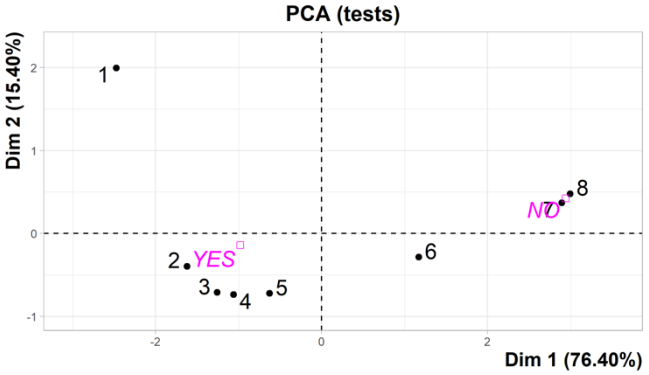

Figure 7. PCA representations of the eight tests

The dataset can be divided into three subsets according to the first two dimensions (with an explained variance of 92%), see Fig. 7. The first point is an extreme value with a very high compression ratio but for errors on hydraulic discharge of $1\ m^3.s^{-1}$. Tests 2 to 5 are more comparable in terms of processing time and gain on file sizes. The last three tests 6 to 8 are more demanding on the loss of information and present the lowest ratios.

Processing times and sizes are clearly anticorrelated to errors, with a correlation coefficient (Pearson) of -0.93 and a strong statistical significance (p-value coefficient of 7.8×10^{-4}) for the link between the file size and the ABS error criterion. The relation with the ratio is positive (ratio increases with the acceptance of a larger error) but less linear.

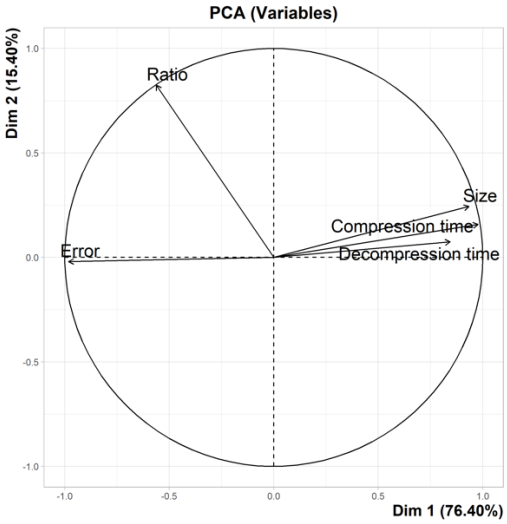

Figure 8. Correlation circle with PCA

The next test of SZ compression performance concerns the relative bound error REL. Only an error value of 10^{-3} is tested here which implies a maximum error of $0.8512\ m^3.s^{-1}$ as $10^{-3} \times (Q_{max} - Q_{min}) \approx 0.8512$. This test is successful as shown in Table 5.

TABLE 5: MASCARET REL TESTS

REL	Size	Compression time	Decompression time	Ratio	Check
0.001	6.3 MB	1'11	26	2623	YES

Lastly PW_REL criterion is tested for six error values as shown in Table 6. Compression and decompression times are not indicated in Table 6 as they are very similar for every test with approximatively $1'30''$ for the compression phase and $50''$ for the decompression one. It can be noticed that the PW_REL value of 10^{-3} can be directly compared to the REL value in Table 5 as they nearly give the same maximal error after decompression ($0.8512\ m^3.s^{-1}$ for REL and $0.84\ m^3.s^{-1}$ for PW_REL) but with a higher compression ratio for the REL algorithm.

PW_REL in Table 6 and ABS in Table 4 can be directly compared but they work differently depending on the compression ratio or the maximum error made.

TABLE 6: MASCARET PW_REL TESTS

PW_REL	Size	Ratio	Max. error ($m^3.s^{-1}$)
10^{-1}	197 KB	86184	83.03
10^{-2}	19 MB	907	8.35
10^{-3}	36 MB	471	0.84
10^{-4}	132 MB	126	0.0864
10^{-5}	256 MB	64	0.00848
10^{-6}	296 MB	56	0.000866

B. *Telemac*

The Telemac test file is about ten times larger than the Mascaret one. For this reason, not all compressions could be done due to the huge amount of RAM required by SZ leading to segmentation faults in some cases. These cases are indicated with a NA value in the following tables.

TABLE 7: TELEMAC ABS TESTS

ABS	Size	Compression time	Decompression time	Ratio	Check
1	4.7 MB	13'10"	4'54	34997	YES
0.1	31 MB	13'12"	4'52"	5299	YES
0.01	211 MB	13'57"	5'44"	770	YES
0.001	1.1 GB	14'9"	5'55"	149	YES
10^{-6}	15 GB	19'11"	14'37"	11	YES
10^{-9}	41 GB	26'58"	33'30"	4	YES
10^{-12}	NA	NA	NA	NA	NA
10^{-15}	NA	NA	NA	NA	NA

With the acceptance of 1 meter error on the water depths, the file size reduction is tremendous. Unfortunately, this maximal error value concerns a large part of the hydraulic domain, as indicated in the distribution graph in Fig. 9. This histogram presents the distribution of the error absolute value on the water depths for a randomly chosen time step. Many of the water depths have an error above $0.8\ m$.

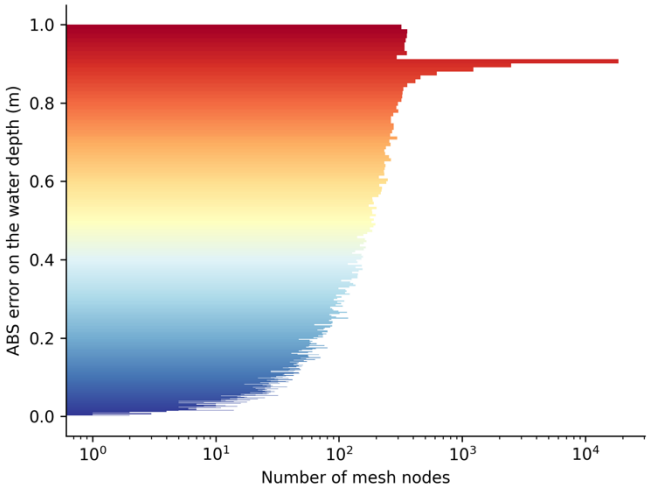

Figure 9. Absolute error distribution for ABS equal to 1 m

SZ does not produce a symmetric error centered on a zero-mean value in this case. Most of the decompressed values are greater than those in the original dataset, see Fig. 10.

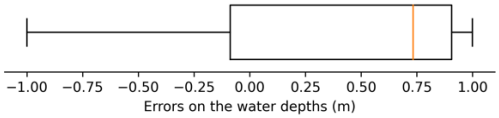

Figure 10. Non symmetric distribution of the errors

REL and PW_REL results are presented in Table 8 and 9 respectively. Once again it was not possible to go to the end of the compression test in both cases for the most restrictive criteria values. However, when the compressions are performed successfully, the compression ratios with a maximum water depth error of the order of a centimeter or less remain very important.

TABLE 8: TELEMAC REL TESTS

REL	Size	Compression time	Decompression time	Ratio	Check
0.001	19 MB	12'54"	5'41"	8726	YES
10^{-6}	2.5 GB	13'55"	5'41"	110	YES
10^{-9}	19 GB	19'51"	19'44"	8	YES
10^{-12}	NA	NA	NA	NA	NA
10^{-15}	NA	NA	NA	NA	NA

TABLE 9: TELEMAC PW_REL TESTS

PW_REL	Size	Ratio	Max. error (m)
10^{-1}	425 MB	381	17.883
10^{-2}	1.5 GB	110	1.8572
10^{-3}	2.8 GB	57	0.1842
10^{-4}	6.2 GB	26	0.0186
10^{-5}	11 GB	14	0.0018
10^{-6}	NA	NA	NA

V. CONCLUSIONS

The purpose of this article is to test a lossy compression tool for shrinking Telemac data. The tool used makes it possible to control the error made by the loss of accuracy. Different error control criteria were tested on two hydraulic data cases. It is shown that files can be compressed heavily compared to standard tools with an acceptable loss of information in many cases. Nevertheless, the consequence of this loss of information is not investigated here whereas it could influence the results of a study, for instance with a poor state initialization of the Telemac computations.

Not all the tests could be completed due to the memory usage that may be too high for the computer used for the tests. One possible solution without changing computers is to split the data files into several pieces so that they are processed separately. This approach has been tested with success with a parallel distribution of compressions on files larger than 1 terabyte.

Finally, not all SZ options have been tested. In particular, it is possible to consider the dependence of the data between each time step in order to achieve better compression performance.

REFERENCES

[1] S. Di and F. Cappello, "Fast Error-Bounded Lossy HPC Data Compression with SZ," 2016 IEEE International Parallel and Distributed Processing Symposium (IPDPS), 2016, pp. 730-739, doi: 10.1109/IPDPS.2016.1

Water Quality

A Hydrodynamic Model of the West Coast of Scotland with Coupled Sea Lice Dispersion

Tom Scanlon[1], Julien Moreau[2] and Matt Stickland[3]

[1]mts-cfd.com, The Barn, Townend of Kirkwood, Stewarton, KA3 3EW, Scotland. tomscanlon63@googlemail.com

[2]Plastic@bay.org, Breadalbane, Durness, IV27 4PN, Scotland. julien.moreau@plasticbay.org

[3]University of Strathclyde, Department of Mechanical and Aerospace Engineering, Glasgow, G1 1XJ, Scotland. matt.stickland@strath.ac.uk

***Abstract*— In order to assess the risk that wild salmon and sea trout will be harmed by parasitic sea lice emanating salmon farms a three-dimensional hydrodynamic and biological model of the West Coast of Scotland has been developed. The model uses TELEMAC-3D-WAQTEL and the computational domain extends from the Mull of Kintyre in the South to Cape Wrath in the North and includes all main islands of the West Coast. The model was successfully validated against observed hydrographic data (water levels and currents) and was found to provide a reasonable description of salinity and temperature levels. In an integrated biological model, virtual particles were constructed within the framework of the open-source particle-tracking code OpenDrift. These were released at each farm site and allowed to disperse into the marine environment. Each particle is a "super-individual", representing a number of sea lice larvae. The biological effects of sea lice production, maturity and mortality rates, salinity avoidance, temperature preference and phototactic vertical swimming behaviour (diel migration) were included. Results show that infective lice copepodids accumulate along tidal and salinity fronts, at the mouths of sea lochs and along shorelines, in different places according to the neap/spring tidal cycle and provide an indication of infestation risk to migrating wild fish.**

I. Introduction

Operational fish farms have the potential to affect the marine environment in several ways, via the release of waste in the form of dissolved nutrients, particulate organic matter, pesticides and live parasitic salmon lice. Farmed salmon are hosts for parasitic sea lice which are proven to harm wild salmon and sea trout [1, 2]. The risk of infestation by sea lice varies according to the density of lice to which the fish are exposed and the duration of that exposure [1, 3]. The wild salmon smolt migration may take place across a period of two months, but individual fish are likely to take only a few days to travel through local lochs to the open sea, so sea lice densities averaged over two months do not best represent the risk they face. In this paper the model outputs are presented in two ways, to demonstrate how the lice density and therefore the apparent risk vary:

1. Infective lice (copepodid) densities averaged over a 15-day period in May/June 2019 - a typical year when four of the seven modelled farms in this study contain high fish biomasses, shown as a heat map.
2. Copepodid densities calculated every hour, and converted to an equivalent daily lice density, shown as an animated series of lice density plots. These are the peak levels that migrating fish are likely to encounter. During their migration journey through the coastal area, they may pass through multiple areas of high lice density.

The oceanography of the west coast of Scotland, including the focus of this paper, Loch Hourn, is an area of complex water circulation exhibiting various levels of density stratification throughout the year. The capture of such three-dimensional phenomena necessitates that a 3D, non-hydrostatic approach is used. Freshwater sources from local rivers discharging into the Loch Hourn area were included to model salinity and temperature differences that act as an important driving force for fluid movement in fjordic systems such as those found on the West Coast. The influence of meteorological wind forcing and atmosphere-water heat exchange on the sea environment was also included for the time of year of the study. The modules employed were TELEMAC-3D-WAQTEL version v8p2. Coupled to the TELEMAC hydrodynamics results is a biological sea lice model, developed within the framework of the open-source particle tracking code OpenDrift [4].

II. Geographic and Hydrodynamic Setting

A. General topography and flow features

North-west Scotland is notable for its complex topography and coastline. Glaciation has formed a great number of islands and peninsulas, while many sounds and fjords penetrate deep into the land. Numerous glacially deepened basins exist, offshore and in the sounds and inlets. The basins and narrow canyons of the sea and loch bed bathymetry are often separated by relatively shallow sills possibly of morainic or resistant rock origin [5]. Fig. 1 shows the regional location with the red inset showing the area of focus around Loch Hourn.

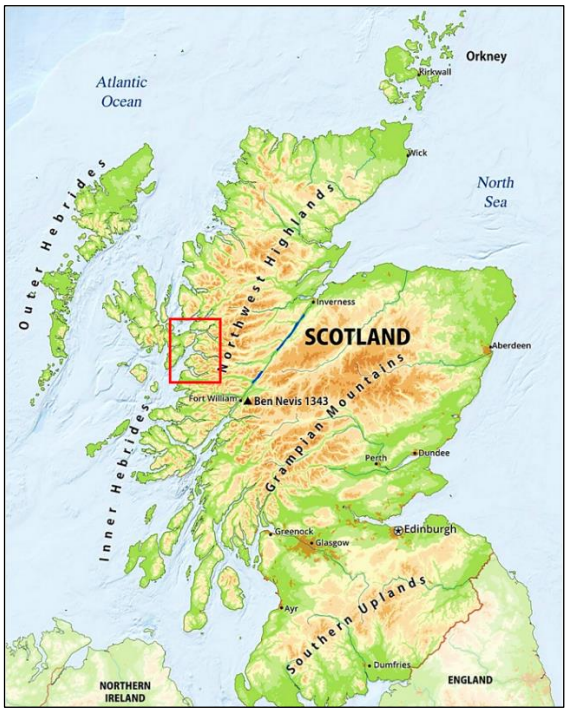

Figure 1. Geographical location with area of focus around Loch Hourn shown in red inset.

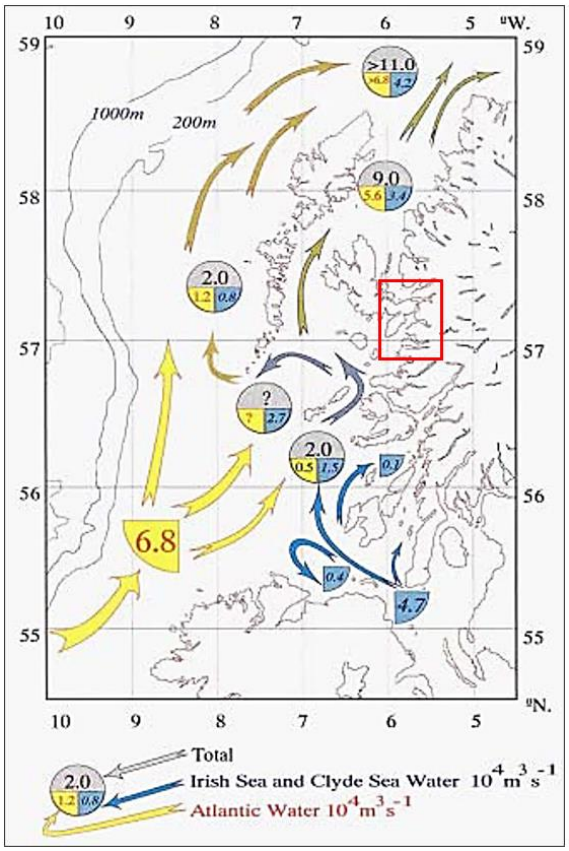

Figure 2. West Coast of Scotland general circulation patterns and approximate volume fluxes [6]. Area of focus around Loch Hourn shown in red inset.

Water in the regional seas around Scotland's West Coast is derived from three sources: oceanic or Atlantic water, Clyde/Irish Sea water and coastal water discharging from the land [6]. Overall circulation patterns (Fig. 2) inferred from the distributions of salinity and temperature, and direct water circulation measurements, indicate a net northward transport along the Scottish West Coast, both through the Sea of the Hebrides and the Minch and to the west of the Outer Hebrides (the Scottish Coastal Current). Flows within the waters closer to coasts and in sea lochs generally represent an arena where freshwater runoff and solar heating act to stratify the water by forming less saline or warmer buoyant layers near the surface, and where winter cooling, wind and tidal mixing tend to homogenise it.

III. AVAILABLE DATA

A. *Bathymetry data*

The bathymetry data for the present study have been collected from a range of different sources including publicly available data sets. These have been provided by Marine Scotland for the Scottish Shelf Model [7], digitised Admiralty charts and bathymetry information from the UK's Digimap

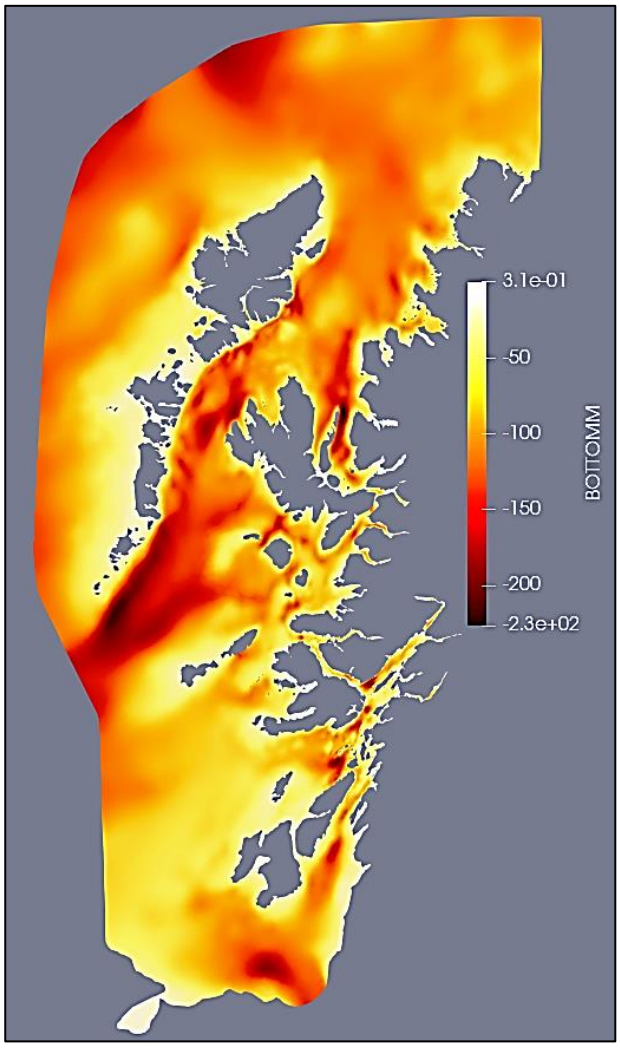

Figure 3. Model bathymetry (m) and spatial extent.

Ordnance Survey Collection [8]. The bathymetry and spatial extent of the model is shown in Fig. 3 while Fig. 4 shows the 3D bathymetry in the vicinity of Loch Hourn.

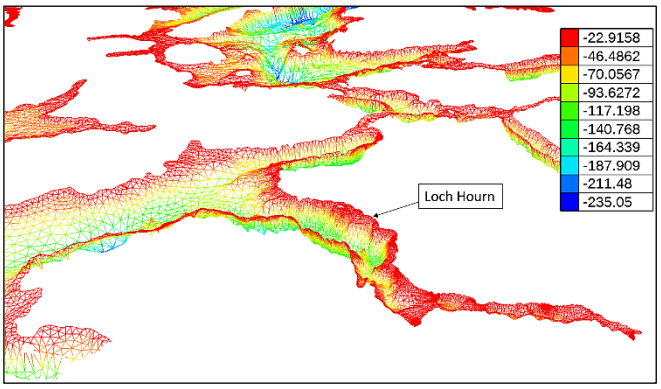

Figure 4. 3D model bathymetry (m) in the vicinity of Loch Hourn.

B. *Sea levels*

Data from the UK Tide Gauge Network is made available through the British Oceanographic Data Centre [9] who have responsibility for the monitoring and retrieval of sea level data.

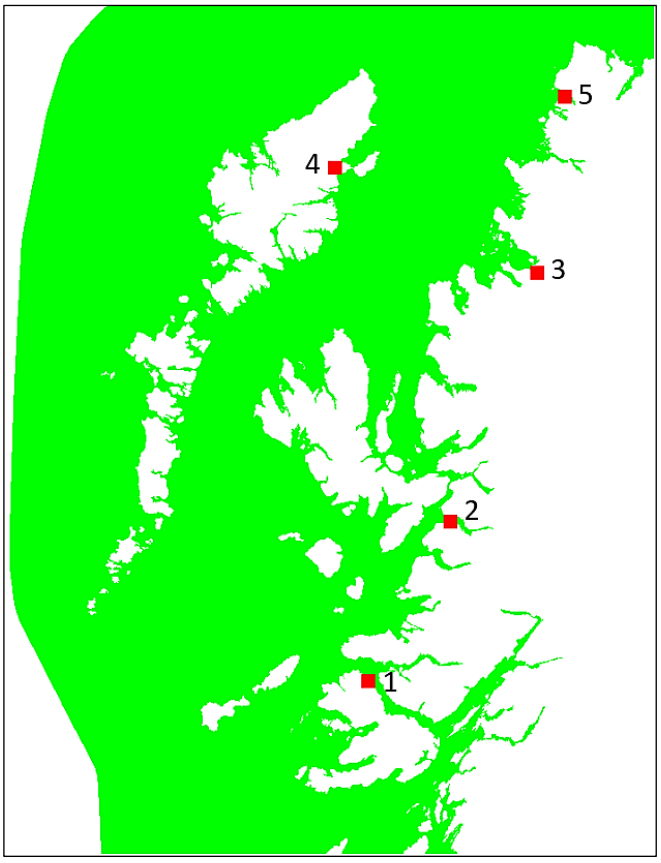

Figure 5. Map showing location of tidal gauge stations.

1 Tobermory, 2 Loch Hourn, 3 Ullapool, 4 Stornoway, 5 Kinlochbervie

The data were extracted from stations 1,3,4 and 5 as shown in Fig. 5 for the period 1st – 31st October 2010. Sea level data were also provided by the aquaculture company Mowi at the Loch Hourn salmon farm for the period 28th November 2018 to the 11th January 2019.

C. *Currents*

Information on current speeds in Loch Hourn were obtained from data produced by the salmon farm company Mowi. These data were recorded during a series of Acoustic Doppler Current Profiler (ADCP) measurements. The ADCP meters are mounted on the seabed and use an acoustic signal to record the current velocities at various depths (bins) through the water column. The near-surface current speed (m/s) was used for model validation purposes.

D. *Wind speed and direction*

Wind speed and direction were extracted from an on-line resource [10]. The historical data are available on a six-hourly average basis and the wind data correlated with the time duration of the model. Wind speed and direction data were extracted at 3 wind station locations across the envelope of the model, these being at Port Ellen, Mallaig and Cape Wrath. Data information between each station was interpolated on to the model.

E. *Freshwater sources*

Data for freshwater sources (i.e., river run off) entering Loch Hourn and the surrounding area were extracted from the

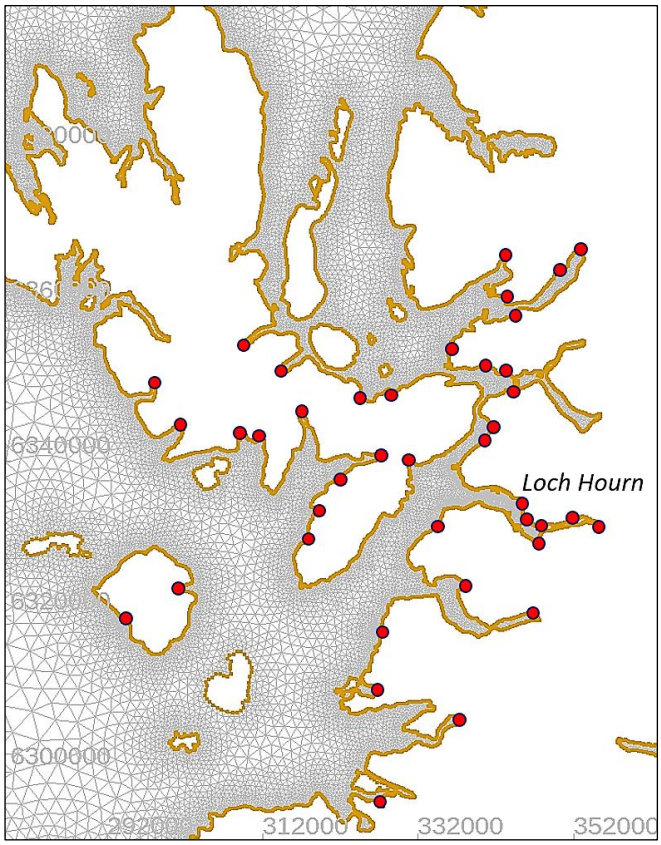

Figure 6. Map showing location of 40 freshwater discharges and the location of Loch Hourn.

historical flow estimates from the network of hydrometric stations operated by the Scottish Environmental Protection

Agency (SEPA) and made available via the National River Flow Archive (NRFA). These data consisted of estimates of daily mean river flow for gauged catchments from 1960 to 2015 [11]. Fig. 6 shows the location of the 40 freshwater discharge locations around Loch Hourn and the surrounding area that were included in the hydrodynamic model.

F. Salinity and temperature

Information on the salinity and temperature fields in Loch Hourn were provided by Mowi at locations close to the salmon farm. This data was used as a resource to allow validation of the TELEMAC-3D hydrodynamic model results

IV. MESHING AND MODEL SET-UP

A. Model domain

The domain of the TELEMAC-3D-WAQTEL model was shown in Fig. 3. The horizontal reference was chosen as UTM Zone 30 N. The model domain extends from the Mull of Kintyre in the south to Cape Wrath in the north and includes all of the main islands and sea lochs of Scotland's West Coast.

The model contains two open (sea) boundaries located in the North Channel and Atlantic Ocean. The northern boundary extends from the north coast of Scotland near Loch Eriboll around the Outer Hebrides and down to Malin Head (Republic of Ireland). The southern boundary spans the North Channel from a location near Torr Head (Northern Ireland) to the Mull of Kintyre (Scotland).

B. Computational mesh

The computational mesh was constructed using a flexible mesh approach with a varying spatial resolution (i.e., element length) across the domain (Fig. 7). Mesh resolution was down to 3 km at open sea boundaries and a few tens of metres at river inlets. Mesh generation was carried out using the freely-available BlueKenue code [12] and there were a total of 672,090 nodes and 991,820 elements in mesh. Six vertical terrain-following sigma layers were employed to account for the sea depth.

C. Open sea boundary conditions

The boundary conditions for the velocities and surface elevations at the offshore open boundaries were obtained from the OSU TPXO8 European Shelf regional model (11 tidal constituents: M2, S2, N2, K2, K1, O1, P1, Q1, M4, MS4 and MN4) [13]. Initial values of temperature and salinity were set to 8 ^{o}C and 34.3 PSU, respectively, and zero-gradient boundary conditions applied at the open sea boundaries.

D. Stratification effects

The annual cycle of stratification along the West Coast of Scotland, due to a combination of solar heating and freshwater inflow, produces gradients in both temperature and salinity that induce flow circulation. A non-hydrostatic approach was adopted as the bathymetry in Loch Hourn can vary from shallow sills to deep canyons of around 200 m in the presence of salinity and temperature gradients. Explicitly including the z-velocity was considered appropriate to capture any 3D effects in such conditions. A hydrostatic approach was not considered. Thus, the effects of freshwater discharges into Loch Hourn and the surrounding area are taken into account in our model and the density is calculated according to the law of state for density as a function of temperature T (^{o}C) and salinity S (PSU)[14]:

$$\rho = \rho_{ref}\left[1 - \left(T\left(T - T_{ref}\right)^2 - 750S\right)10^{-6}\right] \quad (1)$$

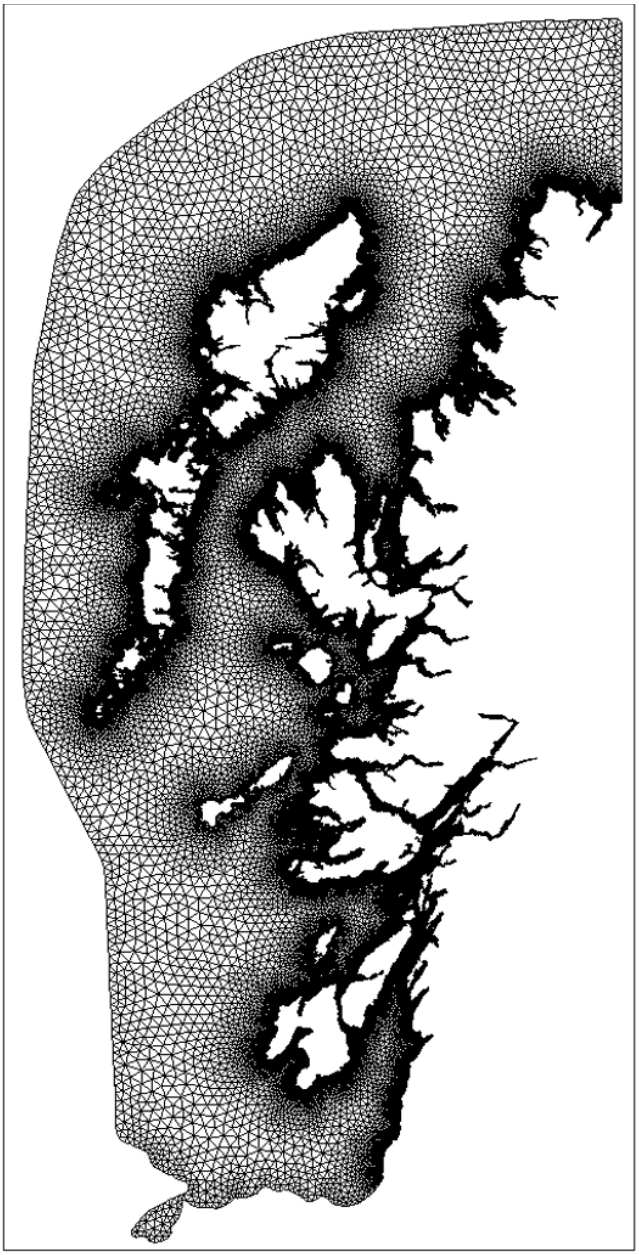

Figure 7. Mesh over entire computational domain.

Brackish water salinities at river outflows on the West Coast can be reduced by a factor of up to 1.5 compared to the far field sea values [15]. The salinity was kept constant in space and time along the river outflow boundaries with values

of S = 20 PSU set for the rivers discharging into sea lochs. The river outflow temperatures were set to follow the air temperature and an average value (film temperature) between the local air temperature and a sea temperature of 8 ºC was employed. The sea temperature value of 8 ºC was deduced from the TELEMAC modelling output – see section V on validation.

Atmosphere-water heat exchange was included in the model using the WAQTEL thermic module and a first-order, lumped parameter approach [16] according to:

$$k\frac{dT}{dz} = -\frac{A}{\rho C_p}(T - T_{air}) \quad (2)$$

The coefficient A includes for phenomena such as sensible and latent heat exchange. Reference [16] expresses the coefficient A, in W/m^2 / ºC, according to the water temperature T and wind velocity V measured at the point under consideration (in m/s) according to:

$$A = (4.48 + 0.049T) + 2021.5b(1 + V)(1.12 + 0.018T + 0.00158T^2) \quad (3)$$

The parameter b varies depending on location and a value of 0.0017 was found appropriate for this study. For turbulence closure the 2-equation *k-epsilon* turbulence model [17] was employed for both vertical and horizontal resolution.

V. MODEL VALIDATION

A. *Sea level*

Validation is against observed hydrographic data in terms of data from long-term sea level gauges as described in section III B. Fig. 8 shows the tidal gauge value comparisons.

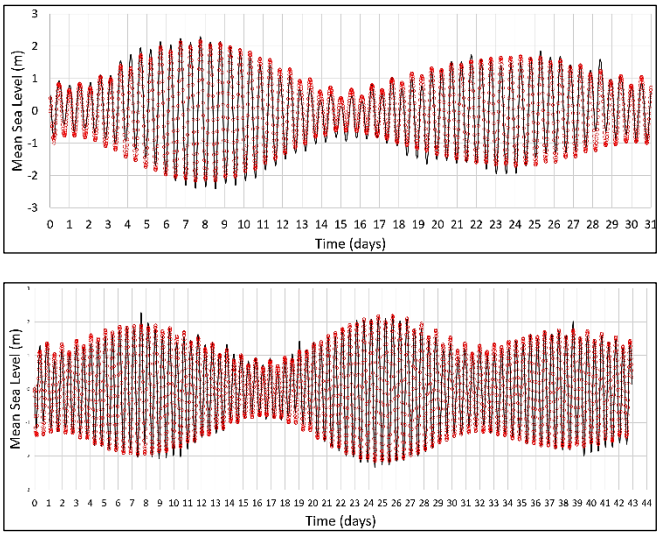

Figure 8. Sea levels at Tobermory (upper) and Loch Hourn (lower). Tobermory figures are for the period 1st – 31st October 2010. Loch Hourn is for the period 28th November 2018 – 11th January 2019. Solid black line is the BODC data and red line with symbols is the TELEMAC-3D model. All data are relative to mean sea level (MSL). Vertical axis is MSL and horizontal axis is time (days).

Fig. 8 demonstrates that the model is able to simulate the propagation of the tide across the envelope of the computational domain. Similar levels of agreement were found at Ullapool, Stornoway and Kinlochbervie (Fig. 5).

B. *Current speed and direction*

Focusing on the salmon farm at Loch Hourn, the predicted current speed magnitudes and directions are also in satisfactory agreement with observed data as shown in Figs 9 and 10.

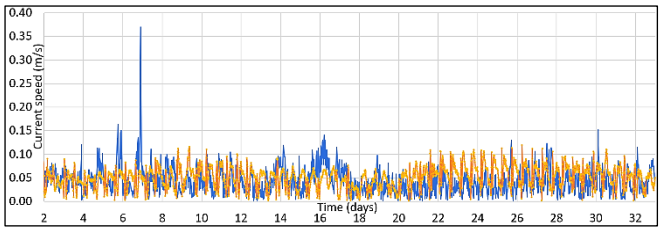

Figure 9. S Near-surface current speed magnitudes at the Loch Hourn salmon farm for the period 1st -30th December 2018. Blue lines are Mowi measured data and orange lines with symbols are the TELEMAC-3D predictions.

The average TELEMAC-3D predicted value was 0.049 m/s while the average measured speed was 0.043 m/s giving confidence that the model is a reasonable representation of physical reality.

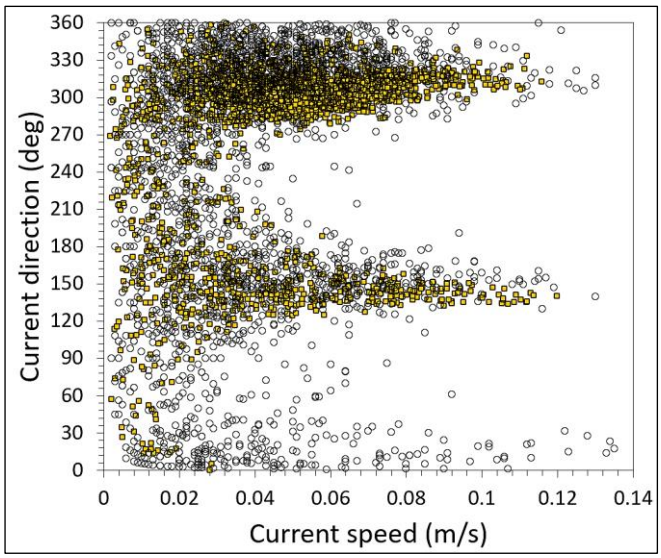

Figure 10. S Near-surface current speed magnitudes and directions for the salmon farm at Loch Hourn. Empty symbols are Mowi measured data, filled symbols are the TELEMAC-3D results.

C. *Further model validation: salinity comparisons*

The methodology for the TELEMAC-3D-WAQTEL solution is to begin with a 3-month (89-days) "spin-up" calculation from 1st Feb. to 30th April 2019. This allows fields of velocity, salinity and temperature to develop in the model. Information on the salinity field in Loch Hourn were provided by Mowi and the TELEMAC-3D predictions of the salinity field are shown in Fig.11. The salinity values appear to be in reasonable agreement with the physical data.

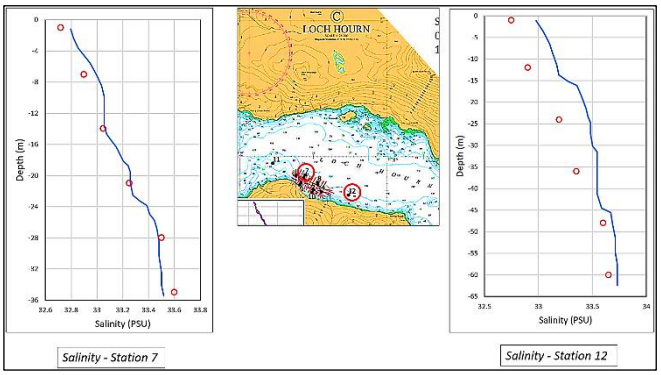

Figure 11. TELEMAC hydrodynamic model salinity versus depth at stations 7 and 12. Lines are Mowi measured data, symbols are the TELEMAC model predictions. Model data was extracted on 1st April 2019

D. *Further model validation: temperature comparisons*

Data on the temperature field in Loch Hourn were provided by Mowi and used for model validation purposes. The TELEMAC-3D hydrodynamic model sea temperature predictions at Station 7 over 89 days from 1st Feb. – 30th April 2019 are highlighted in Figure 12. This plot shows effects of atmospheric heat exchange on sea water initially at 8 ºC. The final hydrodynamic model predictions lie in the range of 7.25 to 7.5 ºC while the Mowi measured values were approximately 7.3 ºC. Although the model and measured values were taken in different years (2019 and 2021, respectively), the magnitudes appear to be in reasonable concurrence.

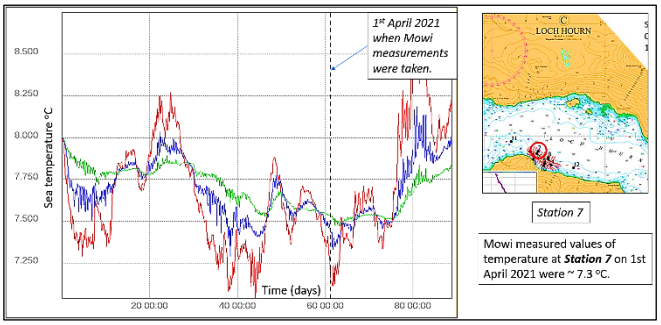

Figure 12. TELEMAC-3D-WAQTEL sea temperature predictions at Station 7 over the 89 day "spin-up" period from 1st Feb. – 30th April 2019. Plot shows influence of atmospheric heat exchange on sea water initially at 8 ºC. Colour represent different depths – red near surface, green near sea-bed.

VI. MODEL METHODOLOGY AND SAMPLE RESULTS

A. *Hydrodynamics*

As described in section V.C, the methodology for the TELEMAC-3D-WAQTEL procedure is to begin with a 3-month "*spin-up*" calculation from 1st Feb. to 30th April 2019. This allows fields of velocity, salinity and temperature to develop in the model. We then use these fields to start the particle tracking sea-lice run, using May-June 2019 data for the freshwater discharge and meteorological wind forcing.

Figures 13 to 15 demonstrate the typical flow fields predicted by the TELEMAC model at the end of the 3-month "*spin-up*" period.

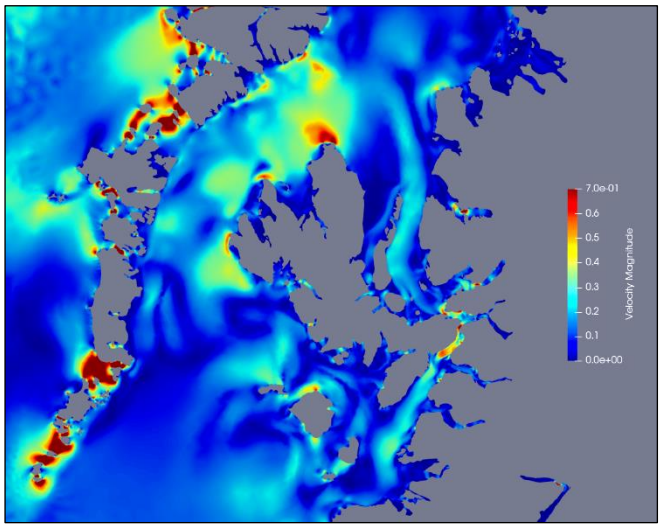

Figure 13. TELEMAC-3D-WAQTEL snapshot example of current speed magnitude (m/s) in the North-West Coast regional seas. Increased flow speeds are evident around coastal headlands, in the channels between islands and in Loch Alsh and the Kyle Rhea.

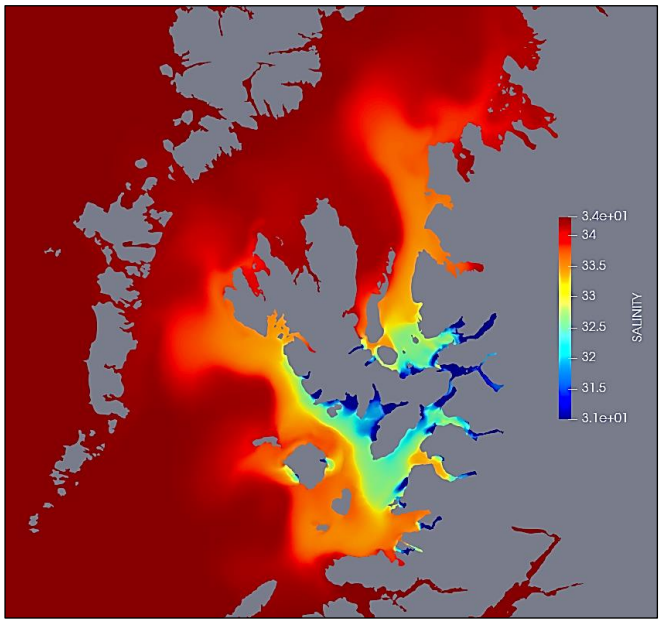

Figure 14. TELEMAC-3D-WAQTEL post- "spin-up" snapshot of near-surface salinity contours (PSU) in the North-West Coast regional seas on 1st May 2019. Freshwater discharge is ONLY from the 40 river inlet locations shown in Figure 6.

B. *Sea lice modelling*

In order to employ the open-source particle tracking code OpenDrift [4], a new reader was developed to integrate the TELEMAC Selafin file format into OpenDrift. OpenDrift was used in place of the particle tracking module in TELEMAC due to the available extra parameterization in the code. The hydrodynamic model produces flow currents for the Lagrangian transport of sea lice "particles" and an integrated biological model is employed in OpenDrift where virtual particles are released at each farm site and allowed to disperse

into the marine environment. Each particle is a "super-individual", representing a number of sea lice larvae, scaled according to the salmon biomass of each farm. The biological effects of sea lice production, maturity and mortality rates and the environmental cues of salinity avoidance, temperature preference and phototactic vertical swimming behaviour (diel migration) were included [18-20].

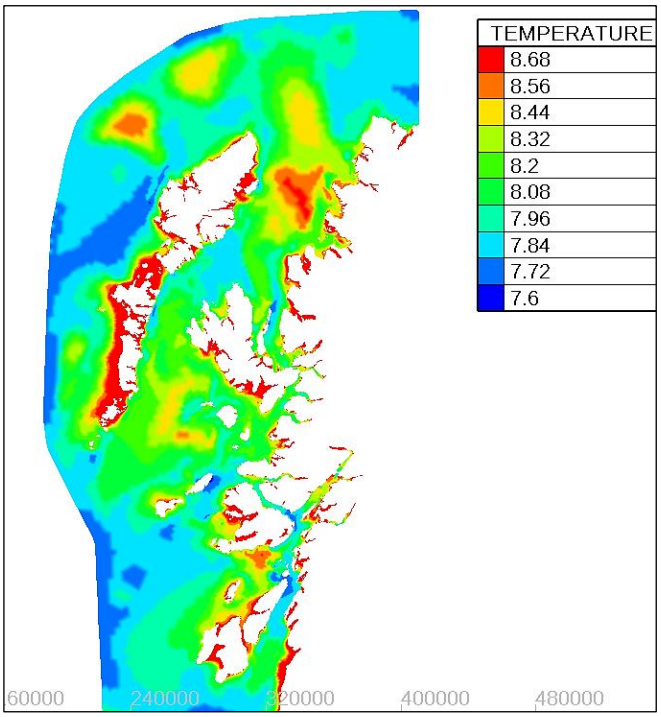

Figure 15. TELEMAC-3D-WAQTEL post- "spin-up" example of near-surface temperature (°C) contours across the North-West Coast regional seas on 1st May 2019.

Particles were introduced into the sea surface layer at the Loch Hourn farm and from 6 surrounding farms in the local area as shown in Figure 16. The period over which the sea lice dispersion model was run was 1st May – 30th June 2019.

Figure 16. The seven salmon farms involved in the sea lice study.

In Fig.17, the dispersion of particles coloured by their farm origin after 60 days is shown. The full model run can be seen as an animation at https://vimeo.com/574392901. The colours in the legend represent particles from different farms. The numbers in the legend have no significance.

This is the first stage in the sea lice modelling process and these particles do not yet represent a particular quantity of sea lice. In subsequent modelling, as each particle ages, sea lice mortality and maturity rates are applied to the population of lice that it represents. These results are then integrated at stated time and spatial intervals to calculate lice density.

Each farm releases the same fixed rate of 50 particles per farm per hour and the number of lice represented by each particle is scaled according to the farm's biomass in a particular year. The Fig. 17 results may also be viewed as indicative of how far sea lice can be transported around the West Coast before they find a fish host or die. There is potential for infective sea lice from different farms to overlap substantially as they disperse.

Results highlight the expected northwestward flow (Fig. 2) and that infective lice copepodids accumulate along tidal and salinity fronts, at the mouths of sea lochs and along shorelines, in different places according to the neap/spring tidal cycle.

Average infective copepodid densities over the period 20th May-3rd June 2019 are shown as a heat map in Fig. 18, while a snapshot of instantaneous copepodid densities is shown in Fig. 19. Both plots highlight enhanced lice densities in the areas around the mouths and southern shorelines of Loch Hourn and Loch Nevis.

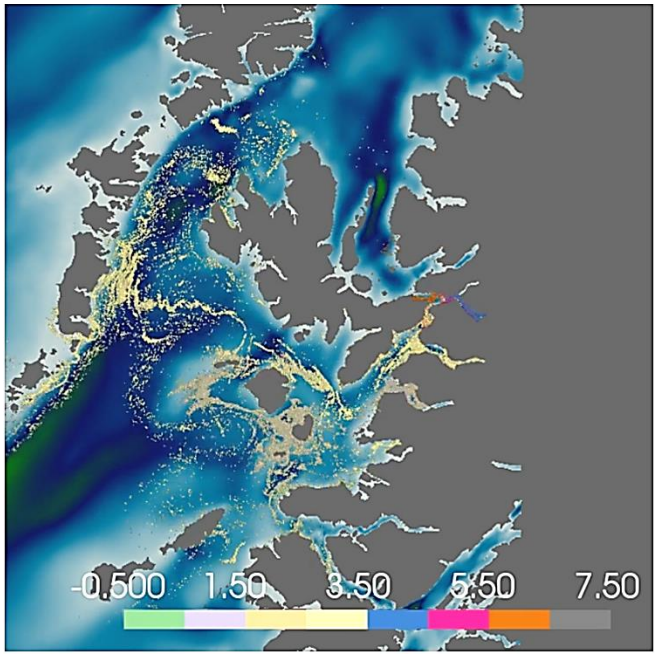

Figure 17. Sea lice distribution coloured by farm origin after **60 DAYS**. Background colour denotes bathymetry contours and the numbers in the legend have no significance. This image highlights the range of dispersion of viable infective lice copepodids but does not quantify any particular density of sea lice – see Figs.18 and 19 for sea lice densities. The full animation can be seen at *https://vimeo.com/574392901*.

VII. Conclusions and Future Work

A hydrodynamic model of the West Coast of Scotland has been created using TELEMAC-3D-WAQTEL. The model includes the effects of complex water circulation, density and temperature gradients that persist in the West Coast seas throughout the year. These 3D phenomena appear to have been adequately captured in the model when compared with physical data. A coupled sea lice transport model has been developed which includes biological parameters for production, maturity and mortality and behavioural cues in terms of salinity, light and temperature based on published scientific literature. The TELEMAC-3D model provides a suitable data basis for modelling sea lice dispersion and an assessment of both the near-field and far-field effects. Future work will consider the risk to wild fish from sea lice originating from a greater number of salmon farms on Scotland's West Coast.

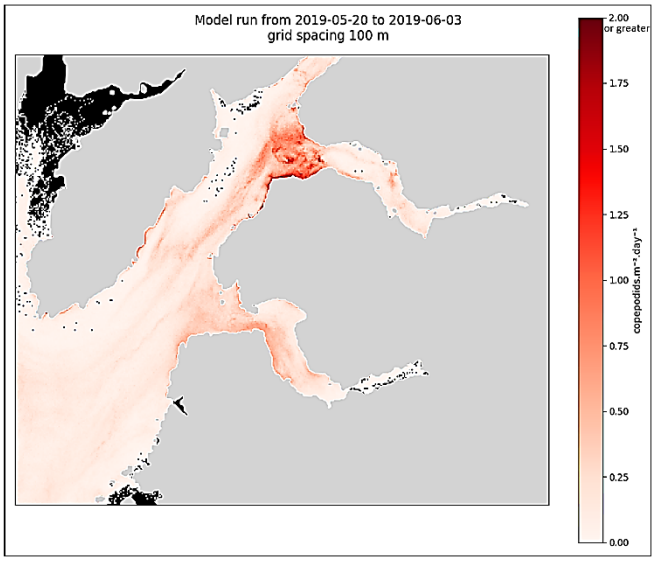

Figure 18. Heat map showing average sea lice densities (copepodids $m^{-2}.day^{-1}$) around Loch Hourn over 15 days of the 61-day run (20th May – 3rd June 2019). Black areas indicate zones where no lice were encountered.

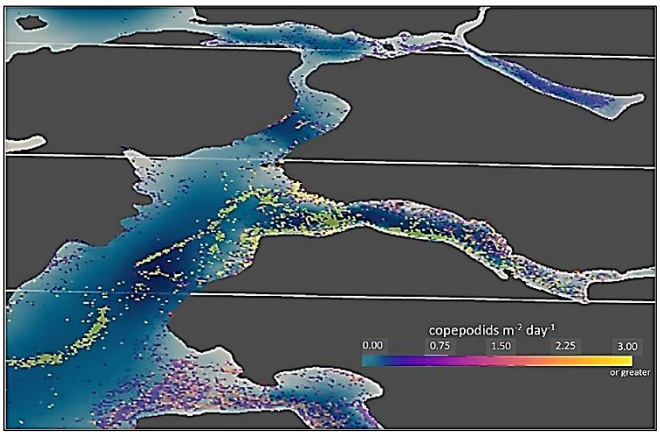

Figure 19. Snapshot of copepodid densities in the Loch Hourn region on **DAY 40** of the 61-day model run, recalculated at hourly intervals and converted to equivalent daily averages. Background colour denotes bathymetry contours. The full animations can be seen at https://vimeo.com/574396820 and https://vimeo.com/574402482.

References

[1] I. A. Johnsen, L. C. Asplin, A. D. Sandvik and R. M. Serra-Llinares, "Salmon lice dispersion in a northern Norwegian fjord system and the impact of vertical movements", Aquaculture Environment Interactions, 99–116, 2016, doi: 10.3354/aei00162.

[2] https://www.gov.scot/publications/summary-of-information-relating-to-impacts-of-salmon-lice-from-fish-farms-on-wild-scottish-sea-trout-and-salmon/ - accessed 10th June 2021.

[3] Myksvoll MS, Sandvik AD, Albretsen J, Asplin L, Johnsen IA, Karlsen Ø, et al., (2018), Evaluation of a national operational salmon lice monitoring system—From physics to fish. PLoSONE 13(7): e0201338. https://doi.org/10.1371/journal.pone.0201338.

[4] https://opendrift.github.io/ - accessed 10th June 2021.

[5] A. Edwards and F. Sharples, "Scottish sea lochs: a catalogue. Scottish Marine Biological Association", Nature Conservancy Council, 110, 1986.

[6] Offshore Energy SEA, https://assets.publishing.service.gov.uk/government/uploads/system/uploads/attachment_data/file/194342/OES_A3d_Water.pdf - accessed 10th June 2021.

[7] http://www.marine.gov.scot/themes/scottish-shelf-model - accessed 10th June 2021.

[8] https://digimap.edina.ac.uk/marine - accessed June 10th 2021.

[9] https://www.bodc.ac.uk/ - accessed June 10th 2021.

[10] https://www.timeanddate.com/weather – accessed 10th June 2021.

[11] V. A. Bell, A. L. Kay, A. C. Rudd and H. N. Davies, "The MaRIUS-G2G datasets: Grid-to-Grid model estimates of flow and soil moisture for Great Britain using observed and climate model driving data", https://doi.org/10.1002/gdj3.55

[12] https://nrc.canada.ca/en/research-development/products-services/software-applications/blue-kenuetm-software-tool-hydraulic-modellers - accessed 10th June 2021.

[13] G. D. Egbert, and S. Y. Erofeeva, "Efficient inverse modeling of barotropic ocean tides." Journal of Atmospheric and Oceanic Technology 19.2 (2002): 183-204.

[14] http://svn.openTELEMAC.org/svn/openTELEMAC/tags/v8p2r1/documentation/TELEMAC3d/user/TELEMAC3d_user_v8p2.pdf accessed 10th June 2021.

[15] *Ecosystem Review*. Scottish Marine and Freshwater Science Vol. 3 No. 4. June 2012. https://www.gov.scot/publications/scottish-marine-freshwater-science-volume-3-number-3-clyde-ecosystem/pages/3/ - accessed 10th June 2021.

[16] H. E. Sweers, "Monograms to estimate the heat-exchange coefficient at the air-water interface as a function of wind speed and temperature; a critical survey of some literature", Journal of Hydrology, 30:375–401, 1976.

[17] B. E. Launder, and D. B. Spalding, (March 1974), "The numerical computation of turbulent flows", Computer Methods in Applied Mechanics and Engineering. 3 (2): 269–289. doi:10.1016/0045-7825(74)90029-2.

[18] I. A. Johnsen, *et al*., "Salmon lice induced mortality of Atlantic salmon during post-smolt migration in Norway", ICES Journal of Marine Science, 2020, doi:10.1093/icesjms/fsaa202.

[19] A. D. Sandvik, I. A. Johnsen, M. S. Myskvoll, P. N. Saevik and M. D. Skogen, "Prediction of the salmon lice infestation pressure in a Norwegian fjord", ICES Journal of Marine Science, Volume 77, Issue 2, March 2020, Pages 746–756, https://doi.org/10.1093/icesjms/fsz256.

[20] N. K. G. Salama, A. G. Murray, and B. Rabe, "Simulated environmental transport distances of Lepeophtheirus salmonis in Loch Linnhe, Scotland, for informing aquaculture area management structures", Journal of Fish Diseases 2016, 39, 419–428. doi:10.1111/jfd.12375.

Aquatic ecological modelling with TELEMAC3D: performance of the ecological library AED2 in a natural ecosystem

Francesco Piccioni, Brigitte Vinçon-Leite
LEESU, Ecole des Ponts ParisTech, UPEC
Champs-sur-Marne, France
francesco.piccioni@enpc.fr

Minh-Hoang Le
LHSV, Ecole des Ponts ParisTech, CEREMA, EDF R&D
Chatou, France

Céline Casenave
UMR MISTEA, Univ Montpellier, INRA, Montpellier SupAgro, Montpellier, France

***Abstract*—This work aims to test the performance of the coupled models TELEMAC-3D / AED2 for reproducing over a seasonal time-horizon the complete phytoplankton growth-cycle. The study site is a small and shallow urban lake that suffers from repeated and severe harmful algal blooms, located in the east of the Great Paris metropolitan area. The lake is equipped with sensors recording data at high-frequency (every 10 minutes) of water temperature, pH, as well as concentrations of dissolved oxygen, nitrate total chlorophyll and phycocyanin. Such an extensive data set allows to test the model thoroughly against multiple variables and at different time scales. In particular, simulation results were evaluated in terms water temperature at different depths to test the ability of the coupled models to simulate thermal stratification in a shallow water body. High-frequency observations of total chlorophyll, phycocyanin, nitrate, dissolved oxygen concentrations, were used to calibrate the biogeochemical model and evaluate its performance. The analysis of model results highlights a feedback between the coupled models, that can be linked to the dynamic calculation of the light extinction coefficient done in the biogeochemical model. The coupled models AED2 and TELEMAC-3D allow to correctly reproduce the overall seasonal phytoplankton growth in a water body, correctly dispatching biomass among the different phytoplankton groups in particular during summer. Furthermore, the model reproduces correctly the overall dynamics recorded in the study site in terms of dissolved oxygen and nitrate. This corroborates the robustness of the coupled models and of the configuration set up for this study.**

I. INTRODUCTION

Water resources are highly impacted by anthropogenic stressors. Urbanization can lead to an increase of pollutant and nutrient input to aquatic ecosystems, enhancing eutrophication [1]. Furthermore, their thermal dynamics are also affected by climate change. Warmer water temperatures and accelerated eutrophication are thought to be the main causes of the expansion of harmful algal blooms observed worldwide during the last decades [2]–[4]. In particular, because of their potential toxicity, cyanobacteria blooms are an ever increasing concern in the management of water resources and represent a serious threat for the balance of aquatic ecosystems [3], [5]. For these reasons, an ever-increasing interest grows around modelling tools capable of simulating the ecological evolution of aquatic ecosystems under different meteorological or eutrophication scenarios, in order to provide stakeholders with reliable projections for decision making [6]. In this context, TELEMAC-3D has recently been coupled by EDF R&D with the well-known ecological library Aquatic EcoDynamics (AED2). Aquatic ecological models often have a complex structure with a high number of parameters to be defined and their calibration is challenging: data deriving from traditional periodic field surveys are sparse in space and time and do not allow for a thorough validation of processes occurring at a time-scale lower than the monitoring frequency.

The aim of our work is to test the performance of the coupled model TELEMAC-3D / AED2 on a full scale experimental site over a seasonal time-horizon with the objective of reproducing the phytoplankton succession. The study site is a small and shallow urban lake located in the east of Great Paris metropolitan area, which suffers from repeated and severe harmful algal blooms during spring, summer and autumn. Aside from the traditional monitoring via field campaigns and water sampling, the study site is equipped with specific sensors recording data at high-frequency (every 10 minutes) of water temperature as well as concentrations of dissolved oxygen, nitrate, total chlorophyll and phycocyanin, which is considered a proxy for cyanobacteria biomass. Such an extensive data set allows to test the model thoroughly against multiple variables and at different time scales.

II. MATERIALS AND METHODS

A. *Study site and measuring instrumentation*

The study site is Lake Champs-sur-Marne. It is a sand-pit lake located in the East of Paris (latitude: 48°51'50" N, longitude: 2°35'52" E), next to the Marne River. It is a small and shallow water body with a surface of 0.12 km^2, mean depth of 2.5 m and maximum depth of around 3.5 m. As shown in Fig. 1, the lake is deeper in the southern part, while depth decreases to under 2 m in the northern part of the lake. The lake is fed primarily by groundwater, and has no inflows nor

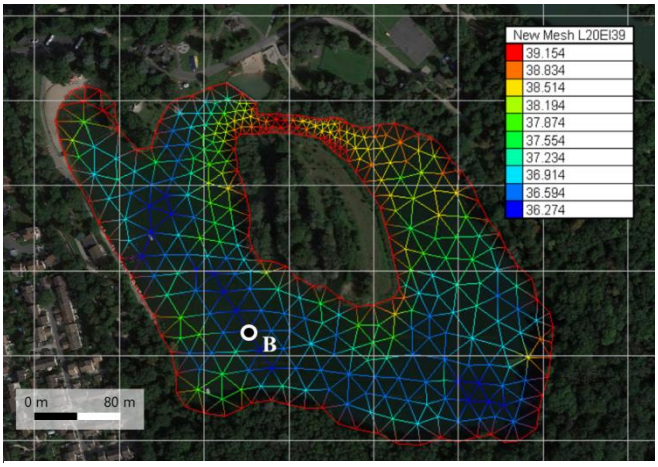

Figure 1: Satellite picture of Lake Champs-sur-Marne and computational domain used for the present study. The colour chart shows the elevation of each point of the grid in meters above sea level and the white dot indicates the measuring site.

outflows. Its water level is influenced by the Marne River that flows from east to west right north of the lake. The lake level varies weakly during the year, with monthly oscillations lower than 0.2 m on average.

Given its shallowness, Lake Champs-sur-Marne is polymyctic and its thermal behaviour is strongly influenced by the meteorological conditions. Between Spring and Autumn, periods of stable thermal stratification that can last up to two or three continuous weeks alternate with complete mixing and overturn of the water column. The lake suffers from strong eutrophic conditions and experiences severe harmful algal blooms, especially between early spring and autumn. These blooms are often dominated by potentially toxic species of cyanobacteria.

For these reasons, the lake is monitored through periodical field surveys during which water samples, profiles and Secchi depth measurements are collected, as well as continuous *in situ* measurements that record data at high-frequency (every 10 min) of relevant physical, biological and chemical variables. In particular, measuring site B (see figure 1) is equipped with two SP2T10 (nke INSTRUMENT®) water temperature sensors at the surface (0.5 m depth) and bottom (2.5 m depth) layers, while at the middle of the water column (1.5 m depth), the MPx multi-parameter sensor (nke INSTRUMENT®) records data in terms of water temperature and total chlorophyll, dissolved oxygen and phycocyanin concentrations. A detailed description of the automated measuring system can be found in [7]. Eventually, high-frequency observations of nitrate concentration are also recorded at 1.5 m depth at site B, through the OPUS UV spectral sensor (OPUS instrumentation). Such data are used in this work to calibrate the model parameters and evaluate the its performance.

B. *Model configuration*

TELEMAC3D (release 8.1.2) coupled with the ecological library Aquatic EcoDynamics is used to run 3D simulations of the thermal dynamics and of the biogeochemical cycle in Lake Champs-sur-Marne. The simulated period covers the season of phytoplankton growth observed on the study site during the year 2019 and goes from the month of February to the end of October.

In the coupled model, TELEMAC3D handles the hydrodynamics, while AED2, through a set of partial differential equations, simulates the biogeochemical cycle [8]. Namely, the AED2 library is called at each time step in order to update the concentration of the variables simulated in the biogeochemical cycle, which are then treated as active tracers by TELEMAC3D. When TELEMAC3D is coupled with AED2, the light extinction coefficient is dynamically calculated at each iteration by AED2 as a function of tracers concentrations and the corresponding specific light extinction coefficients that can be set by the user [8]. This way, AED2 can have a feedback on the TELAMAC3D results in particular in terms of vertical distribution of water temperature and thermal stratification.

The computational domain used to run the coupled models is shown in Fig. 1. It was built with the open-source software BlueKenue™ [9]. It consists of a triangular grid with an average distance between the nodes of 20 m, and a refined zone around the narrower portion of the water body. Bathymetric data were obtained via an echo-sounder. The mesh is composed of 404 nodes (661 elements), with 10 σ-layers for the discretization on the vertical axis and a uniform water level set at an elevation of 40 m a.s.l..

Hydrodynamic model

The Nezu and Nakagawa's formulation of the mixing length model with Viollet's damping function was implemented for vertical turbulence closure. The molecular diffusivity of water is used on the vertical as a background value and was set to 10^{-6} m^2s^{-1}, while horizontal diffusivity was set to 0.01 m^2s^{-1} after similar applications ([10], [11]) and according to the grid size [12]. The model is forced with six meteorological variables: relative humidity [-], air temperature [°C], cloud cover [-], net solar radiation [$J\ s^{-1}m^{-2}$], wind speed [$m\ s^{-1}$] and direction [°N]. Their values were downloaded from the closest Meteo France meteorological station, located at the Orly airport roughly 40 km south-west of the study site. In the heat budget, the contribution of precipitation was neglected both in terms of energy and mass, while for evaporation only the mass flux was neglected. Finally, the model was run with a 60 s time step, and its outputs were saved with a four-hours time step.

Biogeochemical model

Aquatic EcoDynamics (AED2) was recently coupled with the TELEMAC system. AED2 is a modular biogeochemical library, that potentially allows the user to simulate all the processes playing a role in the biogeochemical cycle in aquatic ecosystems, from benthic fluxes and microbial decomposition to primary production, grazing, and macrophytes growth [8]. The model configuration can be customized by the user through the activation and deactivation of its modules. For the present work, focused on

phytoplankton growth, five modules were activated, which are listed in Table 1 together with the relative variables simulated by AED2 and their initial conditions. In the table, particulate (dissolved) fractions of organic carbon, nitrogen and phosphorus are respectively indicated as POC, PON and POP (DOC, DON and DOP). Four phytoplankton groups typically observed on the study site are activated in this configuration: cyanobacteria, green algae, flagellates and diatoms.

TABLE 1: MODULES AND VARIABLES ACTIVATED IN AED2, ALONG WITH THEIR INITIAL CONDITIONS.

Module	Simulated variables	Initial value
Oxygen	Dissolved oxygen	180 mmol O m^{-3}
Phosphorus	Ortho-phosphate	2.6 mmol P m^{-3}
Nitrogen	Ammonium	40 mmol N m^{-3}
	Nitrate	45 mmol N m^{-3}
Organic matter	POC	310 mmol C m^{-3}
	PON	37 mmol N m^{-3}
	POP	1.5 mmol P m^{-3}
	DOC	600 mmol C m^{-3}
	DON	37 mmol N m^{-3}
	DOP	1.5 mmol P m^{-3}
Phytoplankton	Cyanobacteria	1 mmol C m^{-3}
	Green algae	1 mmol C m^{-3}
	Flagellates	1 mmol C m^{-3}
	Diatoms	6 mmol C m^{-3}

C. Initialization and calibration of the model

Data measured at site B were used to initialize the model, uniformly over the study site. High frequency observations allowed to directly set the initial conditions in terms of water temperature, total phytoplankton concentration, dissolved oxygen concentration and nitrate concentration. Water samples collected during two field campaigns carried out in January and February of 2019 granted data to initialize the remaining variables listed in Table 1. Eventually, no data were available to set the initial velocity field, and the model was therefore initialized with water at rest.

The coupled models were calibrated against high-frequency observations recorded at site B in terms of water temperature (at three different layers) and total chlorophyll, cyanobacteria and dissolved oxygen concentration at the middle layer. The calibration of the coupled models was done by trial and error and involved three parameters from the TELEMAC3D hydrodynamic model, deputed to tune the heat-transfer model at the air-water interface, and around 40 parameters proper of the AED2 library. Such parameters were selected as the most sensitive from previous sensitivity analysis. The AED2 parameters were initially set and calibrated based on values found in similar applications in scientific literature (e.g. [8], [13], [14]). The main parameters included in the calibration of the coupled TELEMAC3D and AED2 models are listed in table 2.

In this study, the coupled models were calibrated focusing on the months from February to July of 2019, while they were run for validation until the end of October. In order to evaluate the model performances, the root mean square error (RMSE) between model results and observations was calculated. High-frequency observations were therefore averaged in order to match the model output time step.

TABLE 2: CALIBRATED VALUES OF THE MOST RELEVANT PARAMETERS INCLUDED IN THE PRESENT TELEMAC3D / AED2 CONFIGURATION.

Model	Parameter	Value	Unit
T3D	Coeff. for atm. rad.	0.89	-
	Coeff. for surf. Water rad.	0.93	-
	Coeff. for atm.-wat. heat exc.	0.0017	-
AED	Light ext. coeff. (DOC)	0.002	m^2 mmol C^{-1}
	Light ext. coeff. (POC)	0.002	m^2 mmol C^{-1}

	Phytoplankton				
	Green	**Cyano.**	**Falg.**	**Diat.**	**Unit**
Growth rate (20°C)	1.4	1.2	1.6	3.7	d^{-1}
Temp. coeff. for growth	1.08	1.08	1.08	1.05	-
Std. wat. temp.	20	20	18	4	°C
Opt. wat. temp.	25	28	23	9	°C
Max. wat. temp.	35	36	30	18	°C
Light ext. coeff.	0.005	0.005	0.01	0.005	m^2 mmol C^{-1}
Half sat. const. for light	28	25	28	10	µE m^{-2} s^{-1}

III. RESULTS

Model results at site B in terms of water temperature and concentration of total chlorophyll, cyanobacteria, dissolved oxygen and nitrate are gathered in figures 2 and 3, together with the corresponding observations from high-frequency measurements. The performance of the coupled models is here analysed over the whole simulation period in two separate sections: one concerning the thermal and stratification dynamics, and the second one dealing with the biogeochemical cycle.

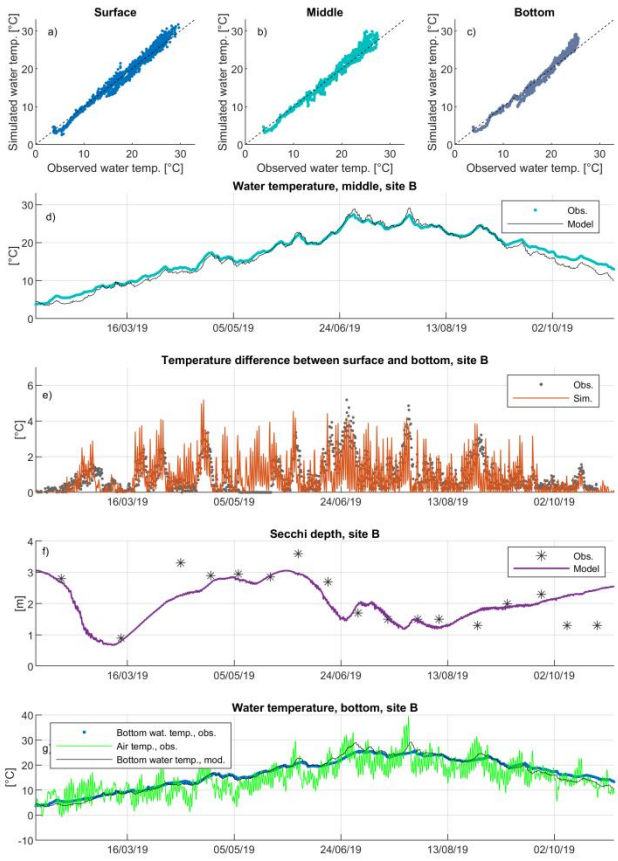

Figure 2: Model results for the seasonal simulation in 2019 in terms of water temperature and Secchi depth. Panels a, b and c: parity diagrams for water temperature at the surface, middle and bottom layers respectively. Panel d: observations and simulation results in terms of water temperature for the middle layer. Panel e: observed and simulated water temperature difference between the surface and bottom layers. Eventually, panel f shows the simulated and observed values for Secchi depth, and panel g shows the comparison between observed and simulated bottom water temperature and the air temperature series used to force the model. All figures are referred to measuring site B.

D. Thermal dynamics

Model results in terms of water temperature are compared with high-frequency observations at site B in figure 2. The parity diagrams in panels a, b and c show a very good agreement between simulated and observed water temperature for all the three layers, with only a small overestimation by the model of the highest temperatures recorded on the study site (in particular for the surface layer) and a slight underestimation of lower water temperatures. Figure 2d shows, as an example for the middle layer, that the evolution of water temperature over the simulation period is correctly reproduced by the coupled models. This is confirmed by the low RMSE values between simulated and observed water temperature at all three layers: respectively of 1.09°C, 1.16°C and 1.20°C for the surface, middle and bottom layers relatively to the whole simulation period.

Figure 2d shows particularly good model performances in terms of water temperature until the end of the month of September. Afterwards, however, a deterioration of the model performance is detectable with an underestimation of water temperature by the model. Similar results were obtained for the surface and bottom layers. Such behaviour was further analysed by comparing the simulated water temperature at site B with the air temperature values used to force the model. Such comparison (Figure 2g) showed how, between the months of October and November, simulated water temperature follows closely the data of air temperature used to force the model. This might be linked with some of the processes neglected in the present configuration, such as water level variations or interactions with groundwater, that might influence the real system.

Between spring and autumn, numerous thermal stratification events are observed on the study site. Such stratification events can last up to two or three consecutive weeks and might reach water temperature differences between the surface and bottom layers around 6°C [11], as shown by panel e of Figure 2. The analyses of the differences between surface and bottom water temperature showed that the model correctly reproduced the stratification events observed on the study site, in particular during the spring season. However, during the months of June and July, when the highest water temperatures are reached, the simulated bottom water temperature is slightly overestimated by the model, causing simulated stratification to be somewhat weaker than the observed one. This could be caused by an underestimation of the light extinction dynamically computed by AED2. To test this hypothesis, the simulated light extinction coefficient (K_d) was calculated over the whole simulation period following equation [8]:

$$K_d = K_w + K_{e,DOC}DOC + K_{e,POC}POC + \sum_{i}^{N_{PHY}} K_{e,i}PHY_{C,i}$$

where K_w is the base light extinction coefficient associated with water, and $K_{e,DOC}$, $K_{e,POC}$ and K_{e_i} represent respectively the specific light extinction coefficient for dissolved organic carbon, particulate organic carbon and for the phytoplankton group i, whose values were known parameters of the model. The concentration of POC, DOC and phytoplankton (PHY_{Ci}) were known as output of the model simulation. Eventually, the light extinction coefficient could be converted into its corresponding simulated Secchi depth S through the Poole and Atkins equation ($S=1.7/K_d$, [15]).

The simulated and measured Secchi depth at site B are shown in figure 2f. The simulated values match closely with the observations, with only four main exceptions (namely in the months of April, June and October). Ultimately, therefore, the slight underestimation of summer thermal stratification found in model results could be partly linked with some simplifications made in the model configuration, such as the constant water level or the absence of exchanges with groundwater. Furthermore, an excess of numerical diffusion might also be introduced by the computational schemes of the hydrodynamic model and could have an impact on model results in terms of thermal stratification, especially on such a shallow water body.

E. Biogeochemical model

The calibration of the model was done by trial and error, comparing its results with high-frequency observations of total chlorophyll, cyanobacteria, dissolved oxygen and nitrate concentration. The analysis of such observations data set, represented through the dotted grey lines in figure 3, shows the presence of a first strong peak of phytoplankton biomass around the beginning of March that surpasses 100 μg l^{-1} of total chlorophyll concentration. It constitutes the strongest bloom of the simulated period and completely consumes the stock of nitrate present in the water column, influencing the subsequent availability of nutrients (and nitrate in particular) to sustain phytoplankton growth during the remaining growing season.

Model results are also shown in figure 3 (coloured solid lines), in terms of total chlorophyll (panel a), cyanobacteria (panel b), dissolved oxygen (panel c) and nitrate concentration (panel d). In terms of total chlorophyll (Fig. 2a), the model reproduces correctly the overall behaviour recorded by the high-frequency sensor. The first algal bloom is correctly simulated, both in terms of timing and intensity. Following, the model correctly reproduces the decrease of phytoplankton biomass, as well as the span and overall concentration magnitude of the phytoplankton during the summer months. Eventually, the end of the growing season is also well captured by the model around the end of October.

The year 2019 was not characterized by particularly strong cyanobacterial blooms. As shown by Fig. 3b, their maximal concentration reaches roughly 40 μg Chl l^{-1} in four separate occasions: once during the late winter bloom, and the remaining times during sudden growth peaks between the end of August and the beginning of October. However, in the present configuration, the group representing cyanobacteria is adapted to warm water temperatures (i.e. optimum temperature of 28°C), and is therefore not capable to reproduce their winter growth. In this configuration in fact, winter growth completely deputed to the diatoms group, which are here parameterized with the lowest optimum temperature (i.e. 9°C). Similarly to what was discussed for total chlorophyll, during Summer the model manages to correctly simulate the span of the growing season for the group of cyanobacteria, as well as their overall concentration magnitude. However, the model fails to reproduce the succession of short term peaks detected by the high-frequency observations.

The dynamics of dissolved oxygen simulated by the model fits very closely that recorded by the high-frequency measurements. Figure 3c shows that the model overestimates slightly the concentration of dissolved oxygen, in particular during the colder months of the simulation: during the strong late winter phytoplankton bloom, as well as during the month of October. In the remaining months of simulation dissolved oxygen concentration is correctly reproduced.

Figure 3d shows the comparison between high-frequency observations and model results at site B in terms of nitrate concentration. The model correctly reproduces the observed nitrate dynamics before and during the late-winter algal bloom. The initial increase in nitrate concentration is modelled here solely through the processes of mineralization of organic matter and nitrification of ammonium. The rapid consumption of all the available nitrate during the late winter algal bloom is also correctly simulated.

Right after the late-winter bloom, during the months of April and May, the phytoplankton observations are very low and correspond to an increase in the observed nitrate concentrations. The nitrate accumulated in the water column during this period is then quickly consumed at the beginning of the second blooming period around the month of June. The lake appears to be nitrogen limited from this point until the end of the growing season. These dynamics are not fully reproduced by the model. At the end of the late-winter bloom the simulated phytoplankton concentration is higher than the observed one, causing, in the model, a stronger consumption of nitrate by the phytoplankton, and ultimately delaying the simulated accumulation of nitrate. Such accumulation of nitrate is necessary to the model in order to sustain phytoplankton growth during the subsequent summer and autumn months. Eventually, at the end of the growing season, in the last portion of the simulation around the end of October, a strong increase of nitrate concentration is recorded in the study site. The model also simulates an increase of nitrate concentration during the month of October, but with a considerably lower rate. In the present model configuration, no external input of nutrients are present, and such nitrate increase is obtained solely through the processes of organic matter mineralization and nitrification. The underestimation of nitrate increase by the model suggests the existence of nitrogen sources into the ecosystem that are not taken into account in the present configuration.

IV. DISCUSSION

In this work, the coupled models TELEMAC3D and AED2 were implemented on Lake Champs-sur-Marne, and were used to simulate the biogeochemical cycle in the study site during the complete phytoplankton growth season recorded in the year 2019, i.e. from February to October.

In their own fields of application, the two models are both well-established tools that, separately, have been employed in various contexts (e.g., for TELEMAC3D: [16]–[18], and [14], [19], [20] for AED2). The coupling of the two models introduces the possibility of modelling the biogeochemical cycle directly through the TELEMAC modelling system. In this work, it was possible to test the behaviour of the coupled models in a natural lake ecosystem and the use of high-frequency observations allowed to evaluate the performance of the models continuously over the simulation period.

During the seasonal simulation of 2019, the coupled models reproduced well the overall water temperature dynamics at all three layers. The underestimation of water temperature found at the end of the simulation for the month of October, as well as the slight overestimation of summer water temperature, could be linked with some of the simplifications introduced in the present configuration, such as a constant water level and the absence of exchanges with groundwater. The latter in particular could somewhat

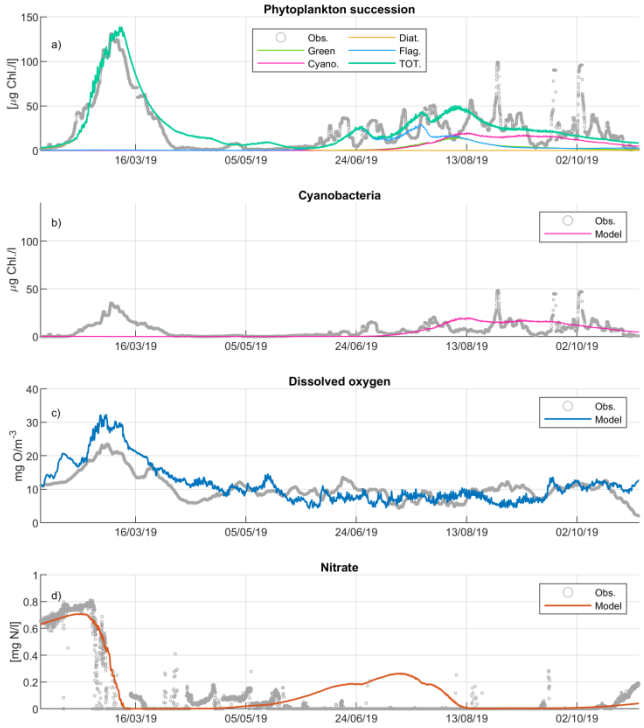

Figure 3: Model results and high-frequency observations in terms of: total chlorophyll (panel a), cyanobacteria concentration (panel b), dissolved oxygen concentration (panel c), and nitrate concentration (panel d). Coloured lines represent model results and grey dotted lines the observation series; all figures are referred to site B.

moderate the seasonal variations of water temperature in the real system. Despite some differences with the measured water temperature series, the overall RMSE values between model and observations were lower than 1.2°C. Similar values are usually considered as good model performances in scientific literature (e.g. [11], [21], [22]). Furthermore, starting in particular from the month of October until the end of January, very low phytoplankton biomass is usually detected on the study site. In this respect, the bias found for water temperature during early autumn should have a reduced impact on the outcomes of the coupled biogeochemical model. Water temperature is a key variable for the simulation of the biogeochemical cycle and in particular for phytoplankton growth. Despite some slight biases, water temperature was overall very well simulated by the coupled models over the simulated period.

This study is focused on phytoplankton growth and on cyanobacteria growth in particular, and the modules activated in the configuration of AED2 (see Table 1) reflect this general objective. Furthermore, the availability of an extensive high-frequency data set allowed to test the model thoroughly, against multiple variables that characterize the biogeochemical cycle exhaustively: in terms of total phytoplankton, cyanobacteria and dissolved oxygen concentration, as well as in terms of an important nutrient such as nitrate.

The biogeochemical cycle was correctly reproduced over the eight months of the simulation. Total phytoplankton concentration was analysed here through phytoplankton chlorophyll content. The four algal groups activated in the present configuration (diatoms, flagellates, green algae and cyanobacteria) are typically related to different optimum water temperatures. Among them, diatoms are usually linked with the lowest optimum water temperatures, while cyanobacteria are typically linked with the highest ones [3]. Following this general assumption, they were here parameterized to respond different optimum water temperatures. This choice allowed the model to correctly reproduce the overall magnitude of total chlorophyll concentration over the simulated period.

The observed late winter phytoplankton bloom showed a considerable presence of cyanobacteria. However, due to the parameterization of their optimum water temperature, cyanobacteria growth is inhibited at low water temperatures. This shows the need to introduce various *genera* of the same algal group with different parameterizations, in order to mimic the complexity of a natural ecosystem.

Also the remaining variables recorded *in situ* (i.e. dissolved oxygen, nitrate, Secchi depth) were well reproduced by the model for 2019. However, some discrepancies were indeed detected when comparing model results to high-frequency observations. Notably, the model did not fully reproduce the sudden peaks of growth and mortlity observed during spring and summer. This could be explained by the absence, in the models configuration, of: (i) nitrogen-fixing cyanobacteria such as *Aphanizomenon*, present on the study site, that should be advantaged under nitrogen-limited conditions, (ii) predation by zooplankton or competition for nutrients and light with other organisms, such as macrophytes, and (iii) by the absence in the model configuration of external nutrient sources, that might locally boost phytoplankton growth over a short period of time. Furthermore, the underestimation of nitrate accumulation during early autumn could be simply originated by an underestimation of the mineralization rate of organic matter implemented in the present configuration.

V. CONCLUSION

In this work, the recent coupling between TELEMAC3D and the biogeochemical library AED2 was tested in a natural ecosystem, Lake Champs-sur-Marne, for which an extensive data set is available. In particular, the availability of high-frequency *in situ* data of variables particularly relevant to the biogeochemical cycle, such as water temperature, dissolved oxygen total chlorophyll, cyanobacteria and nitrate concentrations, allowed to thoroughly test the performance of the coupled models all along the simulation period. In particular, the results show a correct simulation of the light extinction coefficient and highlight the feedback of its dynamic calculation, computed through AED2, on the hydrodynamic model. Furthermore, results show how the mineralization of organic matter can suffice to sustain phytoplankton growth over an annual cycle in the simulation of an ecosystem without direct surface inlets. Through the coupling with AED2, the TELEMAC system is capable of correctly simulating the main features of the biogeochemical cycle and, in particular, phytoplankton growth over a complete growth season.

ACKNOWLEDGEMENT

The authors acknowledge the Base de loisirs du lac de Champs/Marne (CD93) for their logistic support in the field campaigns. The dataset used for model calibration and validation was collected under the OSSCyano (ANR-13-ECOT-0001) and ANSWER (ANR-16-CE32-0009-02) projects. The environmental observatories OSU EFLUVE and OLA contributed to the financial support for equipment maintenance. The first author's PhD grant is funded by Ecole des Ponts ParisTech and the ANSWER project.

REFERENCES

[1] D. M. Anderson, P. M. Glibert, and J. M. Burkholder, "Harmful algal blooms and eutrophication: Nutrient sources, composition, and consequences," *Estuaries*, vol. 25, no. 4, pp. 704–726, Aug. 2002, doi: 10.1007/BF02804901.

[2] J. Heisler *et al.*, "Eutrophication and Harmful Algal Blooms: A Scientific Consensus," *Harmful Algae*, vol. 8, no. 1, pp. 3–13, Dec. 2008, doi: 10.1016/j.hal.2008.08.006.

[3] H. Paerl and T. Otten, "Harmful Cyanobacterial Blooms: Causes, Consequences, and Controls," *Microbial ecology*, vol. 65, Jan. 2013, doi: 10.1007/s00248-012-0159-y.

[4] J. M. O'Neil, T. W. Davis, M. A. Burford, and C. J. Gobler, "The rise of harmful cyanobacteria blooms: The potential roles of eutrophication and climate change," *Harmful Algae*, vol. 14, pp. 313–334, Feb. 2012, doi: 10.1016/j.hal.2011.10.027.

[5] L. Bláha, P. Babica, and B. Maršálek, "Toxins produced in cyanobacterial water blooms – toxicity and risks," *Interdiscip Toxicol*, vol. 2, no. 2, pp. 36–41, Jun. 2009, doi: 10.2478/v10102-009-0006-2.

[6] D. Trolle *et al.*, "A community-based framework for aquatic ecosystem models," *Hydrobiologia*, vol. 683, no. 1, pp. 25–34, Mar. 2012, doi: 10.1007/s10750-011-0957-0.

[7] V. Tran Khac *et al.*, "An Automatic Monitoring System for High-Frequency Measuring and Real-Time Management of Cyanobacterial Blooms in Urban Water Bodies," *Processes*, vol. 6, no. 2, p. 11, Jan. 2018, doi: 10.3390/pr6020011.

[8] M. R. Hipsey, L. C. Bruce, and D. P. Hamilton, "Aquatic Ecodynamics (AED) Model Library. Science Manual.," Oct. 2013, [Online]. Available: http://aed.see.uwa.edu.au/research/models/aed/Download/AED_ScienceManual_v4_draft.pdf

[9] Canadian Hydraulic Centre, *Blue Kenue reference manual*. Ottawa, Ontario, Canada, 2011.

[10] F. Soulignac *et al.*, "Performance Assessment of a 3D Hydrodynamic Model Using High Temporal Resolution Measurements in a Shallow Urban Lake," *Environ Model Assess*, vol. 22, no. 4, pp. 309–322, Aug. 2017, doi: 10.1007/s10666-017-9548-4.

[11] F. Piccioni, C. Casenave, B. J. Lemaire, P. Le Moigne, P. Dubois, and B. Vinçon-Leite, "The thermal response of small and shallow lakes to climate change: new insights from 3D hindcast modelling," *Earth System Dynamics*, vol. 12, no. 2, pp. 439–456, Apr. 2021, doi: 10.5194/esd-12-439-2021.

[12] A. Okubo, "Oceanic diffusion diagrams," *Deep Sea Research and Oceanographic Abstracts*, vol. 18, no. 8, pp. 789–802, Aug. 1971, doi: 10.1016/0011-7471(71)90046-5.

[13] G. Gal, M. Hipsey, A. Parparov, U. Wagner, V. Makler, and T. Zohary, "Implementation of ecological modeling as an effective management and investigation tool: Lake Kinneret as a case study," *Ecological Modelling*, vol. 220, pp. 1697–1718, Jun. 2009, doi: 10.1016/j.ecolmodel.2009.04.010.

[14] A. Fenocchi, M. Rogora, G. Morabito, A. Marchetto, S. Sibilla, and C. Dresti, "Applicability of a one-dimensional coupled ecological-hydrodynamic numerical model to future projections in a very deep large lake (Lake Maggiore, Northern Italy/Southern Switzerland)," *Ecological Modelling*, vol. 392, pp. 38–51, Jan. 2019, doi: 10.1016/j.ecolmodel.2018.11.005.

[15] H. H. Poole and W. R. G. Atkins, "Photo-electric Measurements of Submarine Illumination throughout the Year," *Journal of the Marine Biological Association of the United Kingdom*, vol. 16, no. 1, pp. 297–324, May 1929, doi: 10.1017/S0025315400029829.

[16] C. Villaret, J.-M. Hervouet, R. Kopmann, U. Merkel, and A. G. Davies, "Morphodynamic modeling using the Telemac finite-element system," *Computers & Geosciences*, vol. 53, pp. 105–113, Apr. 2013, doi: 10.1016/j.cageo.2011.10.004.

[17] J. Feng and M. Jodeau, "Three-dimensional numerical modeling of sediment transport with TELEMAC-3D: validation of test cases," p. 9, 2016.

[18] U. H. Merkel, "Thermal Stratification in Small Lakes with TELEMAC-3D: Showcase 'Lake Monsterloch,'" *XXVIth TELEMAC-MASCARET User Conference, 15th to 17th October 2019, Toulouse*, 2019, doi: 10.5281/zenodo.3611576.

[19] L. Zhang, M. R. Hipsey, G. X. Zhang, B. Busch, and H. Y. Li, "Simulation of multiple water sources ecological replenishment for Chagan Lake based on coupled hydrodynamic and water quality models," *Water Science and Technology: Water Supply*, p. ws2017079, May 2017, doi: 10.2166/ws.2017.079.

[20] A. I. Krinos, K. J. Farrell, V. Daneshmand, K. C. Subratie, R. J. Figueiredo, and C. C. Carey, "Including variability in air temperature warming scenarios in a lake simulation model highlights uncertainty in predictions of cyanobacteria," *bioRxiv*, p. 734285, Aug. 2019, doi: 10.1101/734285.

[21] M. R. Magee and C. H. Wu, "Response of water temperatures and stratification to changing climate in three lakes with different morphometry," *Hydrology and Earth System Sciences*, vol. 21, no. 12, pp. 6253–6274, 2017, doi: 10.5194/hess-21-6253-2017.

[22] S. Moras, A. I. Ayala, and D. C. Pierson, "Historical modelling of changes in Lake Erken thermal conditions," *Hydrology and Earth System Sciences*, vol. 23, no. 12, pp. 5001–5016, Dec. 2019, doi: https://doi.org/10.5194/hess-23-5001-2019.

Hydrodynamic modelling for early warning of sanitary risks in open swimming waters

Natalia Angelotti *(1)*, Brigitte Vinçon-Leite *(1)*
(1) LEESU
Ecole des Ponts ParisTech, UPEC
Champs-sur-Marne, France
natalia.angelotti-de-ponte-rodrigues@enpc.fr

Rémi Carmigniani *(2)*
(2): LHSV
ENPC, Cerema, EDF R&D
Chatou, France

***Abstract*— Swimming in open water involves sanitary risks related to the presence of pathogenic microorganisms. To ensure the safety of bathers, a regulatory monitoring in the bathing area, based on faecal indicator bacteria (FIB), is required. Analysis of FIB concentrations can take more than 10 hours with *in situ* devices and more than 24 hours in the laboratory. Hence monitoring and forecasting of the sanitary conditions in urban bathing sites are essential for decision-making on their possible closure and its duration.**

In this paper, TELEMAC-3D hydrodynamic model was used to compute the time and space distribution of water temperature, velocity and contaminant tracers considering hydro-meteorological conditions that can cause noticeable changes on the transfer time of the contaminant to the bathing area.

The study site, La Villette, is an urban canal-basin system with a bathing area, located in Paris. The objectives focus on (i) how thermal stratification affects the transfer time of upstream contamination to the bathing area; (ii) the use of conductivity to track water quality changes after a storm event and (iii) the simulation of conductivity variation.

I. INTRODUCTION

In urban areas, swimming in open water has been increasingly popular, especially in large European cities. However, the bathers can be exposed to infectious diseases caused by pathogens from faecal contamination. To avoid this, the European regulation (bathing water directive 2006/7/EC [1]) requires the implementation of a sanitary control. The regulatory indicators of pathogenic microorganisms are faecal indicator bacteria (FIB). They include *Escherichia coli* (*E. coli*), a coliform bacteria whose concentration analysis can take more than 10 hours with *in situ* devices ([2], [3]) and more than 24 hours in the laboratory [4].

To anticipate possible sanitary risks, the microbiological monitoring can be performed upstream of the bathing area. Considering the transfer time from the measuring point to the bathing area and the delay to obtain the analysis results, the information about the water quality in the bathing area can be available in due time. In addition, a hydrodynamic model can be used for computing the transfer time between the sampling point and the bathing area.

Hydro-meteorological conditions may impact the transfer time, such as flowrate variations and thermal stratification. Vertical thermal stratification causes differences in the flow velocity with depth. Therefore, the arrival time and the duration of the contamination can vary with depth in the bathing area.

On the other hand, an indicator related to faecal contamination and available in real-time would also be very beneficial for decision making about a possible closure or re-opening of the bathing area. After heavy rainfall episodes, due to stormwater network discharge and runoff on contaminated surface and, faecal contamination is observed in urban water bodies. Conductivity is one of the variables that shows good correlation with stormwater discharge, and is possibly able to track faecal contamination ([5]–[7]).

We addressed these issues in the study site of La Villette in Paris. As part of the Paris-Plage summer program, a bathing area has been open in La Villette basin since 2017. Very appreciated by the public, it received around 70 000 bathers in July-August 2019 [8].

The first objective of the study was to investigate how the thermal stratification modifies the transfer time of a microbiological contamination originated from upstream. The first results presented here relate to the contaminant transport during a hot weather episode. Then, after confirming that continuous monitoring of conductivity, upstream and in the bathing area, could track the water quality changes after a heavy rainfall episode, the second objective was to simulate the conductivity variation from upstream to the bathing area. We used the TELEMAC-3D hydrodynamic model to compute the time and space distribution of water temperature, velocity, and contamination tracer. Time series of conductivity were measured with *in situ* sensors installed upstream and at the bathing area.

II. STUDY SITE AND FIELD DATA

The study site, La Villette, is located in the north-east of Paris. It is an urban water body with recreational activities such as boat navigation and the opening of a free bathing area during summer.

The upstream part of La Villette system corresponds to a canal of 25 m wide and 800 m long. Then, it widens to 75 m wide, forming a basin of 700 m long, where the bathing area is located (Fig. 1) [9]. The whole system has a total extension of 1500 m and approximately 3 m of depth. The average annual water flow is 2.7 m^3/s.

At the outlet of the system, a navigation lock towards the St-Martin canal works from 09h00 to 19h00. Additionally, a

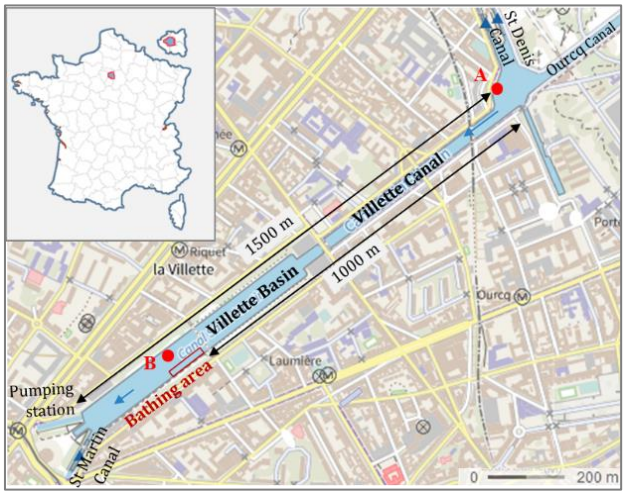

Figure 1: Location of La Villette system and the measurement points A and B (red dots)

water pumping station derives part of the volume to Paris non-drinkable water network.

The monitoring system has two points of measurements. Point A is located at the inlet of the canal, 1000 m upstream of the bathing area. Point B is located downstream, next to the bathing area, at the right bank of the basin (Fig. 1). Both points are equipped with sensors of water temperature and conductivity measured at a 10 min time step. Water temperature has been measured at three depths (0.5 m, 1.2 m, 2.0 m) and conductivity at 1.2 m depth.

III. NUMERICAL MODEL

The numerical simulations were done with TELEMAC-3D (version 8.0). The atmosphere-water heat exchanges were done with the WAQTEL module, where the thermal process was activated. The data pre-processing was carried out with BlueKenue 64 v3.3.4 and the post-processing with MATLAB R2020b.

A. *Modelling domain*

The model domain goes from the canal round-about at upstream to the end of the basin area at downstream. A triangulated mesh (Fig. 2) was created using the data of a bathymetry survey at 6 section profiles [10].

The 3D grid has a total of 10 layers, with approximately 0.30 m of depth. Each layer has 3185 nodes and 5680 elements. The average edge length is of approximately five meters.

The simulation results of layers 2 (bottom), 5 (middle), and 8 (surface) are compared with the field data at 2.0 m, 1.2 m, and 0.5 m, respectively.

B. *Hydrodynamic model*

The simulated variables are the free surface elevation, water temperature, water velocity and an indicator of microbiological quality. In alignment with the European regulation, the faecal indicator bacteria "coliforms" was selected. Water temperature was considered as an active tracer and microbiological indicator as a passive tracer [11].

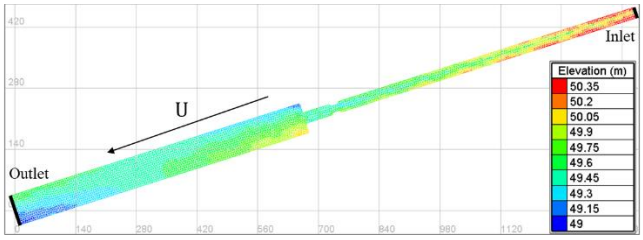

Figure 2: Mesh of the bottom layer of La Villette system

The model was set-up to consider the heat exchange between the atmosphere and the water, through the WAQTEL module.

The water density was expressed as a function of water temperature (1).

$$\rho = \rho_{ref}\left[1 - T\left(T - T_{ref}\right)^2 10^{-6}\right] \quad (1)$$

Where ρ is water density [kg/m³], ρ_{ref} is the reference density (999.972 kg/m³) at the reference water temperature T_{ref} = 4 °C, and T is the water temperature [°C].

The solar radiation attenuation in the water column is calculated according to the Beer-Lambert equation where the extinction coefficient is derived from the field data of Secchi depth [12].

The Strickler law was used for the bottom friction with the default coefficient of 60 $m^{1/3}/s$. The horizontal turbulence model considers a constant viscosity with a coefficient for diffusion of velocities of 0.1 m^2/s. The adopted vertical turbulence model was the Nezu and Nakagawa mixing length (2). All the parameters have the default values.

$$L_m = \kappa z\sqrt{1 - \frac{z}{h}} \quad (2)$$

Where L_m is the mixing length, κ is the von Kármán constant (0.41), z is the distance to the bed [m] and h is the water depth [m].

The upstream boundary condition is defined as an open boundary with prescribed flowrate and tracer values. The downstream open boundary is defined with prescribed water elevation and free tracer values. The lateral boundaries are defined as a solid wall.

The input data include the flowrate and water temperature at the upstream boundary. For the heat exchange with the atmosphere, meteorological data (wind speed and direction, air temperature, atmospheric pressure, relative humidity, nebulosity, and rainfall) are also required. The meteorological data are obtained from the Orly Météo-France station. The input upstream water temperature and conductivity are measured at point A. The flowrates are calculated from the total daily volumes provided by the Service des Canaux de la Ville de Paris.

The time-step of the model computation is of 20 s. The results are given in time-step of 10 min.

C. *Simulation periods*

Two periods were simulated. The first one in August 2020 corresponds to a high temperature episode, to analyse the thermal stratification impact on the distribution of velocity and of the microbiological indicator, "coliforms". The latest was considered as a passive tracer in order to disentangle the effect of the water column stratification from any other biogeochemical process.

The second period, in June 2021, includes a heavy rainfall episode. On this period, the conductivity evolution, which is assumed to be a proxy of the water quality change due to the rainfall event, was simulated.

IV. RESULTS AND DISCUSSION

A. *Simulation from the 7th to the 12th of August 2020: hot weather period*

The first simulated period is from 07/08/2020 to 12/08/2020 (5 days). In addition to water temperature and velocity, the variable "coliforms" was simulated as a passive tracer. It was prescribed as a step input of 1000 MPN/100mL (MPN, Most Probable Number per 100 mL), uniformly distributed in the inlet water column. It lasts for 48 hours, from 08/08/2020 to 10/08/2020. Generally, in the equation of coliforms evolution, the bacterial decrease is represented by an exponential term using a decay rate, which depends on water temperature, light intensity, and salinity [13-15]. Here, in order to assess the single effect of thermal stratification, the decay rate was set to 0. The Secchi depth is 0.9 m.

The water column is stratified during the day and mixes at night (Fig. 3). The simulated and the field data of water temperatures range from 22.8 to 26.3°C.

The simulated temperatures are close to the measured data (RMSE=0.36°C at the surface, 0.35°C at the middle and 0.41°C at the bottom). A good agreement is obtained between field data and model results: $R^2 = 0.84$ at the surface, $R^2 = 0.83$ at the middle and R^2=0.77 at the bottom. The maximum differences between the results and the field data are of 0.84°C at the sub-surface, 0.87°C at the middle, and 1.08°C at the bottom.

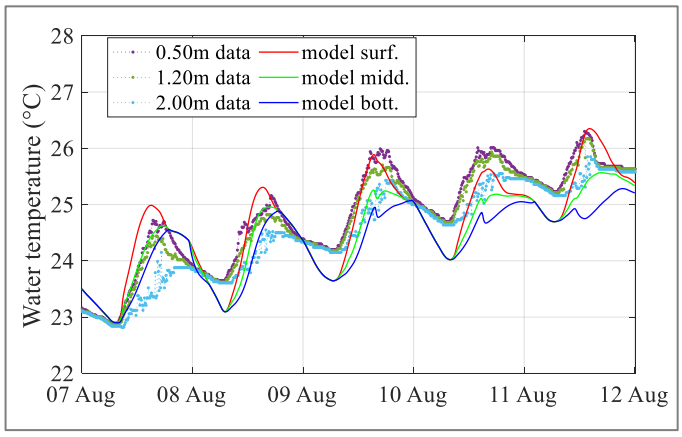

Figure 3: Measured and simulated water temperature at three depths at point B, from 07 to 12/08/2020.

The model slightly underestimates the field data by 0.6% at surface, 1% at the middle and 0.8% at the bottom.

The maximum temperature difference between the surface and bottom layers (ΔTw) can be considered as an indicator of the stratification intensity. It ranges from 0.85°C to 1.35°C for the field data and from 0.95°C to 1.6°C for the simulation results (Fig. 4). The stratification starts at the same time for both field data and model results. However, on the first three days of simulation, the mixing of the water column in the night occurs earlier in the model, 4.5 h to 7 h before the measured data.

The longitudinal current velocity (U-axis, positive towards downstream) and the coliforms concentration at point B, in the surface, middle and bottom layers are presented on Fig. 5.

At the surface, the longitudinal velocities vary from -0.03 m/s to 0.05 m/s. At the bottom, they vary from -0.03 m/s to 0.03 m/s. The velocity range of the middle layer is from 0 to 0.02 m/s, with a mean of 0.01 m/s.

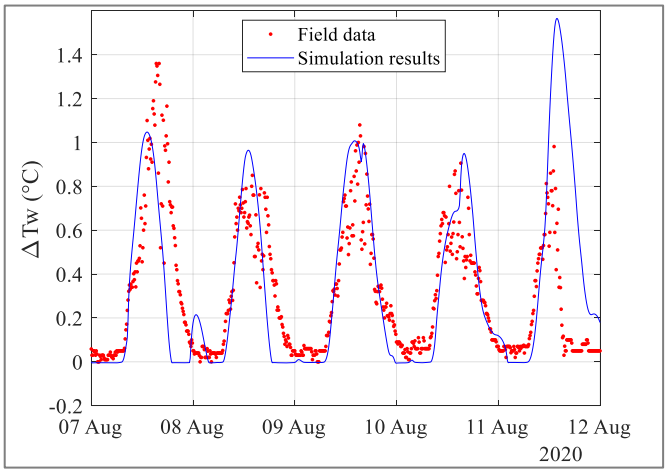

Figure 4: Difference between surface and bottom temperatures, ΔTw (field data: red, simulation results: blue), at point B, from 07 to 12/08/2020.

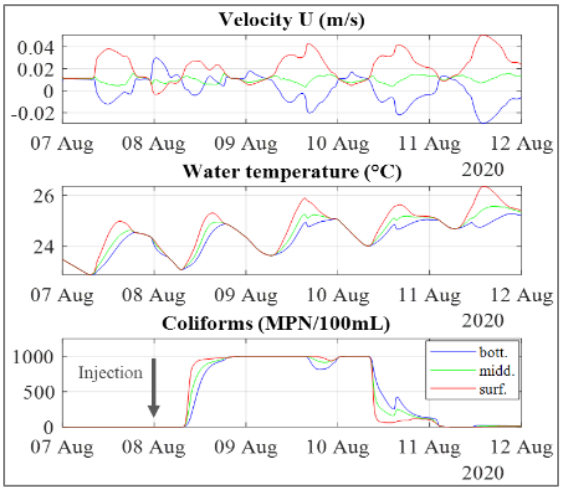

Figure 5: Simulation results of longitudinal velocity (U-axis), water temperature and coliforms concentration at point B, from 07 to 12/08/2020.

The difference between the surface and the bottom velocities is the largest when the water column is stratified, reaching up to 0.08 m/s. A return flow is then observed in the bottom layer. The difference in flow direction between the surface and the bottom layers is due to the thermal stratification on the water column, leading to vertical density gradient. In the case of constant density fluid simulations, these negative velocities at the bottom are not observed.

The arrival time of the coliforms at point B is different at the three depths. The maximum concentration is first reached in the surface layer. The transfer time in the surface layer is 13.3h, in the middle layer is 15.5 h, and at the bottom is 18.7 h.

The decrease of coliforms concentration starts on 10/08/2020 around 08:00 for the three depths. However, the decrease is faster in the surface layer. After 2 h, the surface concentration is around 130 MPN/100mL, and the bottom coliforms is 660 MPN/100mL.The bottom layer takes almost 15h to reach a concentration around 130 MPN/100mL.

B. *Simulation from the 1st to the 10th of June 2021: heavy rainfall event*

The second simulated period goes from 01/06/2021 to 10/06/2021 (9 days). A rainfall of more than 20 mm in one hour took place on 04/06/2021 at 08h00. Conductivity, considered as an indicator of the water quality, was simulated as a passive tracer. For this period, the Secchi depth is 1.5 m.

The field water temperature ranges from 18.2°C to 22.0°C (Fig. 6). The simulation results range from 18.1°C and 20.9°C. The performance indicators (RMSE and R^2) indicate a good agreement between field data and model results: at the surface $R^2 = 0.76$ and RMSE = 0.32°C, at the middle $R^2 = 0.73$ and RMSE = 0.33°C, at the bottom $R^2 = 0.75$ and RMSE = 0.30°C.

The model slightly underestimates the measured temperature, having a maximum difference of around 1.3 °C. The underestimation is of 2.2 % at the sub-surface, 2.8% at the middle, and 2.3% the bottom.

During the simulated period, the water column was stratified during the day and mixed at night. However, after the rainfall event, the water temperature decreased, and the water column remained mixed for the entire day of 05/08/2021.

The stratification decreased during the first four days of the simulation, disappears on 5 June, and occurs again on the four last days (Fig. 7). The model correctly reproduces the mixing on 5 June and the increase of stratification during the last days of the simulation.

The simulation results of longitudinal current velocity (U), water temperature and conductivity in the surface, middle and bottom layers at point B are presented on Fig. 8. The velocities range from -0.03 m/s to 0.04 m/s. The surface layer has the higher velocities. As on the previous simulated period, the velocity is negative in the bottom layer.

At the beginning of the simulated period, the conductivity is uniform in the water column. Following the rainfall event, a continuous decrease of the conductivity was observed upstream (Fig. 9). It dropped from around 790 to 610 µS/cm in 3 days. Afterwards, the conductivity increased continuously for also 3 days.

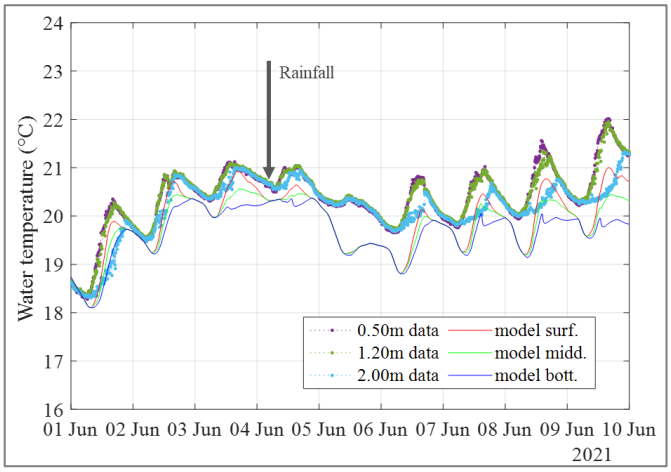

Figure 6: Water temperature at three depths from the simulation results and measured at point B.

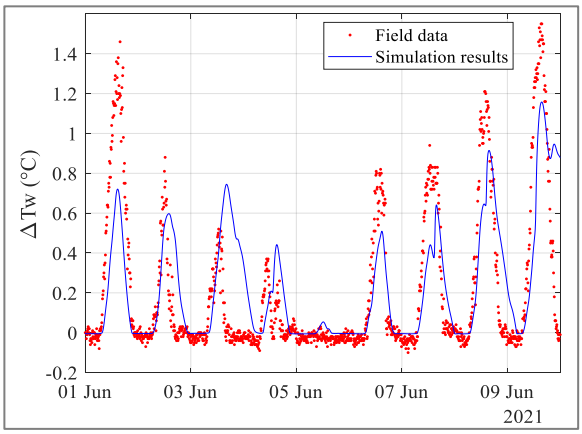

Figure 7: Difference between surface and bottom temperatures, ΔTw (field data: red, simulation results: blue), at point B from the 01 to 10/06/2020.

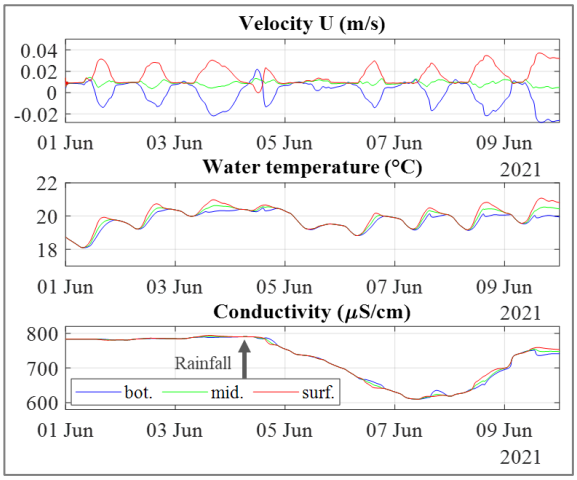

Figure 8: Simulation results of longitudinal velocity (U-axis), water temperature and conductivity, at point B from 01 to 10/06/2021.

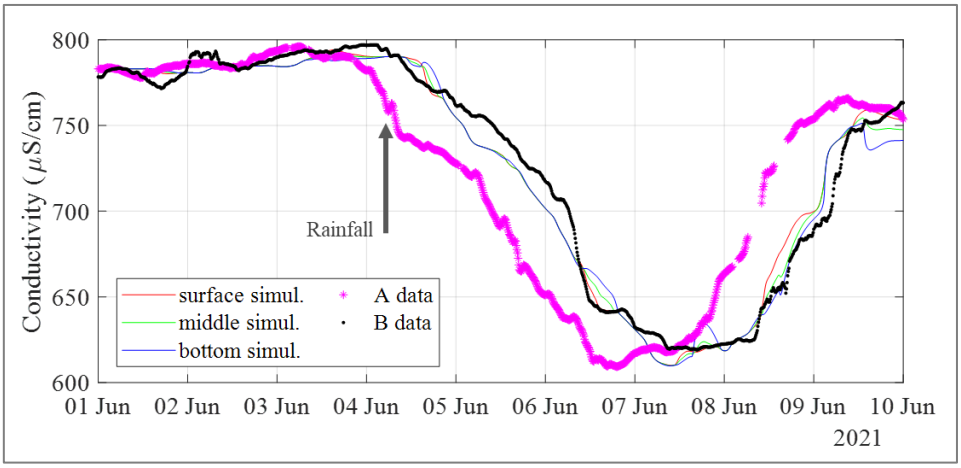

Figure 9: Conductivity measurements at points A (*) and B (·) and simulation results for three depths at point B, from 01 to 10/06/2021.

The conductivity variation observed downstream was well reproduced (Fig. 9). The simulation results and the measured conductivity show a good agreement, $R^2 = 0.98$ and RMSE = 9.0 µS/cm.

On 04/06/2021, a value of around 790 µS/cm is observed at both points (A and B). The minimum value of 610 µS/cm is observed upstream (point A) on 06/06/2021, at 19:10. Downstream, at point B, this minimum value is observed on 07/06/2021, at 11:50 and at 9:50 through the model results.

The transfer time between points A and B (1000 m) can be estimated using the time-lag between the same conductivity values at both points.

The transfer time and the mean velocity according to the simulation results and to the field data are presented in Tab. 1. The values estimated from the model results are close to the field data. The model anticipates by a few hours the arrival of the upstream water.

TABLE 1 TRANSFER TIME AND MEAN VELOCITY ESTIMATION AT MID-DEPTH (1.20 M)

Conductivity	**Date (2021)**			**Transfer time (hh:mm)**		**Mean velocity (cm/s)**	
	Point A	***Point B***	***Simul. result***	***Simul.***	***Field data***	***Simul.***	***Field data***
750 µS/cm	04/06 08:00	05/06 10:00	05/06 01:50	17:50	26:00	1.6	1.1
700 µS/cm	05/06 09:40	06/06 06:20	06/06 00:40	15:00	20:40	1.9	1.3
650 µS/cm	06/06 01:30	06/06 11:30	06/06 15:10	13:40	10:00	2.0	2.8
610 µS/cm	06/06 11:40	07/06 08:40	07/06 03:30	15:50	21:00	1.8	1.3

V. CONCLUSIONS AND PERSPECTIVES

TELEMAC-3D has been applied for microbiological modelling in some studies (*e.g.* [13], [14]) but generally in coastal study sites where the thermal stratification is negligible.

In this study, TELEMAC-3D hydrodynamic model was used to compute the time and space distributions of microbiological contaminant indicators in a thermally stratified water body.

The thermal stratification of the water column during the day was correctly captured by the model as well as the overnight mixing. In particular, the temperature difference between the surface and the bottom of the water column was well reproduced.

During the periods of thermal stratification, the longitudinal velocity is the surface layer is faster. This affects the transfer time of the tracers, depending on the depth.

Regarding the simulated period of June 2021, when a heavy rainfall occurred at the study site and in the upstream catchment, a continuous and strong decrease of the conductivity was observed at upstream and at downstream with a few hour time-lag. This confirms that conductivity can be used to track the water quality changes after a heavy rainfall episode. The simulation results with the conductivity as a passive tracer showed a good agreement with the field data.

In conclusion, the thermal stratification observed in the field data during hot weather periods could be correctly simulated by TELEMAC-3D. It can be used to assess the transfer time of a microbiological contamination measured upstream to the bathing area of La Villette. The model was able to correctly simulate the conductivity evolution to track water quality changes after a rainfall episode in the catchment.

ACKNOWLEDGEMENT

This work is part of the OPUR project. We express our gratitude to our colleagues from ENPC/LEESU particularly for the design and implementation of the system: Philippe Dubois and Duong Tang, and for the field campaigns: Mohamed Saad, Amanda Tolentino Mendes, Guilherme Calabro and Francesco Piccioni.

The authors would like to thank Thierry Mareschal, from the Service des Canaux de la Ville de Paris, for his help and availability. We would also like to thank Yael (responsible of Paris base), César (manager of Paris base) and all the crew from Marin d'Eau Douce for their support for the field work.

REFERENCES

[1] EU, 'Directive 2006/7/EC of the European Parliament and of the Council of 15 February 2006 concerning the management of bathing water quality and repealing Directive 76/160/EEC'. Feb. 15, 2006. Accessed: Nov. 16, 2020. [Online]. Available: https://eur-lex.europa.eu/legal-content/GA/TXT/?uri=CELEX:32006L0007

[2] S. Guérin-Rechdaoui *et al.*, 'Mesure de la qualité microbiologique des eaux de surface par le Système ALERT de fluidion. Présentation des essais laboratoire sur la matrice "eau de Seine"', *EIN*, no. 399, pp. 89–95, 2017.

[3] D. E. Angelescu *et al.*, 'Autonomous system for rapid field quantification of Escherichia coli in surface waters', *J. Appl. Microbiol.*, vol. 126, no. 1, pp. 332–343, Jan. 2019, doi: 10.1111/jam.14066.

[4] A. Tiwari, S. I. Niemelä, A. Vepsäläinen, J. Rapala, S. Kalso, and T. Pitkänen, 'Comparison of Colilert-18 with miniaturised most probable number method for monitoring of Escherichia coli in bathing water', *Journal of Water and Health*, vol. 14, no. 1, pp. 121–131, Feb. 2016, doi: 10.2166/wh.2015.071.

[5] S. Frank, N. Goeppert, and N. Goldscheider, 'Fluorescence-based multi-parameter approach to characterize dynamics of organic carbon, faecal bacteria and particles at alpine karst springs', *Science of The Total Environment*, vol. 615, pp. 1446–1459, Feb. 2018, doi: 10.1016/j.scitotenv.2017.09.095.

[6] D. E. Nnane, J. E. Ebdon, and H. D. Taylor, 'Integrated analysis of water quality parameters for cost-effective faecal pollution management in river catchments', *Water Research*, vol. 45, no. 6, pp. 2235–2246, Mar. 2011, doi: 10.1016/j.watres.2011.01.018.

[7] M. Seo, H. Lee, and Y. Kim, 'Relationship between Coliform Bacteria and Water Quality Factors at Weir Stations in the Nakdong River, South Korea', *Water*, vol. 11, no. 6, p. 1171, Jun. 2019, doi: 10.3390/w11061171.

[8] Seine-Saint-Denis Tourisme, 'Bilan d'activité 2019 et perspectives d'action pour 2020', Agence de développement touristique, 2019. Accessed: Mar. 12, 2021. [Online]. Available: https://ressources.seinesaintdenis.fr/IMG/pdf/2._bilan_activites_organismes_exterieurs_2019_-_annexe_partie2.pdf

[9] SAFEGE, 'Elaboration d'un profil de baignade pour une baignade publique sur le bassin de la Villette à Paris. Rapport de phase 1: Etats des lieux'. Mairie de Paris-Suez, 2017.

[10] F. Bezerra *et al.*, 'Open-water swimming in urban areas: How a three-dimensional hydrodynamic model can help in the microbiological contamination monitoring?', presented at the Novatech Urban Water - Planning and technologies for sustainable management Novatech, Lyon, 2019. [Online]. Available: http://www.novatech.graie.org/documents/auteurs/2B4P-273VIN.pdf

[11] EDF R&D and Telemac3d consortium, *TELEMAC-3D User Manual, Version 8.0*. TELEMAC-MASCARET, 2018.

[12] S. B. Idso and R. G. Gilbert, 'On the Universality of the Poole and Atkins Secchi Disk-Light Extinction Equation', *Journal of Applied Ecology*, vol. 11, no. 1, pp. 399–401, 1974, doi: 10.2307/2402029.

[13] J. King, R. Ahmadian, and R. A. Falconer, 'Hydro-epidemiological modelling of bacterial transport and decay in nearshore coastal waters', *Water Research*, vol. 196, p. 117049, May 2021, doi: 10.1016/j.watres.2021.117049.

[14] J. Dugor, J. Baills, and D. Rihouey, 'Numerical modelling of bacteriologic impacts in the Laïta estuary (France)', presented at the Telemac User Conference 2019 (TUC2019), Toulouse, Jan. 17, 2020. doi: 10.5281/zenodo.3611538.

[15] L. Selméus, 'Dynamic modelling of bathing water quality with biodegradation of Escherichia coli in TELEMAC-3D', Lund University, 2018.

International Marine and Dredging Consultants (IMDC)
Van Immerseelstraat 66
2018 Antwerp
Belgium
tuc2020@imdc.be
https://tuc2020.org/

ISBN 9789464447842